

Molecular Sieves—II

James R. Katzer, EDITOR
University of Delaware

The Fourth International
Conference co-sponsored by
the Divisions of Colloid and
Surface Chemistry,
Petroleum Chemistry, and
Physical Chemistry of the
American Chemical Society
and by the University of
Chicago at the University
of Chicago, Chicago, Ill.,
April 18–22, 1977

A C S S Y M P O S I U M S E R I E S

40

AMERICAN CHEMICAL SOCIETY
WASHINGTON, D. C. 1977



Library of Congress CIP Data

International Conference on Molecular Sieves, 4th, University of Chicago, 1977.

Molecular sieves II.

(ACS symposium series; 40 ISSN 0097-6156)

Papers of the 4th of a series of meetings; papers of the 3rd are entered under the title: Molecular sieves.

Bibliography: p. Includes index.

1. Zeolites—Congresses. 2. Molecular sieves—Congresses.

I. Katzer, James R., 1941- . II. American Chemical Society. Division of Colloid and Surface Chemistry. III. Title. IV. Series: American Chemical Society. ACS symposium series; 40.

TP245.S5159

661'.06'8324

77-720

ISBN 0-8412-0362-8

ACSMC 8

40 1-732

Copyright © 1977

American Chemical Society

All Rights Reserved. No part of this book may be reproduced or transmitted in any form or by any means—graphic, electronic, including photocopying, recording, taping, or information storage and retrieval systems—without written permission from the American Chemical Society.

PRINTED IN THE UNITED STATES OF AMERICA

**American Chemical
Society Library
1155 16th St. N. W.**

Washington, D. C. 20036

ACS Symposium Series; American Chemical Society: Washington, DC, 1977.

ACS Symposium Series

Robert F. Gould, *Editor*

Advisory Board

Donald G. Crosby

Jeremiah P. Freeman

E. Desmond Goddard

Robert A. Hofstader

John L. Margrave

Nina I. McClelland

John B. Pfeiffer

Joseph V. Rodricks

Alan C. Sartorelli

Raymond B. Seymour

Roy L. Whistler

Aaron Wold

FOREWORD

The ACS SYMPOSIUM SERIES was founded in 1974 to provide a medium for publishing symposia quickly in book form. The format of the SERIES parallels that of the continuing ADVANCES IN CHEMISTRY SERIES except that in order to save time the papers are not typeset but are reproduced as they are submitted by the authors in camera-ready form. As a further means of saving time, the papers are not edited or reviewed except by the symposium chairman, who becomes editor of the book. Papers published in the ACS SYMPOSIUM SERIES are original contributions not published elsewhere in whole or major part and include reports of research as well as reviews since symposia may embrace both types of presentation.

PREFACE

With the discovery of the catalytic properties of zeolites in the late 1950s, the level of research activity into zeolite synthesis, structure, and properties changed from one of slow continual progress to intense pursuit. This led to three International Conferences on Molecular Sieves. The first in London in 1967 was in recognition of the pioneering work of R. M. Barrer, the second was at Worcester Polytechnic Institute in 1970, and the third was in Zurich, Switzerland in 1973. About 300 scientists and engineers from many countries and with a broad range of backgrounds attended the sessions. These meetings attempted to cover the scope of molecular sieve science including mineralogy, structure, synthesis, modification, adsorption, diffusion, catalytic properties, and technological applications. This intermingling of disciplines has been a critically important benefit of previous conferences and of the resulting proceedings.

This volume of the ACS Symposium Series contains the program papers of the Fourth International Conference on Molecular Sieves held at the University of Chicago in April 1977. It includes papers on all the aspects of molecular sieve science that were covered at the last three conferences except mineralogy. Due to a Natural Zeolites meeting held in Tuscon, Arizona in June 1976, no mineralogy papers were submitted to this conference. It is unfortunate that this separation has occurred, and a reuniting of these two areas would benefit the entire field of zeolite science.

The program papers have been categorized into the topical sections: Structure, Synthesis and Modification, Adsorption and Diffusion, Catalysis, and Technology. Such categorization was at times subjective because many papers overlapped several topical areas. For example, papers concerning the structure and electronic properties of transition metal complexes in zeolites relate to the structural (location) properties (albeit not framework structure) of zeolites, involve modification, and are of vital interest to the catalytic properties. Similarly papers that characterize metals, partially or completely reduced, are not truly catalytic and were typically included as a modification.

A review paper by M. M. Dubinin is presented first. Reviews on theoretical calculation of zeolite structure (Gibbs et al.), ion exchange (Cremers), adsorption (Schirmer et al.), transition metal complexes in zeolites (Lunsford), the acid catalytic properties of zeolites (Bartho-

meuf), adsorption applications (Anderson), and catalytic cracking technology (Magee) open each topical section.

Our knowledge of zeolite properties and the emphasis in zeolite research has changed markedly over the last two decades as illustrated by the papers in this volume and those of the previous three conferences. Classical framework structural papers are no longer present as they were appropriate when the field was new and growing. They have been succeeded by papers concerned with the locations and electronic properties of cations in the cages and detailed structural information on the location and properties of transition metal complexes in zeolites. The physical-chemical approach of investigating zeolite properties is being replaced by application of sensitive electronic (X-ray emission, XPS), nuclear (NMR, Szilard-Chalmers cation recoil), and other probes (Raman, IR, uv). Catalytic chemistry is marked by two trends. Many studies are concerned now with trying to clarify yet unclear chemistry and to quantify previously stated concepts. In the second trend new, different chemistry is being investigated. An example of the latter is the studies of transition metal complexes in zeolites. Catalytic properties remain the least well characterized properties of zeolites and are the topic of the most papers.

Adsorption and catalytic applications papers were encouraged in recognition of the technological impact of zeolites. Because of the proprietary nature of commercial catalysts and catalytic processing, few papers were obtained in this area.

Thanks are due to the organizing committee which consisted of J. V. Smith (Conference Chairman), D. W. Breck (Technical Program Chairman), J. W. Ward (Financial Committee Chairman), D. M. Ruthven, G. T. Kerr, and J. B. Uytterhoeven (previous chairmen) for all their assistance in getting the program together. Special thanks are due to all of the reviewers who have contributed greatly to the quality of the papers in this volume, to the authors for their excellent preparation of the final manuscripts, to ACS for their cooperation, and particularly to J. B. Uytterhoeven for his advice on paper handling gained from his work on the Third International Conference on Molecular Sieves. Support was obtained from several organizations which are listed in the proceedings of the conference.

University of Delaware
Newark, Delaware
November 18, 1976

JAMES R. KATZER

Investigations of Equilibria and Kinetics of Adsorption of Gases on Zeolites

M. M. DUBININ

Institute of Physical Chemistry, Academy of Sciences of the U.S.S.R.,
Union of Soviet Socialist Republic

ABSTRACT

A thermodynamic theory of adsorption equilibrium based on the vacancy solution model and the analogy between osmotic and adsorption equilibria has been developed to describe adsorption on zeolites over wide ranges of pressure and temperature. New methods for investigating the kinetics of vapor adsorption by microporous adsorbents and for theoretical description of these processes on the basis of a biporous adsorbent model have been proposed. The experimental data agree with theory.

Introduction

For the subject of the opening lecture which I have been invited to deliver, I have chosen the most important results obtained recently at the Sorption Processes Department headed by me at the Institute of Physical Chemistry of the USSR Academy of Sciences. These are theoretical and experimental investigations into equilibrium physical adsorption carried out by B.P. Bering and V.V. Serpinskii with the participation of T.S. Yakubov and A.A. Fomkin, and studies into the kinetics of physical adsorption for biporous-structure adsorbents conducted by P.P. Zolotarev, A.M. Voloshchuk with the participation of I.T. Erashko, V.A. Gonlov, G. Schön and V.I. Ulin.

Based on the sizes of their pores, zeolites are typical microporous adsorbents. The commensurability of the sizes of micropores and the molecules adsorbed leads to a sharply defined effect of increase in adsorption potentials due to dispersion forces. Cations in the zeolite voids considerably enhance (owing to electrostatic interactions) the energy inhomogeneity

of the adsorption space of the micropores as compared with adsorbents of a different chemical nature, such as activated carbons.

Our investigations of equilibrium adsorption of the vapors of various substances in micropores, have lead to the concept that there was a qualitative difference between adsorption in micropores and adsorption on the surface of non-porous and relatively large-pore adsorbents of identical chemical nature. As a reasonable approximation for describing adsorption in micropores, we proposed the theory of volume filling of micropores. A survey of these investigations is given in (1,2).

In development of this theory we meet with some difficulties. The theory indicates only a decrease in differential heats of adsorption with an increase in filling. At temperature $T > T_c$ the theory is inapplicable.

It follows from the foregoing that it is expedient to search for a more perfect model of equilibrium adsorption of gases in micropores and develop a theory free from the above drawbacks. B.P.Bering and V.V.Serpinskii have made a successful attempt to develop and substantiate experimentally a more general thermodynamic theory of equilibrium adsorption, which was named the osmotic theory of adsorption. Its basic principles have been published only in Russian (3). We will consider the main version of the theory as applied to microporous adsorbents, using zeolites as examples.

Fundamental of Osmotic Theory of Adsorption in Micropores

As demonstrated by Hill (4), in describing equilibrium between an adsorbent and the gas phase in physical adsorption, methods of adsorption thermodynamics and of solution thermodynamics can be applied with equal success. Usually, the adsorbent is assumed to be thermodynamically inert in adsorption, and methods of adsorption thermodynamics are used. However the chemical potentials of the microporous adsorbents and particularly of zeolites change in the course of adsorption (5). Therefore the methods of solution thermodynamics are more expedient in this case. In connection with this it was also shown (6) that the linear dimensions of the zeolite crystals change in the course of adsorption.

This approach to the description of adsorption

equilibria has proved to be the most fruitful, when the theory was based on the solution model, which was named "the vacancy solution". In this model, one of the solution components is not a solid adsorbent, as in (5), but so-called "adsorption vacancies". This term means the free elementary volume of the adsorption space of the micropores which is filled by one adsorbate molecule in adsorption. Since the adsorption space of the micropores is limited by their volume, for a unit mass of the adsorbent there is a maximum number of vacancies, which is equal to the limiting number of the molecules adsorbed. The adsorption value tends to this quantity asymptotically with an unlimited increase of the equilibrium pressure in the gas phase.

At any equilibrium pressure of the adsorbate the adsorption space of the micropores contains adsorbed molecules and adsorption vacancies which form a binary vacancy solution. At a constant temperature, the dependence of the equilibrium pressure in the gas phase on the molar fraction of the dissolved substance (adsorbate), i.e. the adsorption value, represents a curve of the partial vapor pressure over the vacancy solution, or the adsorption isotherm. Thus, the adsorption equilibrium of the adsorbent with the gas phase is equivalent to the equilibrium of the vacancy solution with the same gas phase. It is natural to analyse this equilibrium by methods of solution thermodynamics.

Note that these concepts have proved to be particularly fruitful because there is a deep, formally thermodynamic, as well as physical, analogy between adsorption equilibrium and osmotic equilibrium. The idea of the existence of this similarity in the simplest case of adsorption on the surface of a liquid was first suggested by Frumkin as far back as 1925 (7), and then was absolutely clearly formulated by Adam (8). In subsequent years, however, it was not developed on a sufficient scale.

Consider now the physical background of this analogy. Denote the number of moles of the substance adsorbed and the number of vacancies per unit mass of the adsorbent by α and α^* , respectively. At any equilibrium conditions

$$\alpha + \alpha^* = \alpha_m \quad (1)$$

where α_m is limiting adsorption, which is assumed to be temperature invariant. Introduce the concept

of molar fractions of the adsorbate x and of the vacancies x^* , in the vacancy solution:

$$x = a/a_m, \quad x^* = a^*/a_m \quad (2)$$

We will regard the equilibrium of the microporous adsorbent with the gas phase as equilibrium of two vacancy solutions of different concentration. One of these solutions is the vacancy solution in the micropores, and the other, the solution formed by the gas molecules in a vacuum, in which the role of the "solvent" is played by the vacancies in the gas phase. Two solutions of different concentration formed by unlimited soluble components can be at equilibrium only when one of them is in the external potential field. It is easy to show that the effect of this field is formally equivalent to the difference of the hydrostatic pressures existing in these solutions. In the solution theory the difference of these pressures is called the osmotic pressure.

We will now write down the expressions for the chemical potentials of the vacancies in these two solutions, denoting the values referring to the gas phase by the subscript α . Note that a vacancy solution corresponding to the gas phase is always highly diluted ($x_{\alpha}^* \approx 1$; $x_{\alpha} \ll 1$) and therefore can be regarded as ideal

$$\mu_{\alpha}^* = \mu_{\alpha 0}^* + RT \ln x_{\alpha}^* + p_{\alpha} V^* \quad (3)$$

$$\mu^* = \mu_0^* + gRT \ln x^* + pV^* \quad (4)$$

where V^* is the molar volume of the vacancies, and g is the osmotic coefficient, which, like the activity coefficient, characterizes the non-ideality of the vacancy solution in the micropores (9).

At equilibrium, $\mu_{\alpha}^* = \mu^*$, and, according to (3) and (4),

$$\mu_{\alpha 0}^* + RT \ln x_{\alpha}^* + p_{\alpha} V^* = \mu_0^* + gRT \ln x^* + pV^* \quad (5)$$

It is obvious that at $x_{\alpha}^* = 1$, i.e. at zero concentration of the substance in the gas phase $x^* = 1$, $g = 1$ and $p_{\alpha} = p$. Therefore, in (5) $\mu_{\alpha 0}^* = \mu_0^*$. Introducing the notation

$$\Pi = p - p_{\alpha} \quad (6)$$

for the osmotic pressure, we obtain

$$\Pi V^* = -gRT \ln x^* + RT \ln x_{\alpha}^* \quad (7)$$

The second term in Eq. (7) can be neglected. If W is the micropore volume per unit mass of the adsorbent, the quotient W/V^* is the limiting adsorption value a_m

$$W/V^* = a_m \quad (8)$$

In accordance with (7) and (8), we get

$$W\Pi = -a_m g RT \ln(1 - a/a_m) \quad (9)$$

We will now write the Gibbs-Duhem equation for the vacancy solution in the micropores, referring it to the unit mass of the adsorbent at $T = \text{const}$

$$a d\mu + a^* d\mu^* = W d\Pi \quad (10)$$

where μ is the chemical potential of the adsorbate. Since this solution is at osmotic equilibrium, $d\mu^* = 0$, and therefore

$$a d\mu = W d\Pi \quad \text{and} \quad \Pi W = \int_0^a a d\mu = \Phi \quad (11)$$

where Φ is the integral of Gibbs' adsorption equation calculated from the adsorption isotherm. It is obvious that Φ is proportional to the osmotic pressure of the vacancy solution in the micropores.

Adopting the only non-thermodynamic assumption of the constancy of the osmotic coefficient g at $T = \text{const}$, we obtain, proceeding from Eqs. (9) and (11), the adsorption isotherm equation:

$$p^{1/g} = (a/\beta)/(a_m - a) \quad (12)$$

where β is a constant, or

$$a = a_m \beta p^{1/g} / (1 + \beta p^{1/g}) \quad (13)$$

Equations of the type (13) have long been known in the literature as empirical adsorption equations with three parameters a_m, β , and g (10) /See also (11) and (12)/. Their good applicability over wide ranges of fillings, a/a_m supports the adopted assumption of the constancy of the osmotic coefficient g .

As is known from a rigorous thermodynamic analysis of osmotic equilibrium in bulk solutions, the osmotic coefficient g is a linear function of the reciprocal temperature with a constant molar fraction of the solvent (13)

$$g = C(1 - b/T) \quad (14)$$

In developing further the analogy between osmotic equilibrium and adsorption equilibrium, it is expedient to utilize Eq. (14) in the latter case as well. For the discussed binary vacancy solution in the mic-

ropores the constancy of the molar fraction of the vacancies means the constancy of the molar fraction of the adsorbate, i.e. of the adsorption value.

Denoting, for brevity,

$$\varphi(a) = \ln [a/(a_m - a)] \quad (15)$$

we obtain from Eq. (12),

$$\ln p = g\varphi(a) - g \ln \beta \quad (16)$$

Since $\varphi(a) = 0$ at $a = 0.5a_m$, we apply Eq. (16) for this case and obtain

$$\ln p_{0.5} = -g \ln \beta \quad (17)$$

where $p_{0.5}$ is a function of the temperature alone. To express this dependence, we adopt a second non-thermodynamic assumption that the isostere corresponding to $a = 0.5a_m$ is linear:

$$\ln p_{0.5} = C_{0.5} - L_{0.5}/T \quad (18)$$

In Eq. (18), $L_{0.5}$ and $C_{0.5}$ are the slope and the intercept on the $\ln p$ -axis, which are temperature invariant.

We will obtain a thermal equation (19) of the osmotic theory of adsorption of the type $f(a, p, T) = 0$ after substituting g from (14) and $\ln p_{0.5}$ from (17) and (18) into Eq. (16), taking into account (15):

$$\ln p = C_{0.5} - L_{0.5}/T + C(1 - b/T) \ln [a/(a_m - a)] \quad (19)$$

This equation can be represented as

$$\ln p = C_a - L/T \quad (20)$$

where

$$C_a = C_{0.5} + C\varphi(a) \quad (21)$$

and

$$L = L_{0.5} + Cb\varphi(a) \quad (22)$$

are temperature invariant parameters. Their relation with the adsorption values with an allowance for (15) however, is given explicit form.

Thus, on the basis of the previously derived adsorption isotherm equation (12), the thermodynamic dependence of the osmotic coefficient on the temperature (14), and the assumption (18) as an experimental fact, we obtain the "thermal equation of adsorption" (19). To this equation there corresponds the linearity of the isosteres over a wide range of adsorption values. As is well known, the linearity of the adsorption isosteres is one of the very general proper-

ties of adsorption equilibrium and is usually well supported by experiment.

Note that in the initial portion of the adsorption isotherm, when the adsorption values become very low, i.e. when passing over to the ideal, infinitely diluted vacancy solution, the osmotic coefficient g tends to unity and the parameter b , to zero. Therefore, it should be assumed that in the initial portion of any adsorption isotherm $g=1$, and then, as Q increases, this coefficient rapidly changes to a certain value, which remains constant over a wide range of adsorption values.

Experimental Substantiation of Thermal Equation of Osmotic Theory of Adsorption

The thermal equation of adsorption (19) contains 5 parameters: Q_m , $L_{0.5}$, $C_{0.5}$, C and b , for whose determination one must have at least two experimental adsorption isotherms.

The thermal equation (19) of the osmotic theory of adsorption describes with a high accuracy the adsorption equilibrium of gases and vapors on various microporous adsorbents such as zeolites and active carbons over a wide range of temperatures and pressures. To illustrate the agreement between theory and experiment, we will consider only one typical system, namely Xe-zeolite NaX which have been studied at our Laboratory (14). These investigations are of interest per se in the experimental sense, since the constructed equipment enabled us to perform reliable measurements of adsorption equilibria over a very wide range of pressures from hundredths of Torr to hundreds of atm and temperatures from 150 to 600 K.

In Figure 1, in coordinate axes Q - $\log p$, the solid lines show the adsorption isotherms of Xe on crystals of zeolite NaX, calculated for various temperatures from Eq. (19), for the following values of the equation parameters: $Q_m = 4.30$ mmole/g, $L_{0.5} = 1225$ K, $C_{0.5} = 6.76$, $C = 1.14$ and $b = 109$ K.

The experimental points are marked by circles. Within the studies temperature range from 150 to 600 K, which includes the normal critical temperature $T_c = 290$ K, theory agrees well with experiment in the range of filling Q/Q_m from 0.09 to 0.93.

It is worth noting that for systems studied in the above-mentioned ranges of Q/Q_m the adsorption isosteres are linear. The thermal equation of adsorption (19) with the same parameter values is equally

applicable to below- and above-critical temperatures. The good agreement between the calculated and experimental adsorption isotherms and the linearity of the isosteres, in particular at $\alpha = 0.5\alpha_m$, are direct experimental confirmations of the main principles of the osmotic theory of adsorption.

Thermodynamic Functions of Adsorption Equilibrium

On the basis of Eqs. (18) and (22) it is easy to obtain expressions for the main thermodynamic functions of adsorption equilibrium for the range of p and T in which the gas phase can be considered practically ideal. According to (16) and (17), Gibbs' differential free energy G is expressed thus:

$$G = RT \ln p = G_{0.5} + gRT\psi(\alpha) \quad (23)$$

Differentiating this equation with respect to T at $\alpha = \text{const}$ with an allowance for the temperature dependence of g according to (14), we get the expression for the differential entropy of adsorption S .

$$S = -(\partial G / \partial T)_{\alpha} = S_{0.5} - CR\psi(\alpha) \quad (24)$$

If we have an ideal equilibrium gas phase, $RL = Q$, where Q is the differential heat of adsorption. Therefore, according to (22),

$$Q = Q_{0.5} + CbR\psi(\alpha) \quad (25)$$

Proceeding from thermodynamic considerations we can show that the parameter C in Eq. (14) cannot be negative. Therefore it follows from Eq. (25) that at $T = \text{const}$ the dependence of the heat of adsorption Q on α is determined by the sign of the parameter b . When $b > 0$, Q increases with adsorption. For $b < 0$, Q decreases with increasing α .

Figure 2 compares the dependence of the differential heat of adsorption on the adsorption value (solid curve), as calculated by Eq. (25), for the system Xe-NaX in the range of p where the equilibrium gas phase can practically be considered ideal. The circles indicate the experimental isosteric heats of adsorption. Calculation is in good agreement with experiment.

Thus, the osmotic theory of adsorption equilibrium leads to a thermal equation of adsorption which makes it possible to express the isotherms, isosteres, and thermodynamic functions of equilibrium through the same parameters of this equation.

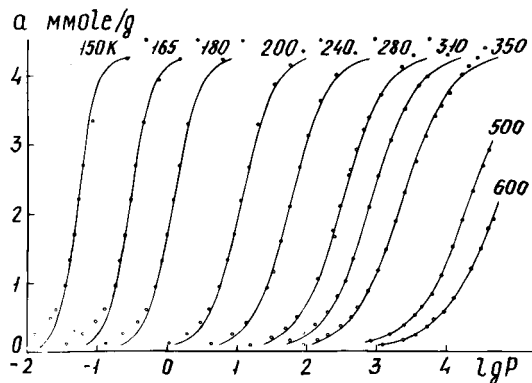


Figure 1. Adsorption isotherms of Xe on zeolite NaX. Solid lines calculated from Ref. 19. Circles denote experiment (α , mmole/gr; p , N/m² or Pa).

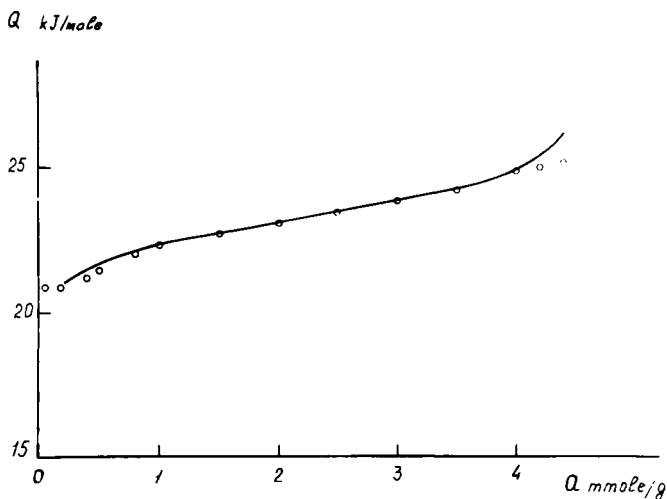


Figure 2. Dependence of differential heat of adsorption of Xe on zeolite NaX on adsorption values α . Solid line calculated from Ref. 25. Circles denote experimental values.

Kinetics of Physical Adsorption by Microporous Adsorbents

According to the classification based on the mechanisms of adsorption and capillary phenomena occurring in adsorbent grains, it is expedient to divide their pores into micropores, supermicropores, mesopores and macropores (2,15).

In many practically important cases it is possible to slightly simplify the real structure of the adsorbent and distinguish only two pore varieties differing substantially in their properties: adsorbing pores (micro- and supermicropores) and transport pores (meso- and macropores). This biporous adsorbent model, which characterizes, in particular, molded zeolites, is presented in simplified form in Fig.3.

In recent years, investigations on the kinetics of adsorption by biporous adsorbents have been conducted in the works of a number of authors (16-19) and in our works (20-27). We considered the equations of internal diffusion in biporous adsorbents in the general case of non-linear adsorption isotherms. Then we generalized these equations for the case of microporous zones (small crystals) of various sizes taking into account the finite diffusion resistance of the external surface of the crystals (21,22,25,27). For linear adsorption isotherms, the application of the statistical moments method made it possible to obtain sufficiently simple analytical equations relating the characteristic times of diffusion in adsorbing τ_a and transport τ_i pores with the moments of the kinetic curves (23,27). In the case of introduction kinetics and microporous zones of identical size, k -order moments have the form

$$M_k = \sum_{\nu=0}^k g_{\nu k} \tau_i^{\nu} \tau_a^{k-\nu} \quad (26)$$

Here,

L and r_0 are the determining dimensions of the granule and the microporous zones, D_i and D_a are the coefficients of diffusion in the transport pores and the microporous zones, Q_0 is the equilibrium adsorption value, C_0 is the adsorptive concentration at the granule surface. The coefficients $g_{\nu k}$ depend on the geometrical shape of the granule and of the microporous zones, respectively. Their values for granules and microporous zones of various shape are given, for instance, in (25). Besides, we developed a procedure for determining the transport coefficients in biporous adsorbents based on the study of adsorp-

tive diffusion from one volume to another through an adsorbent granule (26).

The relations discussed were used by us for calculating the diffusion coefficients separately in adsorbing and transport pores and analyzing the character of mass transfer in real microporous adsorbents (molded zeolites, active carbons) (25,26). This analysis demonstrated the rationality of application of the biporous model in studying real microporous adsorbents.

Along with the case of linear adsorption isotherms the equations of internal diffusion in biporous adsorbents have also been investigated by us theoretically for sharply convex (rectangular) isotherms.

The case of a cylindrical (prismatic) adsorbent grain with an impermeable lateral surface has been considered. The variation in the local concentration of the adsorbate in the grain, $Q(x)$, at different instants of time (x is the distance from the grain end face) and the grain-average relative adsorption, $\gamma(t)$ (kinetic curves), have been investigated. The process pattern essentially depends on the ratio of the characteristic times to adsorption equilibrium in the transport pores and in the microporous zones, τ_i and τ_a .

In the case of sharply convex adsorption isotherms, a pictorial picture, confirming the rationality of the biporous model for molded zeolites and microporous active carbons can be obtained by studying the adsorption kinetics of the vapors of X-ray contrast substances by X-ray technique (22,25). The advantage of this method is the possibility of visual observation of the formation of the adsorption front and its propagation across the grain.

Consider a cylindrical zeolite granule whose lateral surface and one of the end faces are impermeable, and the adsorption of the X-ray contrast substance occurs only from the granule end face (Fig. 3). If the adsorption rate is determined by the diffusion in the zeolite crystals ($\tau_a \gg \tau_i$), the X-ray patterns will show gradual darkening of the entire adsorbent granule (Fig. 3a). If, however, the process is limited by the transfer in the transport pores ($\tau_i \gg \tau_a$) "layer-by-layer" filling of the zeolite granule is taking place (Fig. 3c). In this case the shape of the adsorption wave $Q(x)$ is near-rectangular and the kinetic curve $\gamma(t) \sim \sqrt{t}$.

The intermediate case (when the times τ_i and τ_a

are comparable) is characterized by the formation and propagation, across the grain of an adsorption wave $Q(x)$ with a considerably smeared-out front (Fig. 3b). In this case, as theoretical calculations show, $\gamma(t)$ varies in a more complicated way than by the law \sqrt{t} . The actual form of the dependence $\gamma(t)$ is determined by the type of the kinetic function of the filling of the microporous zones (for instance, of the small zeolite crystals in the granule), $\varphi(t)$ ($0 \leq \varphi(t) \leq 1$). In our opinion, the approximate integral equation obtained by us (for this case) for the law of motion of the forward front of the adsorption wave

$$\hat{l}^2(s) = 2D_i s^{-2} [(a_0/c_0) s \hat{\varphi}(s) + 1/6]^{-1} \quad (27)$$

is of interest. Here, $\hat{l}^2(s)$ and $\hat{\varphi}(s)$ are the Laplace transformants of the function $l^2(t)$ and $\varphi(t)$. Equation (27) makes it possible (in principle) to determine, on the basis of the known law of motion of the forward front of the adsorption wave $l(t)$, the kinetics of adsorption in the microporous zones $\varphi(t)$, and vice versa. The same relation can be used for calculating the diffusion coefficients.

We have also investigated theoretically the law of variation in the front width of the adsorption wave with time in the intermediate case. For the rectangular adsorption isotherm, we found that this value, $\Delta(t)$, decreases with time. The concrete form of the decreasing function $\Delta(t)$ depends on the nature of the kinetic function of the filling of the microporous zones, $\varphi(t)$. In particular, if $\varphi(t) = 1 - \exp(-t/\tau_a)$ then

$$\Delta(t) = \left(\frac{2D_i \tau_a c_0}{a_0} \right)^{1/2} \left[\left(\frac{t}{\tau_a} + \ln(1 - \varepsilon_1) + 1 \right)^{1/2} - \left(\frac{t}{\tau_a} + \ln \varepsilon_1 + 1 \right)^{1/2} \right] \quad (28)$$

Here, $\varepsilon_1 > 0$ is a small value appearing in the definition of the front width of the adsorption wave.

The conclusion about the variation in the adsorption wave front width, which follows from theoretical analysis, can be confirmed experimentally by studying the kinetics of adsorption of X-ray contrast substances by X-ray technique. This method was used by us, in particular, when studying the kinetics of adsorption of ethyl iodide, ethyl bromide, and bromobenzene from a nitrogen flow by molded zeolites CaA, CaX, NaX, and by active carbons. For X-type zeolites and active carbons, in adsorption from the carrier gas flow we observed a clearly defined pattern of "layer-by-layer" filling of the granules (Fig. 3c). When studying zeo-

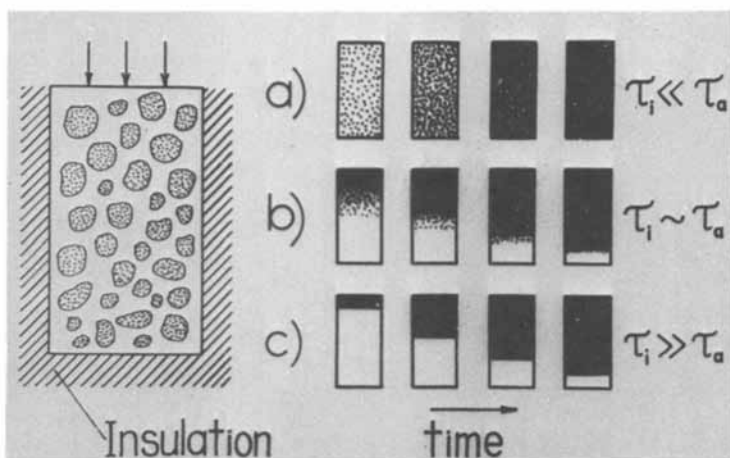


Figure 3. Granule of molded zeolite with impermeable lateral surface and nature of adsorbate distribution in granule of biporous adsorbent

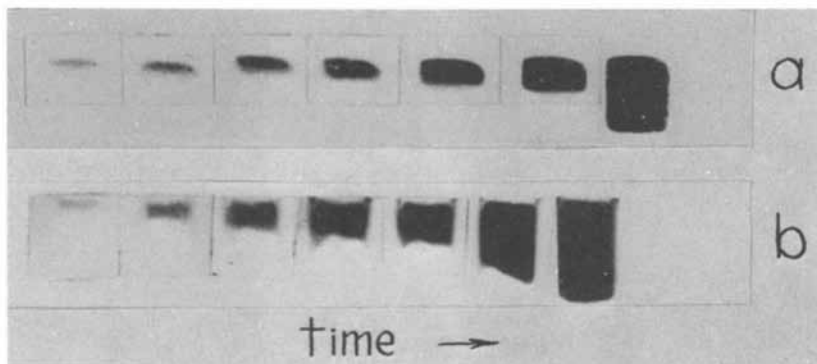


Figure 4. Distribution of bromobenzene (a) and xenon (b) in active carbon granule in successive time intervals

lites CaA, which differ as regards their binders and granule molding conditions, we observed all the possible cases (Fig.3). The pattern typical of the intermediate case ($\tau_i \approx \tau_a$, Fig. 3b) is observed most clearly in studying the kinetics of adsorption of bromobenzene and xenon from a one-component gas phase by microporous active carbons with molecular-sieve properties. The experimental results are depicted in Fig. 4 (a -brom-benzene, P=27 Pa, T=298K; b-xenon, P=6.5 kPa, T=195K).

In all the figures attached, at the initial instants of time one can see a substantially smeared-out adsorption front, which reduces with time, in accordance with theoretical analysis, and at sufficiently large times one observes "layer-by-layer" filling of the granules.

Our investigations, as well as those of other authors, show that the biporous kinetic model holds much promise for studying the kinetics of adsorption by real adsorbents and, in the first place, by molded zeolites. It enables one to interpret correctly the results of experiments which cannot be squeezed into the framework of the classical quasi-diffusion model. At the same time, this model requires further experimental substantiation. This refers, above all, to the nature of mass transfer in the microporous zones. In the final analysis, the application of the biporous model of real adsorbents makes it possible to approach more rationally the choice of adsorbents with the most rational porous structure.

Literature Cited

1. Dubinin M.M., "Chemistry and Physics of Carbon", Vol.2, p.51, M.Dekker, New York, 1966
2. Dubinin M.M., "Progress in Surface and Membrane Science", Vol.9, p.1, Academic Press, New York, 1975
3. Bering B.P., Serpinski V.V., Izv.Akad. Nauk SSSR, Ser. Khim. (1974) 2427
4. Hill T.L., J. Chem. Phys., (1950) 18, 246
5. Barrer R.M., Calabova I.M., Adv. Chem. Series (1973) 121, 356
6. Sarakhov A.I., Kononyuk V.F., Dubinin M.M., Adv. Chem. Series, (1973) 121, 403
7. Frumkin A.N., Z.phys. Chem., (1925) 116, 466
8. Adam N.K., "The Physics and Chemistry of Surfaces" London, 1941

9. Prigogina I., Defay R., "Chemical Thermodynamics", Longmans Green, London, 1954
10. Young D.M., Crowell A.D., "Physical Adsorption of Gases", p.110, Butterworths, London, 1962
11. Cohen G., Thesis, Grenoble, 1967
12. Kisarov V.N., Zh. Fiz. Khim., (1967) 43, 1037
13. Guggenheim E.A., "Modern Thermodynamics by the Methods of Willard Gibbs", Methuen and Co. Ltd, London, 1933
14. Fomkin A.A., Dissertacia, Moskva, 1975
15. Dubinin M.M., Adv. Colloid Interface Sci., (1968) 2, 217
16. Ruckenstein E., Vaidyanathan A.S., Youngquist G.K., Chem. Eng. Sci., (1971) 26, 1305
17. Ma Y.H., Mancel C., Adv. Chem. Series, (1973) 121, 392
18. Haynes H.W., Sarma P.N., AIChE J., (1973) 19, 1043
19. Kochirjik M., Zikanova A., "Adsorbicija i poristost" p. 296, "Nauka", Moskva, 1976
20. Voloshchuk A.M., Dubinin M.M., Zolotarev P.P., "Adsorbicija i poristost", p. 285, "Nauka", Moskva, 1976
21. Zolotarev P.P., Dubinin M.M., Dokl. Akad. Nauk SSSR, (1973) 210, 136
22. Voloshchuk A.M., Dubinin M.M., Dokl. Akad. Nauk SSSR, (1973) 212, 649
23. Voloshchuk A.M., Zolotarev P.P., Ulin V.I., Izv. Akad. Nauk SSSR, Ser. Khim., (1974) 1250
24. Zolotarev P.P., Ulin V.I., Izv. Akad. Nauk SSSR, Ser. Khim., (1974) 2367
25. Dubinin M.M., Erashko I.T., Kadlec O., Ulin V.I., Voloshchuk A.M., Zolotarev P.P., Carbon, (1975), 13, 198
26. Voloshchuk A.M., Dubinin M.M., Nechaeva N.A., Ulin V.I., Dokl. Akad. Nauk SSSR, (1975) 222, 369
27. Zolotarev P.P., Izv. Akad. Nauk SSSR, Ser. Khim. (1975) 193

Molecular Orbital Calculations for Atoms in the Tetrahedral Frameworks of Zeolites

G. V. GIBBS—Department of Geological Sciences, Virginia Polytechnic Institute and State University, Blacksburg, Va. 24061

E. P. MEAGHER—Department of Geological Sciences, University of British Columbia, Vancouver 8, B.C., Canada V6T 1W5

J. V. SMITH and J. J. PLUTH—Department of the Geophysical Sciences, University of Chicago, Chicago, Ill. 60637

ABSTRACT

MO calculations for T_5O_{16} clusters isolated from structures of six zeolites are examined. Variations of observed $T-O$ bond lengths correlate negatively with bond overlap populations and positively with geminal nonbonded repulsions. Longer $T-O$ bonds tend to involve narrower $T-O-T$ and $O-T-O$ angles and oxygen atoms with larger electrical charges, $Q(O)$. Despite the neglect in the calculations of the nontetrahedral cations, M , shorter $M-O$ bonds involve framework oxygen atoms with larger $Q(O)$ values.

Introduction

In the last few decades much work has been devoted to clarifying the structure, crystal chemistry and properties of zeolites. Nevertheless, it has provided little insight into the charge distribution and the nature of the bonding forces in the zeolite framework. Most interpretations of cation distributions and bond length and valence angle variations have been based on ionic theory. For example Dempsey (1, 2) found that Madelung potentials calculated for faujasite type zeolites correlate with cation distributions obtained in x-ray studies. However, because complete ionicity and observed atomic coordinates were assumed and dispersion and closed shell repulsion energies were neglected, the calculations do not improve understanding of the geometry and charge distribution of the tetrahedral framework for which extended Hückel theory (EHT) should be particularly relevant by analogy with earlier calculations on feldspars (3). The calculations for the feldspars predict that the oxygen atoms involving the longer $T-O$ bonds ($T = Al, Si$) have larger electrical charges, $Q(O)$, than those involving the shorter bonds. In addition, Mulliken bond overlap populations, $n(T-O)$, calculated by assuming constant $T-O$ bond lengths with the valence angles clamped at observed values correlate negatively with the observed $T-O$ bond lengths, $d(T-O)$.

The calculations also predict that Si-O bonds in Si-O-Al linkages should be shorter than those in Si-O-Si linkages and that Si-O-Al linkages are more stable than Al-O-Al linkages (4). Because shorter bonds are predicted to involve wider T-O-T angles, tetrahedra involved in wider than average angles are expected to be slightly smaller than those involved in narrower angles (5). Molecular orbital theory has also proved useful in the construction of theoretical and empirical MO diagrams and the interpretation of visible, ultraviolet and x-ray emission and x-ray photoelectron spectra of other silicates (6, 7, 8, 9, 10, 11). The good agreement obtained between the calculated electronic structure of the silicate ion and the available spectra of silicates and the use of the theory to correlate bond length and valence angles in silicates indicate that modern valence theory can provide a meaningful rationalization of the nature of bonding in silicate minerals.

The present study was undertaken to learn whether Mulliken bond overlap populations obtained using molecular orbital theory correlate with T-O bond length variations in six silica rich zeolites (two dehydrated and two rehydrated ptilolites (12, 13, 14, 15, 16) and two offretites (15, 17) and whether the calculated electrical charges for the oxygen atoms in the tetrahedral framework predict especially favorable sites in these zeolites for attaching cations and sorbed molecules.

Extended Hückel Theory and Population Parameters

Because quantum mechanics cannot be applied in general to polyelectronic systems, simplified approximations such as EHT (18) were developed to provide objective algorithms for rationalizing chemical experience. Comparison of experimental observations with such calculations should improve our understanding of the crystal chemistry of the zeolites and other inorganic compounds. Recently it allowed interpretation of the interplay between bond length and valence angle variations in the nontransition metal tetrahedral oxyanions for the second, third and fourth period elements (19). Although the algorithm cannot predict *a priori* the equilibrium bond lengths, it does predict the observations that shorter T-O bonds tend to involve wider valence angles and that interdependence between bond length and valence angle variations improves with increasing electronegativity of the tetrahedral cation.

In EHT, each valence electron is characterized by a normalized molecular orbital extending over the whole oxyanion cluster. This orbital is approximated by a linear combination of atomic orbitals

$$|\psi_k\rangle = \sum_{j=1}^n c_{kj} |\chi_j\rangle$$

where $|\chi_j\rangle$ are single exponent Slater type atomic orbitals and c_{kj}

is a set of linear coefficients. If one electron orbital energies, ϵ_k , are defined, then we may write the integral form of the Schrödinger equation

$$\epsilon_k = \langle \psi_k | h_{\text{eff}} | \psi_k \rangle$$

where h_{eff} is some undefined effective one electron Hamiltonian operator. The variation principle yields the following set of secular equations

$$\sum_{j=1}^n c_{kj} (h_{ij} - \epsilon_k S_{ij}) = 0$$

where $h_{ij} = h_{ji} = \langle \chi_i | h_{\text{eff}} | \chi_j \rangle$ and $S_{ij} = \langle \chi_i | \chi_j \rangle$. A nontrivial solution occurs only when

$$|h_{ij} - \epsilon S_{ij}| = 0$$

holds for the secular determinant.

When the elements of the Hartree-Fock Hamiltonian matrix are replaced by the Wolfsberg-Helmholz approximation (20), EHT is asserted to simulate Hartree-Fock calculations. We employed this approximation, i.e., (1) the diagonal elements of the matrix h_{ii} were taken as measures of the electron attracting power of an atom and were set equal to the negative of the valence orbital ionization potential (VOIP) of the *i*th atomic orbital and (2) the off diagonal matrix elements h_{ij} were taken as proportional to the overlap integral, S_{ij} , according to the parameterization

$$h_{ij} = S_{ij} (h_{ii} + h_{jj}).$$

The overlap integrals were computed using the atomic coordinates of each atom in the oxyanion cluster and the following Clementi-Raimondi orbital exponents, ζ : O(2s) 2.246; O(2p) 2.227; T(3s) 1.634 and T(3p) 1.428. The VOIP's used are: O(2s) -32.33 eV; O(2p) -15.79 eV; T(3s) -14.83 eV and T(3p) -7.75 eV.

When the secular determinant is expanded, the solution to the resulting *n*th order polynomial gives *n* molecular orbital energies, ϵ . Each ϵ_k is then inserted into the secular equations to obtain a set of linear coefficients c_{kj} that define $|\psi_k\rangle$. Once the linear coefficients are found, a Mulliken population analysis may be completed to gain some insight into the charge distribution in the oxyanion cluster. For a TO_4^{-n} tetrahedral oxyanion, the T-O bond overlap population defined by

$$n(T-O) = \sum_k^{MO} N(k) \sum_{i \in T} \sum_{j \in O} c_{ki} c_{kj} S_{ij}$$

is believed to measure the electron density located between T and O where $N(k)$ is the number of electrons in $|\psi_k\rangle$. It is traditional to expect a larger binding force between the nuclei of the two atoms and therefore a shorter $T-O$ bond when the electron density in the bond is large. Accordingly, a negative correlation between $n(T-O)$ and the observed $T-O$ bond length, $d(T-O)$, is anticipated. On the other hand, when the overlap population between two atoms (like two oxygen or two T atoms) is negative (antibonding), the electron density between the nuclei is believed to be reduced. This increases their repulsion and they separate to minimize the potential energy. The sum of all the antibonding overlap populations across a $T-O$ bond is called the geminal nonbonding overlap population, $nb(T-O)$. According to Bartell *et al.* (21), $nb(T-O)$ should measure repulsion forces in a structure that tend to stretch bonds, longer bonds involving larger $nb(T-O)$.

The electrical charges on oxygen are estimated by

$$Q(O) = Z_O^{\text{eff}} - \sum_k N(k) \left[\sum_{i \in O} c_{ki}^2 + \sum_{i \in O} \sum_{j \in T, i \neq j} c_{ki} c_{kj} S_{ij} \right]$$

where Z_O^{eff} is the number of valence electrons on O . The actual number calculated for $Q(O)$ should not be regarded as the actual charge on the atom but as a crude index of the relative charge. An intrinsic defect in EHT is the strong dependence of the resulting energies and wavefunctions on the form of the parameterization. Nevertheless, it appears that trends in bond overlap populations and electric charges estimated for chemically and structurally similar molecules are virtually independent of the exact parameterization. Hence, the correlations are considered to be significant, not the absolute numbers.

Application to Zeolites

In a systematic study of the factors controlling the location of exchangeable cations and adsorbed molecules in ptilolite and offretite, Mortier *et al.* (13, 15, 17) observed moderate to strong correlations between $\Delta d(T-O)$ and $-1/\cos(LT-O-T)$ where $\Delta d(T-O)$ is the variation of the individual $d(T-O)$ value from the mean value for the tetrahedron (Fig. 1a). The correlation is especially well developed for dehydrated H-ptilolite which lacks exchangeable cations or sorbed molecules whose bonding requirements must disturb correlations based only on framework effects. As these correlations are consistent with observational and molecular orbital results for the feldspars, they proposed that covalent bonding may be important in characterizing the steric details of the tetrahedral frameworks in these zeolites. Although the correlation evinced by Figure 1a is highly significant, the scatter of points about the regression line is fairly large. This is not surprising

because (1) $\Delta d(T-O)$ also correlates with the average of the three $O-T-O$ angles adjacent to the bond, $\langle O-T-O \rangle_3$, such that shorter bonds tend to involve larger $\langle O-T-O \rangle_3$ angles (Fig. 1b), and (2) bonding from exchangeable cations and adsorbed molecules was neglected. A multiple linear regression analysis of $\Delta d(T-O)$ versus both $\langle O-T-O \rangle_3$ and $-1/\cos(\angle T-O-T)$ accounts for about three-quarters of the variation in $\Delta d(T-O)$, Figure 1c; on the other hand, only about half was explained in terms of either $\langle O-T-O \rangle_3$ or $-1/\cos(\angle T-O-T)$. Note that no attempt was made to include the bonding effects of the nontetrahedral atoms in the regression analysis.

In order to interpret the correlations in Figure 1 with a covalent bonding model, EHT calculations (Table I) were completed for closed shell T_5O_{16} clusters isolated from ptilolite and offretite following the procedure described for the feldspars by Gibbs *et al.* (3). All $T-O$ distances were clamped at 1.61 Å but $T-O-T$ and $O-T-O$ angles were set at observed values obtained from x-ray crystal structure analyses. The data for dehydrated H-ptilolite were plotted in Figures 1-4 as solid triangles whereas those for the remaining zeolites containing exchangeable cations and sorbed molecules were plotted as solid circles. The larger scatter in data for the latter zeolites may be ascribed to the bonding effects of the cations and molecules not explicitly modelled in the molecular orbital calculations for the framework.

From the plot (Fig. 2) of $\Delta d(T-O)$ versus $\Delta n(T-O)$, the deviation of $n(T-O)$ from the mean value of its host tetrahedron, the shorter bonds are shown to match the larger bond overlap populations as observed for the feldspars. The $\Delta d(T-O)$ values also correlate with $\Delta nb(T-O)$ (Fig. 3), the deviation of the geminal nonbonding overlap population from the mean value of its host tetrahedron. These two correlations support the assertion by Bartell *et al.* (21) that geminal nonbonding repulsions are as important as bond overlap populations in governing trends in bond length variations. Calculations predict that the repulsion forces associated with $nb(T-O)$ become more important as the angles between the tetrahedra in the zeolite framework narrow and as $T-T$ and $O-O$ separations and $n(T-O)$ values decrease (22).

The oxygen atoms involved in the narrower angles within and between the tetrahedra of the framework are predicted by EHT to carry the larger electrical charges, $Q(O)$ (Fig. 4). Because longer $T-O$ bonds tend to be associated with narrower valence angles, longer $T-O$ bonds are predicted to involve the more negatively charged oxygen anions. In spite of the utter neglect of the nontetrahedral cations, M , in the feldspar calculations, the $Q(O)$ values were found to correlate inversely with the number of $M-O$ bonds and the bond strength sums to the oxygen atoms in the framework. For the zeolites, the estimated $Q(O)$ values correlate with the observed $M-O$ bond lengths, shorter bonds involving oxygen atoms with larger electrical charges (Fig. 5). Because the bonding between the M cations and the framework is asserted to be

Table I. Observed T-O bond lengths, $d(T-O)$, Mulliken bond overlap populations, $\underline{n}(T-O)$, geminal nonbonding populations, $\underline{nb}(T-O)$, and electrical charges for oxygen, $Q(O)$, for selected ptilolites and offretites.

Atoms	$d(T-O)$	$\underline{n}(T-O)$	$\underline{nb}(T-O)$	$Q(O)$	Atoms	$d(T-O)$	$\underline{n}(T-O)$	$\underline{nb}(T-O)$	$Q(O)$
Dehydrated Ca-ptilolite									
T ₁ -O ₁	1.605	0.502	-0.094	-1.251	T ₃ -O ₁	1.632	0.501	-0.095	-1.251
T ₁ -O ₃	1.586	0.514	-0.090	-1.227	T ₃ -O ₄	1.594	0.528	-0.086	-1.207
T ₁ -O ₆	1.610	0.505	-0.091	-1.241	T ₃ -O ₉	1.657	0.484	-0.099	-1.287
T ₁ -O ₇	1.604	0.499	-0.095	-1.254					
T ₂ -O ₂	1.591	0.502	-0.093	-1.246	T ₄ -O ₂	1.609	0.503	-0.094	-1.246
T ₂ -O ₃	1.579	0.513	-0.091	-1.227	T ₄ -O ₄	1.607	0.521	-0.089	-1.207
T ₂ -O ₅	1.606	0.499	-0.094	-1.251	T ₄ -O ₁₀	1.610	0.498	-0.095	-1.254
T ₂ -O ₈	1.566	0.518	-0.088	-1.222					
Rehydrated Ca-ptilolite									
T ₁ -O ₁	1.618	0.505	-0.093	-1.247	T ₃ -O ₁	1.638	0.501	-0.095	-1.247
T ₁ -O ₃	1.600	0.512	-0.091	-1.231	T ₃ -O ₄	1.599	0.523	-0.086	-1.211
T ₁ -O ₆	1.617	0.507	-0.091	-1.238	T ₃ -O ₉	1.645	0.496	-0.096	-1.258
T ₁ -O ₇	1.627	0.496	-0.095	-1.260					
T ₂ -O ₂	1.609	0.498	-0.094	-1.252	T ₄ -O ₂	1.622	0.500	-0.095	-1.252
T ₂ -O ₃	1.601	0.512	-0.090	-1.231	T ₄ -O ₄	1.615	0.523	-0.087	-1.211
T ₂ -O ₅	1.620	0.498	-0.095	-1.254	T ₄ -O ₁₀	1.623	0.500	-0.095	-1.251
T ₂ -O ₈	1.584	0.520	-0.088	-1.217					
Hydrated Na-ptilolite									
T ₁ -O ₁	1.628	0.505	-0.093	-1.248	T ₃ -O ₁	1.645	0.501	-0.095	-1.248
T ₁ -O ₃	1.603	0.512	-0.091	-1.230	T ₃ -O ₄	1.618	0.523	-0.086	-1.208
T ₁ -O ₆	1.623	0.506	-0.092	-1.241	T ₃ -O ₉	1.647	0.496	-0.096	-1.260
T ₁ -O ₇	1.633	0.493	-0.097	-1.265					
T ₂ -O ₂	1.615	0.497	-0.096	-1.255	T ₄ -O ₂	1.629	0.499	-0.094	-1.255
T ₂ -O ₃	1.604	0.512	-0.091	-1.230	T ₄ -O ₄	1.607	0.497	-0.086	-1.208
T ₂ -O ₅	1.619	0.498	-0.095	-1.254	T ₄ -O ₁₀	1.632	0.524	-0.094	-1.256
T ₂ -O ₈	1.589	0.521	-0.089	-1.216					
Dehydrated H-ptilolite									
T ₁ -O ₁	1.608	0.507	-0.092	-1.243	T ₃ -O ₁	1.640	0.503	-0.093	-1.243
T ₁ -O ₃	1.600	0.512	-0.091	-1.230	T ₃ -O ₄	1.614	0.520	-0.087	-1.217
T ₁ -O ₆	1.611	0.508	-0.091	-1.236	T ₃ -O ₉	1.636	0.500	-0.093	-1.250
T ₁ -O ₇	1.631	0.497	-0.096	-1.258					
T ₂ -O ₂	1.608	0.500	-0.093	-1.249	T ₄ -O ₂	1.632	0.502	-0.095	-1.249
T ₂ -O ₃	1.596	0.511	-0.090	-1.230	T ₄ -O ₄	1.600	0.520	-0.089	-1.217
T ₂ -O ₅	1.613	0.500	-0.093	-1.249	T ₄ -O ₁₀	1.623	0.503	-0.094	-1.245
T ₂ -O ₈	1.587	0.519	-0.089	-1.220					
Dehydrated offretite									
T ₁ -O ₁	1.618	0.505	-0.093	-1.239	T ₂ -O ₁	1.612	0.511	-0.091	-1.239
T ₁ -O ₂	1.668	0.489	-0.099	-1.278	T ₂ -O ₅	1.681	0.490	-0.100	-1.274
T ₁ -O ₃	1.622	0.496	-0.096	-1.256	T ₂ -O ₆	1.612	0.505	-0.093	-1.242
T ₁ -O ₄	1.618	0.519	-0.089	-1.224					
CO adsorbed offretite									
T ₁ -O ₁	1.631	0.505	-0.093	-1.238	T ₂ -O ₁	1.621	0.512	-0.091	-1.238
T ₁ -O ₂	1.669	0.488	-0.099	-1.279	T ₂ -O ₅	1.697	0.487	-0.100	-1.280
T ₁ -O ₃	1.635	0.496	-0.096	-1.256	T ₂ -O ₆	1.607	0.505	-0.093	-1.242
T ₁ -O ₄	1.621	0.518	-0.089	-1.224					

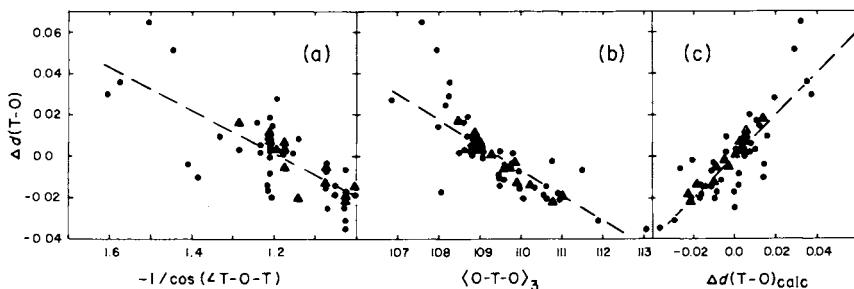


Figure 1. T-O bond length variations $\Delta d(\text{T-O})$ for dehydrated and rehydrated Ca ptilolite, hydrated Na and dehydrated H-ptilolite, dehydrated and CO-adsorbed off-tite vs. (a) $-1/\cos(\angle \text{T-O-T})$, (b) $\langle \text{O-T-O} \rangle_3$, the average of the three angles common to the bond, and (c) $\Delta d(\text{T-O})_{\text{calc}}$ calculated as a linear combination of $-1/\cos(\angle \text{T-O-T})$ and $\langle \text{O-T-O} \rangle_3$.

EHT has shown that $n(\text{T-O})$ varies nonlinearly when plotted against $\angle \text{T-O-T}$ and linearly when plotted against $-1/\cos(\angle \text{T-O-T})$ (23). Because experience has shown that $n(\text{T-O})$ is linearly dependent on $d(\text{T-O})$, $\Delta d(\text{T-O})$ was plotted against $-1/\cos(\angle \text{T-O-T})$ to obtain a linear trend. \blacktriangle , data for dehydrated H-ptilolite, which lacks exchangeable cations and adsorbed molecules; \bullet , remaining zeolites.

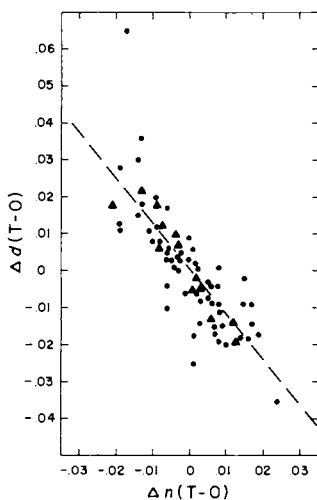


Figure 2. $\Delta d(\text{T-O})$ vs. $\Delta n(\text{T-O})$, the variation of the individual bond overlap population, $n(\text{T-O})$, from the mean value calculated of its host tetrahedron.

The $n(\text{T-O})$ values (Table I) were obtained for the T-O bonds of the central tetrahedron of a T_5O_{16} cluster. Each nonequivalent tetrahedron in the six zeolites was placed in such a cluster, but only the $n(\text{T-O})$ values of the central tetrahedron were used. All the T-O bond lengths in the cluster were set at 1.61 Å, and the O-T-O and T-O-T angles were kept at observed values.

Figure 3. $\Delta d(\text{T-O})$ vs. $\Delta nb(\text{T-O})$, the variation of the geminal nonbonding repulsion from the mean value of its host tetrahedron

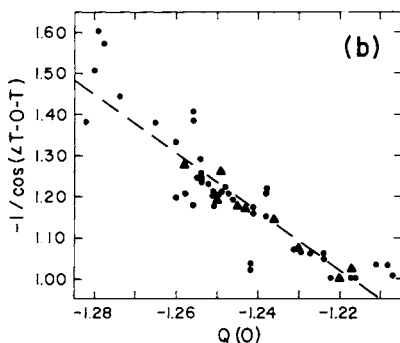
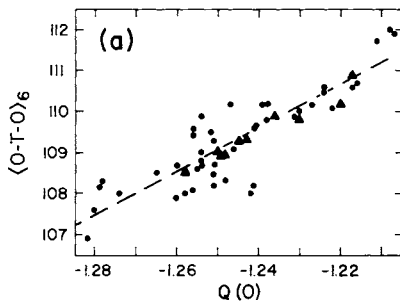
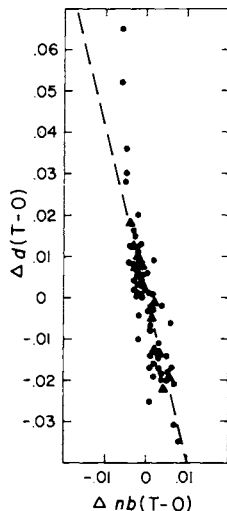


Figure 4. Estimated electrical charge for oxygen $Q(\text{O})$ vs. (a) $\langle \text{O-T-O} \rangle_6$, the average of the six O-T-O angles involving an oxygen in a T-O-T linkage, and (b) $-1/\cos(\angle \text{T-O-T})$. The $Q(\text{O})$ values (Table I) were calculated for the oxygen atoms coordinating the central tetrahedron of a T_4O_{16} cluster.

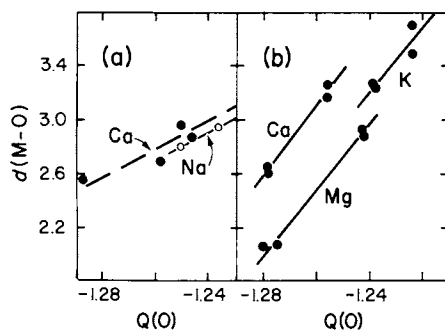


Figure 5. Observed M-O bond lengths ($M = Mg, Na, Ca, K$) vs. the estimated charge on oxygen $Q(O)$ for (a) pitilolite and (b) offretite. In (a), $\circ = Na-O$ bonds, and $\bullet = Ca-O$ bonds.

predominantly ionic in character, an inverse relation between $Q(O)$ and $M-O$ bond length is to be expected. It should be emphasized that partial site occupancy by M cations results in unknown systematic errors in the $M-O$ distances, and that the slopes in Figure 5 should not be interpreted quantitatively. Furthermore, note that small systematic errors in $T-O$ distances and $T-O-T$ and $O-T-O$ angles may result from technical problems of crystal structure refinement when Al,Si substitution occurs, but that such errors are trivial in relation to the above correlations for ptilolite and offretite.

In conclusion, the above discussion indicates that semiempirical molecular orbital theory is a useful model for rationalizing the conformation of the zeolite framework. It may also help in evaluating the role of the framework in sorption, ion exchange and catalysis by providing crude estimates of the charges on the oxygen atoms in the tetrahedral framework.

Acknowledgments

GVG thanks the Earth Sciences Section of the National Science Foundation for grant DES71-00486-A03, EPM thanks the National Research Council of Canada for a supporting research grant, and JVS and JJP thank the Materials Sciences Laboratory (NSF grant CHE75-22451) and Union Carbide Corporation. Prof. P.H. Ribbe read the manuscript and made a number of valuable comments. We also thank R.J. Haycocks, J.A. Speer and I. Baltuska for typing, drafting and technical services.

Literature Cited

1. Dempsey, E., "Molecular Sieves," p. 293, Society of Chemical Industry, London, 1968.
2. Dempsey, E., *J. Phys. Chem.* (1969), 73, 3660-3668.
3. Gibbs, G.V., Louisnathan, S.J., Ribbe, P.H., Phillips, M.W., "The Feldspars," pp. 49-67, Manchester Univ. Press, Manchester, 1974.
4. Cohen, J.P., Ross, F.K., Gibbs, G.V., *Geol. Soc. Am. Abstr. with Progr.* (1975), 1031.
5. Cohen, J.P., Ross, F.K., Gibbs, G.V., *Am. Mineral.* (1977), in press.
6. Collins, G.A.D., Cruickshank, D.W.J., Breeze, A., *J. Chem. Soc., Faraday Trans. II* (1972), 68, 1189-1195.
7. Tossell, J.A., *J. Phys. Chem. Solids* (1973), 34, 307-319.
8. Tossell, J.A., Vaughan, D.J., Johnson, K.H., *Chem. Phys. Letters* (1973), 20, 329-334.
9. Tossell, J.A., *J. Amer. Chem. Soc.* (1975), 97, 4840-4844.
10. Gilbert, T.L., Stevens, W.J., *Phys. Rev. B* (1973), 8, 5977-5998.
11. Pantelides, S.T., Harrison, W.A., *Phys. Rev. B* (1976), 13, 2667-2691.

12. Gramlich, V., Diss. No. 4633, ETH, Zürich (1971).
13. Mortier, W.J., Pluth, J.J., Smith, J.V., *Mat. Res. Bull.* (1975a), 10, 1037-1045.
14. Mortier, W.J., Pluth, J.J., Smith, J.V., *Mat. Res. Bull.* (1975b), 10, 1319-1325.
15. Mortier, W.J., Pluth, J.J., Smith, J.V., *Mat. Res. Bull.* (1976), 11, 15-21.
16. Mortier, W.J., Pluth, J.J., Smith, J.V., *Z. Kristallogr.*, in press.
17. Mortier, W.J., Pluth, J.J., Smith, J.V., *Z. Kristallogr.*, in press.
18. Hoffmann, R., *J. Chem. Phys.* (1963), 39, 1397-1412.
19. Gibbs, G.V., *Abstr., Trans. Am. Geophys. Union* (1975), 56, 1082.
20. Boer, P.F., Newton, M.D., Lipscomb, W.N., *Proc. N.A.S.* (1964), 52, 890-893.
21. Bartell, L.S., Su, L.S., Yow, H., *Inorg. Chem.* (1970), 9, 1903-1912.
22. Gibbs, G.V., Prewitt, C.T., Baldwin, K.J., *Z. Kristallogr.*, in press.
23. Gibbs, G.V., Hamil, M.M., Louisnathan, S.J., Bartell, L.S., Yow, H., *Am. Mineral.* (1972), 57, 1578-1613.

3

Identification and Characterization of Zeolites Synthesized in the $K_2O-Al_2O_3-SiO_2-H_2O$ System

JOHN D. SHERMAN

Union Carbide Corp., Tarrytown Technical Center, Tarrytown, N.Y. 10591

ABSTRACT

Close examination has revealed some confusion in the identification of the various zeolites synthesized in the $K_2O-Al_2O_3-SiO_2-H_2O$ system.

Linde H and Linde M have been found to consist of mixtures of other species. Recent papers have erroneously identified a species as zeolite Z (K-F); in fact, the material most closely resembles Linde F zeolite, not zeolite Z.

Based upon these proper identifications the relationships between the various species reported by different authors have now been clarified.

Introduction

Systematic studies in 1950-1952 of the synthesis of zeolites from gels at low temperatures (50-120°C) in the $K_2O-Al_2O_3-SiO_2-H_2O$ system were undertaken in the Tonawanda Laboratory of Union Carbide Corporation. Several new zeolite phases were discovered (designated herein as Linde F, H, J, L, M, Q and W) (1-7). Additional synthetic zeolite phases K-E, K-F (designated zeolite Z in the patent literature and also herein to avoid confusion), and K-G were subsequently reported by Barrer and Baynham (8,9,10). More recently, another zeolite, K-A, has been reported by Aiello and Franco (11). Because other zeolites provide properties (such as larger pore sizes and pore volumes) of greater practical value, only a few of these eleven zeolites have been studied in any detail (12-22, 26).

Present Studies. During recent syntheses and characterizations of samples of these zeolites, detailed comparisons were made of the X-ray diffraction patterns of the samples and those reported in the literature. Some discrepancies were found in the identification of the various zeolites involved. This led to a detailed examination of some of the zeolite samples synthesized in the early Linde studies and a critical review of the literature. As a result, the nomenclature and relationships among these zeolites have been clarified. The typical properties and relationships among the various zeolites reported by different authors are outlined in Tables I and II and discussed below.

TABLE I
TYPICAL COMPOSITIONS AND SORPTION PROPERTIES OF ZEOLITES SYNTHESIZED IN THE K₂O-Al₂O₃-SiO₂-H₂O SYSTEM

Identification In Present Report	Literature Designation	Typical Composition (Moles/Al ₂ O ₃)			Largest Molecule Sorbed	Approximate Effective Pore Diameter	H ₂ O Sorption		Thermal Stability	
		K ₂ O	SiO ₂	H ₂ O			Temp. (°C)	Pressure (Torr)		Capacity (gms/100 gms active wt)
Zeolite Z (K-F)	K-F (8)	1	2	3	NH ₃ (slowly at 20°C)	2.6 Å	(LOI at 1000°C)	14.3	Decomposed at 600°C/3 days	
	K-F (19)	1	2	3.4	—	—	18	~0.5 P/Po		18.0, 22.0
Linde F	F (1)	1	2	2.9	SO ₂	3.6 Å	25	4.5	Stable to at least 350°C (20)	
	F*						25	4.6		13.0
Linde M (Mixture of F and Kaliophilite)	M (5)	1	2.1	1.7			25	4.5	Stable to at least 350°C (20)	
	M*				SO ₂	3.6 Å				
Zeolite K-G	K-G (8)	1	2.3-4.15	2.6-4.6	CO ₂	3.5 Å	Calculated (from Chem. Analyses)		Stable to 600°C*	
	K-G (19)	1	2.0-4.2	3.8-6.2	—	—	18	~0.5 P/Po		13-20
Linde H (Mixture of Q and K-G)	H (2)	1	2	4	SO ₂	3.6 Å	25	4.5	17.4	Unstable above ~130°C (20)
Linde Q	Q (6)	1	2.2	4.3	SO ₂	3.6 Å	25	4.5	11.5	Unstable above ~130°C (20)
	K-I (19)	1	2	3.8	—	—	18	0.5 P/Po	18.0	Disintegrated at 200°C
	K-I (14)	1	2	4						Decomposes at 168°C
Linde J	J (3)	1	1.9	1.2	SO ₂	3.6 Å	25	25	8.4	Stable to at least 350°C (20)
	K-II (19)	1	2.0	—	—	—	18	~0.5 P/Po	9.0	
Linde L	L (4)	1	6	6	(C ₄ F ₆) ₃ N (slowly at 50°C)	8.1 Å	25	4.5	12.6	
Linde W	W (7)	1	3.6	5.1	SO ₂	3.6 Å	25	4.5	14.4	Stable to at least 250°C (20)
	K-M (19)	1/3.5-4.4; 3.8-4.4					18	~0.5 P/Po	16.4	
	W*						25	17.5	16.4	
Zeolite K-E	K-E (8)	1	4	1	—	—	(LOI at 1000°C)		7.43	—
Zeolite K-A (Mixture of K-E and Kalisilite) (?)	K-A (11)	1	2	4.25	—	—	—	—	—	—

* Present Studies

TABLE II - NOMENCLATURE AND RELATIONSHIPS AMONG ZEOLITES SYNTHESIZED IN THE $K_2O - Al_2O_3 - SiO_2 - H_2O$ SYSTEM

Designation In This Report	Mixtures Identified In The Present Work	U.S. PATENT Designation	DESIGNATION IN TECHNICAL LITERATURE										Related Natural Mineral			
			Barrer & Baynham (1956)	Barrer, Cole & Sticher (1968)	Barrer & Munday (1971)	Barrer & Mainwaring (1972)	Zhdanov & Ovspeyan (1964)	Ovspeyan & Zhdanov (1965)	Taylor & Roy (1964)	Aiello & Franco (1968)	Takahashi & Nishimura (1970)	Bosmans et al. (1973)				
Zeolite Z	---	Z (9)	K-F				K-F	K-F	K-F							Unknown*
Linde F	---	F (1)	K-F	K-F	K-F									B	F	Edingtonite
Linde M	F + Synthetic Kaliophillite	M (5)														---
Synthetic Kaliophillite	---	---	K-D	K-D		K-D										Kaliophillite
Zeolite K-G	---	K-G (10)	K-G	K-G			K-G		K-G				K-Chabazite	C	H	Chabazite
Linde H	Q + K-G	H (2)		K-G+K-I											Q (Impure)	---
Linde Q	---	Q (6)		K-I						K-I				A	Q	Unknown
Linde J	---	J (3)									K-II					Unknown
Linde L	---	L (4)							K-L						L	Unknown
Linde W	---	W (7)	K-M				K-M		K-M			K-H			W	Phillipsite**
Zeolite K-E	---	---	K-E													Analcime
K-A	K-E + Synthetic? Kalsilite	---											K-A			---
Synthetic Kalsilite	---	---	K-N													Kalsilite

*Appears closely related to edingtonite and to Linde F. **Linde W has an X-ray pattern very similar to but different from that of Natural Phillipsite.

Linde F/Zeolite Z (K-F)

The report of the synthesis of zeolite Z (K-F) from gel at 120-150°C by Barrer and Baynham (8,9) was followed later by confirmation of the synthesis from gel at 90°C by Zhdanov and Ovsepyan (12) and from clay at 80°C by Aiello and Franco (11). As may be seen in Figure 1, the reported X-ray patterns are in good agreement. The synthesis of Linde F zeolite was described by Milton (1) and later by Takahashi and Nishimura (13).

A series of recent papers (14-17) described the synthesis of a zeolite designated "K-F", its characterization, and, finally, the determination that it had a framework structure like that of the natural zeolite edingtonite. However, as shown by the comparisons with Linde F zeolite synthesized from gel (present studies) (Figure 1), this zeolite "K-F", the synthesis of which is described in references (14-17), most closely resembles Linde F zeolite.

Further confirmation is provided by comparison of X-ray diffraction patterns of clay-synthesized Linde F (present studies) in both K^+ (as synthesized) and Na^+ exchanged forms, with the X-ray diffraction patterns reported (15) for "K-F" and Na^+ exchanged "K-F" prepared in a similar manner; and also with the computed X-ray powder pattern calculated from the structure reported by Baerlocher and Barrer (17) for the " Na^{ex} K-F". These comparisons are given in Table III. As may be seen, the agreement is excellent. Therefore, it is concluded that the reported (17) structure is that of Linde F and the studies (14-17) were performed on samples most closely resembling Linde F, not zeolite Z [Barrer and Baynham's K-F (8)].

Examination of Figure 1 reveals that zeolites Z and Linde F have similar X-ray patterns. Since the edingtonite framework is very flexible, it may well be that zeolite Z has a distorted structure based upon the same or a closely related framework.

Other reported properties of zeolite Z also differ from those of Linde F. In particular, Na^+ exchange of zeolite Z caused "no appreciable alteration in the lattice" as shown by X-ray diffraction (8). However, as discussed above and shown in Table III, Na^+ exchange of Linde F causes marked alteration of the X-ray diffraction pattern.

Zeolite Z appears to sorb more water than does Linde F, as summarized in Table I. The thermal stability of the K^+ form of Linde F also appears to be much greater than that of zeolite Z. Barrer and Baynham (8) reported the conversion of Z (K-F) to kaliophilite in three days at 600°C; whereas Barrer, Cole and Sticher (14) and Barrer and Mainwaring (16) reported that decomposition of their "K-F" (actually Linde F) did not occur until a temperature of 1095°C was reached in a DTA study. Such a difference cannot be rationalized on the basis of kinetics alone.

Finally, zeolite Z appears to have a smaller effective pore diameter for sorption than does Linde F zeolite. Barrer and Baynham (8) reported that zeolite Z (K-F) sorbed NH_3 very slowly at 20°C, indicating an effective pore diameter of $\sim 2.6 \text{ \AA}$. In contrast to this, Linde F zeolite readily sorbs SO_2 and CO_2 at room temperature, indicating an effective pore diameter of $\sim 3.6 \text{ \AA}$.

It is of interest that the crystal morphologies of both zeolites are very similar. Figure 2a shows the typical tetragonal morphology of the Linde F zeolite (present studies). Barrer and Baynham (8) describe a zeolite Z (K-F) preparation consisting of "small rods", and Aiello and Franco (11) show an electron photomicrograph of their sample of zeolite Z (K-F) revealing a similar morphology. The structural

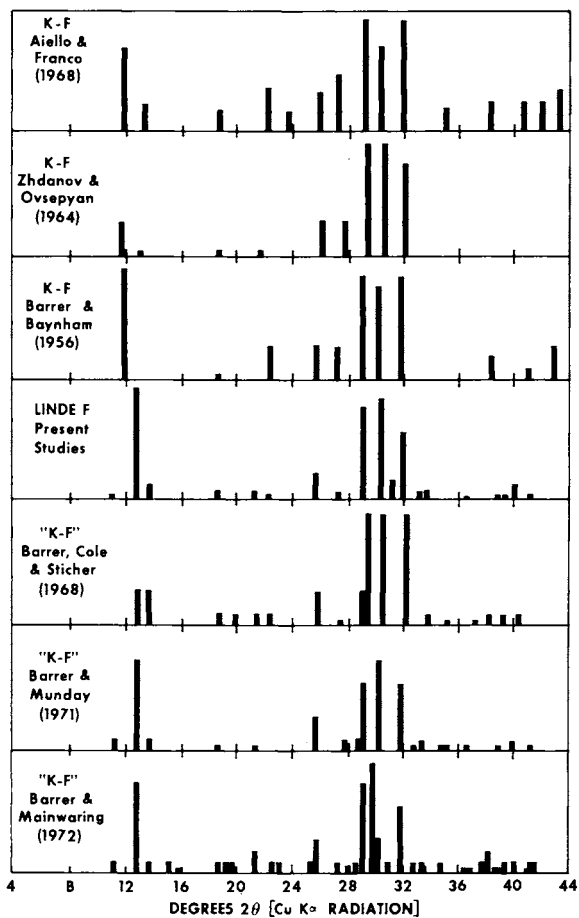


Figure 1. Zeolite Z(K-F)/Linde F

TABLE III. X-RAY POWDER DATA FOR K⁺ AND Na⁺ FORMS OF LINDE F SYNTHESIZED FROM CLAY

K ⁺ FORMS				Na ⁺ EXCHANGED FORMS						
LINDE F (PRESENT STUDIES)		"K-F" BARRER & MUNDAY (1971)		LINDE F (PRESENT STUDIES)		"Na-F" BARRER & MUNDAY (1971)		"Na ^{ex} K-F" CALCULATED FROM STRUCTURE BY BAERLOCHER & BARRER (1974)		
<u>d</u>	<u>l</u>	<u>d</u>	<u>l</u>	<u>d</u>	<u>l</u>	<u>d</u>	<u>l</u>	<u>d</u>	<u>l</u>	<u>hkl</u>
		7.87	W							
6.94	100	6.94	S	7.14	100	7.10	S	7.11	100	110
6.51	13	6.52	W	6.66	15	6.66	M	6.68	25	001
								5.56	4	101
								5.03	1	200
4.80	8	4.78	VW	4.90	17	4.89	M	4.87	17	111
4.17	6	4.18	VW			4.47	VW	4.50	1	210
4.00	4			4.00	5	4.27	VW	4.02	6	201
						4.03	W	3.73	2	211
3.49	22	3.48	M	3.56	12	3.57	MW	3.56	8	220
				3.52 ^{sh}	7					
3.28	7	3.22	W	3.34	5	3.35	W	3.34	4	002
		3.20	VW							
				3.14	94	3.19	W	3.17	14	102, 310
3.11	6	3.11	W			3.15	VS	3.14	62	221
3.09	75	3.08	MS							
2.97	87	2.97	S	3.02	28	3.03	MS	3.02	18	112
2.81	56	2.82	MS	2.88	25	2.88	MS	2.87	18	311
		2.74	VW							
2.68	8	2.69	VW							
2.57	3	2.58	VW							
		2.56	VW			2.56	VW	2.57	1	321
2.46	4	2.46	VW							
				2.52	6	2.52	MW	2.51	3	400
				2.44	8	2.44	MW	2.43	4	222, 410
								2.37	1	302
								2.35	1	401
2.32	5	2.32	VW	2.30	6	2.31	MW	2.30	3	312
2.26	10	2.26	W							
				2.24	4	2.25	W	2.25	2	420
		2.19	VW			2.24	W	2.23	3	331
1.90	4	1.86	VW							
				2.13	3	2.14	VW	2.14	2	322
						2.13	VW	2.12	3	113, 421
						2.01	W	2.01	2	402
								2.00	1	213
1.85	5			1.90	9	1.89	MW	1.89	5	223
						1.87	W	1.86	1	422
						1.83	VW	1.82	1	313
1.74	10	1.74	W	1.78	19	1.78	M	1.78	8	440
				1.73	5	1.73	MW	1.725	1	530
						1.72	VW	1.718	1	441
1.69	9			1.70	4			1.698	2	512
1.67	5							1.670	2	004
								1.623	3	333, 601, 114
								1.590	1	620
								1.585	1	204
								1.547	4	621

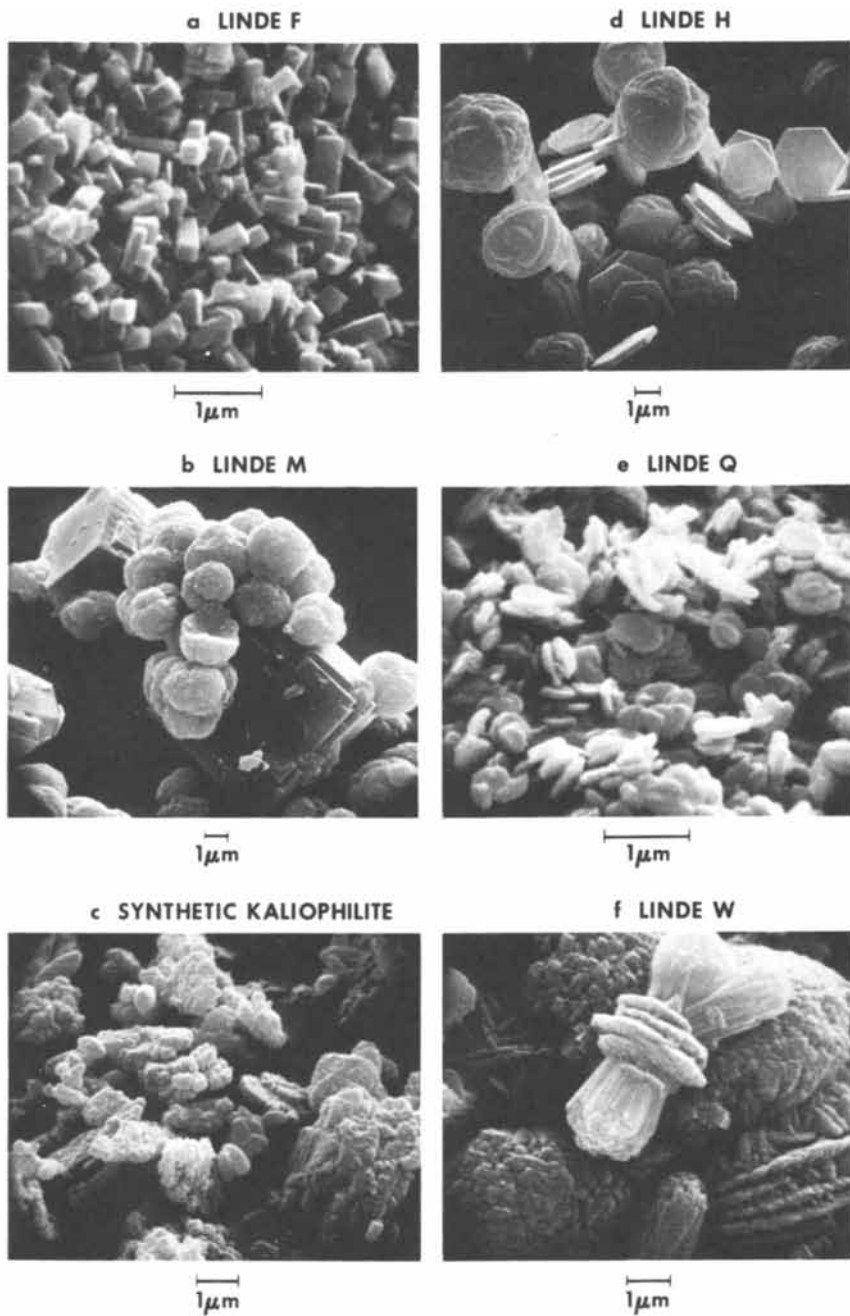


Figure 2.

relationships between zeolite Z and Linde F are not clear. Further study is needed to resolve this question.

Linde F/Linde M/Kaliophilite

The synthesis of Linde M was described by Breck and Acara (5), and it was later shown by Breck and Flanigen (18) that Linde M forms in a portion of the same composition field in which Linde F is synthesized. Barrer, Cole and Sticher (14) concluded later that Linde M is the same as "K-F". But, as discussed above, their "K-F" of reference (14) is identical with Linde F, not zeolite Z (K-F).

To resolve these questions, the original sample of Linde M (5) was obtained and examined. From comparisons of the X-ray diffraction patterns shown in Figure 3, it is concluded that Linde M is a mixture of Linde F and synthetic kaliophilite.

Scanning electron microscopy (SEM) also confirms that this Linde M sample contains particles with two different morphologies (Figure 2b): block-shape crystals of Linde F and rounded intergrown agglomerates of synthetic kaliophilite. The latter are larger but similar in appearance to those found in a synthesis of pure synthetic kaliophilite (Figure 2c). Water sorption and NH_4^+ ion exchange data also confirm the above conclusions and indicate that the fraction of Linde F present ranges from ~25 to 50% in the Linde M samples examined.

Linde Q/Linde H/Zeolite K-G

Breck and Acara (6) reported the synthesis of Linde Q. On the basis of the comparisons in Figure 4, it is concluded that zeolite K-I later reported by Zhdanov and Ovsepyan (12,19), and Barrer, Cole and Sticher (14), is identical to Linde Q. Barrer, Cole and Sticher (14) also noted that they consistently synthesized mixtures of zeolite K-G and zeolite K-I and concluded that Linde H (2) is the same mixture.

The original sample of Linde H described by the X-ray pattern (2) was obtained and examined by X-ray diffraction and scanning electron microscopy. As shown in Figure 4, Linde H is indeed a mixture of Linde Q and zeolite K-G, the latter being similar to, but not identical with, natural chabazite.

SEM reveals that this Linde H sample (Figure 2d) contains particles with two different morphologies: hexagonal plates of Linde Q and rounded spherulites of interpenetrating twins of zeolite K-G. A separate synthesis of pure Linde Q gave very small, poorly formed hexagonal plates (Figure 2e). However, the morphology of the Linde Q in Figure 2d is identical to that reported by Zhdanov and Ovsepyan (12) for Linde Q (K-I). The picture given by Barrer, Cole and Sticher (14) for Linde Q (K-I) showed a morphology more similar to that shown in Figure 2e. The morphology of zeolite K-G shown in Figure 2d is identical to that shown by Barrer and Mainwaring (16).

Single crystal electron diffraction studies by J. M. Bennett of one of the hexagonal Linde Q platelets (in the sample of Linde H) gave the following results: hexagonal symmetry, $\underline{a} = 13.37 \pm 0.09 \text{ \AA}$, $\underline{c} = 26.45 \pm 0.12 \text{ \AA}$. This is in excellent agreement with the results of Zhdanov and Ovsepyan (12) who found hexagonal symmetry with $\underline{a} = 13.41 \pm 0.02 \text{ \AA}$ and $\underline{c} = 13.2 \pm 0.2 \text{ \AA}$ (based on indexing of the powder pattern). The doubling of \underline{c} shown by our electron diffraction results may well be due to Si/Al ordering in this zeolite (which has Si/Al \cong 1).

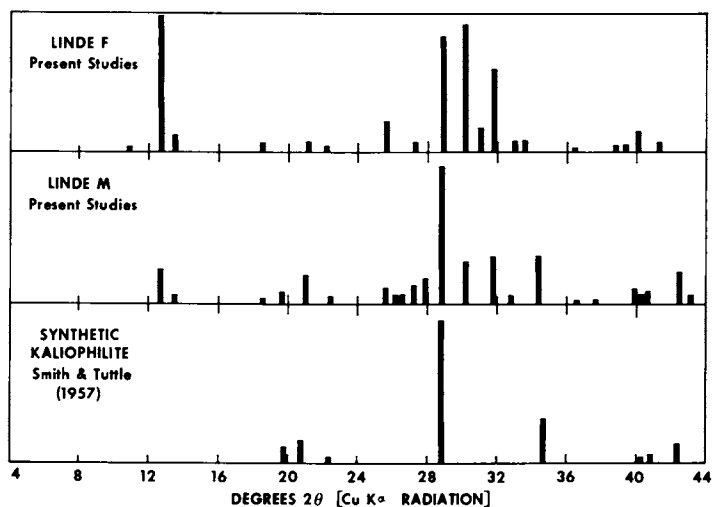


Figure 3. *Linde F/Linde M/synthetic kaliophillite*

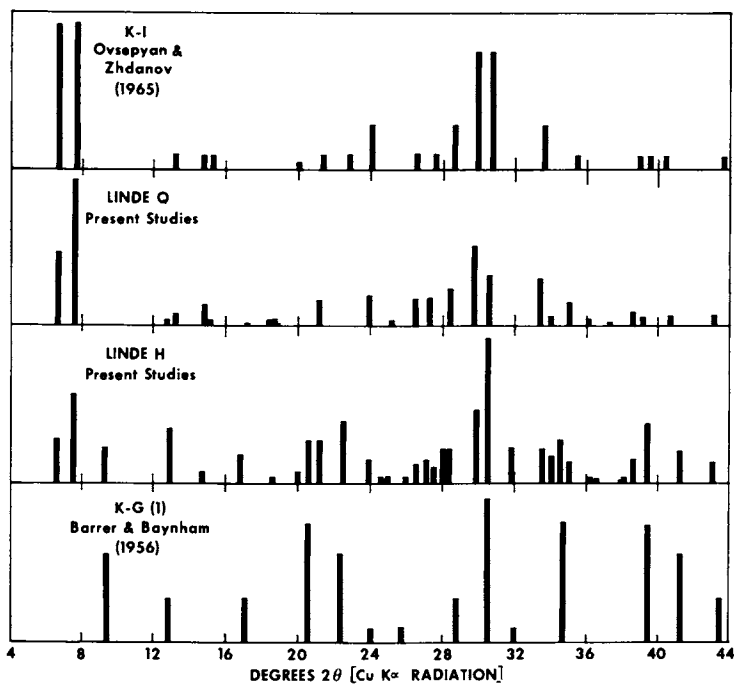


Figure 4. *Linde Q/Linde H/Zeolite K-G*

The low thermal stability of Linde H is also in agreement with these conclusions, and is clearly due to the low thermal stability of the Linde Q portion of the mixture (see Table I).

Linde W/Phillipsite/Zeolite K-G

The synthesis and properties of Linde W were described by Milton (7). Barrer and Baynham (8) also described the synthesis of a zeolite K-M. A sample of the latter zeolite was obtained, examined, and found to be essentially identical with the Linde W synthesized earlier (20).

The X-ray powder patterns of the various zeolites found to be identical with Linde W are given in Figure 5. Comparison is also given with natural phillipsite, zeolite ZK-19, and both synthetic (K-G) and natural chabazite. The latter are included because zeolite K-G has a similar composition and might occur as an impurity in the synthesis of Linde W. Consideration of Figure 5 confirms that the zeolite K-M of Barrer et al. (8,16,22) and the zeolite K-H of Taylor and Roy (21) are identical with Linde W. Also, Linde W is very similar to natural phillipsite.

However, the X-ray patterns for Linde W and phillipsite differ, for example, in the existence in the Linde W of a line at $d = 9.94 \text{ \AA}$. It was believed that this might be due to the presence of a chabazite-type (K-G) impurity with the Linde W. However, close comparison (see Figure 5) with the X-ray pattern for K-G and with that calculated from the chabazite structure of J. V. Smith et al. (23) leads to the conclusion that the discrepancies between the Linde W and phillipsite patterns are not due to a chabazite type impurity. On the other hand, the X-ray powder pattern for zeolite ZK-19 [Kuehl (24)] most closely resembles that of natural phillipsite. [Note: ZK-19 is synthesized in the $K_2O \cdot Na_2O \cdot (K,Na)_3PO_4 \cdot Al_2O_3 \cdot SiO_2 \cdot H_2O$ system.]

SEM also indicates that Linde W comprises a single phase, consisting of "wheatsheaf" bundles as shown in Figure 2f. Therefore, it is concluded that Linde W zeolite has a structure related to, but different from, that of natural phillipsite. Further study is needed to determine the exact structure of Linde W.

K-E/K-A/Kalsilite

Barrer and Baynham (8) described the synthesis from gel of a hydrated potassium zeolite, K-E ($K_2O \cdot Al_2O_3 \cdot 4SiO_2 \cdot H_2O$), having an X-ray powder pattern very close to the zeolite mineral analcime ($Na_2O \cdot Al_2O_3 \cdot 4SiO_2 \cdot 2H_2O$). Aiello and Franco (11) reported the synthesis of a new zeolite, K-A ($K_2O \cdot Al_2O_3 \cdot 2SiO_2 \cdot 4.25H_2O$), from halloysite. The K-A phase was found in a single preparation and subsequent attempts to repeat the synthesis were unsuccessful (25). No other reports of the synthesis of K-A have been found.

Comparison of the X-ray patterns for K-E and K-A reveals great similarity between the two. Furthermore, many of the remaining lines are identical with those of synthetic (K-N) or natural kalsilite. Therefore, it appears that K-A might be a mixture of K-E and kalsilite. Further study of the K-A sample should be of value. If it is indeed a single phase, further attempts to repeat the synthesis would appear desirable.

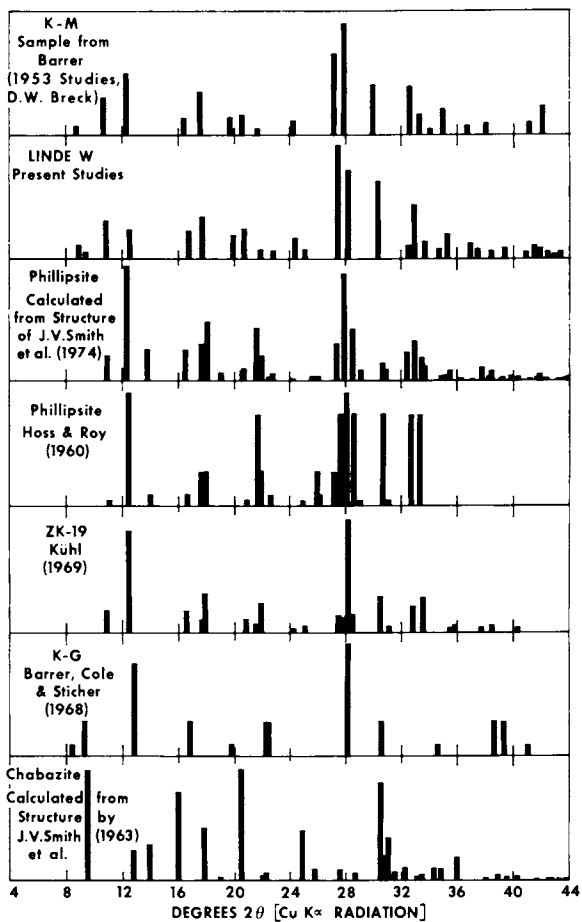


Figure 5. Linde W/phillipsite/chabazite zeolites

Other K⁺ Zeolites

Critical examination of unpublished data and literature reports of the syntheses of other zeolites synthesized in the K₂O-Al₂O₃-SiO₂-H₂O system has confirmed that the zeolite Linde J [Breck and Acara (3)] is a pure phase. Zeolite K-II of Ovsepyan and Zhdanov (19) appears identical to Linde J. Linde L [Breck (4)] has received detailed study (18) establishing that it is a pure phase.

The conclusions from the present studies relating the zeolite phases reported by various authors are summarized in Table II. The identifications of the zeolite phases of Bosmans et al. (26) are based upon examination of copies of the X-ray powder patterns kindly provided by Professor Bosmans (33).

Conclusions

Of eleven zeolites reported synthesized in the K₂O-Al₂O₃-SiO₂-H₂O system, one (Linde H) has been shown to consist of a mixture of two other zeolites (Linde Q and K-G), and another (Linde M) is a mixture of Linde F and kaliophilite. The existence of another zeolite (K-A) has not been confirmed and it is noted that it might be a mixture of a zeolite (K-E) and kalsilite. Therefore, the list simplifies to eight clearly distinguishable zeolite phases [K-E, F, K-G, J, L, Q, W and Z (K-F)] plus one (K-A) yet to be confirmed.

It has been found that all of the other zeolite phases reported synthesized in this system are identical with, or mixtures of, the eight confirmed zeolite species (see Table II).

Recent papers (14-17) describing the structure (edingtonite-type framework) and properties of zeolite "K-F" have, in fact, dealt with samples most closely resembling the Linde F zeolite, not zeolite Z (K-F). However, Linde F and zeolite Z (K-F) appear to have related framework structures. Finally, Linde W zeolite is shown to be closely related to but different in structure from natural phillipsite. The structures of Linde Q and Linde J zeolites are also unknown.

It is hoped that these results will aid others involved in studies of these zeolites and encourage orderly development in a heretofore somewhat confused synthesis field.

Acknowledgements

The author is indebted to Dr. D. W. Breck for noting the need for the Linde H studies and many stimulating discussions. The efforts of Dr. J. M. Bennett for electron diffraction studies, and R. W. Grose for calculations of X-ray powder patterns, are gratefully acknowledged. The effort and skill of D. A. Cook (shown in the SEM pictures of Figure 2) is greatly appreciated. Finally, the assistance of Dr. C. C. Chao and A. J. Gioffre, Jr., made possible the completion of the manuscript in digestible form.

Literature Cited

- (1) Milton, R. M., Zeolite F, U.S. Patent 2,996,358 (1961).
- (2) Milton, R. M., Zeolite H, U.S. Patent 3,010,789 (1961).
- (3) Breck, D. W., and Acara, N. A., Zeolite J, U.S. Patent 3,011,869 (1961).
- (4) Breck, D. W., Zeolite L, U.S. Patent 3,216,789 (1965).

- (5) Breck, D. W., and Acara, N. A., Zeolite M, U.S. Patent 2,995,423 (1961).
- (6) Breck, D. W., and Acara, N. A., Zeolite Q, U.S. Patent 2,971,151 (1961).
- (7) Milton, R. M., Zeolite W, U.S. Patent 3,012,853 (1961).
- (8) Barrer, R. M., and Baynham, J. W., J. Chem. Soc. (1956), 2882-2891.
- (9) Barrer, R. M., and Baynham, J. W., Zeolite Z, U.S. Patent 2,972,516 (1961).
- (10) Barrer, R. M., and Baynham, J. W., Zeolite K-G, U.S. Patent 3,056,654 (1962).
- (11) Aiello, R., and Franco, E., Rend. Accad. Sci. Fis. Mat., Naples (1968), 35, 165-192.
- (12) Zhdanov, S. P., and Ovsepyan, M. E., Dokl. Akad. Nauk SSSR (1964), 157 (4), 913-916.
- (13) Takahashi, H., and Nishimura, Y., Nippon Kagaku Zasshi (1967), 88, 528; (1968), 89, 378; and (1970), 91, 23.
- (14) Barrer, R. M., Cole, J. F., and Sticher, H., J. Chem. Soc. (A) (1968), 2475-2485; and U.S. Patent 3,663,164 (1972).
- (15) Barrer, R. M., and Munday, B. M., J. Chem. Soc. (A), (1971), 2914-2921.
- (16) Barrer, R. M., and Mainwaring, D. E., J. Chem. Soc., Dalton Trans., (1972), (12), 1254-1259.
- (17) Baerlocher, Ch., and Barrer, R. M., Z Kristal, (1974), 140, 10-26.
- (18) Breck, D. W., and Flanigen, E. M., "Molecular Sieves", p. 47, Soc. of Chem. Ind., London (1968).
- (19) Ovsepyan, M. E., and Zhdanov, S. P., "Zeolites. Their Synthesis, Properties, and Applications", Dubinin, M. M., and Plachenov, T. G., eds., (1964), pp. 2-10 through 2-15, Transl. by International Information, Inc.
- (20) Breck, D. W., Union Carbide Corp., unpublished results (Jan. 12, 1953).
- (21) Taylor, A. M., and Roy, R., Amer. Mineral. (1964), 49, 656.
- (22) Barrer, R. M., Baynham, J. W., Bultitude, F. W., and Meier, W. M., J. Chem. Soc. (London) (1959), 195.
- (23) Smith, J. V., Rinaldi, F., and Dent Glasser, L. S., Acta Crystallogr. (1963), 16, 45.
- (24) Kuehl, G. H., Amer. Mineral (1969), 54, 1607.
- (25) Aiello, R., personal communication (June, 1976).
- (26) Bosmans, H. J., Tambuyzer, E., Paenhuys, J., Ylen, L., and Vancluysen, J., Advances in Chemistry Series No. 121, (Mol. Sieves, Int. Conf. 3rd), (1973), 179-188.
- (27) Smith, J. V., and Tuttle, O. F., Amer. J. Sci. (1957), 255, 282.
- (28) Bannister, F. A., Mineralog. Mag. (1931), 22, 569-608.
- (29) Gude, A. J., and Sheppard, R. A., Amer. Mineral. (1966), 51, 909.
- (30) Rinaldi, R., Pluth, J. J., and Smith, J. V., Acta. Crystallogr. (1974) B30, 2426.
- (31) Knowles, C. R., Indian Mineral. (1965), 6, 127.
- (32) Taylor, W. H., Z. Kristal. (1930), 74, 1.
- (33) Bosmans, H. J., personal communication (Oct., 1973).
- (34) Hoss, H., and Roy, R., Beitr. Mineral. Petrogr. (1960), 7, 389.

Properties of Synthesized, Ion-Exchanged, and Stabilized Zeolite Rho

W. H. FLANK

Union Carbide Corp., Molecular Sieve Dept., Tarrytown Technical Center,
Tarrytown, N.Y. 10591

ABSTRACT

Zeolite rho and some of its modifications, including a stabilized form, have been characterized by infrared, sorption, x-ray and thermal techniques. The structure is less open than expected. A distorted structure is suggested, containing two unequal non-intersecting pore networks. Evidence is presented for the presence of a zeolitic H_3O^+ species, and for acidic OH groups. Considerable framework elasticity during sorption-desorption is indicated.

Introduction

The synthesis and characterization of a crystalline zeolite designated zeolite rho has been described by Robson and co-workers(1). The structure initially proposed for this material is that of a cubic array of α -cages linked by double 8-rings. Further characterization, using infrared, sorption, x-ray and thermal analysis techniques, was undertaken to examine in more detail the properties of this material and some of its modifications.

Experimental

The Cs, Na-form of zeolite rho was prepared in accordance with published procedures(1). Ion exchange with 1.25N NH_4Cl solution was accomplished by multiple exchange treatments at reflux temperature, followed by washing with 1% NH_4OH solution. A portion of the NH_4 -rho was stabilized by placing it in a furnace at 523K purged with an 80% steam in air mixture, and raising the temperature to 923K for one hour. Conventional wet chemical analyses were performed on these samples.

Gravimetric sorption data were taken with a quartz spring balance contained in a conventional high-vacuum system. Adsorption data were obtained for n-butane and water at 296K and oxygen at 90K, using vacuum-activated samples of stabilized rho, Cs, Na-rho, NH_4 -rho and NH_4 -rho which had been pre-calcined in air at various temperatures. Additional data were also obtained on samples conventionally exchanged with a number of different ions.

DTA curves were obtained on 50 mg samples with a duPont Model 990 Thermal Analyzer programmed at 10K/min. and air-purged at a rate of 38 $\text{cm}^3/$

min. TG curves on 25.0 mg samples were obtained using a duPont Model 951 TG Analyzer at the same conditions. The latter curves were recorded on a temperature corrected chart, while the former were recorded on a chart which was linear in millivolts.

Infrared spectra were taken with self-supporting wafers after evacuation at room temperature, 523K and 773K, using a Perkin-Elmer Model 225 double-beam instrument. Acid activity and acid strength were examined by observation of band changes after admitting propylene into the infrared cell. The framework region was investigated with pressed KBr discs. Some of the hydroxyl region spectra were obtained with a Perkin-Elmer Model 112 single-beam spectrophotometer.

X-ray powder data were obtained at various conditions using a Norelco diffractometer equipped with a graphite monochromator and pulse height analyzer. A silicon internal standard was used in obtaining the data for calculation of cubic lattice parameters.

Results and Discussion

Chemical Analysis. Data for three forms of zeolite rho are shown in Table I. Some carbonate is frequently present in the synthesized material, and would be expected to remain in the NH_4^+ -exchanged and stabilized forms. (The small band at about 1350 cm^{-1} in the infrared spectra also indicates the presence of cesium carbonate.) Incomplete washing of the NH_4^+ -exchanged sample is also evident, but excess NH_4Cl would not be expected to remain after calcination.

The carbonate-corrected cation to alumina ratio in the as-synthesized sample is 1.02, in agreement with the value of 1.02 reported by Robson et al. (1). There is good agreement in the $\text{SiO}_2/\text{Al}_2\text{O}_3$ ratio (5.86 vs. 5.8). Their molar $\text{Na}_2\text{O}/\text{Cs}_2\text{O}$ value of 3.25, however, differs from the 2.64 reported here, where the carbonate is considered to be present as Cs_2CO_3 . The carbonate- and chloride-corrected cation to alumina ratio for the NH_4^+ -exchanged sample is a reasonable 0.98. An increase in the $\text{SiO}_2/\text{Al}_2\text{O}_3$ molar ratio of the exchanged product was observed, which might be due to aluminum leaching, either from the framework or from unreacted gel, or hydrolysis during the exchange treatment.

It might be noted that essentially all of the Na^+ and most of the Cs^+ were exchanged out of the structure, in contrast to the earlier report that exchange with NH_4^+ removes substantially all of the Cs^+ and over 90% of the Na^+ content of the synthesized product. However, if the cesium in the NH_4^+ -exchanged material is present as carbonate, as appears likely, then the exchanged product is essentially all in the ammonium form.

Adsorption Measurements. It was found that little oxygen sorption occurred with the Cs, Na-form, samples exchanged with monovalent, divalent or trivalent metal cations, or with the NH_4^+ -exchanged form calcined at 623K in vacuum. Water sorptive capacity, however, was appreciable in all of these samples and apparently approached complete void-filling for the calcined NH_4^+ -form, as shown in Table II. This last result may be an artifact, however, and may be due to rehydration of defect aluminum sites. The kinetic diameters for oxygen and water are 3.46 Å and 2.65 Å, respectively(2). The sharp difference in capacities for both n-butane (4.3 Å kinetic diameter) and oxygen between NH_4^+ -rho heated to 623K and NH_4^+ -rho heated to 673K, shown in Table III, indicates that there

TABLE I
CHEMICAL ANALYSIS AND MOLAR RATIO DATA
FOR ZEOLITE RHO SAMPLES

SAMPLE	WT. PERCENT (ANHYDROUS BASIS)						
	Na ₂ O	Cs ₂ O	(NH ₄) ₂ O	SiO ₂	Al ₂ O ₃	C	Cl ⁻
Cs, Na - RHO	7.6	16.8	< 0.1	58.7	17.0	0.15	—
NH ₄ - RHO	< 0.1	3.2	11.2	67.8	18.1	—	2.8
STABILIZED RHO	< 0.1	3.6	< 0.1	75.8	20.4	—	—

SAMPLE	MOLES PER MOLE Al ₂ O ₃						
	Na ₂ O	Cs ₂ O	(NH ₄) ₂ O	SiO ₂	Al ₂ O ₃	C	2Cl ⁻
Cs, Na - RHO	0.74	0.36	—	5.86	1.00	0.08	—
NH ₄ - RHO	—	0.07	1.22	6.35	1.00	—	0.22
STABILIZED RHO	—	0.06	—	6.31	1.00	—	—

TABLE II
SORPTIVE PROPERTIES OF ION-EXCHANGED FORMS OF ZEOLITE RHO^(a)

ION EXCHANGED FORM	O ₂ ADSORPTION AT 90K, 750 TORR		H ₂ O ADSORPTION AT 296K, 20 TORR	
	WT. PERCENT	VOLUME, cm ³ /g	WT. PERCENT	VOLUME, cm ³ /g
(Cs, Na) ^{+(b)}	4.1	0.04	23.3	0.23
NH ₄ ⁺	5.9	0.05	31.5	0.32
Li ⁺	4.7	0.04	23.1	0.23
Na ⁺	4.8	0.04	24.5	0.25
K ⁺	2.6	0.02	21.9	0.22
Mg ⁺⁺	4.7	0.04	24.3	0.24
Ca ⁺⁺	4.3	0.04	27.0	0.27
La ⁺⁺⁺	4.5	0.04	23.3	0.23

(a) ALL SAMPLES ACTIVATED IN VACUUM AT 623K.

(b) AS-SYNTHESIZED FORM

are different kinds of cation exchange sites or positions present, and that only some of the NH_4^+ ions were decomposed at the lower temperature. Complete removal of NH_4^+ ions appears to have occurred only after the high-temperature stabilization treatment.

The data in Table III also show that calcined NH_4 -rho is unstable with respect to water vapor. The measured oxygen and n-butane adsorptive capacities are significantly lower for a vacuum-activated sample which has previously been exposed to water. In contrast, stabilized rho was found not to be adversely affected by exposure to water. The measured oxygen adsorption capacity upon re-activation following exposure to water was within 0.1 relative percent of that for the freshly stabilized material.

Adsorption of n-butane was found to be quite low, approaching 50% of the calculated(3) maximum pore volume of $0.33 \text{ cm}^3/\text{g}$ only for NH_4 -rho samples heated above 673K. After exposure to water and re-activation, such samples generally showed about twice as much loss in n-butane capacity as the loss in oxygen capacity. The maximum size of an 8-ring aperture in a zeolite framework (4) is the same as that of the n-butane molecule. Low adsorption has also been reported for hexane(1), which has the same 4.3 Å kinetic diameter as butane. Zeolite A, which has an 8-ring aperture, adsorbs neither of these molecules at room temperature, most likely because of the presence of cations. If zeolite rho has an 8-ring aperture, then adsorption of such molecules in a structure where the cations have been removed could be expected. Zeolite ZK-5, which appears to have an 8-ring aperture and a dual non-intersecting pore network, after calcination to remove the organic base, adsorbs about 70% of the expected amount of n-hexane(5). However, it is possible that a distorted rho structure containing two non-intersecting three-dimensional pore networks with 8-ring apertures, as was suggested earlier(1), could explain the butane sorption results if the pore networks were unequal, with one allowing, and the other not allowing, passage of the butane molecule. This would be compatible with the thermal and x-ray results discussed below.

Thermal Analysis Data. Curves for the Cs-Na, NH_4 -exchanged and stabilized forms of zeolite rho are shown in Figures 1 and 2. The most noteworthy feature is the presence of hydroxyl groups thermally stable to about 1000K, which are present in the NH_4 -exchanged and stabilized forms. The weight loss associated with these amounts to 2.0% for the NH_4 -exchanged form (on a deaminated basis) and 1.9% for the stabilized form. Endotherms corresponding to these weight losses are clearly evident. A hydroxyl density of about 12×10^{20} per gram of dehydrated zeolite can be calculated for the stabilized material.

It can also be noted that completion of deamination occurs beyond 800K, in agreement with the observations of both Robson and Kerr(6). The present data indicate that two different ammonium ion sites are most likely present in the NH_4 -exchanged product. The endotherm centered at about 610K and the exotherms at about 680K and 765K are not evident in the other zeolite rho forms. There is obviously overlap between these peaks, but the transition from one to the other in the DTA curve corresponds well with the inflection seen in the TG curve at 635K. Alternative explanations involving hydration spheres, hydrolysis, impurities or secondary reactions do not seem to correspond with the heats of reaction or the magnitude of the phenomena involved. Differences based upon distortion of the structure may be more plausible, and would be compatible with the observed

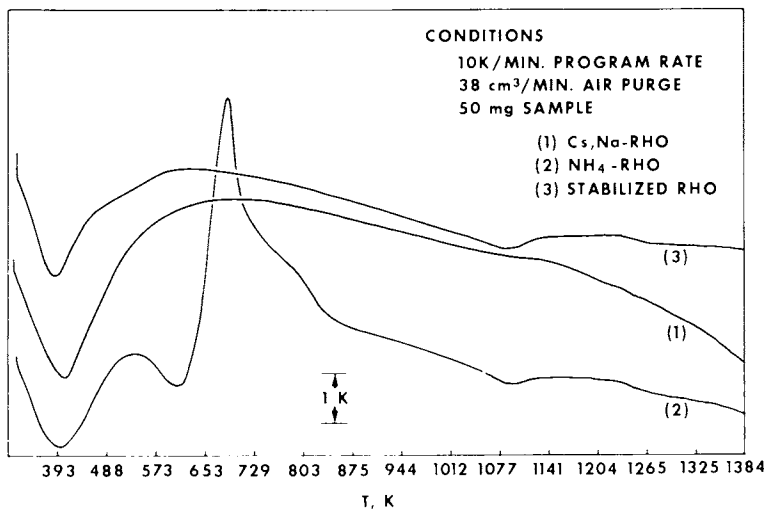


Figure 1. DTA curves for zeolite Rho samples

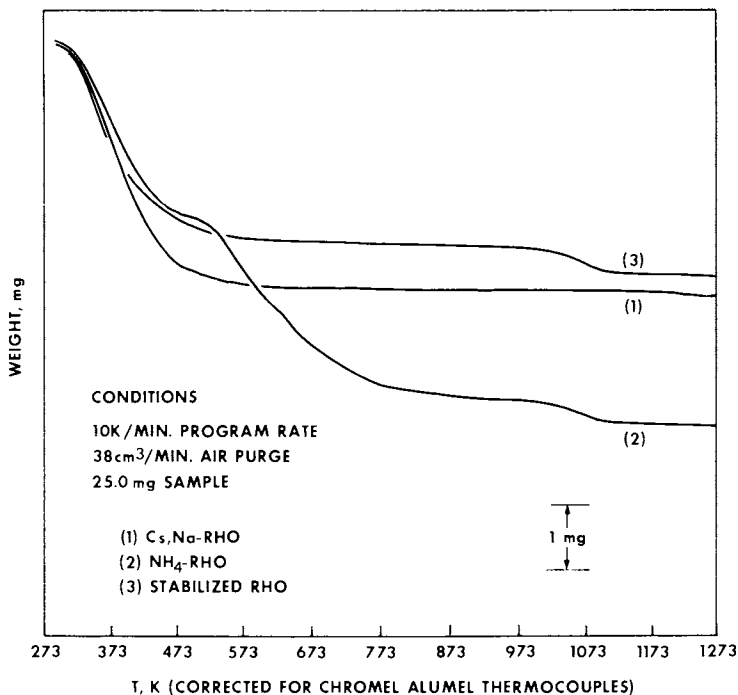


Figure 2. TG curves for zeolite Rho samples

**American Chemical
Society Library**

1155 16th St. N. W.

Washington, D. C. 20036

extended deamination temperature range.

The zeolite rho framework appears to be thermally stable in air to about 1230K. The weight loss due to high-temperature dehydroxylation is about 20% less, or about 0.53 H₂O/Al₂O₃, than would be expected by analogy with similarly treated zeolite Y, which loses about 0.64 H₂O/Al₂O₃ under the same conditions (7), suggesting that the calcined rho structure may be somewhat more defective than the corresponding zeolite Y structure.

Infrared Studies. Several different types of experiments were performed to further characterize the hydroxyl groups indicated by the thermal data. The as-synthesized product showed only a small band at 3740 cm⁻¹ attributable to amorphous silica, and some adsorbed water removable by vacuum activation at 523K. The NH₄⁺-exchanged product, after vacuum activation at 773K, showed, in addition to the small 3740 cm⁻¹ band, a strong band at 3620 cm⁻¹ which has been assigned to a hydroxyl group vibration. The environment of this group has not been clearly defined, however. A very small band at 1420 cm⁻¹ was also observed, indicating that a small amount of NH₄⁺ was still present, in agreement with the thermal data.

The stabilized product exhibited a strong band at 3640 cm⁻¹ which was also not removed by vacuum activation at 523K (which did remove the physisorbed water, however), nor at 773K. The slightly increased size of the 3740 cm⁻¹ band in this material suggests that steaming has effected some aluminum hydrolysis and tetrahedral vacancy formation(8). It can also be noted that the hydroxyl band has shifted 20 cm⁻¹; this can be interpreted as evidence for a change in the structure, or at least a distortion of it.

Exposure of NH₄⁺-exchanged rho and stabilized rho samples, after vacuum activation at 773K, to a 30 torr propylene atmosphere showed that the hydroxyl groups of both materials cause polymerization to occur, but that, in both cases, only a small portion of the hydroxyls interact with the propylene. Broad bands due to hydrogen-bonding between the hydroxyls and the propylene appeared at 3260 cm⁻¹ with the NH₄-rho, and at 3360 cm⁻¹ with the stabilized rho. The bond strength of the O—H bond (as measured by the magnitude of the frequency shift due to hydrogen-bonding of the hydroxyl group) has been related to acid strength. This shift is more pronounced in the NH₄-rho (360 cm⁻¹) than in the stabilized rho (280 cm⁻¹), indicating that the former is more strongly acidic than the latter. This might be due to differences in the environment of some of the aluminum atoms resulting from the stabilization treatment.

Differences in the framework region were also observed between the Cs, Na-rho, the NH₄-rho and the stabilized rho forms. The band positions in cm⁻¹ for these samples are as follows:

Cs, Na-rho	1040	798	730	620	520	432
NH ₄ -rho	1052	804	730	590		440
Stabilized rho	1070	818		605		442

Band shifts, especially for bands in the vicinity of 1050 cm⁻¹ and 800 cm⁻¹, have been related to removal of aluminum from the framework, with higher frequencies being associated with increased SiO₂/Al₂O₃ molar ratios(7,9,10). Some aluminum removal appears to have occurred upon 773K vacuum activation of the NH₄-rho sample, but substantially more seems to have occurred in the stabilized

sample. Additionally, some of the bands in the stabilized sample are broadened and less intense than in the other samples, suggesting some change of ordering in the structure.

It was noted that the spectrum of NH_4 -rho showed a small band at $\sim 1685\text{ cm}^{-1}$. When the sample was exposed to D_2O , the band disappeared and then re-appeared upon subsequent exposure to water vapor, along with the commonly observed physisorbed water band at $\sim 1640\text{ cm}^{-1}$, as shown in Figure 3. Corresponding changes in the broad hydroxyl region at higher frequency were also seen. The band at 1685 cm^{-1} could also be removed by thermal treatment. This may constitute the first experimental evidence for the postulated presence (11) of an H_3O^+ species in zeolites. The predicted position for an H_3O^+ deformation band is $\sim 1690\text{ cm}^{-1}$, with a diffuse hydroxyl band in the region $2500\text{--}3500\text{ cm}^{-1}$, based on salt spectra(12,13). The presence of H_3O^+ has also been established in mineral structures recently, at a slightly higher frequency(14).

X-ray Diffraction Data. The powder patterns for hydrated and dried samples of Cs, Na-rho, dried NH_4 -rho and stabilized rho show that peak intensities change substantially upon hydration of the Cs, Na-form (indicative of considerable movement in the structure), while ion exchange with NH_4^+ results in much higher overall intensity, presumably as a consequence of the removal of cesium. The stabilized form has peak intensities about equal to those of the NH_4 -form, with the [110] peak being much more intense, suggesting that stabilization does not introduce a substantial degree of disorder into the structure. Broadening was noted, however, in the stabilized rho pattern.

The instability of the deaminated NH_4 -form was strikingly seen in the x-ray diffraction pattern for an NH_4 -rho sample which had been calcined at 813K and then exposed to moisture. The intensity of the pattern was reduced by more than an order of magnitude and a considerable amount of amorphous material was evident. This effect is in agreement with the sorption data discussed above, where the behavior of the deaminated and stabilized forms were contrasted.

Judging from the width of some of the peaks in the powder patterns, especially those where overlapping occurs, it appears possible that the rho structure is actually pseudo-cubic, or near-cubic, rather than fully cubic, as suggested earlier(1) and discussed above. Typical dry and humidified Cs, Na-form patterns, together with a stabilized rho pattern, are shown in Figure 4. Apparent impurities present at low levels in the materials prepared include zeolite B, pollucite, quartz, and possibly a trace of zeolite Y.

Of particular interest are the changes in the calculated cubic unit cell parameters that occur as a result of ion exchange, stabilization, and hydration-dehydration. Table IV shows a comparison of these data. The Cs, Na-rho unit cell apparently expands upon hydration by more than 0.4 Angstrom units, or almost 3%. This appears to be one of the largest changes reported so far. (Framework reconstruction or phase transition does not appear to take place in zeolite rho, in contrast to the behavior of thermally dehydrated zeolite B(15), which also exhibits substantial lattice movement.) The NH_4 -rho expands only slightly on hydration, and the stabilized rho does not appear to change at all, in contrast to most other zeolites, which generally change slightly. It is also evident that the stabilized material expands in apparent unit cell size as a result of the stabilization treatment, in contrast to zeolite Y(7). This may be related to the positions assumed by cationic aluminum species. It should be noted that calculations

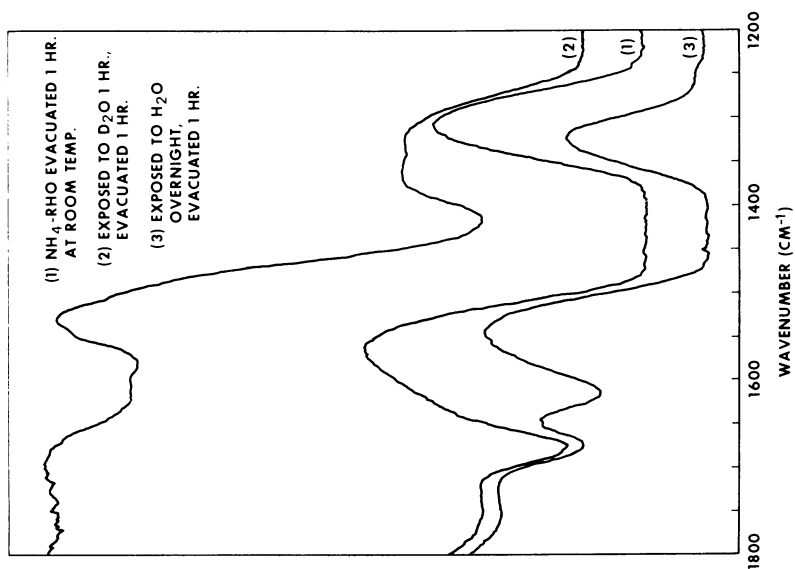


Figure 3. IR spectra of NH_4^+ -Rho showing effect of serial exposure to D_2O and H_2O on postulated H_3O^+ deformation band

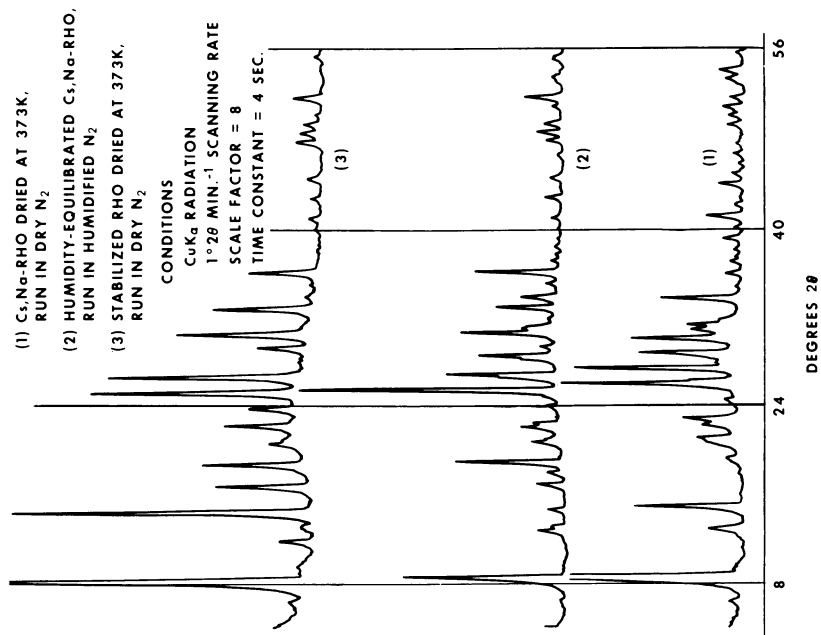


Figure 4. X-ray diffraction patterns for zeolite Rho samples

TABLE III

SORPTIVE PROPERTY CHANGES IN ZEOLITE RHO SAMPLES
TREATED AT DIFFERENT CONDITIONS

SAMPLE	TREATMENT	H ₂ O ADSORPTION AT 296K, 20 TORR		O ₂ ADSORPTION AT 90K, 750 TORR		N-BUTANE ADSORPTION AT 296K, 300 TORR	
		WT. %	V _p , cm ³ /g	WT. %	V _p , cm ³ /g	WT. %	V _p , cm ³ /g
Cs, Na - RHO	ACTIVATED AT 673K IN VACUUM	23.0	0.23	4.5	0.04	1.6	0.03
NH ₄ - RHO	ACTIVATED AT 623K IN VACUUM	31.5	0.32	5.9	0.05	1.7	0.03
NH ₄ - RHO	ACTIVATED AT 673K IN VACUUM	31.8	0.32	32.0	0.28	8.3	0.14
NH ₄ - RHO	RE-ACTIVATED AFTER EXPOSURE TO WATER VAPOR	—	—	17.4	0.15	0.2	—
STABILIZED RHO	ACTIVATED AT 673K IN VACUUM	32.0	0.32	37.7	0.33	—	—
STABILIZED RHO	RE-ACTIVATED AFTER EXPOSURE TO WATER VAPOR	—	—	37.7	0.33	—	—

TABLE IV

COMPARISON OF HYDRATED AND DEHYDRATED
CUBIC LATTICE PARAMETER DATA FOR RHO SAMPLES

FORM	CONDITIONS	CUBIC a ₀ IN Å	STD. DE- VIATION	NO. OF LINES USED
Cs, Na - RHO	DRIED AT 393K ⁽¹⁾⁽²⁾	14.59	0.010	12
	DRIED AT 373K, RUN IN DRY N ₂ ⁽²⁾⁽³⁾	14.66	0.008	11
	HUMIDITY-EQUILIBRATED, RUN IN HUMIDIFIED N ₂ ⁽²⁾⁽³⁾	15.09	0.017	12
NH ₄ - RHO	DRIED AT 373K, RUN IN DRY N ₂ ⁽²⁾⁽³⁾	14.86	0.007	10
	HUMIDITY-EQUILIBRATED, RUN IN HUMIDIFIED N ₂ ⁽²⁾⁽³⁾	14.98	0.006	11
DEAMMINATED RHO	CALCINED AT 813K ⁽¹⁾⁽²⁾	14.96	0.016	10
	CALCINED AT 813K ⁽¹⁾⁽⁴⁾	14.99	0.006	18
	VACUUM-ACTIVATED AT 673K ⁽¹⁾⁽⁴⁾	15.02	0.010	23
STABILIZED RHO	DRIED AT 373K, RUN IN DRY N ₂ ⁽²⁾⁽³⁾	15.06	0.008	10
	HUMIDITY-EQUILIBRATED, RUN IN HUMIDIFIED N ₂ ⁽²⁾⁽³⁾	15.06	0.009	10

(1) DATA FROM REF. 1

(2) CALCULATED FROM LINES BETWEEN 25-40° 2θ

(3) 0.125°/MIN. SCAN RATE

(4) CALCULATED FROM LINES BETWEEN 40-75° 2θ

based on Robson et al.'s data(1) using higher-angle peaks would be expected to give results slightly higher than those for intermediate-angle peaks used in this work, as seen in Table IV. Distortion in the structure is suggested by the different degrees of change observed in hydration-dehydration of the Cs, Na-, NH_4 - and stabilized forms, as well as by the other data noted above.

The data obtained on these rho samples support the view that the zeolite framework structure is not a highly rigid one, and that considerable elasticity is manifested during the sorption-desorption process, as has been noted earlier by Breck(4) and more recently by Dubinin et al.(16). It would appear that, for this structure at least, the strongly hydrated sodium cation is associated with expansion-contraction movement. Steric and electrostatic effects resulting from hydration of the large cesium cation would also be expected to contribute to the strong expansion-contraction phenomenon. The hydrated proton, and aluminum cations possibly present, probably contribute to the absence of an observed expansion-contraction effect in the stabilized structure, while in the NH_4^+ -exchanged form the weakly hydrated NH_4^+ and possibly remaining Cs^+ cations contribute to only a modest effect. This type of interaction probably applies to other adsorbates as well.

Acknowledgements

I would like to acknowledge the significant contributions of T. R. Cannan, who obtained all of the adsorption data, and C. L. Angell and G. W. Skeels, who participated in the infrared aspects of this study.

Literature Cited

- (1) Robson, H. E., Shoemaker, D. P., Ogilvie, R. A., and Manor, P. C., *Advan. Chem. Ser.* (1973) **121**, 106.
- (2) Breck, D. W., "Zeolite Molecular Sieves", Wiley, New York (1974), p. 636.
- (3) *Ibid.*, p. 425.
- (4) *Ibid.*, p. 65.
- (5) Kerr, G. T., *Inorg. Chem.* (1966) **5**, 1539.
- (6) Robson, H. E., *Proceedings, Third International Conference on Molecular Sieves, Zurich, 1973*, p. 20; Kerr, G. T., *ibid.*
- (7) Flank, W. H., in "Analytical Calorimetry, Vol. 3", Plenum Press, New York (1974), p. 649.
- (8) Bennett, J. M., Breck, D. W., and Skeels, G. W., in preparation.
- (9) Flanigen, E. M., Szymanski, H. A., and Khatami, H., *Advan. Chem. Ser.* (1971) **101**, 201.
- (10) Milkey, R. G., *Amer. Mineral.* (1960) **45**, 990.
- (11) Barrer, R. M., *Proc. Chem. Soc.* (1958), 99.
- (12) Taylor, R. C., and Vidale, G. L., *J. Amer. Chem. Soc.* (1956) **78**, 5999.
- (13) Gillard, R. D., and Wilkinson, G., *J. Chem. Soc.* (1964) **No. 323**, 1640.
- (14) Wilkins, R. W. T., Mateen, A., and West, G. W., *Amer. Mineral.* (1974) **59**, 811.
- (15) Taylor, A. M., and Roy, R., *J. Chem. Soc.* (1965), 4028.
- (16) Ivanova, T. N., Sarakhov, A. I., and Dubinin, M. M., *Izv. Akad. Nauk SSSR, Ser. Khim.* (1975) **7**, 1471.

^{23}Na -Resonance in Zeolites of the Faujasite- and A-Type and Its Interpretation by Computer Simulation of the Measured Spectra

H. LECHERT and H. W. HENNEKE

Institute of Physical Chemistry of the University of Hamburg,
Laufgraben 24, 2000 Hamburg, West Germany

ABSTRACT

Na^{23} -spectra of X-zeolites consist of a central component and satellites, assigned to the S1'- and S2-sites, by model calculations. The central component is given by the S1-sites and sites at the cavity-walls with varying coupling constants and high asymmetry parameters. The Y- and A-type spectra cannot be explained satisfactorily by model calculations as yet.

Introduction

The importance of zeolites in catalytic research is mainly based on the fact that these substances have a defined crystal structure, containing the active surface as a part with known geometrical arrangement of the atoms belonging to it. Interactions of sorbed molecules with this surface should, therefore, occur only with a few classes of crystallographically equivalent lattice elements. This has been used, since the very beginning of the application of zeolites, for the development of models of the electric field distribution inside the zeolite cavities, leading, for instance, to the heat of adsorption and its composition of different kinds of interaction (1-5) and also to the development of models of the catalytic action (6). A suitable method to get direct experimental informations on the electric field distribution is the measurement of the magnetic resonances of nuclei with an electric quadrupole moment (7-11), which allows conclusions on the gradient of the electric field at the site of the nucleus. Similar information can be obtained from Mößbauer-spectra (12-14). In some preceding papers (7-11) the behaviour

of the Na 23 and the Li7-resonance has been studied in dehydrated zeolites of the X- and the A-type and tried to explain by model calculations of the electric field gradient (8). For X-type zeolites a single Na23-resonance line has been observed and explained as belonging to the S1-sites. The nuclei of the other sites should have much broader spectra which are usually hidden in the noise. As, however, the probability of occupation of the S1'- and the S2-sites is two to four times higher than that of the S1-sites, these nuclei should be detectable, if the signal-to-noise-ratio is improved by accumulation of spectra.

Nuclear Magnetic Resonance and Quadrupole Effects

Nuclei with spin $I > 1/2$ possess an electric quadrupole moment Q which may interact with the gradient of the electric crystal field at the site of the nucleus. The electric field gradient tensor is usually described by two quantities $e q$ and η called "field gradient" and "asymmetry parameter" measuring the field gradient in the direction its largest value and the deviation of the field perpendicular to this direction from rotational symmetry. The strength of the quadrupole interaction is usually expressed in terms of the quadrupole coupling constant

$$CQ = (1 - \gamma_{\infty}) e^2 q Q / h$$

γ_{∞} is the "antishielding factor" describing the influence of the electronic shell to which the nucleus belongs. In the spectra presented in this paper only the transition $-1/2 \rightarrow 1/2$ can be observed which is affected by second order perturbation. Taking into account the additional dipole-dipole interaction of the nuclei, for different amounts of this interaction and different η the spectra demonstrated in Fig. 1 can be obtained by computer simulation (10). Details shall be discussed later in connection with the measured resonance lines.

Experimental

The samples for the NMR measurements have been prepared following procedures, described elsewhere (19,20). After removing the major part of the water at 100°C at about 10^{-2} torr, the samples were heated to 350°C at 10^{-5} torr for four days. The adsorption of water and other adsorbates was achieved over

the vapour phase where the exact contents could be determined by weight.

The NMR-measurements were carried out with the wide-line unit of a VARIAN DP 60 spectrometer. The measuring frequency has been usually 16 Mc and the frequency of the field modulation 20 c. For the accumulation of the spectra a VARIAN C-1024 time averaging computer was used.

Model Calculations

For the calculation of the field gradients at the sites of the sodium ions in the faujasite lattice a point multipole model has been used. At first the point charge contribution to the fields and field gradients at the sites of all ions of a cubooctahedron was evaluated, carrying the lattice sum over the 26 nearest cubooctahedra. With the values obtained, the strengths of the induced dipoles and quadrupoles were calculated for different polarizabilities of the oxygen ions and the contributions of these multipoles added to the point charge contribution to the field gradient at the site of the wanted Na-ion. The structure has been built up according to the x-ray data of EULENBERGER et.al. (18). The S1- and the S1'-sites are half, the S2-sites fully occupied. For the ions nonlocalizable by diffraction, two models have been chosen. According to BRECK (21), these ions are placed above the four-membered rings (S3 and S3'). S3' and S3 are crystallographically equivalent. The distinction is made only to calculate the influence on the distance of these ions on the field gradient at the neighbouring S1 and S1'-sites. In the other model, the nonlocalizable ions are arranged at the outer side of the double-sixmembered rings according to the suggestions for MORTIER et al. (22). (S4 and S5) The exact positions are drawn from the assumption, that the Na-ions should contact at least three oxygen ions. For the present calculations the distances to these oxygen ions have been chosen as 2.3 Å. OLSON (27) has found, on the other hand, that these ions occupy at least three different sites with strongly varying distances to the nearest oxygen ions.

In Table 1 the results of our calculations are summarized for a dipole polarizability of the oxygen ions of 1.7 \AA^3 and a quadrupole polarizability of 0.1 \AA^5 . Orientational calculations with the data of OLSON (23) show asymmetry parameters above 0.8 and field gradients depending quite sensitively on the

Table 1

Quadrupole Coupling Constants and Asymmetry Parameters for the Possible Sites of the Sodium-ions in Zeolites of the Faujasite Type

	<u>C_q in Mc</u>	<u>η</u>
S1 only S3 occupied	1.486	0.24
S1 only S3' occupied	0.655	0.57
S1, S4 occupied	0.921	0.54
S1, S5 occupied	0.926	0.62
S1' only S3 occupied	3.362	0.04
S1' only S3' occupied	4.165	0.03
S1', S4 occupied	3.288	0.11
S1', S5 occupied	3.270	0.08
S2, S3 occupied	3.917	0.21
S2, S4 occupied	4.535	0.42
S2, S5 occupied	4.720	0.32
S3, S1 occupied	6.15	0.57
S3, S1' occupied	6.18	0.60
S4, S1 occupied	3.61	0.85
S4, S1' occupied	3.50	0.74
S5, S1 occupied	5.09	0.65
S5, S1' occupied	4.81	0.51

choice of the distance of the Na-ion from the nearest oxygen ion.

Results and Discussion

The shape of a Na²³-spectrum, containing the resonance lines of nuclei in the S1-, S1'-, and the S2-sites with the occupancy factors given above, has been simulated by a superposition of the respective spectra of Fig. 1 using the data of Table 1. The broadening parameter has been estimated from the amount of dipole-dipole-interaction with the neighbouring Al²⁷-nuclei (see also (24)). The result is shown in the Fig.2a. It can be seen that the influence of the central resonance comes out surprisingly low and the resonance lines of the S1'- and the S2-sites should be easily detectable. The measurements have, therefore, been repeated accumulating 400 spectra in a time averaging computer. The result is demonstrated in the Fig. 2b and c. Fig.2b shows that, indeed, beside the central resonance, which is too intense to be stored in the computer memory, two peaks can be observed at lower fields. At higher fields the measurement is disturbed by the Al²⁷ resonance of the sample holder of the spectrometer, so

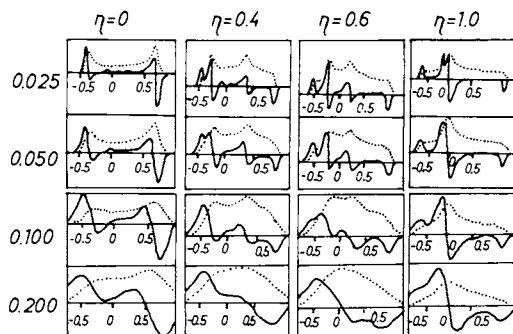


Figure 1. Model-spectra of a quadrupole interaction of the second order for different asymmetry parameters and contributions of the dipole-dipole interactions.

Figures at the left edge give the ratios of the amount of the dipole-dipole interaction and the total width of the spectrum. (· · ·), shape of the actual absorption spectrum; (—), spectrum obtained by the wide-line technique, being the first derivative of the first.

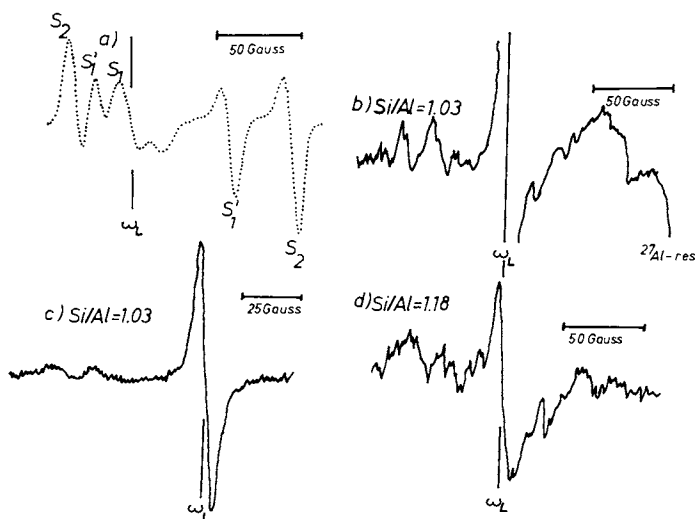


Figure 2. Comparisons of the ^{23}Na -spectra of two dehydrated zeolite samples of the faujasite-type with $\text{Si}/\text{Al} = 1.03$ and 1.18 with a computer simulated spectrum (a) using the data of model calculations of the field gradient

that the respective peaks, being demonstrated in the simulated spectrum, are hidden under this resonance. In the Fig. 2c a run is shown which has been carried out with reduced amplification, to demonstrate the ratio of intensity of the central line and the side peaks. It can be seen that the shape of the spectrum alongside the central line is relatively good reproduced by the simulation. Following the data of Table 1 the outer peak should belong to the S2-sites and the inner to the S1'-sites. Taking the coupling constants from the spectrum of Fig 2b a value of 5.02 Mc for the S1'-sites and 5.69 Mc for the S2-sites can be calculated.

These values are distinctly higher than those of Table 1, although the ratios of the measured and the calculated coupling constants are nearly equal. To explain this discrepancy the lattice parameters have been varied as well as the polarizabilities of the oxygen ions. In the present state of discussion a changed value of the antishielding factor seems to be the best explanation to the author. The observed coupling constants would be explained by the calculated values, if a γ_{∞} of 6.9 is chosen instead of 4.53. Changes of this amount have been discussed several times in the literature to explain the effects of special bond situations of the electronic shell around the nucleus in question (25).

A simulation of various spectra shows that the high intensity of the central line is due to about six ions per cubooctahedron which is much more than the S1-sites available. A considerable part of the intensity of the central line should, therefore, come from the ions, not localizable by x-ray diffraction.

Measuring now spectra of samples with a higher Si/Al-ratio the central line loses intensity quite considerably, whereas the side peaks show only a slight broadening, as is shown for the example of Si/Al = 1.18 in the Fig. 2d.

Similar effects can be observed, if water is added to the zeolite. Fig. 3 shows the example of Si/Al = 1.03 and six molecules of water in the large cage. These effects show, that the central line and the side peaks most likely do not belong to the same ions.

Even, if it is conceded, however, that the assumptions of the S3-, S4- and S5-sites are not correct, it is hard to imagine that any site at the surface of the zeolite cavity should give a low coupling constant. If, on the other hand, the nonlocalizable ions occupy sites with field gradients of asymmetry parameters near $\eta = 1$ and coupling constants, which are

distributed over a certain range, there should be a narrow central component observable and the edges should not have any influence on the spectrum, as is shown in the Fig. 4a. This kind of distribution is also suggested by the data drawn from the results of OLSON (23) mentioned above. The whole spectrum simulated with two lines of relative coupling constants of 1 : 1.8 and the spectrum 4a is demonstrated in the Fig. 4b. It is obvious that from the central line only quite poor information can be drawn about the field distribution at the sites at the walls of the large cages.

Proceeding to higher Si/Al-ratios, the relative intensity of the central line decreases simultaneously with the number of the nonlocalizable ions. Above about Si/Al = 1.3 the side peaks flatten and become unobservable near Si/Al = 1.5 according to the fact that the field distribution at the S1'- and the S2-sites becomes less uniform with increasing Si/Al-ratio. At high Si/Al-ratios above 2.5 a strongly asymmetric line can be observed, as is shown in the Fig. 5. Attempts to explain this line by a simulation based on a model calculation of the above mentioned kind failed until now.

Summarizing, it can be stated that the experimental results can be explained fairly good by model calculations at the sites S1' and S2 for low Si/Al-ratios. The resonance line of the S1-sites is hidden under the line resulting from a relatively large number of nuclei, the behaviour of which suggest the assumption, that this line is given by the nonlocalizable ions. The resonance line apparently does not result from one kind of ion but rather from a number of sites with high asymmetry parameter and varying coupling constants. Another experimental fact which confirms the given explanation of the origin of the central resonance, is that it is strongly affected by sorption of polar molecules, which has been observed already in earlier experiments (7,9). As the coupling constants are rather high at these sites the line widths are strongly dependent on changes of the asymmetry parameter, which lead to a wide spread distribution of the intensity of the central component. At higher coverages for small polar molecules like water and ammonia a strong narrowing of the Na 23 -resonance can be observed, which is due to the fact that a part of the Na-ions becomes movable (7). For larger dipole molecules like tetrahydrofuran and dioxane, at higher coverages obviously complexes with the S2-ions can be observed (9). The coupling-con-

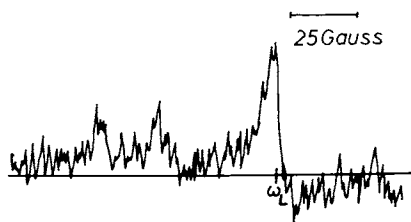


Figure 3. ^{23}Na -spectrum of a zeolite sample of the faujasite type with $\text{Si}/\text{Al} = 1.03$ containing six molecules of water in a cubooctahedron

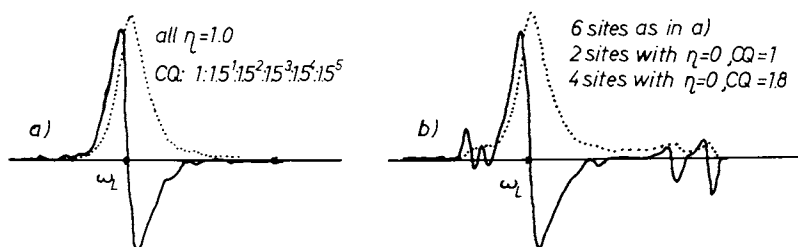


Figure 4. (a) Spectrum of a computer simulation belonging to a number of sites with $\eta = 1$ and coupling constants varying in the given range. (b) Spectrum obtained in (a) superimposed by the spectrum given in Figure 3a.

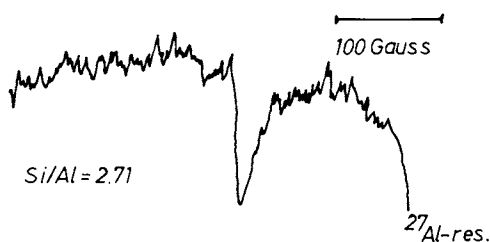


Figure 5. Lineshape of the ^{23}Na -resonance of a dehydrated faujasite sample with $\text{Si}/\text{Al} = 2.71$

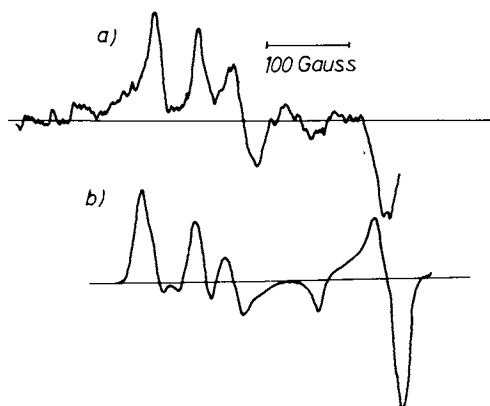


Figure 6. Comparison of the ^{23}Na -resonance of a 4A-type zeolite sample (a) with a computer simulated spectrum (b), fitted to (a) by variation of CQ and η

stant at these sites is decreased considerably by an attached molecule, as can be shown by model calculations of the above mentioned kind. The respective Na²³-spectra show quite intense lines of widths between 10 and 29 kc, depending on Si/Al.

In the Fig. 6 the Na²³-spectrum of a 4A sample is shown. The simulation of the spectrum shows, that it can be composed of two parts with nearly equal intensity and $CQ = 5.13$ Mc with $\eta = 0$

and $CQ = 3.36$ Mc with $\eta = 0.7$

Calculating the field gradient tensors at the site of the ions Na1 and Na2 given by SEFF (26) values of $CQ1 = 7.06$ Mc, $\eta = 0.88$ and $CQ2 = 6.35$ Mc, $\eta = 0.28$ are obtained. Eight ions Na1 are situated above the sixmembered rings at the walls of the large cavities. The Na2 sites lie near the middle of three of the edges of the mentioned sixmembered rings. As for each Na1 only one of these edges is occupied, the threefold symmetry is spoiled, causing the discrepancy, arising between the values drawn from the spectrum and the structural data. For the A-type further discussions and experiments are necessary.

From the discussions of this paper can be seen, that the method of NMR on quadrupole nuclei can be used to supplement the results obtained by structure analysis, especially, if the signal to noise ratio is improved by accumulating spectra, to get enough details for a computer simulation.

The great advantage of the NMR-method is given by the fact, that the influence of sorption on the resonances can be studied more easily than by x-ray diffraction, which has been shown in earlier experiments (2).

Acknowledgements

The authors wish to thank the "Deutsche Forschungsgemeinschaft" and the "Fonds der Chemischen Industrie" for financial support of their work.

Literature Cited

1. Rees, L. V. C., and Williams, C. J., Trans. Farad. Soc. (1964), 60, 1993.
2. Sargent, R. W. H., and Whitford, C. F., ACS Advances in Chemistry Series "Molecular Sieves II" Washington, (1971), 102, 144.
3. Kiselev, A. V., ACS advances in Chemistry Series "Molecular Sieves II" Washington, (1971), 102, 37.
4. Kiselev, A. V., and Lopatkin, A. A., "Molecular

- Sieves", SCI Monograph London, (1968), 252.
5. Barrer, R. M., and Cram, P. J., ACS Advances in Chemistry Series "Molecular Sieves II" Washington, (1971), 102, 105.
 6. Pickert, P. E., Rabo, J. A., Dempsey, E., and Schomaker, V., Act. Int. Congr. Catal. 3rd (1965), 714.
 7. Lechert, H., ACS Advances in Chemistry Series "Molecular Sieves" Washington, (1973), 121, 74.
 8. Lechert, H., Ber. Bunsenges. Phys. Chemie, (1973), 77, 697.
 9. Lechert, H., Habilitation-Theses, Univ.Hamburg, (1973)
 10. Lechert, H., Basler, W. D., and Henneke, H. W., Ber. Bunsenges. Phys. Chemie, (1975), 79, 563.
 11. Lechert, H., and Henneke, H. W., Ber. Bunsenges. Phys. Chemie, (1974), 78, 347.
 12. Delgass, W. M., Garten, R. L., and Boudart, M., J. Phys. Chem., (1969), 73, 2970.
 13. Morice, J. A., and Ress, L. V. C., Trans. Farad. Soc., (1968), 64, 1388.
 14. Garten, R. G., Delgass, W. M., and Boudart, M., J. Catal., (1970) 18, 90.
 15. Goldanskii, V. I., Suzdalev, I. P., Plachinda, A. S., and Shtyrkov, L. G., Proc. Acad. Sci., USSR, Phys. Chem. Sect., (1968), 169, 511.
 16. Dickson, B. L., and Rees, L. V. C., Proc. of the 3rd International Conference on Molecular Sieves, Leuven, (1973), 324.
 17. Abragam, A., "The Principles of Nuclear Magnetism", Oxford University Press, London, 1961.
 18. Eulenberger, G. R., Shoemaker, D. P., and Keil, J. G., J. Phys. Chem. (1967), 71, 1812.
 19. Kacirek, H., and Lechert, H., J. Phys. Chem., (1975), 79, 1589.
 20. Kacirek, H., and Lechert, H., J. Phys. Chem., (1976), 80, 1291.
 21. Breck, D. W., J. Chem. Educ., (1964), 41, 678.
 22. Mortier, W. J., Bosmans, H. J., and Uytterhoeven, J. B., J. Phys. Chem., (1972), 76, 650.
 23. Olson, D. H., private communication.
 24. Stauss, G. H., J. Phys. Chem., (1964), 40, 1988.
 25. Brun, E., and Hafner, S., Z. Kristallographie, (1962), 117, 63.
 26. Seff, K., J. Phys. Chem., (1972), 76, 2601.

6

Measurement of Chemical Shifts in Zeolites by X-Ray Emission

R. L. PATTON, E. M. FLANIGEN, L. G. DOWELL, and D. E. PASSOJA
Union Carbide Corp., Tarrytown Technical Center, Tarrytown, N.Y. 10591

ABSTRACT

Relative $\text{SiK}\beta$ and $\text{AlK}\beta$ X-ray emission band energies have been measured for zeolites A, X, Y, rho, offretite, erionite, and mordenite, as well as some thermochemically treated forms, and correlated with framework aluminum content and structure type. Both $\text{SiK}\beta$ band energies, which are found to linearly increase with increasing framework aluminum content, and $\text{AlK}\beta$ values, which are most responsive to Al coordination changes, shift significantly as thermochemical treatments displace framework Al and transform it to octahedral species.

Introduction

Measurements of $\text{SiK}\beta$ and $\text{AlK}\beta$ X-ray emission bands for a wide variety of silicon and aluminum oxides and aluminosilicates have been reported within the past decade (1-7). These bands, resulting from transition of bonding Al or Si-3p electrons to the inner 1s orbitals, reflect the energy difference between those orbitals. Hence, chemical changes affecting stabilization of bonding orbitals cause a "chemical shift" in the energy of the $\text{K}\beta$ bands. This chemical shift is normally expressed as a quantity " Δ " representing the difference in $\text{K}\beta$ band energy of the sample vs. that of a reference material, usually quartz (SiO_2) or corundum ($\alpha\text{-Al}_2\text{O}_3$).

For $\text{SiK}\beta$ of Si-O bonds of silicates and aluminosilicates, strong correlations of " Δ " have been found with factors such as: d(Si-O) (1,8), silicate structure type (1,4), number and type of species coordinated with the oxygen of the Si-O bond (1,4), T-O-T and O-T-O angles (9), cation type and presence (9), and, for framework aluminosilicates, with Al/Si ratio (1). For $\text{AlK}\beta$ of Al-O bonds in various aluminum oxides and aluminosilicates, large variations in " Δ " have been correlated with d(Al-O) (5,8,10) and with 4 vs. 6-fold coordination of Al (4,7, 10).

Both the Al and $\text{SiK}\beta$ peaks from either tetrahedral or octahedral oxides have been generally accepted to consist of at least two components as evidenced by shoulders or peak asymmetry or distinct peak maxima, the two components of octahedral oxide bands usually being of similar intensity and the tetrahedral oxide band components normally appearing as a weak high energy shoulder on the main component. Several authors (3,4,9,11-17) have presented molecular orbital inter-

pretations, consistent with these K_{β} X-ray emission spectra, of the Si and Al electronic structures in tetrahedral and octahedral coordination with oxygen. Most recently Tossell, in an excellent series (13-17), assigned the high and low energy components of the main K_{β} band to the $5t_2$ and $4t_2$ orbitals for tetrahedral Al and Si oxides and to the $6t_{1u}$ and $5t_{1u}$ orbitals for octahedral oxides, respectively. Alternately, multiple K_{β} band components have simply been interpreted as resulting from distinctly different bonds present in the structure (2). In reality, both interpretations are likely correct, with each different species or bond type present in a material probably contributing multiple molecular orbital components to the total K_{β} band.

To date the only reported K_{β} XES data on zeolites is the brief 1973 report by G. H. K uhl (7) who measured the shift of the AlK_{β} line between sodium zeolite Y and various thermochemical derivatives. The shifts were interpreted as corresponding to transformation of as much as 44% of the original tetrahedrally coordinated framework Al to hexacoordinated non-framework Al, based on a scale using NaY and zinc spinel AlK_{β} lines as standards for 4 and 6-fold coordination, respectively. K uhl additionally mentioned, without detail, that the SiK_{β} line of "dehydroxylated" Y was unshifted.

In this study the SiK_{β} and AlK_{β} emission bands of a variety of typical zeolites, as well as some thermochemically derived forms, have been measured. The SiK_{β} shifts are compared to previous results on non-zeolite framework aluminosilicates, correlated with Al population of the framework, and presented for thermochemically treated products. The AlK_{β} values relative to an $\alpha-Al_2O_3$ standard are reported, and substantial shifts resulting from thermochemical treatment forms of Y, mordenite, and erionite are discussed in terms of framework dealumination reactions.

Experimental

A. Samples. The samples for which X-ray emission data are presented are listed in Table I including origin, history, and chemical composition.

B. Equipment. The X-ray emission data collection equipment and methods have recently been described by Dowell et al., (18). Briefly, a Siemens SRS-1 automatic vacuum path X-ray fluorescence spectrometer was used with CrK_{α} (max. 50 KV, 40 MA) X-ray excitation, and a "PET" (pentaerythritol, $2d = 8.75 \text{ \AA}$) analyzer crystal. A dedicated PDP-11 minicomputer controlled automatic step scanning and digital detector count recording, with each of ten preloaded samples in turn, through a preset diffraction angle range. Filled sample cells, "Somar" brand liquid cups with $\geq 0.5g$ of powder covering "Mylar" polyester bottom windows, were normally vacuum desiccated several hours before loading and pump-down in the spectrometer.

C. Data Collection and Reduction. Each 10-sample set included at least 3 interspersed reference samples: α -quartz for SiK_{β} runs, and $\alpha-Al_2O_3$ for AlK_{β} runs. Sets were normally cycled at least 3 times in automatic overnight or weekend runs, with individual values averaged and with the reference samples serving to verify the stability of the system. Some representative samples were actually step-scanned through the entire K_{β} and K_{β}' peak range of 100.0 to $103.0^{\circ} 2\theta$ for SiK_{β} and 130.0 to $136.0^{\circ} 2\theta$ for AlK_{β} , to characterize the nature of the data and peak

TABLE I: Description of Samples and SiK_β and AlK_β X-ray Emission Results

Description	Notation Used in Figures	Chemical Analysis		Chemical Shift Values (8)	
		$\left(\frac{\text{SiO}_2}{\text{Al}_2\text{O}_3}\right)$	Al fraction $\left(\frac{n\text{Al}}{n\text{Al} + n\text{Si}}\right)$	SiK_β ΔE (e.v.) (vs. quartz)	AlK_β $-\Delta E$ (e.v.) (vs. $\alpha\text{-Al}_2\text{O}_3$)
Zeolites:					
Typical forms: (1)					
Hydroxysodalite	1	2.04	.495	.85 (5)	-
NaA	2	1.84	.521	.77 (5)	1.00 (5)
NaX	3	2.43	.451	.81 (2)	.89 (5)
NaY (3.6)	4	3.61	.357	.69 (7)	.89 (3)
NaY (4.8)	5	4.81	.294	.54 (4)	1.02 (5)
NH_4^{exY}	6, Y0	4.97	.287	.60 (3)	.95 (3)
$\text{NH}_4^{\text{ex rho}}$	7	6.05	.248	.54 (4)	.94 (4)
Na, K, TMA offretite	8	6.70	.230	.38 (5)	1.09 (7)
NH_4^{ex} erionite	9, E0	6.97	.223	.37 (1)	1.17 (5)
Na-Zeolon (mordenite)	10	11.0	.154	.14 (2)	1.24 (4)
Thermochemical forms: (2)					
H-Zeolon:	Z0	12.1	.142	.07 (1)	1.08 (3)
" (AE)	Z0-A	83.6	.023	-.06 (1)	1.14 (11)
" (SS)	Z1	12.1	.142	-.03 (1)	.33 (3)
" (SS, SS)	Z2	12.1	.142	.01 (1)	.35 (3)
" (SS, AE)	Z1-A	>1500	(<.001)	-.05 (1)	1.06 (3)
NH_4^{ex} erionite:	E0	6.97	.223	.37 (1)	1.17 (5)
" (MS)	E1	7.06	.221	.24 (7)	1.05 (6)
" (MS, MS)	E2	7.06	.221	.27 (5)	.98 (6)
" (MS, SS)	E3	7.06	.221	.11 (5)	.46 (5)
" (MS, MS, SS)	E4	7.06	.221	.05 (3)	.39 (6)
" (MS, MS, SS, AE)	E4-A	17.0	.105	.03 (2)	.58 (5)
NH_4^{ex} Y:	Y0	4.97	.287	.60 (3)	.95 (3)
" (MS)	Y1	5.2	.277	.35 (5)	.68 (9)
" (MS, SS)	Y2	5.2	.277	.10 (1)	.27 (*)
" (MS, SS, AE)	Y2-A	17.7	.102	.03 (1)	.27 (*)
Aluminum Oxides:					
$\alpha\text{-Al}_2\text{O}_3$ (Corundum)(3)	0	1	-	-	(-0-)
$\alpha\text{-Al(OH)}_3$ (Gibbsite)(4)	0	1	-	-	.13 (6)
$\alpha\text{-AlO(OH)}$ (Böhmite)(5)	0	1	-	-	-.01 (6)
ZnAl_2O_4 (zinc spinel)(6)	0	1	-	-	-.41 (7)
Silicon Oxide:					
$\alpha\text{-quartz}$ (7)	∞	0	-	(-0-)	-

(1) These zeolites taken from the Linde Research Dept. collection and represent samples of excellent purity and crystallinity. Samples synthesized within Union Carbide except erionite (purified, NH_4^+ exchanged ore) and Zeolons (Norton Co. products).

(2) Thermochemical treatments of the listed starting zeolite forms are coded in parentheses from left to right as performed successively on the material.

-Code:

(AE) - Acid extraction by reflux in excess 6N HCl.

(MS) - Mild steaming - moist air, short term, 500-650°C, followed by ammonium exchange with hot NH_4Cl solution.

(SS) - Severe steaming - 100% steam, long term, 650-850°C.

(3) "Linde" A Corundum (0.3 μ powder)

(4) "Alcoa" C-31

(5) From internal collection - exhibits excellent X-ray powder pattern.

(6) Zinc Spinel (Gahnite) sample courtesy of G. V. Gibbs.

(7) "MIN-U-SIL" (30 μ quartz).

(8) All are triplicate run values except single values marked (*). Numbers in parentheses are actually observed deviations in last reported digit.

shapes. All the main $\text{SiK}\beta$ bands were fairly sharp, strong, narrow bands with half-height widths of 0.3 to $0.5^\circ 2\theta$, symmetric except for a slightly shallower slope on the low 2θ side attributed to the unresolved weak high energy shoulder on the main $\text{K}\beta$ band. The $\text{AlK}\beta$ bands, in contrast, were much wider, ranging at half-height from $\sim 0.75^\circ$ wide for zeolites to $\sim 1.1^\circ 2\theta$ for $\alpha\text{-Al}_2\text{O}_3$, and were characterized by an extremely broad 2θ range for $I \geq 0.9I_{\text{max}}$, or by moderate asymmetry evidenced by different slopes of peak sides and by occasional shoulder appearance. Those samples containing low Al contents resulted in weak, ragged peaks.

The following methods were then developed to produce, for each sample, a value of 2θ characterizing the main $\text{K}\beta$ peak position which, by difference ($\Delta 2\theta$) from corresponding values for accompanying quartz or $\alpha\text{-Al}_2\text{O}_3$ references, represents the "chemical shift" of the sample reported as " ΔE " values, where

$$(1) \Delta E (\text{e.v.}) = [E (\text{sample}) - E (\text{reference})] = -[\underline{k} \times (\Delta 2\theta)^\circ].$$

In our system, with PET crystal, \underline{k} ($\text{SiK}\beta$) = 13.2 and \underline{k} ($\text{AlK}\beta$) = 6.08.

For $\text{SiK}\beta$ shifts, each sample's main $\text{SiK}\beta$ peak was measured in 17 consecutive $0.01^\circ 2\theta$ steps encompassing the top 10-20% of the peak. The data were then fit to a cubic equation to determine the 2θ value of the peak maximum. Such values matched, within the experimental precision, all values for a series of samples derived from a symmetrical curve fit of the entire main $\text{K}\beta$ band.

For $\text{AlK}\beta$, bands were step-scanned in $0.05^\circ 2\theta$ increments over a $3.0^\circ 2\theta$ range encompassing the entire main $\text{K}\beta$ band. Counts vs. 2θ curves were then plotted for each sample, and the center 2θ position measured at peak half-height. When peaks were ragged or asymmetric, each side of the peak was independently approximated by a visually placed straight line; the center 2θ position was then measured midway between these lines at half-height.

The $\text{AlK}\beta$ and $\text{SiK}\beta$ ΔE values determined by the above methods are given in Table I. The precision of these values for all but the most Al-deficient $\text{AlK}\beta$ samples is estimated at ± 0.05 e.v. based on the excellent consistency throughout each run of the quartz and $\alpha\text{-Al}_2\text{O}_3$ values, and the usually excellent agreement of triplicate sample results. The observed maximum deviation is shown in parentheses.

Recently in our laboratories, Dowell et al. (18) developed a computer processing method to resolve the $\text{SiK}\beta$ curves into two symmetrical components. Such two component spectra shown for quartz, α -alumina, gibbsite, and a zeolite crystallization sequence (18), closely resemble the types of bands observed in published higher resolution spectra, and as Dowell et al. noted, are consistent with Tossell's molecular orbital treatment (16,17). However, Tossell's assignments are inconsistent with the use of the two component resolution method for the thermochemically treated zeolites of this study. These samples contain both Al^{IV} and Al^{VI} species, and therefore should have $\text{AlK}\beta$ bands composed of at least four components from the $6t_{1u}$ and $5t_{1u}$ octahedral orbitals and the $5t_2$ and $4t_2$ tetrahedral orbitals. Attempts to resolve the $\text{AlK}\beta$ bands into only two components for these samples were tedious and unsatisfactory, and hence the choice of the single component method described.

Discussion

A. $\text{SiK}\beta$ Results. It follows from the nature of the electronic transition producing the $\text{SiK}\beta$ X-ray emission band, that any perturbation of Si-O bonds resulting in less efficient bonding orbital overlap relative to that in quartz should result in a

positive chemical shift expressed as $\Delta E(\text{SiK}\beta) = [E(\text{sample}) - E(\text{quartz})]$. The most obvious such perturbation in zeolites is the substitution of Al into the tetrahedral silicate framework. Figure 1 shows $\text{SiK}\beta$ results for all the typical zeolite forms (as synthesized or ion-exchanged) that have received no further thermal treatments plotted against $[n\text{Al}/(n\text{Al} + n\text{Si})]$, the fraction of framework positions occupied by Al assuming all chemically analyzed Si and Al to be in the framework. Indeed, ΔE is observed to increase linearly with increasing Al framework substitution and, satisfyingly, the illustrated least-squares line fit of the data indicates that ΔE closely approaches zero for zero Al fraction.

For comparison, the White and Gibbs (1) $\text{SiK}\beta$ chemical shift data for a series of non-zeolite framework aluminosilicates have been replotted vs. Al fraction in Figure 2. Strikingly, the same linear relationship is shown by both zeolites and non-zeolites as illustrated by the near coincidence of the least-squares fit lines.

Thus, $\Delta E(\text{SiK}\beta)$ of framework aluminosilicates is primarily related to the extent of Al occupation of tetrahedral framework positions. The observed deviations from linearity can be expected from secondary effects such as structure type and defects, variation and number of cations, and hydration. It should also be noted that wet chemical analyses, on which all $[n\text{Al}/(n\text{Al} + n\text{Si})]$ values are based, do not distinguish framework from non-framework Al and Si. Thus, for example, the presence of cationic Al species, aluminate stuffing, or amorphous silica will cause the quantity $[n\text{Al}/(n\text{Al} + \text{Si})]$ to incorrectly represent the real framework composition.

Figure 3 shows that the measurement of $\text{SiK}\beta$ shifts can be used to monitor the effects on framework Al of various thermal treatments of ammonium or hydrogen exchanged forms of zeolites erionite, mordenite, and Y. In each case, the displacement of a moderate amount of framework Al by mild steam calcination was reflected by a moderate lowering of $\Delta E(\text{SiK}\beta)$; subsequent displacement of much of the framework Al by severe steaming was reflected by lowering of ΔE to near zero; and the success with which subsequent acid extraction removed extra-framework Al species was shown by the approach to the original zeolite line on the plot of ΔE vs. Al fraction.

Thus, $\Delta E(\text{SiK}\beta)$ can serve to monitor the relative effects of the thermochemical treatments on framework composition. The results, particularly the H-Zeolon series with actual appearance of negative ΔE values, caution, however, that actual quantitative conclusions are not always realistic because of secondary effects on ΔE such as cation changes, creation of structural defects or amorphous silica, or the presence of Si-OH bonds expected to differ from Si-O-Si bonds in $\text{SiK}\beta$ energies.

B. $\text{AlK}\beta$ Results. Unlike $\text{SiK}\beta$, the $\text{AlK}\beta$ results, shown in Table I and Figure 4, only weakly correlate with Al-fraction. This is reasonable because regardless of the Al content of a zeolite, all Al in the framework is tetrahedrally coordinated with 4 (-O-Si) groups as required by Loewenstein's rule (19). Framework Si, on the other hand, is coordinated to both (-O-Si) and (-O-Al), hence the pronounced effect on $\text{SiK}\beta$ of Al-fraction variation.

Any number of secondary differences in the studied zeolites might be invoked in correlations with the observed 0.35 e.v. $\text{AlK}\beta$ variation. Such differences, however, appear to relate to the zeolite structural geometry, the number and type of cations present, and possible structural defects or non-framework Al present. For example, the $\text{AlK}\beta$ values can be separated into three groups based either on framework structure type or framework density as in Table II. These

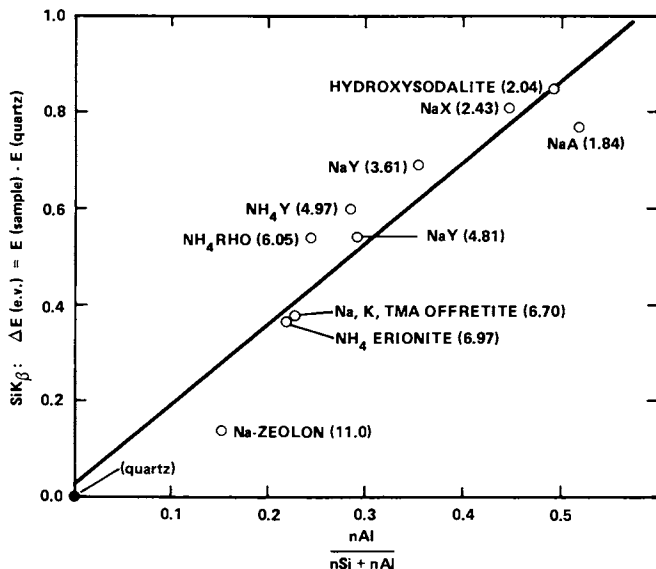


Figure 1. Relative SiK_β band energies of zeolites plotted vs. framework Al fraction calculated from chemical analyses (parentheses show $\text{SiO}_2/\text{Al}_2\text{O}_3$ ratios). Line shown is best linear ($y = a + bx$) least-squares fit with $a = .026$, $b = .0166$.

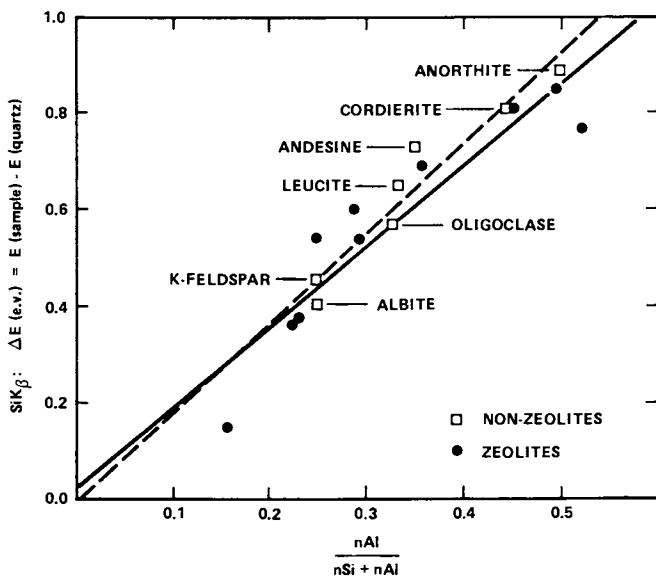


Figure 2. White and Gibbs (1) SiK_β results for non-zeolite tetrahedral framework aluminosilicates plotted vs. Al fraction. Dashed line is best $y = a + bx$ least-squares fit with $a = -.003$, $b = .0185$. Zeolite data from Figure 1 are shown for comparison (solid line and points).

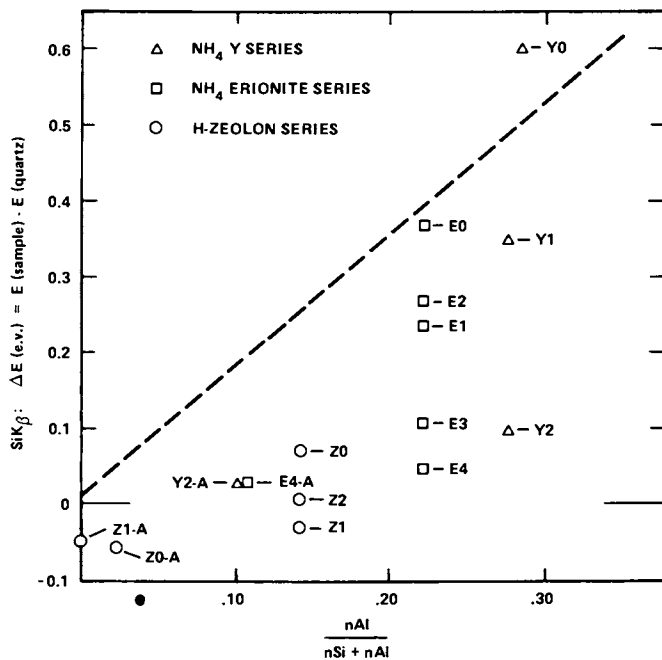


Figure 3. Effects on $\Delta E(SiK\beta)$ of thermochemical treatments of zeolites. Sample notations are identified in Table I. (---), zeolite least-squares fit from Figure 1.

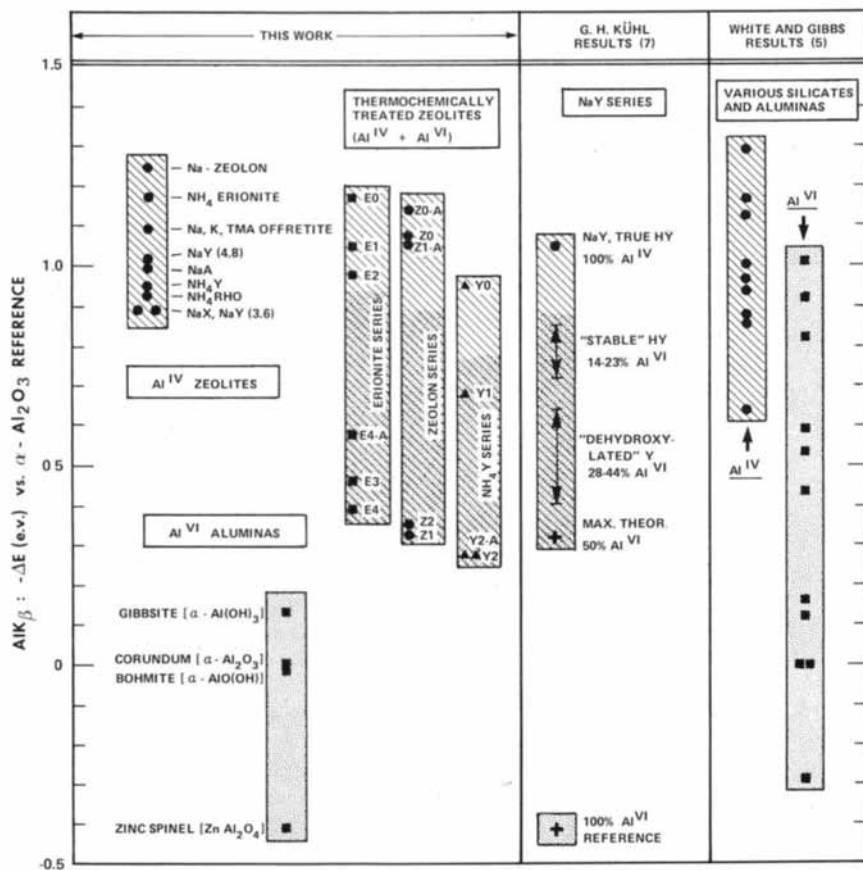


Figure 4. AlK_{β} results for various zeolites (Al^{IV}), aluminas (Al^{VI}), and thermochemically treated zeolites ($Al^{IV} + Al^{VI}$). Results of Kühl (7) and White and Gibbs (5) are shown for comparison.

correlations are reasonable in terms of increasing chemical shifts ($-\Delta E$) representing increased stabilization of the Al-O bonding orbitals from Group 1 to Group 3, and closer approach to perfect tetrahedral coordination of the framework Al. Qualitatively, the denser linked 5-ring mordenite framework should be less strained and the Al atoms less susceptible to approach by, and weak coordination with, extra-framework species. The excellent thermal stability of mordenite is also consistent with these AlK_{β} (and SiK_{β}) chemical shift results.

TABLE II
CORRELATION OF AlK_{β} SHIFTS
WITH FRAMEWORK DENSITY AND STRUCTURE

Group	Zeolites	AlK_{β} shift $-\Delta E$ (e.v.)	Framework Density (g/cc)*	Framework Structural Units*
1	A, X, Y, Rho	0.89 to 1.02	1.25 to 1.41	Truncated octahedra or cuboctahedra
2	Offretite, Erionite	1.09 to 1.17	1.51 to 1.55	Cancrinite Units (ϵ cages)
3	Mordenite	1.24	1.7	Crosslinked 5-ring chains

* Information from Breck (20) except Rho data from Robson et al., (21)

Additionally shown in Figure 4 are our $\Delta E(AlK_{\beta})$ values for the various aluminas and the various thermochemically treated zeolites, together with values reported by K uhl (7) for shifts of various Y's and values from White and Gibbs (5) for a wide variety of silicates separated into 4 and 6-fold Al coordination groups. [K uhl's values were all referenced to zinc spinel and have been plotted vs. our zinc spinel value; his $\Delta 2\theta = .240^\circ$ for NaY translates to a 1.46 e.v. difference and agrees excellently with our NaY (4.8) value. The White and Gibbs values, reported as $\Delta(\text{Å} \times 10^{-4})$ vs. $\alpha\text{-Al}_2\text{O}_3$, are referenced to our $\alpha\text{-Al}_2\text{O}_3$ value and scaled by the relation ΔE (e.v.) = $(-.0195) \times \Delta(\text{Å} \times 10^{-4})$.]

The zeolites (4-coord. Al) and the aluminas (6-coord.) are seen to lie in two distinctly separated broad groups. With successively more severe treatments, the thermochemically treated zeolites are seen to enter successively further into the region between the two groups, as is expected for increasing transformation of tetrahedral Al-O into 6-coordinated species.

K uhl observed this same behavior in his Y series (7) and, in fact, quantitatively estimated the percentage of framework Al transformed to hexacoordinated Al using a linear scale with his NaY and zinc spinel values as standards for 0% and 100% hexacoordinated Al, respectively. Our results support, and extend to other zeolites, K uhl's concept that increasing shifts of the AlK_{β} band from starting zeolite values can be used to monitor the relative degrees of framework dealumination resulting from thermochemical treatments.

It now seems, however, that quantitative estimates of the ratio of tetrahedral to hexacoordinated Al as derived from chemical shifts by K uhl, must be treated

with some caution because of the absence of a clearly defined standard for either 4-fold or 6-fold Al. For example, two hexacoordinated Al species, gibbsite ($\alpha\text{-Al}(\text{OH})_3$) and zinc spinel (ZnAl_2O_4), have shifts differing by 0.54 e.v., equivalent to 37% of the observed NaY to zinc spinel shift. Thus, within the realm of hexacoordinated Al species, a wide range of shifts are encountered depending on the actual oxy- or hydroxy-aluminum bonding present. The ideal standard representing 100% hexacoordinated Al should be the actual species present in the thermally treated zeolite. Unfortunately, variously treated zeolites probably contain more than one type of non-framework Al species with differing coordination with -O and -OH and in differing cationic forms, making selection of a suitable quantitative standard somewhat tenuous.

Even the use of the particular starting zeolite for a 100% 4-fold framework Al standard is precarious as evidenced by the 0.13 e.v. difference between NaY (4.8) and NaY (3.6) indicating that the Al remaining in the framework may itself shift as other Al is removed. Thus the .12 and .19 e.v. shifts for the two mildly steamed erionites, E1 and E2, which would indicate 8-12% hexacoordinated Al by Kühl's method, may simply reflect the changing environment of the framework Al. The data of White and Gibbs (5) shown in Figure 4 further illustrate the care needed in picking realistic standards.

The shifts for the severely steamed then acid extracted products deserve mention. It is apparent that essentially all the hexacoordinated Al was removed from mordenite (Z1-A) and part from erionite (E4-A), but the 6/4-fold ratio seems unaffected in Y (Y2-A). The differing results relate to the extent to which extra-framework Al can be trapped in the different structures, and illustrate the utility of chemical shift measurements in monitoring the effectiveness of chemical extractions.

C. Comparison of $\text{AlK}\beta$ and $\text{SiK}\beta$ Results: Both $\text{AlK}\beta$ and $\text{SiK}\beta$ shifts are plotted against each other in Figure 5, graphically illustrating the consistent, complementary nature of the two measurements. Strikingly, the untreated zeolites all closely fall along the same line, whereas the treated zeolites are all displaced to a degree related directly to the thermal treatment severity.

Summary

The $\text{SiK}\beta$ X-ray emission band energies of a variety of zeolites, as well as other tetrahedral framework aluminosilicates, have been found to increase approximately linearly with increasing substitution of Al into tetrahedral framework sites, implying significant destabilization of silicon bonding orbitals. These $\text{SiK}\beta$ shifts are highly sensitive to thermochemical treatments which remove Al from the zeolite framework, and readily allow comparison of the effects of such treatments.

As expected, $\text{AlK}\beta$ shifts are less sensitive to variation of zeolite framework Al fraction because all framework Al is coordinated to 4(-O-Si) groups regardless of composition. More important is the substantial $\text{AlK}\beta$ difference between 4 and 6-fold coordinated Al. Significant shifts result as tetrahedral framework Al is thermochemically transformed to octahedral extra-framework species. The magnitude of these shifts, as Kühl observed (7), can be used to estimate the extent of transformation, with the caution that quantitative use is complicated by the wide variety, and wide ΔE ($\text{AlK}\beta$) range, of possible extra-framework Al species.

Thus, both $\text{SiK}\beta$ and $\text{AlK}\beta$ chemical shift measurements are powerful, com-

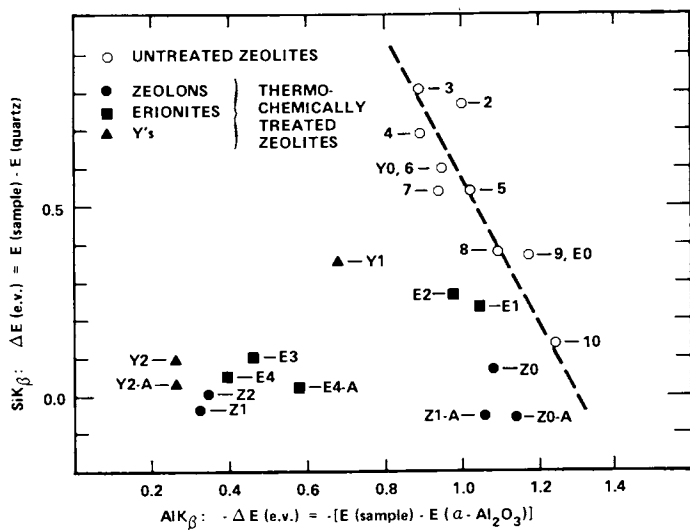


Figure 5. Plot of $\Delta E(\text{SiK}\beta)$ vs. $\Delta E(\text{AlK}\beta)$ for both untreated and thermochemically treated zeolites. Line shown is best linear fit of data for untreated zeolites.

plementary tools to readily monitor zeolite framework compositions and the structural and chemical changes occurring during various thermal and chemical treatments.

Literature Cited

1. White, E. W., Gibbs, G. V., *Amer. Mineral.* (1967) 52, 985.
2. Baun, W. L., *Appl. Spectr. Revs.* (1968) 1, 379.
3. Dodd, C. G., Glen, G. L., *J. Appl. Phys.* (1968) 39, 5377.
4. Dodd, C. G., Glen, G. L., *Amer. Mineral.* (1969) 54, 1299.
5. White, E. W., Gibbs, G. V., *Amer. Mineral.* (1969) 54, 931.
6. Freund, F., in *Proc. Intern. Clay Conf.* (1972) 13.
7. Kühn, G. H., In "Proc. Third Intern. Conf. on Molecular Sieves" Leuven University Press (1973) 227.
8. Tossell, J. A., *J. Phys. Chem. Solids.* (1973) 34, 307.
9. Brown, G. E., Gibbs, G. V., Ribbe, P. H., *Amer. Mineral.* (1969) 54, 1044.
10. Wardle, R., Brindley, G. W., *Amer. Mineral.* (1971) 56, 2123.
11. Jenkins, R., "An Intoduction to X-ray Spectrometry", Heyden and Son, N.Y. (1974).
12. Urch, D. S., *J. Phys. C: Solid St. Phys.* (1970) 3, 1275.
13. Tossell, J. A., *J. Phys. Chem. Solids* (1973) 34, 307.
14. Tossell, J. A., *Geochim. Cosmochim. Acta* (1973) 37, 583.
15. Tossell, J. A., Vaughan, D. J., Johnson, K. H., *Chem. Phys. Lett.* (1973) 20, 329.
16. Tossell, J. A., *J. Amer. Chem. Soc.* (1975) 97, 4840.
17. Tossell, J. A., *J. Phys. Chem. Solids* (1975) 36, 1273.
18. Dowell, L. G., Bennett, J. M., Passoja, D. E., paper presented at 25th Ann. Denver X-ray Conf. (1976), to be publ. in "Adv. in X-ray Anal."
19. Loewenstein, W., *Amer. Mineral.* (1954) 39, 92.
20. Breck, D. W., "Zeolite Molecular Sieves", John Wiley and Sons, N.Y. (1974).
21. Robson, H. E., Shoemaker, D. P., Oglivie, R. A., Manor, P. C., *Advan. Chem. Ser.* (1973) 121, 106.

Zeolite Surface Composition by X.P.S.

J-FR. TEMPERE and D. DELAFOSSE

Cinétique des Réactions Superficielles, E.R. 133, Université Pierre et Marie Curie, 75230 Paris Cedex 05, France

J. P. CONTOUR

Laboratoire de Physico-Chimie Instrumentale, Université Paris VII, 75221 Paris Cedex 05, France

ABSTRACT

In the present paper the silicon and aluminium composition of the external layers in some sodium zeolites or exchanged zeolites have been investigated by X.P.S. Partial dealumination of the surface of these solids is shown to occur.

Introduction

The adsorptive properties of synthetic zeolites are related to their ultramicroporous crystalline structure which confers upon them very high specific areas. But in many cases, the part of the surface really involved in the phenomena of gas adsorptive and catalytic reactions is only a small fraction of the total and can be limited in certain cases to the external layers of the crystal. The external surface of some synthetic zeolites has been studied by means of X.P.S.

Experimental section

Material. The following zeolites are used in the study : NaA, NaX, NaY Linde molecular sieves ; NaZ, HZ Norton zeolons ; partially calcium exchanged NaA, NaX, NaY and NaZ.

Some experiments were performed with Ketjen silica-aluminas containing either 14% or 26,4% by weight of alumina. A series of these oxides, progressively dealuminated in order to obtain samples containing from 0.1% to 26.4% by weight of alumina, was obtained from Dr. D. Barthomeuf.

X.P.S. X-ray photoelectron spectra were recorded on an AEI ES 200B spectrometer with a magnesium anode in the X-ray source (1253,65 eV). The binding energies were calculated by

taking the energy of the 1s electron of carbon contamination as an internal standard (1, 2). In view of previous work, this energy has been fixed at 285 eV. relative to the Fermi level (2). The spectrometer is equipped with an independent sample handling chamber, and a direct introduction system. During recording of the spectrum the pressure is 2×10^{-10} torr, when the sample is introduced via the preparation chamber, and 5×10^{-9} torr when it is introduced via the direct introduction lock. The zeolite powders are compressed onto a copper grid and then, fixed on the sample holder whose temperature can be varied from -180°C to 450°C . When the samples are desorbed "in situ", they are introduced via the preparation chamber and treated under vacuum (10^{-8} torr) at 300°C for 16 hours.

The inhomogeneity of the chemical composition in the external layers can be revealed by an in depth analysis. In the case of zeolite, the use of a sputter ion gun is not suitable when the samples are heterogenous insulator oxides, so that we try to obtain an in depth analysis by using a variable angle sample holder (3, 4). Such a device provides a non destructive analysis over a thickness of about one escape depth (5). Since the samples are compacted powders, the surface roughness of samples must be taken into account in a study of the angular distribution. The sinusoidally rough surface model which is proposed by C.S. Fadley (3) was chosen to describe the surface roughness of our compacted zeolite (Fig. 1). Scanning electron microscopy of the surface shows that the roughness parameter (a/λ) is close to unity. Fig. 2 shows the average value of the actual electron emission angle θ' evaluated over the electron unshaded area on a sinusoidally rough surface for $0.5 < a/\lambda < 2.0$. It is clear that when the apparent emission angle θ decreases the actual angle θ' decreases more and when θ is small, θ' becomes great. Such a θ' variation will exaggerate the surface species, not only for large values of θ , but also for the smallest ones.

Results

Energies of the Al and Si electrons in the zeolites. The energies of the Al_{2s} and Si_{2p} electrons in different zeolites can be grouped according to the value of the ratio (Al/Si) and the mean values are listed in table I. The 2s level of Al does not appear to be displaced and the values are close to those measured for $\gamma \text{Al}_2\text{O}_3$. On the other hand, the energies of the Si_{2p} electrons increase (+ 1.3 eV), on going from zeolite A to Z. The difference ($E_{\text{B Si}_{2p}} - E_{\text{B Al}_{2s}}$) increases in the same way. For the Y and Z zeolites, the binding energy is closer to that measured for silice, for type A and X it is considerably less.

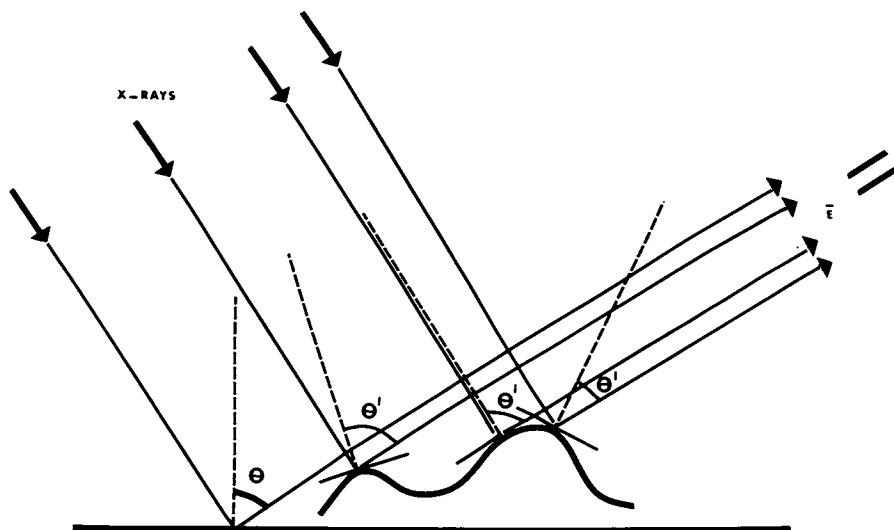


Figure 1. Model of a general rough surface contour with both x-ray and electron shading (after Ref. 3)

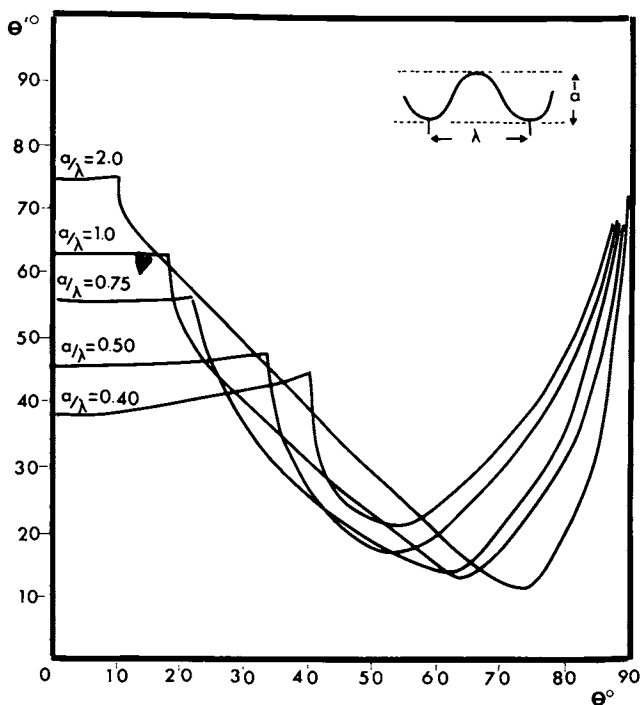


Figure 2. Curve showing the variation of Θ' with Θ for various values of the roughness parameter (after Ref. 3)

Table I. Si_{2p} and Al_{2s} binding energies.

Sample	(Al/Si) _B	E _L ^F Al _{2s} (*)	E _L ^F Si _{2p} (*)	Δ _{Al} ^{Si} eV	T-O (**) ^o Å
A	1	119.10	102.05	-17.05	1.688
X	0.80	119.55	102.70	-16.85	1.678
Y	0.40	119.75	103.25	-16.50	1.648
Z	0.20	119.60	103.35	-16.25	1.629
Ketjen		119.80	103.20	-16.60	
Al ₂ O ₃		119.50			
Si ₂ O ₃			103.20		

(*) The accuracy of this calculation is estimated to be $\pm 0,2$ eV

(**) mean length T-O from Smith (13)

Spectrometer calibration and relative intensity. For a sample of infinite thickness, the relative intensity of the two characteristic peaks is given by (6) :

$$\frac{I_1}{I_2} = \frac{n_1}{n_2} \times \frac{\lambda_1}{\lambda_2} \times \frac{\sigma_1}{\sigma_2} \times \frac{S_1}{S_2} = T_{1,2} \frac{n_1}{n_2} \quad (\text{Eq. 1})$$

with :

λ : mean free path of the photoelectrons of kinetic energy E_C

S : transmission factor of the spectrometer for an energy E_C

σ : effective ionization cross section

n : atomic concentration of the element studied

For the elements given, the ratio is a constant which can be called a "relative spectrometer intensity factor" : $T_{1,2}$. This factor can be determined, by recording the spectra of compounds of known stoichiometry. These calculations and the experimental determinations are presented in table II.

These results provoke two remarks : there is good agreement between our measurements and the ratio of the effective ionization cross sections, but at same time one observes considerable dispersion in the experimental values which suggests that subsequent quantitative analysis will lack precision.

Table II. Relative intensity of peaks Al_{2s} and Si_{2p} : $T_{Si,Al}$

This work		(8)	(9, 10)	(11)	(12)
Na_3AlF_3 Na_2SiF_6	Dealum. Ketjen	σ_{Si}/σ_{Al}		exp. theo.	AlK_{α}
1.37	1.61	1.27	2.53 (9) 1.82(10)	1.11 1.25	0.80*

* Since the energies of the Al_{2s} and Si_{2p} photoelectrons are similar, it is possible to compare the results obtained on different apparatus, since the transmission are close for similar kinetic energies.

Analysis of the surface of zeolites. Equation (1) makes it possible to evaluate the relative atomic concentrations of the two elements of a solid from the relative intensities assuming that the concentration is homogenous. But conversely if there is a concentration gradient, the relative intensities, which correspond only to the analysis of the superficial layers, would reveal a difference relative to the core concentration. The (Al/Si) ratios in the zeolites investigated in this study vary from 0.2 to 1. These ratios denoted by $(Al/Si)_B$ refer to the bulk composition and are obtained from chemical analysis. Another (Al/Si) ratio may be determined from X.P.S. which involves the external layers of the solid. This is referred to as $(Al/Si)_S$ and is based on the relative factor $T_{Si,Al} = 1.37$ which is reported above.

The results of the analysis of the zeolites of the Na series and of the calcium exchanged series are given in Fig. 3 and in table III. "In situ" desorption of samples at 300°C for 16 H causes no significant modifications of the relative intensities measured for the different solids. At higher temperatures the Al/Si ratio increases, and at 450°C the values of the ratios determined for calibration with Na_2SiF_6 are found (Fig. 3). At 850°C the zeolite structure is destroyed as indicated by the X-ray diffraction diagram. One then obtains a very high value, higher than the theoretical value. These analysis reveal an excess of Si^{4+} or an Al^{3+} deficiency for all these samples. The very low values obtained for the HZ zeolites which are decationized by HCl suggest that it is an Al^{3+} deficiency rather than an excess of silicon. We have attempted to verify this aluminium deficiency by using the variation of the relative intensity I_{Al}/I_{Si} with the angle of

photoelectron emission. As we have recalled above, if the surface roughness is taken into account, it can be seen that the effective photoelectron emission angle θ' is large (grazing angle) when the apparent angle θ is very small or very great so that the contribution of entities at the surface to the total signal will be intensified, not only for large apparent angles, but also for small ones. A superficial deficiency in Al^{3+} will appear then, as a decrease in the relative intensity $I_{\text{Al}2s}/I_{\text{Si}2p}$ for θ close to 0° and 90° . This corresponds to the profile recorded when θ was varied from 0° to 90° thus confirming the hypothesis that the external layers of the crystals are dealuminated. With a roughness parameter between 0.5 and 1 the variation of the relative intensity as a function of the effective photoelectron emission angle (Fig. 4a) has the classical form.

Discussion of the results.

a) Binding energy. According to various crystallographic studies on tectosilicates (13), the mean T-O bond length decreases on going from type A zeolite to type Z (see Table I). The binding energies of the $\text{Si}2p$ electrons increase from A to Z. Since this shift cannot be attributed to a variation in the charge of the cations it must be supposed that the modifications of the crystalline structure induces a variation of the Madelung potential which is responsible for this shift. In fact the decrease in the mean T-O length related to dealumination provokes an increase in the influence of near neighbors on the binding energy of the atom studied, it is however impossible to establish a quantitative correlation between the mean length and the binding energies of the $\text{Al}2s$ and $\text{Si}2p$ electrons. The effect of the Madelung potential shows up more clearly on the Si^{4+} ions than on the Al^{3+} ions contrary the results reported by Urch et al. (14) for natural silicoaluminates.

b) Dealumination. In a previous publication (15) we reported results on the X.P.S. analysis of the surface of some synthetic zeolites. However to calculate $(\text{Al}/\text{Si})_S$ we used the relative intensity coefficients of Wagner (12). The use of those coefficients had two disadvantages : first Wagner's tables were based on $\text{Al}_{K\alpha}$ radiations : moreover the Varian IEE 15 spectrometer used by this author has a transmission factor which varies with the kinetic energy differently than our AEI ES 200. These two parameters should not have led to important differences between our determinations and those of Wagner. Since the nature of the radiation has an effect of about 20% on the relative intensity and since the photoelectrons analysed have very similar energies (1135 and 1150 eV) the variation of the transmission factor can

then be neglected. We nevertheless observed considerable disagreement between our results and Wagner's but there is even less agreement between the latter and those of Jørgensen (9, 10) who uses the same type of spectrometer. The diversity of these results demonstrates clearly the great difficulty one meets when one tries to translate relative intensity measurements in terms of atomic concentration. In this work we have used the relative intensity factor determined by analysis of Na_3AlF_6 and Na_2SiF_6 on the AEI ES 200 spectrometer. Since this value is very close to the theoretical value calculated from the effective photoionization cross sections, we have assumed that its use led to the most precise calculation of the superficial atomic concentration (Al/Si) (7). The determination of Al/Si based on these assumptions for variously treated A, X, Y, Z zeolites lead to values which reveal systematic dealumination of the surface layers of those solids (Fig. 3 and Table III). This phenomenon which we have pointed out in a previous publication (15) has now been observed in other solids by other authors (16, 17). The principal objection to such a conclusion is the possibility that there is a matrix effect in the zeolite which lowers the apparent effective photoionization cross section of aluminium thus diminishing the intensity of the signal corresponding to Al^{3+} ions which could then be interpreted as evidence for a decrease in the atomic concentration (18).

Table III.

Bulk and superficial Si and Al composition of various zeolites.

	Linde molecular sieves			Norton zeolons	
	NaA	NaX	NaY	NaZ	HZ
(Al/Si) _B	1	0.8	0.4	0.2	0.2
untreated Na zeolite	0.75	0.65	0.25	0.15	0.041
desorbed 16 h at 300°C Na zeolite	0.68	0.49	0.22	0.17	0.069
(Al/Si) _S desorbed 16 h at 300°C Na,Ca zeolite	0.60	0.55	0.27	0.14	

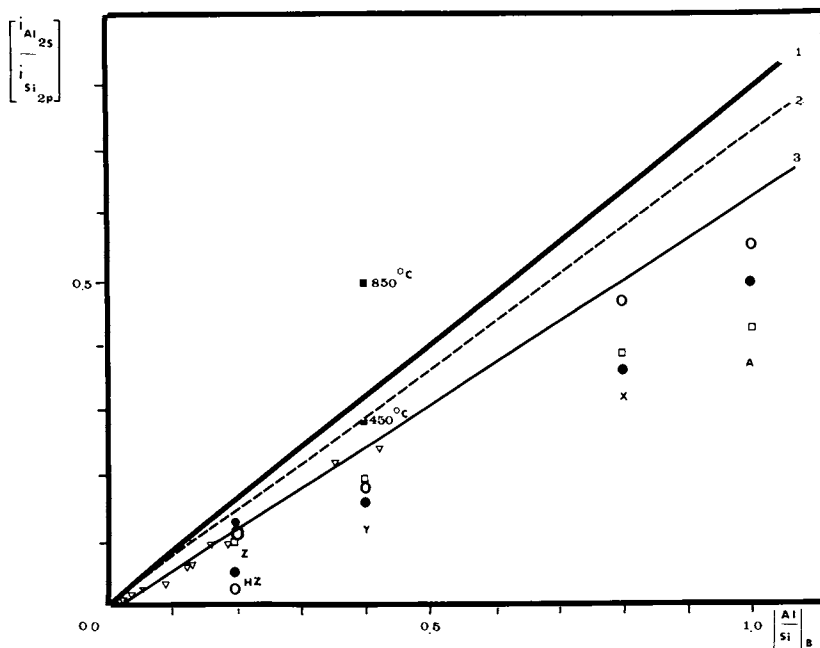


Figure 3. Curve showing the variations of $I_{Al_{2s}}/I_{Si_{2p}}$ with $(Al/Si)_B$. (1), effective ionization cross section. (2), $Na_3AlF_6-Na_2SiF_6$ as standard. (3), (a) ∇ dealuminated Ketjen series; (b) \circ NaA, NaX, NaY, NaZ, HZ; (c) \bullet as (b) but desorbed 16 hr at $300^\circ C$; (d) \square CaA, CaX, CaY, CaZ.

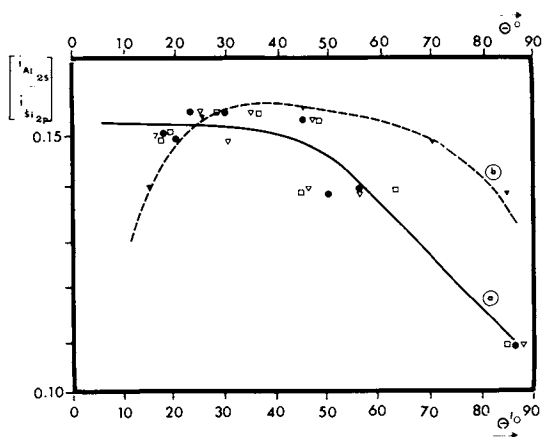


Figure 4. Curve showing the variations of $I_{Al_{2s}}/I_{Si_{2p}}$ with Θ' . (a) (∇) $a/\lambda = 0.5$, (\bullet) $a/\lambda = 0.75$, (\square) $a/\lambda = 1.0$. With Θ (b) \blacktriangledown .

We thought that adsorbed water molecules or the exchangeable cations could cause an effect of this type. We therefore recorded the spectre a) after "in situ" desorption and b) of a series exchanged with calcium ions. Since no significant variation between the three series of measurements could be observed we concluded that the low values of the Al/Si ratio were really due to a superficial Al^{3+} deficiency.

This interpretation is strongly supported by the variation of the relative intensity of Al and Si in function of the photoelectron emission angle assuming that the model proposed by Fadley is applicable to samples studied here. The curves obtained on the basis of these assumptions are given in Fig. 4 and appear to confirm that it is possible to use the model of a surface with sinusoidal roughness for compacted powders. Certain results (19, 20) suggest that the external surface of a particle or even the first external layers of a crystal have non negligible catalytic activity. This would appear to be confirmed by reagents which do not penetrate to the interior of the cavities or which diffuse only partially in the pores. Thus the reduction of benzophenone (19) may occur to a large extent on this external surface. If this is so, such reactions occur upon contact with a partially dealuminated catalyst.

Literature Cited

1. Jörgensen C.K. and Berthou H., Chem. Phys. Lett. (1975), 31, 416.
2. Contour, J.P., and Mouvier, G., J. Electron Spectrosc. (1975), 7, 85.
3. Fadley, C.S., J. Electron Spectrosc. (1974), 5, 725.
4. Larson, P., Private communication.
5. Blaise, G., Contour, J.P. and Leclere, J. Microsc. Spectrosc. Electron, (1976), 2, 247.
6. Carter, W.J., Schweitzer G.K. and Carlson T.A., Electron Spectrosc., (1974), 5, 825.
7. Barbaray, B., Contour, J.P. and Mouvier, G., J. Electron Spectrosc. (to be published).
8. Scofield, J.H., J. Electron Spectrosc. (1976), 8, 129.
9. Jörgensen, C.K. and Berthou, H., Anal. Chem. (1975), 47, 482.
10. Berthou, H., Private Communication.
11. Nefedov, J.I., Sergushin, N.P., Band I.M. Trzhaskovskaya, J. Electron Spectrosc. (1973), 2, 383.
12. Wagner, C.D., Anal. Chem. (1972), 44, 1050.
13. Smith, J.V., Acta Cryst. (1954), 7, 479.
14. Urch, D.S., Murphy, S., J. Electron Spectrosc. (1974), 5, 167.

15. Tempère, J.F., Delafosse, D. and Contour, J.P., *Chem. Phys. Lett.* (1975), 33, 95.
16. Defossé, C., Canesson, P. and Delmon, B. (to be published).
17. Thomassin, J.H., Touray, J.C. and Trichet, J., *C.R. Acad. Sci.* (1976) ser. D, 1229.
18. Nh K.T. Hercules D.H., *J. Electron Spectrosc.* (1975), 7, 257.
19. Shabtai, J., Lazar, R. and Schmidt, G.M., *J. Proceeding of the third International Conference on Molecular Sieves, Zürich sept. 1973*, p. 383, Leuven University Press.
20. Venuto, P.B., Landis, P.S., *J. Catal.*, (1971), 21, 330.

X.P.S. Study of HY Zeolites: Characterization of Superficial Composition and Acidity

C. DEFOSSE and B. DELMON

Groupe de Physico-Chimie Minérale et de Catalyse, Université Catholique de Louvain, Place Croix du Sud 1, B-1348 Louvain-la-Neuve, Belgium

P. CANESSON

Laboratoire de Chimie XI, U.E.R. Sciences Fondamentales et Appliquées, 40, Avenue du Recteur Pineau, F-86022 Poitiers, France

ABSTRACT

The superficial composition of germanium - and silicon-aluminum zeolites has been investigated by X.P.S. The aluminum concentration in the upper layers increases when the crystallinity decreases. Pyridine adsorption at 150°C on an HY zeolite induces a reduction of superficial silicon. Adsorption at room temperature allows a quantitative measurement of Brönsted and Lewis acid centers.

Introduction

The field of application of electron spectroscopy (called X.P.S. or E.S.C.A.) has broadened very quickly and its usefulness in catalysis has been conjectured very early (1). Indeed, the high specificity for surface analysis achieved by this technique allows the qualitative and quantitative characterization of the outermost layers of solids as well as that of adsorbed species. Very recently, some studies have been published dealing with the application of X.P.S. to the study of zeolites (2-6).

This communication concerns some applications of X.P.S. to the characterization of surface properties of zeolites. When catalytic phenomena are considered, diffusion effects may limit the actually active part of zeolites to the few first unit cells below the external surface of the grains, or, at least, give prominent importance to this external region. Since X.P.S. signals originate from the 15 - 30 outermost Angströms, they may give information that is more narrowly related to the observed catalytic activity. Two topics will be considered in the communication. First, the chemical composition of the superficial layers for ordinary (i.e. Si-Al) γ zeolites and for germanium faujasite-type molecular sieves has been determined quantitatively. Second, the superficial acidity of ordinary HY zeolites has been investigated by the adsorption of pyridine

used as a probe molecule. The adsorption state of the molecule can be monitored by X.P.S. and a qualitative distinction of Brønsted and Lewis acidity can be established, quite similar to what is routinely realized using I.R. techniques.

Experimental

1. Material. The germanium faujasite type zeolite has been synthesized according to a procedure described elsewhere (7). The bulk Al/Ge ratio is exactly unity. Sodium and ammonium exchanged (exchange level : 30%) sieves have been studied as well as the ammonium form after framework collapse subsequent to heating overnight in air at 180°C.

Two series of silicon zeolites have been studied. The first one (Union Carbide lot 3606-385) is characterized by a bulk Si/Al ratio of 2.2. Three different samples have been investigated : the original Na Y₁, a 72% exchanged NH₄Y₁, and the same NH₄Y₁ sample calcined in air at 900°C.

The parent NaY₂ zeolite of the second series has been synthesized in our laboratory; its bulk Si/Al ratio is 2.4. 60% exchanged CaNaY₂ and 90% exchanged NiNaY₂ samples have been prepared from the original NaY₂. The crystallinity of both series has been monitored by X-ray powder diffraction.

Pyridine (Merck A.G.) is distilled under vacuum. After thorough outgassing by the freeze - pump - thaw procedure, it is stored over activated 5 Å molecular sieve.

2. Procedure. All the X.P.S. spectra have been recorded on a Vacuum Generators ESCA 2 system equipped with a signal averager (Tracor Northern NS 560). The Al anode was powered at 10 KV and 50 mA. The sample was sprinkled on a double-sided adhesive tape.

In the experiments dealing with pyridine adsorption at room temperature (R.T.) on NH₄Y₁ zeolites, the treatment and sampling sequence are described elsewhere (8). Samples obtained this way are labelled Py 300, Py 400, Py 500 and Py 600, depending upon their activation temperature, expressed in °C.

Experiments have also been carried out on an HY zeolite activated at 300°C. In this case, pyridine was adsorbed and outgassed at 150°C. The cell was kept in liquid nitrogen overnight and a gold backing was used instead of scotch tape.

The Si 2p- or Ge 2p_{3/2} - line has been used as reference for determining binding energies and intensities. In the case of silicon-aluminum type zeolites, it has been proved elsewhere that the carbon contamination overlayer does not perturb the intensity ratios (8) since the kinetic energies of electrons issued from the reference line (Si 2p) and from the investigated one (Al 2p or N 1s) have similar values. For germanium-aluminum type zeolites, the Ge 2p_{3/2} level has been chosen as reference in the absence of any other suitable line; in this case, it

should be noted that the carbon contamination overlayer can artificially increase the Al 2p/Ge 2p_{3/2} intensity ratio because of the large difference in the mean free path of electrons issued from the Ge 2p_{3/2} and Al 2p levels.

The intensities are given as intensity ratios noted R_y^x equal to

$$R_y^x = \frac{I_y}{I_x}$$

where I_x is the planimetered intensity of the reference peak and I_y is the intensity for the line of interest.

Infrared measurements include a similar treatment than for X.P.S. analysis but, in this case, the zeolite is compacted into a wafer of 3 mg.cm² density and pyridine outgassing is achieved at increasing temperatures, namely at R.T., 100°C, 200°C and 300°C. Spectra in the 1750-1400 cm⁻¹ region have been recorded using a Beckman I.R. 12 spectrometer or a Perkin Elmer 180 spectrometer, working in absorbance mode. Intensities are the planimetered surface areas, normalized for the wafer thickness; they are expressed in absorbance units (A.U.) x wavenumber (W.N.; cm⁻¹) x cm² x g⁻¹. Assignments are taken from the literature (9,10).

Results

1. Superficial composition.

a. Germanium zeolites. For all the samples studied the difference in binding energy between the Ge 2p_{3/2} and Al 2p levels is constant, showing that the Ge and Al cations are in a similar surrounding.

For the various samples, namely NaGeX, NaNH₄GeX, and the hydroxysodalite structure obtained by heating the NaNH₄GeX at 180°C (11), the Al 2p/Ge 2p_{3/2} intensity ratios, noted R_{Al}^{Ge} , are given in Table I.

b. Silicon zeolites. Concerning the R_{Al}^{Si} 2p ratios, the influence of the calcination temperature as well as that of the ion exchange have been investigated on Y zeolites. The results for the two series are given in Table I.

TABLE I

intensity ratios for the various samples

Al 2p:	Germanium zeolites			Silicon zeolites						
	Sample:	Na	NH ₄	First series Y ₁	NH ₄ [*]	NH ₄	Second series Y ₂	Na	Ca	Ni
			180°C			900°C				
R	.0193	.0257	.0268	.21	.20+.01	.43	.24	.27	.58	

* Unactivated sample and samples activated at temperatures ranging from 300°C to 600°C.

2. Organic molecules adsorption. The behavior of pyridine adsorbed on NH_4Y zeolites outgassed at various temperatures has been investigated. All the experiments have been made with the NH_4Y_1 zeolite series.

a. Adsorption at 150°C. For the sake of comparison with some infrared studies (12,13), pyridine adsorption has been carried out at 150°C. In this condition, an unexpected result has been observed, as shown in figure 1. A second Si 2p line appears after adsorption at 150°C (figure 1-C). This second line is not observed in any of the following samples : (i) simply outgassed zeolite (I) (curve a), (ii) sample exposed to pyridine at room temperature (R.T.) (II), (iii) previous sample II further outgassed at R.T. (III) (curve b), (iv) sample II slowly heated for 1 hour at 150°C (IV) (curve not shown, similar to b). Similar results are obtained if ethylene is used instead of pyridine; namely a second Si 2p line is observed after adsorption at 150°C (figure 1, curve d).

b. Adsorption at room temperature. The most remarkable feature in the X.P.S. spectra after R.T. adsorption is a shift of -2 eV of the N 1s line from adsorbed pyridine when the activation temperature of the zeolite exceeds 400°C.

We have evaluated the ratio of the number of adsorbed pyridine molecules to the total number of silicon atoms in the near-surface layers. Intensity values, noted $R_{\text{N1s}}^{\text{Si}}$ (1) and $R_{\text{N1s}}^{\text{Si}}$ (2), correspond respectively to the low binding energy line and to the high one. These values, after correcting for the remaining N 1s intensities found in the corresponding blank samples (8) are summarized in table II.

Table II

$R_{\text{N1s}}^{\text{Si}}$ (i) values for the various Py samples.

	$R_{\text{N1s}}^{\text{Si}}$ (1)	$R_{\text{N1s}}^{\text{Si}}$ (2)
Outgassing temperature		
Without any treatment		.33
300	.0	.13
400	.02	.13
500	.18	.02
600	.11	.0

Discussion

1. Superficial composition. The atomic Al/x ratios in the superficial layers analyzed by X.P.S. can be calculated from the R ratios given in table I by the relation :

$$\frac{Al}{x} = R \times \frac{ix}{i Al 2p}$$

where x is Ge or Si and $ix/iAl 2P$ is the relative line intensity ratio taken from the literature (14,15). This above relation assumes that mean free path of electrons inside the solid and transmission factor of the spectrometer are the same for x and Al 2p. These conditions are verified for the Si 2p line: the kinetic energy of electrons for this level (about 1385 eV) is very close to that of the Al 2P line (about 1412 eV). For the Ge $2p_{3/2}$ level, because of the very high value of the binding energy, the relation would artificially enhanced the Al/Ge ratio. The results obtained this way are given in table III.

The surface layers of all well crystallized zeolites, in their initial Na form, are depleted in alumina. This fact had already been observed by other authors. (4)

On the other hand, a destruction of the structure by calcination at 900°C results in a superficial segregation of aluminum in the case of Y silicon zeolites. This is demonstrated by the fact that the Al/Si ratios for NH_4 900 are twice those observed with NaY. The bulk Al/Si ratio is situated between these two extremes.

The situation for germanium zeolites is somewhat different. The calcination in air at 180°C of the NH_4 exchanged material leads to a surface Al/Ge ratio similar to that of the bulk. This difference reflects the fact that, in the case of silicon zeolites, the calcination leads to an amorphous material, whereas with germanium ones, the thermal treatment at 180°C brings about the transformation of the faujasite type structure into hydroxysodalite (11).

As long as the exchange does not affect crystallinity, the superficial composition remains unchanged, as observed for the $NH_4 Y_1$ zeolite. When ion exchange leads to a partial loss of crystallinity, the superficial concentration in aluminum increases. This is illustrated by the Ca exchanged Y_2 zeolite, the X-ray diffraction pattern of which indicates a less crystalline material than the starting NaY_2 zeolite, and by the extensive Ni exchanged one, where this effect is still more enhanced. In both cases, one observes an increase in the Al/Si ratios in the layers analyzed by X.P.S. The same trend is observed for germanium zeolites.

Thus, the partial loss of crystallinity by the exchange process affects the superficial composition in a way similar to a thermal treatment. The loss of crystallinity results in a preferential loss of aluminium tetrahedra in the framework. These aluminum cations are expelled to the external surface of the crystallites.

The above results suggests that the determination of the Al/Si ratio by X.P.S. could constitute a valuable method for evaluating crystallinity.

2. Adsorption of organic molecules

a. Adsorption at 150°C. The second silicon line situated at a binding energy level of 98 eV cannot be attributed to a specific chemisorptive interaction between pyridine and silicon in the framework, since the same behavior is observed in the case of a completely different adsorbed molecule, namely ethylene. The separation between the silicon lines, approximately 4 eV (figure 1, c and d), is too large to be attributed to any specific interaction between the adsorbed molecules and silicon atoms. A shift of 4 eV is comparable near that observed between elemental silicon and SiO_2 (16). This shift is neither observed on the Al 2p line nor on the O1s one. We are therefore led to conclude that, as a consequence of adsorption, some silicon in the zero-valence state is formed on the external surface of the zeolite. In spite of possible interference of other contaminating gases, control experiments indicate that the line attributed to Si^0 disappear in the presence of traces of O_2 . In addition, this line tends to disappear over long periods of ^{22}Ne -x-ray exposure at R.T., probably by a diffusion into the bulk. Nevertheless, a possible reoxidation because of the poor quality of the vacuum cannot be excluded. The critical factor for this reduction of Si^{4+} to Si^0 is the adsorption temperature. The splitting into two lines of the Si 2p spectrum is not observed when the adsorption takes place at R.T. even after a subsequent slow outgassing at 150°C. The reduction to Si^0 apparently can only occur at the outermost surface of the crystallites since it has never been observed by bulk techniques. This surprising result raises the question as to whether such a superficial reduction could modify strongly catalytic properties in certain working conditions.

b. Adsorption at room temperature. Since pyridine adsorption at R.T. does not induce any reduction, X.P.S. can be used for superficial acidity determinations, by monitoring the N 1s level of the probe molecule.

There is a shift of 2 eV of the N1s level towards lower binding energies between Py 400 and Py 500 samples (table II). This shift must be attributed to differences in interactions between the nitrogen atom of the probe molecule and, respectively, a

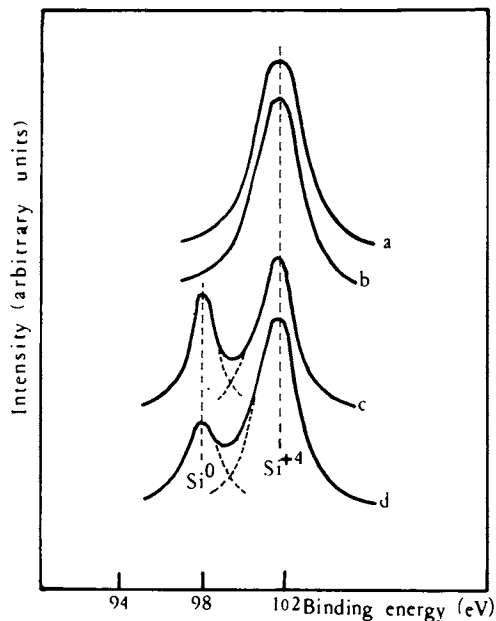


Figure 1. Si 2p profiles for NH_4 zeolite activated at 300°C . (a), with no pyridine adsorption; (b), upon pyridine adsorption at R.T.; (c), upon pyridine adsorption at 150°C ; (d), upon ethylene adsorption at 150°C .

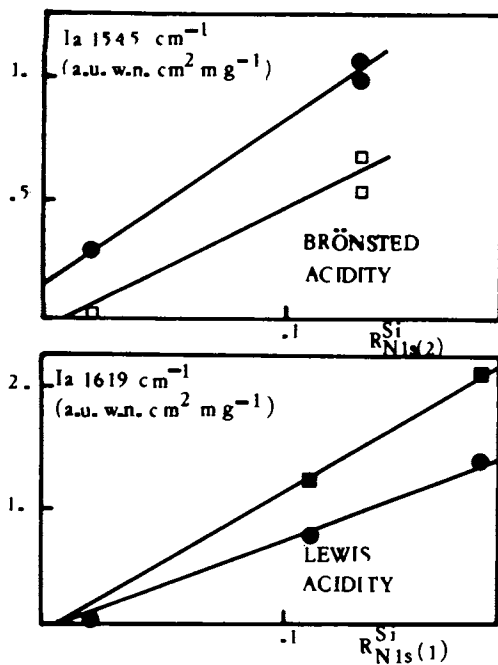


Figure 2. Quantitative correlation between X.P.S. $R_{\text{Ni}}^{\text{Si}^{2p}}$ and infrared absorption intensities for Brønsted and Lewis acid sites. Ni1s data collected at -90°C . I.R. wafer exposed to pyridine and outgassed at 20°C (■), 200°C (●) and 300°C (□).

Brönsted or a Lewis acid site since it is well known that dehydroxylation of HY zeolites occurs between 400°C and 500°C (17,18). Infrared measurements further support this conclusion.

Figure 2 indicates a good correlation between the $R_{N\ 1s}^{Si}$ (1) values characteristic respectively of Brönsted ($i = 2$) and Lewis ($i = 1$) sites and the intensity of the infrared bands at 1545 cm^{-1} (Brönsted sites) and 1619 cm^{-1} (Lewis sites). The comparison of $R_{N\ 1s}^{Si}$ (2) ratios for the initial NH_4Y zeolite and the Py samples shows that roughly one third of the near surface sites accessible to NH_3 can be reached by pyridine molecules.

From the stoichiometry, it is possible to calculate the theoretical intensity ratios of the N 1s and Si 2p lines for the NH_4Y initial zeolite (14). The theoretical intensity ratio is 0.68, and the experimental observed one is 0.33. This indicates that the surface NH_4 content is about 1/2 that of the bulk. This suggests that the surface depletion in aluminum tetrahedra corresponds to a similar depletion in NH_4 . The superficial layers of the crystallites are poorer in acidic centers (by a factor of about 1/2) than the bulk. This relation between Al and acidic center contents confirms that acidic centers are associated with the incomplete charge compensation of Al tetrahedra in the zeolite or alumino-silicate frameworks.

Acknowledgements. One of us (C.D.) thanks the "Fonds National de la Recherche Scientifique" (Belgium) for an "Aspirant" fellowship.

Miss M.L. Oubru and Mr. G. Decamp are gratefully acknowledged for kindly supplying germanium zeolites and some silicon ones.

Litterature Cited

1. Delgass W.N., Hughes T.R. and Fadley C.S., Catalysis Rev., (1970), 4, 179.
2. Minachev Kh. M., Antoshin G.V., Shpiro E.S. and Navruzov T.A., Izv. Akad. Nauk. S.S.S.R., Ser. Khim., (1973), p. 2131.
3. Minachev Kh.M., Antoshin G.V., Shpiro E.S. and Navruzov T.A., Izv. Akad. Nauk. S.S.S.R., Ser. Kim., (1973), p. 2134.
4. Tempere J.F., DELAFOSSE D. and Contour J.P., Chem Phys. Letters, (1975), 33, 95.
5. Defossé C., Friedman R.M. and Fripiat J.J., Bull. Soc. Chim. France, (1975), p. 1513.
6. Defossé C. and Canesson P., React. Kinet. Catal. Letters, (1975), 3, 161.
7. Lerot L., Poncelet G. and Fripiat J.J., Mat. Res. Bull., (1974), 9, 979.

8. Defossé C. and Canesson P., *J. Chem. Soc., Faraday Trans. I*, accepted for publication, in the press.
9. Ward J.W., *J. Colloid Interf. Sci.*, (1968), 28, 269.
10. Pichat P., Mathieu M.V. and Imelik B., *J. Chim. Phys.*, (1969), 66, 845.
11. Poncelet G. Personal communication.
12. Jacobs P.A., Theng B.K.G. and Uytterhoeven J.B., *J. Catalysis*, (1972), 26, 191.
13. Bielanski A. and Datka J., *Bull. Acad. Pol. Sci., Ser. Chim.*, (1974), XXII, 341.
14. Nefedov V.I., Sergushin N.P., Band I.M. and Trzhaskovskya M.B., *J. Electron Spectrosc.*, (1973), 2, 383.
15. Nefedov V.I., Sergushin N.P., Salyn Y.V., Band I.M. and Trzhaskovskaya, *J. Electron Spectrosc.*, (1975), 7, 175.
16. Hollinger G., Jugnet Y., Pertosa P. and Tran Minh Duc, *Chem. Phys. Letters*, (1975), 36, 441.
17. Uytterhoeven J.B., Christner L.G. and Hall W.K., *J. Phys. Chem.*, (1967), 69, 2117.
18. Ward J.W., *J. Catalysis*, (1967), 9, 225.

9

Acidity of Mordenite

G. H. KÜHL

Mobil Research and Development Corp., Paulsboro, N.J. 08066

ABSTRACT

The acidity of hydrogen mordenite was determined by treatment with 0.1N NaOH and back-titration of the excess, and by titration of the extract obtained by successive batch treatments with 2N NaCl or 0.1N AgNO₃. The results show that acid-exchanged mordenites are true hydronium forms. The degree of dehydroxylation of thin-layer calcined NH₄-mordenites can be estimated from the different results obtained by the two methods.

Introduction

When a true hydrogen zeolite Y is contacted with 0.1N NaOH solution, the sodium form of the zeolite is obtained (1). Sorbing water on hydrogen zeolite Y probably produces the hydronium form of the zeolite; the structure collapses upon dehydration of hydronium zeolite Y (1). It is not clear whether any framework-Al hydrolyzes upon contact of HY with water, but since the heat of hydration of a proton is considerable, partial hydrolysis is likely to occur. Similar reactions can be expected upon contact of HY with NaCl solution.

When a stabilized hydrogen zeolite Y is treated with 0.1N NaOH solution, cationic aluminum is removed from the zeolite and replaced by Na⁺ ions (1). Contact of stable hydrogen zeolite Y with 2N NaCl solution also causes removal of cationic aluminum in exchange for sodium, while the pH of the initially neutral solution drops to about 3 and the SiO₂/Al₂O₃ ratio of the remaining solid increases (2). Refluxing of a stabilized hydrogen zeolite Y with several batches of sodium chloride solution resulted in a gradual increase of the pH in sequential batches: 2.7-3.0-3.2-3.35-3.5 (2). It was also found that most of the exchangeable aluminum was removed in the first treatment. The number of sodium ions introduced into the zeolite per aluminum ion removed was close to 3.0 in the first exchange and decreased in subsequent

steps. It, therefore, appears that Al^{3+} ions are exchanged first, followed by $\text{Al}(\text{OH})^{2+}$ and $\text{Al}(\text{OH})_2^+$. In a few samples we found that the ratio $\text{Na}_{\text{in}}/\text{Al}_{\text{out}}$ dropped below 1, indicating the possible presence of a dimeric ion such as $\{\text{HO}-\text{Al} \begin{array}{c} \diagup \text{O} \diagdown \\ \text{O} \end{array} \text{Al}\}^+$.

Similar reactions occur with most zeolites. A notable exception is mordenite. When hydrogen mordenite is treated with NaCl solution at ambient temperature, hydronium ions are exchanged from the zeolite. Unless the contact is prolonged, no aluminum cations appear in solution; it is likely that hydrated aluminum ions are so large at ambient temperature that they cannot easily migrate out of the cavities. This behavior permits easy determination of exchangeable hydrogen ions by titration and may be useful as a model for other zeolites.

Since this work was done, Barrer and Klinowski (3) reported on the exchange of Na-mordenite with H_3O^+ ions and on the reverse reaction. They also reported results with H-mordenite prepared by calcination of NH_4 -mordenite. Therefore, we shall limit this paper to those parts of our work that will provide additional contributions to the understanding of hydrogen mordenite.

Experimental

Materials. Two samples of commercial hydrogen mordenite and three samples of commercial sodium mordenite were obtained from Norton Company; the compositions were (in wt. %):

	<u>Hydrogen Mordenite</u>		<u>Sodium Mordenite</u>		
	<u>A</u>	<u>B</u>	<u>A</u>	<u>B</u>	<u>C</u>
SiO_2	86.4	85.5	78.7	78.8	77.4
Al_2O_3	13.0	12.1	13.35	13.6	12.9
Na_2O	0.39	0.66	7.45	7.4	7.6

Three samples of hydronium mordenite were prepared by ion-exchange of sodium mordenite with 0.1N HCl at ambient temperature. Their compositions were:

	<u>Hydronium Mordenite</u>		
	<u>A</u>	<u>B</u>	<u>C</u>
	<u>A</u>	<u>A</u>	<u>B</u>
From Na-Mordenite			
Dried	Heat Lamp	Heat Lamp	Room Temp
SiO_2	70.9	70.9	69.9
Al_2O_3	10.9	11.7	11.6
Na_2O	0.21	0.33	0.34

NH_4 -mordenite was prepared by successive ion-exchange of sodium mordenite C with 2N NH_4Cl solution at reflux temperature. The composition was 65.2% SiO_2 , 10.7% Al_2O_3 , 0.30% Na_2O , 2.69% N.

Procedures. The thermal analysis was carried out with a DuPont Model 950 thermogravimetric analyzer. Ammonia appearing in the effluent helium was determined by passing the gas through a solution containing 2 ml of aqueous 4% boric acid and 50 ml of water, and titrating with sulfamic acid using an automatic titrator.

Three methods for determining the acid hydrogen were used:

- a) Approximately 1g of zeolite is treated with 20-25 ml of 0.1N NaOH and stirred for one hour. The slurry is then filtered and washed with water. The excess of NaOH is back-titrated with 0.1N HCl to determine the ml 0.1N NaOH consumed. Methyl purple was used as indicator.
- b) Approximately 1g of zeolite is treated with 150 ml of 2N NaCl solution and stirred for fifteen minutes. The slurry is filtered on a fritted disk funnel and the residue washed with water. The filtrate is titrated with 0.1N NaOH. Methyl purple was used as indicator to obtain a very distinct end point, but other indicators can be used. The solid is reslurried with 150 ml of 2N NaCl solution and the treatment repeated until the amount of titrant required is only 0.1 ml for the last batch. The accumulated ml of 0.1N NaOH is plotted over the number of treatments and extrapolated.
- c) Since mordenite, like other zeolites, has a high affinity for Ag^+ ions, 2N NaCl can be replaced by 0.1N AgNO_3 solution. To prevent precipitation of Ag_2O during the titration, NaCl solution is added to each filtrate ($\text{AgNO}_3 + \text{NaCl} \rightarrow \text{AgCl} \downarrow + \text{NaNO}_3$) before titrating with 0.1N NaOH.

No aluminum was extracted by these treatments in the great majority of determinations. In a few experiments, negligible traces of aluminum were observed.

The percentage of aluminum potentially associated with hydrogen ions ("effective" aluminum) was calculated by subtracting the percentage of aluminum associated with sodium or ammonium from the total aluminum content. From this figure and the titration result the atomic ratio of acid hydrogen per effective aluminum, $\text{H}^+/\text{eff. Al}$, was determined. X-ray diffraction of a few selected samples showed full retention of crystallinity.

Results and Discussion

When a mordenite sample containing hydrogen ions is contacted with sodium chloride solution, an exchange $\text{HM} + \text{NaCl} \rightleftharpoons \text{NaM} + \text{HCl}$ takes place. The extent of the exchange is governed by the exchange isotherm (3). Repeated NaCl treatments remove more and more hydrogen ions, the total amount of available acid hydrogen being approached asymptotically. If the accumulated acid removed is plotted over the number of treatments, the curve obtained with five to seven treatments can be extrapolated to

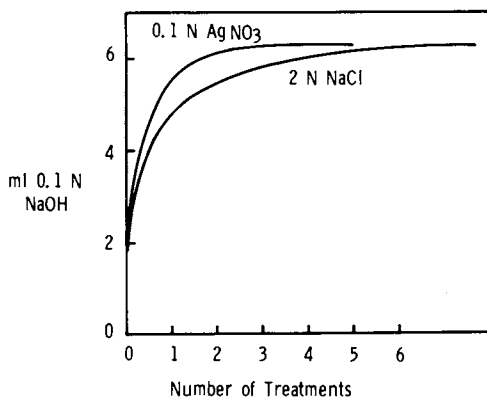


Figure 1. Comparison of Ag and Na exchange of H-mordenite

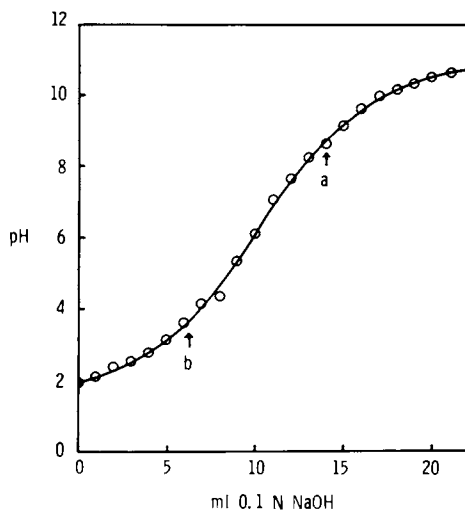
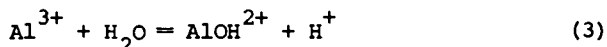


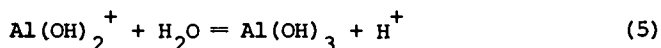
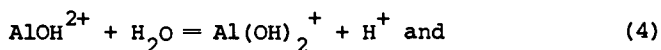
Figure 2. Titration of H-mordenite. 1.0982g H-mordenite A + 10 ml saturated NaCl solution + 100 ml H₂O.

and neutralized upon leaving the zeolite. The equilibrium pH after every addition of NaOH depends on the two coupled rate reactions, hydrolysis of cationic Al(1) and ion-exchange(2).

The points corresponding to the results obtained by the NaCl method(b) and by the NaOH method(a) are marked in Figure 2. It seems likely, therefore, that free hydrogen ions and those generated by



are determined by procedure b), whereas the sum of these hydrogen ions and those generated by the reactions



is obtained by procedure a).

The results obtained indicate that commercial hydrogen mordenites -- or at least the two samples investigated by us -- are not true hydrogen zeolites. Their structure appears to be considerably more complex. Our next goal was, therefore, to prepare a true hydrogen form of mordenite. A mordenite containing hydrogen ions as the only source of acidity should give the same results with both procedures, unless a secondary reaction, such as hydrolysis of framework-aluminum, occurs. An acid form of mordenite can conceivably be prepared by

- a) ion-exchange with an acid,
- b) calcination of ammonium mordenite.

Hydronium Mordenite. Ion-exchange of sodium mordenite with 0.1N HCl produced hydronium mordenite, in agreement with Shikunov, Lafer and Yakerson (4). The analytical data show a small increase in the $\text{SiO}_2/\text{Al}_2\text{O}_3$ ratio for samples B and C, a somewhat greater increase for sample A. The results suggest that treatment with 0.1N HCl extracts some aluminum from the zeolite, in agreement with the findings of Barrer and Klinowski (3). The amount of acid used to prepare sample A was greater than for B and the product contained less sodium and aluminum.

Sodium chloride extracted 0.601 $\text{H}^+/\text{eff. Al}$ from hydronium mordenite A. The treated zeolite sample had a Na/Al atomic ratio of 0.595, in excellent agreement with the result of the titration.

Another sample of hydronium mordenite (sample B) was examined after twelve years of storage. Treatment with 0.1N NaOH neutralized 0.481 $\text{H}^+/\text{eff. Al}$, and NaCl treatment extracted 0.482 $\text{H}^+/\text{eff. Al}$. The perfect agreement of the results indicates that the only acidity present in the zeolite was that of H_3O^+ ions. But the absolute number found is very low suggesting that H_3O^+ ions disappeared, either in the drying procedure or in storage, without generating other potential acidity, such as that of

aluminum cations.

Determination of acid hydrogen in hydronium mordenite C gave 0.648 H^+ /eff.Al with NaOH and 0.663 H^+ /eff.Al with NaCl, i.e. practically identical results by the two methods, again indicating the absence of acidity other than H_3O^+ .

Finally, ammonium mordenite was exchanged with 0.1N HCl but the product was not dried after washing. Treatment of this sample with 0.1N NaOH and back-titration of the excess showed the presence of 0.802 H^+ /eff.Al, calculated on the assumption that the small percentage of Na did not change during the HCl exchange. An identically treated sample was contacted with NaCl and the released acid titrated yielding 0.776 H^+ /eff.Al by this determination, again in agreement with the result obtained by NaOH treatment. The higher H^+ /eff.Al of this sample compared with the dried materials agrees with the statement of Shikunov and co-workers (5) that the presence of molecular water is required for the existence of the hydronium ion.

All samples of hydronium mordenite gave the same results by the two methods employed. This can only happen if hydronium ions are the only source of acidity in the zeolite. In particular, aluminum cations of any composition cannot be present. It is interesting that the acid treatment did extract small amounts of aluminum from the framework, but all intermediate cationic aluminum was then removed by ion-exchange. The always low H^+ /Al ratios suggest that some non-ionic Al is present, possibly still attached to the framework through two oxygen ions and carrying one free hydroxyl group.

H-Mordenite Obtained by Calcination of NH_4 -Mordenite. The decomposition pattern of ammonium mordenite is shown in Figure 3. A helium atmosphere was used to avoid temperature excursions upon oxidation of NH_3 in air, as observed, e.g., by Weeks and co-workers (6). The figure contains the thermogravimetric analysis at 5°/min. heating rate (corroborating the results of Benesi (7) and Shikunov and co-workers (8)), the weight of ammonia released and the weight of water given off. Also included are the rates at which ammonia and water are liberated (in arbitrary units). The temperature at which ammonia begins to escape is about the same as for zeolite Y (9). Whereas the release of ammonia from NH_4Y is practically complete at 460°C (9), it reaches its highest rate for mordenite at 480°C, and is essentially complete at 620°C. The highest rate of dehydroxylation of mordenite is attained at about the same temperature as with zeolite Y, about 670°C. However, whereas dehydroxylation of zeolite Y occurs within a narrow temperature range (9), this reaction in mordenite is drawn out from 525 to 880°C. It is evident that the deammoniation and dehydroxylation reactions overlap in the range of 525 to 620°C. For this reason, it is very difficult, if not impossible, to prepare a pure hydrogen mordenite by calcination of ammonium mordenite. The best chances appear to be in the range 480-525°C.

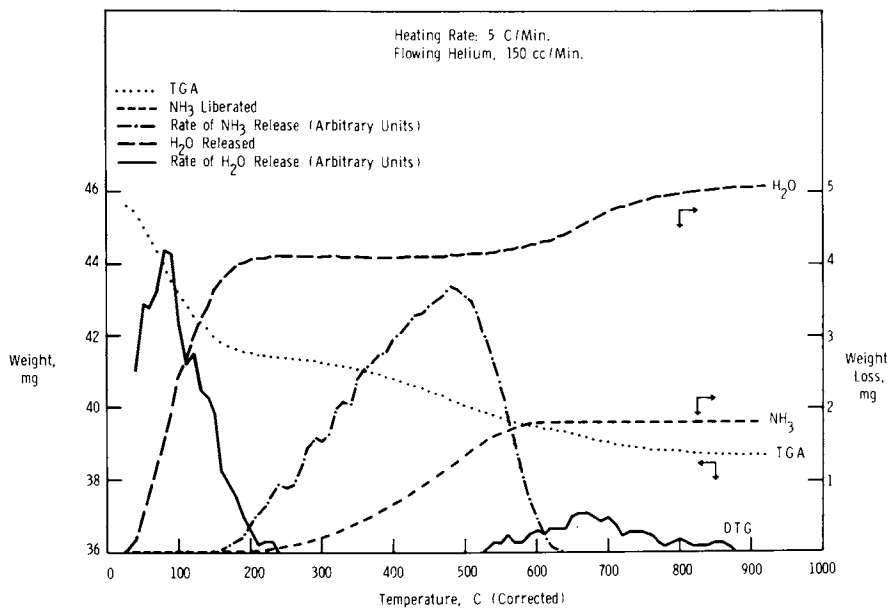


Figure 3. Thermogravimetric analysis of NH_4 -mordenite

In order to prevent hydrolysis of framework-aluminum, it is mandatory to remove gaseous reaction products fast. Several attempts to prepare a pure hydrogen mordenite are outlined in Table I.

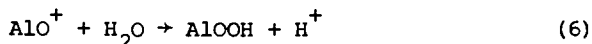
TABLE I.— Attempts to prepare pure H-mordenite

Sample No.	Muffle	Sample in	Heating Rate	Highest Temp.	Time at Highest Temp.	H ⁺ /eff.Al	
						NaOH	NaCl
1	Cold	Crucible	1°/min	480°C	8 hrs	0.539	0.344
2	"	Thin Bed	3°/ "	"	3 "	0.795	0.559
3	"	" "	" "	"	1 hr	0.855*	0.695*
4	"	" "	" "	500°C	3 hrs	0.816	0.631
5	"	Crucible	1°/ "	515°C	" "	0.539	0.453
6	"	"	" "	550°C	" "	0.508	0.189
7	Hot	"	-	480°C	" "	0.669	0.518
8	"	"	-	550°C	" "	0.479	0.250

*Contains 0.156 residual NH₄⁺/Al, all other samples <0.008.

Kerr (1) produced a true hydrogen zeolite Y by "shallow bed" calcination. Samples 2 to 4 were prepared by the same method, calcinations 2 and 4 gave complete deammoniation. The titration results indicate more dehydroxylation at 480°C than at 500°C, whereas the opposite should be the case. The data are evidence of the degree of reproducibility attainable for shallow bed calcination in this temperature range. Less acid hydrogen was found in a sample calcined for one hour at 480°C (sample 3), but the product still contained 0.55% N. If the effective Al is reduced by the corresponding amount, the highest H⁺/eff.Al was found in this sample; but the result is still only 85% of that expected if all acid hydrogen initially formed in the deammoniation process was retained. Evidently some dehydroxylation occurred even in one hour at 480°C, before deammoniation was complete.

For all three thin layer calcined samples, especially for samples 3 and 4, it is evident that the amount of acid hydrogen lost is twice as great for the NaCl procedure as for the NaOH method. Assuming that no "deep bed" (1) reactions occurred during the calcination, only dehydroxylation has to be considered. As reported earlier (10), X-ray spectrometry results suggest that, in dehydroxylated zeolites, one half of the aluminum is tetrahedrally coordinated (framework-Al) and the other half is probably present as AlO⁺ cations to give the combination AlO⁺ AlO₂⁻. AlO⁺ can hydrolyze according to



This reaction occurs when dehydroxylated mordenite is treated with

0.1N NaOH, thus generating 1 H⁺/2 Al. The exchange equilibrium between Na⁺ and H⁺ does not permit this reaction to proceed when the zeolite is treated with NaCl solution. In a partially dehydroxylated true hydrogen mordenite, NaCl extracts only hydronium ions formed by hydration of protons, whereas 0.1N NaOH determines also those generated by equation (6). Thus, 70% of the effective aluminum in sample 3 is associated with protons, 15% is present as AlO⁺ ions associated with another 15% of the effective Al in the framework: (H⁺)_{.70}(AlO⁺)_{.15}(AlO₂⁻)_{.85}

(sample 2: (H⁺)_{.56}(AlO⁺)_{.22}(AlO₂⁻)_{.78}; sample 4: (H⁺)_{.63}

(AlO⁺)_{.185}(AlO₂⁻)_{.815}). The other samples in Table I, calcined

in crucibles, have characteristics intermediate between shallow bed and deep bed calcination with some degree of dehydroxylation added. The closest to deep bed calcination with the least amount of dehydroxylation is expected from a fast calcination at the lowest temperature (sample 7). The titration results can be

interpreted if a dimeric cation {Al₂O₂OH⁺} is assumed: H⁺_{.52}

(Al₂O₂OH⁺)_{.15}(AlO₂⁻)_{.67}. It is questionable whether hydrogen

ions can coexist with the dimeric cation, and other explanations may be possible.

Dealuminized Mordenite. The number of acid sites in a hydrogen mordenite can be reduced by mere calcination or steaming. However, oxy- and hydroxy-aluminum cations and possibly aluminum oxide are deposited in the channels of the zeolite. These materials, which may block passage of hydrocarbons in catalytic applications, can be removed by acid extraction.

Prolonged heating of any hydrogen mordenite to a temperature of about 480°C or higher causes a decrease of the H⁺/Al ratio by dehydroxylation (Table II).

TABLE II.- Dehydroxylation of hydrogen mordenite

Sample, SiO ₂ /Al ₂ O ₃	H ⁺ /Al after drying at 120°C	H ⁺ /Al after calcination at 550°C for	
		3 hours	16 hours
H-Mordenite B, 12.0	0.31	0.29	0.06
H-Mordenite, 14.8 ^a	0.65	0.50	0.12
H-Mordenite, 23.8 ^b	0.63	0.53	0.14

a) Prepared by refluxing Na-mordenite C with two batches of 20% H₂SO₄ for four hrs. each.

b) Prepared by refluxing NH₄-mordenite A with 6N HCl for eight hrs.

The data for H^+/Al in this table were obtained from NaCl treatments; this procedure was chosen because it does not extract H^+ generated by hydrolysis of hydroxylated aluminum cations, and the data obtained in this way should be more meaningful.

TABLE III.- Dealuminized mordenite -
Effect of steaming and acid treatment

Starting Material SiO_2/Al_2O_3	Steamed		Refluxed		Product	
	hours	°C	hours	with	SiO_2/Al_2O_3	H^+/Al
23.8 ^a	24	760	8	1N HCl	38	0.05
38	24	760	8	6N HCl	41.5	0.02
23.8 ^a	-	-	24	6N HCl	47	0.56
11.3 ^b	-	-	6x8	6N HCl	75	0.58
75	24	760	4x8	6N HCl	102	0.29
11.3 ^b	-	-	5x8	6N HCl	62	0.69
62	2	538	5x8	6N HCl	112	0.46 ^c
10.2 ^d	-	-	6x8	6N HCl	59	0.62 ^e
59	2	538	3x8	6N HCl	125	0.39 ^e

- a) See Table II.
 b) Hydrogen mordenite A.
 c) After two-hour calcination at 480°C.
 d) Sodium mordenite C.
 e) After two-hour calcination at 540°C.

Table III contains results obtained by NaCl treatment of dealuminized mordenites; the effect of steam treatment on the hydrogen content was examined. When a mordenite of 23.8 SiO_2/Al_2O_3 was steamed at 760°C for a day, acid hydrogen was almost completely lost. The same treatment decreased the H^+/Al ratio of a 75 SiO_2/Al_2O_3 sample by only 50%. Steam treatment at lower temperature (538°) (11) and for a shorter period (two hours) retained considerably more H^+/Al in the preparation of high-silica dealuminized mordenite.

The results indicate that high-temperature steaming of hydrogen mordenite causes removal of aluminum from the framework and deposition within the zeolite as polymeric oxoaluminum cations of low charge and probably even as neutral aluminum oxide. These species appear to have a low rate of dissolution at a hydrogen ion concentration present in the zeolite channels and cannot be extracted very readily.

Acknowledgment

The valuable assistance of Mr. G. R. Landolt in the experimental procedures of the thermal analysis is gratefully acknowledged.

Literature Cited

1. Kerr, G. T., *J. Catal.* (1969), 15, 200.
2. Kühl, G. H., unpublished results.
3. Barrer, R. M., and Klinowski, J., *J. Chem. Soc., Farad. Trans. I*, (1975), 71, 690.
4. Shikunov, B. I., Lafer, L. I., and Yakerson, V. I., *Dokl. Akad. Nauk SSSR* (1971), 200, 1119.
5. Shikunov, B. I., Lafer, L. I., Yakerson, V. I., and Rubinshtein, A. M., *Izv. Akad. Nauk SSSR, Ser. Khim.* 1971, 1595.
6. Weeks, T. J., Jr., Hillery, H. F., and Bolton, A. P., *J. Chem. Soc., Farad. Trans. I*, (1975), 71, 2051.
7. Benesi, H. A., *J. Cat.* (1967), 8, 368.
8. Shikunov, B. I., Mishin, I. V., Piloyan, G. A., Klyachko-Gurvich, A. L., Lafer, L. I., Yakerson, V. I., and Rubinshtein, A. M., *Izv. Akad. Nauk SSSR, Ser. Khim.* 1973, 767.
9. Kerr, G. T., and Chester, A. W., *Thermochimica Acta* (1971), 3, 113.
10. Kühl, G. H., "A Study of Aluminum Coordination in Zeolites Using the K β Line", Recent Progress Report, Proceedings of the Third International Conference on Molecular Sieves, page 227 (1973). Full paper in preparation.
11. Chen, N. Y., and Smith, F. A., *Inorg. Chem.* (1976), 15, 295.

Electronic Structure and Stability of Transition Metal Ions in Zeolites

KAMIL KLIER and PAUL J. HUTTA
Lehigh University, Bethlehem, Penn. 18015

RICHARD KELLERMAN
Xerox Corp., Webster, N.Y. 14580

ABSTRACT

A theory of the electronic structure of transition metal ions in zeolites which takes into account the site symmetry and vibrational-electronic interactions is presented. The relative stabilities in trigonal sites ($\text{Cu}^{\text{II}} \approx \text{Ni}^{\text{II}} > \text{Co}^{\text{II}} > \text{Fe}^{\text{II}} > \text{Mn}^{\text{II}}$, $\text{Cr}^{\text{II}} \approx \text{V}^{\text{II}} > \text{Ti}^{\text{II}}$), redox potentials, axial and off-axial distortions, and optical transitions are calculated and compared with published data.

Introduction

It is well established that transition metal ions in zeolites act as specific chemisorption centers (1-4), form intrazeolitic complexes (5,6), undergo redox reactions (7-10), and are catalytically active in oxidation reactions (11). These properties stem from the electronic structure of the ions in coordinatively unsaturated sites of the zeolite internal surfaces, and are accompanied by well defined physical properties such as optical absorption, photoluminescence, magnetic moments, and magnetic resonances, characteristic of both the metal ion and its environment.

A theory that accounts for these phenomena must take into consideration the site symmetry, interelectronic repulsion, vibrational-electronic interactions, spin-orbit coupling, and interactions with electromagnetic fields where present, and to compare the chemical properties and stabilities of the individual ions, such a theory should encompass the whole transition series.

The interelectronic repulsion and site potential energies for D_{3h} and C_{3v} symmetries were first analyzed for the Ni^{2+} ion and compared with the optical spectra of the NiA zeolite (12,13). In this paper an analysis is presented for all the d^n configurations. Further discussion is devoted to the effects of vibronic coupling on the stability of ions in trigonal and tetrahedral sites, and to the consequences of combined crystal-field, Jahn-Teller effect, and spin-orbit coupling.

Observations and Physical Model

The observable quantities in transition metal ion containing zeolites are associated with either the electronic ground states or transitions between the ground and excited states. To the first category belong chemical properties such as redox potentials and stabilization energies, static and dynamic distortions, magnetic moments, and magnetic resonances. Phenomena of the second class are exemplified by optical absorption spectra and color changes induced by chemisorption, photoluminescence, and as yet unreported but expectable photochemical reactions. Theoretical relationships among various observable quantities can be found in terms of a small number of physically meaningful parameters related to the symmetry of ligand charge distributions.

We consider the Hamiltonian given by

$$H = T + V_R + V_G + H_{LS} + H_{JT} \quad (1)$$

where T is the kinetic energy, V_R the interelectronic repulsion, V_G the ligand field potential at a site of the symmetry group G , H_{LS} the spin-orbit coupling energy, and H_{JT} the Jahn-Teller (vibronic) coupling energy. While $T + V_R + H_{LS}$ are basically atomic (i.e., spherically symmetric) properties of the ion, $V_G + H_{JT}$ describe the interaction of the ion with its environment. The symmetry of V_G is the full site symmetry but the symmetry of H_{JT} is generally that of less than fully symmetric irreducible representations of the group G . The site symmetry G may be obtained from crystallographic data but the model presented here is sufficiently general to allow for continuous transitions from one symmetry position to another and for determination of the site symmetry from optical data where crystallographic positions are not available.

The prevailing site symmetries in zeolites have in common a trigonal axis, and the model for such a site is depicted in Fig. 1. The site symmetry in this picture is C_{3v} and contains the limiting cases of planar trigonal (D_{3h}) symmetry for $L_1 = L_2 = L_3$, $L_4 = 0$, $\beta = 90^\circ$; tetrahedral (T_d) for $L_1 = L_2 = L_3 = L_4$, $\cos \beta = -1/3$; and half-octahedral for $L_1 = L_2 = L_3$, $L_4 = 0$, $\cos \beta = -1/\sqrt{3}$. Two identical assemblies with $L_4 = 0$ may also be superimposed from the positive and negative z -direction so as to form sites of symmetries D_{3v} or D_{3h} with six oxygen atoms surrounding the metal ion. The SI site in zeolites is accordingly D_{3v} symmetry while the SII-type sites have C_{3v} or D_{3h} symmetries. The ligand field potential for the model in Fig. 1 is given by (14)

$$\begin{aligned}
 V_{C_{3v}} = V(r, \theta, \phi) = & 3V_{00}^B z_{00}^B + V_{00}^A z_{00}^A \\
 & + \left\{ \frac{3}{2} V_{20}^B (3 \cos^2 \theta - 1) + V_{20}^A \right\} r^2 z_{20}(\theta, \phi) \\
 & + \left\{ \frac{3}{8} V_{40}^B (35 \cos^4 \theta - 30 \cos^2 \theta + 3) + V_{40}^A \right\} r^4 z_{40}(\theta, \phi) \\
 & + \frac{3\sqrt{70}}{4} V_{40}^B \sin^3 \theta \cos^2 \theta r^4 z_{43}(\theta, \phi) \quad (2)
 \end{aligned}$$

where
$$Y_{k0} = \frac{4\pi}{2k+1} \int_0^\pi \frac{P_k^0(\cos \theta)}{r^{k+1}} z_{k0}(\theta, \phi) dr$$

and
$$z_{k0} = Y_{k0} z_{k0}^C; z_{k1} = \frac{1}{\sqrt{2}} (Y_{k-1} + \bar{Y}_{k-1})$$

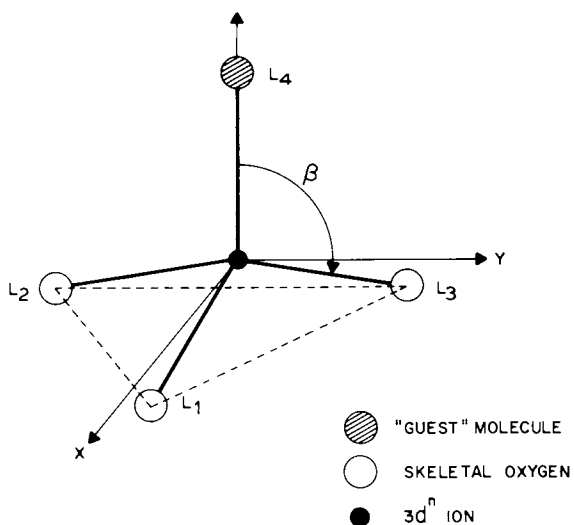


Figure 1. The C_{3v} ligand field model for intrazeolitic transition-metal ion complexes. The three base ligands L_1 , L_2 , L_3 are the proximal oxygens of the distorted hexagonal oxygen window of the sodalite unit. Ligand L_4 represents an adsorbed 'guest molecule.'

The superscripts A, B in the γ 's refer to axial or basal ligands respectively, $V_{C_{3v}}$ is the potential felt by an electron at $\underline{r} \equiv (r, \theta, \phi)$ and $\rho(\underline{R})$ is the charge density of the ligands at $\underline{R} \equiv (R, \Theta, \Phi)$. For $\beta = 90^\circ$ the potential in eq. 2 becomes independent of the in-plane angle ϕ in which case the trigonal field behaves as a circular field and one can rigorously replace the ligands L_1, L_2 , and L_3 by a "halo" of negative charge. The circularly symmetric field allows the orbital angular momentum to remain a good quantum number and results in high orbital contributions to the magnetic moment. When ligand L_4 has off-axial symmetry components, as in the case for π -bonded olefins (4), the low symmetry component may be introduced as a perturbation.

The individual parts of the Hamiltonian (eq. 1) are often of comparable magnitude but for the first and second transition series the contributions to energy from $T + V_R + V_C$ are much larger than those from $H_{LS} + H_{JT}$. We therefore describe the major effects due to electron repulsion and ligand field energies in Parts III - IV and follow with the analysis of Jahn-Teller effect and spin-orbit coupling in Part V.

Energy Spectra of Ions in Trigonal Fields with Electron Repulsion

The neglect of H_{JT} and H_{LS} amounts to admitting an adiabatic potential for vibration-electronic interactions, and the total spin of the system as a good quantum number. Under these circumstances the states of the system split into spin multiplets in which each term is labeled by the irreducible representations of the group $C_{3v}(D_{3h}, T_d)$. The explicit form of the Hamiltonian (eq. 1) becomes

$$H_c \equiv T + V_{C_{3v}} + V_R = \sum_{i=1}^n \left[-\frac{\hbar^2}{2m} \nabla_i^2 - \frac{Ze^2}{r_i} + V_{C_{3v}}(\underline{r}_i) \right] + \sum_{i < j} \frac{e^2}{r_{ij}} \quad (3)$$

The eigenfunctions of H_c are built up from Slater determinants of the atomic d-orbitals by standard group-theoretical techniques (14, 15) and the matrix of H_c is then diagonalized in the basis of the multielectron functions to obtain the energy spectrum. The electron repulsion matrix elements are evaluated in terms of the Racah parameters B and C (15). The matrix elements of $V_{C_{3v}}(V_{D_{3h}}, V_{T_d})$ are evaluated in terms of parameters which characterize the ligand field distribution and strength:

$$G_4 = \sqrt{\frac{9}{4\pi}} \gamma_{40} \langle r^4 \rangle_{ion}; \quad G_2 = \sqrt{\frac{5}{4\pi}} \gamma_{20} \langle r^2 \rangle_{ion}$$

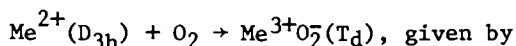
The physical significance of G_2 and G_4 is that of a convolution of the ligand charge distribution with the functions Z_{20}/R^3 and Z_{40}/R^5 where the spherical harmonics Z_{20} and Z_{40} are directed along the ion-ligand axis.

From qualitative arguments as well as from calculations for various ligand charge distributions it appears that (i) G_2 and G_4 are positive for negatively charged ligands; (ii) G_4 decreases, and the ratio G_2/G_4 increases, with increasing ligand-ion distance; (iii) both G_2 and G_4 correspond to short range interactions not reaching beyond the nearest neighbor distances; (iv) for the divalent ions of the first transition series the range of values of G_4/B is between 2.2 and 6.0 while that of G_2/G_4 is between 10 and 3.5. Energy term diagrams are presented in Fig. 2 for the D_{3h} site. Only the highest spin multiplicity terms and the lowest energy low spin terms are shown. Inspection of these diagrams in the neighborhood of $(G_4/B) = 2.2 - 3.0$ shows that: (i) all ground states have high spin multiplicity; (ii) the ground states A_1' of the d^1 and d^6 and A_2' of the d^3 and d^8 systems are non-degenerate; (iii) the ground states E' of the d^4 and d^9 systems are doubly degenerate, and (iv) the ground states of the d^2 and d^7 systems are either doubly degenerate E'' or nondegenerate A_2' depending upon the ligand strength G_4/B . Accidental degeneracy of A_2' with E'' is possible. Degeneracy of the ground state plays an important role in off-axial distortions and in the temperature dependence of the magnetic moment. The energy term diagrams in Fig. 2 can also be used to assign the main optical transitions observed in various metal substituted zeolites (2,3,9). A detailed quantitative interpretation of optical spectra, including their fine structure, requires an account of further term splitting by $H_{JT} + H_{LS}$ and a refinement of the ion position with respect to the angle β .

Stabilization Energies and Redox Potentials

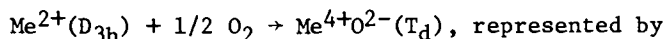
It can be seen from the term diagrams in Fig. 2 that the ground states of the $d^8(d^3)$ and $d^9(d^4)$ ions are strongly stabilized compared to their spherically symmetric ($G_4 = 0$) state. The energy difference $E_c = E_{\text{ground}}(G_4) - E_{\text{ground}}(G_4 = 0)$ is the crystal field stabilization energy which, since it is in some cases quite large, will be an important contribution to various thermodynamic quantities which determine relative stabilities and redox reactions of the ions. We have elected to demonstrate the patterns of relative stabilities and redox potentials for the following cases:

- (1) Stabilization of a divalent ion in the D_{3h} site, represented by the energy $-E_c$;
- (2) One-electron oxidation potential for oxidations



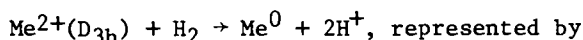
$$\Delta E(1) = -I_3 - E_c[\text{Me}^{3+}(T_d)] + E_c[\text{Me}^{2+}(D_{3h})];$$

(3) Two-electron oxidation potential for oxidations



$$\Delta E^{(2)} = -I_3 - I_4 - E_{\text{c}}[\text{Me}^{4+}(\text{T}_\text{d})] + E_{\text{c}}[\text{Me}^{2+}(\text{D}_{3\text{h}})];$$

(4) Reduction potential for reductions to neutral atoms



$$\Delta E^{(3)} = I_1 + I_2 + E_{\text{c}}[\text{Me}^{2+}(\text{D}_{3\text{h}})];$$

(5) Reduction potential for reduction to bulk metal represented by $\Delta E^{(4)} = \Delta E^{(3)} - \Delta U$ where ΔU is the cohesion energy of the metal.

Here I_n is the n -th ionization potential of the metal under consideration. Energy contributions common to all the ions such as the Madelung energies, dissociation energies of oxygen and hydrogen, the ionization potential of hydrogen and the electron affinities of oxygen, need not be considered in estimates of relative energies. The energies of the processes 1 - 5 have been calculated for $(G_4/B) = 3$, $(G_2/G_4) = 10$ (16) from the term diagrams in Fig. 2, tabulated values of ionization potentials (17), cohesion energies (18), Racah's parameters B (19), and ground state energies of tetrahedral complexes (20). The results are summarized in Fig. 3.

Several points of interest arise from the data in Fig. 3: (i) the d^4 and d^9 (Cr^{2+} and Cu^{2+}) ions are as strongly stabilized in the $\text{D}_{3\text{h}}$ sites as the d^3 and d^8 ions, in contrast to tetrahedral or octahedral sites; (ii) the one-electron oxidation potentials of Fe^{2+} and Cr^{2+} are nearly the same, and since Cr^{2+} has been shown to be a reversible one-electron oxygen carrier (9), Fe^{2+} in zeolites is a likely candidate for the same reaction; (iii) the two-electron oxidations exhibit a steeply varying redox potential and there will be a dividing line above which all ions will undergo the two-electron oxidations and below which none will; (iv) copper is most easily reducible to bulk metal but zinc displays the greatest reducibility to atoms. Since similar calculations have led to a quantitative account of redox potentials in oxides (21) the results in Fig. 3 are expected to be a fairly accurate picture of the relative energies for the listed reactions in zeolites.

Distortions and Spin-Orbit Coupling

Axial distortions. The changes of electronic energy associated with the movement of an ion in a $\text{D}_{3\text{h}}$ site along the trigonal axis are given in ref. 16, Fig. 6 for the case of a single d -electron. As the symmetry changes from $\text{D}_{3\text{h}}$ to $\text{C}_{3\text{v}}$, there is little change in electronic energies for values of the angle β between 90 and 100° ,

and further excursion only results in destabilization of the system. Similar conclusions hold for multielectron systems. Thus the in-plane D_{3h} position is *electronically* the most stable but no significant energy penalty is paid upon excursions up to half-way to the tetrahedral position. This result is in agreement with crystallographic analysis showing the ion probability ellipsoids centered near the plane of the proximal oxygens and elongated along the trigonal axis (22). It is also noted that due to a general relationship between the D_{3h} and C_{3v} groups, no degeneracies are removed upon axial distortions.

Off-axial Distortions. Off-axial motion of the ion in the $D_{3h}(C_{3v})$ site is associated with degenerate vibrations having the symmetry of the E' (E) representations of the $D_{3h}(C_{3v})$ groups. As there exist many such vibrations in the phonon manifold of the crystal lattice, Toyozawa and Inoue (23) have shown that for the analysis of vibronic interactions, normal modes of the same symmetry may be assembled into a single "interaction mode." The interaction mode E' (E) is doubly degenerate with components Q_x and Q_y localized in the vicinity of the metal ion and similar to the E' (e) normal modes of a trigonal XY_3 molecule (24). The displacements Q_x and Q_y give rise to potentials V_x and V_y which remove the degeneracies of the electronic states E' and E'' and exemplify the Jahn-Teller effect in our system. The vibronic interaction Hamiltonian H_{JT} and its matrix in the basis of the electronic functions $\{|E'1\rangle, |E'-1\rangle\}$ of an E' state are

$$H_{JT} = V_x(\xi)Q_x + V_y(\xi)Q_y \quad (4)$$

and

H_{JT}	$ E'1\rangle$	$ E'-1\rangle$	
$\langle E'1 $	0	$-\frac{ib}{\sqrt{2}}(Q_x + iQ_y)$	
$\langle E'-1 $	$\frac{ib}{\sqrt{2}}(Q_x - iQ_y)$	0	(5)

where b is a coupling constant (25). An identical matrix is obtained for the E'' electronic states of D_{3h} and E of C_{3v} and therefore the same analysis applies to all doubly degenerate states of the D_{3h} and C_{3v} groups for systems with any number of d -electrons. The vibronic energies obtained by diagonalizing H_{JT}

$$E^\pm = \pm \frac{b}{\sqrt{2}} R, \text{ where } R = \sqrt{(Q_x^2 + Q_y^2)} \quad (6)$$

and energies involving the adiabatic potential R^2 and anharmonicity $BR^3 \cos 3\phi$ (B is the anharmonicity constant and ϕ the angle between

\bar{R} and \bar{Q}_x) are given by (26)

$$E_{JT}^{\pm} = R^2 \pm \frac{b}{\sqrt{2}} R + \underline{BR}^3 \cos 3\phi.$$

It is noted that this result is formally but not physically equivalent to the vibronic splitting of octahedral E-states by the E-vibrations (27). The energy surfaces corresponding to (7) are represented in Fig. 4. Case A is representative of non-degenerate electronic states with anharmonic vibrations ($\underline{b}=0$, $\underline{B}\neq 0$), case B corresponds to a dynamic Jahn-Teller effect ($\underline{b}\neq 0$, $\underline{B}=0$) on the doubly degenerate states, and case C represents the static Jahn-Teller effect ($\underline{b}\neq 0$, $\underline{B}\neq 0$) in which the combination of vibronic coupling with anharmonicity results in new trigonally symmetric stable positions of the central ion. These positions are either in the direction between two proximal oxygens at 60° , 180° , and 240° for $\underline{B}>0$, or point to the proximal oxygens for $\underline{B}<0$, and should be crystallographically observable at low temperatures (while case B results in an angular motion about the center at all temperatures). Sufficiently large combined vibronic coupling and anharmonicity may result in low saddle points (cf. one at 180° in Fig. 4C), the trajectory over which may lead to the destruction of the complex, i.e., to an ion-skeletal chemical reaction. On the basis of qualitative chemical behavior and the magnetic moments of the individual ions in zeolites, it is suggested that case B is approached by Cr^{2+} and case C by Cu^{2+} in Type A zeolites. When the energy surfaces from Fig. 4 are superimposed upon the electronic energies from the term diagrams Fig. 2, the removal of degeneracy of the E electronic states is apparent from the existence of the two surfaces in Fig. 4B or C.

The Trigonal Site with an Adsorbed Molecule. In the case where a molecule L_4 (Fig. 1) is adsorbed with a strength comparable to that of the skeletal oxygens $L_{1,2,3}$, certain combinations of states will produce the triply degenerate states T_1 and T_2 of the tetrahedral group ($A_1 + E = T_2(T_d)$ and $A_2 + E = T_1(T_d)$) which will split into symmetric triplets. Such triplets are apparent in the optical transitions into the excited states of Co(II) sieves with adsorbed water, ammonia (3), and imidazole (6).

Spin-orbit Coupling. A full treatment of spin-orbit (LS) coupling requires a diagonalization of the LS operator for each individual ion within all terms of a d^n configuration. However, simplifications arise in trigonal fields from the fact that suitable bases for the E-representations are pairs of functions $\{|SL M_S M_L\rangle$, $|SL M_S -M_L\rangle\}$ in which the $\lambda \underline{L} \cdot \underline{S}$ operator (λ is the spin orbit coupling constant of the $2S+1L$ term) is diagonal with eigenvalues $\pm \lambda M_L M_S$. The $|SL M_S \pm M_L\rangle$ functions behave as the $|E \pm 1\rangle$ components and inspection of equation (5) shows that the operators $\lambda \underline{L} \cdot \underline{S}$ and H_{JT} have opposite effects on the energies of the E-states: *the*

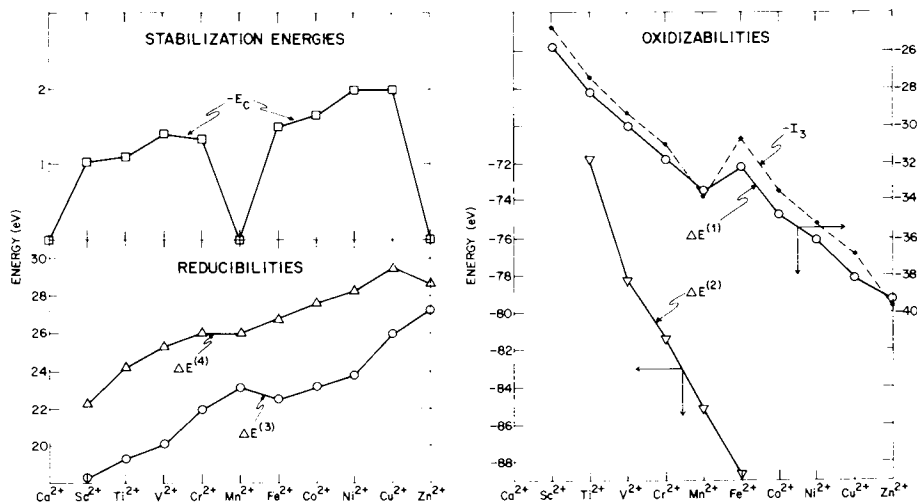


Figure 3. Stabilization energies (E_c), reducibilities to metal atom ($\Delta E^{(3)}$) and bulk metal ($\Delta E^{(4)}$), and one-electron ($\Delta E^{(1)}$) and two-electron ($\Delta E^{(2)}$) oxidizabilities for the divalent ions of the first transition series in the D_{3h} sites.

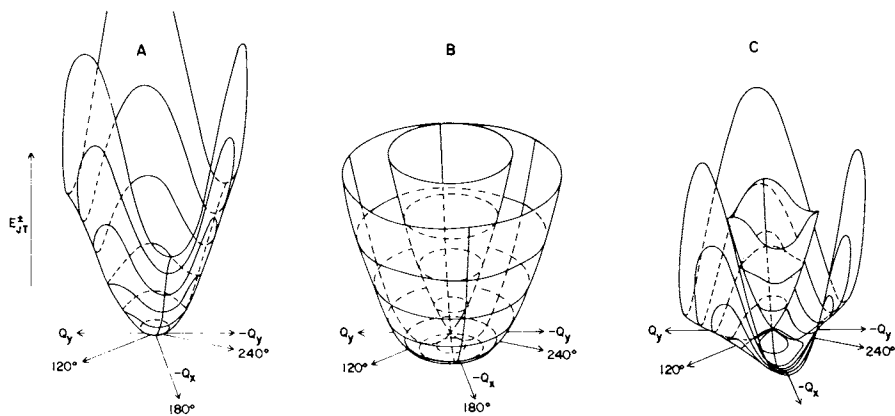


Figure 4. Energy surfaces in the space of interaction modes Q_x and Q_y of the $E'(D_{3h})$ or $E(C_{3v})$ vibrations according to equation (7) in text. Case A, a non-degenerate electronic state with anharmonicity ($b = 0$, $B = 0.375$); Case B, a degenerate electronic state without anharmonicity ($b = 0.94$, $B = 0$); Case C, a doubly degenerate electronic state with comparable Jahn-Teller coupling and anharmonicity ($B = 0.4$, $b = 0.375$).

Jahn-Teller effect tends to reduce the energy differences between states with M_g differing by 1 compared to those of the free ion terms. This effect results in smaller splittings of the lowest lying states and should significantly influence both magnetic susceptibilities and electron paramagnetic resonance spectra.

Conclusions

The properties of transition metal ions in zeolites are adequately described by the theoretical treatment outlined herein. The structure of the theory allows qualitative assignments to be made to the ground and excited states of any d^n configuration, on the basis of which the various phenomena such as relative stabilities, redox properties, vibronic coupling, and magnetic properties may be predicted and explained. Data on temperature dependence of optical band splitting and magnetic moments will be required for the quantitative determination of relative magnitudes of the various coupling constants in each individual system.

Acknowledgment

The authors are grateful for grants from Chevron Research Corporation and the Donors of the Petroleum Research Fund of the American Chemical Society which enabled this work, and to Carol Troy who typed the manuscript.

Literature Cited

1. Seff, K., Accounts of Chemical Research (1976), 9, 121.
2. Klier, K. and Ralek, M., J. Phys. Chem. Solids (1968), 29, 951.
3. Klier, K., Advances in Chemistry Series (1971), 101, 480.
4. Klier, K., Kellerman, R. and Hutta, P.J., J. Chem. Phys. (1974), 61, 4224.
5. Vansant, E.F. and Lunsford, J.H., Advances in Chemistry Series (1973), 121, 441.
6. Kellerman, R. and Klier, K., "Imidazole Complexes in Type A Zeolite," to be published.
7. Delgass, W.N., Garten, R.L. and Boudart, M., J. Phys. Chem. (1969), 73, 2970.
8. Kellerman, R., Hutta, P.J. and Klier, K., J. Amer. Chem. Soc. (1974), 96, 5946.
9. Texter, J., Strome, D.H., Herman, R.G. and Klier, K., to be published.
10. Mochida, I. and Takeshita, K., J. Phys. Chem. (1974), 78, 1653.
11. Mochida, I. *et al.*, J. Catal. (1975), 36, 361.
12. Polak, R. and Cerny, V., J. Phys. Chem. Solids (1968), 29, 945.
13. Polak, R. and Klier, K., J. Phys. Chem. Solids (1969), 30, 2231.
14. Hutta, P.J., Thesis, Lehigh University 1974.

15. Griffith, J.S., *The Theory of Transition Metal Ions*, Cambridge University Press 1964, p. 84.
16. These values are justified as an average choice for fitting a number of optical spectra of various D_{3h} ions, cf. also Kellerman, R. and Klier, K., *Surface and Defect Properties of Solids* (Chem. Soc. London) (1975), 4, 1.
17. Moore, Ch.E., *Atomic Energy Levels*, NBS Circular 467, Revised Dec. 1971.
18. *Handbook of Chemistry and Physics*, The Chemical Rubber Co., 56th Ed., 1975-76.
19. Ref. 15, p. 83.
20. Sugano, S., Tanabe, Y. and Kamimura, H., *Multiplets of Transition-Metal Ions in Crystals*, Academic Press, N.Y. 1970, pp. 106-112.
21. Klier, K., *J. Catal.* (1967), 8, 14.
22. See e.g. Riley, P.E. and Seff, K., *Inorg. Chem.* (1974), 13, 1355.
23. Toyozawa, Y. and Inoue, M., *J. Phys. Soc. Japan* (1964), 19, 1274.
24. Herzberg, G., *Molecular Spectra and Molecular Structure II*, Van Nostrand Reinhold Co., N.Y. 1945, pp. 110 and 179.
25. The coupling coefficients for this matrix were obtained by transforming V_x and V_y into complex conjugate pairs and using the tables in G.F. Koster et al., *Properties of the Thirty-Two Point Groups*, MIT Press, Cambridge, Mass. 1963. A convention is employed $V_{E\pm 1} = \pm i/\sqrt{2}(V_x \pm iV_y)$.
26. The anharmonic contributions to the potential are those combinations of the cubic terms Q_x^3 , Q_y^3 , $Q_x^2Q_y$, and $Q_xQ_y^2$ which are invariant under the symmetry group $D_{3h}(C_{3v})$. The only non-vanishing symmetric term, cubic in powers of the interaction coordinates, is one proportional to $(Q_{E1}^3 - Q_{E-1}^3)$, utilizing the convention as sub 25.
27. Ref. 20, pp. 235-239.

Redox Chemistry and Complexation of Divalent Chromium Ion-Exchanged Zeolite A

RICHARD KELLERMAN

Xerox Corp., Webster Research Center, N.Y. 14580

KAMIL KLIER

Department of Chemistry and Center for Surface and Coatings Research,
Lehigh University, Bethlehem, Penn. 18015

ABSTRACT

Spectroscopic, magnetic and gravimetric analysis show that the Cr^{+2} ion in anhydrous type-A zeolite is trigonally coordinated and that it forms complexes with N_2O , CO_2 , C_2H_4 and O_2 at room temperature. At 150°C O_2 and N_2O dissociate producing a near tetrahedral Cr^{+4} ion which is reduced to the original trigonal Cr^{+2} ion by CO at 300°C .

Introduction

The multiple valence states available to transition metal ions, their characteristic electronic absorption spectra and magnetic properties, and the strong dependence of all three on local environment have stimulated a large amount of research on the physics and chemistry of transition metal ion exchanged zeolites (1,2). Studies of the stability of such zeolites (3,4), their catalytic activity, particularly to redox reactions (5,6), and of the geometry of various sorption complexes formed with guest molecules (1,2) have established that most if not all of the d ions can be exchanged into various zeolites, that the exchanged zeolite may be dehydrated leaving the exchanged ions in crystallographically well defined sites which are usually accessible, and that these ions can form complexes with guest molecules or molecular fragments which may be present in the zeolitic cavities.

The ease of oxidation of the divalent chromium ion suggests that this ion, in addition to forming complexes in which the oxidation state of the ion does not change, should also give rise to ionic chemisorption with suitable electron acceptors. Changes in the oxidation state of transition metal ions are expected to be important in catalytic reactions and study of a model system such as exchanged type-A zeolite may lead to further understanding of

the catalytic behavior of these ions.

We report here on the optical and magnetic properties of the divalent Cr^{+2} ion in anhydrous type-A zeolite, the interactions of the Cr^{+2} ion with N_2O , CO_2 , and C_2H_4 at room temperature, interactions which will be shown to be weak and, in the case of CO_2 and N_2O reversible, and on the oxidation of Cr^{+2} by N_2O or O_2 and subsequent reduction by CO . Finally we show that the chromium ion in zeolite A acts as a catalytic center in the oxidation of CO by O_2 .

Experimental

Fully hydrated zeolite A was washed several times in distilled water prior to being loaded into an anaerobic ion exchanger (7). After adjustment of pH to 7 and deoxygenation of the aqueous zeolite slurry, crystals of chromous sulfate pentahydrate were added and ion exchange proceeded with agitation by an oxygen-free nitrogen stream for one hour at room temperature. The pale blue zeolite so produced was air stable and was filtered and washed without anaerobic precautions. For low Cr^{+2} contents (1 - 1.5 Cr^{+2} ions per unit cell) exchange was essentially complete as indicated by the absence of visible coloration in the air oxidized exchange supernatant. The supernatant sulfate ion concentration was shown by gravimetric analysis to be the same before and after exchange. Samples containing 1, 1.5 and 3 Cr^{+2} ions per unit cell or per large cavity and hereinafter referred to as $\text{Cr}_1(\text{II})\text{-A}$, $\text{Cr}_{1.5}(\text{II})\text{-A}$ and $\text{Cr}_3(\text{II})\text{-A}$ were prepared, and were stored over saturated aqueous calcium nitrate solutions prior to use. The samples were dehydrated at $\sim 110^\circ\text{C}$ overnight and then at $\sim 350^\circ\text{C}$ for two hours. Vacuum was maintained by a liquid nitrogen cooled zeolite 5A sorption pump activated under vacuum at 350°C prior to use. The anhydrous zeolite was transferred without loss of vacuum from the shallow bed vessel in which activation took place to the cell used for spectrophotometric measurements. Similar procedures were used to prepare samples for magnetic susceptibility measurements.

A Cary 14 spectrophotometer was used to collect diffuse reflectance spectra over the range $2.19 - 0.25\mu$ ($4566.2 - 40,000\text{cm}^{-1}$). The output of the spectrophotometer ($-\log_{10} R_\infty$, where R_∞ is defined as the reflectance ratio $R_{\text{sample}}/R_{\text{standard}}$ for materials of sufficient thickness that no transmission occurs) was digitalized by an analog to digital converter (8) which was triggered by the spectrophotometer monochromator scan drive. The ordinate resolution was $\pm 0.001 \log_{10} R_\infty$ units and the wavelength trigger interval was 1nm . A preselected number of spectral points was stored by a Data General "Nova 2" minicomputer which also controlled the wavelength scan drive. FORTRAN coded programs were used to transform wavelength to a linear energy scale, and $\log_{10} R_\infty$ to the Schuster-Kubelka-Munk function ($F(R_\infty) = (1-R_\infty)^2/(2R_\infty)$) (9). The function $F(R_\infty)$ is equal to K/S where K is the absorption coefficient and is therefore equal, but for a scattering coefficient S which may be shown to be a constant for the particle size

and energy range of interest here, to the absorbance of the sample (9). Plots of E (reciprocal centimeters) *vs.* $F(R_\infty)$ were prepared on an incremental plotter.

Anhydrous magnesium oxide was used as a reflectance standard for all measurements and corrections were made for instrumental baseline effects. The sharp negative absorption visible in most of the spectra at approximately $7,300\text{cm}^{-1}$ is due to hydroxyl infrared absorption in the Cary 14 optics.

Nitrous oxide, carbon dioxide, ethylene and oxygen gas (Linde, 99.9% purity) could be admitted to the sample without air contamination. Pressures were measured in the range 10^{-4} –1000 torr using Datametrics capacitance manometers. A Cahn RG electrobalance and a McBain-Bakr spring balance were used to measure the uptake of the various gases under controlled temperature and pressure conditions. A Uthe Technology Incorporated 100C quadrupole residual gas analyzer was used for gas analysis. Magnetic susceptibilities were measured using a Gouy balance and a Princeton Applied Research Foner Vibrating Sample Magnetometer.

Results

Complete dehydration of pale blue, air stable $\text{Cr}_1(\text{II})\text{-A}$ produced a pale blue-grey material with the spectrum given, along with those of $\text{Cr}_{1.5}(\text{II})\text{-A}$ and $\text{Cr}_3(\text{II})\text{-A}$, in Fig. 1a curves 1, 2 and 3 respectively. There is a small Cr^{+2} concentration dependence of the position of the band at $17,000\text{cm}^{-1}$ and the expected dependence of the intensities of both bands on the Cr^{+2} concentration. The magnetic susceptibility of $\text{Cr}_1(\text{II})\text{-A}$ was measured at 10,000 Oe at room temperature with the vibrating sample magnetometer and the magnetic moment of the Cr^{+2} ion was calculated to be 5.8 μB . The value of 5.0 μB calculated from Gouy balance data and previously reported by us (10) is considered to be less reliable.

Exposure of the anhydrous $\text{Cr}(\text{II})\text{-A}$ zeolites to 1000 torr of N_2O caused an immediate color change from pale blue-grey to turquoise. The spectra of $\text{Cr}_1(\text{II})\text{-A}$, $\text{Cr}_{1.5}(\text{II})\text{-A}$ and $\text{Cr}_3(\text{II})\text{-A}$ equilibrated with 1000 torr N_2O are given in Fig. 1b curves 1, 2 and 3 respectively, from which it can be seen that the $12,000\text{cm}^{-1}$ peak is only slightly affected by N_2O and that the shift in the $17,000\text{cm}^{-1}$ peak is dependent on Cr^{+2} concentration, being larger at higher Cr^{+2} loadings. The N_2O could be pumped out at room temperature to restore the original spectrum of all of the samples.

The effect of N_2O at 1, 10, 100 and 1000 torr at room temperature on the spectrum of $\text{Cr}_1(\text{II})\text{-A}$ is shown in Fig. 1c and the room temperature adsorption isotherm over the same pressure range is given in Fig. 2. From both figures it can be seen that the interaction of the N_2O with the Cr^{+2} ion is weak, and the absence of any plateau in the isotherm at one N_2O molecule per cavity indicates that the interaction is of the same order as that of N_2O with the nonexchanged Na^+ ions. The fraction of adsorbed N_2O bound irreversibly at room temperature (Fig. 2) could be completely

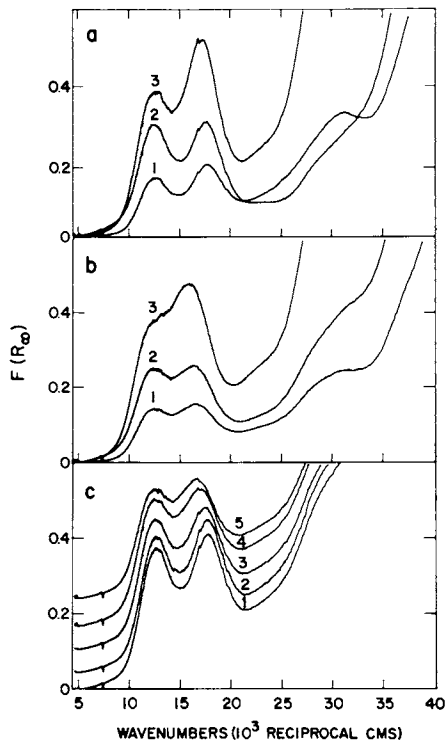


Figure 1. Diffuse reflectance spectra of anhydrous chromium(II)-exchanged type-A zeolite containing 1, 1.5, and 3 Cr^{2+} ions per unit cell (a, curves 1, 2, 3, respectively) and the same under 1000 torr of N_2O (b, curves 1, 2, 3, respectively). The effect of pressure on the spectrum of $\text{Cr}_1(\text{II})\text{-A}$ in equilibrium with N_2O is shown in c, where each of the curves is offset for clarity, for N_2O pressures of 0, 1, 10, 100, and 1000 torr (curves 1, 2, 3, 4, and 5).

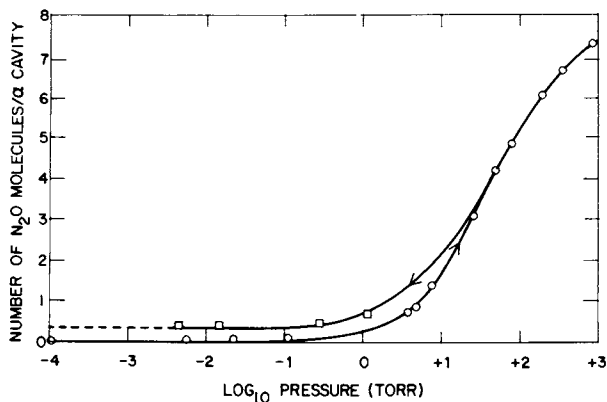


Figure 2. The room temperature adsorption isotherm for nitrous oxide on anhydrous $\text{Cr}_{1.5}(\text{II})\text{-A}$. The isotherm shows no plateau at N_2O contents corresponding to 1 N_2O molecule per Cr^{2+} ion.

removed by evacuation at 150°C. Nitrous oxide at 760 torr caused only a slight decrease in the magnetic moment of the $\text{Cr}_{1.5}(\text{II})\text{-A}$ material.

Ethylene and carbon dioxide show a behavior similar to N_2O and the spectra of $\text{Cr}_1(\text{II})\text{-A}$ in equilibrium with 1000 torr of these gases are given, along with the bare site spectrum, in Fig. 3a curves 1, 2 and 3 respectively. Carbon dioxide adsorption was completely reversible at room temperature as indicated by the restoration of the bare site spectrum by evacuation. Color changes similar to those produced by N_2O were observed. Color changes attending C_2H_4 adsorption were more subtle, as can be seen from the spectrum.

The narrow, low intensity peaks in the 4500-6000 cm^{-1} region of the spectra of samples under 1000 torr of C_2H_4 , CO_2 or N_2O are overtone/combination vibrational bands. Examination of these bands under higher magnification for $\text{Cr}_1(\text{II})\text{-A}$ shows that for CO_2 and N_2O their shapes and positions are, within noise and resolution limits, the same as the shapes and positions of the vibrational bands of CO_2 and N_2O in unexchanged sodium-A. This is perhaps not surprising since $\text{Cr}_1(\text{II})\text{-A}$ contains 5 Na^+ ions for each Cr^{+2} ion. Similar results however, are obtained for $\text{Cr}_3(\text{II})\text{-A}$ in which there are only 2 Na^+ ions for each Cr^{+2} ion. Only the intensities change, being greater for the exchanged zeolite.

Although the effects of brief exposure of $\text{Cr}(\text{II})\text{-A}$ to N_2O were largely reversed by pumping at room temperature and completely reversed by pumping while slowly heating to 150°C, prolonged exposure (several weeks) of either $\text{Cr}_1(\text{II})\text{-A}$ or $\text{Cr}_{1.5}(\text{II})\text{-A}$ to N_2O at 1000 torr at room temperature caused a color change from turquoise to lilac which could not be reversed either by pumping at room temperature or at 150°C. Curve 1 in Fig. 3b is the spectrum of the 150°C evacuated lilac sample. The spectrum of the room temperature evacuated sample differs only in intensity. Re-admission of N_2O to the lilac material at 150°C intensified and deepened its color to red-brown and produced a material with the spectrum given in Fig. 3b curve 2 which, it should be noted, is approximately ten times the intensity of the spectrum of the original $\text{Cr}_{1.5}(\text{II})\text{-A}$ sample (Fig. 1a curve 2).

Prior to pumping out the N_2O in the lilac samples the pressure in the sample cell with a glass extension tube immersed in liquid nitrogen was measured and found to be about 500 torr, showing that a large fraction of the original N_2O had dissociated to N_2 .

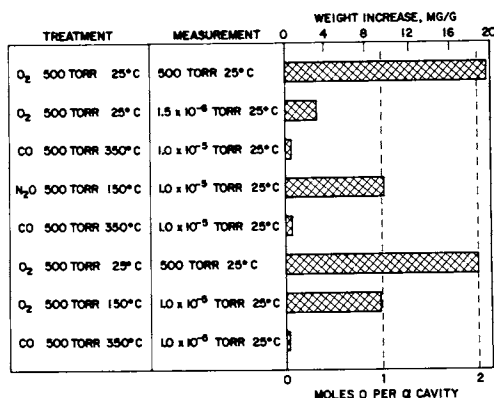
The magnetic moment of the chromium ion subsequent to 150°C N_2O oxidation was 2.9 μB .

Exposure of $\text{Cr}_3(\text{II})\text{-A}$ to O_2 at 760 torr at room temperature produced a deep grey material with the spectrum given in Fig. 3c. This spectrum is similar to that of $\text{Cr}_{1.5}(\text{II})\text{-A}$ exposed to O_2 under the same conditions (10). At 150°C anhydrous $\text{Cr}(\text{II})\text{-A}$ turned red-brown in the presence of oxygen at 500 torr. The spectrum of this material differs from that of the 150°C N_2O treated sample only in the presence of an additional band at 36,700 cm^{-1} .

The red-brown products of 150°C oxidation by either N₂O or O₂ were reduced to the starting Cr(II)-A material by CO at 300–350°C and 500–760 torr with the formation of CO₂. This reduction was demonstrated both spectroscopically and by vacuum microbalance analysis (see below). The spectra of the reduced samples matched those of the virgin anhydrous material but exhibited some broadening of the absorption bands.

The results of a vacuum microbalance analysis of the interaction of anhydrous Cr₁(II)-A with O₂, N₂O and CO are presented in Table I. The sequence of measurements was from top to bottom. The analyses are thought to be accurate to ±5%. All reactions

TABLE I.- Gravimetric Analysis of Cr₁(II)-A Interaction with O₂, N₂O and CO



were complete within minutes except for molecular oxygen uptake which was instantaneous, and molecular oxygen desorption which was incomplete even after 12 hours evacuation. The Cr₁(II)-A sample contained one Cr⁺² ion per unit cell or per α cavity so that a weight uptake equivalent to one oxygen atom per α cavity corresponds to a Cr/O ratio of unity.

The catalytic oxidation of CO by oxygen suggested by these observations was confirmed in a flow experiment in which a mixture of CO and O₂ was passed through an anhydrous Cr₁(II)-A bed which could be heated. The mass spectrometer was set to display the 30–46 mass region. At room temperature the mass spectrum was dominated by the molecular oxygen peak but at 300°C the CO₂ peak was dominant.

X-ray diffractograms of the hydrated freshly prepared Cr_{1.5}(II)-A and of re-hydrated dehydrated Cr_{1.5}(II)-A showed no significant structure loss had occurred.

Discussion

The location of transition metal ions in water free A-type zeolites is generally the oxygen six-ring linking the α and β cages (1,2). Distortion of this ring by the coordinated ion gives rise to a site symmetry which is in general C_{3v} and which becomes D_{3h} in the event that the central ion lies in the plane of the three proximal oxygens. Accordingly the spectra of the various Cr(II)-A anhydrous zeolites are interpreted using the simplified term diagram for a d^4 (Cr^{+2}) ion in a D_{3h} (trigonal planar) ligand field given in Fig. 4. Only the high spin ($2S+1=5$) terms are given (solid lines). The definition and the significance of the ligand field parameter G_4 have been discussed elsewhere (11). The solid line D_{3h} terms in Fig. 4 have been calculated for a fixed G_2/G_4 value of 10 which is physically reasonable for the zeolite framework oxygen ligands (11). The lowest lying triplet and singlet states of the Cr^{+2} ion under a D_{3h} field cross the quintet ground state at $ca.$ $(G_4/B)=5$ and $(G_4/B)=7$ respectively so that the ground state at $(G_4/B)=2.2$ is the quintet state and the two major bands observed for the anhydrous Cr(II)-A zeolite (Fig. 1a) may be assigned to the ${}^5E' \longrightarrow {}^5E''$ and ${}^5E' \longrightarrow {}^5A_1'$ transitions predicted in Fig. 4. The best fit is at $(G_4/B)=2.2$ for a Racah B parameter of $830cm^{-1}$ (12) but agreement between the predicted and observed values of the ${}^5E' \longrightarrow {}^5A_1'$ transition is only fair. The discrepancy can be attributed to a Jahn-Teller distortion of the doubly degenerate electronic ground state (11), which displaces the equilibrium position of the ion in the ground state from that in the excited ${}^5A_1'$ state and thereby increases the energy of the Franck-Condon transition between the two.

The small but significant dependence of the ${}^5A_1'$ state energy on the Cr^{+2} concentration (Fig. 1a) may be due to the motion, driven by electrostatic forces, of the Cr^{+2} ion along the C_3 axis of the oxygen six-ring site since it has been shown that there is only a small electronic energy barrier for small motions of the 3d ions along the C_3 axis (11).

The narrow weak band at $17,000cm^{-1}$ in Fig. 1a probably arises from a spin forbidden transition into a triplet state, the most likely being the $({}^3P) {}^3A_2'$ state (13) which is nearly parallel to the quintet ground state and so should give rise to a narrow band. The magnetic moment of $5.8\mu_B$ of the Cr^{+2} ion in $Cr_1(II)$ -A confirms that the system ground state is a spin quintet and the large orbital contribution to the d^4 spin only value of $4.89\mu_B$ is expected for a D_{3h} complex (11).

Admission of any molecule into the zeolite framework opens the possibility that complexation of the highly coordinatively unsaturated Cr^{+2} ion will occur. Thus small and reversible changes in the spectrum of Cr(II)-A are caused by N_2O and CO_2 (Fig. 1b, c and Fig. 3a curve 2) and these changes are interpreted as arising from a change from a D_{3h} complex to a C_{3v} complex in which the fourth (axial) ligand is the guest molecule (1,13). A choice of $(G_2/G_4)=17$

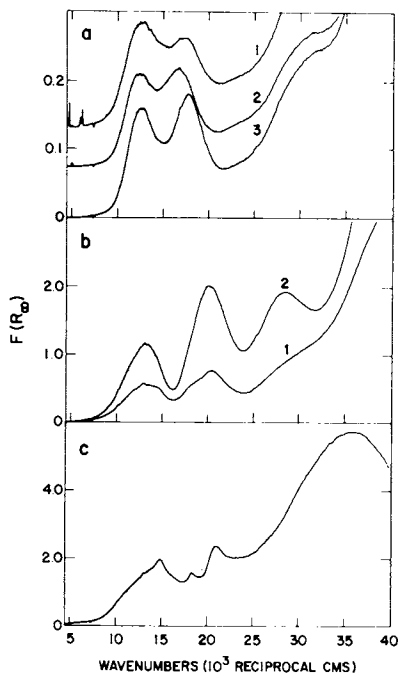


Figure 3. Diffuse reflectance spectra of (a) Cr(II)-A in equilibrium with 1000 torr of C_2H_4 and CO_2 at room temperature and of "bare" Cr(II)-A (curves 1, 2, and 3, respectively); (b) Cr(II)-A left in contact with 1000 torr N_2O at room temperature for 5 weeks and of the same material heated under 1000 torr N_2O to 150°C (curves 1 and 2); and (c) Cr(II)-A under 760 torr O_2 . The ordinate scales of a, b, and c are not the same.

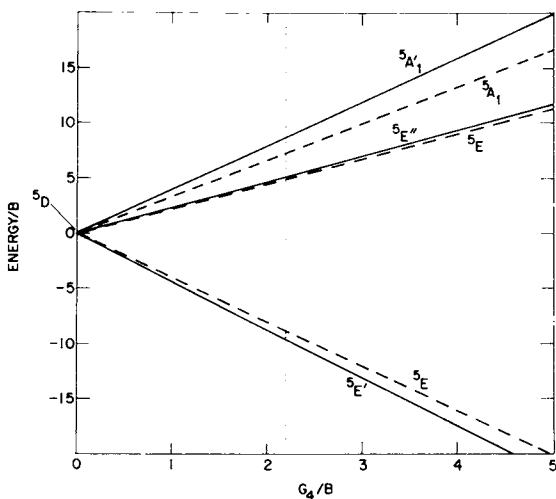
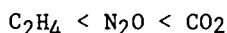


Figure 4. The term diagram for a d^4 (Cr^{2+}) D_{3h} complex (—) and the same for a d^4 (Cr^{2+}) C_{3v} complex in which a weak axial ligand lowers the symmetry from D_{3h} to C_{3v} (---). The vertical dotted line at $(G_4/B) = 2.2$ best matches the observed transitions of the D_{3h} Cr^{2+} ion in anhydrous Cr(II)-A . The same value of G_4/B is used in interpreting the spectrum of the Cr^{2+} ion perturbed by weak ligands.

and a relative axial ligand strength of 0.7 was used in calculating the C_{3v} (dashed line) terms in Fig. 4 and the effect of a weak fourth ligand is qualitatively well described - the separation between the ground 5E (C_{3v}) term and the first excited 5E term decreases less than that between the excited 5E and 5A_1 terms.

The electronic spectrum of ethylene saturated $Cr_1(II)$ -A (Fig. 3a curve 1) may be interpreted in the same way as the CO_2 and N_2O perturbed $Cr(II)$ -A spectra and a spectrochemical series for the Cr^{+2} ion in anhydrous type-A zeolite may be written.



The shift in the $17,000cm^{-1}$ band on exposure of $Cr_n(II)$ -A to N_2O shows a small but significant dependence on n (Fig. 1a and b), being larger for larger n , and it is reasonable to speculate that larger n values are associated with a Cr^{+2} ion displaced into the α cavity and so more exposed to guest molecules.

The positions of the infrared absorption bands of N_2O and CO_2 on $Cr_1(II)$ -A are given in Table 2 column 1. The assignments of

TABLE 2.- Near Infrared Absorption Bands of N_2O and CO_2 on $Cr_1(II)$ -A

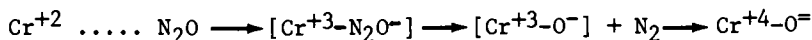
BAND ENERGY, CM^{-1}		ASSIGNMENT		
ADSORBED	GAS PHASE	ν_1	ν_2^t	ν_3
4775	4734.0	2	0°	1 N_2O
4835	4860.5	0	4°	1 $\left. \begin{array}{l} \\ \\ \end{array} \right\} CO_2$
4970	4983.5	1	2°	1 $\left. \begin{array}{l} \\ \\ \end{array} \right\} CO_2$
5090	5109.0	2	0°	1 $\left. \begin{array}{l} \\ \\ \end{array} \right\} CO_2$

these bands and their gas phase energies are given in columns 2 and 3 (14). As can be seen from this table, only small shifts in the infrared absorption spectra are caused by the sorption of CO_2 and N_2O , confirming, as is already apparent from the electronic spectra of sorbed N_2O and CO_2 (Fig. 1b and c and Fig. 3a curve 2 respectively), that these molecules interact only weakly with the Cr^{+2} ion in anhydrous $Cr(II)$ -A. A discussion of the ethylene infrared spectrum will be given in a separate publication.

The guest molecule/ Cr^{+2} interactions discussed so far have been weak and reversible and have not involved any change in the oxidation state of the chromium ion. We now show that both N_2O and O_2 are able to induce such oxidation state changes, N_2O irreversibly through dissociation, and oxygen reversibly *via* the O_2^- anion

or irreversibly through dissociation.

The magnetic moment (2.9 μ B), stoichiometry (one oxygen atom per chromium ion) and optical spectrum of the red-brown product of the oxidation of Cr(II)-A by N₂O at 150°C may all be understood in terms of the reaction



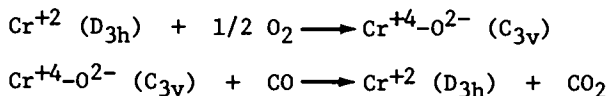
in which an electron is transferred from the Cr⁺² ion to N₂O forming the unstable intermediate N₂O⁻ which decomposes yielding N₂ and leaving a single oxygen atom bound to the Cr⁺³ ion. A similar mechanism, involving dissociation of the precursor O₂⁻ is proposed for the oxidation of Cr(II)-A by O₂ at 150°C. The species Cr⁺³-O⁻ must itself be unstable against further oxidation of the Cr⁺³ ion to Cr⁺⁴ because neither the magnetic moment nor the spectrum of the red-brown complex are attributable to a d³ ion. Therefore it is concluded that the red-brown product of N₂O or O₂ oxidation at 150°C of Cr(II)-A has a tetravalent (Cr⁺⁴) ion in near T_d coordination defined by three zeolitic oxygen atoms and the axial oxygen derived from N₂O or O₂. Accordingly the three bands of Fig. 3b arise from the ³A₂ → ³T₂, ³A₂ → ³T₁ and ³A₂ → ³T₁ transitions predicted by the Tanabe-Sugano diagram for a T_d high spin d² ion (15). The ³A₂ → ³T₂ transition is symmetry forbidden in T_d complexes but it is argued that the Cr⁺⁴ complex has C_{3v} symmetry and that small departures from T_d symmetry may have large effects on selection rules, though not on absorption band positions. The origin of the additional band at 36,700cm⁻¹ produced by O₂ oxidation at 150°C is unknown but this band is believed not to arise from a d-d transition of the Cr⁺⁴ ion. The above assignments of the three bands in Fig. 3b curve 2 imply a Δ_{tet} value of 13,000cm⁻¹ for a Racah B parameter of 875cm⁻¹ of the Cr⁺⁴ ion. For a formally tetravalent ion a value of Δ_{tet}=13,000cm⁻¹ is reasonable since it is well known that ligand field splitting parameters increase with increasing charge on the central ion. A nephelauxetic reduction of the free Cr⁺⁴ ion B value of 1039cm⁻¹ (12) to 875cm⁻¹ reflects the extent to which the binding in the red-brown Cr⁺⁴ complex is covalent rather than purely ionic. The tenfold increase in intensity in going from the D_{3h} Cr⁺² ion to the C_{3v} Cr⁺⁴ ion (Figs. 1a curve 2 and 3b curve 2 respectively) is expected for a reduction in symmetry which involves the loss of the horizontal mirror plane. A detailed discussion of the electric dipole transition selection rules for D_{3h} systems has been given in Ref. 13.

The bands in Fig. 3b do not show the splitting generally observed for Co⁺² T_d complexes (1) and attributed to a dynamic Jahn-Teller effect, indicating that the Jahn-Teller coupling constants for the excited states are small.

Behavior similar to that reported here for N₂O on Cr(II)-A has been reported for N₂O on α-chromia (16, 17) with which N₂O may either form weak sorption complexes or undergo dissociation to O⁻_{ads} and N₂, but not form stable N₂O⁻_{ads} species.

We have already reported upon the reversible adsorption of molecular oxygen by Cr_{1.5}(II)-A (10) and only note here that Cr₃(II)-A also reversibly adsorbs O₂ but that the degree of reversibility appears to be less. In both cases the irreversibly bound fraction (i.e., that oxygen which could not be pumped off at room temperature and 5 x 10⁻⁷ torr) may be due to slow decomposition, as observed for N₂O, or may simply correspond to strongly bound molecular O₂. The spectrum of the Cr₃(II)-A/O₂ complex (Fig. 3c) is most likely due to a species in which the electrons are shared between the O₂⁻ ligand and the Cr⁺³ ion and therefore cannot be interpreted satisfactorily within the context of ligand field theory.

The reduction of the red-brown Cr⁺⁴ complex by CO at 300–350°C and the formation of this complex from Cr(II)-A and N₂O or O₂ suggest that the catalytic oxidation of CO by O₂ to CO₂ exhibited by Cr(II)-A involves the following reaction sequence:



Acknowledgement

The authors are grateful to the Chevron Company for partial support, to Dr. M. O'Horo for assistance in the magnetic susceptibility measurements, to M. Ishler for assistance in computer interfacing of the Cary and to Carol Troy for typing the manuscript.

Literature Cited

1. Kellerman, R. and Klier, K., "Surface and Defect Properties of Solids, Vol. 4." A Specialist Periodical Report published by The Chemical Society, London, 1975.
2. Seff, K., *Accounts of Chemical Research* (1976), 9, 121.
3. Bremer, H., Mörke, W., Schödel, R. and Vogt, F., *Advan. Chem. Ser.* (1973), 121, 248.
4. Maes, A. and Cremers, A., *Advan. Chem. Ser.* (1973), 121, 230.
5. Mochida, I., Hayata, S., Kato, A. and Seiyama, T., *J. Catal.* (1971), 23, 31.
6. Leach, H.F., *Annual Reports* (1971), 68A, 195, published by The Chemical Society, London.
7. Details of the anaerobic ion exchange procedure are available from R.K., Xerox Corporation, Bldg. 114, 800 Phillips Rd., Webster, New York 14580, U.S.A.
8. Aviv Associates Model CI-14 (106 Glenn Ave. Lakewood, New Jersey 08701, U.S.A.)
9. Kortüm, G., "Reflectance Spectroscopy," 1969, p. 104ff. Springer-Verlag, New York.

10. Kellerman, R., Hutta, P.J. and Klier, K., *J. Amer. Chem. Soc.* (1974) 96, 5946.
11. Klier, K., Hutta, P.J. and Kellerman, R. This conference (0000), 000, 000.
12. di Bartolo, B., "Optical Interactions in Solids," p. 185ff., J. Wiley, New York, 1968.
13. Hutta, P.J., Ph.D. Thesis, Lehigh University, Bethlehem, Pennsylvania 18015, 1974.
14. Hertzberg, G., "Molecular Spectra and Molecular Structure II. Infrared and Raman Spectra of Polyatomic Molecules," p. 275 and 278, Van Nostrand, New York, 1964.
15. Tanabe, Y., Sugano, S. and Kaminura, H., "Multiplets of Transition Metal Ions in Crystals," p. 108, Academic Press, New York, 1970.
16. Borello, E., Cerruti, L., Ghiotti, G. and Guglieminotti, E., *Inorg. Chim. Acta.* (1972), 6, 45.
17. Zecchina, A., Cerruti, L. and Borello, E., *J. Catal.* (1975), 25, 55.

Optical Spectroscopy of Hydrated and Ammoniated Cu(II)-Exchanged Zeolites, Types X and Y

WILLY DE WILDE, ROBERT A. SCHOONHEYDT, and JAN B. UYTTERHOEVEN

Centrum voor Oppervlaktischekunde en Colloidale Scheikunde, Katholieke Universiteit Leuven, De Croylaan 42, B-3030 Heverlee, Belgium

ABSTRACT

Hydrated Cu(II) zeolites with Na^+ and La(III) as co-exchanged cations contain mainly $\text{Cu(II)(H}_2\text{O)}_6$ in the supercages with bonding characteristics similar to those of $\text{Cu(II)(H}_2\text{O)}_6$ in solution. With K^+ as co-exchanged cation most of the hydrated Cu(II) ions are in the sodalite cages at low exchange levels. Saturation with NH_3 gives $\text{Cu(II)(NH}_3)_4$ with increased π -bonding character with respect to $\text{Cu(II)(NH}_3)_4$ in single crystals. Desorption and adsorption were studied, and the species $(\text{O})_3\text{-Cu-OH}_2$ and $(\text{O})_3\text{-Cu-NH}_3$ were characterized spectroscopically.

Introduction

Epr studies of hydrated Cu(II) ions in synthetic faujasites revealed the presence of the $\text{Cu(II)(H}_2\text{O)}_6$ species in the supercages (1-8), and a partially hydrated Cu(II) ion immobilized against the cavity walls (2,4-6). The latter species could not be identified from the optical spectroscopic measurements while the former absorbed around 12500 cm^{-1} (3,9-12). Upon adsorption of NH_3 on a dehydrated Cu(II) zeolite, epr measurements indicated that the square planar $\text{Cu(II)(NH}_3)_4$ is immediately formed. However, for a quantitative reaction to occur, the pretreatment conditions are extremely important as vacuum dehydration leads to a partial reduction of Cu(II) to Cu(I) (2,6-8, 13-18). The optical spectra of ammoniated Cu(II) zeolites were not interpreted as uniformly as the epr data and pentammine as well as hexammine complexes have been proposed (9-11). Upon desorption of NH_3 intermediates of the type $\text{Cu(NH}_3)_x\text{O}_2$, with x

ranging from 1 to 3 and O_l indicating lattice oxygens, were identified but there was no agreement among the authors (8-11,13). We report the electronic spectra of hydrated and ammoniated X and Y zeolites with different Cu(II) loadings, and with Na^+ , K^+ and La(III) as co-exchanged cations. The study includes adsorption and desorption of H_2O and NH_3 .

Experimental

Samples. Zeolites X and Y in their Na^+ forms were exchanged in 1N NaCl solution at room temperature for 72×10^3 s prior to use. Parts of these samples were converted to their K^+ form by repeated exchange (5x) in 1N KCl. Four runs were performed at room temperature, the fifth at 343°K. La(III) was exchanged into NaY from 0.1N $La(NO_3)_3$ solutions at room temperature for 72×10^3 s. These Na^+ , K^+ and La(III) loaded zeolites were exchanged with $CuCl_2$ solutions at room temperature for 1 day. The solid:liquid ratio varied from 2-10 kg/m^3 . Maximum exchange levels were obtained in 0.1N Cu(II) solutions. Lower exchange levels were obtained from solutions containing the necessary amount Cu(II) to realize a fixed exchange level. All the samples were washed until Cl^- free, airdried at 333°K and stored in a desiccator over a saturated NH_4Cl solution. Na^+ , K^+ and Cu(II) were determined by atomic absorption. La(III) was determined with the atomic absorption spectrometer in the emission mode. The analytical data are given in Table I, together with the sample symbols. The co-exchanged cation Na^+ is not indicated. The numbers after each symbol are the number of Cu(II) ions per unit cell. In the same table the charge deficit due to proton exchange, and excess Cu due to exchange or precipitation of polynuclear Cu-complexes, are indicated also (19).

Desorption and adsorption of H_2O . The recording of the spectra of the hydrated zeolites was followed by a stepwise vacuum desorption up to 723°K with intervals of $\sim 50^\circ K$. At each interval the desorption time was 1.728×10^5 s prior to recording the spectra. O_2 was added at 623°K and, after a one night contact, evacuated at room temperature. The samples were then equilibrated with water vapour at room temperature or at 353°K for several days and the spectra taken again.

Adsorption and desorption of NH_3 . The zeolites were degassed up to 773°K, except CuX26.8 and CuX36, which were degassed at 623°K because of lattice

destruction at 773°K. In our earlier experiments no O₂ treatment was given prior to adsorption of NH₃. In the other experiments the dehydration was followed by an O₂ treatment as described above. After this O₂ treatment the spectra of the dehydrated zeolites were taken. NH₃ was allowed to adsorb in slugs of ~ 1 NH₃ molecule per Cu(II) ion up to 6 NH₃/Cu(II). The final adsorption step was an equilibration of the zeolite in NH₃ vapor. After addition of each slug the zeolite was allowed to equilibrate for 1.728×10^5 s and the spectra recorded. Adsorptions were performed at room temperature and at 353°K. In some cases the saturation of the zeolite with NH₃ was followed by a stepwise desorption as described for the desorption of water.

TABLE I.- Number of exchangeable cations per unit cell

Samples	Cu(II)	Na ⁺	K ⁺	La(III)	charge excess (+) or deficit (-)
CuY1.3	1.3	54.8	-	-	-
CuY2.6	2.6	52.1	-	-	-
CuY3.8	3.8	47.1	-	-	- 1.3
CuY8.8	8.8	37.3	-	-	-
CuY11.8	11.8	31.4	-	-	-
CuY17.5	17.5	21.4	-	-	-
CuY18.0	18.0	20.0	-	-	-
CuY19.0	19.0	18.5	-	-	-
CuKY3.1	3.1	0.9	49.1	-	-
CuLaY4.6	4.6	17.3	-	6.9	- 8.8
CuLaY6.8	6.8	5.2	-	8.6	-11.4
CuX4.5	4.5	76.8	-	-	-
CuX8.5	8.5	65.4	-	-	- 3.6
CuX10.9	10.9	60.7	-	-	- 3.5
CuX26.8	26.8	38.9	-	-	+ 6.5
CuX36.0	36.0	21.7	-	-	+ 7.7
CuKX4.4	4.4	1.5	76.3	-	-

Spectral measurements. The spectra were recorded at room temperature in the range 1800-350 nm with a Cary 17 instrument equipped with a type II reflectance unit. The output was digitalized and processed in a computer to obtain plots of the Kubelka-Munk function (20) against wavenumbers. The standard was MgO. Samples and standard were placed in quartz reflectometric cells (21) fitted with a small volume for pre-

treatment and a sidearm with a greaseless stopcock for connection to the vacuum system.

Results

Hydrated zeolites. Figure 1 shows typical spectra of hydrated X-type zeolites with Na^+ as co-exchanged cation at different Cu(II) loadings. The spectra show 1 band, slightly asymmetric at its low frequency side. The shape is independent of the Cu(II) content. The band is centered at 12430 cm^{-1} with a standard deviation of 71 cm^{-1} . The half band width increases with increasing Cu(II) loadings in the range $5100\text{--}6300 \text{ cm}^{-1}$. For Y-type zeolites with 8-19 Cu(II) ions per unit cell and Na^+ as co-exchanged cation, the same band is observed at a slightly lower frequency, $12150 \pm 50 \text{ cm}^{-1}$ with a half band width of $5700 \pm 135 \text{ cm}^{-1}$. The La(III) exchanged sieves have their band maximum at $12350 \pm 150 \text{ cm}^{-1}$ with a half band width of $6200\text{--}6700 \text{ cm}^{-1}$. The original band of CuY1.25 and CuY2.6 (Figure 2) is centered around 14000 cm^{-1} , but after rehydration the band maximum shifted to 13000 cm^{-1} . For all the other zeolites rehydration at room temperature completely restored the original spectra, while rehydration at 353°K resulted in a shift of $\sim 200 \text{ cm}^{-1}$ to lower wavenumbers. For hydrated zeolites with K^+ as co-exchanged cation the spectra are totally different (Figure 3). Both for X and Y type zeolites the band maximum is at 11100 cm^{-1} with a clearly distinguishable shoulder at 9200 cm^{-1} . After a dehydration rehydration cycle the same spectrum is recovered. A 0.1 N Cu(II) solution has a band with maximum absorption at 12300 cm^{-1} , slightly asymmetric towards the low frequencies. The half band width is 5000 cm^{-1} .

Partially hydrated zeolites. The spectral changes observed during dehydration are very similar for all the samples except the K^+ co-exchanged zeolites. Figure 2 shows the results for CuY2.6. Room temperature vacuum degassing gives a band broadening due to the appearance of low and high frequency shoulders around 10200 cm^{-1} and 15000 cm^{-1} respectively with the band maximum still around 12500 cm^{-1} . Upon heating a 2 band spectrum appears with maxima at 10600 cm^{-1} and 12200 cm^{-1} , which persist up to 418°K . For the Y type zeolites with higher Cu(II) loadings and also for those with La(III) as co-exchanged cation the 3 band spectrum obtained for CuY2.6 after room temperature vacuum degassing persists up to $\sim 373^\circ\text{K}$. Between 373°K and 423°K a broad band is observed with its maximum stret-

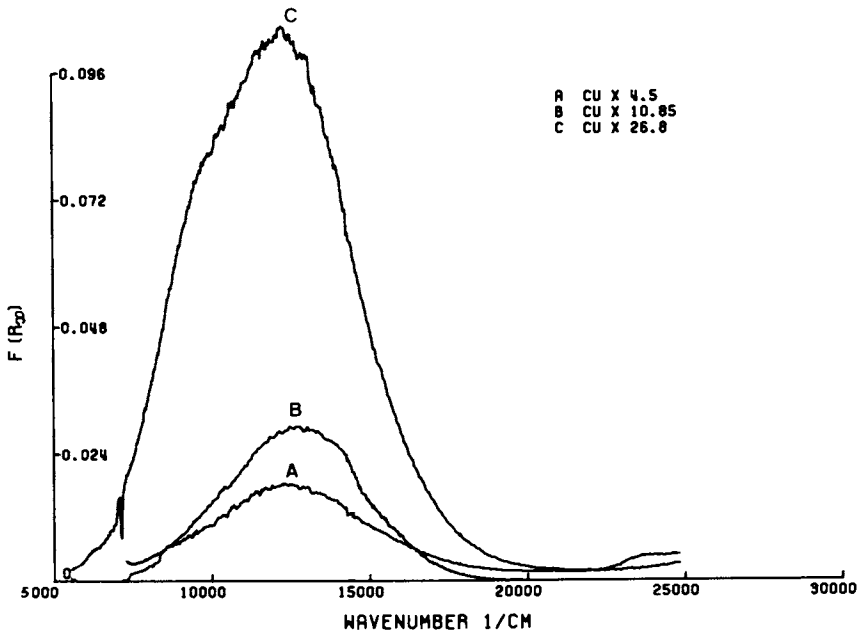


Figure 1. NIR-VIS spectra of hydrated zeolites. (A) CuX 4.5; (B) CuX 10.85; (C) CuX 26.8.

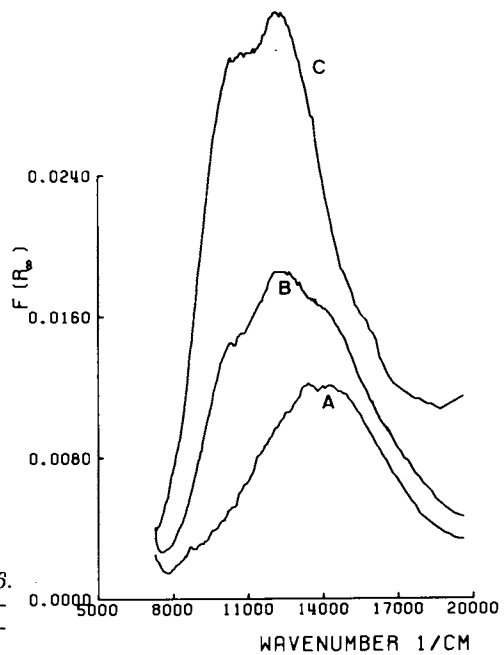


Figure 2. NIR-VIS spectra of CuY 2.6. (A) hydrated; (B) after vacuum desorption at 298 K; (C) after vacuum desorption at 418 K.

ching from 11500 to 13200 cm^{-1} . It clearly covers several components. For the X type zeolites with Na^+ as co-exchanged cation room temperature vacuum degassing results in a narrowing of the 12430 cm^{-1} band for CuX4.5 and the appearance of a 10000 cm^{-1} shoulder for CuX26.8. At 373°K the 3 band spectrum similar to that of CuY2.6 (Figure 2) is obtained with the band maximum at 13100 cm^{-1} and the shoulders around 17000 cm^{-1} and 10000 cm^{-1} . Above 373°K a broad band in the range 12500-14500 cm^{-1} shows up and persists up to 475°K. Above 423°K for Y type and above 475°K for X type zeolites the spectra are typical for Cu(II) in dehydrated zeolites with a band maximum at 10800 cm^{-1} and a shoulder around 14500 cm^{-1} (see Figure 4A). Figure 3 shows the typical spectra for CuKY3.1 obtained after several dehydration stages. The spectra of CuKX4.4 are identical. The band system of the completely hydrated system shifts to higher frequencies, decreases in intensity and a new band appears at 16000 cm^{-1} which persists up to 438°K. At 566°K this spectrum is destroyed and that of a dehydrated Cu(II)-zeolite shows up.

Cu(II) ammonia complexes. The spectral behavior upon adsorption of NH_3 is similar for zeolites X and Y and is independent of the degree of exchange, of the type of co-exchanged cation, Na^+ or La(III) and of the adsorption temperature. Figure 4 shows a typical example. At low NH_3 :Cu(II) ratios a two band spectrum is visible with absorption maxima around 11000 cm^{-1} and 12400 cm^{-1} and a weak shoulder around 16000 cm^{-1} . At high Cu(II) loadings the two absorption maxima overlap too strongly to be distinguishable. This spectrum persists up to 1 NH_3 per Cu(II). At higher NH_3 :Cu(II) ratios the 16000 cm^{-1} component increases at the expense of the lower frequency bands. This causes a shift of the band system to higher frequencies. The NH_3 saturated samples have their band maximum at $16300 \pm 200 \text{ cm}^{-1}$ at high exchange levels (CuX26.8, CuY17.5, CuY18, CuY19) and at $15600 \pm 300 \text{ cm}^{-1}$ at low exchange levels (CuX4.5, CuY1.25, CuY2.58, CuY3.8, CuLaY4.6, CuLa6.7). Irrespective of the position of their band maximum the bands of these NH_3 saturated zeolites are asymmetric towards their low frequency side. This is especially evident for CuX4.5 where the shoulder could be localized around 11300 cm^{-1} . The spectrum of a Cu(II)(NH_3)₄ solution had its band maximum at 16500 cm^{-1} . In 6.1N NaCl the Cu(II)(NH_3)₄ complex absorbed at 16660 cm^{-1} . These bands are asymmetric at their low frequency sides.

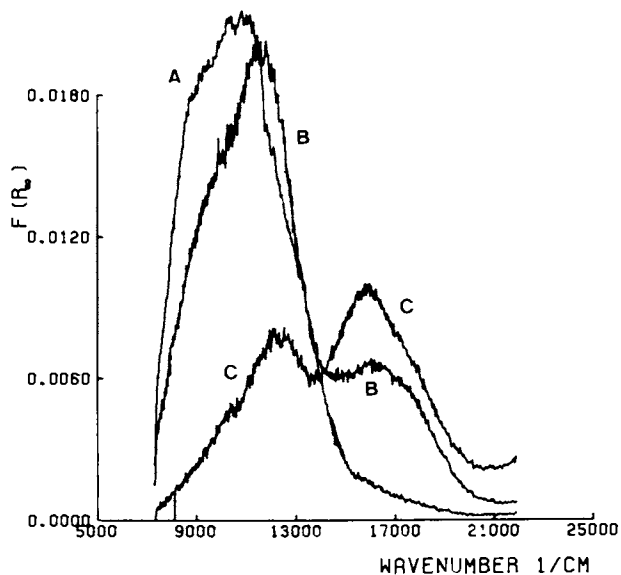


Figure 3. NIR-VIS spectra of CuKY 3.1. (A) hydrated; (B) after vacuum desorption at 327 K; (C) after vacuum desorption at 438 K.

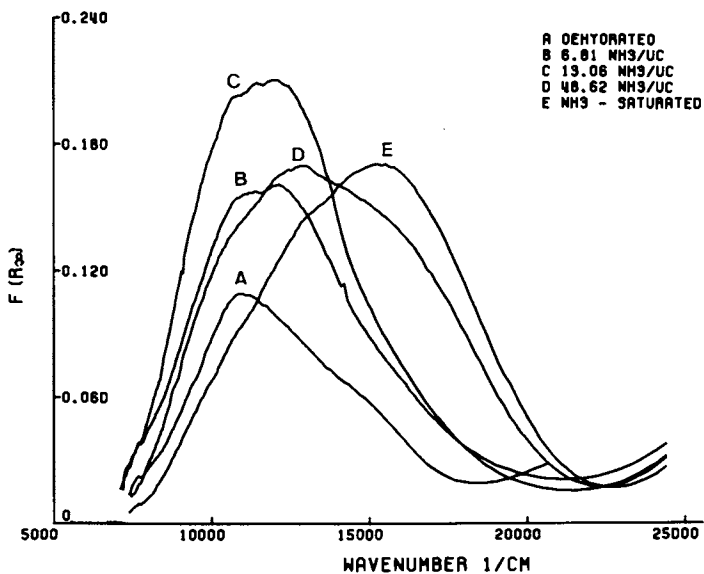


Figure 4. NIR-VIS spectra of CuLaY 6.7. (A) dehydrated; (B) 6.81 $\text{NH}_3/\text{U.C.}$; (C) 13.06 $\text{NH}_3/\text{U.C.}$; (D) 46.62 $\text{NH}_3/\text{U.C.}$; (E) saturated with NH_3 .

$\text{Cu(II)(NH}_3)_4$ was also exchanged onto a NaY zeolite a zeolite. Degassing yields, between 356°K and 383°K , an intense spectrum wherein 2 bands could be resolved at $\sim 10500\text{ cm}^{-1}$ and 12200 cm^{-1} . At higher temperatures this spectrum decreases in intensity and the spectrum of a dehydrated Cu(II) zeolite is recovered after addition of O_2 . The NH_3 desorption of the same sample followed in a McBain balance revealed in the temperature range $363^\circ\text{K} - 400^\circ\text{K}$ a distinct loss at 0.5 NH_3 molecules per Cu(II) ion. Desorption of NH_3 from the NH_3 saturated zeolites in the range $356^\circ\text{K} - 400^\circ\text{K}$ gave a broad band between 10000 and 12500 cm^{-1} for CuY1.25 and CuLaY4.6. For CuX4.5 and CuX26.8 the desorption in the same temperature range gave spectra with band maxima at higher frequencies. Clearly the desorption was not so advanced as for the corresponding Y type zeolites.

Discussion

Aqueous Cu(II) ions in zeolites X and Y. The spectra of Cu(II) ions in hydrated and rehydrated zeolites with Na^+ or La(III) as co-exchanged cations confirm the epr data (1-8) in that they are due to $\text{Cu(II)(H}_2\text{O)}_6$ species in the supercages. Indeed, the band frequencies of 12150 cm^{-1} and 12430 cm^{-1} for Y and X type zeolites respectively agree with the 12300 cm^{-1} for $\text{Cu(II)(H}_2\text{O)}_6$ in solution. The frequency difference for $\text{Cu(II)(H}_2\text{O)}_6$ between X and Y indicates a slight increase of the octahedral crystal field parameter $10 Dq$ from Y to X. The same effect has been observed for Ni(II) in dehydrated A, X and Y type zeolites by Garbowski and Mathieu (22). They ascribed it to the difference in isomorphic substitution. A similar explanation may be invoked here but should be handled with care as the framework is screened by the adsorbed water molecules and the co-exchanged cations.

The combination of our spectral data with the epr parameters published sofar (1-8) allows a better estimate of the above mentioned idea. $\text{Cu(II)(H}_2\text{O)}_6$ is a tetragonally distorted complex. The effective spin-orbit coupling constants can be calculated both from the isotropic and axially symmetric g-values (1-8) and the observed band frequencies (23). The results are given in Table II. This table contains also the coefficients of the molecular orbitals (M.O.'s) of the complex, calculated according to the theory of Kivelson and Neiman (24). α , β_1 and β are respectively the coefficients of the $d_{x^2-y^2}$, d_{xy} and d_{xz} or d_{yz} orbitals

of Cu(II) in the M.O.'s of Cu(II)(H₂O)₆. We conclude from the values of these coefficients in Table II that the bonding characteristics of Cu(II)(H₂O)₆ are not significantly different in zeolites X and Y. The values of α , which is a measure of the extent of σ -bonding, is equal to its value in aqueous solution (25). Usually π -bonding is negligible i.e. $\beta^2 = \beta_1^2 = 1$ (25). In zeolites these coefficients are less than 1, suggesting that some π -bonding may occur.

When the zeolites are not completely hydrated Cu(II) is present as Cu(II)(H₂O)₄ as suggested by the 14000 cm⁻¹ band of CuY1.25 and CuY2.6. The spectra of CuKX4.4 and CuKY3.1 necessitate a different explanation. Indeed, the 9200 cm⁻¹ shoulder is indicative for the presence of a distorted tetrahedral configuration (26-28). We therefore think that in CuKX4.4 and in CuKY3.1 most of the Cu(II) ions are in the sodalite cages on sites I' or II' and co-ordinated to 1 or 2 water molecules. We conclude that K⁺ is easier to replace in the sodalite cages than Na⁺. This phenomenon reflects the different hydration properties of K⁺ and Na⁺ as discussed by Costenoble et al. (29).

The spectral changes observed during dehydration are similar to those described by Kuzmenko and Lygin (10). The appearance of high and low frequency shoulders on the Cu(II)(H₂O)₆ band indicates the formation of less hydrated species. The high frequency shoulder (15000-17000 cm⁻¹) is clearly observed on CuKX4.4 and CuKY3.1 (Figure 3). The assignment of this band is not clear, although the rather high frequency may indicate a square planar character for the Cu(II) environment. The low frequency shoulder around 10000 cm⁻¹ is part of the stable 2 band spectrum observed clearly at higher degassing temperatures (Figure 2). The frequencies of 10600 cm⁻¹ and 12200 cm⁻¹ are in agreement with a C_{3v} symmetry model i.e. a Cu(II) ion linked to 3 lattice oxygens of sites I', II' or II and 1 water molecule. At high Cu(II) concentrations these bands overlap strongly and cannot be resolved. It is interesting to note that the degassing temperature necessary for the formation of this species increases with increasing Cu(II) loading and is higher for X than for Y type zeolites.

Cu(II) ammonia complexes. The band frequencies and band shapes of the spectra after saturation with NH₃ are similar to those for Cu(II)(NH₃)₄ in solution. We assign our spectra to this species, in agreement with the interpretation of the epr and ir data (6-8, 13, 15-17), but in disagreement with Kuzmenko's and

Kiselev's interpretation (10,11). The difference in band frequency between samples with small and high Cu(II) loadings reflects slightly different crystal field parameters. The asymmetry of the band is partially due to the presence of uncomplexed Cu(II), especially in CuX4.5, and partially to the asymmetric nature of the band of Cu(II)(NH₃)₄ itself. The effective spin-orbit coupling constants and the coefficients of the molecular orbitals of Cu(II)(NH₃)₄ in zeolites are given in Table II. No significant differences were found for Cu(II)(NH₃)₄ at low and high loadings, except some increased π -bonding character in the former case. With respect to single crystal studies of Cu(II)(NH₃)₄ the spin-orbit coupling constant λ calculated from g is significantly less (30). This may indicate an increased π -bonding character of Cu(II)(NH₃)₄ in zeolites with respect to the same species in crystals. The same trend was observed for Cu(II)(H₂O)₆.

TABLE II.- Effective spin-orbit coupling constants and coefficients of M.O.'s of Cu(II)(H₂O)₆ and Cu(II)(NH₃)₄.

	Cu(II)(H ₂ O) ₆		Cu(II)(NH ₃) ₄	
	Y	X	low Cu(II)	high Cu(II)
g_{iso} (± 0.01)	2.18	2.18	-	-
λ_{eff} ($\pm 31 \text{ cm}^{-1}$)	513	525	-	-
g	2.38	2.369	2.245	2.245
A (cm^{-1})	0.0137	0.0139	0.0164	0.0164
g	2.08	2.084	2.039	2.039
λ ($\pm 40 \text{ cm}^{-1}$)	600	599	487	508
λ ($\pm 90 \text{ cm}^{-1}$)	533	575	298	305
α^2 (± 0.05)	0.84	0.83	0.77	0.77
β_1^2 (± 0.05)	0.78	0.85	0.75	0.86
β_2^2 (± 0.05)	0.71	0.76	*	*

* g too inaccurate to calculate a reliable value.

Partial saturation of a dehydrated Cu(II) zeolite or partial desorption of a NH₃-saturated sample leads to the formation of a 2 band spectrum, analogous to that assigned to (O)₃-Cu-OH₂. We ascribe it to the complex (O)₃-Cu-NH₃. This species has been characte-

rized by epr too, but only after partial desorption (7,8,13). The values $g = 2.24$ and $g = 2.012$ confirm our interpretation in terms of a distorted tetrahedral complex. The desorption experiments indicate that, as for $\text{Cu(II)(H}_2\text{O)}_6$, desorption of NH_3 is somewhat faster in zeolites Y than in zeolites X.

Acknowledgment

W.D.W. is indebted to the I.W.O.N.L. (Belgium) for a Ph.D. grant. R.A.S. acknowledges the N.F.W.O. for a grant as "Bevoegdverklaard Navorsers". The authors are grateful to J. Pelgrims for the chemical analysis of the samples. This research was made possible by the Belgian Government (Staatssekretariaat voor Wetenschapsbeleid).

Literature Cited

1. Nicula, A., Stamires, D., and Turkevich, J., *J. Chem. Phys.* (1965), 42, 3684
2. Turkevich, J., Ono, Y., and Soria, J., *J. Catalysis* (1972), 25, 44.
3. Mikheikin, I.D., Shvets, V.A., and Kazanskii, V.B., *Kin. Kat.* (1970), 11, 747.
4. Trif, E., Cociu, L., and Nicula, A., *Rev. Roum. Phys.* (1973), 18, 451.
5. Soria Ruiz, J.A., and Turkevich, J., *An. Fisica* (1971), 67, 435.
6. Leith, I.R., and Leach, H.F., *Proc. Royal Soc. London* (1972), A330, 247.
7. Naccache C., and Ben Taarit, Y., *Chem. Phys. Lett.* (1971), 11, 11.
8. Maksimov, N.G., Anufrienko, V.F., and Ione, K.G., *Dokl. Akad. Nauk. SSSR* (1973), 212, 142.
9. Kiselev, A.V., Kuzmenko, N.M., and Lygin, V.I., *Russian J. Phys. Chem.* (1973), 47, 88.
10. Kuzmenko, N.H., and Lygin, V.I., *Proceedings, Third International Conference on Molecular Sieves*, ed. J.B. Uytterhoeven, Leuven University press (1973), 347.
11. Kiselev, A.V., Kuzmenko, N.H., and Lygin, V.I., *Zh. Fiz. Khim.* (1975), 49, 3043.
12. Shinkarenko, V.G., Anufrienko, V.F., Boreskov, G.K., Ione, K.G., and Yur'eva, T.M., *Dokl. Akad. Nauk. SSSR* (1975), 223, 410.
13. Vansant, E.F., and Lunsford, J.H., *J. Phys. Chem.* (1972), 76, 2860.
14. Huang, Y.-Y., and Vansant, E.F., *J. Phys. Chem.* (1973), 77, 663.

15. Vadrine, J.C., Derouane, E.G., and Ben Taarit, Y., *J. Phys. Chem.* (1974), 78, 531.
16. Derouane, E.G., Vadrine, J.C., and Ben Taarit, Y., *Bull. Soc. Chim. Belge* (1974), 83, 189.
17. Flentge, D.R., Lunsford, J.H., Jacobs, P.A., and Uytterhoeven, J.B., *J. Phys. Chem.* (1975), 79, 354.
18. Jacobs, P.A., De Wilde, W., Schoonheydt, R.A., Uytterhoeven, J.B., and Beyer, H., *J. Chem. Soc. Faraday I* (1976), 72, 1221.
19. Schoonheydt, R.A., Vandamme, L.J., Jacobs, P.A., and Uytterhoeven, J.B., *J. Catalysis*, (1976), 43, 292.
20. Kortüm, G., *Reflectance Spectroscopy*, Springer Verlag, Berlin (1969).
21. Klier, K., *Catalysis Rev.* (1967), 1, 207.
22. Garbowski, E., and Mathieu, M.-V., *C.R. Acad. Sci. Paris* (1975), 280, 1125.
23. Bleaney, B., Bowen, K.D., and Pryce M.H.L., *Proc. Royal Soc.* (1955), A228, 166.
24. Kivelson, D., Neiman R., *J. Chem. Phys.* (1961), 35, 149.
25. Walker, F.A., Sigel, H., and McCormick, D.B., *Inorg. Chem.* (1972), 11, 2756.
26. Karipides, A.G., and Piper, T.S., *Inorg. Chem.* (1962), 1, 970.
27. Tom Dieck, H., *Inorg. Chim. Acta* (1973), 7, 397.
28. Harlow, R.L., Wells III, W.J., Watt, G.W., and Simonsen, S.H., *Inorg. Chem.* (1975), 14, 1768.
29. Costenoble, M.L., Mortier, W.J., and Uytterhoeven, J.B., *J. Chem. Soc. Faraday I* (1976), 72, 1877.
30. Tomlinson, A.A.G., Hathaway, B.J., Billing, D.E., and Nichols, P., *J. Chem. Soc. (A)* (1969), 65.

Adsorption and Decomposition of Metal Carbonyls Loaded in Y-Type Zeolite

P. GALLEZOT, G. COUDURIER, M. PRIMET, and B. IMELIK

Institut de Recherches sur la Catalyse, 79, boulevard du 11 Novembre 1918, 69626 Villeurbanne Cédex, France

ABSTRACT

$\text{Mo}(\text{CO})_6$, $\text{Re}_2(\text{CO})_{10}$, $\text{Ru}_3(\text{CO})_{12}$, adsorbed on HY zeolite, were located by crystal structure analysis and their bonding with the framework has been investigated by IR spectroscopy. Initially, they occupy positions near the supercage center (Re) or near the supercage aperture (Mo, Ru). On partial decomposition Mo and Re complexes are displaced and bonded to the framework.

Introduction

In recent years, considerable effort has been devoted to developing a new class of heterogeneous catalysts whose preparation involves the linking of transition metal complexes to the surface atoms of a solid support (1). These catalysts are expected to combine the advantages of homogeneous and heterogeneous catalytic systems. One way of using zeolites is to introduce transition metal cations by ion-exchange. After dehydration, the coordinatively unsaturated cations not in hidden sites are available to form complexes with molecules entering the zeolite framework (2). Detailed structural informations on a number of complexes in A zeolites have been given by Seff (3, 4, 5). In this laboratory, the Cu^{2+} ions migration induced by reagents (6) and the activity of Ni^{2+} ions located in supercages towards the cyclotrimerisation of acetylene (7) were studied.

An alternative way of grafting metal complexes in zeolites has been tried in the present work. It consists in adsorbing uncharged coordination complexes on the zeolite which may be subsequently treated in order to eliminate part of the ligands so that the metal atom might bond to the zeolite framework acting as a polydentate ligand. This process has been tried using metal carbonyls $\{\text{Mo}(\text{CO})_6, \text{Re}_2(\text{CO})_{10} \text{ and } \text{Ru}_3(\text{CO})_{12}\}$ as adsorbate and HY zeolite as adsorbent.

Experimental

Materials. The starting materials were a NaY zeolite supplied by the Linde Co (SK 40 Sieves) and $\text{Mo}(\text{CO})_6$, $\text{Re}_2(\text{CO})_{10}$ and $\text{Ru}_3(\text{CO})_{12}$ obtained from commercial sources. The ammonium form, NH_4Y , was prepared by conventional ion-exchange procedure in NH_4NO_3 solutions. The unit cell composition derived from chemical analysis was $(\text{NH}_4)_{46}\text{Na}_{10}\text{Y}(\text{Y} = \text{Al}_{56}\text{Si}_{136}\text{O}_{384})$.

Metal carbonyls loading. The metal carbonyls were sublimated under vacuum and their vapours were adsorbed on the activated zeolite. This was achieved in a cell having two branches connected through a grease-free stopcock. The NH_4Y zeolite set in the first branch was heated for 15 hours in oxygen and for three hours in vacuo (10^{-5} Torr) at 350°C in order to obtain the activated HY form.

For X-ray investigations, the metal carbonyl in suitable amount to get a given loading was set in the second branch and evacuated at 25°C . The branches were then connected and the cell was set into a thermostated oven and $\text{Mo}(\text{CO})_6$, $\text{Re}_2(\text{CO})_{10}$ and $\text{Ru}_3(\text{CO})_{12}$ were adsorbed at 60, 110 and 120°C respectively. It was gravimetrically checked that the zeolite took up the whole amount of carbonyl within 15 hours or less. In this way three samples containing 8 $\text{Mo}(\text{CO})_6$, 4 $\text{Re}_2(\text{CO})_{10}$ and 3 $\text{Ru}_3(\text{CO})_{12}$ per unit cell were prepared.

For volumetric measurements, the first branch of the cell was then a classical adsorption bulb. For the IR studies, the adsorption of $\text{Mo}(\text{CO})_6$ and $\text{Re}_2(\text{CO})_{10}$ were performed at room temperature by connecting the HY zeolite with a small bulb containing the carbonyl compound purified by repeated distillations under vacuum and dried on 4 A molecular sieves.

Thermal decomposition. The metal carbonyls adsorbed on zeolites were decomposed in a closed system by heating at various temperatures the cell used for metal carbonyl loading. The decomposition was monitored by measuring the pressure changes in the cell with a Texas Instruments pressure gauge. With proper calibration for dead space and correction for physically adsorbed CO, it was possible to determine the amount of CO evolved per mole of metal carbonyl.

IR investigations. The NH_4Y zeolite was compressed under a pressure of 1 Ton cm^{-2} so as to give discs of 18 mm diameter and of weight comprised between 5 and 8 mg. The disc, placed in a quartz sample holder, was inserted into an infrared cell equipped with KBr windows and treated in flowing oxygen at 350°C , then in vacuo as described above.

Infrared spectra were recorded at 25°C using a Digilab FTS - 14 Fourier transform interferometer, with a resolution of 4 cm^{-1} and a number of scans equal to 200. For each set of spectra, a reference spectrum of the HY zeolite was obtained at the beginning

and stored in the 128 K disc incorporated in the FTS - 14 spectrometer. Subsequent spectra containing additional bands from adsorbed molecules were recorded in the same conditions. The ratio of the two stored spectra gave a spectrum from which the bands of the reference sample have been eliminated.

Results

Volumetric measurements. The number of moles of CO evolved per mole of metal carbonyl loaded in HY zeolite on heating the solid, is given in figure 1.

Crystal structure determination. In order to locate the metal carbonyls, the crystal structures of four samples described in table I have been determined. The resolution methods were the same as those used in previous work (8). The least squares refinement of crystallographic parameters was performed from the intensities of X-ray reflections up to $h^2 + k^2 + l^2 = 395$ derived from powder data. Attempts to determine the precise location of the metal atoms have failed because any atom occupying a general position in space group $Fd\bar{3}m$ has a very low occupancy factor (1/192). Nevertheless, the intensities of the reflections at low Bragg angles were considerably modified by the presence of the adsorbed complexes in the four samples investigated. This indicates that the complexes find "nests" of higher occupancy probability. The best way of handling this problem is to suppose that the unlocated atoms statistically occupy random positions within a sphere of given radius and to refine the occupancy factor of the sphere. As first approximation, only the metal atom of the complex has to be taken into account. This was achieved by means of the liquid scattering functions introduced by Simpson and Steinfink (9). The method has already been successfully applied to account for unlocated molecules and cations (10, 11) and for reduced palladium and platinum atoms in Y zeolite (8, 12).

Sample I. Without taking into account the adsorbed complexes, the least squares refinement resulted in $R = 0.114$ for the whole set of structure factors. However, considerable discrepancies were noticed for the low indexes reflections: for the 27 first structure factors (from 220 to 555) $R_{1,j} = 0.147$. The liquid scattering functions were introduced assuming that the Mo atoms were in spheres centered either at $x = y = z = 0.375$ (center of the supercage) or at $x = y = z = 0.5$ (center of the 12 membered ring aperture of the supercages). This last location gave by far the best R values. The influence of positions and radius of the sphere were then systematically studied. The lowest R values ($R = 0.089$ and $R_{1,j} = 0.090$) were obtained by refining the Mo population assumed to be distributed within a 1.5 Å radius sphere at $x = y = z = 0.475$; this yielded 10.5 Mo atoms. The excess of scattering matter with respect to the 8 Mo introduced, may be partly explained because the CO have not been taken into account.

Sample II. Structure refinement without taking into account the 4 $\text{Re}_2(\text{CO})_{10}$ per unit cell gave $R = 0.138$ and $R_{1,j} = 0.265$. Difference Fourier maps indicated that the unlocated scattering matter was probably concentrated near the center of the supercage. Considering that the Re atoms were distributed throughout a 2 Å sphere centered at $x = y = z = 0.375$, a considerable improvement of R values was obtained ($R = 0.101$ and $R_{1,j} = 0.150$). The refinement gave a population of 7.5 Re per unit cell which is in good agreement with the number of Re atoms introduced, moreover it can be noted that the 2 Å radius sphere just encompasses the Re - Re pair present in $\text{Re}_2(\text{CO})_{10}$.

Samples III and IV. The Re and Ru atoms were assumed to be distributed in a 3 Å radius sphere centered at $x = y = z = 0.5$. Sample III refinement produced a drop of R and $R_{1,j}$ from 0.139 and 0.140 to 0.125 and 0.108 respectively. The population of the sphere was found to be 9 Re atoms. For sample IV, R values dropped from 0.123 and 0.167 to 0.113 and 0.148 respectively. The results obtained from sample III and IV are less accurate than for sample I and II. The use of liquid scattering functions results in a lower decrease of R indexes and the spheres are much larger. The locations of the Re and Ru atoms in samples III and IV are therefore comparatively ill-defined.

The crystallographic parameters of the four structures investigated are given in table I. Listings of the observed and calculated structure factors are available upon request to the authors.

IR spectroscopy results. Adsorption of $\text{Mo}(\text{CO})_6$. At 25°C $\text{Mo}(\text{CO})_6$ introduced onto HY zeolite gave a spectrum in the $\nu(\text{CO})$ range containing four bands at 2125 (weak), 2050 (medium), 1995 (strong) and 1955 (strong) cm^{-1} (fig. 2a). The intensity of these bands increased with the amount of adsorbed $\text{Mo}(\text{CO})_6$ and a 592 cm^{-1} band developed (fig. 2b). The OH groups of the zeolite were also perturbed: the 3640 cm^{-1} band decreased and a broad band developed at about 3500 cm^{-1} . For large amounts of $\text{Mo}(\text{CO})_6$, the 3540 cm^{-1} band also decreased, the intensity of the 3500 cm^{-1} band became very important and two new bands at 925 and 840 cm^{-1} appeared.

When the loaded sample was heated under vacuum between 60°C and 110°C, the band at 3500 cm^{-1} due to hydrogen bonded hydroxyl groups and the band at 592 cm^{-1} disappeared, while a band at 920 cm^{-1} developed. The $\nu(\text{CO})$ bands were strongly modified and gave an intermediate spectrum with bands at 2045, 1965, 1905, 1835 and 1670 cm^{-1} (fig. 2c).

Upon heating at 150°C (fig. 2d), the sample gave an infrared spectrum with $\nu(\text{CO})$ bands at 2070, 2020 and 1985 cm^{-1} whereas the 920 cm^{-1} bands was shifted to 895 cm^{-1} . The IR spectrum showed a decrease of the $\nu(\text{OH})$ bands at 3640 and 3540 cm^{-1} in comparison with the initial zeolite sample. At 220°C (fig. 2e), the $\nu(\text{CO})$ bands were missing and the 895 cm^{-1} band was shifted to 875 cm^{-1} .

Adsorption of $\text{Re}_2(\text{CO})_{10}$. $\text{Re}_2(\text{CO})_{10}$ adsorbed onto HY zeolite at 25°C led to the appearance of 4 $\nu(\text{CO})$ bands at 2130 (weak),

American Chemical
Society Library

1155 16th St., N.W.

In Molecular Sieves—II; Katzer, J.;
Washington, D.C. 20036

Table I
Crystallographic parameters

		Sample I	Sample II	Sample III	Sample IV
Preparation		Mo(CO) ₆ adsorbed at 60°C	Re ₂ (CO) ₁₀ adsorbed at 110°C	Sample II heated at 300°C	Ru ₃ (CO) ₁₂ adsorbed at 120°C
Composition		Na ₁₀ H ₄₆ ^Y .8Mo(CO) ₆	Na ₁₀ H ₄₆ ^Y .4Re(CO) ₁₀	Na ₁₀ H ₄₆ ^Y .4Re ₂ (CO) _x ^a	Na ₁₀ H ₄₆ ^Y .3Ru ₃ (CO) ₁₂
T(S1,A1)	x	0.1241(2)	0.1246(2)	0.1253(2)	0.1248(2)
	y	- 0.0532(2)	- 0.0535(2)	- 0.0524(2)	- 0.0528(2)
	z	0.0358(2)	0.0364(2)	0.0362(2)	0.0356(2)
	B ^b	1.5(2)	1.5(2)	2.2(2)	1.2(2)
O(1)	x=y	0.1061(4)	0.1098(4)	0.1065(5)	0.1067(5)
	z	0.0	0.0	0.0	0.0
	B	3.3(5)	3.4(5)	3.4(5)	2.5(5)
O(2)	x=y	- 0.0009(4)	- 0.0004(5)	- 0.0032(5)	- 0.0013(4)
	z	0.1418(4)	0.1436(6)	0.1424(6)	0.1426(6)
	B	2.3(3)	4.5(4)	2.3(4)	1.4(5)
O(3)	x=y	0.1770(4)	0.1750(4)	0.1767(5)	0.1748(5)
	z	- 0.0341(5)	- 0.0337(5)	- 0.0342(6)	- 0.0337(6)
	B	3.2(4)	1.5(4)	2.4(4)	2.1(4)
O(4)	x=y	0.1742(4)	0.1769(4)	0.1769(5)	0.1751(5)
	z	0.3201(5)	0.3219(6)	0.3245(7)	0.3236(7)
	B	3.0(3)	2.7(4)	3.1(4)	3.3(5)
Na(1)	x=y=z	0.0	0.0	0.0	0.0
	B	3.0	3.0	3.0	3.0
	P ^c	6(1)	5(1)	8(1)	5(1)
Na(1')	x=y=z	0.059(2)	0.059(2)	0.056(2)	0.056(2)
	B	3.0	3.0	3.0	3.0
	P	4(1)	6(1)	7(1)	8(1)
Na(11)	x=y=z	0.239(3)	0.245(3)		
	B	3.0	3.0		
	P	3(1)	7(1)		
M ^d		10.5(1.0)Mo	7.5(1.0)Re	9(1.5)Re	10(2)Ru
		1.5 Å sphere	2 Å sphere	3 Å sphere	3 Å sphere
		x=y=z=0.475	x=y=z=0.375	x=y=z=0.5	x=y=z=0.5
R ^e		0.089	0.101	0.114	0.113
a(Å) ^f		24.75(1)	24.75(1)	24.73(1)	24.70(1)

(a) - From the decomposition curve : x = 7. (b) - Temperature factor (Å²)

(c) - Population per unit cell. (d) - Metal atom of the complex localized by liquid scattering function. (e) - R = Σ |F_o| - |F_c| / Σ |F_o| (f) - Unit cell constant

Estimated standard errors in parentheses.

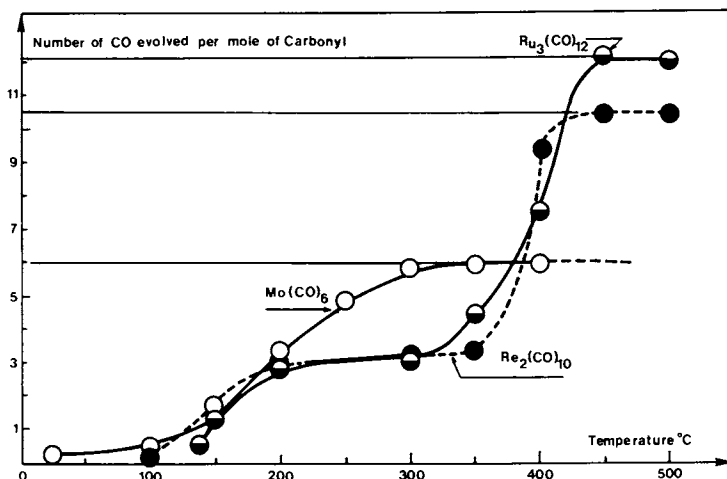


Figure 1. Decomposition curves of the metal carbonyls absorbed on HY zeolite

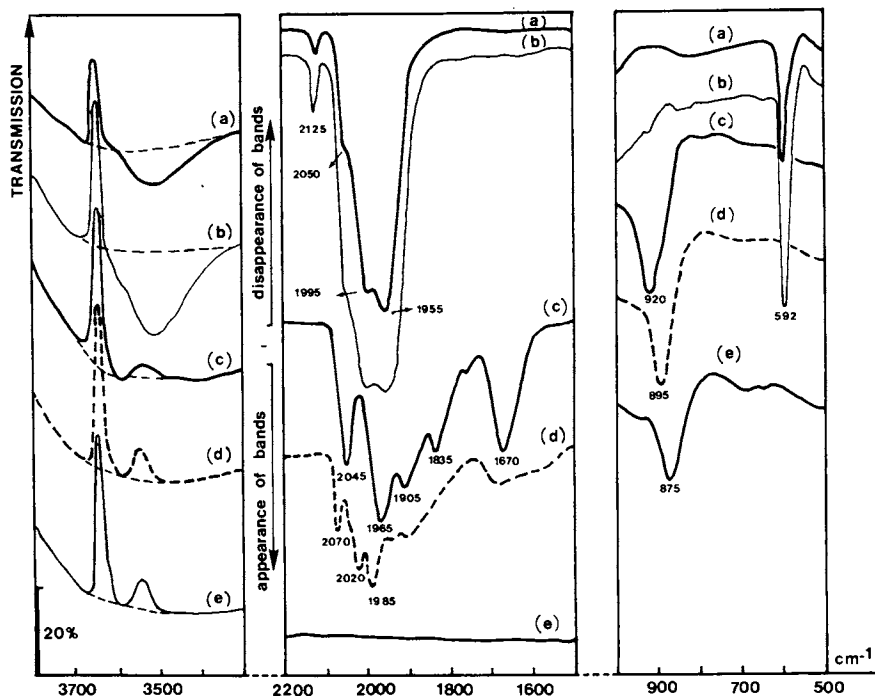


Figure 2. Infrared spectra of $\text{Mo}(\text{CO})_6$ adsorbed on HY zeolite. (a) HY zeolite contacted at R.T. with vapor of $\text{Mo}(\text{CO})_6$ for 15 sec; (b) HY zeolite contacted at R.T. with vapor of $\text{Mo}(\text{CO})_6$ for 30 sec; (c) sample (b) treated under vacuum at 70°C for 90 min; (d) sample (b) treated under vacuum at 150°C for 150 min; (e) sample (b) treated under vacuum at 220°C for 11 hrs. (· · ·), base line spectrum.

2080 (strong), 2020 (strong) and 1940 (medium) cm^{-1} (fig. 3a). On increasing the amount of $\text{Re}_2(\text{CO})_{10}$, the $\nu(\text{OH})$ band at 3640 cm^{-1} decreased, a band near 3500 cm^{-1} appeared while a band at 585 cm^{-1} developed. The spectrum was not modified by evacuation of the sample at 25°C .

On heating from 25°C to 150°C , a band at 915 cm^{-1} appeared. Above 150°C , the band at 585 cm^{-1} disappeared, and the $\nu(\text{CO})$ bands were strongly modified (fig. 3b). Near 300°C , the IR spectrum showed 4 main bands at 2050 (strong), 1950 (strong), 1895 (strong) and 1810 (weak) cm^{-1} . Above 400°C , the $\nu(\text{CO})$ bands and the peak at 915 cm^{-1} disappeared. The adsorption of CO on this sample produced a new band at 2045 cm^{-1} but the spectrum of the initial carbonyl was restored.

Discussion

Adsorption and decomposition of $\text{Mo}(\text{CO})_6$. The $\text{Mo}(\text{CO})_6$ adsorption at 25°C occurs without any loss of CO ligands since the decomposition curve in closed system (fig. 1) indicates that no CO evolved at room temperature.

Since 8 $\text{Mo}(\text{CO})_6$ have been introduced per unit cell, there should be statistically 1 $\text{Mo}(\text{CO})_6$ per supercage. Crystal structure of sample I demonstrates that the Mo atoms are actually distributed at random throughout a 1.5 Å radius sphere centered at $x = y = z = 0.475$ on the [111] axis. Each $\text{Mo}(\text{CO})_6$ molecule is therefore situated in the vicinity of the 12 membered ring and it can be inferred that these positions are occupied because the CO groups interact with the atoms of the aperture.

The spectrum of adsorbed $\text{Mo}(\text{CO})_6$ can be interpreted by a lowering of the symmetry of the molecule from O_h to C_{4v} (13) probably due to the interaction of CO groups with the framework. Moreover the decrease, after $\text{Mo}(\text{CO})_6$ adsorption, of the 3640 cm^{-1} band attributed to $O_1 - H$ groups and the simultaneous increase of a broad band at 3500 cm^{-1} attributed to hydrogen bonded OH groups strongly suggest that the CO groups are in interaction with the $O_1 - H$ species of the 12 membered oxygen rings. One may wonder why the $\text{Mo}(\text{CO})_6$ molecule is not bonded to 3 O_1 atoms maintaining a C_{3v} symmetry (in this case, the Mo atom should be situated on the (111) axis). This does not occur probably because 3 equivalent O_1H groups would be required on 8 rings which is unlikely, from the Dempsey's studies (14).

The decomposition curve (fig. 1) shows that a continuous evolution of CO takes place on heating the $\text{Mo}(\text{CO})_6$ loaded zeolite. The characteristic low angles diffraction pattern observed for sample I progressively disappears; thus at 180°C it is essentially similar to that of a dehydrated HY zeolite but with a more intense background on films. This indicates that the Mo atoms now occupy quite random positions and give incoherent scattering.

Upon heating above 70°C , IR spectra show that the initial adsorption mode no longer holds. The broad band near to 3500 cm^{-1}

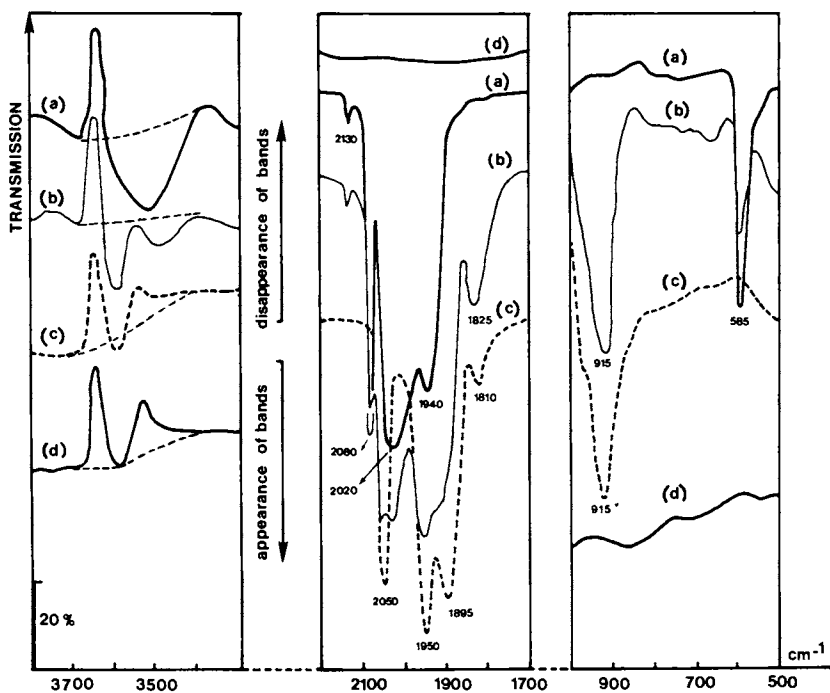
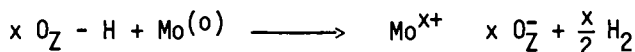


Figure 3. Infrared spectra of $\text{Re}_2(\text{CO})_{10}$ adsorbed on HY zeolite. (a) HY zeolite contacted at R.T. with vapor of $\text{Re}_2(\text{CO})_{10}$ for 3 hrs then the sample is desorbed at 150°C for 2 hrs; (b) at 300°C for 1 hr 30 min, (c) at 400°C for 2 hrs. (· · ·), base line spectrum.

assigned to OH groups in interaction with CO groups and the band at 592 cm^{-1} attributed to $\delta(\text{MCO})$ vibrations decrease and vanish while the band at 920 cm^{-1} develops. This last band which is shifted to lower frequencies at higher temperatures (895 cm^{-1} at 150°C) can be attributed to Mo-O vibrations similar to those observed for the IR spectra of molybdenum oxides and molybdates (15, 16). The Mo-O bond formation supposes that the Mo atoms are oxidized to a certain extent. The oxidation scheme could be :



where O_7 is a framework oxygen. The rôle played by the protons as oxidizing agents is confirmed by, (i) the strong decrease of the $\nu(\text{OH})$ band intensity correlated with the amount of $\text{Mo}(\text{CO})_6$ introduced, (ii) the formation of hydrogen in the gas phase detected by mass spectrometry.

At 150°C , the spectrum exhibits three $\nu(\text{CO})$ bands at 2070, 2020 and 1985 cm^{-1} . This is consistent with a complex $\text{Mo}(\text{CO})_4$ (17) where the Mo atom is directly bonded to two framework oxygen atoms. This arrangement accounts for the disappearance of the Mo atoms from their initial position and corresponds well with the number of CO molecules evolved (fig. 1).

For activation temperatures under vacuum above 220°C the complete loss of carbonyl ligands occurs and the observance of Mo-O bond shows that at least some of the molybdenum atoms are oxidized in agreement with UV spectroscopy results (18, 19).

Adsorption and decomposition of $\text{Re}_2(\text{CO})_{10}$. The decomposition curve (fig. 1) proves that $\text{Re}_2(\text{CO})_{10}$ is adsorbed without appreciable loss of CO at 110°C . The Re atoms of the molecules (statistically 1 $\text{Re}_2(\text{CO})_{10}/2$ supercages) have been located with a comparatively good precision within a 2 \AA radius sphere centered at $x = y = z = 0.375$. This situation is in agreement with the stereochemistry of the molecule, the sphere just encompasses the Re-Re pair and the supercage is large enough to allow the molecule to stretch across the cage with the possibility to be hydrogen-bonded at each end with two framework oxygen atoms.

The IR spectrum of the adsorbed $\text{Re}_2(\text{CO})_{10}$ exhibits $3\nu(\text{CO})$ bands at 2080, 2025 and 2014 cm^{-1} which are shifted with respect to the $\nu(\text{CO})$ of free $\text{Re}_2(\text{CO})_{10}$ ($2070, 2014$ and 1976 cm^{-1}) plus a band at 2132 cm^{-1} which is normally inactive in IR but active in Raman spectroscopy (20). These features can be interpreted by assuming that the structure of the molecule is preserved but that it undergoes a weak distortion probably due to lateral interactions. The bonding of the complex with the framework involves the formation of hydrogen bonds with the hydroxyl groups as described for $\text{Mo}(\text{CO})_6$ adsorption.

The decomposition curve of $\text{Re}_2(\text{CO})_{10}$ exhibits a large plateau between 200 and 300°C which corresponds to 3 CO molecules evolved per molecule, but it is possible to ascertain whether this plateau

corresponds to a definite intermediate complex or to several species. The X-ray investigation on a sample heated at 300°C (sample III) shows that the Re atoms no longer occupy the 2 Å radius sphere at the center of the supercages but a rather imprecise region delimited by 3 Å radius sphere at $x = y = z = 0.5$. This result means that most of the Re atoms are in the vicinity of the 12 membered oxygen ring much closer to the oxygen atoms than the Mo atoms were in sample I. Therefore the Re atoms of the partially decomposed complexes are likely to be bonded with the oxygen atoms of the ring.

The main feature in IR, at the beginning of the thermal decomposition of adsorbed $\text{Re}_2(\text{CO})_{10}$ is the appearance of a band at 910 cm^{-1} which reaches its maximum at 300°C. This band can be attributed to Re-O stretching vibration (15, 16) indicating that the Re atoms are actually bonded to framework oxygen atoms. Also at 300°C, except a weak 1810 cm^{-1} band which probably corresponds to bridging CO, there are 3 $\nu(\text{CO})$ bands at 2050, 1950 and 1895 cm^{-1} . Since they are very similar to those observed in $\text{Re}(\text{CO})_3\text{Py}_2$ (21) ($2041, 1934, 1891 \text{ cm}^{-1}$) they can be tentatively assigned to $\text{Re}(\text{CO})_3$ species. There is no direct proof that the Re-Re bond has been broken since the Re-Re vibrations occur at frequencies too low to be observed. However, the displacement of the complex from the center of the supercage to the vicinity of the supercage aperture, the formation of Re-O bonds and the $\text{Re}(\text{CO})_3$ structure are hardly compatible with the presence of Re-Re bonds.

Above 300°C, a rapid decrease of the $\nu(\text{CO})$ bands corresponds to the departure of CO complete at 400°C. Moreover, the 910 cm^{-1} band also vanishes indicating that no Re-O bonds remain after the Re atoms have lost all the CO ligands. This suggests that an agglomeration of Re atoms takes place, possibly yielding very small metal particles encaged in the zeolite. Indeed, the adsorption of CO on this solid produces a band at 2045 cm^{-1} , which also appears when CO is adsorbed on $\text{Re}/\text{Al}_2\text{O}_3$ (22). Metal particles fitting into the supercages cannot be detected from line broadening or crystal structure analysis as shown in a previous paper (12), however on heating at 900°C, broad lines of hexagonal crystallites of rhenium metal have been detected.

Adsorption and thermal decomposition of $\text{Ru}_3(\text{CO})_{12}$. The adsorption occurs without evolution of CO (fig. 1). The location of Ru atoms is comparatively inaccurate; this is probably due both to the irregular occupancy of the cages (since there are 3 $\text{Ru}_3(\text{CO})_{12}$ per unit cell, only 3 cages out of 8 are occupied) and to the fact that the bulky triangular molecule cannot be encompassed in a "precise" sphere centered on the ternary axis. The results only mean that the $\text{Ru}_3(\text{CO})_{12}$ complexes are well adsorbed in the zeolite cages and that they are in the vicinity of the supercage apertures.

The diffraction pattern of the sample heated at 300°C (plateau of the decomposition curve) is similar to that found for a HY zeolite with a strong additional background, the Ru atoms are thus completely at random in the cages. At 500°C, broad reflections cor-

responding to ruthenium crystallites are detected. Therefore, the decomposition of $\text{Ru}_3(\text{CO})_{12}$ ultimately gives the metal. This is corroborated by the IR study of CO adsorbed on these materials: $\nu(\text{CO})$ bands occur at frequencies similar to those found by Dalla Betta (23).

Conclusion

The crystal structure analysis using liquid scattering functions to locate the adsorbed metal carbonyls do not give the precise position of the extra framework atoms nor the stereochemistry of the complexes. On the other hand, this method enables us to determine which regions of the zeolite cages are initially occupied by most of the adsorbed molecules. Moreover, volumetric and infrared results provide essential data allowing to precise the bonding of the complex with the zeolite framework.

This study shows that the adsorption of uncharged metal complexes like the metal carbonyls is a valuable method to load the zeolite with transition metals, specially for elements which cannot be easily ion-exchanged. Moreover, the complexes are too bulky to enter sodalite cage so that the whole loading occurs in the supercages unlike ion-exchange procedures which introduce cations everywhere and specially on hidden sites.

When the carbonyl complexes are partly decomposed, the metal atoms still retaining CO ligands are directly bonded to the framework oxygen anions. These grafted species are accessible to reagents and might have interesting catalytic properties in heterogeneous processes. On the other hand, the total decomposition of metal carbonyl on zeolites could also be a valuable method to obtain high metal dispersions.

Literature cited

1. Delmon, B., Jannes, G.J., "Catalysis Heterogeneous and Homogeneous", Elsevier Amsterdam (1975).
2. Lunsford, J.H., Catal. Rev. (1975), 12, 137.
3. Riley, P.E., Seff, K., Inorg. Chem. (1974), 13, 1355.
4. Riley, P.E., Seff, K., Inorg. Chem. (1975), 19, 714.
5. Riley, P.E., Kunz, K.B., Seff, K., J. Amer. Chem. Soc. (1975), 97, 537.
6. Gallezot, P., Ben Taarit, Y., Imelik, B., J. Catal. (1972), 26, 481.
7. Pichat, P., Védrine, J., Gallezot, P., Imelik, B., J. Catal. (1974), 32, 190.
8. Gallezot, P., Imelik, B., Adv. Chem. Ser. (1973), 121, 66.
9. Simpson, H.D., Steinfink, H., Acta Crystallogr., Sect. A (1970) 26, 158.
10. Mortier, W.J., Costenoble, M.L., Uytterhoeven, J.B., J. Phys. Chem. (1973), 77, 2880.
11. de Boer, J.J., Maxwell, I.E., J. Phys. Chem. (1974), 78, 2395.
12. Gallezot, P., Alarcon Diaz, A., Dalmon, J.A., Renouprez, A.J., Imelik, B., J. Catal. (1975), 39, 334.

13. Howe, R.F., Davidson, D.E., Whan, D.A., *J. Chem. Soc., Faraday Transactions, I* (1972), 68, 2266.
14. Dempsey, E., *J. Catal.* (1975), 39, 155.
15. Cotton, F.A., Wing, A.M., *Inorg. Chem.* (1965), 6, 867.
16. Adams, D.M., "Metal-Ligand and Related Vibrations", Chapter 5, E. Arnold Publishers, London, (1967).
17. Adams, D.M., "Metal-Ligand and Related Vibrations", Chapter 3, E. Arnold Publishers, London, (1967).
18. Coudurier, G., Gallezot, P., Praliaud, H., Primet, M., Imelik, B., *C.R. Acad. Sci.* (1976), 282 C, 311.
19. Praliaud, H., (Private communication).
20. Braterman, P.S., "Metal Carbonyl Spectra", p. 195, Academic Press, London, (1975).
21. Abel, E.W., Wilkinson, G., *J. Chem. Soc.* (1959), 1, 1501.
22. Primet, M., *J. Catal.* (in press).
23. Dalla Betta, R.A., *J. Phys. Chem.* (1975), 79, 2519.

Esr Study of Bivalent Rhodium Complexes Formed in Zeolites

CLAUDE NACCACHE and YOUNÈS BEN TAARIT

Institut de Recherches sur la Catalyse, 79 boulevard du 11 Novembre,
1918 - 69626 - Villeurbanne, France

MICHEL BOUDART

Department of Chemical Engineering, Stanford University, Stanford, Calif. 94305

ABSTRACT

Rhodium (III) exchanged zeolites were prepared starting from NaY and $[\text{Rh}(\text{NH}_3)_5\text{Cl}]^{2+}$ aqueous solution $[\text{Rh}(\text{II})(\text{NH}_3)_5]^{2+}$ was shown to form at the early stages of the thermal activation of the zeolite around 480 K. At higher temperatures, 770-600°K, Rh(II) species bound directly to the lattice were formed. Part of these species also resulted from the thermal treatment and appeared to form μ -peroxo-species upon oxygen addition; the symmetry of these various paramagnetic species is discussed.

Introduction

Recent studies of transition metal complexes formed in zeolites (1, 2, 3, 4) suggest that the zeolite framework could serve as a "solid solvent". Furthermore transition metal-ion-exchanged zeolites have shown catalytic properties very similar to those of soluble transition metal complexes (5, 6). More recently it has been shown that ethylene was selectively dimerized to n-butenes over rhodium exchanged Y zeolite and the authors suggested that zero-valent well dispersed rhodium atoms within the zeolite cages constituted the source of active sites (5). The object of this paper is to report on the esr measurements of rhodium exchanged Y zeolites to determine the oxidation state and the environment of rhodium ions in zeolite activated in various conditions.

Experimental

The rhodium Y form was obtained by stirring NaY zeolite (SK 40) in an aqueous solution of rhodium pentaammine chloride: $[\text{Rh}(\text{NH}_3)_5\text{Cl}]^{2+}\text{Cl}_2$ for 6 h. The pentaammine complex was prepared by refluxing $\text{RhCl}_3 \cdot x \text{H}_2\text{O}$ in concentrated ammonia at 80°C. Chemical analysis for both sodium and rhodium showed that 5 rhodium complexes were introduced per unit cell.

The zeolite samples were heated in flowing oxygen while the temperature was slowly raised up to 480 K or 770 K. The samples were then outgassed at either 480 K or 770 K and then transferred in vacuo into esr quartz tubes.

For adsorption experiments pure oxygen and carbon monoxide were dehydrated over 5 Å molecular sieve. ^{17}O enriched O_2 (58 % in ^{17}O) and ^{13}C enriched CO (90 % in ^{13}C) were obtained from the French Atomic Energy Agency and used without further purification.

The esr measurements were performed on a Varian E. line spectrometer equipped with a dual cavity and operating in the X band mode. g -values were measured using D.P.P.H. as a standard ($g = 2.0036$). All esr spectra were recorded at 77 K unless otherwise stated.

Results

The esr spectra of NaY form dehydrated up to 770 K and RhY heated up to 420 K revealed only a weak signal around $g = 4$ which is attributed to Fe^{3+} impurities. In contrast paramagnetic species were formed when RhY zeolite was heated at 480 K. The esr spectrum of this species (species A) is shown in figure 1a. This spectrum characterized by $g_{\perp} = 2.09$, $g_{\parallel} = 2.06$, $g_3 = 1.97$ was recorded also at 295 K without appreciable line broadening. Hence it appeared that spin-lattice relaxation time (T_1) did not control the line width. The spectrum was reversibly broadened by oxygen.

RhY samples activated at 770 K ($\text{O}_2 - \text{vacuo}$) revealed an axial esr spectrum with $g_{\perp} = 2.68$ and $g_{\parallel} = 2.006$, which could be observed at 77 K and 295 K. The g_{\perp} component of this species B was progressively shifted to $g_{\perp} = 2.60$ by addition of small amounts of water. Furthermore no dipolar line broadening was observed in the presence of oxygen.

The temperature range over which ammonia evolved from decomposition of pentaamino-chlororhodium complexes was determined by testing the emerging oxygen stream with moist paper litmus. Up to 480 K almost no ammonia was detected in the exit stream which suggests that no appreciable release of the NH_3 ligands has occurred. Above 480 K ammonia was detected in the emerging oxygen stream up to 620 K. Moreover the disappearance of the infrared bands due to NH_3 ligands when the RhY zeolite was calcined at 770 K confirmed that $[\text{Rh}(\text{III})(\text{NH}_3)_5\text{Cl}]^{2+}$ complex was completely decomposed.

Carbon monoxide adsorption. The addition of ^{12}CO at 295 K to RhY activated at 770 K resulted in the formation of a new paramagnetic species (species C); its esr spectrum shown in figure 1b is typical of a species of axial symmetry whose g components are $g_{\perp} = 2.191$, $g_{\parallel} = 1.991$. The g_{\parallel} component was further split into two hyperfine lines due to the interaction of the unpaired electron with Rh nucleus ($I = 1/2$). This signal was not altered by an evacuation at 77 K but disappeared following desorption at 295 K for 5 minutes. When ^{13}CO was used the resulting esr spectrum (figure 1c) showed that the perpendicular component was split into a doublet while the parallel component was split into a doublet of doublets while the same features observed when ^{12}CO was used also appeared due to unlabelled species. Hence a monocarbonyl species appears to be formed. The ^{13}CO anisotropic hyperfine splitting constants were $A_{\perp} = 105 \text{ Oe}$ and $A_{\parallel} = 115 \text{ Oe}$. This spectrum was not observed at

room temperature.

Oxygen adsorption. Upon $^{16}\text{O}_2$ adsorption either at 77 K or at 295 K on RhY activated at 770 K the esr signal shown in figure 2a with $g_{\parallel} = 2.015$, $g_{\perp} = 1.931$ appeared (species D). This signal was unobservable at room temperature and reversibly broadened by increasing the oxygen pressure. Furthermore experiments carried out with ^{17}O enriched molecular oxygen at a pressure low enough to avoid dipolar line broadening gave the esr spectrum shown in figure 2b. Hyperfine lines resulting from the interaction of the unpaired electron with ^{17}O nuclei ($I = 5/2$) were not resolved; however the $^{17}\text{O}_2$ - adduct esr spectrum was considerably broader compared with that of the unlabelled oxygen - adduct. As for CO - adduct the oxygen adsorption was reversible at room temperature with the subsequent disappearance of the paramagnetic oxygen - adduct.

Effect of water adsorption. The oxygen experiments were performed in the absence of water traces. However a new esr spectrum at $g_1 = 2.11$, $g_2 = 2.016$, $g_3 = 1.98$ (figure 2c) developed when RhY sample activated at 770 K was exposed to the atmosphere. Subsequently a series of RhY samples activated at 770 K were exposed to water vapor alone or to water plus oxygen at room temperature. Water adsorption produced no effect while the simultaneous adsorption of water and oxygen resulted in the appearance of the esr signal shown in figure 2c (species E). Furthermore the adsorption of water on a sample which has previously been contacted with O_2 to form the oxygen - adduct species D leads to the formation of species E with the subsequent disappearance of species D. Species E was stable and observable at room temperature but was destroyed by outgassing the sample at about 673 K. Finally, adsorption of CO at 295 K followed by adsorption of O_2 at 77 K on the same RhY sample pretreated at 770 K resulted in both species C and D thus suggesting that carbon monoxide and oxygen adducts involved different sites.

Interpretation of the esr spectra

All known stable Rh(III) species are diamagnetic with low spin d^6 configurations. However thermal treatment of Rh(III) exchanged zeolites produced paramagnetic species as evidenced by the observed esr signals. The large departure of the g values from g_e is a clear indication that the odd electron should be associated with a rhodium species since rhodium has a large spin-orbit coupling which may account for the observed large g shifts from g_e .

Among the various oxidation states of rhodium only Rh(0) $4d^9$, Rh(II) $4d^7$, Rh(IV) $4d^5$ are paramagnetic with $s = 1/2$.

Species A :

The powder esr spectrum of species A showed three principal g -values which indicated that it is experiencing a rhombic crystal field. By ignoring the small deviation from axial symmetry, one

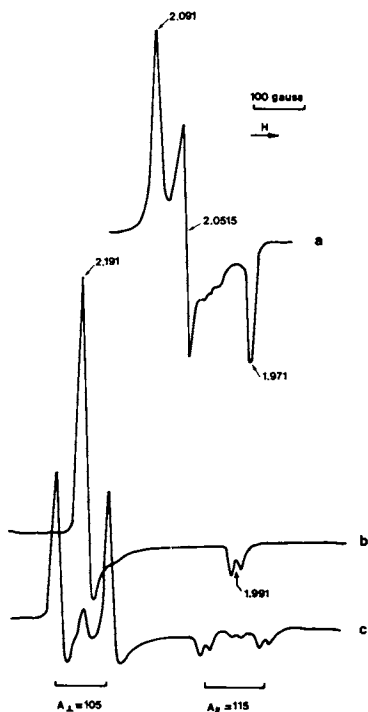


Figure 1. ESR spectra of (a) rhodium zeolite activated at 480 K; (b) ^{12}CO adsorbed on rhodium zeolite activated at 770 K; (c) the ^{13}CO -adduct

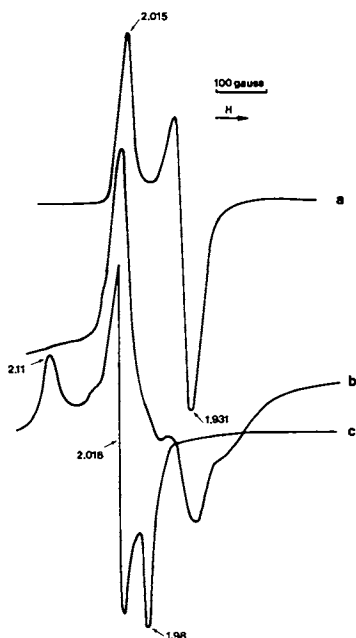


Figure 2. ESR spectra of (a) oxygen adsorbed on RhY activated at 770 K; (b) the $^{16}\text{O}_2$ -adduct; (c) the $^{17}\text{O}_2$ -adduct; (c) the $^{16}\text{O}_2$ -adduct contacted with water.

might consider $g_{\parallel} = 1.97$ and $g_{\perp} = 1/2 (g_1 + g_2) = 2.07$, then $g_{\perp} > g_{\parallel} \approx g_e$. ESR spectrum of neutral rhodium in $(\text{RhCl}_6)^{6-}$ has been reported (7) and interpreted in terms of Rh(0) under tetragonal compression with $g_{\parallel} > g_{\perp} \approx g_e$, in contrast with the present results. Furthermore since the formation of Rh(0) atoms within the zeolite cages would require a three-electron reduction per Rh(III), production of neutral rhodium in the oxidizing atmosphere used during thermal activation in oxygen is highly unlikely. On the other hand assignment of signal A to Rh(IV) can be equally ruled out on the following basis: the 4 d^5 low-spin configuration ground state would be $e^4 b_2^1$ and regarded as a single hole in the a_2 shell. In this configuration the g-values would be very anisotropic with g_{\parallel} much less than g_e (8). The spin-lattice relaxation would be very short and the corresponding esr spectra observed only at very low temperature. Indeed Rh(IV) in MgO gave esr spectrum only at 20 K with $g = 1.667$ (9). With the above considerations obviously species A should be assigned to Rh(II) complex. For a d^7 system with $g_{\parallel} \approx g_e$ the odd electron is localized in the metal $a_1(dz^2)$ orbital. Assuming a rhodium (II) complex in a square pyramidal configuration, the a_1 orbital will be destabilized with respect to the $b_2(dx_y)$ and (dxz, dyz) orbitals. The electronic configuration for the metal complex is therefore $e^4 b_2^2 a_1^1$ with the unpaired electron in the a_1 orbital. Tilting the fifth ligand away from the tetragonal axis results in a splitting of the degenerate e orbital pair and the three principal g-values given by the relation (10): $g_{zz} = 2N^2$, $g_{xx} = 2N^2 + 6Na_1$, $g_{yy} = 2N^2 + 6Na_2$ where $a_1 = \lambda / (E_{dyz} - E_{dz^2})$, $a_2 = \lambda / (E_{dxy} - E_{dz^2})$. N is a normalized coefficient and λ the reduced spin-orbit coupling constant allowing covalency ($\lambda = 0.6 \lambda_0$). Setting $\lambda_0 = 1235 \text{ cm}^{-1}$, the calculated $E_{dyz} - E_{dz^2}$ and $E_{dxy} - E_{dz^2}$ energy differences are respectively 33,000 and 43,000 cm^{-1} . Hence species A is assigned to Rh(II)L₅ complex in a square pyramidal arrangement.

Species B :

For the same reason stated above assignment to Rh(0) or Rh(IV) was ruled out. Since species B showed esr spectrum with $g_{\perp} > g_{\parallel} \approx g_e$ the unpaired electron is in a dz^2 orbital. The g-value expressions given for species A are also valid in this case with $a_1 = a_2$. Then $E(dxz, dyz) - E(dz^2) = 11,000 \text{ cm}^{-1}$ (RhCl₆)⁴⁻ centres (11) gave esr spectrum at $g_{\perp} = 2.48$, $g_{\parallel} = 2.00$, very close to those found for species B. The results are then consistent with Rh(II) ions in a tetragonally distorted octahedral crystal field.

Species C :

CO radical may be considered as a possible result of the reaction of CO with RhY zeolite. However this suggestion was ruled out since CO radical showed g-values close to g_e and very large hyperfine constants when ¹³CO was used (19). Moreover it is unlikely that CO was formally reduced or oxidized in its adduct. We feel the ad-

duct is best described as a CO-Rh(II) complex with the unpaired electron spin being mainly in a rhodium orbital. Indeed the doublet with a splitting of about 18 Oe appearing at the g_{\parallel} component indicates that the odd electron is associated with rhodium d-orbital. The esr spectrum can be analyzed in terms of an axially symmetric g-tensor with $g_{\perp} > g_{\parallel}$ and is consistent with a $(d_{xy}, d_{yz}, d_{xz})^6 (d_{z^2})^1$ ground state. Again from the theoretical g_{\perp} expression given above a value of 24,000 cm^{-1} for the $d_{xz}, d_{yz} \rightarrow d_{z^2}$ transition was obtained. The g_{\perp} and g_{\parallel} components of the ^{13}C O adduct were each split into two lines indicating that this signal is due to the Rh(II) complex in which a rhodium ion is coordinated to one carbon atom. The A_{\perp} and A_{\parallel} anisotropic ^{13}C coupling constants provide, using the relation $a_{\text{iso}} = 1/3 (A_{\parallel} + 2A_{\perp})$, $a_{\text{iso}}(^{13}\text{C}) = 108.3$ Oe then $b_{\text{dip}} = 3.3$ Oe. The molecular orbital coefficients C_{2s}^2 and C_{2p}^2 which characterize the spin density on the respective 2s and 2p carbon orbitals can then be estimated, as $C_{2s}^2 = a_{\text{iso}}/1110.8$, $C_{2p}^2 = b_{\text{dip}}/32.4$. The spin densities on 2s and 2p ^{13}C orbitals are then 0.098 and 0.101 respectively. The carbon donor orbital that mixes with the rhodium d_{z^2} orbital has a carbon 2p/2s ratio close to 1 in good agreement with the expected sp hybrid donor orbital for carbon monoxide. The total spin density delocalised on the CO molecule is about 0.20 hence the spin density on the metal orbital is 0.80 which confirms our former suggestion that the odd electron is mainly localized on the rhodium metal orbital. From a molecular orbital standpoint the wave function of the unpaired electron may be described as a linear combination of d_{z^2} metal orbital and 3 σ sp carbon orbital.

Species D :

The anisotropic esr signal due to the oxygen-adduct showed $g_{\parallel} > g_e > g_{\perp}$. The large departure of g_{\perp} from g_e ($\Delta g = 0.07$) and the absence of any resolved hyperfine splitting when ^{17}O enriched molecular oxygen was used suggest that the unpaired electron orbital is essentially metal d orbital in character. However the line broadening observed when $^{17}\text{O}_2$ was used, resulted probably from unresolved hyperfine splitting due to ^{17}O nuclei and indicates that a small electron spin density is present on the oxygen nuclei in the rhodium-oxygen complexes. The experimental order $g_{\parallel} > g_e > g_{\perp}$ corresponds to the d^7 configuration with the unpaired electron in the $4 d_{x^2 - y^2}$ orbital, the g values calculated from the ligand field theory being (12) :

$$g_{\parallel} = 2 + \frac{8\lambda}{(E_{2-x^2-y^2} - E_{xy})}, \quad g_{\perp} = \frac{2-2\lambda}{(E_{2-x^2-y^2} - E_{xz, yz})}$$

From experimental g_{\perp} value and $\lambda = 0.6 \lambda_0$ one ends up with $E_{xy} - E_{2-x^2-y^2} = 21,000 \text{ cm}^{-1}$. The effective metal oxidation state in rhodium-oxygen complex is 2, resulting probably from electron transfer from metal ion to oxygen through the π^* antibonding oxygen orbital.

Species E :

Since this species was formed from the reaction of H_2O on

Rh(II) - O₂ species one could suggest that no change in the formal oxidation state of Rh(II) has occurred, but rather a change in the crystal field symmetry. We find that this complex has g_{zz} (g_1)

$> g_{yy}$ (g_2) $> g_{xx}$. These results are typical of square planar or bipyramidal trigonal d⁷ low-spin systems where the unpaired electron sits mainly in d_{xy} orbital (11, 12, 20). Furthermore the orthorhombic g-tensor obtained for species E implies that a deviation from pure tetragonal or trigonal crystal field has occurred. Species E may be ascribed to Rh(II) coordinated to oxygen and to H₂O. The esr signal of rhodium (II) tetraphenyl-porphyrin complex with $g_1 = 2.089$, $g_2 = 2.029$, $g_3 = 1.99$, very close to the g-values obtained for E species, has been reported (13) and tentatively assigned to bivalent four coordinate rhodium.

Discussion

The experimental esr results and their interpretations have shown that several bivalent rhodium species might be generated within the zeolite cages starting from $[\text{Rh(III)(NH}_3)_5\text{Cl}]^{2+}$ complex. These results have proved the ability of zeolites to stabilize transition metal-ions in unusual oxidation states. The thermal treatment at 473 K produced a reduction of Rh(III) into Rh(II) ions. Two possible ways of Rh(II) ions formation may be suggested: either chlorine atom is removed from the complex with the concomitant reduction of Rh(III) leading to $[\text{Rh(NH}_3)_5]^{2+}$ or a reductive dissociation of NH₃, the resulting complex being $[\text{Rh(NH}_3)_4\text{Cl}]^+$. In both cases the rhodium complex would have a square pyramidal symmetry and should be located in the supercages. Because of steric restrictions imposed by the ammine groups this species appeared unreactive to other ligands such as CO, O₂. The effect of the thermal treatment at 500°C was to completely decompose $[\text{Rh(II)(NH}_3)_5]$ complex. The bare Rh(II) ions hence migrate within the zeolite cages and coordinate with lattice oxygen ions in S_I, S_{I'}, S_{II} or S_{II'}. It is obvious from our results that, at least, part of the total amount of Rh(II) is localized inside the hexagonal prisms. However quantitative measurements showed that only 10% of the total rhodium content was found in the form of Rh(II) ions sited on S_I. Hence one could suggest that either a large amount of Rh(II) escapes esr detection or that a disproportionation reaction $2\text{Rh(II)} \rightarrow \text{Rh(I)} + \text{Rh(III)}$ has occurred. Partial oxidation of Rh(II) into Rh(III) by O₂ at 770 K could also be achieved. The carbon monoxide and oxygen results prove that both suggestions are plausible. There are few mononuclear Rh(II) complexes. Magnetic properties of rhodium(II) acetate compounds indicated a diamagnetic dimer structure $\text{Rh}_2(\text{OAc})_4$ with a strong metal-metal interaction (14). Formation of rhodium (II)- aquocomplex has been reported (15) the compound was found to be a binuclear $(\text{Rh}_2(\text{H}_2\text{O})_{10})^{4+}$ complex. Considering the complex of $(\text{Rh(NH}_3)_5)^{2+}$ which arises from the chlorine atom removal, it is obvious that only one pentaammine complex is present per supercage owing to the large size of the rhodium complex. However as NH₃ ligands were removed from the rhodium coordination sphere,

the Rh(II) ions tend to bind with lattice oxygen ions either at the hexagonal windows or possibly inside the hexagonal prisms. When two Rh(II) ions were present either in the supercage or in the sodalite cavity, for example, in $S_{I'}$, and $S_{II'}$, or in S_{II} , then metal-metal bonding would produce diamagnetic binuclear Rh(II) complex typical of rhodium (II) compounds (15, 16). One could represent this species as $[(O^{2-})_3Rh - Rh(O^{2-})_3]^{4+}$ with a C_{3v} or D_{3h} symmetry. To allow a better metal-metal binding it is probable that the rhodium ions move away from the trigonal axis thus lowering the symmetry of the crystal field they are experiencing. In some phosphine complexes metal-metal interaction over long distances (4 Å) has been suggested (17); such interaction would be rather small and would allow the insertion of a strong donor ligand such as CO. Hence the binuclear bivalent rhodium complex may pick up carbon monoxide with the subsequent formation of mononuclear bivalent rhodium-carbon monoxide adduct showing paramagnetic properties. As CO could not enter the sodalite cage it appears that the binuclear rhodium species reacting with CO was previously in the supercage. The effect of CO was mainly to remove the metal-metal bond without changing the formal oxidation state of Rh(II).

We have shown that oxygen was probably adsorbed on different sites as those for CO. Rh(II) aquocomplex exhibited reaction with oxygen similar to Co(II) ammine complex forming the classical μ -peroxo compound $Rh-O-O-Rh$ (16). However Rh(I) species might also be oxidized into paramagnetic Rh(II) with the simultaneous formation of the superoxide ion O_2^- . In particular, it was claimed that the Rh(I) cyclooctene complex was oxidized into Rh(II) with the formation of O_2^- (18). By contrast it was reported that Rh(II) compounds could be reduced by hydrogen and reoxidized by oxygen apparently without formation of O_2^- (13). In the present study, we could see no evidence suggesting the formation of the superoxide ion as Rh(I) species were oxidized and therefore we favour the scheme where a single O_2 molecule reacts with two close enough Rh(I) ions giving rise to the μ -peroxo species $Rh-O-O-Rh(II)$ due to the transfer of two electrons into the antibonding π^* molecular orbital of oxygen resulting in the diamagnetic O_2^{2-} ion bridging two Rh(II) ions. As the CO-adduct, the oxygen-adduct is localized in the supercage. The oxidation of rhodium from 1 to 2 oxidation state upon oxygen adsorption which was reversible in the absence of water is irreversible in the presence of H_2O . The probable reaction which occurs might be the coordination of one H_2O molecule per Rh atom to Rh(II)- O_2^- -Rh(II) in a trans position, hence the H_2O molecule being localized in the sodalite cage. This geometry would show a trigonal bipyramidal arrangement of the ligands around the Rh ion as proposed to interpret the esr results, the rhodium ion being in the plane of three lattice oxygen ions and in trans position one H_2O and one oxygen atom slightly away from the trigonal axis. As a square planar Rh(II) complex could account for the esr results one could also suggest that the adsorption of O_2 and

H₂O on two Rh(I) ions likely forms mononuclear Rh(II) species from



In conclusion this work has provided information not only concerning the zeolite as a unique host matrix for unusual transition metal oxidation states but also showed the solvent behaviour of the zeolite framework.

Concerning the chemistry of rhodium, apart from the characterization of paramagnetic rhodium species, the work emphasizes the ability of rhodium complexes solvated in the zeolite framework to behave in similar fashion as in solution and particularly to activate two chief reagents in organometallic chemistry, CO and oxygen.

Acknowledgments

C. NACCACHE wishes to thank the C.N.R.S. and the Stanford University Chemical Engineering department and National Science Foundation for trainships awards. The authors are also indebted to H. URBAIN for the chemical analysis and G. WICKER for the esr measurements.

Literature cited

1. Jermyn, J.W., Johnson, T.J., Vansant, E.F. and Lunsford, J.H., *J. Phys. Chem.*, (1973), 77, 2964.
2. Naccache, C., and Ben Taarit, Y., *Chem. Phys. Letters*, (1971), 11, 11.
3. Laing, K.R., Lubner, R.L. and Lunsford, J.H., *Inorg. Chem.*, (1975), 14, 1400.
4. Vansant, E.F., and Lunsford, J.H., *Third Internat. Conf. Molecular Sieves*, *Adv. Chem. Series 121*, Amer. Chem. Soc., (1973), 441.
5. Yashima, T., Ushida, Y., Ebisawa, M. and Hara, N., *J. Catalysis*, (1975), 36, 320.
6. Pichat, P., Vedrine, J.C., Gallezot, P. and Imelik, B., *J. Catalysis*, (1974), 32, 190.
7. Wilkens, J., De Graag, D.P. and Hell, J.N., *Phys. Lett.*, (1965), 19, 178.
8. Griffiths, J.H.E., Owen, J. and Ward, I.M., *Proc. Roy. Soc.*, (1963), *Ser. A* 219, 526.
9. Raizman, A., Suss, J.T. and Szapiro, S., *Phys. Lett.*, (1970), 32 A, 30.
10. Krigas, T., and Rogers, M.T., *J. Chem. Phys.*, (1971), 55, 3035.
11. Shock, J.R., and Rogers, M.T., *J. Chem. Phys.*, (1975), 62, 2640.
12. Fujiwara, S., Watanabe, T. and Tadano, H., *J. Coord. Chem.* (1971), 1, 195.
13. James, B.R. and Stynes, D.V., *J. Amer. Chem. Soc.*, (1972), 94, 6225.
14. Kitchens, J. and Bear, J.L., *J. Inorg. Nucl. Chem.*, (1970), 32

- 49.
15. Ziolkowski, J.J., and Taube, H., *Bull. Acad. Science Poland*, (1973), 21, 113.
 16. Ziolkowski, J.J., *Bull. Acad. Science Poland*, (1973), 21, 119.
 17. Master, C. and Shaw, B.L., *J. Chem. Soc.*, (1971), A, 3679.
 18. James, B.R., Ng, F.T.T., and Ochiai, Ei., *Canda., J. Chem.*, (1972), 50, 590.
 19. Vedrine, J.C., and Naccache, C., *Chem. Phys. Letters*, (1973), 18, 190.
 20. Kuska, H.A., and Rogers, M.T., Martell, A.E., *Coordination Chemistry A.C.S., Monograph Van Nostrand Reinhold Co., New York*, (1971), 1, 186.

Szilard-Chalmers Cation Recoil Studies in Zeolite L

LOVAT V. C. REES and PAUL A. NEWELL

Physical Chemistry Laboratories, Imperial College of Science and Technology,
London SW7 2AY EnglandABSTRACT

Szilard-Chalmers recoil effects have been studied in zeolite L exchanged with the monovalent cations, Li^+ , Na^+ , K^+ , Rb^+ , Cs^+ , NH_4^+ and Ag^+ . The percentage of the neutron capture products of these cations recoiling from the various sites in this zeolite into those sites exchangeable to NH_4^+ ions at room temperature has been determined. From these recoil probabilities the sites occupied by the various cations as a function of temperature has been deduced.

Introduction

In a previous study [1] the Szilard-Chalmers recoil of Rb^+ , Cs^+ , Ba^{2+} , La^{3+} , Co^{2+} , Zn^{2+} , Cu^{2+} and Na^+ cations from their sites in the sodalite cages (sites I' and II') and hexagonal prisms (site I) into the supercages of zeolites X and Y was ascertained. It was found that these cations recoiled with a probability of $\sim 90\%$ from sites I' and II' and between 40 and 50% from site I depending on the cation. It was thus possible to establish the preferences shown by these cations for these "locked" sites as a function of temperature of calcination, T_c , concentration and type of other cations contained in these sites. This paper describes some further recoil studies of monovalent cations in zeolite L.

Theory

When a nucleus captures a neutron ~ 8 MeV of binding energy is released in a prompt gamma cascade. The emitting nucleus receives an instantaneous momentum increment equal and opposite to the vector sum of the momenta, P , of the emitted gamma photons. If n photons are emitted isotropically and are equal in energy then the mean kinetic energy, \bar{K} , of recoil in eV is given by

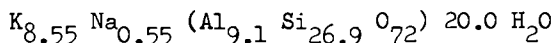
$$\bar{K} \approx 537 \frac{E_{\gamma}^2}{Mn} \quad (1)$$

where E_{γ} is the sum of the gamma photon energies in MeV and M is the mass of the nucleus in atomic mass units. Although equal gamma ray energies are seldom, if ever, encountered the average recoil energy associated with a (n, γ) reaction must be of the order of a few hundred electron volts and excitation of electrons of the medium traversed by the recoiling species is thus an unlikely event. The recoil kinetic energy may be assumed, therefore, to be dissipated only by elastic collisions.

Assuming that it requires a minimum energy of 25eV to move an atom from its normal location into an interstitial position it is possible to calculate the mean free path, L_S , of the recoiling atom using a hard sphere model [2]. This calculation was made for ^{24}Na in Na L and L_S was found to be 1.84nm. L_S is thus equal to the a - axis unit cell length but greater than the c - axis value of 0.75nm of zeolite L [3].

Experimental

The unit cell composition of the zeolite L as supplied by Union Carbide Corporation, U.S.A. (batch no. 12508-86) was



The experimental techniques employed in these studies are similar to those more fully described previously [1], [2], [4]. On return from irradiation in a neutron flux the zeolite samples were divided into two unequal portions and weighed. The larger portion was eluted, at room temperature, with 100 cm³ of saturated ammonium chloride solution overnight. The zeolite was then filtered, washed, dried at 110°C for an hour and counted along with the non-eluted smaller portion. The percentage elution, γ , of a particular neutron-capture product is given by

$$\gamma = \left(1 - \frac{C_{\text{ext}}}{C_{\text{non}}} \right) 100\% \quad (2)$$

where C represents the count rate per g. of zeolite and subscripts "ext" and "non" represent the extracted and non-extracted zeolite respectively.

In exploratory experiments it was found that NH_4^+ ions exchanged with the cations located in both C and D sites (see later for a description of these sites) whereas Na^+ and Ba^{2+} ions only exchanged with cations located in D sites when these exchanges were carried out at room temperature. In the determination of C_{ext} above, therefore, when NH_4Cl was used as the eluent, the cations sited in C and D sites have been removed leaving those cations which were sited in A and B sites.

The samples which were calcined to 650°C before irradiation were heated in two stages (a) dehydration of the sample at 110°C for at least 8 hours followed by (b) calcination at 650°C for 16 hours.

Results and Discussion

Hydrated zeolite L has four different cation sites [3]. Site A is at the centre of the hexagonal prism; site B is at the centre of the cancrinite cage; site C is located midway between two adjacent cancrinite cages and site D is near the wall of the main channel. On dehydration small cations occupying D sites may withdraw to site E which is located midway between two adjacent hexagonal prisms. In zeolite L of composition $K_6Na_3Al_9Si_{27}O_{76} \cdot 21H_2O$ the occupancies of the 4 sites by the Na and K ions given in Table I have been suggested [3].

Table I Site Occupancies by Cations in Zeolite L.

Cation	Site	Type [†]	No. of sites per u.c.	No. of Cations per u.c.
Na ⁺ , K ⁺	A	Locked	2	1.4 [†]
K ⁺	B	Locked	2	2
K ⁺	C	Open	3	2.7
Na ⁺	D	Open	6	3.6
			<u>13</u>	<u>9.7</u>

† Assumes partial occupancy by Na⁺; if only K⁺ ions occupy this site then a value of 0.8 is obtained which leads to a total of 9.1 cations per u.c. in good agreement with the figure of 9 found by chemical analysis.

‡ Cations in locked sites cannot, while cations in open sites can, be exchanged by NH₄⁺ ions at room temperature.

The various ion exchanged samples of zeolite L will be represented by M(T₁)-L(T_C)N. M is the target cation and T₁ is the temperature at which the ion M was exchanged into the parent L zeolite. In these studies T₁ = 25 or 95°C. When T₁ = 25°C the symbol will be omitted. T_C is the temperature at which the sample was calcined after the introduction of the cation M. When no calcination was carried out this symbol is omitted. N is the cation used to ion exchange the sample subsequent to the introduction of ion M or on cooling to room temperature after the calcination step. In these experiments N is either NH₄⁺, Na⁺ or Ba²⁺. If N = NH₄⁺ then all M ions in sites C and D are replaced by NH₄⁺ ions in this exchange. If N = Na⁺ or Ba²⁺ then only the M ions in site D are replaced in this exchange (see experimental section). If no exchange with cation N was carried out this

symbol is omitted. Although K^+ ions are always present in these samples they are not included in the representation for the sake of clarity.

Recoil Studies A number of neutron-capture products, *M , were studied, namely; 3H (from 6Li), ^{24}Na , ^{42}K , ^{86}Rb , ^{134}Cs and ^{110m}Ag . The recoil of these products was investigated in the following three sets of samples.

M-L Target cations, M , were ion exchanged into the parent zeolite L at room temperature. The target ions will be mainly sited in D sites although exchange into C sites is found to occur in certain cases.

Following neutron irradiation of these samples the recoil products sited in C and D sites were removed by elution with concentrated NH_4Cl solution and the percentage elution, γ , determined (see experimental section). Thus in this set of samples recoils from open to open sites were studied.

M(95)-L Target cations, M , were ion exchanged into the parent zeolite L at $95^\circ C$. Some target cations will exchange with cations sited in locked sites at this elevated temperature. Following neutron irradiation of these samples the recoil products sited in C and D sites were removed by elution at room temperature with concentrated NH_4Cl solution and γ determined. In this set of samples therefore, both open and locked to open recoils were studied.

M-L(650)N The M-L zeolites were calcined at $650^\circ C$. On cooling, when $N = NH_4^+$, the cations in C and D sited were replaced with NH_4^+ ions. When $N = Na^+$ or Ba^{2+} only the cations in D sites were replaced with Na^+ or Ba^{2+} respectively. Following neutron irradiation of these samples the recoil products in C and D sites were removed by elution at room temperature with concentrated NH_4Cl solution and γ determined. In this set of samples, therefore, only locked to open recoils were studied.

M-L Zeolites : Open to Open Recoils. The number of K^+ and M^+ ions per u.c. present in zeolite L after introduction of the M^+ ions at room temperature are given in columns 3 and 4, Table II, respectively. The capacity at room temperature for alkali metal cations is found to be approximately linearly dependent on the size of the entering cation, increasing from 2.35 Li^+ ions per u.c. to 5.50 Cs^+ ions per u.c.

The percentage elution, γ , of ^{42}K and *M , found after irradiation of the above samples, are given in columns 5 and 6, Table II, respectively. The K^+ ions in these samples were not sited only in open sites and these recoils are not, therefore, open to open site recoils. The low γ (^{86}Rb) and γ (^{134}Cs) values are probably due to incomplete removal by the NH_4^+ eluate of the $^{86}Rb^+$ and $^{134}Cs^+$ ions, which have recoiled into site C.

The γ (^{42}K) values in Table II are interesting. NH_4 -L (sample 7) has 2.86 K^+ ions per u.c. inaccessible to exchange by NH_4^+ ions at room temperature. Table I suggests that these K^+

ions are likely to be sited in A and B sites. $\gamma(^{42}\text{K}) = 77.2\%$ in $\text{NH}_4\text{-L}$ should represent, therefore, the probability of $^{42}\text{K}^+$ ions recoiling from sites A and B into sites C and D and can be written as $\gamma_{\text{A+B}}(^{42}\text{K})$. In sample 3, Na-L, there are 5.75 K^+ ions and in Ba-L, not listed, there was found to be 5.58 K^+ ions per u.c. $\gamma(^{42}\text{K})$ for these two samples was found to be 78.4 and 78.5% respectively. From the figures given in Table I it would seem reasonable to place these K^+ ions in sites A, B and C. Making the reasonable assumption that

$$n_{\text{T}} \gamma = \sum_i n_i \gamma_i \quad (3)$$

where n_i and γ_i represent the number and percentage elution of M ions located on the i^{th} site (where $i = \text{A, B, C}$ or D) respectively and n_{T} and γ the total number and overall percentage elution of M ions in the zeolite respectively it is possible to calculate $\gamma_{\text{C}}(^{42}\text{K})$ the percentage elution of K^+ ions located in site C before irradiation. $\gamma_{\text{C}}(^{42}\text{K})$ is so found to be 80%. Similarly, as zeolites L and K-L have K^+ ions in all four types of sites it is now possible to obtain $\gamma_{\text{D}}(^{42}\text{K})$, the percentage elution of K^+ ions sited in D sites before irradiation. Assuming that the K^+ ion occupancies of sites A, B, and C are unchanged and as given in Table I a value of 93.5% is obtained for $\gamma_{\text{D}}(^{42}\text{K})$. The accuracy of the experimentally determined percentage elutions depends on several factors and is spread over the range 0.15% to 3% for γ values of 95 to 55% respectively. The γ_{C} and γ_{D} values calculated above could be in error by $\pm 2\%$.

In an attempt to ascertain the sites occupied by the Rb^+ and Cs^+ ions in Rb-L and Cs-L (samples 5 and 6 respectively) these samples were exchanged at room temperature with NH_4^+ and Ba^{2+} or Na^+ ions to produce samples 9-12.

Nearly all of the 5.5 Cs^+ ions per u.c. in Cs-L were exchanged by NH_4^+ . Cs-L NH_4 (sample 11) had only 0.25 Cs^+ ions per u.c. remaining after exchange. $\gamma(^{134}\text{Cs})$ for these remaining Cs^+ ions is shown in Table II to be 85.9%. This figure is very close to the value of 85.8% found for the parent Cs-L suggesting that the remaining Cs^+ ions in Cs-L NH_4 are sited on the same sites as all the Cs^+ ions in Cs-L. As the Cs^+ ions in Cs-L were introduced at 25°C the obvious site for these Cs^+ ions is site D. The small amount of Cs^+ still remaining in the D sites of Cs-L NH_4 , after exchange with NH_4^+ , suggests that Cs^+ ions interact very strongly with the framework oxygens and are not readily exchanged by NH_4^+ ions. When Cs-L was exchanged with Na^+ to give Cs-L Na (sample 12) 27% of the original Cs^+ content remained unexchanged. $\gamma(^{134}\text{Cs})$ for these remaining 1.35 Cs^+ ions per u.c. was 85.5%, very close to the figure of 85.8% for the parent Cs-L, and consistent with the suggestion above that all Cs^+ ions in Cs-L are sited in site D. Na^+ is less efficient than NH_4^+ in removing these strongly bound Cs^+ ions from the open channel sites.

γ (^{86}Rb) for Rb-L is shown in Table II to be 86.4%. When Rb-L, containing 5.45 Rb^+ ions per u.c., is exchanged with NH_4^+ and Ba^{2+} the Rb-L NH_4 and Rb-L Ba (samples 9 and 10 respectively) produced contain 0.89 and 2.92 Rb^+ ions per u.c., respectively. γ (^{86}Rb) for Rb-L NH_4 is 82% and for Rb-L Ba is 85.7%. The low percentage elution for ^{86}Rb in Rb-L NH_4 suggests that some of these Rb^+ ions are located in a site other than site D with site C being the obvious choice. Assuming that γ_C (^{86}Rb) is 80% (i.e. the same as deduced for ^{42}K recoils: in reference 1 it was shown that the percentage elution was not dependent on the type of cation when these cations were sited in the supercages and sodalite cages of zeolites X and Y) it is possible to calculate by equation (3) that 0.65 Rb^+ ions per u.c. are located in site C in Rb-L and Rb-L NH_4 and that γ_D (^{86}Rb) is 87.2%. If these values for γ_C and γ_D are taken good agreement with the experimental value of 85.7% for γ (^{86}Rb) in Rb-L Ba is obtained when 0.65 Rb^+ ions are placed in site C.

Table II Cation Contents and Percentage Elutions of M-L Zeolites.

Sample No.	Sample	$\text{K}^+/\text{u.c.}$	$\text{M}^+/\text{u.c.}$	$\gamma(^{42}\text{K})$	$\gamma(^*\text{M})$
1	Parent L	8.55	0.5(Na)	84.0	95.5
2	Li-L	6.82	2.35	78.4	95.7
3	Na-L	5.75	3.32	78.4	95.9
4	K-L	9.14	-	84.2	-
5	Rb-L	3.63	5.45	81.2	86.4
6	Cs-L	3.60	5.50	~77	85.8
7	NH_4 -L	2.86	6.26	77.2	-
8	Ag^+ -L	4.83	4.29	76.7	89.5
9	Rb-L NH_4	2.71	0.89	78.5	82.0
10	Rb-L Ba	3.25	2.92	79.5	85.7
11	Cs-L NH_4	2.82	0.25	78.1	85.9
12	Cs-L Na	3.65	1.35	-	85.5

Assuming, firstly, that 2.8 K^+ ions per u.c. can be accommodated in A+B sites and, secondly, that a further 2.7 ions per u.c. can be contained in C sites it is now possible to produce the distribution of K^+ and M^+ ions in the C and D sites given in Table III.

The percentage elution figures listed in Table II are consistent with the distributions given in Table III except for the low γ (^{42}K) value of 76.7% in Ag^+ -L. However the ^{42}K activity was weak and was measured in the presence of a strong $^{110\text{m}}\text{Ag}$ activity and this low γ figure could have an error > 2% arising from statistical counting errors.

M(95)-L Zeolites : Open to Open and Locked to Open Recoils.
The number of K^+ and M^+ ions per u.c. present in these zeolites, after introduction of the M^+ ions by exchange at 95°C, are given in columns 3 and 4 respectively of Table IV. The extent of

Table III Cation Distributions in M-L Zeolites

Sample No.	Sample	C sites		D sites	
		K ⁺	M ⁺	K ⁺	M ⁺
1	Parent L	2.70	-	3.05	0.50(Na ⁺)
2	Li-L	2.70	-	1.32	2.35
3	Na-L	2.70	-	0.25	3.32
4	K-L	2.70	-	3.64	-
5	Rb-L	0.43	0.65	0.4	4.80
6	Cs-L	0.80	-	-	5.50
7	NH ₄ -L	0.06	2.64	-	3.62
8	Ag-L	2.03	0.67	-	3.62

exchange at 95°C is NH₄⁺ > Cs⁺ > Rb⁺ > Ag⁺ > Na⁺ and follows the same order, therefore, as found for exchange at room temperature where only open sites were involved. The high degree of exchange found with NH₄⁺ (80.2%) compares well with the figure determined by Barrer and Kanellopoulos [5]. They postulated that NH₄⁺ ions had replaced the K⁺ ions located on all sites other than those on B sites. However, the following recoil results suggest that ~1 K⁺ per u.c. from the cancrinite cages is exchanged.

The Rb(95)-L NH₄ and Rb(95)-L Ba zeolites (samples 20 and 21) in Table IV both contain 2.5 K⁺ ions per u.c. Since NH₄⁺ exchange replaces ions in sites C and D while Ba²⁺ exchange only replaces ions in site D the constant K⁺ concentration in these two samples indicate that no K⁺ ions remain in site C after exchange with Rb⁺ at 95°C. Similarly Table IV indicates that

Table IV. Cation Contents and Percentage Elutions of M(95)-L Zeolites.

Sample No.	Sample	K ⁺ /u.c.	M ⁺ /u.c.	Y(42K)	Y(*M)
13	Na(95)-L	4.05	5.05	79.2	95.5
14	Na(95)-L NH ₄	2.82	-	77.8	-
15	Na(95)-L Ba	4.09	0.11	78.5	93.0
16	K(95)-L	9.10	-	85.0	-
17	K(95)-L NH ₄	2.78	-	77.7	-
18	K(95)-L Ba	4.85	-	80.7	-
19	Rb(95)-L	3.13	5.98	83.3	85.8
20	Rb(95)-L NH ₄	2.53	1.61	79.2	81.5
21	Rb(95)-L Ba	2.50	3.11	79.6	81.0
22	Cs(95)-L	2.83	6.30	-	82.3
23	Cs(95)-L NH ₄	2.26	1.65	80.8	74.8
24	Cs(95)-L Na	2.25	3.25	-	80.9
25	NH ₄ (95)-L	1.80	7.30	72.0	-
26	NH ₄ (95)-L NH ₄	1.72	7.34	72.1	-
27	NH ₄ (95)-L Ba	1.90	3.85	72.5	-
28	Ag(95)-L	3.86	5.25	84.2	84.5
29	Ag(95)-L NH ₄	2.21	0.55	83.2	55.0
30	Ag(95)-L Na	3.85	0.65	82.0	58.5

no K^+ ions remain in site C after exchange with Cs^+ at $95^\circ C$ (see samples 23 and 24). Secondly, the number of K^+ ions per u.c. is < 2.8 in these four samples indicating that K^+ ions have been removed from sites A and/or B. This may mean that Rb^+ and Cs^+ ions have entered the hexagonal prisms and/or cancrinite cages.

The number of K^+ ions in $K(95)-L NH_4$ is 2.8 per u.c. suggesting that no redistribution of K^+ ions from sites A and B have occurred at $95^\circ C$. By comparing the Na^+ contents of samples 13, 14 and 15 it may be deduced that Na^+ exhibits a strong preference for the main channel D sites at $95^\circ C$. A similar comparison of samples 28, 29 and 30 shows that Ag^+ ions, however, enter the locked sites at $95^\circ C$. The 0.55 Ag^+ ions per u.c. that have entered the hexagonal prisms and/or cancrinite cages corresponds well with the 0.59 K^+ ions per u.c. that have vacated these sites.

The percentage elution figure of 95.5 for ^{24}Na in $Na(95)-L$ (sample 13, Table IV) agrees well with the figure of 95.9 found with $Na-L$ (sample 3). Since the recoils from locked to open sites usually occur with a lower efficiency these very similar γ results indicate that the Na^+ ions in $Na(95)-L$ are still all located in the main channel confirming the ion exchange results above.

The percentage elution figures for ^{42}K in $Na(95)-L NH_4$ and $Na(95)-L Ba$ (samples 14 and 15) agree with the previously derived values of 77% for $\gamma_{A,B}$ and 80% for γ_C confirming that no K^+ ions are present in D sites. A very low γ figure of 55% is found for ^{110m}Ag in $Ag(95)-L NH_4$ (sample 29). The Ag^+ ions are sitting in site A and/or site B. Lai and Rees [1] found that γ was frequently around 50% for ions located in the hexagonal prisms of zeolites X and Y. It is likely, therefore, that the Ag^+ ions are all, or nearly all, sited in A sites.

If $\gamma_A(^{42}K)$ is also assumed to be 55% then, using equation (3) to the results obtained with NH_4-L , $\gamma_B(^{42}K)$ is found to be 86%. These two percentage elution figures now allow us to estimate the K^+ contents of sites A and B in other samples. A value of 2.0 per u.c. for K^+ in site B is found for $Ag(95)-L NH_4$ confirming that site A is the location of the locked Ag^+ ions in this sample. Similarly a value of 1.0 per u.c. for K^+ in site B is obtained for $NH_4(95)-L$. The K^+ contents of site B in Rb and $Cs(95)-L$ are found to be 2.0 and 1.9 per u.c. respectively implying that only sites A and C are available for the locked Rb^+ and Cs^+ ions. If $\gamma_A(^{86}Rb$ or $^{134}Cs)$ is taken to be 55% and $\gamma_C(^{86}Rb$ or $^{134}Cs)$ is 80% [i.e. same as $\gamma_C(^{42}K)$] then it is calculated that 0.26 Rb^+ and 0.32 Cs^+ ions per u.c. are sited in the hexagonal prisms and 1.35 Rb^+ and 1.33 Cs^+ ions per u.c. are in site C.

From these various deductions the distribution of cations among the four sites given in Table V may be obtained. The total ion population of site A is ~ 0.8 per u.c., as found in the parent zeolite L, and of site B is ~ 2.0 per u.c. with NH_4^+ being the only ion to replace K^+ in this site.

Table V. Cation Distributions in M(95)-L Zeolites

Sample No.	Sample	Site A		Site B		Site C		Site D	
		K ⁺	M ⁺	K ⁺	M ⁺	K ⁺	M ⁺	K ⁺	M ⁺
13	Na(95)-L	0.75	-	2.07	-	1.27	0.11	-	4.94
16	K(95)-L	0.70	-	2.08	-	2.07	-	4.25	-
19	Rb(95)-L	0.53	0.26	2.00	-	-	1.35	0.63	4.37
22	Cs(95)-L	0.38	0.32	1.90	-	-	1.33	0.58	4.65
25	NH ₄ (95)-L	0.77	-	0.95	1.05	0.18	2.80	-	3.45
28	Ag(95)-L	0.20	0.55	2.01	-	1.64	0.10	-	4.60

M-L(650)N Zeolites : Locked to Open Recoils. The number of K⁺ and M⁺ ions remaining in the M-L zeolites (described previously) after calcination at 650°C and exchange with N ions on cooling to room temperature are given in columns 3 and 4 of Table VI. This table [M-L(650)NH₄ samples] shows that the total amount of cation locked in the A and B sites increases from the 2.8 K⁺ ions per u.c. of the starting materials on calcination. M⁺ cations now, do not exchange with K⁺ ions in these sites in a 1:1 ratio. A marked preference for these locked sites is now apparent.

The $\gamma(^{24}\text{Na})$ value in column 6 of Table VI of 54.2% for the Na-L(650)NH₄ sample indicates that the Na⁺ ions are sited in the hexagonal prisms. The small amount of Na⁺ locked outside the A and B sites in Na-L(650)Ba is probably located in site E.

Little change in the distribution of K⁺ ions among the various sites is found on calcining K-L to 650°C. This finding confirms that the distribution of K⁺ ions in zeolite L is an energetically favourable one. The percentage elution of ⁴²K in the K-L(650)NH₄ and K-L(650)Ba samples may be used to derive another estimation of $\gamma_{\text{C}}(^{42}\text{K})$. The value of 79% is in reasonable

Table VI. Cation Contents and Percentage Elutions of M-L(650)N Zeolites.

Sample No.	Sample	K ⁺ /u.c.	M ⁺ /u.c.	$\gamma(^{42}\text{K})$	$\gamma(*\text{M})$
31	Li-L(650)NH ₄	1.30	1.8	78.5	71.5
32	Li-L(650)Na	3.20	2.25	82.0	-
33	Na-L(650)NH ₄	2.45	0.85	78.5	54.2
34	Na-L(650)Ba	4.65	0.95	75.1	58.1
35	K-L(650)NH ₄	2.81	-	76.5	-
36	K-L(650)Ba	5.70	-	77.6	-
37	Rb-L(650)NH ₄	1.48	2.47	81.9	74.1
38	Rb-L(650)Ba	2.18	3.46	80.0	81.9
39	Cs-L(650)NH ₄	2.52	0.63	80.5	55.5
40	Cs-L(650)Na	3.64	1.75	-	71.5
41	H-L(650)NH ₄	1.25	4.25	72.0	-
42	H-L(650)Ba	2.15	4.20	76.5	-
43	Ag-L(650)NH ₄	1.98	2.00	70.2	71.0
44	Ag-L(650)Na	2.80	2.50	82.0	76.0

agreement with the previous value of 80% considering the small differences in γ in samples 35 and 36.

The Li ions in Li-L(650)NH₄ are found to divide themselves fairly evenly between A and B sites assuming γ_A is 59% and γ_B is 86% in equation (3). The value of 0.85 Li⁺ per u.c. in site A agrees with the corresponding value found for Na⁺ and K⁺. Due to their small size the remaining 0.45 Li⁺ per u.c. locked outside the A and B sites are assumed to occupy site E.

Hydrogen ions, formed in the calcination of NH₄-L are present in quantities more than sufficient to fill A and B sites. As no recoil studies can be made with this ion two assumptions have to be made. Firstly, 0.85 H⁺ per u.c. are allocated to site A. NH₄⁺ ions could migrate into the hexagonal prisms when the sample is heated to 110°C prior to the calcination at 650°C. This figure is taken in order to agree with the similar figure found with Li⁺, Na⁺, and K⁺. Secondly, the cancrinite cage is assumed to be fully occupied. Thus, 1.31 H⁺ per u.c. are allocated to those B sites which contain 0.69 K⁺ per u.c. from the recoil result. The remaining 2.09 H⁺ per u.c. are allocated to site C in order to completely fill this site. It would appear that NH₄⁺ ions do not elute H⁺ ions from site C and, like Ba²⁺, exchange only with the H⁺ ions in D sites.

A complete filling of the two A and two B sites in each u.c. is calculated from equation 3 for the Ag-L(650) sample. This marked preference for locked sites is probably the result of stronger covalent bonding between the Ag⁺ ions and the oxygens of the framework. The 0.5 Ag⁺ per u.c. locked to Na⁺ exchange (compare samples 43 and 44) gave a calculated percentage elution of 96% and are allocated to site E. The 1.79 Ag⁺ ions per u.c. exchanged by Na⁺ (compare sample 8 and 44) are allocated to site D in the usual way.

Only a small fraction of the Cs⁺ ions migrate to locked sites on calcination. The percentage elution of these ions is 55.5% indicating that site A is preferred to site B. Presumably, due to the large size of the Cs⁺ ion the locked site with the greater cation-oxygen distance is preferred. The smaller Rb⁺ ion shows a different behaviour. The percentage elution is 74.1 for Rb-L(650)NH₄ and the Rb⁺ content of 2.47 per u.c. is much higher than found with Cs⁺. If 0.85 Rb⁺ per u.c. are allocated to site A to be consistent with the findings for Li⁺, Na⁺ and K⁺ and 0.72 Rb⁺ per u.c. located in site B (1.28 K⁺ per u.c. established from the recoil measurements) to bring the loading of that site to the expected 2 per u.c. the remaining 0.90 Rb⁺ per u.c. have to be allocated to site C. Taking this distribution and assuming the normal percentage elutions for these three sites an overall percentage elution figure of 73.2 can be derived from equation (3). This figure, when compared with the experimental figure of 74.1%, indicates that the postulated distribution of Rb⁺ ions is a reasonable one. As in the case of Cs⁺, and as assumed previously

for these two ions, the additional ions locked to Ba^{2+}/Na^+ exchange are located in site D.

A summary of the cation distributions which result on heating the M-L zeolites to 650°C is given in Table VII.

Table VII. Cation Distributions in M-L(650) Zeolites.

Sample No.	Sample	Site A		Site B		Site C		Site D		Site E
		K ⁺	M ⁺	K ⁺	M ⁺	K ⁺	M ⁺	K ⁺	M ⁺	M ⁺
2	Li-L(650)	0.27	0.85	1.03	0.95	1.90	-	3.62	0.10	0.45
3	Na-L(650)	0.59	0.85	1.86	-	2.20	-	1.10	2.37	0.10
4	K-L(650)	0.86	-	1.95	-	2.89	-	3.44	-	-
5	Rb-L(650)	0.20	0.85	1.28	0.72	0.70	0.90	1.45	2.98	-
6	Cs-L(650)	0.45	0.63	2.07	-	1.12	-	-	4.87	-
(7)	H-L(650)	0.56	0.85	0.69	1.31	0.90	2.09	0.71	2.08	-
8	Ag-L(650)	1.00	0.97	0.98	1.03	0.82	-	2.03	1.79	0.50

Conclusion

From these studies and others not reported in this paper it has been shown that the cancrinite cage prefers K^+ , NH_4^+ and Ba^{2+} ions. It appears, therefore, that this cage prefers ions of about 0.135 - 0.140 nm radius. There is a strong possibility that each cancrinite cage forms around a K^+ ion as a precursor to crystallisation of the zeolite. Similarly, it has been found that ions of radius ~0.115 nm are preferred by the hexagonal prisms.

Szilard-Chalmers recoil studies have been shown to be a useful new technique for establishing the sites preferred by various cations.

Literature Cited

1. Lai P.P. and Rees L.V.C. J.C.S. Faraday I, (1976)72, 1827
2. Lai P.P. and Rees L.V.C. J.C.S. Faraday I, (1976)72, 1818
3. Barrer R.M. and Villiger H. Z. Kristallogr., (1969)128, 352
4. Lai P.P. and Rees L.V.C. J.C.S. Faraday I, (1976)72, 1809
5. Barrer R.M. and Kanellopoulos A.G. J.Chem.Soc. (1970) A765

Ion Exchange in Zeolites

ADRIEN CREMERS

Centrum voor Oppervlaktescheikunde en Colloidale Scheikunde,
Katholieke Universiteit Leuven, de Croylaan 42, B-3030 Heverlee, Belgium

ABSTRACT

This paper reviews advances in zeolite ion exchange which have taken place since the Second International Conference and focuses attention on some remaining problem areas. Ion exchange in zeolites A, X, Y, mordenite and chabazite is covered. The review is in three sections: thermodynamic aspects, equilibria and kinetics.

Introduction

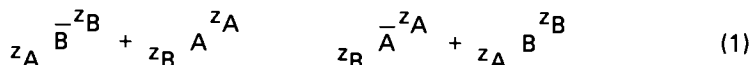
The changing of the nature of the cations in a zeolite structure is a relatively simple task and a variety of homoionic or mixed ionic forms can be prepared using alkali- and alkaline earth- or transition metal- and rare earth ions. In some cases, the exchange reaction may go to completion or fail to do so, depending on the nature of the ion, the zeolite and the temperature. The fact that such changes in ionic composition may produce some marked changes in properties such as thermal stability (1), sieving (2), sorptive (3) (4) and catalytic functions (5) is from the purely practical point of view, one of the most important aspects of zeolite chemistry.

Thermodynamic Formalism For Ion Exchange Reactions

In contrast to ion exchange materials such as clays and organic resins, it is a distinctive feature of many zeolites, as established by X-ray diffraction, that the exchangeable cations may take positions in widely different crystallographic environments. The number of possible sites generally exceeds the crystal charge deficit which in turn may lead to a pattern of charge neutralization which is characteristic for a given ion or group of ions and which is generally quite sensitive to the state of hydration of the sample. It is also known that differences between two cationic forms of the zeolite are not limited to characteristic site preferences of the ions; significant differences may also occur with regard to the total number of cations and solvent molecules which may be localized and in the distribution of the solvent over the various possible sites.

Of course, one may rightfully ignore the foregoing complications in deriving

the overall free energy effect for some arbitrary ion exchange reaction and apply a standard thermodynamic procedure (7) to the equilibrium (bar refers to zeolite phase)



The overall thermodynamic equilibrium constant K_a is defined as

$$K_a = \frac{A^{z_B} m_B^{z_A} f_A^{z_B} \gamma_B^{z_A}}{B^{z_A} m_A^{z_B} f_B^{z_A} \gamma_A^{z_B}} \quad (2)$$

in which the zeolite phase composition is defined on the equivalent fraction scale (represented by the capitals A, B) and the bulk solution composition specified as m_A , m_B , on the molal scale; f_A/f_B and γ_B/γ_A represent the ion activity coefficient ratios in the two phases and z_A , z_B refer to the ionic valences.

Equation (2) implies the following expression for the free energy content of an adsorbed ion (omitting valence sign for simplicity)

$$\mu_A = \mu_A^\circ + RT \ln A f_A \quad (3)$$

in which the excess free energy, resulting from changes in composition is specified as $f_A = \exp(u_A^{\text{exc}}/RT)$. However, in applying such an overall approach to a heterogeneous material, one must be aware that the "overall" activity coefficients may have very limited bearing on non-ideality effects "per se", such as site-site interactions, but are carrying the heavy burden of the site heterogeneity of the material as well. These coefficients serve a very limited purpose in terms of gaining a better understanding of the effect of charge heterogeneity on the ion exchange behavior of zeolites.

An attempt to relate the overall equilibrium constant to the properties of the individual site groups was made by Barrer and Klinowski who considered the exchanger to contain a number of site groups (8). The sites within each group are taken as equivalent but differing from the sites in the other groups. The exchange reaction in each particular group may therefore be specified in terms of a characteristic equilibrium constant K_i , i.e. the analog of equation (2) for the i^{th} group.

$$K_i = \frac{A_i^{z_B} m_B^{z_A} (f_i)^{z_B} \gamma_B^{z_A}}{B_i^{z_A} m_A^{z_B} (f_i)^{z_A} \gamma_A^{z_B}} \quad (4)$$

Consequently, the overall standard free energy effect is related to the free energy terms for the n groups of sites through the equation

$$\Delta G^\circ = \sum_1^n X_i \Delta G_i^\circ \quad \text{or} \quad K_a = \prod_1^n K_i^{X_i} \quad (5)$$

in which X_i represents the equivalent fraction of all cations in group i . These relations allow the overall selectivity coefficient K_C , to be related to the selectivity coefficients within the various site groups according to the equation

$$K_C = \frac{\prod_1^n X_i B_i^{z_A/z_B} (K_C^i)^{1/2 B_i} z_B}{\prod_1^n X_i B_i} z_A \quad (6)$$

Using various combinations of S_i and K_i and simple composition dependences of the ion activity coefficient ratios within each group i.e. f_A^i/f_B^i (or synonymously taking K_C^i a simple function of the composition in the i th set) the authors were able to successfully predict Kielland plots which agreed closely with experimental data.

One of the crucial points in this approach seems to be the assignment of a characteristic non-ideality pattern to each site group. Implicit in such a choice is the existence of the analog of eqn(3) for each group of sites, i.e.

$$\mu_i^A = \mu_i^{\circ A} + RT \ln A_i f_A^i \quad (7)$$

in which f_A^i is some function of the composition in the i th set and for which $f_A^i \rightarrow 1$ as $A_i \rightarrow 1$. More specifically, the excess chemical potential of an ion in the i th set is defined exclusively in terms of the composition within this set. It is however quite possible that the excess free energy function of a particular ion-site combination is very sensitive to composition changes in other sets and nearly independent of the composition of the sites belonging to its own group: for example, one may imagine the case of a given type of site surrounded by sites belonging to another group. It would therefore appear that the interaction of a given group of sites on the exchange phenomenon in another site group through this influence on the activity coefficients in this other group, as invoked by Barrer, Klinowski and Sherry (9), is hard to reconcile with the fact that such effects, however likely, are outside the scope of the definitions; in other words, the definition of the activity coefficient contains no provision for such interactions. Consequently, it would seem that the thermodynamic constants K_i for the various site groups are not to be considered as thermodynamic quantities "sensu stricto" but rather as a quantitative measure of the relative affinities of a pair of ions for a given site group.

A characteristic feature of many ion exchange reactions in zeolites is the failure to proceed to completion. Barrer and co-workers (23), followed by Sherry (10), introduced a normalization procedure which amounts to expressing the composition of the zeolite sites which are accessible to both exchanging ions with reference to the maximum exchange level for the ingoing cation. Thermodynamic quantities for this limited exchange process are then obtained by standard procedures. In some cases the maximum exchange level is temperature dependent. For this reason, and on the grounds that the Barrer method might fail to take into account a possible effect of unexchanged ions and also because redistributions may occur between small cages and supercages, Vansant and Uytterhoeven (12) presented an alternative normalization procedure. This method however was criticized by Barrer, Klinowski and Sherry (9) and shown to contain some inaccuracies. In

the same paper, three possible cases of incomplete exchange were envisaged. The first case, in which no thermodynamic treatment is justified is a pseudo-equilibrium which shows a time dependent drift in the ion distribution. The second case corresponds to a temperature-independent maximum exchange level which is independent of the time scale used. The third case is identical to the second but the maximum exchange level changes reversibly with the temperature. Several practical cases were discussed and some doubt was expressed whether case 3 is actually ever encountered.

When measuring ion exchange distributions between ions of different charge, it is well known that the ion of higher charge is more selectively adsorbed with increasing dilution of the liquid phase, i.e. the electrovalence effect. This is one of the main reasons for carrying out the exchange reaction at a constant total normality, c_0 . The quantitative calculation of an isotherm at some arbitrary value of c_0' from a known isotherm at c_0 , including the effect of solution concentration on activity coefficient ratios, was worked out by Barrer and Klinowski (13). It was shown that, when working at relatively low c_0 values, the terms pertaining to water activity effects (7) can generally be ignored in zeolites. Perhaps, it is appropriate in this context to recall the thermodynamic relation between selectivity coefficient and water activity, as derived by Laudelout and Thomas (14, 15):

$$\left(\frac{\delta \ln K_c}{\delta \ln a_w A} \right) = n_w^A - n_w^B \quad (8)$$

in which A is the ingoing ion and n_w^A , n_w^B represent the water contents of the monoionic zeolites. This equation is based on the reasonable assumption that the water content of zeolites is independent of ionic strength. It was successfully tested in the case of clays (18) but no such tests were made in zeolites, for which pronounced differences in water content may occur, for example between NaX and CsX (16). An even better case would be the KY and alkylammonium Y zeolites (17) in which the water content decreases from 240 in KY to values ranging between 125 and 100 water molecules/u.c. for the c_1 , c_2 , c_3 mixed K-alkyl ammonium forms.

Ion Exchange Equilibria

Alkali and Alkaline Earth Metal Ion Exchange in Zeolites X and Y. Rather few new data have appeared on the ion exchange behavior of X and Y zeolites since the earlier review by Sherry (6). The study by Wolf and co-workers (19) on the Na/Ca equilibrium in NaX is in essential agreement with the work of Sherry (20). In contrast to Ca, it was shown by Wolf (19) that the maximum exchange level for Mg ions was only 60%. More recently, Lai and Rees (21) reinvestigated the adsorption of alkali and alkaline earth metal ions. As expected, Rb and Cs failed to displace all the Na ions: in zeolite Y, 25 out of 68 ions/u.c. could not be displaced. This number is intermediate between the values found by Sherry (22) and Barrer, Davies and Rees (23), i.e. 16 ions in NaY and 32 in NaX could not be displaced. In view of the known occupancies of Na in hydrated NaX (24), the reasons for incomplete exchange are not merely a question of steric effects. In contrast the data on Ba (21) in X and Y fitted exactly with the exchange limit of 68 and 82% in NaY and NaX, corresponding to the 16 Na ions/u.c. in the small cages. Of course, the

exchange process can be activated at higher temperature, and complete exchange can be achieved for Ca and Ba-ions as shown by Sherry (20).

One of the main difficulties in understanding the peculiar behavior of X and Y zeolites is to account for the fact that in both cases, 16-17 ions per u.c. are localized in the small cages (24) (25) and that all the remaining ions can sometimes not be displaced, either by bulky ions which, for steric reasons, cannot penetrate the small cages, or by ions such as calcium for which no steric reasons can be invoked. Usually, the strong hydration of divalent ions and the necessity of a partial dehydration is thought to be associated with difficulty of displacing the residual Na-ions.

Another hypothesis to account for limited exchange to levels which are inconsistent with cation localization studies is that the ingoing ions may lead to a rearrangement of the other ions in the zeolite (26), which may lead to a different type of charge neutralization. In the absence of appropriate structural data, none of the foregoing hypotheses could be submitted to a quantitative test. Some recent structural data on monoionic and bionic hydrated zeolites provide strong indications that ion exchange reactions are accompanied with a rearrangement of the ions in the zeolite. Table I shows a comparison of cation localizations, as obtained from X-ray diffraction in NaX, NaY, KX, KY and CaY (24) (26) (27). These data show that for NaX and KX, the pattern is fairly similar, i.e. about 9 ions per u.c. in S_1 , 7-8 ions/u.c. in S_1' and 23-24 in S_{11} . In zeolite Y however, some very distinct differences occur: the total number of ions in the small cages is 15-17, nearly exclusively localized in S_1' ; however, contrary to predictions made by Smith (28) on the basis of the absence of six-rings with 3 Al-atoms followed by Sherry (10) (11) on the absence of ion siting in the supercages in Y zeolite, a significant number of ions is found on S_{11} , 20 in KY, and 10 in NaY, and 3 in CaY. Pronounced differences are seen in the localization of water molecules: in NaY, 13 water molecules are localized in S_{11} , whereas in KY, none were localized in this site; in CaY, 31 water molecules were localized in S_{11} , i.e. about 3 per Ca ion localized in S_1' , and were thought to be coordinated to the calcium ions.

One of the common features in most ion exchange work in zeolites is that the selectivity is mostly referred to the Na ion, the Na form being generally used as starting material. Mortier, Costenoble and Uytterhoeven (27) have shown that the calcium exchange levels which may be reached, using room temperature conditions, are very much dependent upon the nature of the outgoing cation. Using the same treatment, .6M CaCl_2 for 6 days at room temperature, the calcium saturations were 68% in NaY and 90% in KY. These data show that properties of the ingoing cation are not the sole factor controlling the exchange levels at a given temperature. From these data one may attempt a rough estimate of the ion selectivity of K to Na ions, as expressed with reference to the calcium ion. It would appear that the Na ion is strongly preferred ($K_{\text{Na-K}} \cong 20$), which is in contrast with the equilibrium data by Sherry (10) and Barrer, Davies and Rees (23) which point to a very slight preference of K: $K_{\text{K-Na}} \cong 1.5$. This would indicate that, when using the Na form of the zeolite, a pseudo- or metastable equilibrium is reached. The comparison of ion localization in NaCaY and KCaY (27), also shown in Table I, is also revealing. The data show that, when using NaY, no calcium is detected in S_1' , whereas the water occupancy in the NaCaY is roughly identical to NaY (about 1 $\text{H}_2\text{O}/\text{Na}$ ion in S_{11}). In contrast, when using the KY, 10.6 Ca ions are found in S_1' which is accompanied by a strong increase in water occupancy in S_{11} , roughly identical to CaY, i.e. 3 H_2O molecules per Ca ion. It would appear that partial dehydration to account for the difficulty could not be invoked as an important factor to account for the limited

exchange of ions such as calcium. The authors point out that, in addition to a partial dehydration, the calcium ion must displace a stable Na-hydrate structure which is non-existent in KY, forming a stable hydrate structure itself, i.e. being coordinated to three O_3 oxygens and three water molecules in the sodalite cage.

A further indication that ion redistributions may occur in the course of an ion exchange reaction is shown in an X-ray study on K-alkylammonium zeolite Y (29, 30). It was shown that the exchange of K by alkylammonium ions leads to a progressive decrease of the water content in KY, a process which was accompanied with a K occupancy increase in S_I from 1.3 to 5.4 and from 13.3 to 16.5 in S'_I in the case of propylammonium, which corresponds to a total occupancy of nearly 22 ions/u.c. for the small cages. At the same time, the K occupancy in S_{II} decreased from 20 ions/u.c. in KY to about 15 in K-propylammonium Y zeolite. The significant fact however is that such a distribution is nearly identical to the one found for dehydrated KY (30), an observation which led the authors to interpret the shift of K ions to the small cages as resulting from a decrease in hydration level.

The foregoing data indicate that, in general, the relative occupancies of the various sites are interdependent and that the hydration level is a very important factor in the pattern of charge neutralization. In the case of monoionic zeolites, the quantitative relations between the relative occupancies of the various sites and the energy differences between these sites were shown to be related quantitatively through a Maxwell-Boltzmann expression for the case of K zeolites (31).

Transition Metal Ion Exchange in Zeolite X, Y, A and Mordenite. In spite of the importance of transition metal ion exchanged zeolites as potential catalysts, the interest in the ion exchange thermodynamics of these ions in zeolites remains rather limited (19) (21) (32-40). Some of the well known features common to the behaviour of alkaline earth metal ions are also found in the case of transition metal ions: sigmoidal-shaped isotherm, incomplete exchange and temperature-dependent maximum exchange levels. Consequently, interpretations rely heavily on earlier views, especially since there are practically no data available on the localization of these ions in hydrated systems.

The maximum exchange levels show some rather large variations which can, in part, be accounted for by differences in experimental conditions such as equilibrium time and concentration of the saturating solutions. It appears that only in rare cases (21) are maximum exchange levels obtained which are consistent with the number of sodium ions known to be localized in the large cages. In zeolite X, complete exchange seems possible with the ions Cu, Cd and Zn (19) (37) (40), although lower values have been reported for Cu (21) and Zn (21) (38). The values for other ions cover the range .75 - .85 for Co (37) (38), .70 - .80 for Ni (35) (37) (38) and .80 for Mn (35). The maximum limits in Y zeolite vary within even wider ranges: .85 - 1 for Cu (37) (42), .75 - .95 for Zn (36) (37) (40), .6 for Cd (36), .70 - .75 for Ni (35) (36) (37), .65 - .80 for Co (35) (36) (37) and .78 for Mn (35). In the case of zeolite A complete exchange is possible for Cd and Zn and a maximum of about .8 is obtained for Co and Ni (32) (33). In Mordenite, the maximum exchange levels range from .45 to .50. The diversity in these data is surprising in view of the nearly identical values of the Pauling radii (about .7 Å except for Cd for which the value is .97). Therefore, the reasons for incomplete exchange should not be ascribed exclusively to steric effects or partial dehydration, particularly in view of the fact that ions which are so closely similar in dimensions behave so drastically different, and that the Cd ion which has the largest radius seems to pene-

trate relatively easy in the small cages.

The shape of the ion exchange isotherms is similar to what is found for alkali earth metal ions. Some typical examples are shown in figures 1 and 2. Judging from the foregoing data on maximum exchange levels, it appears that some of the ions do take positions in the small cages. It is tempting to adhere to the interpretation which is used for other bivalent ions (6): the sites in the small cages prefer Na ions to divalent ions and the inability of divalent cations to displace Na ions from the sodalite cages results from an unfavorable exchange equilibrium (23), particularly in the case of zeolite Y. The data on calcium exchange in KY and NaY (26) have shown that the ability to take positions in the small cages is not exclusively related to the properties of the divalent ion but is very much dependent on the nature of the outgoing cation.

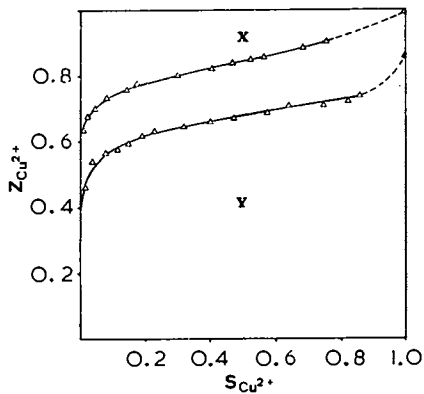
A rather different point of view was expressed by Maes and Cremers (34, 37, 41) in ascribing a preference of bivalent ions for the small cage sites. Such a view is based on the finding that at a low overall loading of the zeolite, the relative occupancy of small cage sites exceeds the value in the supercages. In some cases, and for reasons which are probably kinetic in origin, complete exchange may not be achieved within reasonable time limits. Preference of (some) transition metal ions for small cage sites is likely to have a direct influence on the exchange phenomena in the supercages. That such interactions do occur has been demonstrated by Schoonheydt and De Wilde (43) and Schoonheydt and Velghe (44) for dehydrated zeolites. They showed that the filling of the small cages with divalent ions such as Ca or Cu, i.e. putting a high positive charge density in the small cages, increases the potential energy of the cations in S_{II} and consequently leads to a decrease in the activation energy for migration. This effect is more pronounced in the case of Cu, a finding which agrees with the fact that Ca prefers site I (45) and Cu site I' (46). The oxygen atoms of the hexagonal prism provide a better shielding effect for S_{II} sites.

Additional evidence may be found in hydrated systems. Maxwell and de Boer (42) have shown that in hydrated Cu faujasite 6.3 ions/u.c. were found in S'_I ; no other Cu ions were localized. In view of the theoretical argument by Mortier (31) connecting site occupancy numbers and site energy differences, it would follow that in hydrated faujasite, site I' is by far the energetically most favorable site for copper ions. It is not unlikely that a similar interpretation may even hold for calcium ions. Relying on the calcium occupancies shown in Table I for CaY, it is seen from the ratio of S'_I/S_{II} occupancies, that S'_I is energetically the most favored site.

The selectivity values among the transition metal ions at low loading increases in the order $Ni < Co \leq Zn < Cu < Cd$ in X, Y and A (32, 33, 37, 38). This is the sequence reported by Barrer and Townsend (39) for mordenite. In view of the fact that in zeolite X, Y and A, different normalization factors, i.e. different standard states, were used, we are somewhat reluctant to compare ΔG° values since a more or less pronounced involvement of small cage sites may be implied. It is perhaps more important that this selectivity sequence coincides with the order found by Ahrland for the relative concentration of inner sphere complexes of these ions with sulfate anions (47). It is also relevant that Ni and Co ions, which seem most reluctant to penetrate the small cages, have been shown to exist as fully hydrated octahedrally coordinated species in hydrated zeolite X, Y and A (48-50). Upon dehydration these ions pass through an intermediate near-tetrahedral stage and more finally to the hexagonal prisms (51) where they return to an octahedral coordination.

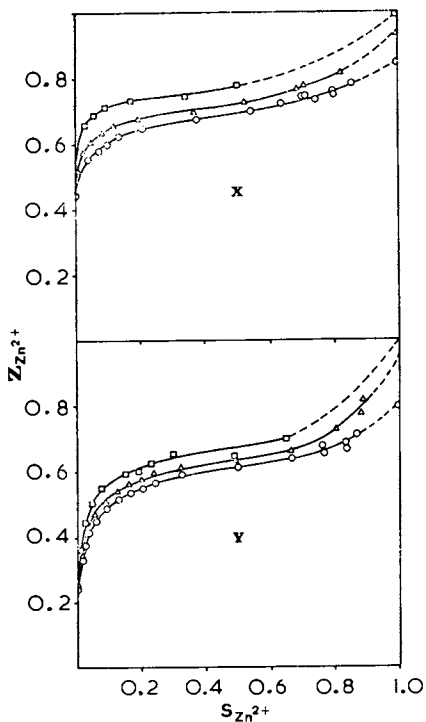
Journal of the Chemical Society,
Faraday Transactions I

Figure 1. Ion exchange isotherm for Cu
in NaX and NaY at 25°C (37)



Journal of the Chemical Society,
Faraday Transactions I

Figure 2. Ion exchange isotherm for Zn
in NaX and NaY at 45°C, 25°C, 5°C
(from top to bottom) (37)



The foregoing shows that the thermal history of transition metal exchanged zeolites determines the ion distribution in that high temperature conditions leave these ions in the small cages where they seem irreversibly locked upon rehydration (21). A similar process may occur when submitting fully hydrated zeolites to a higher temperature (34, 41); upon returning to a lower temperature, part of the ions which moved to the sodalite cages, no longer participate in the ion exchange equilibrium. In studying ion exchange equilibria of the ions it is strictly necessary not to submit the hydrated samples to any higher temperature prior to equilibrium studies at a lower temperature. Only under these conditions can reversibility be ensured.

An attempt to resolve ion exchange isotherms in terms of more than one group of sites was made by Gallei, Eisenbach and Ahmed (35). They showed that the isotherms for Na-Co, Na-Ni and Na-Mn in the supercages of X and Y zeolite could be described on the basis of a model of two groups of sites with a characteristic selectivity coefficient. A similar attempt was made by Costenoble and Maes (52) and Maes and Cremers (53) in a combined X-ray and ion exchange study of silver ions in zeolite Y. They showed that the Ag-Na exchange in zeolite Y could be described in four types of sites I, I', II and U (unlocalized) in which Ag showed the highest selectivity for site I. The Ag-Na exchange in the presence of a large excess of Cs ions was shown to be confined to the small cages and could be described in terms of two groups of site I and I'. The important fact was that the presence of Cs ions in the supercages had a lowering effect on the silver selectivity for site I. More significantly, the occupancy of silver ions in S_I was reduced by a factor of 2 which again demonstrates the possibility of interactions between site groups: These data show that, as already emphasized by Sherry, an entering ion does not necessarily take the leaving ion's place in the crystal.

Ion Exchange Equilibria in Chabazite and Mordenite. Barrer and Klinowski (54) have studied the exchange of alkali- and alkaline earth metal ions in a high framework charge chabazite-type zeolite (55) and compared its behavior with that found earlier for natural chabazite (56). Except for Cs, the alkali metal ions exchange readily; the exchange for the divalent cations is slow although full exchange is achieved. The incomplete exchange of Cs is explained in terms of electrostatic repulsion due to its large size. The slow rate of exchange of the ions Ca, Sr, Ba is interpreted on the basis of the tightly held hydration sheath. The thermodynamic affinity sequence is $Cs > K > Na > Li$ and the differences in affinity between a given pair of ions is larger in the zeolite of lower charge density, as is found in X and Y zeolite (23). The effect is explained in terms of a dielectric theory based on the consideration that the local dielectric constant in a given cationic form of the zeolite of higher charge density exceeds the value of the zeolite of lower charge.

Perhaps some care should be taken in generalizing this result to other silicates. For example, the opposite effect is found in the case of a series of isostructural montmorillonites of different charge density (57) which had been prepared by a method based on the Hofmann Klemen effect (58).

The ion exchange adsorption of alkali and alkaline earth metal ions was studied in synthetic mordenite by Barrer and Klinowski (59). The thermodynamic affinity sequence for monovalent cations is $Cs > Na > Li$, which is typical for some other zeolites, provided that normalization methods are used in case of incomplete exchange. The extent of exchange which could be achieved for divalent ions is

.60 for Ca, .62 for Sr and .84 for Ba and is thought to be associated with strong hydration and the corresponding difficulties in entering the side pockets in this zeolite.

Complex Ions in Zeolites. It is well known that transition metal ions may form stable complexes in dehydrated zeolites such as X and Y (60) (61) (62) and that the adsorption of ligands may lead to a shift of metal ions from the small cavities to the supercages (63) (64) (65). Such cationic complexes may form in hydrated zeolites and may be introduced by simple ion exchange methods (60) (67). Although some studies have been carried out in other silicates (68), very limited attention was given to these phenomena in zeolites (66) (69). In general it is seen that the adsorption behavior of such complexes in aluminosilicates is quite different from the one found for the hydrated cations. The formation of adsorbed complexes may be characterized in quantitative thermodynamic terms, as is commonly done in aqueous solution. A preliminary treatment of the quantitative relations between adsorption behavior and excess stability was presented by Pleysier and Cremers (68). More recently, a more rigorous thermodynamic approach on these interrelations was presented by Maes, Marynen and Cremers (70).

A systematic study of the stability of the ethylenediamine complexes of Cu, Zn, Ni and Cd in hydrated X and Y was carried out by Peigneur (66). It was shown that the one-complexes were stabilized by some two to three orders of magnitude whereas the two complexes were strongly destabilized, as inferred from the shift of the metal ions into the liquid phase at high ethylenediamine concentrations.

Ion Exchange Kinetics

Isotopic exchange kinetics were studied for Zn ions in zeolite X and Y by Dyer and Townsend (71) and in zeolite A by Radak, Gal and Salai (72). Dyer and Townsend showed that the self-diffusion of Zn ions in X and Y could be described by a simple equation relating to the case of self diffusion out of a sphere into a well stirred fluid. Two Y zeolites, with Si/A1 ratio 1.87 and 2.62, and X zeolite were studied at low and high temperature. In all cases the resulting τ vs t plots were linear. Except in the case of ZnX at high temperature, the Arrhenius plots were linear for all cases. A summary of the kinetic data is shown in Table II. These results were discussed in terms of differences in the ordering of the zeolitic water by the diffusing Zn ion.

The activation energies for Zn diffusion were similar to these reported by Radak, Gal and Salai (72), who analyzed the self-diffusion of Zn in zeolite A on the basis of the Brown-Sherry-Krambeck (73) model of a fast diffusion process coupled with a slow first order exchange between mobile and sited cations. This model has been found adequate for Na self-diffusion in zeolite X and A (74) but no tests were made as yet on transition metal ions. The kinetic data are shown in Table III. A comparison of the data for the two particle sizes shows that, as required by the model, the diffusional frequency B, depends on the reciprocal of R^2 , i.e. $B = \pi^2 D/R^2$. The rate constants for the slow intracrystalline exchange step, which should be independent of particle size, are seen to be systematically lower in the large particle size by a factor of about 2. A comparison of the relative rates for the two processes in ZnA and NaA is relevant. In zeolite A, the two rates are of a similar magnitude whereas in ZnA, the diffusional frequency B exceeds the rate constant for the slow process by an order of magnitude. Although the two

TABLE I. Ion Localization in hydrated zeolites NaX, KX, NaY, KY, CaY (26.8 ion/u.c.) CaNaY (19.3 Ca ions/u.c) and CaKY (25 Ca ions/u.c.)
Data are taken from references (24) (26) (27).

Site	NaX	KX	NaY	KY	CaY	CaNaY	CaKY
I	9 Na	8.9 K		1.3 K			
I	8 Na 12 H ₂ O	7.2 K	17.3 Na	13.3 K	9.7 Ca	17.3 Na	10.6 Ca
II	26 H ₂ O		13.4 H ₂ O		30.7 H ₂ O	15.4 H ₂ O	25.2 H ₂ O
II	24 Na 8 H ₂ O	23.2 K	10.2 Na	20 K	3.1 Ca	6.0 Ca	6.5 Ca

TABLE II. Kinetic data for Zn isotopic exchange (71)

Zn-zeolite	Temp. range (°C)	Δ_0 m ² sec ⁻¹	E _A (KJ/mole)	ΔS^\ddagger J/°/mole	ΔG^\ddagger KJ/mole
X	54.5 - 94.5	4.35.10 ⁻⁴	89.6	35.6	76.6
1.87 Y	-36 - -12	2.88.10 ⁶	119.8	224.0	50.2
1,87 Y	64 - 108	3.04.10 ⁻¹⁰	59.8	-82.5	82.0
2.62 Y	-36 - -12	2.59.10 ¹	87.5	127.3	51.5
2.62 Y	75 - 106.5	1.06.10 ⁻¹⁰	53.8	-91.3	78.3

TABLE III. Diffusion coefficients and rate constants for the self-diffusion of Zn in zeolite A(72) on the basis of the Brown-Sherry-Krambeck model (73).

Particle radius (μm)	Temp °K	$B(\pi^2 D/R^2)$ sec ⁻¹	D m ² sec ⁻¹	Parameters for diffusion process	Exchange rate k ₂ (sec ⁻¹)	Parameters for exchange rate	B/k ₂
30	298	2.05.10 ⁻⁶	1.87.10 ⁻¹⁶	D ₀ = 10 ^{-3.97}	2.25.10 ⁻⁷	k ₀ = 10 ^{3.05}	9.11
	313	8.11.10 ⁻⁶	7.39.10 ⁻¹⁶	m ² sec ⁻¹	6.92.10 ⁻⁷	sec ⁻¹	11.72
	333	3.39.10 ⁻⁵	3.09.10 ⁻¹⁵		1.98.10 ⁻⁷		17.12
45	298	8.89.10 ⁻⁷	1.82.10 ⁻¹⁶	E ₀ = 67.1	7.14.10 ⁻⁸	E _k = 56.6	12.45
	318	5.19.10 ⁻⁶	1.05.10 ⁻¹⁵	KJ mol ⁻¹	3.44.10 ⁻⁷	KJ mol ⁻¹	15.09
	333	1.68.10 ⁻⁵	3.44.10 ⁻¹⁵		9.48.10 ⁻⁷		17.72

processes remain coupled in ZnA, the diffusional movement is by far the faster process indicating the more pronounced siting in the case of Zn. The activation energy values for both processes are significantly higher than in NaA ($E_D=22.4$ and $E_K=42.5$ KJ/mole). The activation energy for the slow exchange process is lower than for the diffusional process, although the expected order is found for the free energies of activation ($\Delta G^\circ = 117$ KJ/mole). This is related to the very large entropy loss for the exchange process ($\Delta S_K = -194$ and $\Delta S_D^* = 27$ J.K⁻¹ mol⁻¹). The authors suggest that in the activated state the delocalization of the Zn ion from the sites is accompanied by considerable water dipole ordering around the strongly hydrated Zn ion.

Tracer diffusion studies of Na and K ions were made in homoionic and biionic chabazite by Duffy and Rees (75) using the Carman Haul equation (76). It was shown that, in the homoionic zeolite, the self-diffusion coefficient of K, D_K^* , exceeds the value of D_{Na}^* by a factor of 4 ($D_{Na}^* = 10^{-12}$ m².sec⁻¹). The activation energies are 52.8 and 28.4 KJ.mol⁻¹ for Na and K respectively. The activation entropies for the self-diffusion are 33 to 37 (Na) and -20 to -25 J.mol⁻¹ K⁻¹ (K) depending on the value chosen for the jump distance.

The D^* values in the mixed zeolite show a rather peculiar behavior: D_K^* decreases by a factor of 10 in going from the pure K-chabazite to the Na form, i.e. the trace self diffusion coefficient of K in Na chabazite, as obtained by extrapolation, is about 4.10^{-13} m².sec⁻¹. D_{Na}^* increases from the value of 10^{-12} to about $2.2 \cdot 10^{-12}$ m².sec⁻¹ in the K-chabazite. Such a change in D^* values may qualitatively be understood on the basis of the selectivity behavior of this pair of ions (56): in the initial stages of replacement of K, Na ions may take those sites least favorable towards K and D_K^* may be expected to decrease. The converse effect may arise on the other side of the composition scale.

Whatever the exact quantitative reason for these effects, these data illustrate the complexity of the situation in that, even in equilibrium systems, self-diffusion coefficients may differ by an order of magnitude from those in the pure ionic forms. It is therefore not surprising that the Helfferich-Plesset equation, although reasonably satisfactory for resins (77), is not adequate for describing ion exchange kinetics in zeolites. Undoubtedly, such failure is related to the heterogeneous nature of zeolite exchangers. Brooke and Rees (78) attempted, with limited success, to improve the Helfferich-Plesset theory by including ion activity coefficients for the solid phase. However, the nature of such overall ion activity coefficients is rather complex and the way in which the site heterogeneity is carried by such coefficients cannot clearly be specified.

One of the difficulties in the Helfferich-Plesset equation is that it predicts a higher exchange rate when the more mobile species is initially present in the solid. Inasmuch as the self-diffusion coefficients in chabazite (75) are directly relevant to the ion exchange kinetics, one would predict that the displacement of K by Na should proceed at a higher rate than the opposite reaction. Similar to what is found in the case of Sr/Ba in chabazite, the reverse effect is found. Kinshofer, Bunzl, Sansoni and Schwab (79) have shown in a study of differential ion exchange rates in chabazite that the rate in the direction of K uptake is faster than for K release at all compositions; however, the differences in rates become very small at high K saturation of the zeolite. The Na/Cs behavior, reported in the same paper, is different in that a change in differential rates occur which become identical at a Cs occupancy of about .65. The relevance of self-diffusion data, even in mixed systems, to ion exchange kinetics is not clear as yet; undoubtedly, water transport

may play an important role, as can qualitatively be expected from the significant changes in water content in going from the pure Na-chabazite to the K-chabazite (75).

No further tests have been made at describing ion exchange kinetics on the basis of the Brooke-Rees model. However, Wolf and coworkers at the Martin-Luther University, Halle-Wittenberg, made a rather extensive experimental study on the ion exchange kinetics of divalent ions in NaA, NaY and NaX zeolites (80-84). They attempted a description of the exchange rates in terms of the Paterson equation (85). Interdiffusion coefficients were found to depend strongly on ion composition, the effects amounting to two orders of magnitude in some cases. The data were interpreted in terms of a relatively fast diffusion process and a relaxation phenomenon, relating to the exchange between the more mobile and the sited ions. Qualitatively, such a picture corresponds with the model of Brown, Sherry and Krambeck (73) for the case of self-diffusion.

Literature Cited:

- (1) Takaishi, T., Yatsurugi, Y., Yusa, A., Kuratomi, T., J.C.S. Faraday I, (1975), 71, 97.
- (2) Bremer, H., Morke, W., Schodel, R., Vogt, F., Adv. Chem. Ser. (1973), 121, 249.
- (3) Barrer, R. M., Galabova, I. M., Adv. Chem. Ser. (1973), 121, 357.
- (4) Egerton, T. A., Stone, F. S., J.C.S. Faraday I, (1973), 1, 22.
- (5) Minachev, Kh. M., Isakov, Ya. I., Adv. Chem. Ser. (1973), 121, 451.
- (6) Sherry, H. S., Adv. Chem. Ser. (1971), 101, 350.
- (7) Gaines, G. L., Thomas, H. C., (1953), 21, 714.
- (8) Barrer, R. M., Klinowski, J., J.C.S. Faraday I, (1972), 68, 73.
- (9) Barrer, R. M., Klinowski, J., Sherry, H. S., J.C.S. Faraday II, (1973), 69, 1669.
- (10) Sherry, H. S., J. Phys. Chem., (1966), 70, 1158.
- (11) Sherry, H. S., J. Phys. Chem., (1968), 72, 4086.
- (12) Vansant, E. F., Uytterhoeven, J. B., Trans. Faraday Soc., (1971), 67, 2961.
- (13) Barrer, R. M., Klinowski, J., J.C.S. Faraday I, (1974), 11, 2080.
- (14) Laudelout, H., Thomas, H. C., J. Phys. Chem., (1965), 69, 339.
- (15) Laudelout, H., Van Bladel, R., Robeyns, J., Soil Sci. Soc. Amer. Proc. (1972), 36, 30.
- (16) Lai, P. P., Rees, L. V. C., J. C. S. Faraday I, (1976), 72, 1840.
- (17) Mortier, W. J., Costenoble, M. L., Uytterhoeven, J. B., J. Phys. Chem., (1973), 77, 2880.
- (18) Laudelout, H., Van Bladel, R., Robeyns, J., Soil Sci., (1971), 111, 211.
- (19) Wolf, F., Ceacareanu, D., Philchowski, K., Z. Phys. Chemie, Leipzig, (1973), 252, 50.
- (20) Sherry, H. S., J. Phys. Chem., (1968), 72, 4086.
- (21) Lai, P. P., Rees, L. V. C., J.C.S. Faraday I, (1976), 72, 1809.
- (22) Sherry, H. S., J. Phys. Chem., (1966), 70, 1158.
- (23) Barrer, R. M., Davies, J. A., Rees, L. V. C., J. Inorg. Nucl. Chem. (1969), 31, 2599.
- (24) Olson, D. H., J. Phys. Chem., (1970), 74, 2758.
- (25) Theng, B. K. G., Vansant, E., Uytterhoeven, J. B., Trans. Faraday Soc., (1968), 64, 3370.

- (26) Mortier, W. J., Bosmans, H. J., *J. Phys. Chem.*, (1971), 75, 3327.
- (27) Costenoble, M. L., Mortier, W. J., Uytterhoeven, J. B., *J.C.S. Faraday I*, (1976), 72, 1877.
- (28) Smith, J. V., *Adv. Chem. Ser.*, (1971), 101, 171.
- (29) Mortier, W. J., Costenoble, M. L., *Proc. 3rd Int. Conf. Mol. Sieves*, (1973), 125.
- (30) Mortier, W. J., Bosmans, H. J., Uytterhoeven, J. B., *J. Phys. Chem.* (1972), 76, 650.
- (31) Mortier, W. J., *J. Phys. Chem.* (1975), 79, 1447.
- (32) Gal, I. J., Jancovic, O., Malcic, S., Radovanov, P., Todorovic, M., *Trans. Faraday Soc.*, (1971), 67, 999.
- (33) Lomic, S., Gal, I. J., *Croat. Chem. Acta*, (1972), 44, 403.
- (34) Maes, A., Cremers, A., *Adv. Chem. Ser.* (1973), 121, 230.
- (35) Gallei, E., Eisenbach, D., Ahmed, A., *J. Catal.*, (1974), 33, 62.
- (36) Radak, V. M., Gal, I. J., *Proc. 3rd Int. Conf. Mol. Sieves*, (1973), 201.
- (37) Maes, A., Cremers, A., *J.C.S. Faraday I*, (1975), 71, 265.
- (38) Gal, I. J., Radovanov, P., *J.C.S. Faraday I*, (1975), 71, 1671.
- (39) Barrer, R. M., Townsend, R. P., *J.C.S. Faraday I*, (1976), 72, 661.
- (40) Dyer, A., Townsend, R. P., *J. Inorg. Nucl. Chem.*, (1973), 35, 2993.
- (41) Maes, A., Cremers, A., *Proc. 3rd Int. Conf. Mol. Sieves*, (1973), 192.
- (42) Maxwell, I. A., de Boer, J. J., (1975), 79, 1874.
- (43) Schoonheydt, R. A., De Wilde, W., *J.C.S. Faraday I*, (1974), 70, 2133.
- (44) Schoonheydt, R. A., Velghe, F., *J.C.S. Faraday I*, (1976), 72, 172.
- (45) Smith, J. V., *Adv. Chem. Ser.*, (1971), 101, 171.
- (46) Gallezot, P., Ben Taarit, Y., Imelik, B., *J. Catal.*, (1972), 26, 295.
- (47) Ahrland, S., *Coord. Chem. Rev.*, (1972), 8, 21.
- (48) Wichterlova, B., Jiru, P., Curinova, A., *Z. Phys. Chem., Frankfurt A. Main*, (1974), 88, 192.
- (49) Egerton, T. A., Hagan, A., Stone, F. S., Vickerman, J. C., *J.C.S. Faraday I*, (1972), 68, 723.
- (50) Egerton, T. A., Vickerman, J. C., *J.C.S. Faraday I*, (1973), 69, 39.
- (51) Gallezot, P., Imelik, B., *J. Phys. Chem.* (1973), 77, 652.
- (52) Costenoble, M. L., Maes, A., submitted for publication
- (53) Maes, A., Cremers, A., submitted for publication
- (54) Barrer, R. M., Klinowski, J., *J.C.S. Faraday I*, (1972), 68, 1956.
- (55) Barrer, R. M., Mainwaring, D. E., *J.C.S. Dalton*, (1972), 1252.
- (56) Barrer, R. M., Davies, J. A., Rees, L. V. C., *J. Inorg. Nucl. Chem.*, (1969), 31, 219.
- (57) Maes, A., Cremers, A., submitted for publication
- (58) Hofmann, K., Klemen, R., *Z. Anorg. Allgem. Chem.*, (1950), 262, 95.
- (59) Barrer, R. M., Klinowski, J., *J.C.S. Faraday I*, (1974), 70, 2362.
- (60) Naccache, C., Ben Taarit, Y., *Chem. Phys. Lett.*, (1971), 11, 11.
- (61) Simpson, H. D., Steinfink, H., *J. Amer. Chem. Soc.*, (1969), 91, 6225.
- (62) Vansant, E. F., Lunsford, J. H., *J. Phys. Chem.* (1972), 76, 2860.
- (63) Huang, Y. Y., Vansant, E. F., *J. Phys. Chem.*, (1973), 77, 663.
- (64) Gallezot, P., Ben Taarit, Y., Imelik, B., *J. Phys. Chem.*, (1973), 77, 2556.
- (65) Flentge, D. R., Lunsford, J. H., Jacobs, P. A., Uytterhoeven, J. B., *J. Phys. Chem.*, (1975), 79, 354.
- (66) Peigneur, P., (1976), Ph. D. Thesis, Leuven.
- (67) Lunsford, J. H., Peigneur, P., Schoonheydt, R. A., submitted for publication.

- (68) Pleysier, J., Cremers, A., *J.C.S. Faraday I*, (1975), 71, 256.
- (69) Pleysier, J., Cremers, A., *J.C.S. Faraday I*, (1975), 71, 256.
- (70) Maes, A., Marynen, P., Cremers, A., submitted for publication.
- (71) Dyer, A., Townsend, R. P., *J. Inorg. Nucl. Chem.*, (1973), 35, 3001.
- (72) Radak, V. M., Gal. I. J., Salai, I. J., *J.C.S. Faraday I*, (1976), 72, 1150.
- (73) Brown, L.M., Sherry, H. S., Krambeck, F. J., *J. Phys. Chem.*, (1971), 75, 3846.
- (74) Brown, L. N., Sherry, H. S., *J. Phys. Chem.*, (1971), 75, 3855.
- (75) Duffy, S. C., Rees, L. V. C., *J.C.S. Faraday I*, (1974), 70, 777.
- (76) Carman, P. C., Haul, R. W. A., *Proc. Roy. Soc. A.*, (1954), 222, 109.
- (77) Helfferich, F., Plesset, M. S., *J. Phys. Chem.*, (1958), 28, 418.
- (78) Brooke, N. M., Rees, L. V. C., *Trans. Faraday Soc.*, (1968), 64, 3383.
- (79) Kinshofer, G. S., Bunzl, K., Sansoni, B., Schwab, G. M., *Z. Phys. Chem. Frankfurt a. Main*, (1973), 87, 218.
- (80) Danes, F., Wolf, F., *Z. Phys. Chemie, Leipzig*, (1972), 251, 329.
- (81) Danes, F., Wolf, F., *Z. Phys. Chemie, Leipzig*, (1973), 252, 15.
- (82) Wolf, F., Danes, F., Pilchowski, K., *Z. Phys. Chemie, Leipzig*, (1973), 252, 33.
- (83) Wolf, F., Ceacareanu, D., Pilchowski, K., *Z. Phys. Chemie, Leipzig*, (1973), 254, 83.
- (84) Wolf, F., Ceacareanu, D., Pilchowski, K., *Z. Phys. Chemie, Leipzig*, (1973), 254, 96.
- (85) Paterson, S., *Proc. Phys. Soc.*, (1947), 59, 50.

Mechanism of Zeolite A Synthesis

C. L. ANGELL and W. H. FLANK

Union Carbide Corp., Molecular Sieve Department,
Tarrytown Technical Center, Tarrytown, N.Y. 10591

ABSTRACT

Experiments utilizing several different characterization techniques as a function of time, including chemical analyses, Raman spectra, x-ray diffraction, sorption and particle size measurements, have been performed to determine the mechanistic pathway in 4A synthesis. The evidence supports a mechanism involving formation and subsequent dissolution of an amorphous aluminosilicate intermediate, with solution transport from the gel to the growth surface of the crystallite.

Introduction

Two different zeolite synthesis mechanisms have been discussed in the recent literature. McNicol *et al.* (1,2) argue in favor of a solid phase transformation mechanism and Flanigen(3) discusses surface diffusion in the absence of substantial liquid transport, while Sand *et al.* (4,5), Kacirek and Lechert(6), and Zhdanov(7) present evidence in support of a solution transport mechanism. To aid in resolving this conflict, a variety of techniques were applied to the study of the 4A synthesis system as a function of time.

Experimental

Portions of a 4A gel synthesis formulation were placed in sample tubes which were withdrawn from constant temperature baths after aging at 25°C or crystallization at 96°C for various times, and centrifuged while hot in an insulated holder. The reaction rate in this series of unagitated experiments was relatively slow. The gel was formed by mixing solutions of sodium silicate and sodium aluminate, and utilized ratios of Na₂O/Al₂O₃, SiO₂/Al₂O₃ and H₂O/Al₂O₃ of 1.96, 1.98 and 83.0, respectively. The liquid and solid phases were promptly scanned in a Jarrell-

Ash Model 25-300 laser Raman spectrometer. Several of the samples were re-scanned after standing for some time and showed no marked changes. Band assignments were made on the basis of data reported in the literature for the aluminate ion(8,9), silica species (10,11) and zeolite A(11).

A similar 4A gel synthesis formulation master batch was prepared and samples were withdrawn as a function of time during the course of the reaction. The reaction rate in this series of agitated experiments was moderately fast. Solid and liquid phases were separated by hot centrifugation in an insulated holder, and the solids were washed with weighed portions of water. The various sample fractions were weighed and subjected to chemical analysis. Material balance closures, with one exception, were better than 96% and averaged 97.0%.

Another 4A gel synthesis formulation master batch was prepared, with samples also being withdrawn as a function of time during the course of the reaction. The gel was formed by mixing solutions of sodium silicate and sodium aluminate, and utilized ratios of $\text{Na}_2\text{O}/\text{Al}_2\text{O}_3$, $\text{SiO}_2/\text{Al}_2\text{O}_3$ and $\text{H}_2\text{O}/\text{Al}_2\text{O}_3$ of 1.97, 1.88 and 63.2, respectively. In this case, the solid product samples were evaluated for degree of crystallinity by x-ray powder diffraction via comparison with a 4A standard, O_2 adsorption capacity at 100 torr and 90 K, water content removable by 350°C vacuum activation after humidity equilibration at 50% relative humidity, and mean equivalent spherical diameter as determined by a Sedigraph 5000 Particle Size Analyzer. The reaction rate in this series of experiments was fairly rapid, reflecting the use of a lesser amount of water in the formulation.

Results

The data obtained from the Raman spectra are summarized in Table I and Figure 1. These results, particularly during the crystallization step, can be contrasted with those reported in the literature by McNicol and co-workers(1,2), who observed no changes with time other than the appearance of zeolite A. The terms silica and silicon-containing species are used in a general sense. While the observed band positions correspond to reported values for oxygenated silicon species, it is recognized that the degree of ordering in these materials is variable. The spectra show that conversion to framework silica occurs from precursor material. This may consist of localized concentrations of silica gel formed in the initial mixing of reactants, or by precipitation from a supersaturated solution, or an aluminosilicate gel with a variable degree of cross-linking.

Analysis of liquid and solid phases shows, as illustrated in Figure 2, that the ratio of alumina in the liquid phase to that in the solid phase is relatively high during aging, and decreases during crystallization at elevated temperature. The silica to alumina ratio in the liquid phase is seen to increase sharply

TABLE I
LASER RAMAN SPECTROSCOPY DATA AS A FUNCTION
OF TIME DURING ZEOLITE A SYNTHESIS

AGING TIME, HRS.	CRYST. TIME, HRS.	BAND POSITION, CM ⁻¹	BAND INTENSITY AND SHAPE	SPECIES
LIQUID PHASE				
0	0	620 400-500,700-800	STRONG, SHARP VERY WEAK	ALUMINATE SILICA (?)
1	0	UNCHANGED	UNCHANGED	UNCHANGED
2	0	"	"	"
3	0	"	"	"
4	0	"	"	"
0.5	1	620 450,800	MEDIUM, SHARP WEAK	ALUMINATE SILICA (?)
0.5	2	620 400-500,700-800	WEAK WEAK	ALUMINATE SILICA (?)
0.5	3	UNCHANGED	UNCHANGED	UNCHANGED
0.5	4	620 400-500,700-800	VERY WEAK WEAK, BROAD	ALUMINATE SILICA (?)
SOLID PHASE				
0	0	405 450 800	WEAK STRONG, BROAD WEAK, BROAD	SILICA SILICA SILICA
1	0	UNCHANGED	UNCHANGED	UNCHANGED
2	0	"	"	"
3	0	"	"	"
4	0	"	"	"
0.5	1	450 800	STRONG, BROAD WEAK, BROAD	SILICA SILICA
0.5	2	UNCHANGED	UNCHANGED	UNCHANGED
0.5	3	490	NEW SHOULDER	ZEDLITE A
0.5	4	450,800 490 340, 700, 1040	WEAK, BROAD STRONG, SHARP WEAK	SILICA ZEOLITE A ZEOLITE A

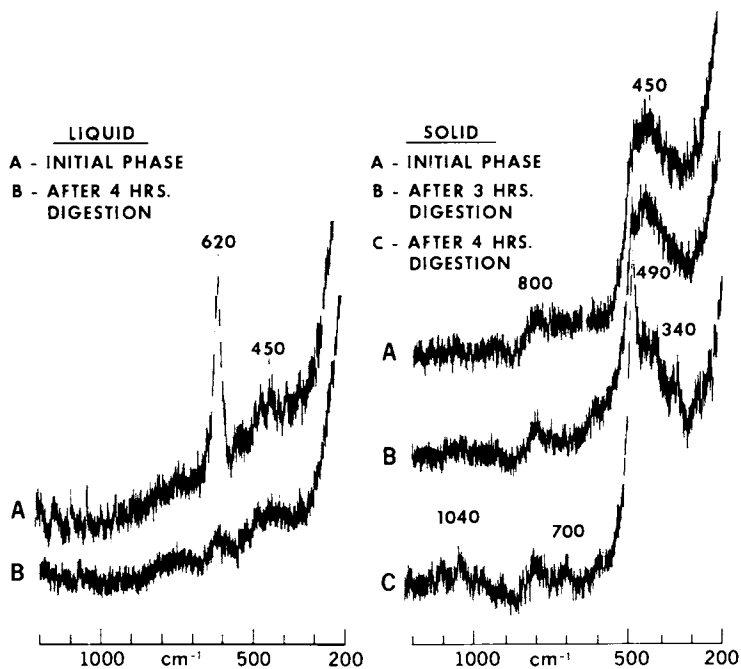


Figure 1. Raman spectra of solid and liquid phases in zeolite A synthesis

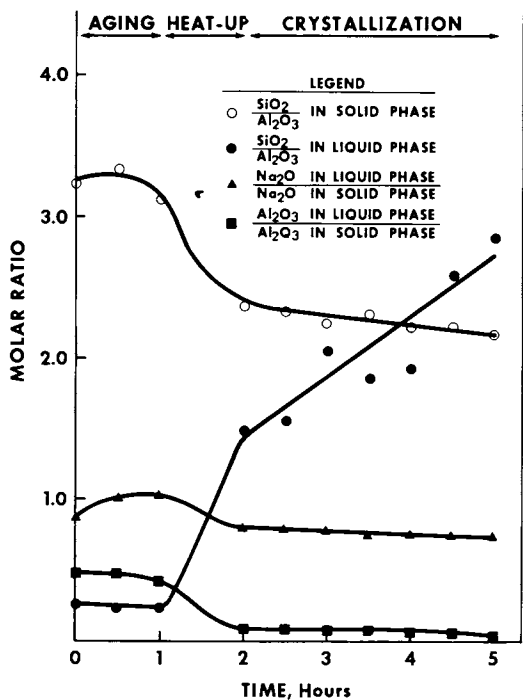


Figure 2. Composition of Gel 4A synthesis system as a function of time

after aging, with the increase continuing during the crystallization period. This is indicative of the increase in liquid phase silica concentration at higher temperature as well as the depletion of alumina in the liquid phase as crystallization proceeds. The silica to alumina ratio in the solid phase is seen to drop sharply during heat-up, and more gradually thereafter, approaching the ideal value of two as the reaction proceeds toward completion. Significant compositional changes as a function of time are thus clearly established.

The fractions of the synthesis composition found in the separated solid phase, as a function of time during the synthesis reaction, are shown in Figure 3. The plotted data are normalized and are derived from material balance data which had closures averaging 97.0%. The changes with time that are seen in the plot indicate significant mass transport between the solid and liquid phases during the reaction.

A ternary mole fraction composition diagram for the solid phase, shown in Figure 4, can be used to illustrate the distinctive compositional changes occurring along the reaction trajectory, as the reaction proceeds through the several synthesis stages. Total initial solids are shown at Point (1). The initially formed amorphous sodium aluminosilicate, shown at Point (2), briefly becomes depleted in soda and enriched in silica content, then steadily is depleted in silica and enriched in soda and alumina content as the zeolite forms.

The mean equivalent spherical diameter is plotted in Figure 5 as a function of time through the heat-up and crystallization periods(12). All of the samples were ultrasonically dispersed. The amount of agitation required to achieve a stable size distribution decreased significantly as crystallization approached completion. During the aging period, however, the mean particle size is both small and unstable with respect to degree of agitation. Beyond this point, the amorphous particles are more firmly cross-linked and are relatively large, but the minimum mean diameter in the series is found after 30 minutes at 96°C. This corresponds to about 35% conversion to zeolite, as indicated in Figures 6 and 7, and shows that some dissolution of the amorphous gel particles takes place prior to crystal growth. The increase with time of x-ray diffraction intensity and oxygen adsorption capacity for the product, indicative of the degree of crystallinity, parallel each other very closely, as shown in Figures 6 and 7, and quickly reach maximum values(12). Figure 7 also shows that the amorphous solid is indeed hydrous and is undergoing change prior to the appearance of detectable crystallinity.

Discussion

Several papers in recent years have attempted to distinguish between direct solid phase transformation of gel to crystalline material(1,2), or re-ordering of gel to an ordered crystalline

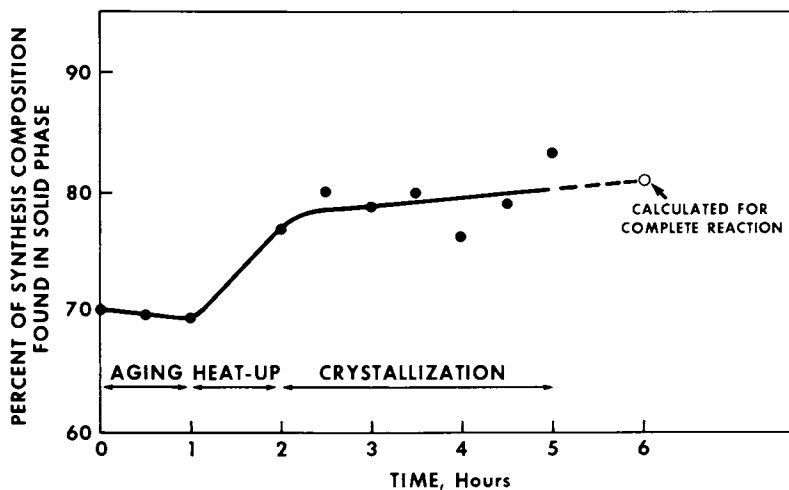


Figure 3. Solids content as a function of time during synthesis

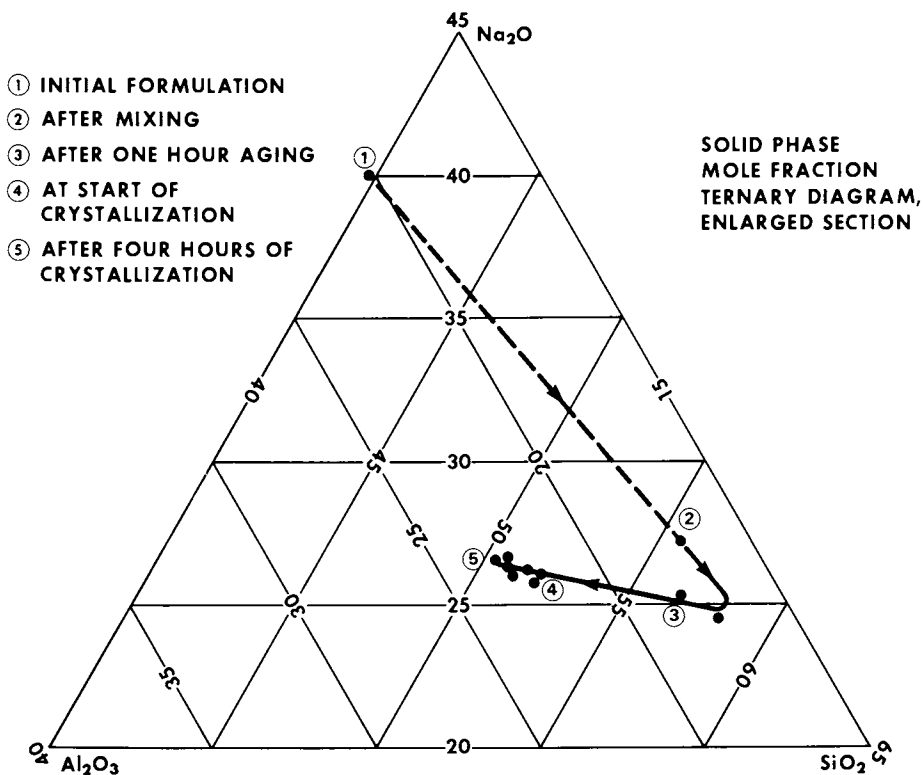


Figure 4. Synthesis reaction trajectory

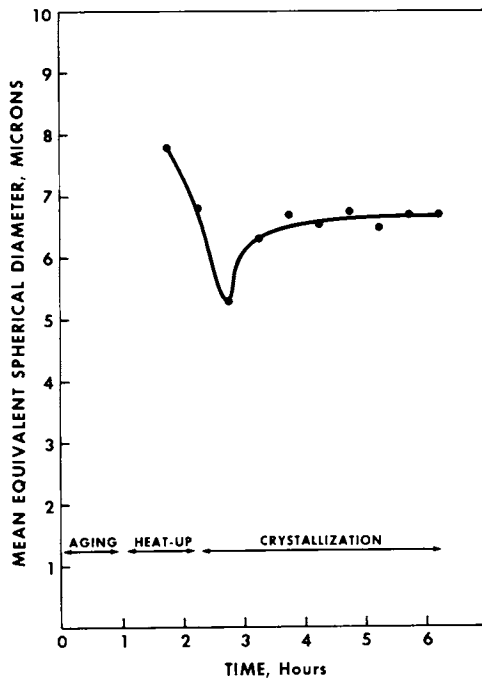


Figure 5. Mean particle size as a function of time during synthesis

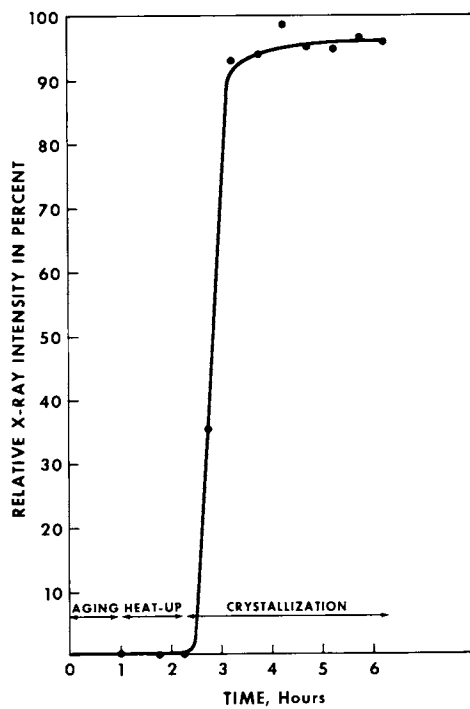


Figure 6. X-ray intensity as a function of time during synthesis

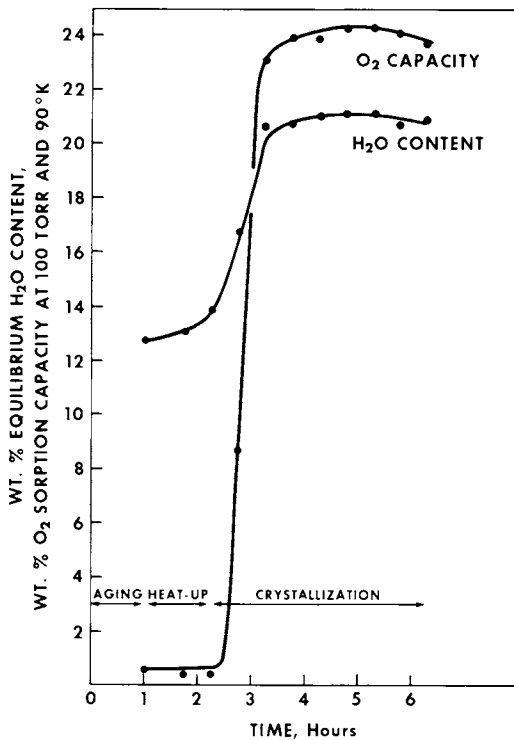


Figure 7. Wt % equilibrium H₂O content and O₂ sorption capacity as a function of time during synthesis

state via surface diffusion(3), and crystallization via liquid phase mass transport(4,5,6,7) as the operative mechanism in zeolite synthesis. We have employed a number of different techniques to characterize the liquid and solid phases of the reacting zeolite A synthesis system as a function of time along the reaction coordinate. An attempt has been made to adequately sample the system at a number of points, covering the several stages of the synthesis process, to help identify the mechanistic route involved.

The Raman data establish that, during the aging step conducted at ambient temperature, the liquid phase is rich in aluminate ion and the solid phase is rich in silica gel. The observed band intensities remain relatively unchanged during this period, as noted in Table I. The analytical data shown in Figure 2 are in good general agreement with this, but it can be noted that a more detailed examination of the solid phase composition reveals that small changes are indeed occurring during the aging period, as evidenced by the data in Figure 4. Also indicative of a change in the system during aging are the data in Figure 3, which suggest that an ambient temperature quasi-equilibrium solubility limit for the amorphous sodium aluminosilicate gel is being approached. Such a compositional plateau is common to a number of aluminosilicate systems(7,13).

During the period in which the reaction mixture is being heated from ambient temperature to 96°C, a number of very significant changes are observed to occur. It can be noted, however, that the x-ray diffraction intensity and oxygen sorption capacity characteristic of zeolite A are absent during this period, as shown in Figures 6 and 7. The hydrous nature of the solids present during heat-up is apparent in Figure 7. Alumina is transferred from the liquid phase to the solid phase and silica goes into the liquid phase, as can be seen in Figures 2 and 4. This finding is analogous to that reported earlier by Schwochow and Heinze(14). There is a net increase in the solid to liquid ratio in the system (see Figure 3), and at the same time the average size of the gel particles is seen in Figure 5 to decrease. This indicates that material is being transferred between the liquid and solid as new solubility product relationships are established as a function of temperature. There is the further indication, supported by the data of Zhdanov(7) and of Aiello and co-workers(15,16), that the initially formed sodium aluminosilicate gel is converted via solution transport to an apparently amorphous aluminosilicate intermediate. It is this latter material which is converted to crystalline zeolite via dissolution by the basic medium.

The conditions to which a gel or aluminosilicate intermediate are exposed must be controlled to provide the necessary liquid phase composition for formation of the desired crystalline phase(17). Zhdanov has recently demonstrated this point very well(18). He showed the influence of gel aging on crystallization

time for the reaction and on crystallite size, as well as evidence for solution transport and participation of the liquid phase in directing the course of the reaction, supporting the conclusion that liquid and solid phases are in dynamic equilibrium. The existence of a complex set of liquid-solid dynamic equilibria during both the aging and crystallization periods, and the influence of these on the rate and direction of the reaction are thus apparent. Concentration of silica and alumina species in the liquid phase is constrained by a solubility product limit for sodium aluminosilicate solids, which changes as a function of temperature. It appears likely that primary nucleation is preceded by the formation of a hydrous aluminosilicate intermediate which contributes to both crystal growth and secondary nucleation (i.e., that which occurs during crystal growth), while the initially formed gel continues to furnish "dissolved" species for crystal growth and further formation of aluminosilicate intermediate.

In the elevated-temperature crystallization stage of the synthesis process, the Raman and chemical analysis data confirm that aluminate disappears from the liquid phase, while the concentration of silica species increases modestly. The fraction of the synthesis composition found in the solid phase, which dropped slightly during aging and then increased sharply upon heating the system to 96°C, continues to increase slowly as a function of crystallization time. The silica to alumina ratio in the liquid phase, which rose sharply during heat-up, continues to increase as crystallization proceeds.

The silica to alumina ratio in the solid phase, which was at a high level during aging and dropped sharply upon heating the system to crystallization temperature, continues to drop slowly during crystallization toward the ideal value of two for zeolite A. The solid phase soda to alumina ratio, derivable from Figure 4, is constant during crystallization, showing that, as aluminum is incorporated into the solid, a corresponding amount of sodium is associated with it, apparently as an ordered moiety (possibly a hydrated ion pair), transported from the intermediate to the crystal growth surface.

The mean particle size of the solids in the system drops as the system goes through heat-up and the initial portion of the crystallization period, at the same time that the solids to liquid ratio is increasing. The subsequent increase in mean particle size is not accompanied by a concomitant change in the solids to liquid ratio. It can be concluded from these observations that a hydrous sodium aluminosilicate intermediate, differing in composition from the initially formed gel, is formed during the heat-up period and that mass transport from this intermediate occurs through the liquid phase to the growth surface.

The Raman data show that the concentration of non-framework silicon-containing species in the solid decreases with time and zeolite A, after an induction period, appears and increases with

time. There is a definite time lag between the beginning of aluminum disappearance from the liquid and the appearance of zeolite A in the solid phase. This is also borne out by the data in Figures 3 and 4.

Wet chemical analysis indicates that silica, the dominant phase in the solid, is relatively unchanged in concentration during both aging and crystallization. However, unlike Raman spectroscopy, it cannot distinguish between amorphous silica gel and silica present in the zeolite framework. It is apparent, nonetheless, that a small steady-state concentration of a liquid phase silicon-containing species is present, and that it increases with temperature. Since the temperature coefficients for the solubility of the various species in the system are not equal, dynamic equilibria must be re-established during heat-up and the initial portion of the crystallization period, giving rise to the various changes observed.

The evidence discussed in this work supports a synthesis reaction mechanism involving formation and subsequent dissolution of an amorphous sodium aluminosilicate intermediate, with solution transport from the gel to the growth surface of the nucleated zeolite crystallite. It is not clear whether ordered moieties formed in the system represent nucleation centers, or building blocks for crystal growth as proposed by Barrer(19) and by Breck(20). This may be difficult to determine because of overlap of the several reaction steps involved. However, these building blocks would not have to be in the form of discrete cage units, as assumed by McNicol and co-workers(2). Ciric concluded that the most likely building-block units were dimer or cyclic tetramer species with dinegative charge(21). It might be speculated that the weak bands observed in the Raman spectra for the liquid phase could be attributable to such species.

It is apparent that dissolution of gel intermediate occurs during the course of crystallization, in agreement with the earlier results of Kerr(22) and Ciric(21), and that a direct gel transformation does not take place in the system. It might be argued that these differing views are not totally irreconcilable, since in most synthesis processes of practical interest, rather short transport distances obtain in the porous hydrogel network. It must be remembered, however, that depletion of local concentration zones in a diffusion-controlled process would require some longer-range mass transfer, as shown mathematically by Ciric(21). It has also been pointed out that the colloidal nature of some of the species involved may obscure the mechanistic picture to some degree(3), but this would not obviate the need for liquid phase participation in the process, as noted by Kerr(22).

While the mechanistic discussion originally presented a number of years ago(23) has been often mis-interpreted(4,22), it was noted therein that "formation of zeolite nuclei requires the solubilization of silicate anions from the colloidal silica particles and a resulting interaction with the aluminate ion

present in the solution". "After the initial gel formation", it was further noted, "the room temperature aging equilibrates the heterogeneous gel with the solution"(24). A concise discussion of this can be found in the monograph on molecular sieves by Breck(25). It is clear that the "solid" gel phase contains a considerable amount of aqueous solution in which liquid transport can occur.

Additional support for liquid phase involvement in zeolite crystal growth can be found upon examination of the zeolite A micrographs in Breck's monograph showing multiple layered growth steps on crystal faces(26). This type of surface structure would be expected in growth from solution, both on theoretical grounds and as a result of observational experience(27). Counterparts to a number of other observations of zeolite crystal habit can be found in crystals of various kinds grown from solution. Annealed metals seem to be the only corresponding structures formed via solid-state crystallization.

It can be further noted that earlier Raman work(1) was apparently not continued far enough into the crystallization period to observe the changes which are reported here. Although the later work(2) pursued the search for "cage-like building blocks" into the crystallization period without success, it is not clear why the changes reported here were not observed, although it is true that a highly dilute system was employed, compared to that employed here, and that no aging step was used.

Finally, the possibility of crystallization occurring by an Ostwald ripening mechanism and surface diffusion is not supported by recent work on the ripening process by Kahlweit(28), who demonstrated that particle growth rate as a function of time approaches zero after going through a maximum, rather than approaching a constant rate. The lack of constancy found in the present work in solids to liquid ratio, and distribution of chemical species in the solid and liquid as a function of time, are not consistent with a ripening process as the dominant crystallization pathway.

In summary, based on sampling of the synthesis system at a number of points covering the several stages of the process, and using a variety of characterization techniques, it can be concluded that the trajectories of the observed physical and chemical parameters in the system are incompatible with a solid phase transformation mechanism, but agree quite well with solution transport considerations.

Literature Cited

- (1) McNicol, B. D., Pott, G. T., and Loos, K. R., *J. Phys. Chem.* (1972) 76, 3388.
- (2) McNicol, B. D., Pott, G. T., Loos, K.R., and Mulder, N., *Advan. Chem. Ser.* (1973) 121, 152.
- (3) Flanigen, E. M., *Advan. Chem. Ser.* (1973) 121, 119.

- (4) Cournoyer, R. A., Kranich, W. L., and Sand, L. B., *J. Phys. Chem.* (1975) 79, 1578.
- (5) Culfaz, A., and Sand, L. B., *Advan. Chem. Ser.* (1973) 121, 140.
- (6) Kacirek, H., and Lechert, H., *J. Phys. Chem.* (1975) 79, 1589.
- (7) Zhdanov, S. P., *Advan. Chem. Ser.* (1971) 101, 20.
- (8) Moolenaar, R. J., Evans, J. C., and McKeever, L. D., *J. Phys. Chem.* (1970) 74, 3629.
- (9) Glastonbury, J. R., *Chemistry and Industry* (1969), 121.
- (10) Fortnum, D., and Edwards, J. O., *J. Inorg. Nuclear Chem.* (1956) 2, 264.
- (11) Angell, C. L., *J. Phys. Chem.* (1973) 77, 222.
- (12) Flank, W. H., and Hinchey, R. J., unpublished data.
- (13) Flank, W. H., unpublished data.
- (14) Schwochow, F. E., and Heinze, G. W., *Advan. Chem. Ser.* (1971) 101, 102.
- (15) Aiello, R., Barrer, R. M., and Kerr, I. S., *Advan. Chem. Ser.* (1971) 101, 44.
- (16) Aiello, R., Cotella, C., and Sersale, R., *Advan. Chem. Ser.* (1971) 101, 51.
- (17) Flank, W. H., *Advan. Chem. Ser.* (1971) 101, 43.
- (18) Zhdanov, S. P., *Proceedings of the Third International Conference on Molecular Sieves, Zurich* (1973), p. 25.
- (19) Barrer, R. M., Baynham, J. W., Bultitude, F. W., and Meier, W. M., *J. Chem. Soc.* (1959), 195.
- (20) Breck, D. W., *J. Chem. Education* (1964) 41, 678.
- (21) Ciric, J., *J. Colloid & Interface Sci.* (1968) 28, 315.
- (22) Kerr, G. T., *J. Phys. Chem.* (1966) 70, 1047.
- (23) Flanigen, E. M., and Breck, D. W., presented at the 137th Meeting of the American Chemical Society, Division of Inorganic Chemistry, Cleveland, Ohio, April 1960; Breck, D. W., and Flanigen, E. M., *Molecular Sieves, Soc. Chem. Ind., London* (1968), 47.
- (24) Breck, D. W., personal communication.
- (25) Breck, D. W., "Zeolite Molecular Sieves", Wiley, New York (1974), p. 338.
- (26) *Ibid.*, p. 343.
- (27) Elwell, D., and Scheel, H. J., "Crystal Growth from High-Temperature Solutions", Academic Press, London (1975), Chapters 4 and 5.
- (28) Kahlweit, M., presented at the International Conference on Colloids and Surfaces, San Juan, Puerto Rico, June 1976.

Mechanisms of Synthesizing Pseudomorphic Zeolite Particulates Using High Concentration Gradients

ANIL K. PATEL and L. B. SAND

Department of Chemical Engineering, Worcester Polytechnic Institute,
Worcester, Mass. 01609

ABSTRACT

A hypothesis is proposed for the mechanisms of gelation and crystallization which occur during the reaction between activated alumina or sodium aluminate particles and sodium silicate solutions to produce pseudomorphic zeolite A, zeolite B and zeolite HS particulates containing up to 100% zeolite with rapid sorption rates.

Introduction

The objective of this work was to make a systematic study on direct syntheses of zeolite A, B, and HS (hydroxysodalite) particulates pseudomorphic after a suitable reactant particle using high concentration gradients in the synthesis system. This had been accomplished using sodium aluminate particles as precursors in a previous study on faujasite-type zeolites (1), in which it was found that sodium salt additions were effective in promoting the mechanism. The first phase of this study, therefore, was to determine the effect of salt additions on the kinetics of crystallization. If successful syntheses were achieved, an examination of the mechanisms involved in the process of pseudomorphic transformations was to be made. A review of the patent literature on reacting preformed shapes in-situ to zeolites is given by Breck (2), and a summary of the work in the U.S.S.R. is given by Mirskii *et al.* (3). These were also pseudomorphic transformations, starting generally with a silica-alumina particle. This study reports on the use of sodium aluminate or activated alumina as the particle precursor and the effects of synthesis parameters on the pseudomorphic conversion.

The term pseudomorphic conversion is used in the broad sense, as with petrified wood, to describe the process of in-situ replacement of one species by another while retaining the size and shape of the original.

Zeolites A, B, and HS were selected for the study, as they are closely related phases in the soda-alumina-silica-water system to the faujasite-type zeolites on which similar successful studies had been made in our laboratories.

Experimental

The materials used were sodium aluminate particles (Nalco, $1.1\text{Na}_2\text{O}\cdot\text{Al}_2\text{O}_3\cdot 3\text{H}_2\text{O}$), activated alumina (ALCOA F-1, $\text{Al}_2\text{O}_3\cdot 0.4\text{H}_2\text{O}$), sodium silicate solution (Phila. Quartz, $0.3\text{Na}_2\text{O}\cdot\text{SiO}_2\cdot 7.3\text{H}_2\text{O}$), distilled water, and reagent grade NaOH, NaCl, NaF, NaBr, and NaI.

Syntheses were made in 15ml capacity low carbon stainless steel vessels placed in controlled drying ovens with pressure developed autogenously.

Using synthesis information summarized by Breck (4), the conditions for zeolite synthesis were determined by conventional techniques to obtain 100% yield of each phase as polycrystalline powder prior to the particulation study. The effects of anion additions on the kinetics of zeolite A crystallization then were determined. The order of mixing of reactants was found to be critical to achieve pseudomorphic conversion of the precursor particles: 1) the solution of distilled water, sodium hydroxide and sodium silicate, 2) sized sodium aluminate or alumina particles, and 3) salt. After reaction, the product was washed with distilled water on a suction-filtered Buchner funnel to near pH7 and then dried at 40-60°C. The samples were analyzed quantitatively by X-ray powder diffraction using a Philips model 3000 diffractometer with monochromatic Cu radiation.

Morphology was determined with the use of a Jeolco U-3 scanning electron microscope for which the samples first received a Au-Pd coating. Rates of adsorption were obtained with a sorption balance designed and constructed in our laboratories (5). Rates of gelation of the sodium aluminate particles were determined by leaching out the unreacted aluminate and of the activated alumina particles by following the decrease in boehmite content by XRD analysis. Induction period was defined as the time required for zeolite crystals to be detected by XRD analysis.

Results

The starting batch composition used to study the effect of salt additions on zeolite A crystallization was $1.6\text{Na}_2\text{O}\cdot\text{Al}_2\text{O}_3\cdot 1.4\text{SiO}_2\cdot 96\text{H}_2\text{O}$ reacted at 100°C. Examples of the effect of sodium salt additions to this batch composition on the reaction rates are given in Figure 1: without salt addition and with addition of 2 moles of NaF, NaI, NaCl or NaBr per mole of Al_2O_3 at 100°C. Additional data on this effect are given by Patel (6). It was found that for the reaction condition selected, sodium salt additions inhibited the rate of crystallization for zeolite A.

Assuming that the formation of stable nuclei is an energetically activated process, and as the nucleation process is rate-determining during the induction period, the apparent activation energy for nucleation, E_n , was determined by the relation

$$\frac{d \ln (1/\theta)}{d (1/t)} = E_n/R$$

where θ is the induction time (7). Table I lists the apparent activation energies for nucleation in the system without salt addition and with salt additions.

Table I. Apparent activation energies for nucleation of Zeolite A from batch composition 1.6Na₂O-Al₂O₃-1.4SiO₂-96H₂O with and without salt additions

<u>Salt addition to batch composition</u>	<u>Temp. Range °C</u>	<u>E_n kcal/gmole</u>
---	10-100	10.5
2NaF	80-120	13.7
2NaCl	60-100	11.1
2NaBr	60-100	11.1
2NaI	80-100	17.3

Pseudomorphic conversions were made with salt additions, which previously had been found effective in promoting faujasite-type particulation by this mechanism, but in the systems chosen for zeolites A, B, and HS, the best results were obtained with no salt additions. Figure 2 is a scanning electron micrograph of zeolite A particulates crystallized from a batch composition 3.2Na₂O-Al₂O₃-1.05SiO₂-60.5H₂O at 65°C using activated alumina as the precursor particle. As can be seen in Figure 2 (top), zeolite A particulates are formed in the 500 μ m to 1000 μ m size range. Figure 2 (bottom) shows the surface of one of these particulates in which the individual crystals can be seen. The crystals are twinned cubes and in the 5 μ m and 6 μ m size range.

Figure 3 (top) is a scanning electron micrograph of zeolite B particulates in the 200 μ m to 1000 μ m size range synthesized using sodium aluminate particles as precursors. Figure 3 (bottom) shows the surface of these particulates in which small spheroid crystals of zeolite B in the 2 μ m to 3 μ m size range are visible.

Figure 4 (top) is a scanning electron micrograph of zeolite HS particulates in the 400-500 μ m size range synthesized from batch composition 4.5Na₂O-Al₂O₃-3.6SiO₂-60.8H₂O at 105°C. Figure 4 (bottom) shows the individual crystals in the 0.1-0.3 μ m size range.

Figure 5 gives the crystallization curves resulting in the particulates of zeolites A, B, and HS shown in Figures 2, 3 and 4, respectively. Table II summarizes the batch composition and

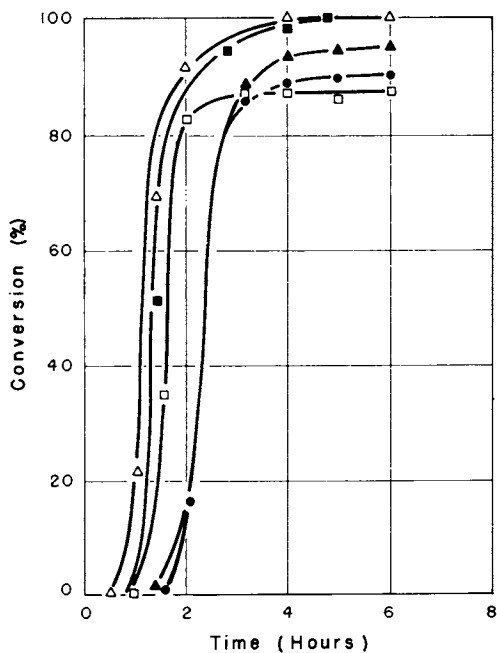


Figure 1. Crystallization curves for zeolite A from overall batch composition $1.6 \text{ Na}_2\text{O}-\text{Al}_2\text{O}_3-1.4 \text{ SiO}_2-96 \text{ H}_2\text{O}-X \text{ salt}$ at 100°C . Δ , no salt; \blacksquare , $X = 2 \text{ NaF}$; \square , $X = 2 \text{ NaI}$; \blacktriangle , $X = 2 \text{ NaBr}$; \bullet , $X = 2 \text{ NaCl}$.

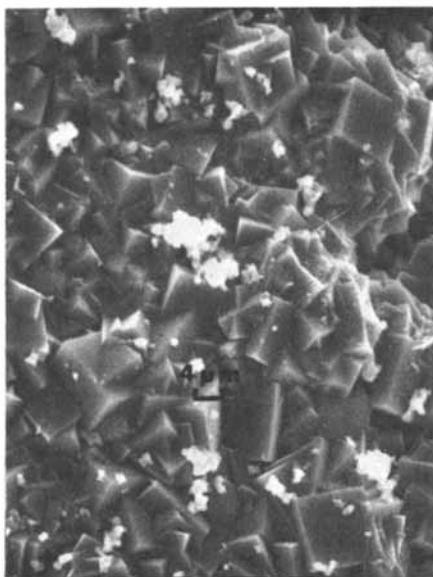
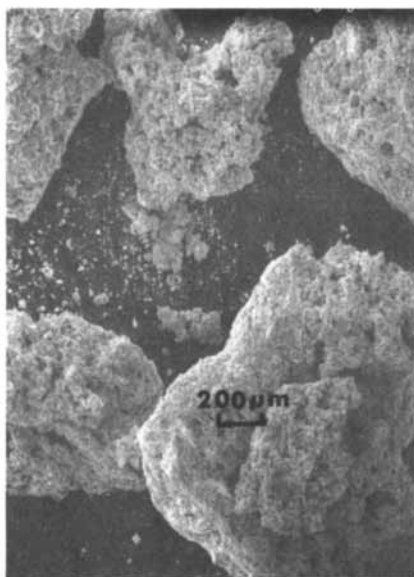


Figure 2. (left) Scanning electron micrograph of pseudomorphic zeolite A particulates from the overall batch composition $3.21 \text{ Na}_2\text{O}-\text{Al}_2\text{O}_3-1.05 \text{ SiO}_2-60.5 \text{ H}_2\text{O}$ at 65°C . (right) Scanning electron micrograph of surface of the zeolite A particulate of Figure 2.

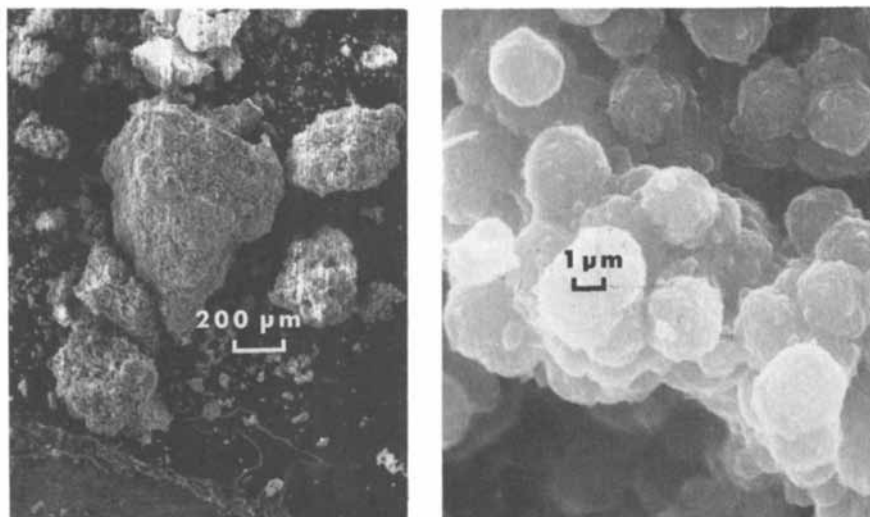


Figure 3. (left) Scanning electron micrograph of pseudomorphic zeolite B particulates from the overall batch composition $12.33 \text{ Na}_2\text{O}-\text{Al}_2\text{O}_3-20 \text{ SiO}_2-223.05 \text{ H}_2\text{O}$ at 105°C . (right) Scanning electron micrograph of surface of the zeolite B particulates.

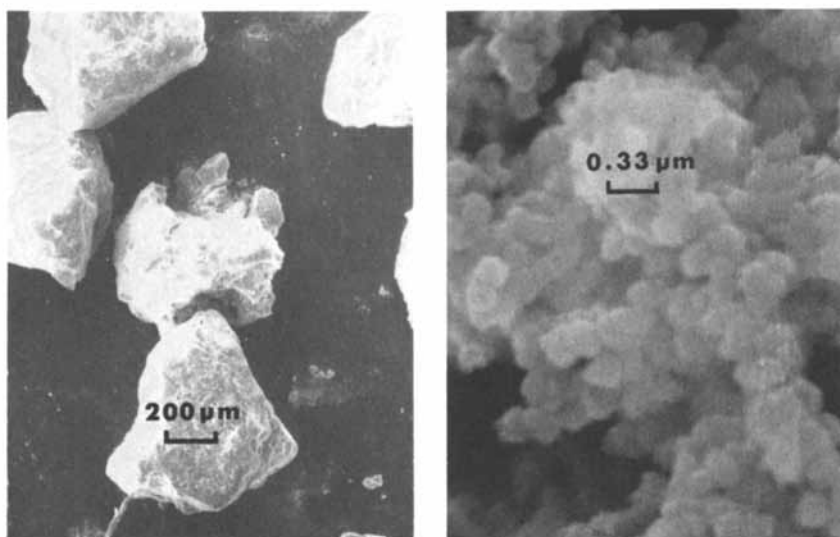


Figure 4. (left) Scanning electron micrograph of pseudomorphic zeolite HS particulates from the overall batch composition $4.45 \text{ Na}_2\text{O}-\text{Al}_2\text{O}_3-3.64 \text{ SiO}_2-60.83 \text{ H}_2\text{O}$ at 105°C . (right) Scanning electron micrograph of surface of the zeolite HS particulates.

the size range of the particulates and individual crystals obtained. Table III lists the induction periods and crystallization rates.

Table II. Size range of particulates and individual crystals in the particulates of zeolites A, B and HS formed from certain batch compositions.

Batch Composition (Na ₂ O/Al ₂ O ₃ /SiO ₂ /H ₂ O)	Zeolite type	Particulates (μm)	Crystals (μm)
11.4/1/3.00/169.8	A	100-500	1-3
3.2/1/1.05/35	A	500-1000	4-6
12.3/1/ 20 /223	B	200-1000	2-3
4.5/1/3.6 /60.8	HS	400-500	0.1-0.3

Table III. Typical induction periods and crystallization rates for zeolites A, B and HS particulates

Batch Composition (Na ₂ O/Al ₂ O ₃ /SiO ₂ /H ₂ O)	Particle	Temp. °C	Zeolite type	Induction Period, hrs.	Cryst. Rate %/hr
3.21/1/1.05/60.5	a.a.	100	A	1.5	13.0
12.3/1/ 20 /223	s.a.	105	B	1	40.0
4.45/1/3.64/60.6	s.a.	105	HS	1.5	14.7

a.a. = activated alumina
s.a. = sodium aluminate

Depending on the system, the rates of gelation varied considerably. For example, the overall rate of gelation for zeolite A was 10%/hr as compared to 10%/min for zeolite B. Figure 6 shows a typical rate curve obtained during gelation of sodium aluminate particles in a system producing zeolite A particulates.

Figure 7 shows two results of a scanning electron microscopic study of the gel particles as they crystallize into zeolite A from the overall batch composition 1.6Na₂O-Al₂O₃-1.4SiO₂-96H₂O-NaCl at 100°C. After about 1 hour at 100°C, the gel particles degrade, and holes develop on the surface of the particles as can be seen in Figure 7 (top). This differential dissolution and breaking down of the particle can lead to the unusual tubular configuration of the gel as is shown in Figure 7 (bottom). This phenomenon is noted when the system does not produce strong particulate pseudomorphs but produces either weak particulates or dispersed polycrystalline powder.

Figure 8 gives a plot of grams of SO₂ adsorbed per 100 grams of adsorbent against time at 25°C and 80mmHg pressure. The rate

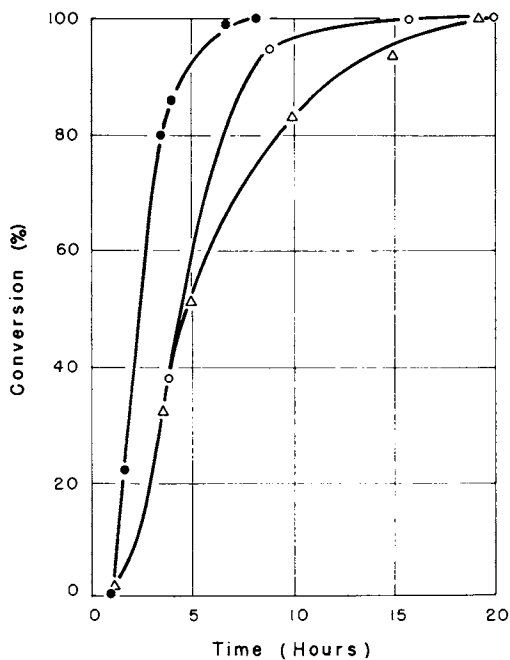


Figure 5. Crystallization curves resulting in pseudomorphic zeolite A, B, and HS particulates. Batch compositions and temperatures are listed in Table 3; ●, zeolite HS; ○, zeolite B; △, zeolite A.

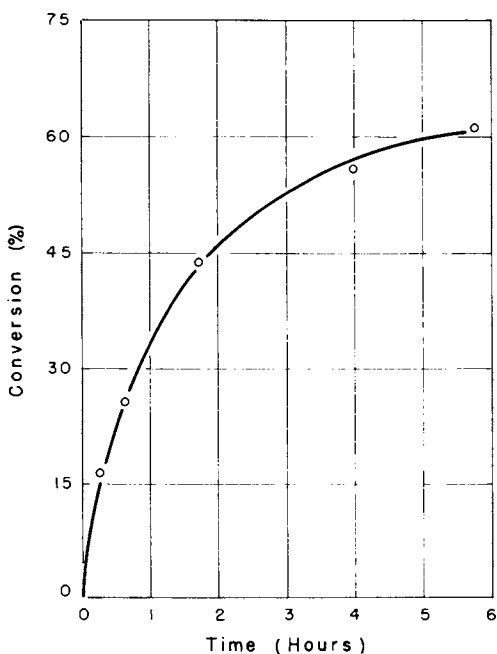


Figure 6. Gel formation rate for the overall batch composition $3.21 \text{ Na}_2\text{O}-\text{Al}_2\text{O}_3-1.05 \text{ SiO}_2-60.50 \text{ H}_2\text{O}$, at room temperature using sodium aluminate as the precursor particle

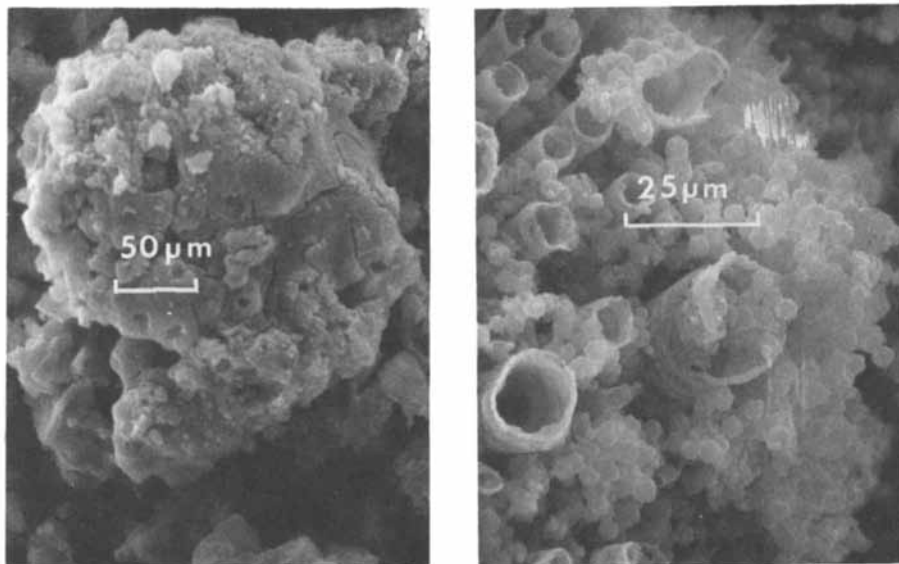


Figure 7. (left) Scanning electron micrograph of a gel particle from the batch composition $1.6 \text{ Na}_2\text{O}-\text{Al}_2\text{O}_3-1.4 \text{ SiO}_2-96 \text{ H}_2\text{O}-2 \text{ NaCl}$ after 1 hr at 100°C . (right) Scanning electron micrograph of a gel particle from the same batch composition after $2\frac{1}{2}$ hr at 100°C .

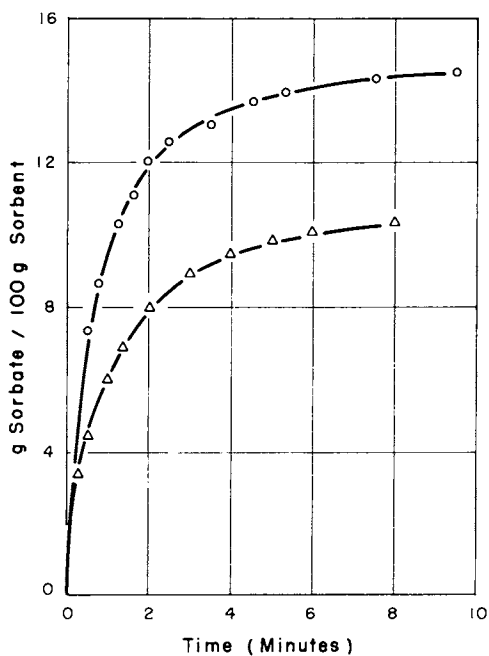


Figure 8. Rates of SO_2 adsorption on pseudomorphic zeolite A particulates (O) and on zeolite A extrudates (Δ) at 25°C and 80 mmHg pressure

of SO₂ adsorption on zeolite A particulates was 6 wt%/min. as compared with 4 wt%/min. for commercial extrudates averaged over the first 2 min. The adsorption capacity after ten minutes for zeolite A particulates was 14 wt% as compared to 10 wt% for the extrudates, due to the higher zeolite content in the particulates.

Results on the flat plate crushing strength of these particulates showed that large particulates of zeolite A had a 0.5% decrease in flat-plate crushing strength after a solution life test as compared to a 13% decrease for the commercial zeolite A extrudates. This is significant in that ion exchanges can be performed without physical deterioration.

Discussion

Pseudomorphic zeolite particulates with rapid sorption rates can be obtained over a wide particle size range by direct synthesis using reactant particles which have a high concentration gradient relative to the solution.

It was found that to obtain particulates by this method with the desired properties of size distribution, dry and wet strength, and rapid sorption rates, much experimentation is required for each zeolite type and for each different condition for crystallization of a given zeolite. The complex dynamic systems are difficult to delineate, but they are reproducible once the conditions are determined. Although further research is needed to fully understand the process mechanisms, the initial studies indicate that the batch composition must be sufficiently viscous to inhibit nutrient transfer among particles to control rates of gelation, nucleation, and crystallization. Conditions which did not produce the desired pseudomorphic conversions showed a phenomenon that provides an insight into the mechanism. The gel particles developed vent holes on the surface; and in some cases in an intermediate stage of crystallization, a tubular configuration of the gel developed on the surface as is shown in Figure 7 (bottom). The 5 μ m particles are zeolite A crystals. It is proposed that when the gel particles in these non-optimum systems were exposed to the temperature of crystallization, the contained fluid phase vented at the surface. The venting fluids developed the cylindrical gel structure. This breaking down of the particle is prevented if viscosity of the surrounding solution is high enough to contain the vapors and the precursor particle is strong enough to allow the reaction to proceed to completion.

Salt added to increase the solution viscosity did not promote the mechanism in these synthesis systems, but the study did demonstrate that the synthesis of pseudomorphic zeolite particulates by this method is not necessarily dependent on salt additions. This raises the possibility that better pseudomorphic faujasite-type particulates might be achieved in a system without salt additions than had been obtained in the previous study.

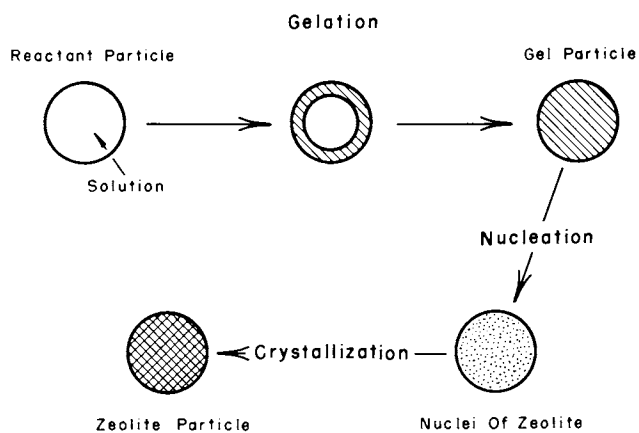


Figure 9. Schematic sequence of proposed mechanism of forming pseudomorphic zeolite particulates

The proposed sequence of gelation and crystallization that a reactant particle undergoes is diagrammed in Figure 9. In starting with a high concentration gradient between the reactant particle and an alkali silicate solution, a gel forms on the surface of the particle and progresses to the center to result in the formation of an intermediate gel particle pseudomorphic after the original particle. In other words, because of the high concentration gradient between the solution and the surface of the reactant particle, the silicate solution diffuses into the reactant particle and forms the gel phase. When the reaction front reaches the center of the particle, the reactant particle is replaced completely by an intermediate gel particle pseudomorphic after the precursor. This contrasts with the usual synthesis method in which a solution of sodium aluminate is mixed simultaneously with a solution of sodium silicate to precipitate dispersed gel particles. Those individual gel particles contain a solid and liquid phase which react to form dispersed zeolite crystals. However, with the technique of this study a coprecipitated gel is not formed instantaneously; and with a high concentration gradient between the aluminum and silicon sources, the particulation process can proceed.

After exposing these pseudomorphic gel particles to the temperature required for crystallization, it is proposed that a very large number of nuclei form simultaneously. Because of this simultaneous nucleation and with uniform crystal growth, the resulting small intergrown crystals form aggregates which retain the same size and shape of the gel particles. It is these small, intergrown crystals which give strength to the final pseudomorphic zeolite particulates.

The more rapid rate of adsorption on these zeolite A particulates observed in a comparative test with extrudates indicates an additional advantage of this method to form particulates in either the fluidized or fixed bed size ranges.

As the particulates could be formed by this technique on the first four zeolites chosen, it appears likely that other alkali zeolite particulates can be produced by this method.

Acknowledgments

The Petroleum Research Fund, Grant No. 8866-AC3,7 and the Backlund Fund of Worcester Polytechnic Institute provided financial support.

Dr. R.R. Biederman and Mr. George Schmidt are gratefully acknowledged for their assistance in using the scanning electron microscope in their laboratories.

Literature Cited

1. Dhanak, B., M.S. Thesis, Dept. of Chem. Eng., Worcester Polytechnic Institute, Worcester, MA, 1975.

2. Breck, D.W., Zeolite Molecular Sieves, John Wiley & Sons (1974) 736.
3. Mirskii, Ya. V., Aleksandrova, I.L., Budovskaya, L.V., Kosolapova, A.P., Golovko, V.G., Adsorbently, Ikh Poluch., Svoistua Primen., Tr. Uses. Soveshch. Adsorbentam, 3rd 1969 (Pub. 1971), 63-5 (Russ.), CA 77,52636W (1972).
4. Breck, D.W., Zeolite Molecular Sieves, John Wiley & Sons (1974) 270.
5. Keisling, C.A., Hayhurst, D.T., Sand, L.B., I&EC Fundamentals, in press.
6. Patel, A.K., M.S. Thesis, Dept. of Chem. Eng., Worcester Polytechnic Institute, Worcester, MA (1976).
7. Culfaz, A. and Sand, L.B., Adv. in Chem. Series, 121 (1973) 144.

Crystallization Kinetics and Properties of Na, K-Phillipsites

DAVID T. HAYHURST* and L. B. SAND

Department of Chemical Engineering, Worcester Polytechnic Institute,
Worcester, Mass. 01609

ABSTRACT

Crystallization kinetics are reported for synthetic sodium, potassium phillipsites. Pure phillipsite was synthesized in the temperature range of 25-175°C under autogenous pressure and with K/(Na+K) ratios in the starting batch composition of 0.05 to 0.35. Reaction rate expressions developed for nucleation and crystallization were determined to be second order in hydroxide concentration. The kinetic diameter of the synthesized phillipsites was determined to be 2.60 to 2.65 \AA .

Introduction

This paper reports the synthesis conditions, crystallization kinetics and some sorptive properties on Na, K-phillipsites formed in a portion of the soda-potash-silica-alumina-water system with and without chloride additions. Phillipsite is one of the most abundant natural zeolites, forming in both sedimentary rocks of marine and continental deposits and in fissures and cavities of extrusive flows, mainly basalts. The name phillipsite was proposed in 1825 by Levy in honor of the British mineralogist W. Phillips, who discovered the first crystals of this mineral in Aci Castello, Sicily (1). Phillipsite predominates in low-silica, alkali-rich rock, while the zeolite clinoptilolite is dominant in high-silica rock (2). Together, phillipsite and clinoptilolite form the largest quantity of all zeolite deposits.

Phillipsite contains the 4-ring (Al, Si)₄O₈ unit as the smallest structural unit and is classified as a Group I zeolite by Meier (3). The phillipsite framework consists of layers of tetrahedra composed of 4- and 8-membered rings lying approximately in the (100) plane. The layers are linked vertically by 4-rings which form crankshafts with the horizontal 4-rings (4,5). Some confusion has arisen in the literature among the structure types. The same letter has been used to name different synthetic species.

*Present address: Cleveland State University, Department of
Chemical Engineering, Cleveland, Ohio 44115

Thus, zeolite Na-B refers to a synthetic analcime-type zeolite (6); zeolite B refers to a synthetic phase originally reported by Barrer et al. (7) who called the same synthetic phase zeolite P_C. The term zeolite P_C was used to indicate a "phillipsite-type" structure. However, the framework structure of zeolite P_C and of zeolite B is actually that of gismondine (8). The phillipsite reported in this work has an X-ray diffractogram identical with that reported by Steinfink (9) for natural phillipsite.

Although a large amount of work has been done on zeolite synthesis in the last thirty years, the conditions of synthesis for phillipsite had not been clearly established even though it is one of the most common zeolite minerals. There are only two reported syntheses of phillipsite analogues in the literature. Sersale et al. (10) reports the preparation of a synthetic phillipsite from a high-potassium, high-calcium volcanic glass by treatment with sodium or potassium hydroxide solutions at temperatures above 240°C for 30 hours. Kuhl (11) also reports the formation of a synthetic phillipsite, designated ZK-19, whose X-ray powder pattern was found to agree very closely with that of a phillipsite obtained from a marine environment. Pure zeolite ZK-19 crystallized from mixtures having molar silica/alumina ratios in the range of 4 to 16 and Na₂O/(K₂O+Na₂O) molar ratios in the range of about 0.3 to 0.85.

EXPERIMENTAL

The reactants used for phillipsite synthesis were an amorphous silica-alumina gel (Al₂O₃-10.38SiO₂-5.18H₂O, Davison Chemical), sodium aluminate (1.1Na₂O-Al₂O₃-2.98H₂O-Nalco Co.), sodium silicate solution (N-type, Na₂O-3.326SiO₂-24.12H₂O, Philadelphia Quartz Co.), microfine precipitated silica (Quso G20, Philadelphia Quartz Co.), and reagent grade sodium and potassium hydroxide and sodium and potassium chloride.

Syntheses were made in modified Morey-type autoclaves of 3 and 15 ml capacity at autogenous pressures. For some runs below 100°C, runs were made in a mechanically stirred triple-neck distilling flask under reflux. For the quiescent runs, the reactants were mixed with a mortar and pestle into a homogeneous mix and loaded into the autoclaves. Crystallization kinetics at 100°C in a stirred flask were determined by first mixing the soluble salts with water and heating the solution to temperature. When at temperature, the gels were added and this was considered time zero. Crystallization was followed by analyzing the solid product quantitatively by X-ray powder diffraction. Prepared mixtures of a well-characterized sample of phillipsite and the amorphous substrate of near-phillipsite composition were used to establish a calibration curve for quantitative phase identification based on a summation of X-ray peak intensities. Crystallization curves were obtained by analyzing the solid product from either a number of identically charged autoclaves kept at the

crystallization temperature for different times or from aliquots taken from the stirred flask at various times.

Adsorption tests were conducted with a constant-pressure, constant-volume adsorption balance in which the weight change of the adsorbent was measured. Samples typically were activated overnight by heating to 300°C under 3×10^{-3} torr vacuum. The activated zeolite then was cooled to the temperature at which the adsorption determination was made.

RESULTS AND DISCUSSION

Synthesis. Na, K-phillipsites were synthesized using a variety of starting batch compositions in the $\text{Na}_2\text{O}-\text{K}_2\text{O}-\text{Al}_2\text{O}_3-\text{SiO}_2-\text{H}_2\text{O}$ system over a temperature range of 25°C to 175°C, with sodium and potassium chloride added in some cases. Typical batch compositions, times, temperatures, and starting materials that produced phillipsite as a pure phase are listed in Table 1. A ternary diagram of the batch compositions used in the synthesis of phillipsite is shown in Figure 1. Phillipsite formed as the stable phase from the less siliceous starting batch compositions. As the amount of silica was increased in the batch, phillipsite was more metastable, with other zeolitic phases forming with or completely replacing it. These other phases were mordenite, erionite and zeolite L. Clinoptilolite was indicated in some of the high-silica runs in which calcium, usually in the form of salt, was added to the system.

In order to determine the critical parameters in phillipsite synthesis, batch compositions were varied with respect to sodium-potassium ratios, and chloride addition. The sodium-potassium ratio was varied from the pure sodium to the pure potassium end-members while maintaining constant all other system parameters such as temperature and silica-alumina ratios. The $\text{K}/(\text{Na}+\text{K})$ ratios used were 1.00, 0.75, 0.50, 0.45, 0.40, etc. to 0. The metastable phase transformations were studied in the system with a starting batch composition of $3.2(\text{Na}_2\text{O}, \text{K}_2\text{O})-\text{Al}_2\text{O}_3-10.38\text{SiO}_2-150\text{H}_2\text{O}-6(\text{NaCl}, \text{KCl})$ and reaction temperature of 120°C. This diagram is shown in Figure 2. Approximately 200 experimental runs were used to establish the phase boundaries.

The phases that were found to coexist with phillipsite were zeolite L, mordenite, gismondine and analcime. Phillipsite formed stably (or persisted metastably for 1000 hours) in a $\text{K}/(\text{Na}+\text{K})$ range of 0.10 to 0.20, although it formed metastably over the $\text{K}/(\text{Na}+\text{K})$ range of 0.05 to 0.40. As the amount of potassium was increased, phillipsite was replaced by mordenite and subsequently by zeolite L. At the high potassium contents, phillipsite did not form and zeolite L was the only crystalline phase observed. From the high sodium compositions, sodium gismondine formed, which was replaced in time by analcime.

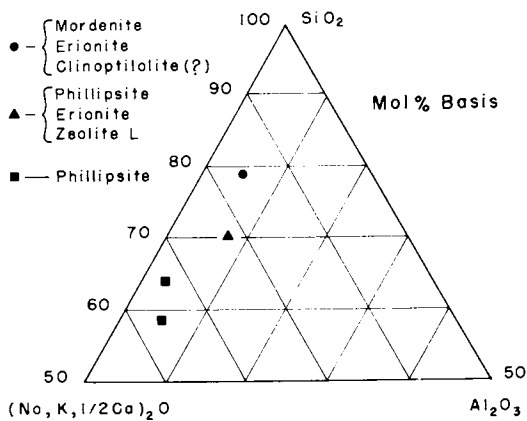


Figure 1. Ternary diagram of the starting batch compositions used in synthesis

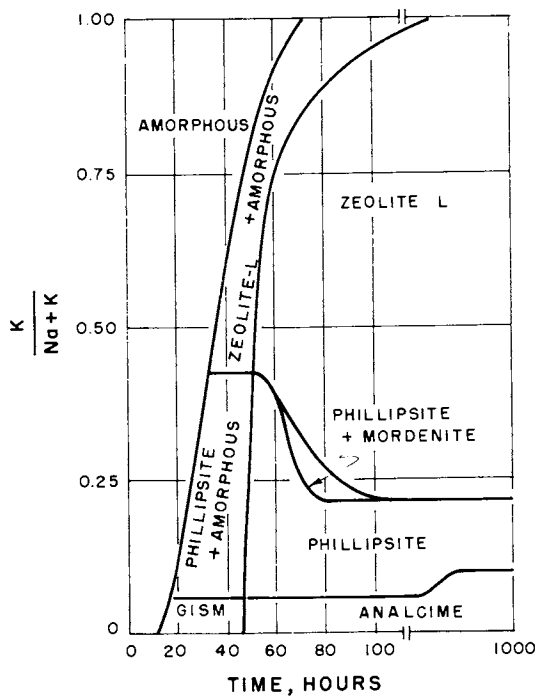


Figure 2. Metastable phase transformation diagram for the system $3.2 (\text{Na}_2\text{O}, \text{K}_2\text{O})-\text{Al}_2\text{O}_3-10.38 \text{SiO}_2-150 \text{H}_2\text{O}-6 (\text{NaCl}, \text{KCl})$ reacted at 120°C

Table I.-Typical Synthesis Runs Producing Pure Phillipsite

Run No.	Batch Composition Na ₂ O/K ₂ O/Al ₂ O ₃ /SiO ₂ /H ₂ O/NaCl/KCl	Starting Materials	Temp °C	Time (Hours)
N-3	2.4/0.8/1.0/10.38/150/4.5/1.5	Davison Gel, NaOH, KOH	120	36
N-6	6.4/0/ 1.0/10.38/150/6/ 6	Davison Gel, NaOH	120	48
N-7	6.95/3.50/1.0/20/325/0/ 0	Na-silicate Na-aluminate KOH	100	68
N-10	10.0/0/ 1.0 20.0/300/5/5	Davison Gel, Quso NaOH	175	2.2
N-10	" " "	"	125	4.5
N-10	" " "	"	100	3.3
N-10	" " "	"	60	96
N-10	" " "	"	25	744

The effect of the addition of chloride was evaluated by developing a metastable phase transformation diagram for the system $3.2(\text{Na}_2\text{O}, \text{K}_2\text{O})-\text{Al}_2\text{O}_3-10.38\text{SiO}_2-150\text{H}_2\text{O}-0.20(\text{NaCl}, \text{KCl})$ using the same reaction temperature of 120°C . The composition was essentially the same as that used in Figure 2, except the amount of chloride was substantially reduced. This diagram is shown in Figure 3. In this low-chloride case, the phases that were found to coexist with phillipsite were erionite, zeolite L, gismondine and analcime. As found in the high-chloride system, phillipsite persisted as a phase over the $\text{K}/(\text{Na}+\text{K})$ range of 0.10 to 0.20. However, phillipsite formed with co-existing phases over the much wider range of $\text{K}/(\text{Na}+\text{K})$ of 0.05 to 0.80. Zeolite L formed as a single phase only at the $\text{K}/(\text{Na}+\text{K})$ ratios greater than 0.80. In the high-sodium region, gismondine persisted as a phase for a greater time, again being replaced by analcime. It is interesting to note that in the low-chloride system erionite formed with phillipsite, while in the higher-chloride system mordenite replaced phillipsite.

The phillipsites that were synthesized had silica-alumina ratios from 4.51 to 5.24, and these are summarized in Table II. It was found that during synthesis, phillipsite selectively took up potassium from the reacting solution. A plot of this selective uptake is given in Figure 4.

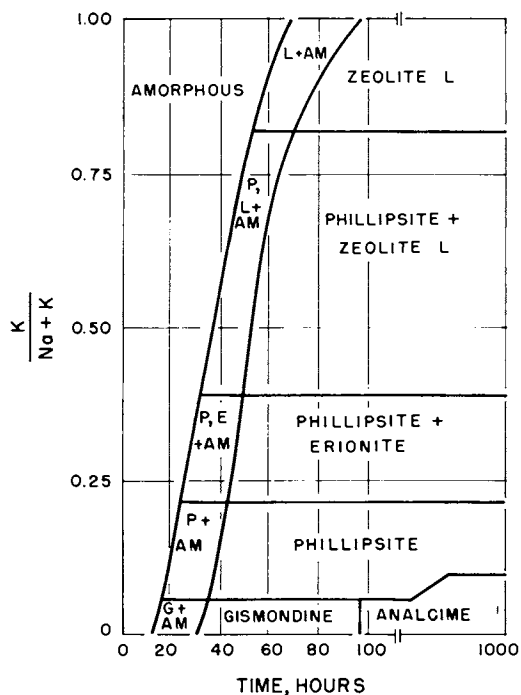


Figure 3. Metastable phase transformation diagram for the system, $3.2(Na_2O, K_2O)-Al_2O_3-10.38 SiO_2-150 H_2O-0.20 (NaCl, KCl)$ reacted at $120^\circ C$

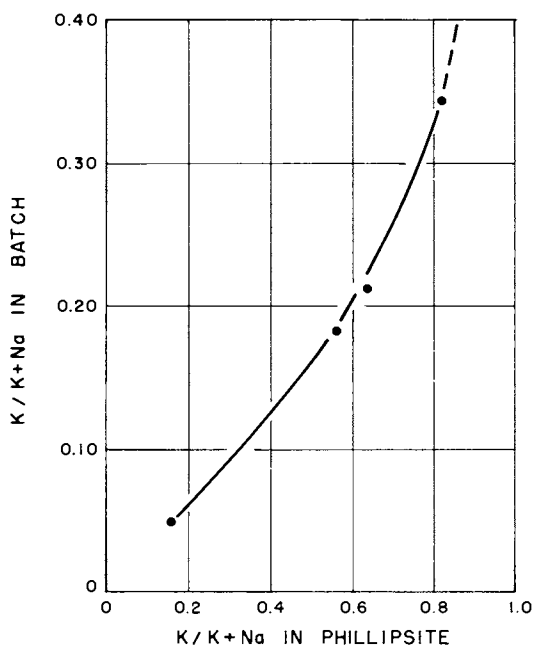


Figure 4. Selected uptake of potassium by phillipsite from the synthesis batch

Table II.-Silica-Alumina Ratios of Synthetic Phillipsites

<u>Run Number</u>	<u>Silica/Alumina</u>
N-7	5.24
N-6	5.01
N-10	4.51

Activation energies for nucleation and crystallization were calculated for Run Number N-10 using an Arrhenius relationship at three temperatures. The data are plotted in Figure 5 where θ is the induction time. Results are summarized in Table III.

Table III.-Apparent Activation Energies

	<u>Nucleation, E_n</u> <u>(Kcal/gmole)</u>	<u>Crystallization, E_c</u> <u>(Kcal/gmole)</u>
Stirred	13.46	15.25
Non-Stirred	14.30	14.76

Crystallization Kinetics. The functional dependence of the zeolite crystallization kinetics on alkalinity was developed for phillipsite synthesis. In Figure 6, crystallization curves for phillipsite are shown in which the same starting batch composition is reacted, but the alkalinity of the system is varied. This was accomplished by replacing hydroxide with chloride and assuming that for this range of concentrations, the chlorides do not affect the alkalinity significantly and therefore also do not significantly affect the nucleation or crystallization reactions. The mixture was reacted at 100°C under reflux while maintaining temperature and stirring rate constant. The batch compositions used are listed in Table IV.

Table IV.-Batch Compositions Used in the Kinetic Studies

<u>Batch Compositions</u> <u>(Na₂O/Al₂O₃/SiO₂/H₂O/NaCl/KCl)</u>	<u>Hydroxide Concentration</u> <u>(gmoles/liter)</u>
9.0/1.0/20.0/300/7/5	3.50
10.0/1.0/20.0/300/5/5	3.89
11.0/1.0/20.0/300/3/5	4.30

As can be seen in Figure 6, the rates of nucleation and crystallization increased as the alkalinity of the system was increased; therefore, a functional dependence of nucleation and

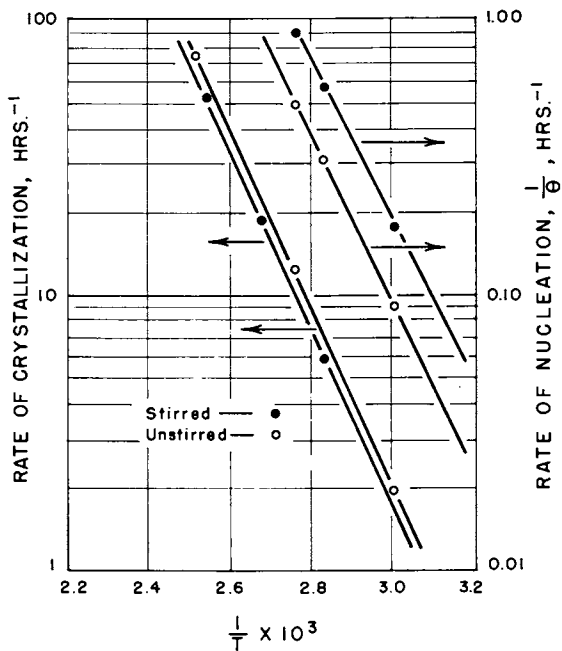


Figure 5. An Arrhenius-type plot determining nucleation and crystallization activation energies

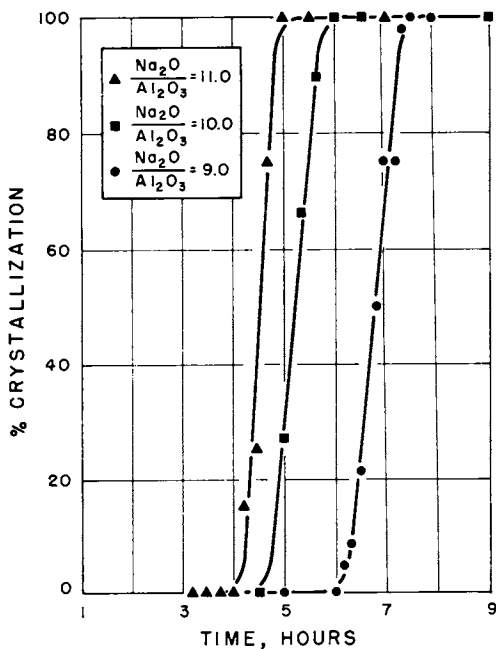


Figure 6. Dependence of nucleation and crystallization rates on alkalinity

crystallization rates on alkalinity could be derived. To investigate the kinetics, crystal growth was considered to be independent of nucleation, as suggested by the uniform particle size (3.1 to 3.5 μm) of the synthetic phillipsite crystals. Therefore, the rate of nucleation can be expressed by the equation

$$\left(\frac{dN}{dt}\right)_T = K_n C_n^a \quad (1)$$

where N is the number of nuclei (a critical number of nuclei are required for crystal growth to begin), K_n is a reaction rate constant, C_n was taken to be the hydroxide concentration and a is the reaction order. The induction period is taken to be equivalent to the nucleation rate. The order of the reaction was evaluated by plotting $\log (dN/dt)_T$ versus $\log (\text{OH}^-)$. The nucleation reaction was found to be second order in hydroxide concentration as shown in Figure 7, where θ again is the induction time (when crystal growth commences).

In a similar manner, an expression was developed for the rate of crystallization as a function of alkalinity. The crystal growth rate can be expressed by the equation

$$\left(\frac{dW_c}{dt}\right)_T = K_c C_c^a \quad (2)$$

where W_c is the crystal growth, K_c is a reaction rate constant, C_c is the concentration of the hydroxide and a is the reaction order. The quantity $(dW_c/dt)_T$ is the rate of crystallization and was taken to be equal to the maximum slope of the crystallization curve which was found to occur at 50% crystallization.

The reaction order for crystallization was evaluated in the same manner as that for nucleation, and from Figure 7 the order was found to be 1.75 or approximately second order. The values of the reaction rate constants and orders are summarized in Table V.

Table V.—Reaction Rate Orders and Rate Constants for
Phillipsite Nucleation and Crystallization

	Reaction Order a	Rate Constant $K_{100^\circ\text{C}}$
Nucleation	1.96	$0.013 \text{ l}^2/\text{hr mole}^2$
Crystallization	1.75	$6.748 \times 10^{-12}/\text{hr mole}^2$

From these experimental data for phillipsite crystallization, it was concluded that (1) the nucleation and growth rates increased with hydroxide concentration, (2) the rates of nucleation and crystallization were proportional to the hydroxide concentration according to second-order kinetics and (3) as the phillipsite crystals were not found to be pseudomorphic with the

reacting alumina-silica gel, phillipsite probably was formed by a condensation-polymerization reaction with some dissolved aluminosilicate species. These data are consistent with those of Ciric (12) for zeolite A crystallization, in which at relatively low alkalinities, the growth rate of zeolite A was found to be second order in hydroxide concentration. Ciric concluded from this second order relationship that dimers or cyclic tetramers possibly are the building blocks for the zeolite.

The experimentally determined order for crystallization was 1.75. As crystal growth takes place very rapidly, the difference between the expected reaction order of 2.00 and the observed 1.75 may reflect mass transfer limitations in the availability of nutrients for the crystal growth.

Properties. The synthetic phillipsite was characterized with respect to thermal stability and sorptive properties and some comparisons were made with natural K, Na-phillipsite from Rome, Oregon. The thermal stabilities of the phillipsites were determined by heating a sample to a set temperature, maintaining it at this temperature for eighteen hours, cooling, and measuring the crystallinity of the activated sample by X-ray techniques. Samples were heated to progressively higher temperatures and the results of this thermal treatment are shown in Figure 8. The synthetic phillipsites are stable to 300°C, with the one having the higher silica-alumina ratio being somewhat more stable. The natural phillipsite from Rome, Oregon, demonstrated a high thermal stability due to its high silica-alumina ratio of 6 to 7.

The phillipsites were characterized further by determining their effective pore diameters by adsorbing molecules of various dimensions into the activated zeolite. At the low gas pressures (less than one atmosphere), it was found that the only gases that any of the phillipsites tested would adsorb were water and ammonia. From this, it can be concluded that the effective pore diameter of phillipsite is 2.60 to 2.65 Å, which is consistent with the crystal structure of phillipsite.

The effect of activation temperature on adsorption capacity was determined on a synthetic phillipsite (Run Number N-7) using ammonia as the sorbate gas. The phillipsite was activated by heating to a set temperature while under a vacuum of less than 0.003 mmHg and maintained at that temperature and pressure for 12 hours. The sample was allowed to cool to 25°C and the adsorption capacity was determined at 100 mmHg. As also can be seen in Figure 8, the adsorption capacity for phillipsite was found to be sensitive to activation temperature, with a maximum capacity achieved with a 300°C to 350°C activation. This sensitivity indicates the high degree of coordination of water to the cations.

Equilibrium adsorption isotherm data were developed for synthetic N-7 phillipsite at 25°C using ammonia as the sorbate.

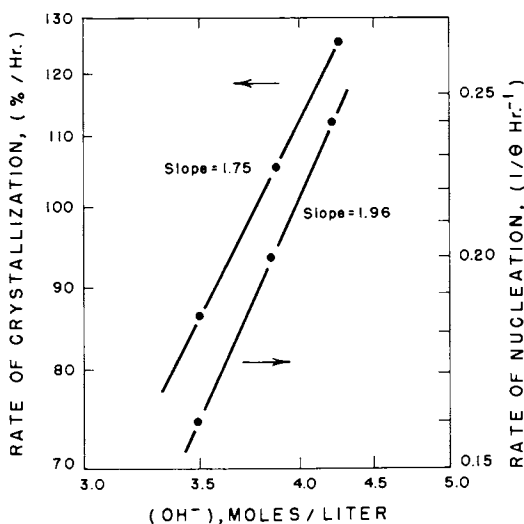


Figure 7. Determination of the reaction rate order for nucleation and for crystallization

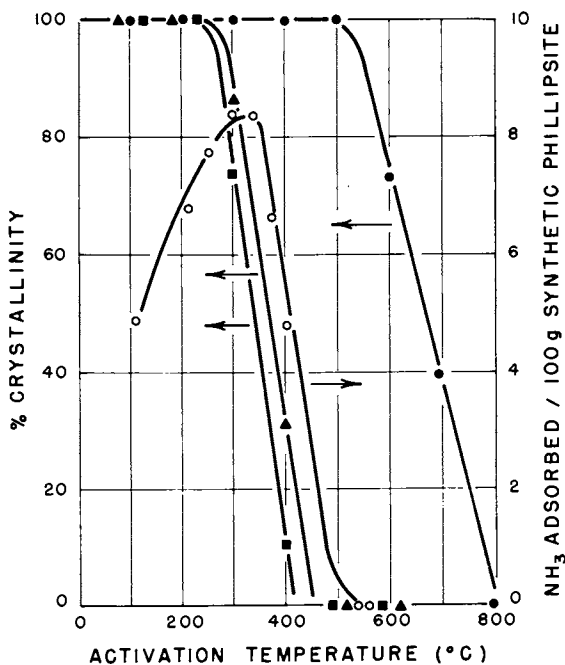


Figure 8. Thermal stability of various phillipsites and dependence of adsorption capacity on activation temperature. \blacktriangle , synthetic phillipsite, $\text{SiO}_2/\text{Al}_2\text{O}_3 = 5.24$; \blacksquare , synthetic phillipsite, $\text{SiO}_2/\text{Al}_2\text{O}_3 = 4.51$; \bullet , natural phillipsite, Rome, Ore.; \circ , synthetic phillipsite, $\text{SiO}_2/\text{Al}_2\text{O}_3 = 5.24$.

The material was activated to 325°C under vacuum for 12 hours and the results are plotted in Figure 9. Adsorption rate data were developed for both ammonia and water sorbed into the synthetic phillipsite. These rate data were essentially identical to those reported for the Rome, Oregon phillipsite (13,14). At 65°C, phillipsite rapidly adsorbed both water and ammonia with capacities of 9.55 wt.% (22 mmHg) and 5.25 wt.% (80 mmHg), respectively. At 25°C, however, phillipsite rapidly adsorbed ammonia, but the rate of adsorption of water was slow. The rate curve was almost linear, with a slope of 0.033 wt.% per minute, suggesting that phillipsite might be of use in removing ammonia in a water-containing system as has been reported in another paper (13).

CONCLUSIONS

The general objectives of this research were to (1) delineate the conditions of synthesis for phillipsite, (2) experimentally determine the nucleation and crystallization kinetics for phillipsite formation and (3) characterize some of the properties of this zeolite.

Phillipsite was found to form most readily from the less siliceous batch compositions; and as the amount of silica in the batch was increased, phillipsite became less stable and other zeolitic phases were found to form with or replace it. It has been reported that phillipsite is the dominant phase in natural zeolite deposits where the activity of silica is low; and phillipsite is less common, if not totally absent, in deposits with high silica activity (15). Clinoptilolite formation was indicated in the siliceous batch compositions in which some calcium was added.

The ratio of sodium to potassium in the starting reaction mixture was also a critical parameter in the synthesis of phillipsite as a single phase. The range of sodium-potassium ratios in the batch mixture, in which phillipsite formed stably as a pure phase, was narrow (between $K/(Na+K)$ of 0.10 to 0.20).

In the reacting systems where chloride was added, the anion addition had a strong effect on the metastable zeolitic phases found to occur with phillipsite. In the high-chloride synthesis system studied (Figure 2), mordenite was found to replace phillipsite; whereas in using the same batch composition with much less chloride added (Figure 3), phillipsite formed with erionite. In both the high- and low-chloride systems, analcime was found to be a transformation product of the phillipsite. An analogy was found between this synthesis system and the natural occurrence of phillipsite in the sedimentary deposits of Owens and Searles Lakes, California. These lakes were connected during the Pleistocene Period, and received detrital sediments and rhyolitic ash from the same source (2). Water progressively passed from Owens to Searles Lake where salinities were consistently high. There is, however, an absence of saline minerals in Owens Lake. In the saline, alkaline environment, phillipsite was the primary zeolite found

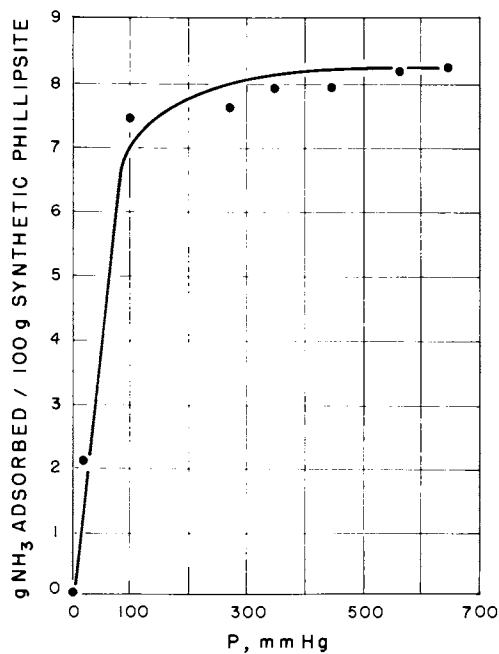


Figure 9. Equilibrium adsorption isotherm for phillipsite at 25°C

along with analcime. In non-saline Owens Lake, phillipsite was found to occur with erionite, clinoptilolite and analcime. The absence of clinoptilolite from the synthetic runs in the system studied may reflect a lack of calcium or a lack of silica activity.

For the kinetics of phillipsite formation, the rates of nucleation and crystallization increased with alkalinity as a second order function of the hydroxide concentration. These data are consistent with that of Ciric (10) for zeolite A crystallization and would indicate that dimers or cyclic tetramers are the building blocks for phillipsite.

Property data confirmed phillipsite to be a small-pore molecular sieve zeolite with an effective pore diameter of 2.60 to 2.65 Å. Phillipsite might be of particular interest in an adsorption process in which it is desired to remove either ammonia or water from a gas stream, or in removing ammonia from a water-containing system.

References

1. Levy, A., *Ann. Phil. New Ser.*, London, 10:361 (1825).
2. Hay, R.L., Zeolites and Zeolitic Reactions in Sedimentary Rocks, GSA Special Paper, No.85 (1967).
3. Meier, W.M., Molecular Sieves, Society of Chemical Industries, London (1968).
4. Smith, J.V., *Mineral. Soc. America, Spec. Paper No.1* (1963).
5. Rinaldi, R., Pluth, J.J. and Smith, J.V., Molecular Sieves, Recent Progress Reports, Leuven University Press (1973).
6. Barrer, R.M., and White, E.A.D., *J. Chem. Soc.*, 1561 (1952).
7. Barrer, R.M., Baynham, J.W., Bultitude, F.W., and Meier, W.M., *J. Chem. Soc.* 195 (1959).
8. Beard, W.C., Molecular Sieve Zeolites, ADV. Chem. Ser. 101, A.C.S., Washington, D.C. (1971).
9. Steinfink, H., *Acta Crystallogr.*, 15:644 (1962).
10. Sersale, R., Aiello, R. and Vero, E., *Periodico di Mineralogie*, Anno. XXXIV, N.2-3 (1965).
11. Kuhl, G.H., *Amer. Mineral.*, 54:1607 (1969).
12. Ciric, J., *J. Colloid Interface Sci.*, 28:315 (1968).
13. Hayhurst, D.T., Zeolite '76, An International Conference on the Occurrence, Properties and Utilization of Natural Zeolites, Pergamon Press (1976) in press.
14. Hayhurst, D.T., Ph.D. Thesis, Worcester Polytechnic Institute, Worcester, Mass. (1976).
15. Hay, R.L., *Amer. Mineral.*, 49:1366 (1964).

Synthesis of Faujasite by Recrystallization of High-Silica Zeolites

HARRY E. ROBSON and KENNETH L. RILEY

Exxon Research and Development Laboratories, Baton Rouge, La.

DALE D. MANESS

University of Texas, Austin, Tex.

ABSTRACT

Hector clinoptilolite was observed to recrystallize to faujasite by a treatment in 30% NaOH at 100°C. Other clinoptilolites and other high SiO₂/Al₂O₃ zeolites did not show this reaction. The differences were traced to chloride content of the source material and to the Na⁺ and K⁺ contents of the minerals. Silica/alumina ratio of the faujasite phase was 4.2. This could be increased to 4.7 by partial neutralization of the NaOH at an intermediate point in the recrystallization process.

Introduction

Natural faujasite is so rare a mineral that it would hardly rate a footnote in geology literature were it not the prototype for Molecular Sieve Types X and Y. Indeed the conditions for its formation seem so particular and peculiar that its occurrence outside the laboratory is most unlikely. Still X and Y are tonnage commodities and the search for low cost materials for their synthesis continues. It is predictable that this search should turn to natural materials and that synthesis conditions should converge on what we believe were the conditions which produced natural faujasite.

Sudo and Matsuoka(1) treated volcanic glass with NaOH/NaCl and obtained sodalite + faujasite (1959). More recently Miyata and Okazaki(2) reported conversion of mordenite and clinoptilolite to a faujasite-type and P-type zeolites. Negishi and Nakamura(3) treated clinoptilolite with NaOH-NaCl solutions at 100°C and observed the conversion sequence clinoptilolite → amorphous material → X-type zeolite → sodalite.

We observed the recrystallization of mordenite to faujasite as an accidental side effect of attempts to prepare silica-deficient mordenite by caustic extraction.(4) Similar treatments of other high SiO₂/Al₂O₃ materials revealed several

which are recrystallized to faujasite by simple NaOH treatment. Best results were obtained on clinoptilolite from Hector, California. Other clinoptilolites from Western USA were inactive. The difference has been attributed to specific composition differences between the Hector sample and the other minerals. The results of this study appear relevant to the conditions which are supposed to have produced natural faujasite.

Experimental

Clinoptilolite samples in this work are all from Western U.S.A. The sample from Hector, Calif. was purchased from Ward's Natural Science Establishment. Nevada clinoptilolites were supplied by K. S. Deffeyes; their proximate locations are given in Tables II and III and more completely described in the literature.^(5,6) Natural mordenite is from Nova Scotia, Canada, and wash purchased from Wards. One synthetic mordenite came from Huber Corp., the other from Norton and was designated by them as "ultra pure". Sources of other high-silica materials which were tested are given in Table I.

Natural materials were ground to about 100 mesh in a mortar for earlier experiments or with a Braun Pulverizer for later samples. Synthetic materials and pumice were received in powder form and tested as received.

The standard recipe used for the conversion reaction was (by weight) one part high-silica zeolite, for example, clinoptilolite, 1 part water, and 0.3 parts NaOH. In a typical run 10 grams of high-silica zeolite was slurried with 7 milliliters of deionized water, followed by the addition of 6 grams of a standard 50% by weight NaOH solution. This mixture was well stirred, poured into a 2 ounce square sample bottle* and capped (including a polyethylene film seal). The vessel was immersed in an oil bath maintained at 100°C and removed the next day (16 hours was the usual reaction time). After air-cooling, the sample was washed with deionized water until the pH of the wash was 10.5 or below. The solid portion was dried overnight at 130°C and analyzed by x-ray diffraction.

In most cases different slurry compositions were achieved by changing the ratio of the three components: clinoptilolite, 50% NaOH solution, water. Multiple samples of the slurry were bottled and heated for progressively longer times in the oil bath before washing. Samples treated above 100°C were contained in 200 ml. monel autoclaves at autogenous pressure.

Water soluble promoters were added to the formula by substituting an aqueous solution of the promoter for the deionized water. When the dissolution of the promoter could

*To check for a container effect, selected experiments were repeated in polyethylene lined containers; results were substantially equivalent.

not be effected at the desired level, the solid was premixed with the high silica zeolite followed by the standard sequence. The promoters were all of B & A reagent grade quality as were other chemicals utilized in the conversion and in normal laboratory procedures. When the inhibiting effect of certain cations on the recrystallization became apparent, the clinoptilolite was pretreated (4 hr. at reflux) with 2N HCl. In some cases sodium aluminate was added to the formula to replace alumina extracted by pretreatment; these recrystallization experiments are described in Table VI.

Later in the project, we observed higher $\text{SiO}_2/\text{Al}_2\text{O}_3$ in the faujasite product by partial neutralization of the NaOH after the initial digestion period. This was accomplished by removing the sample from the oil bath, adding a calculated amount of 12N HCl, agitating, and returning the bottle to the oil bath to complete the recrystallization. These experiments are described in Table VII.

Crystallization was followed by analysis of the solid product quantitatively by x-ray powder diffraction. Prepared mixtures of Hector clinoptilolite and Linde Na-Y were used to establish a calibration curve for the fraction faujasite present in the mixture based on sum of intensities of the ten strongest faujasite lines. Unit cell size of the faujasite phase was calculated from the observed 2θ value of the 664 line; $\text{SiO}_2/\text{Al}_2\text{O}_3$ was estimated from unit cell size. Surface area was calculated from N_2 sorption by Langmuir method. Particle size was estimated from the transmission electron micrograph.

Results and Discussion

Mild caustic treatment of mordenite is known to extract silica; vigorous caustic extractions produce recrystallization to "lower zeolites" such as phillipsite or non-zeolites such as sodalite. By a simple caustic treatment, Huber mordenite was recrystallized to a "lower zeolite", faujasite. Since this result was unexpected,* other mordenite samples and a variety of high silica materials were tested under these conditions as shown in Table I. Natural mordenite and ultra-pure synthetic mordenite (Norton) showed only a trace of faujasite after similar treatment. Ferrierite and erionite were unconverted; pumice and equilibrium silica/alumina cracking catalyst showed significant amounts of faujasite along with gmelinite or phillipsite. By far the best result was obtained on clinoptilolite from Hector, Calif. which gave faujasite as the only crystalline product and 54% of the crystallinity of Linde's Na-Y.

Optimum conditions for recrystallization of Hector clinoptilolite to faujasite were 0.22 NaOH/mineral and 0.5 H_2O /mineral (weight basis) treating 16 hours at 100°C. None of these optima

*This work predated publication of references 2 & 3.

TABLE I.- Caustic treatment of mordenite and other high-silica materials
(1.0 H₂O/Mineral, 0.30 NaOH/mineral, 100°C, 16 hr.)

Exp.	Source Material	Product*
1	Mordenite (Huber)	faujasite
2	Mordenite (Norton)	mordenite + faujasite
3	Mordenite (Nova Scotia)	unidentified + faujasite (trace)
4	Ferrierite (Br. Columbia)	ferrierite
5	Erionite (Jersey Valley, Nev.)	erionite + sodalite
6	Pumice (J. T. Baker)	faujasite (13)
7	SiO ₂ /Al ₂ O ₃ Catalyst (Davison)	faujasite (09) + gmelinite
8	Clinoptilolite (Hector, Calif.)	faujasite (54)

*numbers in parenthesis following "faujasite" indicate crystallinity compared to Linde Na-Y from intensity of x-ray diffraction pattern.

were sharp; there seems to be a reasonable operating range which is not difficult to find. However, the optimized process gives a faujasite product only slightly better than the initial experiments (63% of the crystallinity of Na-Y). At 150°C, analcime was the principal product although some faujasite was observed at that temperature. Excessive NaOH (0.5 NaOH/mineral) produced sodalite instead of faujasite. At the preferred composition, some conversion to faujasite was observed at 25°C after 21 days exposure.

Unit cell sizes for these products are 24.78 to 24.80 Å indicating a SiO₂/Al₂O₃ of 4.0 to 4.3 for the faujasite phase which places them intermediate between Type Y and Type X. Particle size is about 0.1 μm as observed by electron microscope; this is significantly less than either X or Y. Surface areas were 650-700 m²/g. calculated by the Langmuir method; this is nearly proportional to observed faujasite crystallinity by X-ray diffraction.

At this point, the study was expanded to include a number of other natural clinoptilolites from western U.S.A. as shown in Table II, the resulting products showed no faujasite except in the case of Hector.

TABLE II.- Recrystallization* of Clinoptilolites From Western USA

<u>Exp</u>	<u>Source of Mineral</u>	<u>Product</u>
9	Hector, Calif.	Faujasite (63)
10	Red Canyon, Nev.	Clinoptilolite
11	Elko, Nev.	Phillipsite
12	Eastgate, Nev.	Unidentified
13	Fish Creek Mtns.	Phillipsite
14	Rome, Ore.	Phillipsite

*treated 24 hr. at 100°C with 1.0 H₂O/mineral and 0.3 NaOH/mineral.

This posed the question: what is the peculiar property of the Hector source which makes it more suitable for recrystallization to faujasite than other natural clinoptilolites? Or the parallel question: why does the mordenite supplied by Huber readily recrystallize to faujasite whereas other synthetic mordenites and natural mordenite do not?

Conversion of the source materials to the hydrogen form was instructive. Acid pretreatment and washing destroyed the capacity to recrystallize to faujasite for both Huber mordenite and Hector clinoptilolite. Further when the HCl extract was concentrated by evaporation and added to an inert mordenite (Norton), it greatly enhanced the faujasite yield by NaOH treatment. It appeared that some metallic cation in Huber mordenite and Hector clinoptilolite was promoting recrystallization to faujasite. This proved to be in error; the actual promoter was chloride ion present in the source materials but removed by acid treatment.

The Hector clinoptilolite contained significant levels of chloride, (2.9 wt. % chloride), while in general the chloride contents of the inactive Nevada clinoptilolites were low (less than 1% chloride). However, the lower Jersey Valley sample possessing an intermediate level of chloride showed zero activity for the conversion. Although the chloride content is important, other factors were found to exert considerable influence on the formation of faujasite from clinoptilolite.

The clinoptilolite sample from Fish Creek Mtns. was selected as a reference material for this study because the x-ray diffraction pattern was quite similar to Hector clinoptilolite. Samples were treated with increasing concentrations of NaCl to promote conversion to faujasite. The results are shown in Figure 1. Chloride concentration has a pronounced effect up to about 8 wt. percent, beyond this point, more chloride has relatively small influence on conversion.

TABLE III.- Analyses on Natural Clinoptilolites (Wt. %-dry basis)

<u>Sample</u>	<u>Hector, Calif.</u>	<u>Fish Creek Mtns, Nev.</u>
SiO ₂	70.3	74.0
Al ₂ O ₃	12.3	12.9
Na	7.86	1.83
K	1.02	2.44
Fe	0.80	0.88
CaO	2.20	2.81
MgO	0.53	0.63
Cl	2.9	0.0

Clinoptilolite from Hector contained 2.9 wt. % chloride as received; additional chloride gave no improvement in its conversion to faujasite. By sequential washing, the chloride content of Hector clinoptilolite was reduced to 0.8 and 0.2 wt. %. As shown in Figure 1, this washing substantially reduced faujasite content after standard recrystallization treatment. However, at all chloride levels, the Hector sample gave more faujasite than Fish Creek Mountains clinoptilolite.

Other anions were tested for promotion of faujasite recrystallization by adding their sodium salts to Fish Creek Mountains clinoptilolite; concentration was equivalent to 3 wt. % chloride. Of the anions tested, cyanide and nitrate were nearly as effective as chloride; bromide was active but at a much lower level. Other anions were substantially ineffective. The promoting effect of chloride ion has been observed previously (2,3) but not explained. Chloride has long been recognized as a "mineralizer" or crystallization aid in geochemical systems.

Other Nevada clinoptilolites were tested for recrystallization to faujasite after including sufficient NaCl in the standard formula to give 3 wt. % chloride on mineral. Table IV shows the response to the treatment together with sodium and potassium ion contents of the mineral as received. The combination of high initial Na⁺ and low K⁺ content seems to be necessary for conversion to faujasite. There remain unexplained differences in these samples' capacity to make faujasite after chloride content has been equalized and the Na⁺ and K⁺ contents considered. For example Red Canyon, North should be a better source material than Red Canyon, Shoshone R. whereas the results in Table IV indicate the opposite. The most probable reason is K⁺ ions in non-exchangeable positions which are not equilibrated with excess Na⁺ in the liquid at 100°C. The Fish Creek Mountains sample was again chosen for further study because it showed the

TABLE IV.- Recrystallization of Nevada Clinoptilolites with Chloride Promotion (3 wt. % Chloride)

<u>Experiment</u>	<u>Sample</u>	<u>Wt. % K*</u>	<u>Wt. % Na*</u>	<u>% Faujasite</u>
15	Fish Creek Mtns.	2.44	1.83	25
16	Lower Jersey Valley	2.46	2.46	17
17	Red Canyon, Shoshone R.	3.39	0.26	8
18	Elko Oil Shale Plant	2.48	0.66	Trace
19	Red Canyon, North	1.61	0.81	0
20	Hector (reference)	1.02	7.86	45

*as received

most improvement in conversion activity when promoted with NaCl. Various metal chloride salts were added as promoters in the standard recrystallization treatment; all experiments contained 3 wt. % chloride ion. Results are given in Table V.

TABLE V.- Cation Effect in Recrystallization* of Fish Creek Mtns. Clinoptilolites

<u>Experiment</u>	<u>Additive</u>	<u>% Faujasite</u>
21	LiCl	21
15	NaCl	25
22	KCl	5
23	RbCl	0
24	CsCl	0
25	MgCl ₂	18
26	CaCl ₂	8
27	SrCl ₂	4
28	BaCl ₂	1
29	NH ₄ Cl	10
30	FeCl ₂	16
31	FeCl ₃	12
32	ZnCl ₂	0
33	CdCl ₂	17
34	AlCl ₃	10

*treated 16 hrs. at 100°C with 1.0 H₂O/mineral and 0.3 NaOH/mineral; 3 wt. % chloride on mineral.

Since sodium ion is the major cation present due to NaOH in the formula, NaCl addition should be neutral regarding the cation. All other cations appear to be inhibitors to some degree, but with some interesting differences in their effectiveness.

The inhibiting effect of potassium ion is quite understandable in view of the synthesis literature.(7) It seems logical that still larger Rb^+ and Cs^+ should be still more potent inhibitors. Likewise Ca^{+2} , Sr^{+2} , and Ba^{+2} are progressively more poisonous while Mg^{+2} is comparatively innocuous. Zinc appears unique as an inhibitor; its near neighbors in the periodic chart are much less potent.

In order to remove inhibiting cations (particularly potassium) from the Nevada clinoptilolites, samples were refluxed 4 hrs. in 2 N HCl. After washing and drying, they were tested in the standard recrystallization treatment and found to be inert. However addition of sodium aluminate to replace alumina extracted by HCl restored their capacity to recrystallize to faujasite. Results are shown in Table VI.

TABLE VI.- Recrystallization* of Nevada Clinoptilolites After HCl Pretreatment

Exp.	Sample	Wt. % Chloride	NaAlO ₂ /Mineral	% Faujasite
35	Fish Creek Mtns.	3	--	0
36	Fish Creek Mtns.	3	0.08	33
37	Fish Creek Mtns.	3	0.18	58
38	Fish Creek Mtns.	6	0.18	66
39	Jersey Valley, lower	6	0.17	46
40	Red Canyon, Shoshone R.	6	0.53	33
41	Elko Oil Shale Plant	6	0.33	42
42	Red Canyon, north	6	0.40	55

*treated at 100°C with 1.0 H₂O/mineral and 0.3 NaOH/mineral

With this treatment and increasing chloride level to 6 wt. %, all the Nevada clinoptilolites were active.

Kinetics of the recrystallization reaction were studied using the Hector sample under standard conditions with multiple samples; one sample was withdrawn from the 100°C. batch at 30 minute intervals, cooled and washed. Results are shown in Figure 2. Three regions were identified: (1) induction, crystallinity of source material disappears; (2) faujasite crystallization, rapid faujasite formation building to maximum crystallinity;

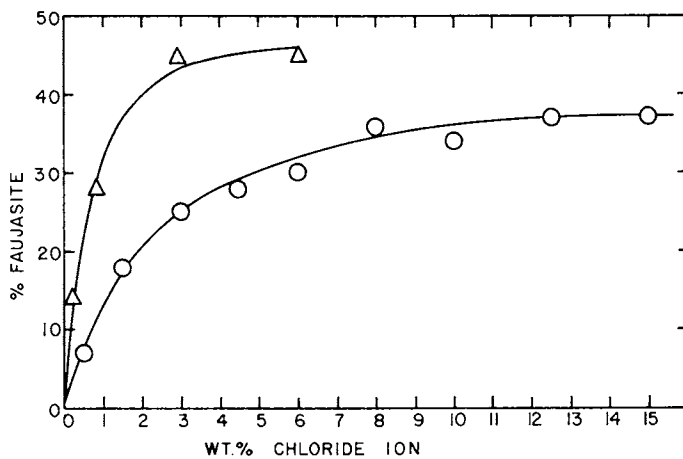


Figure 1. Effect of chloride on recrystallization. Δ , Hector; \circ , Fish Creek mountains.

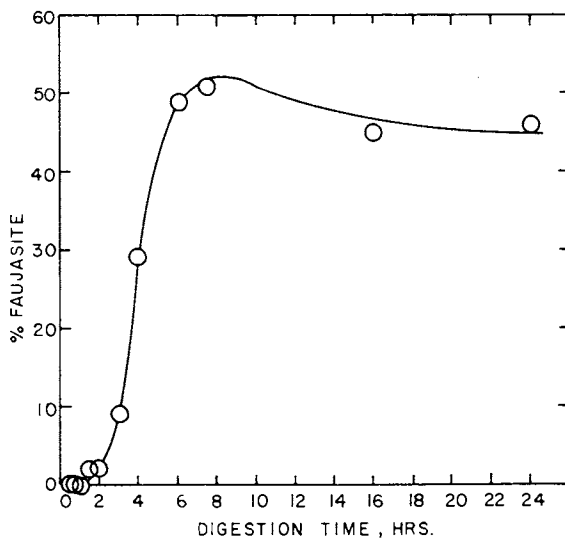


Figure 2. Effect of digestion time on recrystallization of Hector clinoptilolite

(3) aging, constant or decreasing crystallinity. Nucleation of the faujasite occurs in the first or induction period at high pH. However, once nucleated, faujasite crystal growth can proceed at milder conditions. Reducing the alkalinity at the end of the induction period substantially increases the silica content of the faujasite phase.

Multiple samples of Hector clinoptilolite were prepared with the standard recrystallization formula. After selected induction periods (100°C), samples were removed from the oil batch, selected amounts of 12 N HCl added, the contents mixed, and the bottles resealed and returned to the batch for 16 hours. Results are given in Table VII.

TABLE VII.- Partial Neutralization After Induction Period
(Hector sample, standard recrystallization)

<u>Exp.</u>	<u>Time at 100°C</u> <u>Before HCl</u> <u>Addition (hr.)</u>	<u>NaOH/mineral</u> <u>After HCl</u> <u>Addition</u>	<u>%</u> <u>Faujasite</u>	<u>Unit Cell</u> <u>Size (Å)</u>
20	no HCl added	0.30	45	24.80
43	1.5	0.24	44	24.77
44	1.5	0.19	40	24.70
45	1.0	0.19	22	24.71
46	2.0	0.19	17	24.68
47	2.5	0.19	12	too weak to measure

For Hector source, neutralization to 0.19 NaOH/mineral at 1.5 hours is near optimum. This causes only a small loss in faujasite content but reduces unit cell size of the faujasite phase to 24.70 Å which is equivalent to $\text{SiO}_2/\text{Al}_2\text{O}_3 = 4.7$. This compares to 24.80 Å and $\text{SiO}_2/\text{Al}_2\text{O}_3 = 4.2$ for the standard recrystallization without partial neutralization.

Conclusions

All zeolites are thermodynamically unstable and should be expected to recrystallize toward sodalite given favorable conditions; a highly alkaline liquid medium and sufficient time near 100°C often produces recrystallization. It is surprising that there is a considerable area of metastability which permits recrystallization to faujasite instead of sodalite or phillipsite. This study shows that the temperature range extends at least from 25° to 150°C.

Hector clinoptilolite appears uniquely suited for recrystallization to faujasite because of its high soda and low potassa

content and because of its natural chloride content. However these conditions probably exist in a great many natural materials such as pumice or volcanic ash. If minerals are used as source materials for faujasite synthesis, addition of NaCl or NaAlO₂ seems quite feasible; acid treatment to reduce potassa is less attractive. It is improbable that precrystallization to morde-nite or clinoptilolite is a necessary step in faujasite synthesis.

High silica faujasite by nucleation at high pH followed by crystal growth at more moderate alkalinity as reported here could have occurred in ground water action or volcanic deposits. If the lava were also low in potassium and if chloride were present in the lava or ground water, conditions would be favorable for crystallization of natural faujasite. Nucleation at high pH plus crystal growth and lower pH is in principal similar to the seeding techniques now used commercially(8) to prepare Zeolite type Y.

Literature Cited

1. Sudo, T., and Matsuoka, M., *Geochim. Cosmochim. Acta*, (1959), 17, 1.
2. Miyata, Y., and Okayaki, S., *Kogyo Kagaku Zasshi*, (1970), 73, 1940-6.
3. Negishi, T., and Nakamura, H., *Kobutsugaku Zasshi*, (1970), 10, 72-81.
4. Young, D.A., U.S. Patent 3,326,797 (June 20, 1967).
5. Deffeyes, K. S., *J. Sedim. Petrol*, (1959), 29, 602.
6. Sheppard, R.A., "Molecular Sieve Zeolites," Vol. 101, p. 279, American Chemical Soc., Washington D.C. (1971).
7. Khatami, H., *Proceedings of the Third International Conference on Molecular Sieves*, No. 116, Zurich (1973).
8. Jenkins. E. E., U.S. Patent 3,492,090, (January 27, 1970).

Kinetic Studies of the Growth of Zeolites of the Faujasite and N-A Type

HARTMUT KACIREK and HANS LECHERT

Institute of Physical Chemistry of the University of Hamburg,
Laufgraben 24, 2000 Hamburg 13, West Germany

ABSTRACT

The results of kinetic studies of faujasite growth are compared with those of the growth of the zeolite N-A in a TMA/Na-system. A model of crystallization is developed from the experimental results. From this, methods of preparation of N-A zeolites can be deducted.

Introduction

Earlier studies of faujasite growth in the hydrothermal system $\text{Na}_2\text{O}/\text{Al}_2\text{O}_3/\text{SiO}_2/\text{H}_2\text{O}$ resulted in methods of preparation of faujasites of compositions varying in a wide range, using small amounts of seed crystals of zeolite X with small average radii. Under certain conditions the growth can be described by a simple kinetic equation of the form

$$\frac{dx}{dt} = 3 k \cdot x^{2/3} \cdot x_0^{1/3} \cdot \bar{r}_0^{-1} \quad (1)$$

where x and x_0 are the amounts of faujasite at times t and t_0 , \bar{r}_0 is the average radius of the seeds and k the rate constant, describing the linear rate of the growth. Further it was shown that crystal growth takes place at the interface between crystals and solution. A direct solid-solid conversion from amorphous material to crystalline products could be excluded.

For final products of equal Si/Al ratios, the rate constant k proves to be proportional to the silicate concentration in the liquid phase. For Si/Al ratios between that of zeolite X and a silica-rich Y type, rate constants vary over three orders of magnitude. Simultaneously, the activation energy in-

creases considerably. A model for the faujasite crystallization was developed in which the rate-determining step of growth seems to be given by the condensation of silicate species, specific for the special structure. A relation of the silicate species, which might be present in solution during the crystallization process, to k , was discussed(2).

Undoubtedly, the TMA/Na system is more complicated than the Na system because of additional parameters given by different TMA concentrations, the TMA/Na ratio and the possibility of additional silica species.

Since the studies of Barrer and Denny(3) many zeolites have been synthesized in systems with organic bases, especially alkyl ammonium hydroxide. Numerous papers published on these experiments are summarized by Breck(4). In agreement with Aiello and Barrer(5), in the TMA/Na system within the ranges of concentration we studied, the following zeolites were found by x-ray diffraction: Na-,TMA-gismondine (N-P), only from batches with low TMA concentrations; Na-,TMA-faujasites (N-X, N-Y); Na-,TMA-erionite (N-E); Na-,TMA-sodalite (N-T); Na-,TMA- A type zeolite(N-A). In the following text, we will use the notation N-A instead of ZK-4 or α .

Despite the complexity of the TMA/Na system, results obtained by Wieker(6) on the distribution of anions in silicate solutions containing TMA ions make studies on this system highly interesting in the light of our model on faujasite growth. In 1.8 M solutions with $\text{TMA}/\text{SiO}_2 = 1$, Wieker found as the only silicate species an ion with the structure of a double-four-membered-ring (DFR). With increasing dilution, mono-, di-, cyclotetra-, cyclohexa-, and double-three-ring silicate could be detected.

Following our crystallisation model for faujasite growth, it can be asked whether these DFR-species can be used as building units of the N-A structure.

Experimental

Analysis of the Crystalline Products. For the kinetic measurements, mixtures of pure N-A and amorphous aluminosilicate ($\text{Si}/\text{Al} = 1$) were prepared, and the intensity of some characteristic peaks, obtained by diffraction measurements with the Guinier method with Cu-K α radiation, were compared with the noise level of the measurements. The measured relative intensities have been plotted against the compositions. The limit of error of the quantitative analysis of

the N-A amount was about five percent.

The Si/Al ratio was determined by x-ray fluorescence analysis within a limit of error of about one percent.

Sample Preparation. All reactant mixtures were crystallized in polyethylene, or, preferably, in teflon vessels. At certain time intervals samples were taken, filtered and washed to near-neutrality.

The aluminosilicate gels were prepared by mixing alkaline aluminate solutions or TMA-aluminate solutions with water glass solutions or TMA-silicate solutions. In some cases TMA-Cl or NaCl was added and small amounts of NaA seeds with an average radius of about 0.25 μm were suspended in the reaction mixture after gelling.

TMA-aluminate solutions were prepared by dissolving $\text{Al}(\text{OH})_3$ in excess TMA-OH.

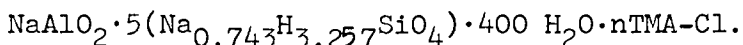
TMA-silicate solutions were prepared by dissolving freshly precipitated silicic acid in TMA-OH (TMA/SiO₂ = 1). These solutions were 1.1 to 1.4 normal.

TMA-OH solution was prepared from TMA-Cl by using a strongly basic ion-exchanger packed in a column. The exchange was carried out until at least ninety percent of the chloride was exchanged.

Results and Discussion

Preliminary experiments show that, similar to the growth of Y-type zeolites, formation of zeolite N-A can be accelerated by adding seeds of zeolite A, and the yield of N-A can be increased considerably.

For the study of the crystallisation curves gels with different concentrations of TMA and the following compositions have been prepared by mixing sodium aluminate solution and water glass solution. The mixtures correspond to zeolite N-A of a final product with an Si/Al ratio of 2.5. The composition of the reactant mixtures was



TMA-chloride and 5 % seeds of A-type with respect to the expected quantity have been added after the formation of the gel. It can be seen that the growth of zeolite N-A occurs, even if the TMA ion is added subsequently as the chloride (table I). The completely crystallized product contains a mixture of N-A and Y zeolite.

TABLE I.- Influence of TMA-concentration on the linear growth rates k (equ.3) and k' (equ. 5)

[TMA]/[Na]+[TMA]	Si/Al	k	k'	samples
		$\mu\text{m/h}$	$\mu\text{m/h}\cdot\text{moles}$	
0.333	2.32	$6.9\cdot 10^{-3}$	$1.1\cdot 10^{-2}$	412
0.5	2.40	6.1 "	1.0 "	413
0.6	2.44	4.9 "	1.0 "	414
0.667	2.58	3.2 "	1.0 "	415

As can be seen from Fig.1 the rate of crystallization of N-A is increased with increasing concentration of TMA ions, if the Na concentration is kept constant. The crystallization curves for the growth of zeolite N-A and zeolite Y have, in principle, a similar course.

Applying an expression, which has been developed for the growth of Y-zeolite in an earlier paper(1), one gets

$$x = (x_0^{1/3} + k \cdot x_0^{1/3} / \bar{r}_0 \cdot t)^3 \quad (2) \quad \text{or}$$

$$k = (x^{1/3} / x_0^{1/3} - 1) \bar{r}_0 / t \quad (3)$$

where the values of k can be taken from the experimental curves. For the growth of faujasites it has been shown that the rate constant k should be proportional to the concentration of silicate in the solution phase in a wide range of concentrations for the same Si/Al ratio in the final product:

$$k = k' \cdot c_{\text{SiO}_2} \quad (4).$$

According to the model developed for the growth of faujasite(2), only the concentration and the rate of reformation of those silicate species which are needed to build up the respective zeolite structure should be taken into account.

The rate of crystallization of zeolite N-A vanishes in a system containing only Na ions, and reaches a finite value if the hydrothermal system also contains TMA ions. This leads to the assumption that the presence of TMA favors the formation of a silicate species which is essential for the crystallization of desired N-A zeolite. Following this the concentration

of such a species should be proportional to the concentration of TMA with respect to the entire concentration of the alkaline ions given by $[TMA] + [Na]$. The good agreement of the values of

$$k' = k \cdot [TMA] / ([TMA] + [Na]) \quad (5)$$

taken from the curves of Fig.1 seems to be a proof for this idea. Fig.2 shows raster scan micrographs of the used A-type seeds and the mixture of zeolites N-A and N-Y of sample 414.

The aim of the following experiments was to develop procedures for the synthesis of pure zeolite N-A in a wide range of Si/Al ratios. Further, the variation of different parameters should give clues to a possible mechanism of the crystallization.

The experiments, which sometimes gave only poor information, are summarized below.

Influence of the Ratio TMA/Na on the Amount of Zeolite N-A in the Final Product. The Batches were prepared from TMA aluminate with a high excess of TMA-OH, SiO₂ as freshly precipitated silicic acid, different amounts of NaCl, and 2.5-3% of A-type seeds. The crystallization temperature was 88°C. The compositions of the reactant mixtures were TMA·AlO₂·5 TMA-silicate·400 H₂O·n NaCl.

TABLE II.- Formation of zeolite N-A from batches with different amounts of sodium ions

<u>Sample</u>	<u>[TMA]/[Na]</u>	<u>time h</u>	<u>%N-A</u>	<u>by-products</u>
1 N		92	trace	amorphous
1 N2/1	2	92	11	N-Y, N-E, N-T
1 N4/1	4	92	70	N-Y, (N-E), (N-T)
1 N6/1	6	92	90	N-Y
1 N8/1	8	92	90	N-Y

As mentioned above, no crystallization occurs if Na ions are absent. If TMA/Na exceeds 4, good yields of zeolite N-A can be obtained, but no pure products.

Preparation of Products with Different SiAl Ratio by Variation of $[OH^-]/[SiO_2]$, and $[H_2O]/[AlO_2^-]$. The batches were prepared from Na aluminate, silicic acid and TMA-Cl with 2.5% A-type seeds, and crystallized

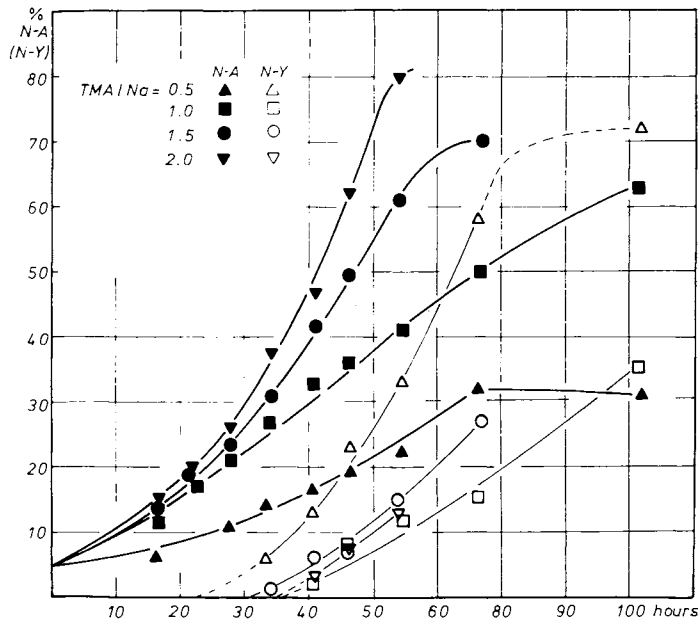


Figure 1. Crystallization curves for zeolite N-A (and N-Y) from batches with different concentrations of TMA

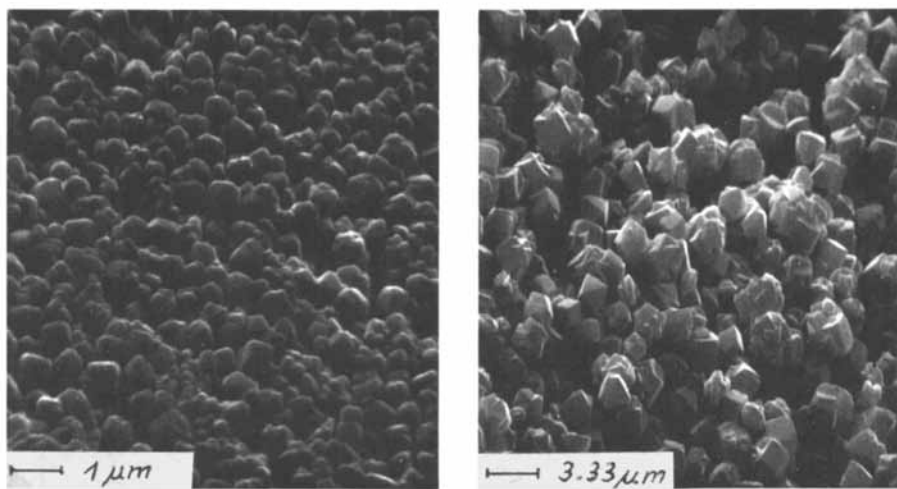


Figure 2. Raster scan micrographs of the used A-type seeds and of sample 414, which contains zeolite N-A (cubic form) and zeolite N-Y (octahedra)

at 88°C.

TABLE III.- Formation of zeolite N-A with different Si/Al ratios

Sample	$\frac{[\text{SiO}_2]}{[\text{AlO}_2^-]}$	$\frac{[\text{TMA}]}{[\text{Na}]}$	$\frac{[\text{OH}^-]}{[\text{SiO}_2]}$	$\frac{[\text{H}_2\text{O}]}{[\text{AlO}_2]}$	%N-A	by-products	Si/Al
428	1.5	5	0.533	200	100	---	1.46
429	1.75	5	0.457	200	100	---	1.61
430	2.00	5	0.400	200	55	N-E, N-T, N-Y	1.80
431	2.25	5	0.356	200	50	N-E, N-T(N-Y)	1.91
432	1.3	5	0.192	100	55	N-E, N-T	1.10
433	1.6	5	0.156	100	20	N-E, N-T	1.42
434	1.9	5	0.132	100	--	N-T	1.64
435	2.2	5	0.114	100	--	N-T	1.98

The results show that zeolite N-A with low Si/Al ratio can be prepared with high purity in this system. At higher Si/Al, however, nucleation and growth of zeolites N-E and N-T are dominant. As has been observed already for the syntheses of faujasite in the hydrothermal system containing only Na ions, at higher concentrations of silicate in the solution, corresponding with a lower ratio $[\text{H}_2\text{O}]/[\text{AlO}_2^-]$, nucleation of zeolites is favored in comparison with crystal growth.

Batches from Na Aluminate and TMA Silicate Solutions. The purpose of these batches was to favor the crystallisation of N-A by adding the silicate as DFR-silicate to the reaction mixture at the very beginning. The batches had the following compositions: $\text{NaAlO}_2 \cdot 0.25 \text{ NaOH} \cdot 3, 5, 7, 10 \text{ TMA-silicate} \cdot 240, 362, 486, 670 \text{ H}_2\text{O}$. After three days at room temperature and even after heating to 50° for one day no formation of a gel could be observed. After adding to the batches 1 mole of SiO_2 (as a sodium silicate solution) for each mole of aluminate, gelling was finished after one day. Following this, 3% of A-type seeds were suspended and the mixture heated to 88°C. The crystallization of the above-noted batches leads to the products summarized in table IV.

The results seem to be good, even for products with higher Si/Al ratios.

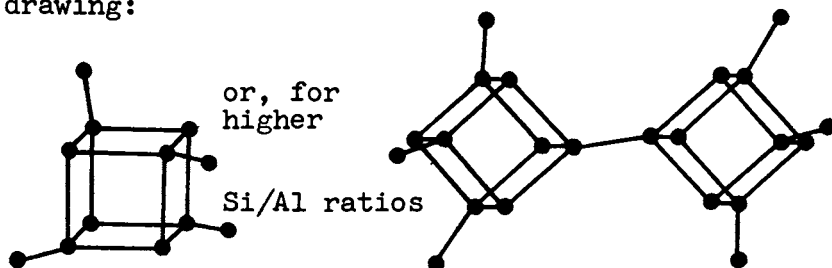
Altogether, the results remain unsatisfactory, however, which needs further reflection and examination.

Table IV.- Formation of zeolite N-A from TMA-silicate, sodium aluminate, and additional sodium silicate

Sample	$\frac{[\text{SiO}_2]}{[\text{AlO}_2]}$	$\frac{[\text{H}_2\text{O}]}{[\text{AlO}_2]}$	$\frac{[\text{TMA}]}{[\text{Na}] + [\text{TMA}]}$	%N-A	by-products	Si/Al
438	4	260	0.621	40	N-E, N-Y(N-T)	2.07
439	6	382	0.73	85	N-Y	2.21
440	8	506	0.793	80	N-Y	2.25
441	11	690	0.845	90	N-Y	2.65

Looking at a model of the A-type structure and considering that intact double-four-membered rings of the TMA-silicate are built into the structure, it can be seen that this structure can be constructed exclusively from the DFR-silicate ions and monomeric aluminate and silicate. These relations are demonstrated in the Fig. 3 a and b which show "pressed" graphs of the N-A structure. This kind of graphs are useful to represent arrangements of a large number of AlO_4 and SiO_4 tetrahedra.

Of the zeolites crystallizing from our reaction mixtures, only N-A contains double-four-membered rings. Using the model developed for the growth of faujasites, four monomers of silicate should condense with the DFR-silicate, giving the silicate species demonstrated in the following schematic drawing:



Otherwise, this model contains only Si-O-Al bonds. Referring to our model the rate of crystallization is determined by linking these silica species and crystal surface. These considerations, at first glance, seem to oversimplify the processes taking place during crystal growth.

In the following experiments, we will try, however, to choose conditions in the course of the syntheses which guarantee that mainly DFR-silicate and

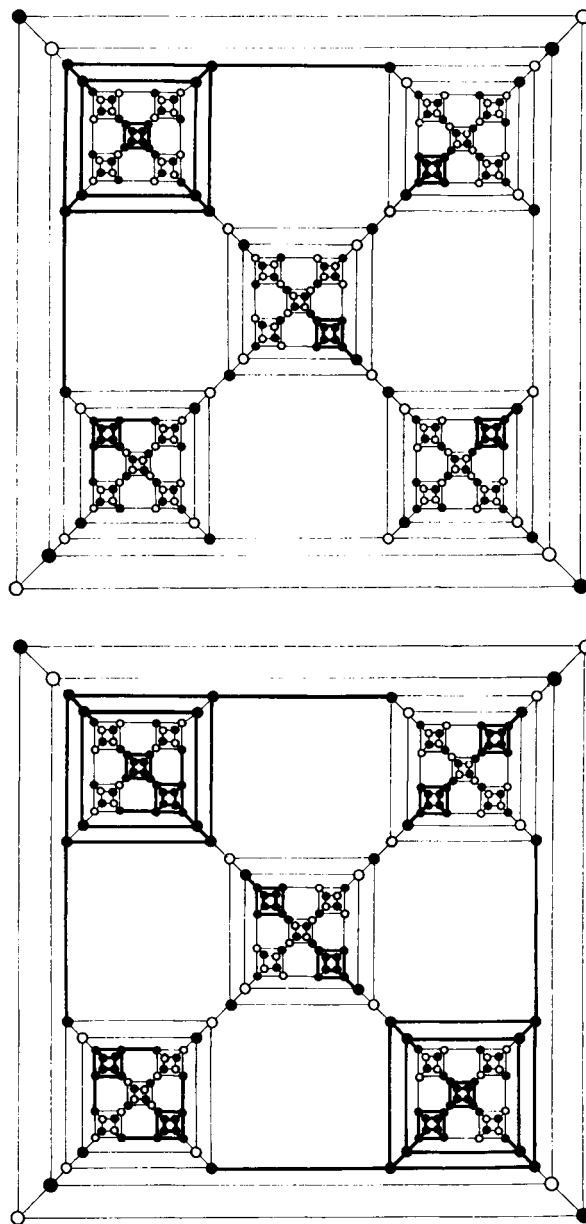


Figure 3. "Pressed" graphs of the N-A structure for Si/Al ratios of 1.5 and 2.33 referring to 30 DFR or 10 cubooctahedra

monomeric silicate and aluminate are present in the solution phase of the reaction mixture. As already mentioned, we know from our studies in the Na-system that the growth of the crystals takes place from the silicate and aluminate components in the solution.

The experiments fulfilling the described conditions were carried out as follows.

An aluminosilicate gel was prepared from a strongly alkaline silicate solution, where the silicate is present as a monomer, and a sodium aluminate solution. Such gels are usually used in the syntheses of A-type zeolites. The gel was washed to near-neutrality. Further procedures are carried out with the wet gel.

The Si/Al ratio, determined by x-ray fluorescence analysis, was 0.99.

By hydrolysis of this gel a mixture of monomeric silicate and aluminate should result.

Appropriate quantities of the amorphous product were then treated with a TMA silicate solution and mixed with 2-3% of A-type seeds. Finally the mixture was brought to 88°C.

The results of these experiments are given in the following table.

TABLE V.- Formation of zeolite N-A from TMA-silicate and sodium aluminosilicate gel (Si/Al=1)

<u>Sample</u>	<u>compositions</u>	<u>product</u>	<u>Si/Al</u>	<u>time</u>
454	NaAlO ₂ ·SiO ₂ ·0.5TMA Si· 53H ₂ O	pure N-A	1.50	7 [d]
455	" 1.0TMA Si· 70H ₂ O	"	1.80	7
456	" 1.5TMA Si· 86H ₂ O	"	2.10	8
457	" 2.0TMA Si·103H ₂ O	"	2.26	8
458	" 3.0TMA Si·119H ₂ O	"	2.33	8
442	" 4.0TMA Si·200H ₂ O	"	2.58	8

It can be seen that from all mixtures pure N-A zeolite can be obtained. Leaving the crystals three additional days in contact with the reaction mixture did not produce even traces of by-products which could be detected by x-ray diffraction. No nucleation of other zeolite species had occurred.

Beside the fact that the described procedure is a simple and reproducible method to get zeolites N-A in a wide range of Si/Al ratios, it represents a strong argument for our model of crystallization.

Following the suggestions of this model the single steps for the crystallization of N-A are the same for all Si/Al ratios, in contrast to the faujasite growth, where the formation of the needed different silicate species on the surface of the crystals seems to be the rate-determining step of the crystallization process.

Therefore, the rates of crystallization should, in the case of N-A, vary only slightly with the Si/Al ratio of the final product, which is also in contrast to the faujasite growth.

The Arrhenius activation energies should also be independent of the Si/Al ratio.

Suggestions of these peculiarities of the N-A growth can be seen from the crystallization times of batches 454 to 458.

In the following experiments the temperature dependence of the crystallization rate was studied for batches with two different Si/Al ratios in the final product at temperatures of 98, 88, 78 and 68°C (I, II, III, IV).

Fig. 4a and 4b demonstrate the crystallization curves at the above temperatures for mixtures with the composition $\text{NaAlO}_2 \cdot \text{SiO}_2 \cdot 0.5 \text{ TMA-silicate} \cdot 60 \cdot \text{H}_2\text{O}$ (4.8 % seeds),

$\text{NaAlO}_2 \cdot \text{SiO}_2 \cdot 4.0 \text{ TMA-silicate} \cdot 210 \text{ H}_2\text{O}$ (4.3 % seeds).

The following Si/Al ratios in the final product were observed.

		<u>Si/Al</u>			<u>Si/Al</u>
462	I	1.48	463	I	2.47
	II	1.45		II	2.41
	III	1.48		III	2.45
	IV	1.48		IV	2.43

The course of the crystallization shows that the growth of the crystals cannot be described by a simple kinetic equation as in the case of faujasite-type zeolites. Before the period of rapid crystallization, a period of 20 - 50 hours is observed where the system obviously changes into the state in which the crystallization is possible. It can be assumed that in this period a partial dissolution of the gel occurs, until a sufficient concentration of monomeric silicate and aluminate is present in the solution with the DFR-silicate. The processes taking place in this period are less temperature dependent than the crystallization itself. As can be seen from Fig. 5,

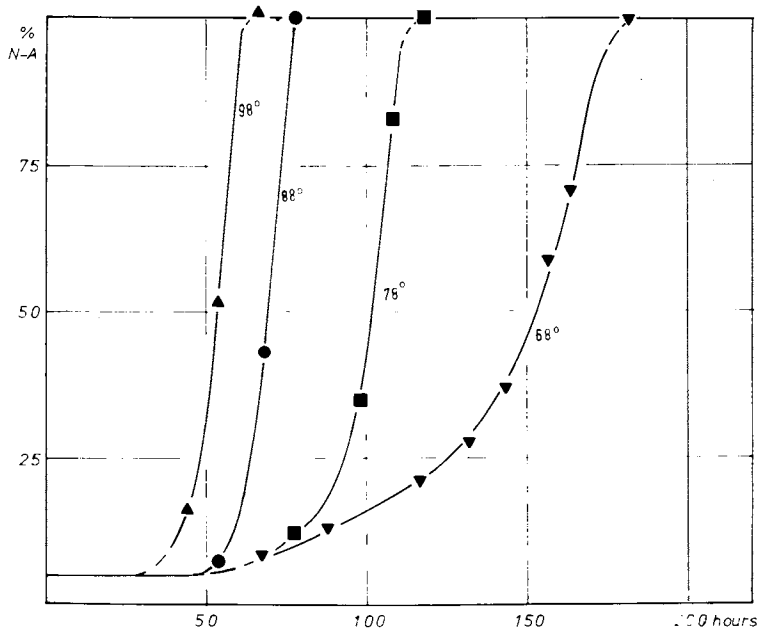
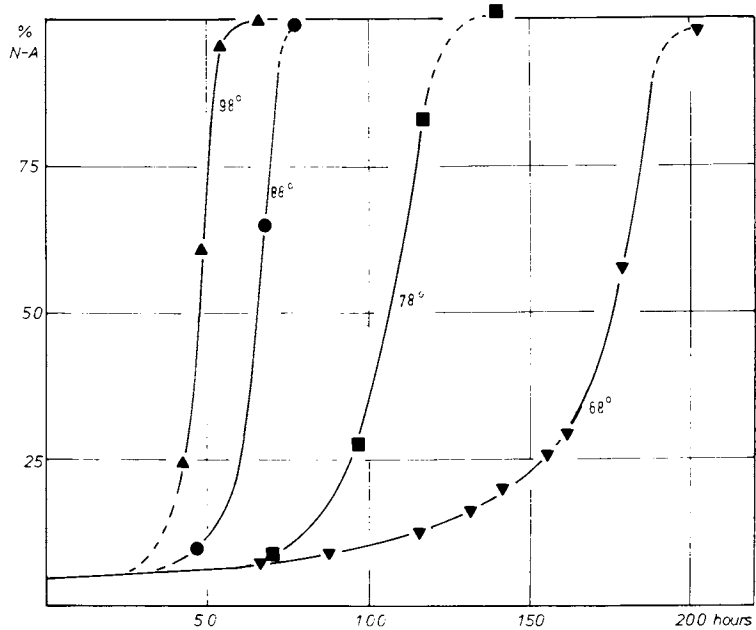


Figure 4. Crystallization curves for zeolite N-A with Si/Al ratios of about 1.5 (a) and 2.5 (b) at 98°, 88°, 78°, and 68°C

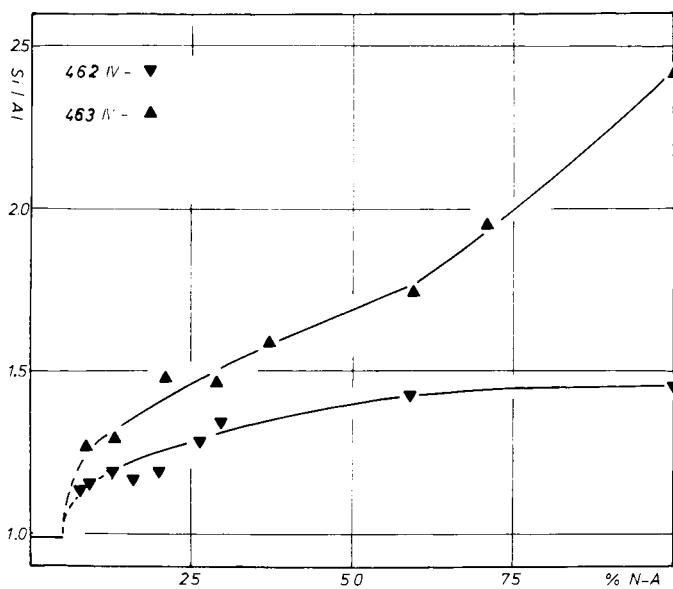


Figure 5. Si/Al ratio as a function of the crystallinity of zeolite N-A for two different Si/Al ratios in the final product

the crystallinity is not proportional to the Si/Al ratio. As can be expected, the silica content of the samples increases with increasing crystallinity. In addition, it seems that the amorphous material takes up some DFR-silicate in the period before the actual crystallization, as can be seen from x-ray fluorescence measurements on the gel.

The crystallization rate and its temperature dependence for products of type N-A with different Si/Al ratios vary only slightly as expected from the model considerations described above. The data for the faujasites show in the observed range of Si/Al ratios, variations of these rates over two orders of magnitude.

It can be seen that an activation energy cannot be derived from these experiments.

Further experiments to determine activation energy are in progress. However, it can be seen from the curves given in Figures 4a, b, that the crystallization curves of different Si/Al ratios are quite similar for a given temperature.

The authors thank the "Deutsche Forschungsgemeinschaft" and the "Fonds der Chemischen Industrie" for financial support of their work.

Literature Cited

1. Kacirek, H., Lechert, H., *J. Phys. Chem.* (1975) **79**, 1589
2. Kacirek, H., Lechert, H., *J. Phys. Chem.* (1976) **80**, 1291
3. Barrer, R.M., Denny, J., *J. Chem. Soc.* (1961) 971
4. Breck, D.W., "Zeolite Molecular Sieves" p.304 ff, John Wiley & Sons, New York 1974
5. Aiello, R., Barrer, R.M., *J. Chem. Soc. A* (1970) 1470
6. Wieker, W., "Neuere Entwicklungen der anorganischen Chemie, VEB Verlag der Wissenschaften, Berlin 1974

Silanation of Zeolites

R. M. BARRER, R. G. JENKINS, and G. PEETERS

Physical Chemistry Laboratories, Chemistry Department, Imperial College,
London SW7 2AY England

ABSTRACT

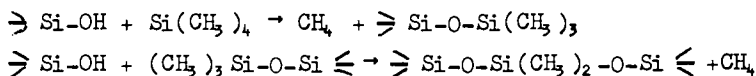
Na-Y, its ~31%, ~54% and 73% H-exchanged forms, Na- and H-mordenites and partially dealuminated H-mordenite have been silanated with SiH₄. From 30 to 210°C chemisorption involves exposed -OH groups:

$$\begin{aligned} & \geq \text{SiOH} + \text{SiH}_4 \rightarrow \geq \text{Si-O-SiH}_3 + \text{H}_2 \\ & \geq \text{Si-O-SiH}_3 + \text{HO-Si} \leq \rightarrow \geq \text{Si-O-SiH}_2\text{-O-Si} \leq + \text{H}_2 \end{aligned}$$

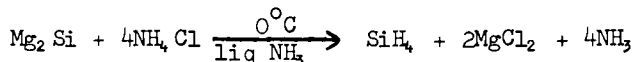
At temperatures of 300° and 360°C further reactions occur. If silanated zeolites are treated with water ratios of total H₂ evolved to SiH₄ consumed approach 4. New -OH groups so introduced also react with SiH₄.

Introduction

There has been much interest in the hydrogen zeolites and their properties (1). Two reports concern reactions between H-zeolites and organosilanes. In one (2) Si(CH₃)₄ was reacted with H-Y in the range 250° to 650°C. Two steps were postulated:



Grey products resulted which became white when heated in air. In the second (3) it was reported that (CH₃)₃SiH reacted rapidly with H-Y at an unspecified temperature. No prior study of the modification of H-zeolites by SiH₄ has been reported and an account of chemisorption of silane by H-zeolites is accordingly presented. Silane is made on an industrial scale by the reaction (4):



Experimental

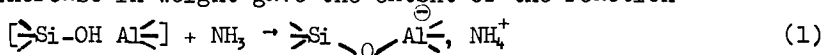
The silane was freed of ~4% of hydrogen by freezing out at 77K and pumping off hydrogen. Pure O₂ and N₂ were used as sorbates and NH₃ to titrate [\geq Si-OH Al \geq] groupings.

The zeolites studied were Na-mordenite, H-mordenite, H-mordenite partially dealuminated, Na-Y (Si/Al=2.51) and (Na,H)-Y forms with ~31%, ~54% and 73% replacement of Na by H (derived by heating (Na,NH₄)- forms at 360°C). About 1g was supported on a sintered glass membrane through which gas could be circulated continually, using a mercury piston pump with two pistons and a reciprocating action which minimized pressure fluctuations during pumping. The circulating system contained a U-tube with glass beads for freezing out condensable gases (e.g. SiH₄). The zeolite was outgassed at 360°C. Oxygen, nitrogen or water could be supplied to the circulation system, after pumping out unreacted silane, to react with chemisorbed SiH₄, or to measure sorption isotherms of O₂ or N₂ in situ. Also the silanated zeolite could be transferred to a volumetric sorption unit (sorption of O₂ and N₂) or a gravimetric unit (sorption of NH₃).

Amounts of H₂ evolved, SiH₄ chemisorbed and SiH₄ physically sorbed were monitored as follows:

1. The circulating pump was stopped at time *t* and the total non-sorbed gas (SiH₄+H₂) determined from the pressure and the known volumes and temperatures of the parts of the system.
2. Gaseous and physically sorbed SiH₄ were condensed in the U-tube at 77K. The residual pressure gave the amount of H₂, and hence the gaseous SiH₄ of step 1.
3. The doser volume containing the trap was isolated, the trap brought to room temperature and the condensed SiH₄ evaporated. The amount of H₂ in the doser volume was calculated (from the total H₂ and the known volumes and temperatures of the relevant parts of the apparatus) and hence the total gaseous and physically sorbed SiH₄. The amount of SiH₄ of step 3 less that of step 1 gave the physically sorbed SiH₄.
4. Finally, subtracting the SiH₄ of step 3 from the SiH₄ available at *t*=0 before any reaction occurred gave the quantity chemisorbed.

When titrating $[\text{Si-OH Al}]$ with NH₃, excess ammonia was first sorbed and then the physically sorbed ammonia was pumped off, until the weight of the crystals in the gravimetric unit became constant. The increase in weight gave the extent of the reaction



Infra-red absorption measurements were made, and also X-ray powder photographs of silanated products and the parent zeolites gave changes of intensity and shifts in the d-spacings. Sorption by the parent and the silanated products was compared using N₂ and O₂.

Silanation of Mordenite and Zeolite Y

Some of the original H-mordenite was dealuminated by treatment with 6N HNO₃. The X-ray diffraction pattern was little changed so that lattice alteration was slight. Compositions are given in Table I. Both these zeolites and also a Na-mordenite were treated

with silane as summarized in Table II. Na-Y and several (Na,H)-Y forms with 73, ~31 and ~54% exchange of Na by H were also silanated, as summarized in Table III. In Table III the results are referred to lg outgassed (dry) weight of zeolite; in Table II dry weights of the samples to which the results refer are given in column 1. The kinetics of chemisorption of silane and release of hydrogen are illustrated for typical experiments in Figure 1 a to d. Chemisorption is initially rapid at the higher temperatures but then tends to reach a plateau. Chemisorption also occurs at temperatures as low as 30°C. Hydrogen evolution exceeds chemisorption, but follows a similar course. Each temperature rise liberated a fresh burst of hydrogen. Each dose of water vapour introduced at a fixed temperature also liberated a burst of hydrogen, being itself consumed in the process, until the supply of chemisorbed $-\text{SiH}_x$ and $-\text{SiH}_y$ groups became exhausted.

Table I Analyses of mordenites

(a) Parent H-mordenite

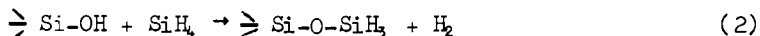
	w/w %	moles/100 g	SiO ₂ :Al ₂ O ₃
SiO ₂	74.06	1.233	
Al ₂ O ₃	10.35	0.102	12.09
H ₂ O	15.59	0.866	

(b) Dealuminated mordenite

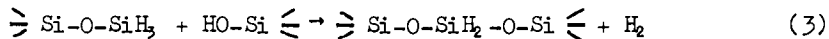
SiO ₂	80.53	1.340	
Al ₂ O ₃	4.79	0.047	28.51
H ₂ O	14.68	0.816	

Discussion of Results

Na-zeolites The small amount of reaction of SiH₄ with Na-Y and Na-mordenite (Tables III and II) compared with the much larger chemisorption by the hydrogen forms showed that the chemisorption process at low and intermediate temperatures (30°C to 210°C) involved the silanol groups of the hydrogen forms. Few hydroxyls are expected in the Na-forms and indeed the chemisorption represents about 7% of the Na replaced by H in Na-mordenite and 3.5% in the Na-Y. The -OH groups could be largely terminal hydroxyls at the external surfaces of the crystals, produced by local hydrolysis. The primary reaction was considered to be



which gives a ratio of H₂ produced to SiH₄ consumed of unity. Within error this could be true of Na-mordenite, but not of Na-Y where this ratio was 1.89 (Table III). This implies secondary reactions, one of which could be



and which could raise the ratio H₂:SiH₄ to 2 if all the pendant -O-SiH₃ groups reacted according to eqn 3. This reaction implies

Table II Reactions of SiH₄ with mordenites

Sample (Dry wt)	Ideal silanol contents of sample (mmol)	Reaction conditions	SiH ₄ consumed (mmol)		H ₂ produced		Ratio H ₂ /SiH ₄	Wt % of Si added
			In the stages	In total	In the stages	In total		
H ₂ mordenite (1.02)	-	100°C for 39 hrs	-	0.14	-	0.127	0.91	0.39
H-mordenite (1.00)	2.04	Room temp. for 176 hrs + unreacted SiH ₄ pumped off + 160°C for 49 hrs + 210°C for 256 hrs	0.56	0.56	0.69	0.69	1.23	1.57
H-mordenite (0.955)	1.95	100°C for 88.25 hrs + 150°C for 65.25 hrs + unreacted SiH ₄ pumped off + 200°C for 47.5 hrs	0.972 +0.18	0.972 1.15	1.412 +0.488	1.412 1.90	1.45 1.65	3.40
H-mordenite (0.63)	1.29	First dose SiH ₄ , 300°C for 113 hrs + second dose, 300°C for 190 hrs + unreacted SiH ₄ pumped off + reaction with O ₂ at 21.7°C consuming 0.637 mmol O ₂	0.91	0.91	-	-	-	-
Dealuminated mordenite (0.615)	3.15 (in nests of four) + 0.58 (as single silanols)	300°C for 75 hrs	0.68	1.59	-	3.02	1.90	7.06
			0.465	0.465	1.06	1.06	2.28	2.48

Table III Reactions with zeolite Y

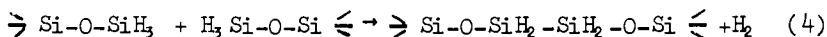
Sample (g dry wt.)	Chem. dose from SiH ₄ (mmol)	High freq. hydroxyls (mmol)	Reaction conditions	SiH ₄ consumed (mmol)		H ₂ produced (mmol)		H ₂ /SiH ₄	Chem. dose from SiH ₄ (mmol)	% Si added
				In the stages	In total	In the stages	In total			
Na-Y	-	-	60 hrs at 160°C + unreacted SiH ₄ evac. + 110 hrs at 160°C + 50 hrs at 210°C + 96 hrs at 300°C	0.15	0.15	0.28	0.28	1.89	-	0.42
(Na,H)-Y (73)	3.17	2.10	150 hrs at 30°C + 150 hrs at 90°C + unreacted SiH ₄ evac. + 20 hrs at 90°C + 122 hrs at 160°C	0.16	0.16	0.25	0.25	1.52	-	1.12
(Na,H)-Y (73)	3.17	2.10	First dose SiH ₄ , 43 hrs at 210°C + 2nd dose SiH ₄ , 86 hrs at 210°C + unreacted SiH ₄ evac. + 27 hrs at 210°C + 4 doses of H ₂ O vap. at 200°C + temp. raised to 300°C at last dose	0.89	0.89	1.33	1.33	1.50	2.02	-
(Na,H)-Y (73) first treatment	3.17	2.10	150 hrs at 210°C, large XS SiH ₄ + unreacted SiH ₄ evac. + 116 hrs at 300°C and 170 hrs at 360°C + 2 doses H ₂ O vap. at 210°C and 1 dose at 210°C and then 300°C	1.23	1.23	2.10	2.10	1.71	-	3.45

Table III Reactions with zeolite Y (continued)

Sample (lg dry wt)	Chemical formula	Top of silanols (mmol)	High freq. hydroxyls (mmol)	Reaction conditions	SiH ₄ consumed (mmol)		H ₂ produced (mmol)		H ₂ /SiH ₄	Chemical formula	Top of silanols (mmol)	% Si added
					In the stages	In total	In the stages	In total				
Second treatment same sample	-	-	-	+ 173 hrs at 210°C with SiH ₄ + unreacted SiH ₄ evac. + 144 hrs at 300°C + reaction with H ₂ O vap. at 300°C	0.37	2.10	1.70	6.44	3.07	-	-	5.93
(Na ₄ H)-Y (51)	1.33	1.15	1.15	122 hrs at 210°C with SiH ₄ + unreacted SiH ₄ evac. + H ₂ O vap. 24 hrs at 30°C + 3 doses H ₂ O vap. at 210°C + 1 dose H ₂ O vap. at 210°C and then at 300°C	1.01	1.01	1.14	1.14	1.12	-	1.10	2.84
(Na ₄ H)-Y (54)	2.34	1.84	1.84	107 hrs at 210°C with SiH ₄ + unreacted SiH ₄ evac. + 122 hrs at 300°C + 26 hrs at 360°C + H ₂ O vap. at 210°C + 2nd dose H ₂ O vap. at 210°C + 3rd dose H ₂ O vap. at 210°C and then at 300°C, 66 hrs)	1.51	1.51	1.83	1.83	1.21	-	-	4.25
							0.66	2.49	1.65			
							0.40	2.89	1.91			
							1.01	3.90	2.58			
							0.80	4.70	3.12			
							0.43	5.13	3.40			

* on modified zeolite equal to lg original sample.

pairs of silanol -OH groups near enough to react, as would be the case in the Na-zeolites if they were concentrated as terminal hydroxyls on external surfaces. A further reaction which with reaction 1 gives an upper limit for $H_2:SiH_4$ of 2 is



although at low temperatures this seems less likely than reaction 3. It is seen that reaction 2 introduces permanent new $\rightarrow Si-O-Si \leftarrow$ bonds.

H-zeolites Although much more chemisorption occurs with the H-zeolites the uptake in the primary process does not equal the total hydroxyl content. In H-mordenite this content was estimated from the analysis assuming the ideal number of silanols expected from the composition. In the (Na,H)-Y zeolites it was determined according to reaction 1. The failure of all silanol hydroxyls to react with SiH_4 is expected if some hydroxyls are not sufficiently exposed to react. In zeolite Y two infrared absorption bands correspond with hydroxyls in two kinds of location. The exposed ones have the higher frequency, and in going from Na-Y through (Na,H)-Y to H-Y the relative numbers of high and low frequency hydroxyls for each (Na,H)-Y composition have been determined (5). The exposed high frequency -OH's are preferentially generated up to a limit expected from the number of possible sites Table III column 3 gives the numbers of exposed hydroxyls expected in each (Na,H)-Y studied. Even so, the primary chemisorption of SiH_4 does not equal the number of exposed hydroxyls. The primary reaction increases in rate and extent with temperature, as seen from the experiments with (Na,H)-Y (73) in Table III, and can approach the number of high frequency, most exposed OH groups for (Na,H)-Y (31) and (Na,H)-Y (54) of the table.

The extent of reaction with exposed hydroxyls must be considered in relation to the H_2 evolved. Since $H_2:SiH_4$ exceeds unity, (Figure 1 a to d), secondary reactions proceed simultaneously with the primary process. If only exposed hydroxyls react with SiH_4 and the secondary reaction is eqn 3, also involving only exposed -OH groups, then the primary process must always be less than corresponds with the exposed -OH groups. Moreover, if one considers the first stages at $210^\circ C$ of the last three experiments of Table III the H_2 produced in primary plus secondary reactions is equal to the number of the exposed -OH groups. This is expected if H_2 evolved is the sum of reactions 2 and 3, the amount of reaction 2 being metered by the SiH_4 chemisorbed, and reaction 3 accounting for the remainder.

When temperatures of $300^\circ C$ and $360^\circ C$ were involved more complex results were noted in two instances. In the fourth experiment in Table II the silane consumed exceeded the total -OH content so that reactions of silane other than reaction 2 are involved. The zeolite and part of the glass wall of the reaction vessel were stained brown and a condensation-polymerisation process was sus-

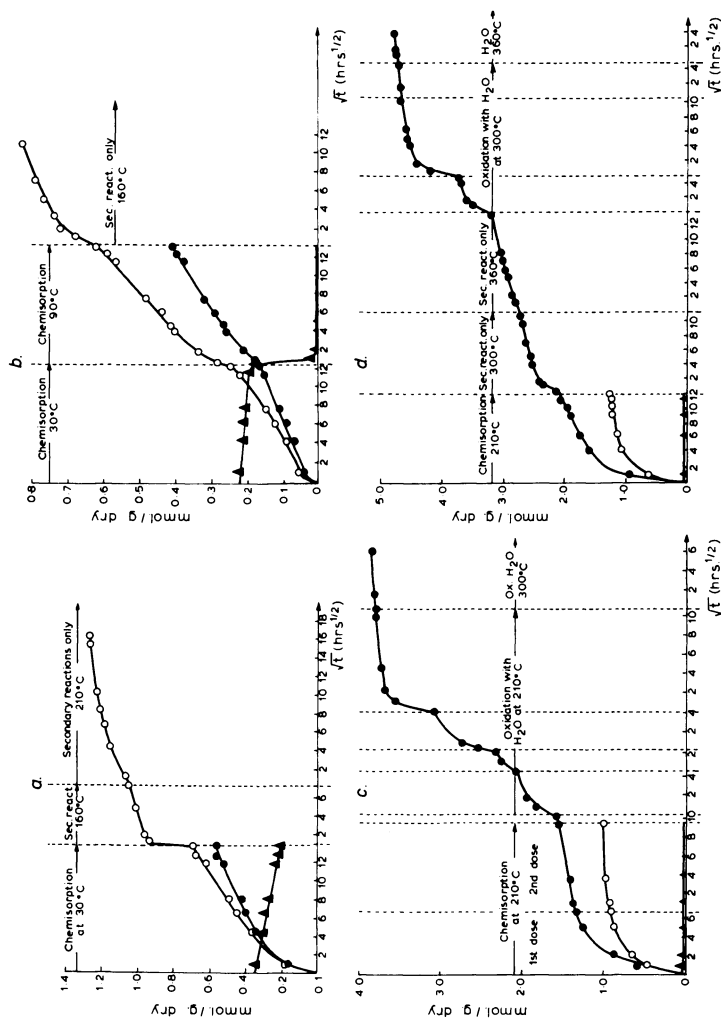
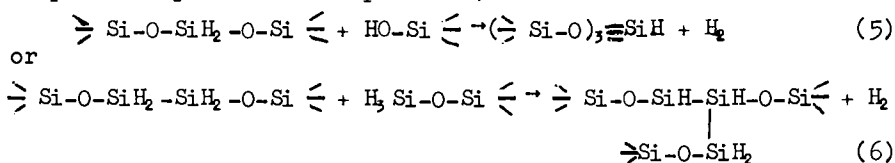


Figure 1. (a) Chemisorption of SiH_4 on H-mordenite and further reactions. In (a) and (b) \bullet = chemisorbed SiH_4 ; \circ = H_2 evolved. In (a)-(d) \triangle = physisorbed SiH_4 . (b) Chemisorption of SiH_4 on H-Y and further reactions. (c) Higher temperature chemisorption and further reactions of SiH_4 with H-Y, followed by progressive treatments with H_2O vapor. In (c) and (d) \circ = chemisorbed SiH_4 ; \bullet = H_2 evolved. (d) As for (c), with further reactions up to 360°C and then progressive treatments with H_2O vapor.

pected, occurring simultaneously with reactions 2 and 3, to give a somewhat volatile polysilane, Si_xH_x , with evolution of some additional hydrogen. The brown modified mordenite slowly sorbed oxygen at room temperature and became somewhat lighter in colour. When heated in air at 850°C the mordenite again became white. A similar result was obtained with (Na,H)-Y (54) in the final experiment recorded in Table III. A brown stain appeared on part of the glass wall of the reaction cell after the chemisorbed SiH_x was heated to 300°C , though the zeolite was still white. After heating at 360°C the zeolite had also become brown. Treatment with water vapour, as described in Table III, restored the white colour of the zeolite Y but did not remove the colour on the glass wall.

As noted, the primary reaction 2 and the secondary reaction 3, do not together give $\text{H}_2:\text{SiH}_x$ ratios above two. Up to 210°C this is correct, but heating at 300°C or 360°C gave $\text{H}_2:\text{SiH}_x$ ratios above two, so that tertiary reactions also occur at these temperatures. Since only two experiments gave at 300°C or 360°C the brown colours referred to in the previous paragraphs, other higher temperature processes are possible, such as

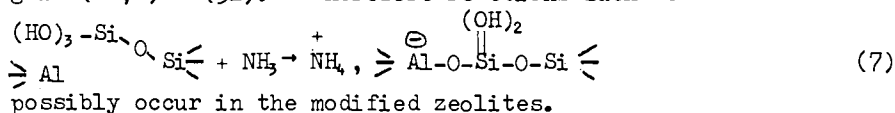


These, with reactions 3 or 4 could give $\text{H}_2:\text{SiH}_x$ ratios up to three

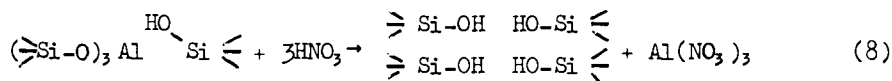
If all chemisorbed silane is made to react with -OH groups the limit to the ratio of H_2 formed to SiH_x consumed is four, unless -Si-Si- bonds such as those introduced by reactions 4 and 6 remain unattacked, in which case ultimate $\text{H}_2:\text{SiH}_x$ ratios less than four would result. This aspect was investigated by treating the chemisorbed silane with doses of water vapour and measuring the evolution of hydrogen. Final ratios $\text{H}_2:\text{SiH}_x$ were 3.82, 3.86, 3.99 and 3.74 (Table III). The ratio 3.40 in the last experiment of Table III is probably low because of unreactive material forming the brown stain on the glass. Since still more prolonged treatment with water vapour could possibly have produced a little more hydrogen the results suggest virtually complete hydroxylation of pendant $-\text{O-SiH}_2$, and of other forms of chemisorbed $-\text{SiH}_x$ and $-\text{SiH}_y-$.

That treatment of $-\text{SiH}_x$ or $-\text{SiH}_y-$ with water vapour yields hydroxylated products was supported by infrared measurements of such water-treated and then outgassed materials. These showed a broad hydroxyl band somewhat like that in silica gel engulfing the separate bands characterizing the non-exposed and exposed OH groups of H-Y. That the new -OH groups would then chemisorb fresh amounts of SiH_x was confirmed in the second treatment of (Na,H)-Y (73) recorded in Table III, 4th experiment. In some of the experiments in Table III the chemisorption of ammonia was measured, to find how many groups of the type

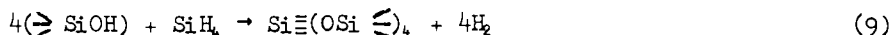
remained. The figures in the second to last column indicate considerable numbers of these. In the examples studied the ammonia titre normally exceeded the number of non-exposed -OH groups in the zeolites Y, which is 1.07 mmol/g in (Na,H)-Y (73) and 0.18 mmol/g in (Na,H)-Y (31). Therefore reactions such as



Dealuminated Mordenite. Nests of hydroxyls should be the primary result of the de-alumination reaction

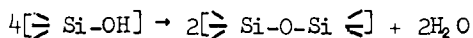


If any of these nests of hydroxyls survive outgassing, the reaction



is possible with original Al isomorphously replaced by Si. This would give crystalline silicas with no exchange ions and the open topology of the parent zeolite framework.

Dealuminated mordenite after outgassing overnight at 360°C was treated at 300°C with SiH₄. The result is shown in the last experiment in Table II. Chemisorption of silane is a little less than the ideal amount of \ge SiOH available as single silanols. However the yield of H₂ exceeds that possible for 0.465 mmol of silane chemisorbed according to reaction 2 followed by reaction 3 until all single silanols were used up. This would give 0.56 mmol of H₂ as against 1.06 mmol actually observed. Tertiary reactions therefore also occur, which may include a small amount of reaction 9. However reaction 9 certainly is not important and the temperatures employed have probably resulted in loss of water from the nests of hydroxyls:



The Modified Zeolites. X-ray powder diffraction of the modified mordenites gave clear mordenite patterns although that of the most heavily silanated product of Table II was somewhat weakened. Na-Y treated with SiH₄ gave a powder pattern unchanged from that of the parent Na-Y. The parent (Na,H)-Y (73) gave weaker intensities than Na-Y. The modified (Na,H)-Y (31) gave the same line intensities as the parent material, and the modified (Na,H)-Y (54) gave slightly diminished intensities relative to its parent zeolite.

N₂ was sorbed in the parent mordenite and the samples with 1.57, 3.40 and 7.06 weight % of added Si (Table II, last column). Isotherms at 77K are shown in Figure 2a and the rate of uptake in the mordenite with 3.4% added Si in Figure 2b. After silanation sorption capacities were in the sequence

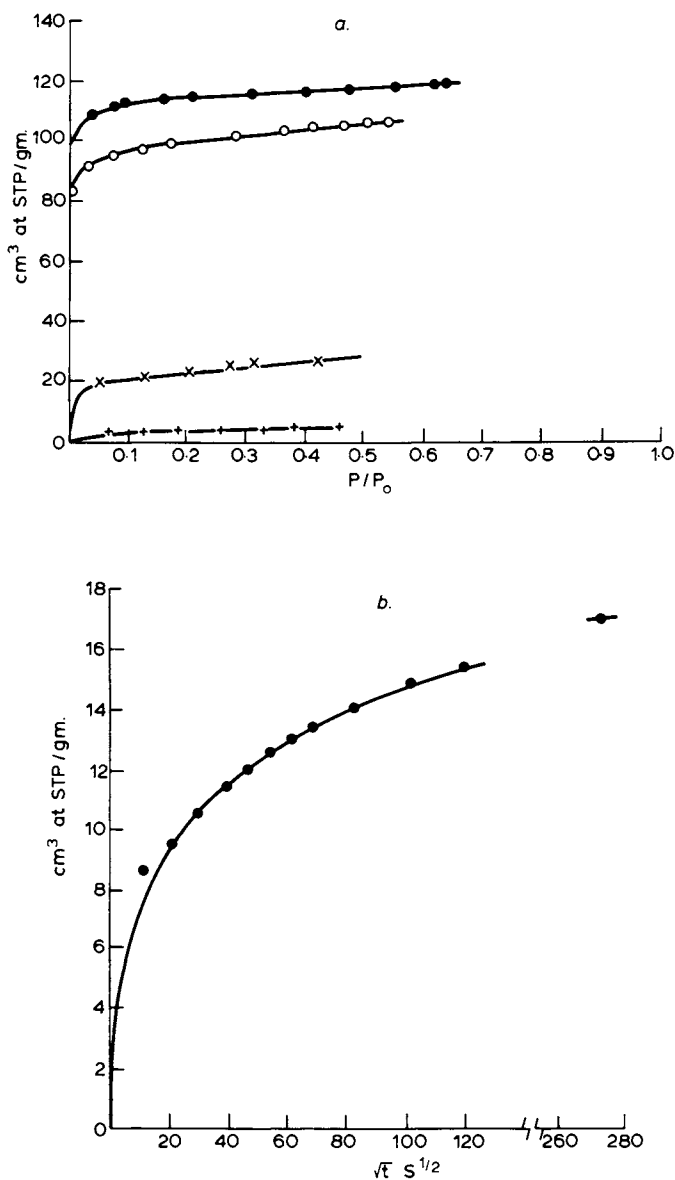


Figure 2. (a) Sorption of N_2 at 77K by ●, parent H-mordenite; ○, H-mordenite with 1.57% by weight of added Si; ×, H-mordenite with 3.40% added Si; +, H-mordenite with 7.06% added Si. (b) Rate of uptake of N_2 at 77K by H-mordenite with 3.40% added Si.

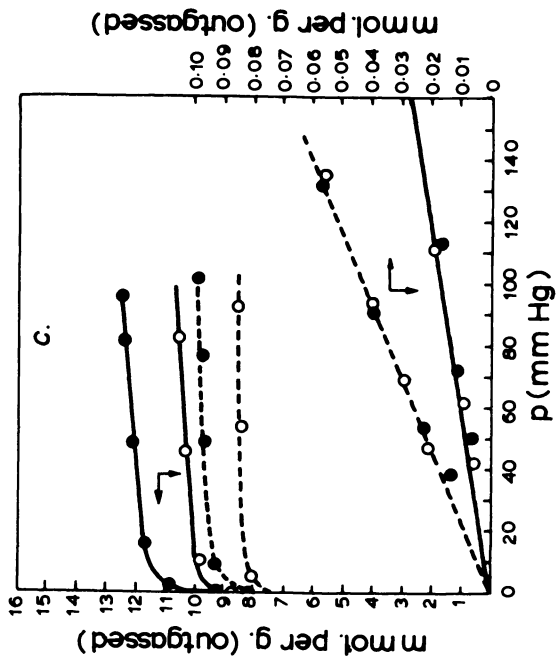
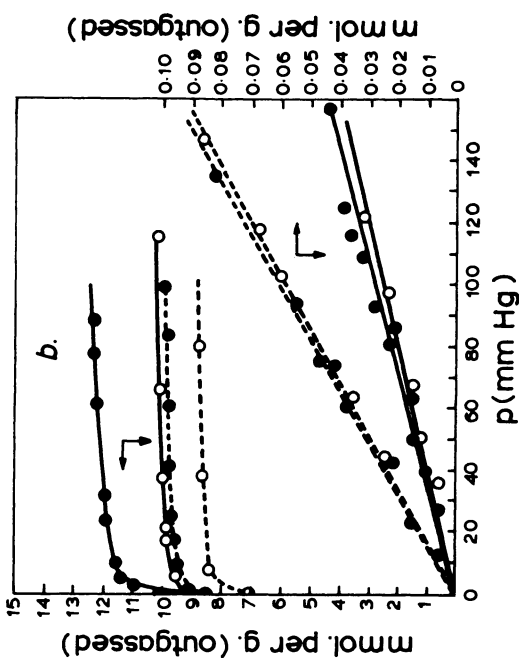
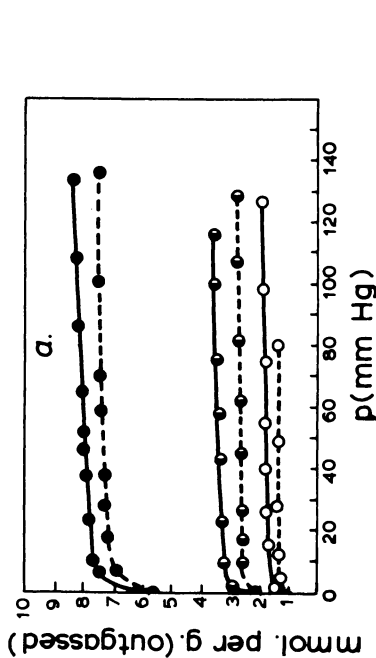


Figure 3. Sorption of O_2 and N_2 by silanated zeolites Y. (—), O_2 ; (---), N_2 . (a) \bullet parent (Na,H)-Y (73); \circ , parent with 2.84% by weight of added Si; \circ , parent with 5.99% added Si. $T = 77K$. (b) \bullet parent (Na,H)-Y (31); \circ , parent with 2.84% added Si. In both (b) and (c) for left hand ordinate, $T = 77K$ and for right hand ordinate $T = 273K$. (c) \bullet parent (Na,H)-Y (54); \circ , parent with 4.25% added Si.



Parent H-mordenite > 1.57% > 3.40% > 7.06%.

For the most heavily silanated product uptake of N_2 is minimal, and for the mordenite with 3.40% added Si sorption at 77K is slow. Silanation can therefore change sorption drastically.

Measurements of the uptake of O_2 and N_2 at 77K are given in Figure 3a for (Na,H)-Y (73) and this zeolite with 2.84% and 5.99% Si added. The sorption capacities decrease rapidly with increased silanation. Figure 3a may be compared with Figure 3b where (Na,H)-Y (31) and its modification with 2.84% added Si are the sorbents. Despite the identical extent of silanation with that of one of the modified zeolites in Figure 3a the saturation capacity for O_2 and N_2 is well maintained as is the uptake and the selectivity for N_2 over O_2 at 0°C. The same is true of (Na,H)-Y (54) with 4.25% Si (Figure 3c). Also nitrogen isotherms, measured at each stage of treatment for (Na,H)-Y (31), showed only minor changes in capacity at 77K and in the Henry's law adsorption constants at 273.2K.

Concluding Remarks

Silanation is a versatile method for permanent modification of hydrogen zeolites. It can be made progressive to almost any degree allowed by the intracrystalline free volume, by converting $-SiH_x$ and $-SiH_y$ groups to $Si(OH)_x$ and $-Si(OH)_y$ and then chemisorbing more silane by reaction 2. It can be controlled in extent by varying the amount of silane chemisorbed in this primary reaction, or by varying the Na:H ratio in the parent zeolite. Further modification can be effected by varying the amount of secondary reactions such as those represented by eqns 3 or 4 compared with the extent of the primary process of eqn 2. Silanation would appear to be possible for any zeolite able to yield at least a partial hydrogen form and open enough to admit SiH_4 .

Literature Cited

1. Breck, D.W., "Zeolite Molecular Sieves", John Wiley and Sons, New York (1974), p.460 et seq.
2. McAteer, J.G., and Rooney, J.J., Advances in Chemistry Series No.121, Editors W.M. Meier and J.B. Uytterhoeven, "Molecular Sieves" p.258 ACS (1973).
3. Kerr, G.T., in "Proceedings of 3rd International Conference on Molecular Sieves", Editor J.B. Uytterhoeven, Zurich, September 3rd - 7th, (1973), p.38.
4. Yusa, A., Yatsurugi, Y., and Takaishi, T., J. Electrochem. Soc. (1975), 122, 1700.
5. Bosáček, V., Patzelová, V., Hybl, Č., and Tvarůžkova, Z., J. Catal. (1975), 36, 371.

Zeolite Chemistry II. The Role of Aluminum in the Hydrothermal Treatment of Ammonium-Exchanged Zeolite Y, Stabilization

D. W. BRECK and G. W. SKEELS

Union Carbide Corp., Tarrytown Technical Center, Tarrytown, N.Y. 10591

ABSTRACT

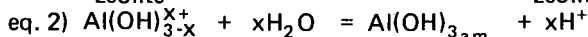
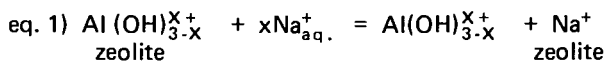
Ammonium exchanged zeolite Y was steam calcined at 573 to 1043K. Treatment with KF or NaCl solution removed 24 of the 56 original framework Al atoms per unit cell, which probably formed μ -trioxotrialuminum cations in the β cages. These complex cations contribute to the increased stability of the structure.

Introduction

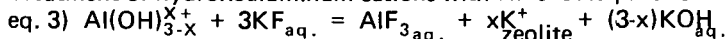
Hydrothermal treatment at elevated temperature of highly ammonium exchanged zeolite Y (NH_4Y) produces a zeolite product that is different from a dry air- or vacuum-calcined NH_4Y . A high degree of crystallinity following hydrothermal treatment is maintained even at temperatures as high as 1300 K; dry-air fired NH_4Y loses X-ray crystallinity at temperatures near 825 K. The preparation of "stabilized Y", the reaction stoichiometry and the physical properties of the stable and unstable products that are formed as a result of various chemical, thermal and hydrothermal treatments have been extensively studied (1,2). Kerr (3,4) proposed that hydrothermal treatment of NH_4Y at elevated temperatures promotes hydrolysis of framework aluminum to form hydroxo-aluminum cations, leaving vacant tetrahedral sites in the zeolite framework (defect sites). Kerr (2) and others (5,6) have further suggested that silicon substitution in the hydrothermally created defect sites, increasing the framework Si/Al ratio, may be the cause of the increased stability. Despite these extensive studies, the source of the increased stability has not been conclusively demonstrated. It is the purpose of this study to establish a mechanism for stabilization and to propose a model for the structure of stabilized zeolite Y.

Part I of this series (7) described the use of potentiometric titrations to verify the formation of hydroxoaluminum cations, and to determine the reaction stoichiometry when NH_4Y is air-calcined. In the current work we have relied on the same principles, namely:

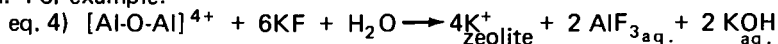
1) The ion exchange of hydroxoaluminum cations with aqueous NaCl will yield an acidic solution containing aluminum cations.



2) Treatment of hydroxoaluminum cations with KF should produce free OH.



3) Treatment of polynuclear oxoaluminum cations with NaCl will not exchange the aluminum cations, but treatment with KF should produce a basic solution. For example:



We have carried out potentiometric titrations with HCl on the fluoride-treated samples and NaOH titrations of the samples treated with NaCl solution following the steaming of NH₄Y zeolite at temperatures from 573 to 1043 K.

Experimental

The composition of the NH₄Y zeolite was Na₈(NH₄)₄₈ [(AlO₂)₅₆ (SiO₂)₁₃₆] · n H₂O. One gram samples in shallow dishes (30 mm X 40 mm X 4 mm) were placed under a thermocouple in a preheated oven (3300 cm³ volume). Three samples were steamed at each temperature; T/K = 573, 673, 773, 873, 973 and 1043. The steaming rate was 40 dm³ hr⁻¹ flowing directly over the samples. The samples were removed from the oven after two hours and cooled in a desiccator.

One of the steamed samples was slurried in 50 cm³ of 3.4 mol dm⁻³ NaCl solution, stirred at room temperature for two hours, filtered and washed with 25 cm³ of the NaCl solution, and finally washed with 25 cm³ distilled water. The combined filtrates were titrated with 0.1 mol dm⁻³ NaOH in one cm³ increments to a pH of about 11. A second sample was slurried in 50 cm³ of 3.4 mol dm⁻³ KF solution, similarly equilibrated for two hours, and the slurry titrated with 0.1 mol dm⁻³ HCl in one cm³ increments. The third sample was used to determine the extent of NH₄⁺ removal at each calcination temperature by chemical analysis.

The samples treated with NaCl solution were further analyzed by X-ray powder diffraction and infrared spectroscopy; the chemical composition (SiO₂, Al₂O₃, M₂O) was determined by standard wet chemical methods. The filtrate was also analyzed for SiO₂ and Al₂O₃ following the titration.

Results

The potentiometric titration curves for the NaCl-treated samples showed that very little acidity was produced. The titration endpoints, calculated as H⁺/unit cell in the NaCl treatment, or OH/unit cell in the KF treatment, together with partial unit cell compositions calculated from the chemical analyses, are shown in Table I. Chemical analyses of the titrated filtrates showed that a negligible amount of silica was removed from the zeolites and that only a small amount of hydroxoaluminum cations were ion-exchanged during NaCl treatment. Chemical analyses of the zeolite phase showed the absence of fluoride ion. There was extensive cation deficiency, even after steaming at 573 K, with the deficiency increasing as the steaming temperature was increased. Coincident with the cation deficiency observed in the NaCl-treated samples, a substantial amount of base

TABLE 1

1.) Unit cell compositions, titration data, and X-ray data calculated for steamed NH_4Y treated in NaCl , 3-425 mol dm^{-3} or titrated in KF , 3-425 mol dm^{-3}

UNIT CELL COMPOSITION, NaCl TREATED SAMPLES			CALCULATED FROM TITRATION ENDPOINTS					
T/K	Si/u.c.	Al/u.c. + M ⁺ /u.c.	Removed Al/u.c. ^{4.)}	Additional cation deficiency/u.c. ^{5.)}	NaCl Treatment H^+ /u.c.	KF Treatment OH^- /u.c.	X-Ray I/I_S ^{2.)}	a_0 in Å
NONE	135.8	56.2	NONE	NONE	- -	- -	100	25.71
		55.6 ^{3.)}						
573	135.8	53.6	2.6	30.2	5.23	- -	69	24.57
673	135.8	53.4	2.8	38.9	7.39	42.76	75	24.52
773	135.8	53.9	2.3	46.1	3.87	43.90	77	24.45
873	135.8	54.2	2.0	44.4	3.64	48.22	73	24.36
973	135.8	52.5	3.7	42.6	3.64	31.84	81	24.41
1043	135.8	55.3	0.9	46.0	4.09	15.13	69	24.37

1.) Based on $\text{Si/u.c.} = 135.8$

2.) I/I_S = Crystallinity of NaCl -treated sample, based on the intensities of 5 reflections, relative to the untreated sample of NH_4Y .

3.) The sample of untreated NH_4Y contained 48.0 NH_4^+ cations per unit cell and 7.6 Na^+ cations per unit cell.

4.) Removed $\text{Al/u.c.} = 56.2 - \text{Col. 4}$

5.) Cation deficiency/u.c. = $56.2 - (\text{Col. 4.} + \text{Col. 5})$

was produced by the KF treatment, which decreased with steaming temperatures above 873 K.

The hydroxyl region of the infrared spectra of the NaCl-treated samples is shown in Figure 1. The infrared sample wafers were vacuum-activated at 473 K to remove only physically adsorbed H_2O . All samples show a very broad OH band ($3745\text{--}3000\text{ cm}^{-1}$) assigned to $(\text{OH})_4$ nests in tetrahedral coordination situated in vacant framework sites (8). The broad OH band is found in the sample steamed at 573 K, and remains uniform in size until steaming temperatures above 873 K are achieved, whereupon it is reduced in size.

Superimposed upon the broad OH band are two additional OH bands normally observed with steamed or "deep bed"-treated NH_4Y (9,10,11). The largest OH band is initially found at 3587 cm^{-1} following steam treatment at 573 K, shifting to higher wave numbers with increasing steam temperature. The smaller OH band is initially found as a shoulder on the larger OH band at about 3670 cm^{-1} , becoming more distinct with possibly a doublet at about 3685 cm^{-1} , as the steaming temperature is increased to 873 K, but finally disappearing after steaming at 1043 K. The infrared wafer of the 873 K-steamed sample was vacuum-activated at 773 K and subsequently exposed to 60 torr benzene vapor at ambient temperature, re-activated at 473 K, then exposed to 200 torr of ammonia gas at ambient temperature. The spectra are shown in Figure 2. Following activation at 773 K, the 3685 cm^{-1} OH band has shifted to 3695 cm^{-1} , the 3600 cm^{-1} band is substantially reduced and the broad OH band is eliminated. With both benzene and ammonia, the 3695 cm^{-1} band is completely eliminated. Vacuum activation at 473 K following adsorption restores the 3695 cm^{-1} band.

In a subsequent experiment, a sample of NH_4Y was steamed at 873 K, suspended in 3.4 mol dm^{-3} NaCl solution and the slurry titrated to pH 11 with 0.1 mol dm^{-3} NaOH. The infrared hydroxyl region of the washed product was examined and both the 3685 cm^{-1} and the 3600 cm^{-1} OH bands were found to be unaffected by the additional NaOH treatment.

Discussion

In Part I of this series (Z) it was shown that during dry air calcination of NH_4Y in a shallow bed, 16 hydroxoaluminum cations (in a unit cell containing 56 aluminum atoms) are formed. The stepwise reaction first produces $16\text{ Al}(\text{OH})_3$ and 16 defect sites in the zeolite framework. As deamination progresses, the $\text{Al}(\text{OH})_3$ subsequently reacts to produce $\text{Al}(\text{OH})_2^+$ and water, then $\text{Al}(\text{OH})_2^{2+}$ and water, and finally at $\sim 823\text{ K}$, $[\text{Al-O-Al}]^{4+}$, or μ -oxodialuminum cations. The formation of these species was confirmed by the substantial acidity produced in the NaCl titrations, and the moderate amount of base produced in the KF titrations.

In the current work, very little acid is produced and very few hydroxoaluminum cations are exchanged when steamed NH_4Y is treated with NaCl solution. On the other hand, treatment with KF solution produces a quantity of base nearly three times that produced by the 16 hydroxoaluminum cations found in dry air-calcined NH_4Y . The hydroxyl region infrared spectra do not show the presence of substantial OH groups to account for it. Interpretation of the data for dry air-fired NH_4Y ascribed the cation deficiency in the NaCl-treated samples to either hydrolyzed hydroxoaluminum cations trapped in the sodalite cage, or to μ -oxodialuminum cations. With the steamed samples this interpretation no longer holds,

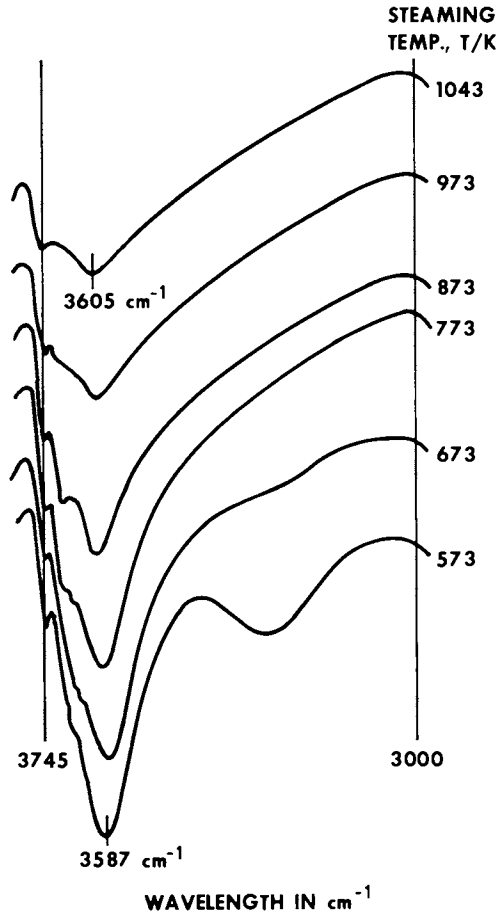


Figure 1. Hydroxyl infrared spectra of steamed NH_4Y following treatment with 3.4 mol dm^{-3} NaCl ; wafers activated in vacuum at 473 K.

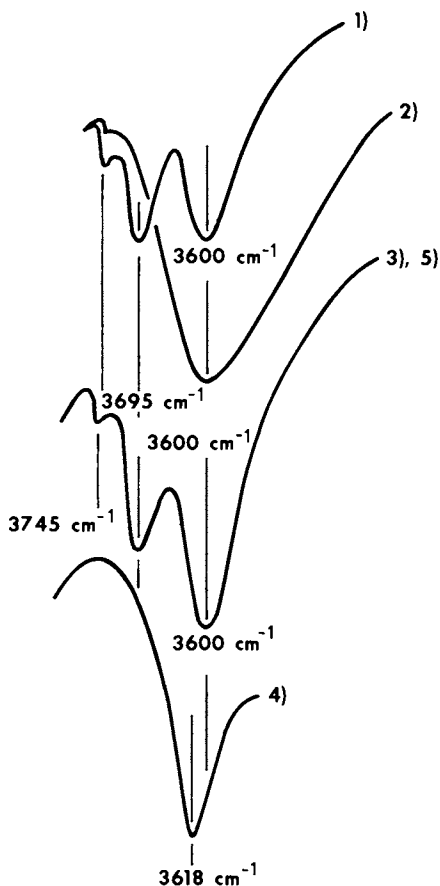
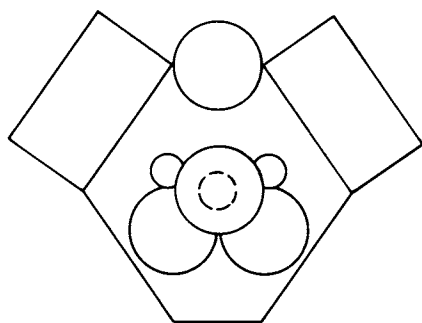
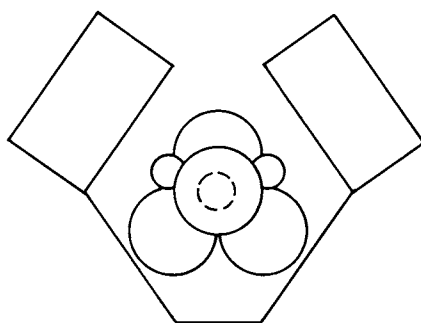


Figure 2. Effect of C_6H_6 and NH_3 on the 3600 cm^{-1} and 3695 cm^{-1} OH infrared bands found in steamed NH_4Y following treatment in 3.4 mol dm^{-3} NaCl. (1) NH_4Y steamed at 873 K , vacuum activated at 773 K ; (2) $60\text{ torr } C_6H_6$ at RT; (3) vacuum activated at 473 K ; (4) $200\text{ torr } NH_3$; (5) vacuum activated at 773 K .



A - FRAMEWORK O_4 IN NORMAL POSITION



B - FRAMEWORK O_4 MOVED INTO SITE II

Figure 3. Illustration of $[Al-O-Al-O-Al]^{3+}$ of stabilized Y in the sodalite unit. Small circles, Al; large circles, oxygen.

TABLE II
 EXPECTED VS. MEASURED OH FORMATION IN STEAMED NH_4Y
 TITRATED IN KF SOLUTION

STEAMING TEMP., T/K	673	773	873	973	1043
SUGGESTED ALUMINUM SPECIES	(1)	(1)	(1)	(1)	(2)
CALCULATED OH/ u_c (3)	49.12	52.20	49.98	16.66	49.86
MEASURED OH/ u_c	42.76	43.90	48.22	31.84	31.84
RATIO, CALCULATED/MEASURED VALUE	1.15	1.19	1.04	0.52	1.57

(1) from $\text{Al}(\text{OH})_2^+$, μ -trioxotrialuminum cations

(2) from $\text{Al}(\text{OH})^{2+}$, μ -oxodialuminum cations

(3) The Calculated OH value is based on the suggested aluminum species

oxygen atoms along the framework, and framework silicon atoms flipping through one position in a chain reaction (17). This could be described as migration of the tetrahedral vacancies, as proposed by Peri (6). However, the data of the present experiments indicate some of the non-framework aluminum is also reinserted into the framework, causing an increase in unit cell size and resulting in less base being produced in the KF titrations. The base produced in KF solution following steaming at 1043 K corresponds to $8[\text{Al-O-Al}]^{4+}$ species. This model is consistent with the X-ray structure data of Bennett and Smith (13), who found density equivalent to 16 Al atoms in Site I' and at least 5 oxygen atoms in Site U when ultra-stable Y was heated at 973 K.

The infrared spectra of steamed NH_4Y show that very few hydroxyl groups are present in the zeolite, particularly when the optical densities of the spectral bands are compared to the OH bands in air- or vacuum-activated NH_4Y . In addition to the broad OH band assigned to hydroxyl nests, there are two relatively small hydroxyl bands observed with stabilized Y which differ in position from air- or vacuum-activated NH_4Y . Most authors seem to agree that the relative positions of the infrared bands are near 3600 and 3700 cm^{-1} , but they have disagreed on structural assignments and relative acidity (6,9,10,11).

Based on the current study and the proposed model for stabilized Y, it seems reasonable to conclude that the OH groups responsible for the 3600 cm^{-1} band are in relatively inaccessible positions, possibly associated with the μ -trioxotri-aluminum cations inside the sodalite cage. The 3600 cm^{-1} band is affected slightly by benzene and NH_3 , and not all by NaCl or dilute NaOH solution and is, therefore, not strongly acidic. Steaming above 873 K, where framework annealing takes place, nearly eliminates this hydroxyl group. The OH groups responsible for the 3695 cm^{-1} band are definitely accessible and are completely eliminated by both benzene and NH_3 . They are not strongly acidic, since both NaCl and dilute NaOH solution do not affect the size of the OH band. This hydroxyl group may be associated with the defect centers in the zeolite framework, since steaming at 1043 K completely eliminates the infrared band.

Literature Cited

- 1) Breck, D. W., "Zeolite Molecular Sieves: Structure, Chemistry and Use", (Wiley-Interscience, New York, 1974), p. 474-483, 507-518.
- 2) Kerr, G. T., Adv. Chem. Ser., Amer. Chem. Soc. (1973) 121, Mol. Sieves, Internat. Conf. 3rd, 219.
- 3) Kerr, G. T., J. Phys. Chem. (1967) 71, 4155.
- 4) Kerr, G. T., J. Catal. (1969) 15, 200.
- 5) Maher, P. K., Hunter, F. D., and Scherzer, J., Adv. Chem. Ser., Amer. Chem. Soc. (1971) 101, Mol. Sieves, Internat. Conf. 2nd, 266.
- 6) Peri, J. B., Proc. 5th Internat. Congress on Catalysis (1972), 329.
- 7) Breck, D. W., and Skeels, G. W., Proc. 6th Internat. Congress on Catalysis (1976).
- 8) Bennett, J. M., Breck, D. W., and Skeels, G. W., to be published.
- 9) Scherzer, J., and Bass, J. L., J. Catal. (1973) 28, 101.
- 10) Ward, J. W., J. Catal. (1970) 19, 348.
- 11) Jacobs, P. A., and Uytterhoeven, J. B., J. Catal. (1971) 22, 193.
- 12) Kerr, G. T., J. Phys. Chem. (1968) 72, 2594.
- 13) Bennett, J. M., and Smith, J. V., Private communication.

- 14) K \ddot{u} hl, G. H., *Mol. Sieves, Internat. Conf. 3rd, Recent Progress Reports* (Leuven University Press, 1973), 227
- 15) Antoshin, G. V., Minachev, Kh.M., Sevastjanov, E. N., and Kondratjev, D. A., *Russ. J. Phys. Chem.* (1970) 44, 1491.
- 16) Peri, J. B., *J. Phys. Chem.* (1975) 79, 1582.
- 17) Lacy, E. D., *Acta Cryst.* (1964) 18, 149.

Formation of Nickel (I) Ions by Hydrogen Reduction of Nickel (II)-Loaded Y Zeolite

EDOUARD GARBOWSKI,* MICHEL PRIMET, and MICHEL-VITAL MATHIEU

Institut de Recherches sur la Catalyse, 79, boulevard du 11 Novembre
1918, 69626, Villeurbanne Cédex, France

ABSTRACT

Hydrogen reduction of a NiCaNaY zeolite has been studied by U.V. reflectance, E.P.R. and I.R. spectroscopies. The formation of Ni^I ions as well as of finely divided metal is observed at the expense of accessible Ni(II) ions. Both species are reoxidized into Ni(II) ions by reaction with oxygen or nitric oxide.

Introduction

Zeolites containing transition metal ions are very interesting catalysts because of their high activity and selectivity. It has been demonstrated that the cations play an important rôle and are in many cases responsible for the modifications of the catalytic activity (1). Transition metal ions are usually introduced into the framework by exchange methods using aquo or amino complexes. During the thermal activation of the loaded zeolites, it was observed that ligands removal induced cations migration to specific zeolite sites (2, 3). Conditions of the activation treatment are determining factors for the location of cations in the framework. These zeolite sites possess their own geometry so that the located cation acquires rather special coordination. Moreover, unusual oxidation states can be stabilized in the zeolite framework, as observed in the case of Cu(I) ions (4).

Some transition metal ions can be easily reduced under specific conditions and lead to finely dispersed metal within the zeolite cavities (5, 6). High and homogeneous dispersions have been obtained for platinum zeolite systems (7). Interactions of the metal particles with the zeolite support can modify the catalytic properties of the supported metal (8).

The present work deals with the modifications of the properties of Ni(II)-loaded faujasites caused by hydrogen reduction. Electronic changes are studied by E.P.R. and U.V. spectroscopies ; the varia-

* U.E.R. de chimie-biochimie, Université Claude Bernard LYON I.

tions in the chemisorption properties are investigated using I.R. spectroscopy.

Experimental

The starting material was a NaY zeolite with $\text{SiO}_2/\text{Al}_2\text{O}_3 = 4.8$ supplied by the Linde Co. (SK-40). Two successive exchanges were performed : (i) part of the sodium ions were first exchanged by stirring a suspension of the NaY form with a solution of 0.03 M calcium nitrate, (ii) nickel ions were then introduced in the obtained sample using a 0.01 M nickel nitrate solution. The exchanged zeolite was then washed until free of nitrate ions, and dried at 100°C in air. Analysis by flame photometry and colorimetric methods led to the following formula : $\text{Ni}_{9.5} \text{Ca}_{12.2} \text{Na}_{10}\text{Y}$.

The diffuse reflectance spectra were recorded at room temperature using an Optica Milano CF_4 NI spectrometer with magnesium oxide as reference. Infrared measurements were carried out at room temperature on a Perkin Elmer grating spectrometer (model 125). Zeolite powder was pressed into pellets (15 mg cm^{-2}) under a pressure of about 1 Ton cm^{-2} . The E.P.R. spectra were recorded at 77 K on a VARIAN E 9 spectrometer operating in the mode X-band.

The sample resulting from the exchange procedure was treated under oxygen up to 500 or 600°C for 10 hours, then evacuated at the same temperature for 2 - 4 hours. In the following parts, such samples will be referred to as oxidized samples. Oxidized samples were reduced at 200°C by hydrogen for 3 hours, then evacuated at the same temperature for 2 hours ; such samples will be referred to as reduced samples.

The gases used in the present work (CO , H_2 , O_2) were pure. Water was removed by using preactivated 4A molecular sieves. Nitric oxide was purified by the freeze-pump-thaw technique in order to eliminate traces of N_2 and NO_2 .

Results

Oxidized samples : After dehydration, all the samples showed a pink color characteristic of dehydrated nickel (II) zeolites (9). The U.V. spectrum showed two main bands at 21800 and 10000 cm^{-1} , a shoulder at 17000 cm^{-1} and a very weak band at ca. 5500 cm^{-1} (figure 1 a). Carbon monoxide or oxygen adsorption did not modify the U.V. spectrum. The infrared spectrum presented only a weak $\nu(\text{OH})$ band at 3635 cm^{-1} . Carbon monoxide adsorption gave two I.R. absorption bands at 2215 and 2195 cm^{-1} ; desorption at room temperature led to the disappearance of the latter, whereas the former was weakened (figure 2 A). Nitric oxide adsorption led to the formation of an intense band at 1900 cm^{-1} which disappeared when the sample was heated under vacuum above 200°C. No paramagnetic signal attributable to nickel species could be detected.

Reduced samples : After hydrogen reduction, the solid exhibited a brilliant malachite green color and drastic changes were observed in the U.V. spectrum (figure 1 b). Two strong bands appeared at

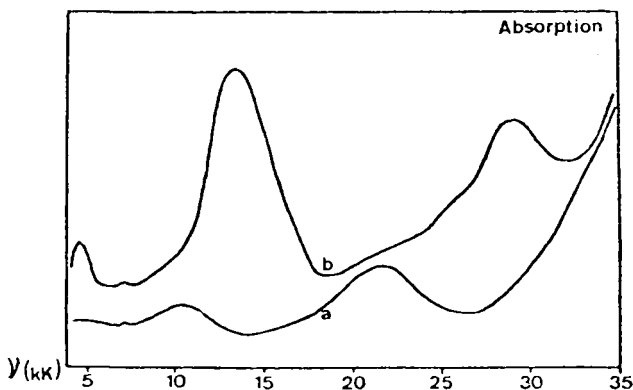


Figure 1. *Uv* reflectance spectra of NiCaNaY zeolite. (a), oxidized sample (oxygen and vacuum treatment at 500°C); (b), reduced sample (oxidized sample reduced by hydrogen at 200°C, then evacuated at 200°C).

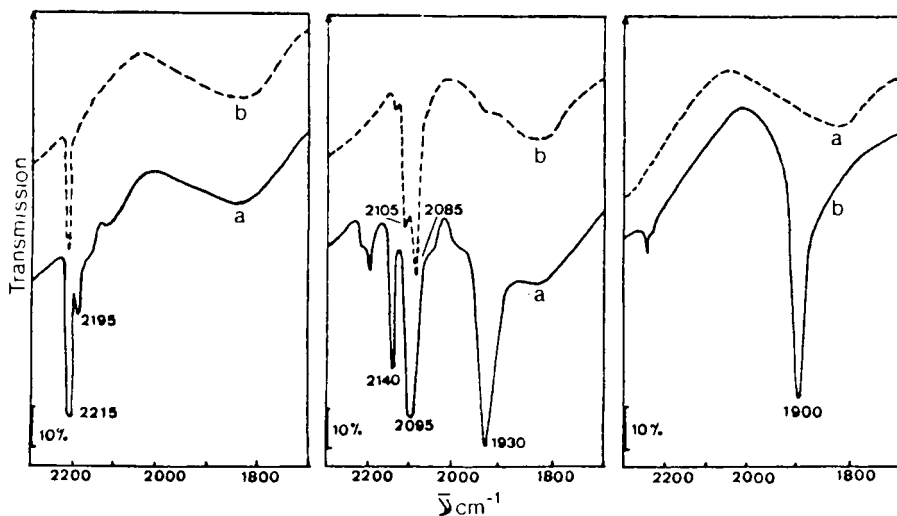


Figure 2. *Infrared* spectra of NiCaNaY zeolite.

A, CO adsorption on oxidized sample. (a), oxidized sample contacted with a 20-torr CO pressure at 25°C; (b), sample (a) evacuated at 25°C. B, CO adsorption on reduced sample. (a), reduced sample contacted with a 20-torr CO pressure at 25°C; (b), sample (a) treated under vacuum at 25°C. C, NO adsorption on reduced sample. (a), background of the reduced sample; (b), introduction of a 10-torr NO pressure at 25°C.

13500 and 29500 cm^{-1} , a weak one at 4700 cm^{-1} and a shoulder near 25000 cm^{-1} . Oxygen adsorption at room temperature caused a strong decrease of the previous bands. On heating under oxygen between 100 and 200°C for several hours, these bands completely vanished and the spectrum observed for oxidized samples was restored. NO adsorbed onto the reduced sample caused, at room temperature, the disappearance of the U.V. spectrum observed for the reduced sample.

The reduction caused only a small increase of the intensity of the $\nu(\text{OH})$ bands. CO adsorption gave a more complicated spectrum than for the oxidized sample: four bands at 1930, 2095, 2140 and 2195 cm^{-1} were observed (figure 2 B). By evacuation at 25°C, the bands at 1930, 2140 and 2195 cm^{-1} disappeared, whereas the 2095 cm^{-1} band is split into two components at 2085 and 2105 cm^{-1} . These last two bands vanished when the sample was contacted with oxygen at 25°C. Upon heating the obtained sample under oxygen at 200°C followed by an evacuation at the same temperature, CO adsorption gave only two bands at 2215 and 2195 cm^{-1} . NO adsorption at 25°C on the reduced sample produced an intense band at 1900 cm^{-1} and a small doublet near 2200 cm^{-1} due to gaseous or weakly adsorbed N_2O (figure 2 C).

Reduced samples exhibited paramagnetic species giving an E.P.R. signal attributed to d^9 species in axial symmetry ($g_{\perp} = 2.095$ and $g_{\parallel} = 2.48$ and 2.80) (figure 3a). Oxygen adsorption between 25 and 100°C caused the disappearance of the previous signal and the formation of one triplet ($g_1 = 2.0015$, $g_2 = 2.008$ and $g_3 = 2.045$) (figure 3b). NO adsorbed at 25°C onto the reduced sample gave a new E.P.R. signal which presented two values of g_{\perp} (2.16 and 2.19) and two values of g_{\parallel} (2.36 and 2.42) (figure 3c).

Discussion

Oxidized samples: on oxidized and dehydrated NiCaNaY samples, U.V. bands at 21800 and 10000 cm^{-1} must be attributed to transitions between 3F and 3P states of $3d^8$ electronic configuration of Ni(II) ions in octahedral field (9). In hexaquo complexes, these transitions produce bands at 25000 and 13500 cm^{-1} ; the intense bathochromic shift encountered for nickel-loaded zeolites is mainly due to the weak crystal field of the zeolite sites. We have previously studied the modifications of the U.V. spectra of Ni(II) ions loaded in different zeolites (A, X and Y forms) (10). In every case, the bathochromic effect was observed; the weaker the crystal field, the stronger the bathochromic effect. X-ray studies performed on NiNaY zeolite showed that Ni(II) cations were mainly located in S_I sites (3). In these sites, the cation to oxygen distances were anomalously long; the shorter the cation-ligand distance, the stronger the crystal field. Since similar U.V. spectra were observed both on NiNaY and NiCaNaY forms, the majority of the Ni(II) ions must be located in S_I sites (11).

On the other hand, Ca(II) ions show also a great tendency to occupy the same S_I sites (12); it seems that in NiCaNaY zeolite

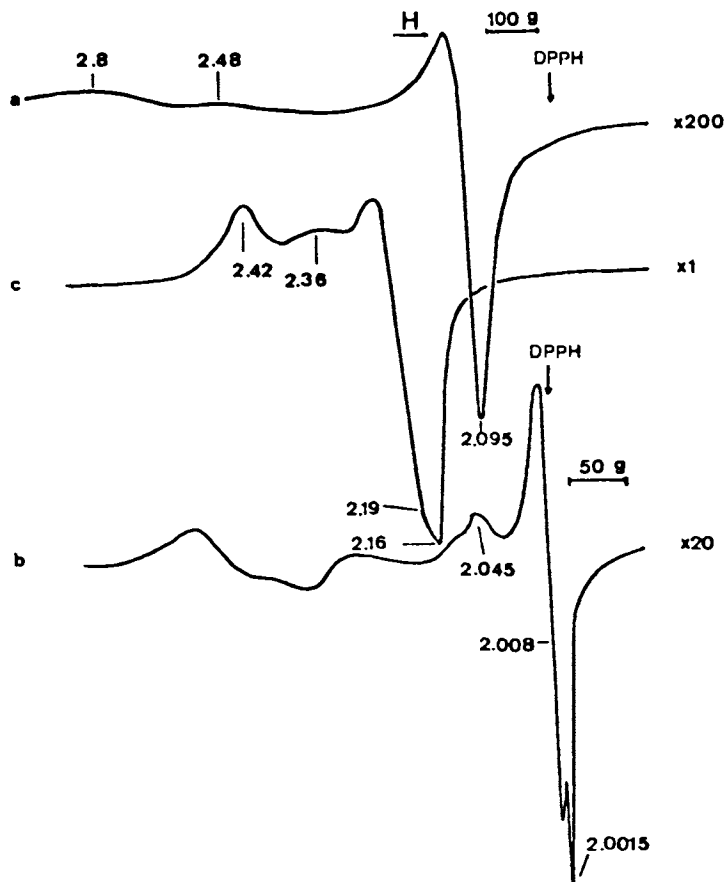


Figure 3. E.P.R. spectra of NiCaNaY zeolite. (a), reduced sample; (b), reduced sample contacted with oxygen at 100°C; (c), reduced sample contacted with NO at room temperature.

a competition occurs between Ca(II) and Ni(II) to occupy S_I sites. Some discrepancies appeared in the literature about the preferential occupation of the sites by Ca(II) or other divalent cations (12, 13, 14). Carbon monoxide adsorption onto oxidized samples gives two \sqrt{CO} bands. These bands are weak and correspond to small amounts of accessible ions, i.e., in the supercages; it must be recalled that CO does not enter the sodalite unit or the hexagonal prism. The 2195 cm^{-1} band must be attributed to CO bonded to Ca(II) ions, whereas the 2215 cm^{-1} band is correlated with the presence of Ni(II) ions (15). This last band is not observed for $\text{Ni}_9\text{Na}_{38}\text{Y}$ sample although the nickel content is similar to that of NiCaNaY . For $\text{Ni}_{19}\text{Na}_9\text{Y}$, the 2215 cm^{-1} band has about the same intensity (for same CO pressures) as for NiCaNaY . These results show that in NiCaNaY samples, some Ni(II) are not in hidden positions (S_I sites for example), but do occupy sites accessible to CO. In the supercage sites, Ni(II) ions can be octahedrally coordinated only if OH groups or molecular water are available to insure complete coordination. The failure to detect sufficient amounts of hydroxyl groups or water in dehydrated samples allows us to rule out this hypothesis. Since no additional bands appear in the U.V. spectra the concentration of Ni(II) ions present in the supercages (and tetrahedrally coordinated) must be low.

Finally, Ni(II) ions in $\text{Ni}_9\text{Ca}_{12}\text{NaY}$ zeolite are mainly located in S_I sites; however, some Ca(II) and Ni(II) ions occupy accessible positions, probably in supercages, but their number must be small in comparison with that of ions in hidden sites.

Reduced samples : After hydrogen reduction, the U.V. spectrum shows two strong bands at 13500 and 29500 cm^{-1} which cannot be attributed to Ni(II) ions in any symmetry. The experimental results can be explained by the formation of Ni(I) ions; the U.V. spectra are due to transitions between the ground state ($3d^9$) and excited states ($3d^8 4s^1$).

This $3d^9$ ion (Ni^I) is isoelectronic with Cu(II) ion and is likely to behave similarly in the zeolite lattice, with respect to preferential occupancy of trigonal sites (S_I' or S_{II}). In these sites, the crystal field is weak, and weaker for Ni(I) than for Cu(II), since the charge of Ni(I) is smaller. Then, the low frequency band (4700 cm^{-1}) is assigned to a d-d transition of Ni(I) ions, whereas the same transition occurs at 5800 cm^{-1} for Cu(II) in tetrahedral coordination (16).

The two other strong bands (13500 and 29500 cm^{-1}) are due to (d - s) transitions from ground state to upper excited states belonging to the $3d^8 - 4s^1$ configuration. Some states (2F 2D and 2P) have the same spin as the ground state, and mixing of odd parity p orbitals both in ground state and excited states allows transitions which become partially Laporte-allowed with increase in intensity. As the crystal field effect will be small, the transitions should have the same energy as the 2F (13600 cm^{-1}) and 2P (29500 cm^{-1}) states of the $3d^8 - 4s^1$ configuration (17). For the 2D state, the transition should occur at ca. 23000 cm^{-1} ; only

a shoulder is observed near this value in the left side of the transition at 29500 cm^{-1} . Recently, Mc. Clure et al. (18, 19) have studied transitions of the M(II) first transition row beyond the inner shell region. They observed (d - s) transitions with oscillator strength about two orders of magnitude greater than those of (d - d) transitions. A similar band close to 13500 cm^{-1} was also reported (20) for reduction studies of Ni(II) ions by sodium vapors. On the other hand, Jacobs et al. (21) observed a (d - d) transitions for Cu(II) (d^9) in Y zeolite at 10700 cm^{-1} . In view of this result, (d - d) transitions for Ni(I) also d^9 ion) should occur at lower frequencies since the charge of the cation is smaller, therefore we believe that we are actually observing a (d - s) transition. More recently, Minachev et al. (22), studying the reduction of Ni(II)-loaded zeolite, have obtained evidence for the presence of Ni(I) ions.

Infrared spectra of CO adsorbed on reduced samples show drastic changes by comparison with the oxidized state. The band at 2215 cm^{-1} attributed to CO bonded to Ni(II) ions does not appear ; it seems that Ni(II) ions in accessible positions have been eliminated by hydrogen reduction. The small band at 2195 cm^{-1} is assigned to CO interacting with Ca(II) ions. The band at 2140 cm^{-1} possesses a \checkmark CO frequency which is intermediate between those of CO adsorbed on Ni(II) ions and nickel in metallic state. Some years ago, Peri (23) reported a similar frequency for a NiO/SiO₂ sample reduced under mild conditions ; he concluded it was due to the formation of Ni(I) state. The conditions of formation of this band and its frequency, as well our U.V. results, lead us to identify the adsorption center as a Ni(I) ion in accessible positions.

The attribution of the 2095 and 1930 cm^{-1} bands is more ambiguous. I.R. studies of CO adsorption onto Ni/SiO₂ catalysts indicate the formation of bands attributed to CO adsorbed in a linear form (\checkmark CO = 2058 cm^{-1}) and in a bridged form (\checkmark CO = 1940 cm^{-1}) (24, 25). The band at 2095 cm^{-1} must be assigned to CO adsorbed on metallic nickel in a linear for since this band disappears by room temperature oxygen treatment. The 1930 cm^{-1} band could be attributed to CO bonded to Ni(0) atoms in the bridged form, but usually this band is not removed by a room temperature evacuation. Assignment of the band at 1930 cm^{-1} to CO bridged between two Ni(I) ions seems unlikely for stability and frequency range reasons. We prefer to assign this band to Ni - CO ~ Ni species ; the poor stability towards vacuum treatment could be tentatively explained by the small size of the nickel particles occluded into the cavities. The failure to observe a ferromagnetic resonance signal is in agreement with the formation of small metal clusters.

The formation of Ni(I) ions is also in agreement with the E.P.R. measurements. On the oxidized sample, no paramagnetic species can be detected, except Mn(II) impurities introduced during the exchange procedure. After heating at 200°C in hydrogen, a signal characterized by an axially symmetric g tensor was recorded. The fact that two values for g_{\parallel} are observed may mean that two

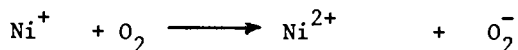
types of Ni(I) ions are present in zeolite in two slightly different environments. The observed g values are very close to those reported for Cu(II) ions in dehydrated zeolites :

	g_{\perp}	g_{\parallel}
Cu(II) Y zeolite (26)	2.065	2.32
NiCaNaY (present work)	2.095	2.48 and 2.80

The similarity of both spectra (disregarding the hyperfine interaction) indicates that in both cases the 3 d^9 ions are in similar sites. However, for nickel samples, two types of Ni(I) ions can be postulated since two values are observed for g_{\parallel} . From quantitative E.P.R. measurements, Ni(I) form represents ca. 4 % of the overall nickel content ; the reduction process is thus very limited. Similar results have been previously reported by Rabo et al. (20), but the reactivity of the obtained species ($g_{\perp} = 2.09$) seems different. These differences may be explained by the use of another exchanged zeolite (without Ca) and by a different reduction process (Na vapor at 580°C)

Reactivity of Ni(I) species : This reactivity was checked towards oxygen and nitric oxide.

With oxygen, Ni(I) ions react almost completely at room temperature : U.V. and E.P.R. bands are strongly weakened ; they disappear by oxygen treatment at 100°C and the U.V. spectrum of Ni(II) ions is restored. E.P.R. results can be interpreted by the formation of O_2^- species ($g_1 = 2.0015$, $g_2 = 2.008$ and $g_3 = 2.045$) adsorbed on divalent cations. On the other hand, CO adsorbed on reduced samples treated by O_2 at 100 - 200°C gives only bands due to Ni(II) and Ca(II) ions ; no absorptions caused by Ni(I) or Ni(0) species are observed. Ni(I) ion oxidation could be represented by the scheme :



This oxidation-reduction process is reversible at around 200°C. The interaction with oxygen molecules concerns mainly one of the two Ni(I) types, probably the species which are in accessible positions.

Infrared spectra of NO adsorbed at room temperature on reduced samples are quite similar to those observed on oxidized samples, e.g., a single ν (NO) band (1900 cm^{-1}) is observed in both cases. Upon NO adsorption, U.V. spectroscopy shows also the disappearance of the Ni(I) signal and the formation of a new signal. This last one was first reported by Ben Taarit et al. (27) during the NO adsorption on Ni(II)-loaded zeolites. It seems unlikely that Ni^+ , NO^+ pairs are formed in this process because of the observation of a ν (NO) band at too low a frequency to be due to NO^+ ion. NO^+ ion has been observed when NO adsorption occurs onto Pd^{3+} ions

(28) according to the scheme : $\text{Pd}^{3+} + \text{NO} \rightleftharpoons \text{Pd}^{2+}, \text{NO}^+$, where the disappearance of the E.P.R. signal due to Pd^{3+} ions is correlated with the formation of $\nu(\text{NO})$ bands at 2175 and 2025 cm^{-1} . The E.P.R. signal observed by NO adsorption on Ni(II) or Ni(I) ions may be explained by a delocalization of the odd electron of NO into a molecular orbital with a large d character.

Both disappearance of E.P.R. signal and U.V. spectra attributed to Ni(I) ions by NO adsorption show that all the Ni(I) ions have been reached and oxidized to the divalent state. The presence of N_2O confirms the oxidizing role of nitric oxide, as previously mentioned (28).

These results clearly show that by hydrogen reduction of a Ni(II) Y zeolite a new species is formed : this species behaves as a reducing agent which is strongly oxygen and nitric oxide-sensitive. The responsible entity is most probably a Ni(I) ion in monomeric form because of the observation of an E.P.R. signal. This unusual oxidation state for nickel is certainly stabilized by the zeolite framework.

Conclusion

In this paper, it has been shown that under mild conditions of reduction, Ni(II)-loaded zeolites do not lead to bulk metal. Moreover, univalent cations are formed and stabilized by the zeolite framework. U.V. and E.P.R. spectroscopies showed new results interpreted in terms of monomeric Ni(I) complexes. Ni(I) cations are located in two different types of sites. Adsorption of oxygen or nitric oxide leads to the rapid disappearance of Ni(I) by oxidation into the divalent state. This reducibility of Ni(II) is thought to be due to some accessible Ni(II) ions located in sites in which they are stabilized with a low energy. All these results emphasize the special coordinating rôle of the zeolite lattice and the stabilization of cations in unusual valence states.

Literature cited

1. Minachev, K.M., and Isakov, Y.I., *Adv. Chem. Ser.* (1973) 121, 451.
2. Gallezot, P., Ben Taarit, Y., and Imelik, B., *J. Catalysis* (1972) 26, 481.
3. Gallezot, P., and Imelik, B., *J. Phys. Chem.* (1973) 77, 652.
4. Naccache, C., Che, M., and Ben Taarit, Y., *Chem. Phys. Letters* (1972) 13, 109.
5. Dalla Bèta, R.A., and Boudart, M., *Proceedings Vth Int. Cong. Catal.*, Palm Beach (1972) paper n° 100.
6. Gallezot, P., and Imelik, B., *Adv. Chem. Ser.* (1973) 121, 66.
7. Gallezot, P., Alarcon-Diaz, A., Dalmon, J.A., Renouprez, A., and Imelik, B., *J. Catalysis* (1975) 39, 334.
8. Figueras, F., Gomez, R., and Primet, M., *Adv. Chem. Ser.* (1973) 121, 480.

9. Garbowski, E., Kodratoff, Y., Mathieu, M.V., and Imelik, B., *J. Chim. Phys.* (1972) 69, 1386.
10. Garbowski, E., and Mathieu, M.V., *C.R. Acad. Sci. Paris* (1975) 280C, 1125.
11. Garbowski, E., Thesis, Lyon (1976).
12. Bennett, J.M., and Smith, J.V., *Mater. Res. Bull.* (1968) 3, 633.
13. Egerton, T.A., and Stone, F.S., *Trans. Farad. Soc.* (1970) 66, 2364.
14. Egerton, T.A., and Vickerman, J.C., *J. Chem. Soc. Farad. Trans. I.* (1973) 69, 39.
15. Angell, C.L., and Schaffer, P.C., *J. Phys. Chem.* (1966) 70, 1413.
16. Weakliem, H.A., *J. Chem. Phys.* (1962) 36, 2117.
17. Moore, C.E., Atomic Energy Levels, Nat. Bur. Stand., Circular n° 467, Washington (1952) Vol. II.
18. Chase, D.B., and Mc. Clure, D.S., *J. Chem. Phys.* (1976) 64, 74.
19. Sabatini, J.F., Salwin, A.E., and Mc. Clure, D.S., *Phys. Rev. B.* (1975) 11, 3832.
20. Rabo, J.A., Angell, C.L., Kasaï, P.H., and Schomaker, V., *Disc. Farad. Soc.* (1966) 41, 328.
21. Jacobs, P.A., De Wilde, W., Schoonheydt, R.A., Uytterhoeven, J.B. and Beyer, H., *J. Chem. Soc., Faraday. Trans. I* (1976) 72, 1221.
22. Minachev, K.M., Antoshin, G.V., Shpiro, E.S., and Yusifov, Y.A. *Proceedings of the VIth Int. Cong. Catal. London* (1976) paper B.2.
23. Peri, J.B., *Disc. Farad. Soc.* (1966) 41, 121.
24. Eischens, R.P., and Pliskin, W.A., *Adv. Catal* (1958) 10, 1.
25. Dalmon, J.A., Primet, M., Martin, G.A., and Imelik, B., *Surface Science* (1975) 50, 95.
26. Naccache, C., and Ben Taarit, Y. *Chem. Phys. Lett.* (1971) 11, 11.
27. Naccache, C., and Ben Taarit, Y., *J. Chem. Soc., Farad. Trans I,* (1973) 69, 1475.
28. Che, M. Dutel, J.F., Gallezot, P., and Primet, M., *J. Phys. Chem.* (in press).

Formation of Iron Clusters in Zeolites with Different Supercage Sizes

F. SCHMIDT, W. GUNSSER, and J. ADOLPH

Institute of Physical Chemistry, University of Hamburg,
Laufgraben 24, D-2000 Hamburg 13, West Germany

ABSTRACT

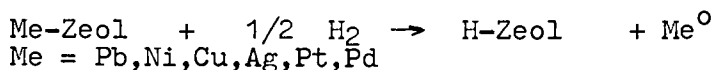
Mössbauer spectroscopy, electron microscopy and magnetic measurements of Na reduced $\text{Fe}^{2+}\text{-X}$, $\text{Fe}^{2+}\text{-Y}$, and $\text{Fe}^{2+}\text{-A}$ zeolites show formation of iron particles outside the zeolite cavities with mean diameter of 60 Å, but preferably formation of iron clusters with extremely narrow particle size distribution and diameters less than 13 Å.

Introduction

Transition metal ion-exchanged zeolites have been used to obtain well dispersed metal catalysts. Some cationic forms of dehydrated zeolites can be reduced by heating the zeolite in a reducing atmosphere like hydrogen. This leads either to highly dispersed metal atoms in the channels and cavities of the zeolite or to external deposition of small metal crystallites.

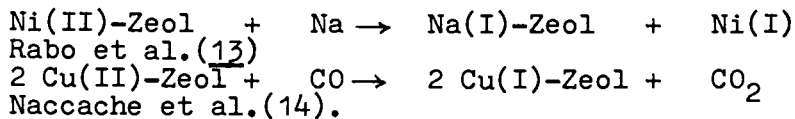
Some methods of reduction of transition metal ion-exchanged zeolites are listed in Table I. Some transition metal ions may be stabilized in unusual oxidation states - i.e. Ni(I), Pd(I).

Table I



Lewis(1), Rabo et al.(2), Yates(3), Bredikhina et al.(4), Romanowski(5), Riekert(6), Richardson(7), Reman et al.(8), Kudo et al.(9), Dalla Betta et al.(10), Minchev et al.(11), Beyer et al.(12).

Table I(continued)



As reported by Küspert (15), hydrogen reduction of ferrous ion-exchanged zeolites is possible only at and above 1023 K. But these conditions lead to lattice destruction. Furthermore, X- and A-type zeolites in the hydrogen forms are not known to be stable. So we reduced our samples by sodium vapour at 673 and 573 K. Thus the initial sodium form of zeolite was prepared, containing reduced electroneutral metal.

In the present study we were especially interested in the magnetic properties of small metallic iron clusters. These particles should be formed within the zeolite cavities and their diameters should be limited by the supercage sizes.

Experimental Methods

Sodium A, X, and Y-zeolites were obtained from the Linde Division of Union Carbide. All steps of preparation were made in a nitrogen atmosphere. Only oxygen free distilled water was used. The iron X and Y zeolites were prepared by treating the sodium form of Linde zeolite with an aqueous solution of ferrous sulphate in a nitrogen atmosphere at $p_{\text{H}} 5$ for 3 hours as described by Delgass (16).

For preparing the ferrous exchanged form of A-type zeolite the ferrous salt solution was obtained by dissolving 1,88 g ferrous sulphate hepta hydrate in 45 cm³ water thus reaching a p_{H} of 4. A few grains of ascorbic acid were added to reduce any ferric ions present. The exchange was allowed to proceed for 2 and 20 hours respectively at 293 K and at $p_{\text{H}} 8$ as described by Dickson et al. (17).

Because of the poor crystallinity thus obtained we chose another method for ferrous sulphate preparation. By dissolving between 5 and 200 mg iron in a calculated volume of 2N sulphuric acid diluted in approximately 6 cm³ water we got a ferrous sulphate solution of $p_{\text{H}} 5$. The ferrous ion-exchanged form of A-type zeolite was prepared by treating 0,5 g oxygen free zeolite with the sulphate solution at 293 K for 3 h and at 343 K for 0,1 and 0,3 h respectively.

This method was changed to prevent formation of iron gel completely. The suspension of 0,5 g oxygen free A-zeolite in about 2 cm³ water was initially adjusted to pH 5 with about 6 ml of standard acetic acid buffer solution. Then the zeolite was ion-exchanged several times. After being washed ten times, the exchanged ferrous A-zeolite was dehydrated at 673 K for 24 h.

After dehydration under high vacuum at 673 K for 24 h the samples were reduced with a calculated amount of sodium. Sodium was placed at the bottom of a glass tube. The dehydrated zeolite sample was supported 3 cm above it on a small glass frit. The top of the tube was formed as a Mössbauer cell. A full-length heating mantle was brought to 673 K. After a heating period of 5, 10, 15, 20, 25, 30, 48 h, respectively the heating mantle was removed and the tube was allowed to cool. Then the zeolite was brought into the Mössbauer cell. This cell was sealed and then mounted in a Mössbauer spectrometer.

Analysis for iron was made of all samples by X-ray fluorescent spectroscopy. The crystallinity of the ferrous A, X and Y zeolite after ion-exchange, after dehydration and after reduction was examined by X-ray powder diffraction without exposure to air. Sharp lines in the powder patterns indicated that no structural breakdown had occurred with X- and Y-type zeolites and with A-type zeolites using the second and third method of preparation.

The Mössbauer spectra were taken on a Friesseke & Hoepfner constant acceleration spectrometer in conjunction with a multi-channel analyser using a ⁵⁷Co in Cu source. All isomer shifts are reported with respect to standard α -Fe. Spectra taken at 300 K were made with the glass cells. Spectra from 4 K to 300 K were made with a beryllium sample holder mounted in a Leybold cryostat. The zeolite was placed in the beryllium holder without exposure to air. The data from each spectrum were analysed by a least squares fitting program.

Magnetic susceptibility data were obtained by the Felddifferenzen-method at temperatures between 77 K and 650 K and variable fields up to 1,25 T. We also used a Foner magnetometer at temperatures between 4 K and 500 K.

Results and Discussion

The X-ray diffraction pattern shows that the Fe²⁺ ion-exchanged A-type zeolite was partly amorphous

if prepared according to the first method. This was expected because of the arguments reported by Ione (18) in the last conference. The second method using exchange times of 3 h (at 293 K), 0,1 and 0,3 h (at 343 K) and the third method using exchange times shorter than 0,3 h (at 293 K) lead to complete crystalline samples.

Figure 1a shows the characteristic room temperature spectrum of crystalline, dehydrated Fe^{2+} -A zeolite obtained by using the second method of preparation for 0,3 hours. We attributed the doublet with i.s. = 0,19 mm/s \pm 6% and q.s. = 0,91 mm/s \pm 2% to iron gel. This is in agreement with the arguments of Ione (18). Therefore, we chose the third method of ion-exchange: a buffer solution was used to prevent iron gel formation and the exchange time was shortened. The spectra of these samples show only two doublets (Figure 1b). Therefore, our supposition of iron gel formation was confirmed. In the resulting spectrum the doublet with i.s. = 0,61 mm/s \pm 0,3% and q.s. = 0,47 mm/s \pm 0,8% is associated with Fe^{2+} ions on the sodalite window sites with 3-fold coordination to lattice oxygens as reported by Dickson (17). We cannot yet render a distinct explanation of the doublet with i.s. = 0,87 mm/s \pm 1,2% and q.s. = 2,26 mm/s \pm 1%, but we suppose that a second site for iron ions exists in A-type zeolites detectable only at small degrees of ion-exchange and using ^{57}Fe .

So it seems to us that the best method preparing ferrous ion-exchanged A-type zeolite is using the buffer solution, low temperatures and short exchange times. The spectra of Fe^{2+} -X and Fe^{2+} -Y zeolite are similar to those reported by Garten et al. (19) and by Morice et al. (20). Detailed discussions of these spectra are given by those authors.

All the reduced samples show the ferrous oxidation state spectra and the superparamagnetic spectra of small iron clusters. The ratio of area of these groups depends on the rate of reduction.

In an assembly of noninteracting particles, the relaxation time for a spontaneous change of the direction of the magnetization vector is given by the Néel equation

$$(1) \quad \tau_0 = \frac{1}{a \cdot f} e^{\frac{2 K v}{kT}}$$

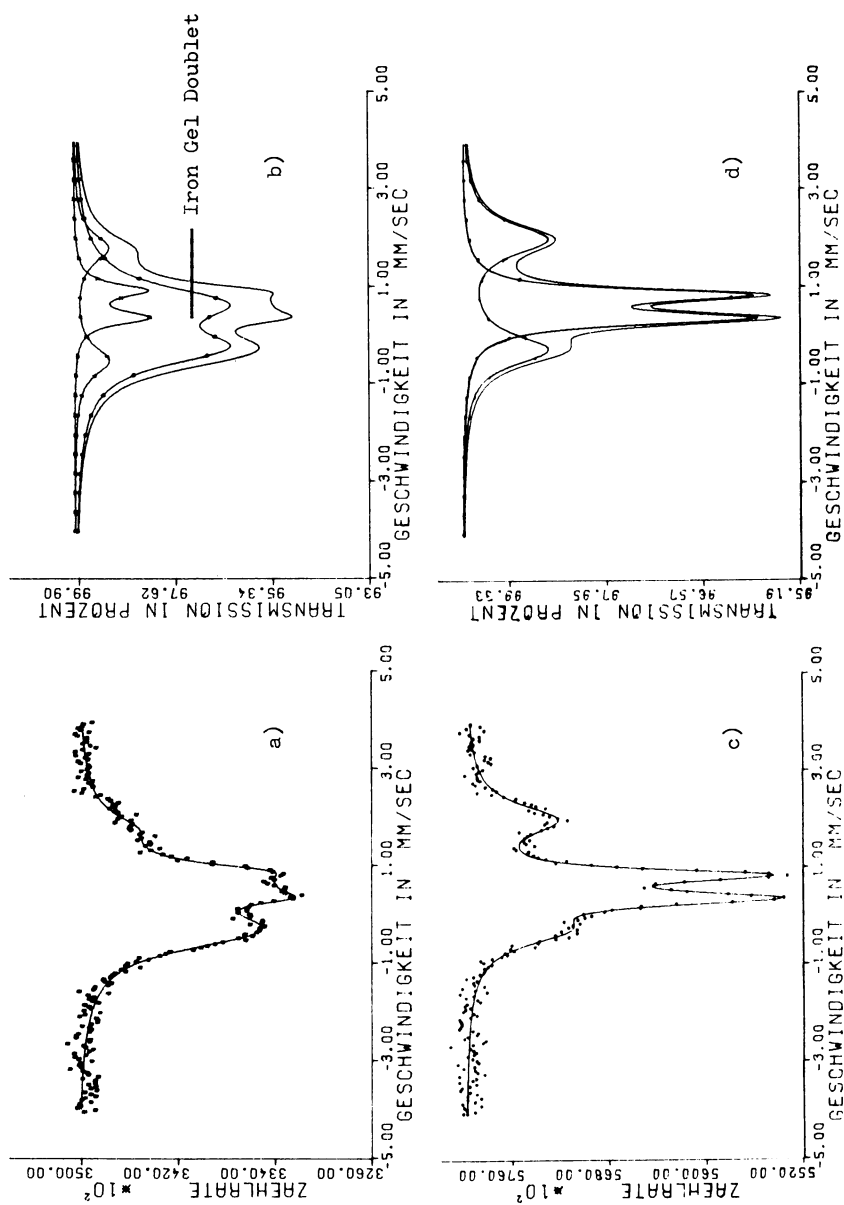


Figure 1. Mössbauer spectra at 295 K, $v = \pm 4$ mm/s. (a), Fe-A, prepared according to the second method; (b), computer fit; (c), third method; (d), computer fit.

in which a is a geometrical factor, v the volume, K the anisotropy constant of the particle. The frequency factor f is the Larmor frequency of the magnetization vector in an effective field; $f = (KA) / (\gamma N_p h)$. A is the atomic weight. If the relaxation time is greater than the time required for the measurement, one can see a snapshot; i.e. if $\tau_0 \gg 1/\nu_L$: Zeeman splitting is observed - ν_L is the Larmor frequency of the nuclear spin around the effective field. For iron $1/\nu_L \sim 10^{-8}$ sec. For $\tau_0 \ll 1/\nu_L$ only the time mean value is observed - i.e. the Zeeman splitting will disappear.

For the fraction of the particles in a sample which are superparamagnetic, the observed spectrum will give a pure quadrupole-split center line if any electric field gradient is present. In Figure 2 a Mössbauer spectrum of a partially reduced ferrous ion-exchanged Y-zeolite is shown. The central doublet is due to superparamagnetic iron clusters. Besides the Fe^{2+} -doublet the usual magnetically split six-peak spectral component of the larger iron particles is to be seen. Taking the ratio of the area corresponding to the quadrupole doublet to the total spectral area, the fraction of the small iron clusters can be estimated (assuming the f -values for the two states are similar). Using the Néel equation and taking the values for iron reported by Arnold (21), the maximum size of the small iron clusters can be calculated from Mössbauer data: $V^{1/3} < 15,6 \text{ \AA}$.

In order to make sure that the central doublet is not due to atomically dispersed iron and to study the small iron particles in greater detail, electron micrographs of ultramicrotome cut reduced samples were taken at several magnifications from 40 000 to 200 000 times. These micrographs show a small number of larger particles with diameters up to about 500 \AA , but preferably they show a formation of iron clusters with extremely narrow particle size distribution. The maximum of the particle size distribution function was found to be 20 \AA . But the corresponding real particles could be 15 \AA or less because of a diffraction zone of approximately 2 \AA on each side of the particle diameter. Furthermore, the electron micrographs do not show particles of this size neither between the zeolite crystals nor on the outer surface of the zeolites, except a greater number of them in the middle of the cut zeolite crystallites. So we can conclude that all detectable particles are only inside the cavities. The distribution of par-

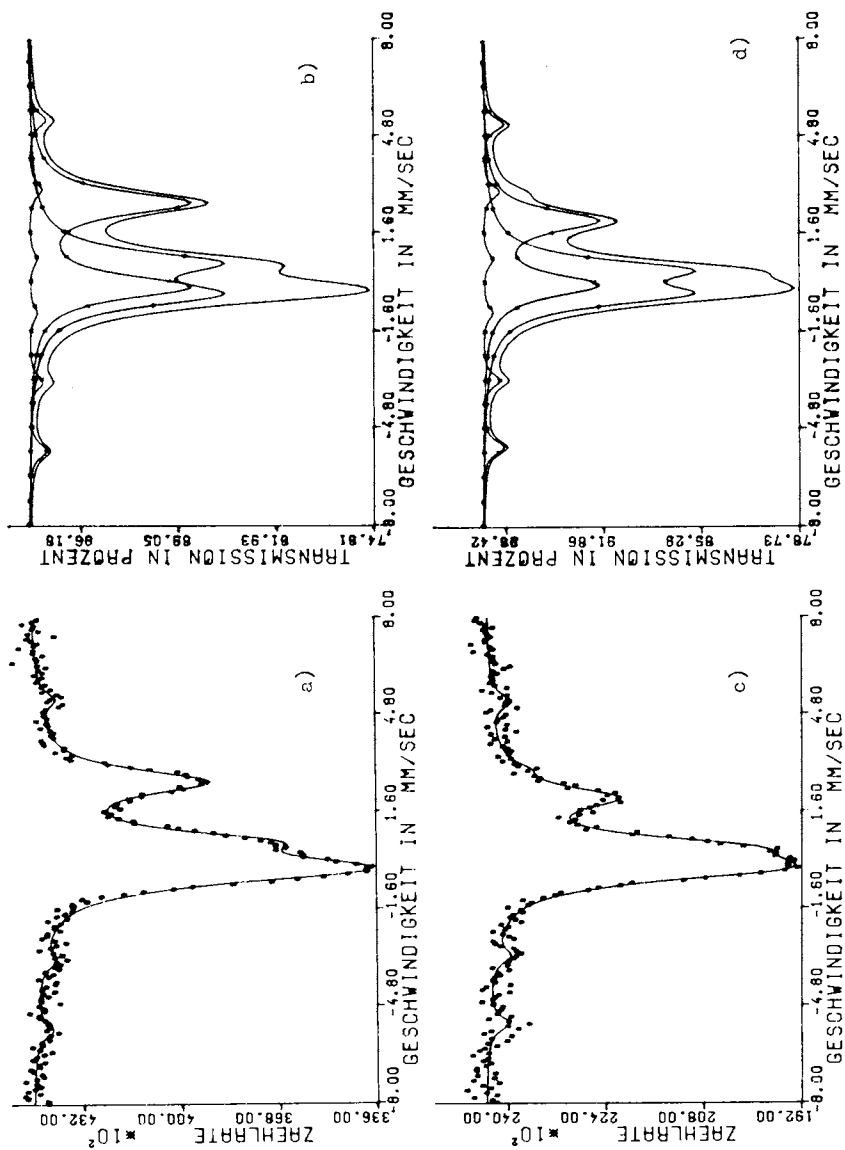


Figure 2. Mössbauer spectra of $\text{Fe}^0\text{-Y}/\text{Fe}^3\text{-Y}$, $v = \pm 8$ mm/s. (a), at 4.3 K; (b), computer fit; (c), at 295 K; (d), computer fit.

ticle sizes could be due to lattice imperfections like local derivations of the Si/Al ratio from the mean value resulting in a distribution of supercage sizes. This matter is still under investigation by STEM EDAX technique.

The magnetic susceptibilities of the dehydrated ferrous ion-exchanged zeolites were measured as a function of temperature. Measured susceptibilities were corrected for the diamagnetism of the aluminosilicate framework and of the sample holder and for the effects of a small amount of ferromagnetic impurity. The temperature dependence of the Fe^{2+} -ion susceptibility of a Y-zeolite could be represented by the Curie-Weiss-law with $p_{\text{eff}} = 5,54 \mu_B$ and $\theta = 105$. Because of the two types of Fe^{2+} -ion sites p and θ are only mean values. But the large θ value which reflects the magnetic exchange interaction within the system, is consistent with the model of the ion sites reported by Garten et al. (19).

Typical results of magnetization versus magnetic field of a reduced sample are given in Figure 3. Measured magnetizations were corrected for the diamagnetism. Taking the fraction of the unreduced iron from Mössbauer data, the field dependence of the magnetization of the reduced iron was calculated. The susceptibility of the small iron clusters which are paramagnetic from 150 K to 650 K and up to a field of 1 T was calculated by plotting the $\Delta G / \Delta H$ values versus $1/H^2$ and extrapolating to $1/H^2 \rightarrow 0$ according to the formula

$$(2) \quad \chi = \frac{d(L(x))}{dx} = \frac{1}{x^2} ; \quad x = \frac{p \cdot H}{k T} ; \quad x > 4$$

Corrections of the paramagnetism of the small iron clusters thus obtained were made, and by plotting the resulting magnetization curves versus H/T superposition was obtained from approximately 150 K to 650 K. Furthermore, no remanence could be detected in this temperature range. Analysing these curves, particle diameters of the large iron particles were obtained.

To estimate the volume v of the small clusters by means of the paramagnetic susceptibility the temperature dependence of the spontaneous magnetization $I_{\text{sp}}(T)_{\text{FeZeolite}}$ must be determined by equation (3). These values were plotted versus T/T_c , with T_c the Curie temperature of bulk iron. The Weiss curves lie distinctly below those of bulk iron, calculated according to the mean field theory.

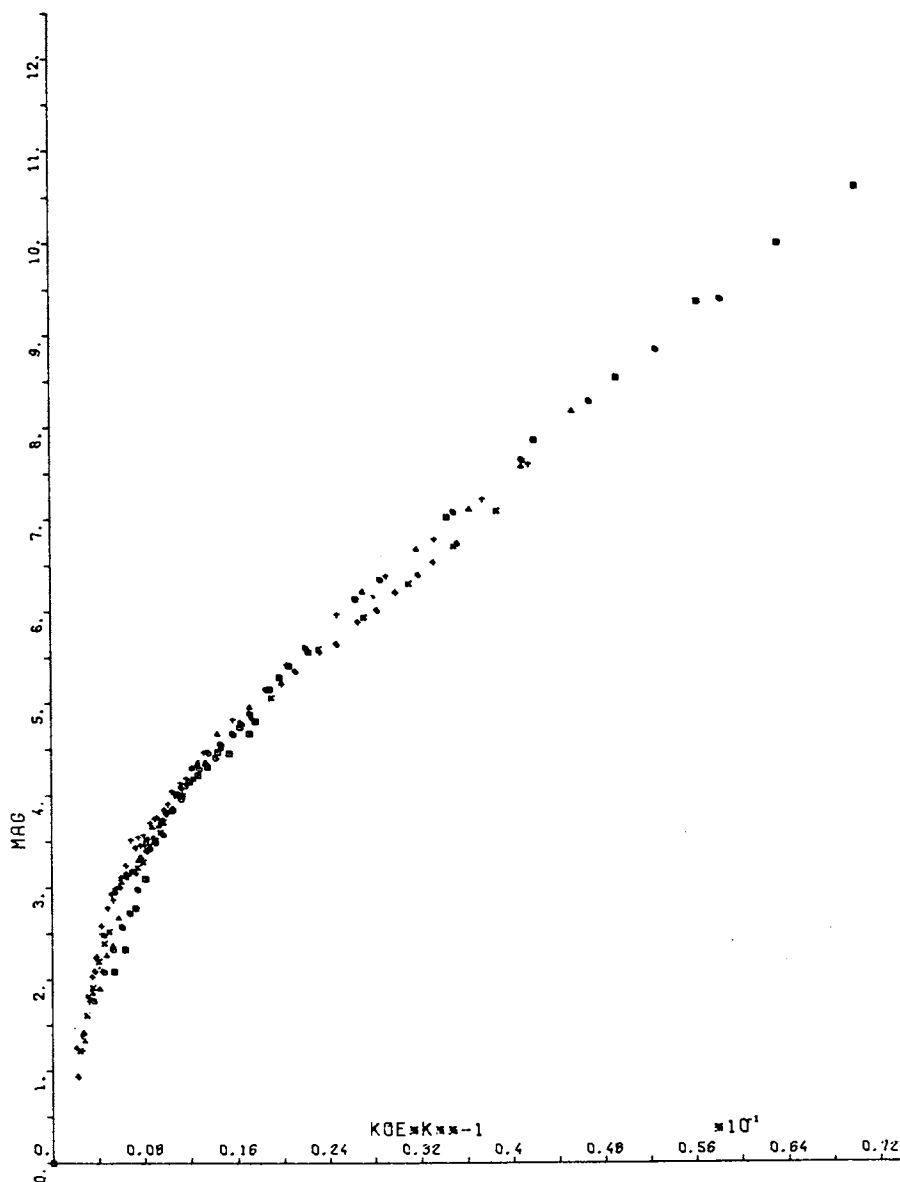


Figure 3. Magnetization (Gauss cm^3/g) vs. H/T curves of $\text{Fe}^\circ\text{-Y}/\text{Fe}^{2+}\text{-Y}$. \square , $T = 178$ K; \circ , $T = 214$ K; \triangle , $T = 273$ K; $+$, $T = 295$ K; \times , $T = 316$ K; \diamond , $T = 343$ K.

$$(3) \quad \frac{I_{sp}(T)}{I_{sp}(T_0)} = \frac{(\chi_T \cdot T)^{1/2}}{(\chi_{T_0} \cdot T_0)^{1/2}}$$

Taking the new Curie temperatures, new Weiss curves were calculated, from which the spontaneous magnetization I_{sp} -cluster can be taken. Thus the particle size can be derived from susceptibility data.
 $v^{1/3}$ FeNaY = 9 Å, $v^{1/3}$ FeNaA = 8 Å.

$$(4) \quad \chi = (I_{sp-clust})^2 V / (3 \rho kT)$$

The i.s. values of the Fe^0 doublet of the Mössbauer spectra (i.s. of $Fe^0 Y = 0,01$ mm/s, i.s. of $Fe^0 A = 0,41$ mm/s) are due to electron transfer from the surface shells of the iron clusters to the zeolite framework, but the values indicate that this electronic interaction is not very strong.

The large q.s. values of $Fe^0 Y$ of 0,69 mm/s show that not only the next nearest iron ions contribute to the electronic field gradient at the iron nuclei, but the zeolite framework also has an important influence on the q.s. values of the iron clusters. The q.s. as well as the i.s. values indicate, that the small iron clusters must be inside the zeolite holes.

Conclusion

Iron(II)-zeolites have been prepared by ion-exchange of faujasite-type zeolites with different Si/Al ratios under conditions preserving the zeolite structure and preventing iron gel formation. After dehydration the zeolites have been reduced with alkali metal vapour at 573 and at 673 K. Mössbauer spectroscopy of the reduced samples shows formation of some iron particles with diameters greater than 20 Å, but a preferred formation of iron clusters with extremely narrow particle size distribution and diameters less than 13 Å. The greater iron particles are outside the cavities. Their diameters are between 20 and 500 Å as was shown by electron microscopy and magnetic measurements. The iron clusters within the zeolite holes are superparamagnetic and their Mössbauer spectra show no HFS, even at 4 K. The iron particles outside the zeolite framework show the usual magnetically split six-peak spectral component at all temperatures between 4 and 300 K. By taking the ratio of the area corresponding to the quadrupole doublet to the total spec-

tral area, the fraction of the iron clusters inside the zeolite cavities has been estimated. The spontaneous magnetization of the small iron clusters has been measured from 4 to 650 K. The Weiss-curves lie distinctly below those of bulk material. Particle sizes of both fractions have been calculated from the separated magnetization curves.

Literature Cited

1. Lewis, P.H., *J.Phys.Chem.* (1963) 67 2151
2. Rabo, J.A., Schomaker, V., *Discuss.Faraday Soc.* (1966) 41 328
3. Yates, D.J., *J.Phys.Chem.* (1965) 69 1676
4. Bredikhina, T.N. and Evdokimov, V.B., *Russ.J.Phys. Chem.* (1967) 41 1601
5. Romanowski, W., *Roczniki Chemie Ann.Soc.Chim.Polonium* (1971) 45 427
6. Riekert, L., *Ber.d.Bunsenges.* (1969) 73 (4) 331
7. Richardson, J.T., *J.Catal.* (1971) 21 122
8. Reman, W.G., Ali, A.H. and Schuit, G.C.A., *J. Catal.* (1971) 20 374
9. Kudo, T., *Bull.of the Chem.Soc.of Japan* (1972) 45 607
10. Dalla Betta, R.A., *Proc.Intern.Congr.Catalysis V Amsterdam* (1972) 100
11. Minchev, H., Steinbach, F., Penchev, V., *Z.Phys. Chem.NF* (1976) 99 223
12. Beyer, H., Jakobs, P.A., Uytterhoeven, J.B., *Trans. Faraday Soc.* (1976) 674
13. Rabo, J.A., Agnell, C.L., Kasai, P.H., Schomaker, V., *Discuss.Faraday Soc.* (1966) 329
14. Naccache, C.M., Ben Taarit, Y., *J. Catal.* (1971) 22 171
15. Kuspert, B., *Dissertation Berlin* (1970)
16. Delgass, W.N., Garten, R.L., and Boudart, M., *J. Chem. Phys.* (1969) 50 4603
17. Dickson, B.L., Rees, L.V.C., *J.Chem.Soc., Faraday I* (1974) 70 2038
18. Ione, K.G., *Third Int.Conf.on Molecular Sieves* (1973) 2 330
19. Garten, R.L., Delgass, W.N., and Boudart, M., *J. Catal.* (1970) 18 90
20. Morice, J.A. and Rees, L.V.C., *Trans.Faraday Soc.* (1968) 64 1388
21. Arnold, D., *Z. Chem.* (1971) 11 409

Thermodynamics of Adsorption on Zeolites

W. SCHIRMER, K. FIEDLER, and H. STACH

Zentralinstitut fuer physikalische Chemie der Akademie der
Wissenschaften der DDR, Berlin-Adlershof, East Germany

ABSTRACT

Comprehensive experimental data on adsorption in zeolites show an influence of structure. Statistical-thermodynamic approaches consider this, the constants of equations are determined by adaption, according to their physical meaning. Empirical correlations within homologous series of chemical compounds represent important characteristics of zeolitic adsorption. All observed phenomena can be explained quantitatively.

Introduction

Although scientific and technical application of adsorption has supplied us, during the last ten years, with comprehensive experimental data, we, at present, are far from being able to formulate a generally valid theory of adsorption on microporous solid bodies. Such a theory especially, when it is applied to zeolites, must take into account the following structural characteristics:

- separate sorption cavities, accessible to adsorbed molecules only by crossing an activation barrier
- small size of the cavities, limiting the number of adsorbed molecules to a few and for long-chain paraffins) to one per cavity, so that the idea of a special adsorbed phase can only be used to a very limited extent
- heterogeneity of the field of adsorption in the cavity, causing the existence of special molecular arrangements for both non-polar molecules (paraffins) and polar molecules (H_2O , NH_3).

An examination of the fundamentals of the actually prevailing theoretical approaches,

- the equation of Langmuir [1],
- the potential theory of adsorption [2],
- the theory of volume filling [3],
- virial equations [4,5,6]

shows, particularly with regard to molecular sieves, that obviously none of them meets the above-mentioned conditions exactly. A comprehensive theoretical approach could be based in our opinion, on statistical thermodynamics. Here we present the first results of our attempts to derive such an approach. By applying the equations in a semi-empirical manner we avoid the need for a quantummechanical treatment which is in principle possible but too difficult for the moment. We present comprehensive experimental material, which we obtained during our research on the adsorption on zeolites of the faujasite type using different classical and modern methods [7,8,9,10]. On the basis of our experiments and the statistical-thermodynamic approach we are able to draw a number of conclusions of a theoretical nature.

Experimental Results

We investigated the adsorption equilibria of nonpolar, easily polarizable, and polar molecules on zeolites of the types A, X, and Y, which, usually, were not pelletized. Normal-paraffins were chosen as adsorbates because they show the following characteristic properties:

- 1) Carbon-chains of various length permitting us to vary the maximal occupation of one zeolite cavity from ten molecules down to one molecule.
- 2) Possibilities of various conformations leading to new, adapted structures of the adsorbed molecule in the cavity.

We further investigated the adsorption of normal-olefins, benzene, water, and ammonia [7,12].

Figure 1 represents our experimental results on isotherms and isosteres in a special manner, which in our case represents the data clearly, but may not be appropriate to all adsorption systems [13]: the adsorbed quantity a is plotted against a value ξ , equal to

$$\xi = \ln \frac{p/p_0}{T/T_0} - \frac{E_0}{RT} \quad (1)$$

Eq. (1) is based on the following known equations

$$\Delta \bar{S}(a, T) = \frac{\Delta \bar{H}(a, T)}{T} \quad (2)$$

$$\frac{\Delta \bar{S}^{\infty}(a, T)}{R} + \ln \frac{p/p_0}{T/T_0} = \frac{\Delta \bar{H}(a, T)}{RT} \quad (3)$$

$$\frac{\Delta \bar{H}(a, T) - E_0}{RT} - \frac{\Delta \bar{S}^{\infty}(a, T)}{R} = \xi \quad (4)$$

E_0 representing an average value for $\Delta \bar{H}(a, T)$;
Solving equation (4) yields the function

$$a = f(\xi, T) \quad (5)$$

from which we derive with the help of the permutation entropy $-R \ln a$ and the decomposition $\Delta \bar{S}^{\infty} = -R \ln a + \Delta \bar{S}^{\infty*}$

$$a = e^{\xi - \frac{\Delta \bar{H} - E_0}{RT} + \frac{\Delta \bar{S}^{\infty*}}{R}} \quad (6)$$

Eq. (5) has the following advantages:

If $\Delta \bar{H} \approx E_0$ and $\Delta \bar{S}^{\infty*}(a, T) \approx \Delta \bar{S}^{\infty*}(a)$ [11], then the coverage a is nearly independent of temperature:

$$a \approx f(\xi) \quad (7)$$

In this case, all isotherms of the system adsorbate/zeolite are approximately represented in figure 1 by a single curve. The characteristic behaviour of the entropy $\Delta \bar{S}^{\infty}$ is expressed by a unique form of the curve $a=f(\xi)$.

For an ideal gas with a volume of adsorption W_0 and a potential E_0 we derive

$$\Delta \bar{S}^{\infty} = -R\xi, \Delta \bar{H} = E_0, \Delta \bar{S}^{\infty*} = R \ln \frac{W_0}{V_0}, a = \frac{W_0}{V_0} e^{\xi} \quad (8)$$

For a real gas, we have to replace W_0 by the free volume of configuration:

$$a = \frac{W_f(a)}{V_0} e^{\xi} \quad (9)$$

which for small values of a leads to

$$a = \frac{W_f(0)}{V_0} e^{\xi} \quad (10)$$

$W_f(0)$ depending only on the size of the molecule. Equation (5) permits us to correlate the various results of many authors concerning the adsorption of n -paraffins in a uniform manner [14,15,16].

Figure 1 shows the adsorption isotherms of the n -paraffins and the rare gases krypton and xenon on zeolite NaCaA in the coordinates $a = f(\xi)$. For every n -paraffin, the value of E_0 was calculated by a procedure, explained below, determining the state of coverage of 1 molecule per cavity (energy of adsorption E_{11}). The isotherms of the light n -alkanes are fairly well represented by a single curve, while longer-chain n -paraffins show some scattering for higher coverages. For n -hexane and n -heptane results obtained at higher temperatures are used.

Methane corresponds well to the exponential character of equation (10). The curve for krypton is the same as for methane, proving that the size and the symmetric character of the particles are comparable, see also Ruthven [17]. All curves of the n -paraffins show an exponential range, diminishing with increasing chain-length. For longer-chain n -paraffins, the curves have steps corresponding to an adsorbed quantity of approximately one molecule per cavity. We observe correlations between the value of ξ and the number of CH_2 -groups per cavity which we discussed elsewhere [18].

The isosteres in the system n -heptane/zeolite are curved [19], a fact which can be explained by the assumption of two different groups of states of energy for the heptane molecules. We observed curved isosteres for the adsorption of n -hexane, n -decane, NH_3 , and benzene on A- or X-zeolites. We draw the conclusion that deviations from the linear character of adsorption isosteres may be rather a common phenomenon, the investigation of which demands a high accuracy of measurements.

We interpret the two groups of states of energy as

- 1) a group of states of low energy with localised positions near the wall of the cavity
- 2) a group of states of high energy, non-localised, situated in the centre.

Between these two groups of states, a temperature-dependent transition of molecule is observed, which is of high order and may be regarded as quasi-Schottky transition. The curves $c_p = f(T)$ must therefore go through a maximum, which we indeed detected by calorimetric measurements.

As a result of our experimental work on the adsorption of water (together with H. Pfeifer *et al.*, [9]) we observed that, especially at low coverage, high values of enthalpy correspond to low values of entropy, thus pointing to special states of adsorption. By the combined application of the above-mentioned physical methods we found that water-molecules can be adsorbed in faujasite-cavities in five different states, strongly distinguished by their correlation time τ_c (measured by NMR-pulse-technique). For details see [9].

Statistical-Thermodynamic Approach

A theoretical treatment of the zeolitic adsorption must be able to describe complicated functions of coverage, temperature-dependent molecular transitions, and special structures of the adsorbate. The statistical thermodynamic treatment developed by Hill and first applied to zeolitic systems by Bakaev [20] and independently by Ruthven [15] and also by Fiedler [21] offers the most promising approach.

On the base of statistical thermodynamics and owing to the separate sorption cavities of the zeolites, particularly characteristic for type A, the grand partition function Ξ of the zeolite can be represented as the product of the grand partition functions Ξ_i of the single cavities (total number = N_c)

$$\Xi = \Xi_i^{N_c} = \left(1 + \sum_{i=1}^m Q_i \lambda^i\right)^{N_c} \quad (11)$$

Under the condition, that the canonical partition function Q_i contains the same residual contributions of moments, rotations, and internal motions as the gas we derive the equation

$$Q_i \lambda^i = (p/RT)^i Q_{i,\text{conf}} \quad (12)$$

In the range of temperature in which we measured the adsorption values we replace the integral expressions of $Q_{i,\text{conf}}$ [6] by finite sums, whose l summations correspond to different energy levels. In this way it is possible to describe different states of energy and their transitions. We put $l = 1$ for a cavity which, for a given coverage, is energetically homogeneous, while in other cases $l = 2$ different states may be regarded as sufficient.

The sums are represented by

$$Q_i \lambda^i = \left(\frac{p/p_0}{T/T_0} \right)^i \sum_{j=1}^l e^{i \frac{S_{ij}^\circ T - E_{ij}}{RT}} \quad (13)$$

S_{ij}° are constants for the (T, V_0) -standard-differences of entropy, E_{ij} = energy constants of the corresponding levels. If the cavity contains only one molecule, we get the value E_{11} , already used in figure 1 ($E_0 = E_{11}$).

The isotherm equation $\alpha = \partial \ln \bar{z} / \partial \ln \lambda$ transforms into

$$\alpha = N_c \frac{\sum_{i=1}^m i Q_i \lambda^i}{1 + \sum_{i=1}^m Q_i \lambda^i} = N \sum_{i=1}^m i \theta_i = N_c \theta \quad (14)$$

where

$$\theta_i = \frac{Q_i \lambda^i}{1 + \sum_{i=1}^m Q_i \lambda^i}, \quad \theta = \sum_{i=1}^m i \theta_i \quad (15)$$

are valid, considering the structure (13). θ_i expresses the probability for the existence of a cavity of an i -fold occupation.

Equation (14) suffices, in connection with (13), to describe transitions of molecules in the cavity, for a given degree of coverage. By a change of θ_i with temperature it is possible to describe another kind of molecular transition, that between different cavities. The differential specific heat of the state of coverage i of a cavity, therefore, contains two summations

$$\Delta \bar{c}_i + i (\Delta \bar{E}_i - \Delta \bar{E})^2 / RT^2 \quad (16)$$

the first one representing transitions within a cavity, the second one between the cavities.

Application of the Approaches

Equation (14) depends on the constants N_C , S_{ij}^{∞} , and E_{ij} , which are superior to virial coefficients in that the form of their dependence on pressure and temperature is known. The dependence of the coverage a on pressure and temperature is expressed explicitly by the substitution of equation (13) in (14). The values of N_C , S_{ij}^{∞} , and E_{ij} are determined in the following two ways:

1) As they have a concrete physical meaning, they may be calculated from molecular data on the adsorbents. Till now we have had such reliable molecular data for only a few systems [22]. We do not know the deviations from ideal values for most real systems, so that this way may not frequently be used. We shall not follow up it here.

2) Equation (14) is adapted to the characteristic properties of the zeolites. It is possible to determine the values of the constants by means of a method of parameter determination using the measured equilibrium data $a(p,T)$.

By this procedure, we finally can calculate the thermodynamic functions and other characteristic quantities such as the distribution functions θ_i . Studies about the relations of the constants within homologous series of chemical compounds and for different types of zeolites will give us insight into the mechanism of adsorption.

Ruthven et al. considered the free volume under van-der-Waals-conditions introducing an additional correlation between the constants S_{ij}^{∞} . This is advantageous for small molecules, for example for short-chain *n*-alkanes. In using a general form of a relations whose constants are independent on one another, we are able to treat more complicated zeolitic systems. It is, however, more difficult to obtain the necessary information data.

Results

1) Equation (14) fits well the experimental data of the equilibria measured for *n*-paraffins of 1 - 18 C-atoms in zeolite NaCaA, over the whole range of investigation. The value for the quantity of cavities, N_C , amounts constantly, within a homologous series, to approximately 0.80 of the theoretical

value corresponding to an ideal structure of the zeolite. The N_C -values of different types of zeolites differ in the same proportion as the theoretical values. The maximal quantity m of molecules, adsorbed in one cavity, decreases with increasing length of chain. For n -alkanes above n -C₁₀, the value for m is 2, the second molecule only enters the cavity at low temperatures and high pressures. Figure 1 shows distinctly that the adsorption range for one molecule per cavity is well separated from the two-molecules range. For one molecule in a cavity equation (14) reduces to the Langmuir equation. This is the reason why, in this range, the Langmuir equation can be successfully applied to technical processes. For n -C₅ to n -C₇: $m = 4$; we found $m = 6$ for the representation of the data for methane to propane.

The number of values l necessary to describe the levels of energy is equal to one for each coverage of the cavity except in the case of n -hexane and n -heptane, where we found $l = 2$. We observed, especially for these two hydrocarbons, curved isosteres, referring to temperature-dependent heats of adsorption.

The energy constants E_{i1} display, as figure 2 shows, a nearly linear dependence on the number of the C-atoms of the n -paraffins. This enables us to extrapolate to long-chain n -paraffins for which adsorption data are not available. A linear dependence could also be found for E_{i1} -values with $i > 1$. The curve $E_{i1} = f(i)$ decreases from an i -value, which corresponds to a total number of 12 C-atoms in the paraffin molecule adsorbed in one cavity.

The curve of the entropy constants S_{i1}° begins to decrease beyond n -paraffins with more than 12 C-atoms. This tendency becomes very clear for the adsorption of n -octadecane. In these cases, obviously, strong restrictions in the possibility of display of various conformations are dominating. At high temperatures T ($RT \gg E_{ij}$), the influence of the energy constants E_{ij} on equation (14) and that of E_0 on ξ disappear. N_C and S_{ij}° , therefore, alone permit calculation of the temperature-independent curve $a=f(\xi)$ in figure 1. This shows once more that this curve especially represents the entropic factor of the zeolitic adsorption. The values of S_{i1}° determine the character of $a=f(\xi)$, especially in the range of low coverages a . They, therefore, are directly responsible for the shift of the exponential part of the curve in figure 1 to the right with

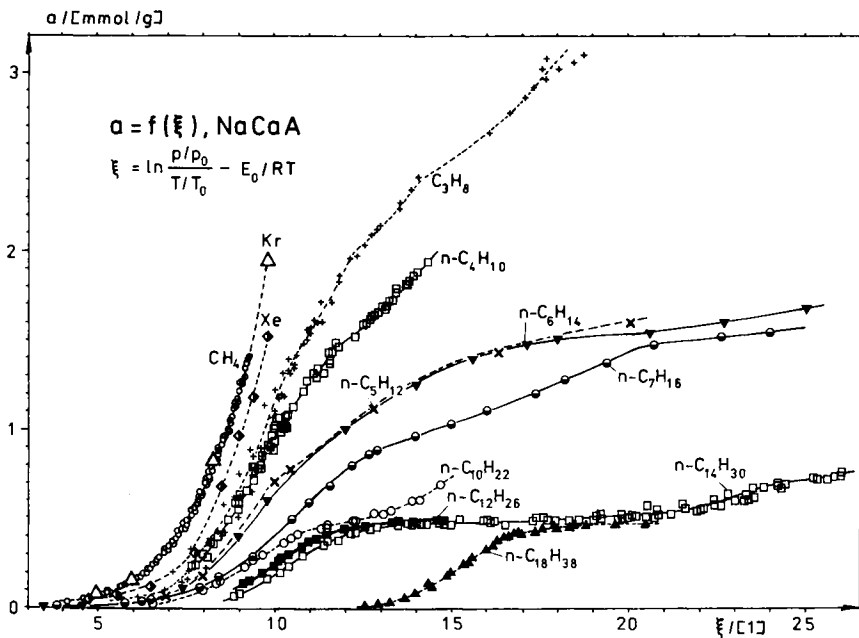


Figure 1. Experimental data of the adsorption equilibria of rare gases (Kr, Xe) and *n*-paraffins on zeolite NaCaA in the plot a vs. ξ

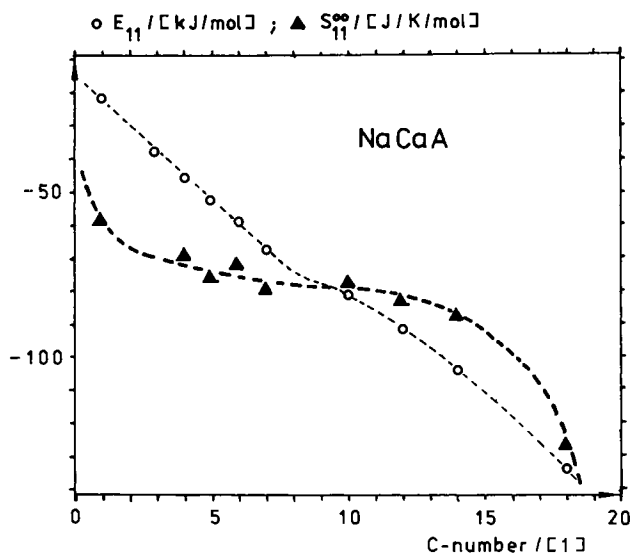


Figure 2. Dependence of the isotherm constants E_{11} and S_{11}^{00} on the number of C-atoms of the *n*-paraffins

increasing chain-length of *n*-paraffins or with increasing atom size for the rare gases.

2) In figure 3 we represent results obtained for the system *n*-decane/zeolite NaMgA using equations (13) and (14). They distinctly show the changes of the thermodynamic functions after the adsorption of the second molecule in the cavity. We demonstrate the effectiveness of the equations by extrapolation to low temperatures.

3) The idea of the separability of the zeolite is no longer valid when the adsorbate molecules are larger than the cavities of the 5A-zeolites. In such cases, adsorbed molecules for instance of *n*-tetradecane or *n*-octadecane, occupy two cavities at the same time, thus reducing the separation of two cages. We considered this fact by introducing thermodynamic systems consisting of cells of two or four cavities. This treatment favours the interactions going on in the interior of the system and neglects, to a certain extent, the processes on the inner surface. This method proved to be valuable for zeolite NaX, for which the equilibria of many adsorbates only could be described by larger cells. We were able to demonstrate states for *n*-hexane and benzene in zeolite NaX.

4) The adsorption of olefines was included in the evaluation of equation (14). Figure 3 represents some thermodynamic functions of the system trans-butene-2/NaX. We see that the heat of adsorption reaches a maximum at high coverages.

5) For the adsorption of polar molecules, we transform equation (14) into the following sum:

$$a = \sum_{k=1}^q N_{c,k} \theta^{(k)} \quad (17)$$

By means of this equation we could describe the adsorption of ammonia and water in the zeolites NaCaA and NaMgA. Figure 4 shows some thermodynamic functions for the system NH_3/NaMgA . All values of *m* and *l* were placed = 1, so that each summation of equation (17) was equal to the right-hand side of a Langmuir equation. The energy constants, highly different for various values of *k*, are responsible for the step-like decrease of the heat of adsorption.

Summarizing our results we state that the comprehensive experimental material can be

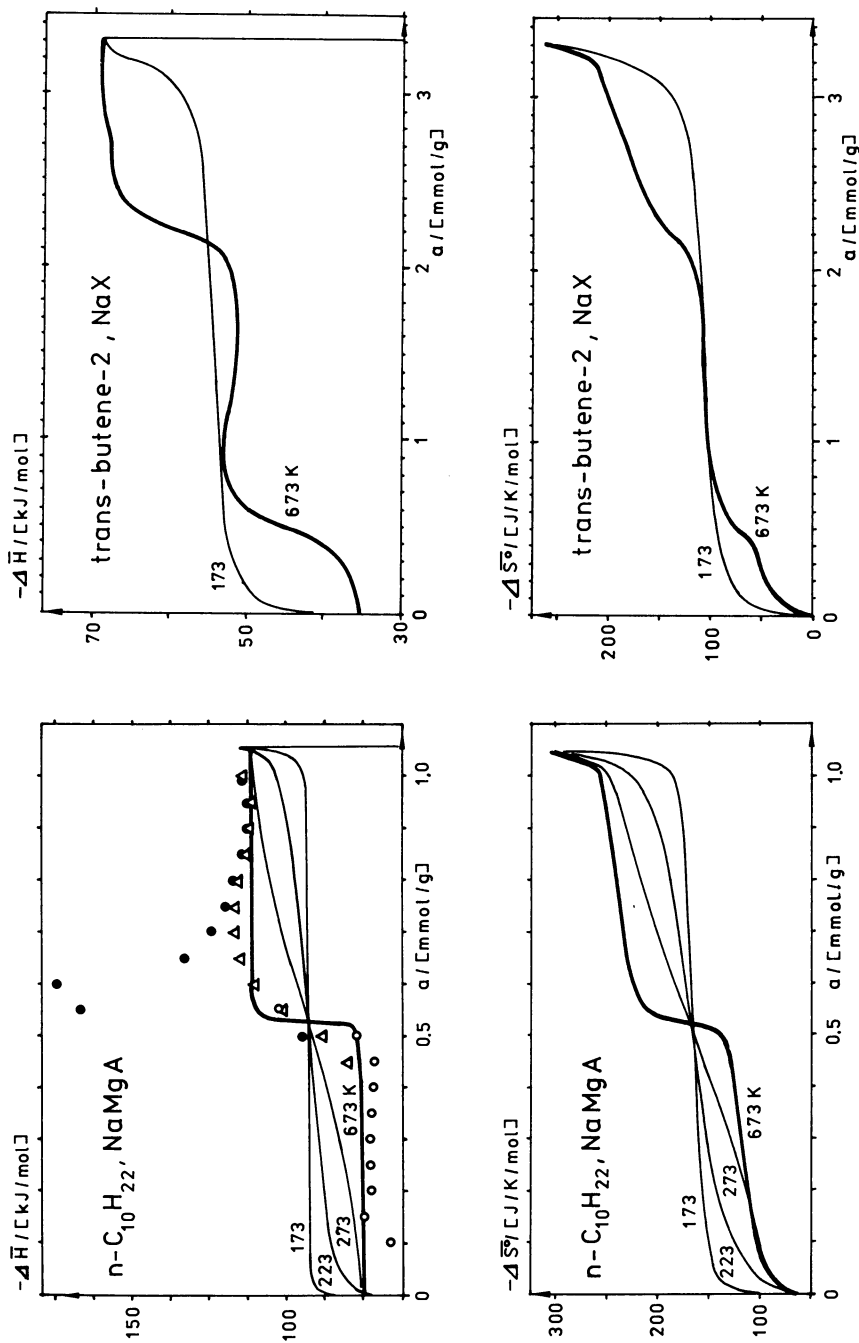


Figure 3. Thermodynamic functions of the adsorption of *n*-decane and *trans*-butene-2 on zeolites NaMgA and NaX

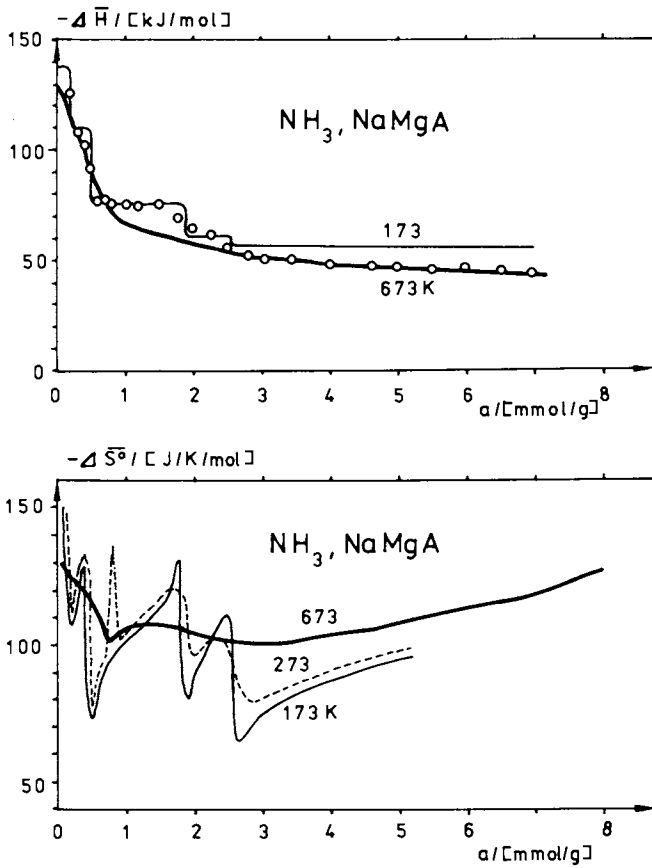


Figure 4. Thermodynamic functions of the adsorption of NH_3 on zeolite NaMgA

represented in a form which allows us to notice the influence of the adsorbent structure. The basic approaches of the statistical thermodynamics, considering the principal features of zeolitic sorption, are developed in a simplified form so that their application becomes possible. The physically established constants are determined by application to experimental data. States of different energy level, molecular transitions, processes of reorganization of adsorbed molecules and maxima in the curves of heats of adsorption are explained. All observed phenomena can be treated quantitatively. A further development of these approaches seems possible.

Nomenclature

$a, a(p, T)$	adsorbate concentration	[mmol/g]
E_0	estimated or calculated suitable constant for heat of adsorption	[kJ/mol]
E_{11}	constant for high-energy ($j=1$) for 1 molecule/cavity ($i=1$)	[kJ/mol]
E_{ij}	molar constant for energy (j -th level) for i molecules/cavity	[kJ/mol]
$f(\xi, T), f(\xi)$	empirically reduced isotherms	[mmol/g]
$f(i)$	empirical function from i	[kJ/mol]
i	number of molecules/cavity	[1]
j	integer for energy level	[1]
k	integer for type of cavity	[1]
l	number of energy levels	[1]
m	maximum number of molecules/cavity	[1]
$N_C, N_{C,k}$	number of cavities, type k	[1] or [mmol/g]
p	equilibrium adsorbate pressure	[Pa]
p_0	standard pressure = 1 [atm] = 101 325	[Pa]
q	number of types of cavities	[1]
Q_i	canonical partition function for i	[1]
$Q_{i,conf}$	contribution of configuration to Q_i	[1]
R	gas constant = 8.31434	[J/K/mol]
\bar{S}	differential entropy adsorbate	[J/K/mol]
$\bar{S}_{gas}(T, V_0)$	molar entropy of ideal gas	[J/K/mol]

$S_{ij}^{\circ\circ}$	molar constant for (T, V_0) -standard-difference of entropy	[J/K/mol]
T	temperature	[K]
T_0	standard temperature = 273.15	[K]
V_0	standard volume = RT_0/p_0	[m ³ /mol]
W_0	volume of adsorption	[m ³ /kg]
$W_f(a), W_f(0)$	free volume of configuration	[m ³ /kg]
$\Delta\bar{c}_i$	molar integral difference of heat capacity for i molecules/cavity	[J/K/mol]
$\Delta\bar{E}$	differential diff. of energy	[kJ/mol]
$\Delta\bar{E}_i$	molar integral difference of energy for i molecules/cavity	[kJ/mol]
$\Delta\bar{H}(a, T)$	differential diff. of enthalpy	[kJ/mol]
$\Delta\bar{S}(a, T)$	differential diff. of entropy	[J/K/mol]
$\Delta\bar{S}^{\circ\circ}(a, T)$	differential (T, V_0) -standard-difference of entropy = $\bar{S} - \bar{S}_{gas}(T, V_0)$	[J/K/mol]
$\Delta\bar{S}^{\circ\circ*}$	not permutation reduced (T, V_0) -standard-difference of entropy	[J/K/mol]
$\theta, \theta^{(k)}$	average number of molecules/cavity, of type k of cavities	[1]
θ_i	probability for i molecules/cavity	[1]
λ	absolute activity	[1]
ξ	variable for representation	[1]
Ξ, Ξ_1	grand partition functions for the whole zeolite, for the single cavity type 1	[1]

Literature Cited

-
- [1] FLOOD, E. A., 'The Solid-Gas Interface', Marcel Dekker, New York, 1967
 - [2] BRUNAUER, S., COUPLAND, L., and KANTRO, D., in FLOOD, E. A., [1]
 - [3] DUBININ, M. M., 'Adsorption and Porosity' (russ.), Moskau, 1972
 - [4] BARRER, R. M., and GIBBONS, R. M., Trans. Faraday Soc. (1963) 59, 2569

- [5] BEZUS, A. G., KISELEV, A. V., and PHAM QUANG DU, *J. Colloid. Interf. Sc.* (1972) 40, 223
- [6] STEELE, W. A., in FLOOD, E. A., [1]
- [7] KUNATH, D., SPANGENBERG, H.-J., STACH, H., and SCHIRMER, W., *Z. Chem.* (1970) 10, 11
- [8] SPANGENBERG, H.-J., FIEDLER, K., ORTLIEB, H.-J., and SCHIRMER, W., *Z. phys. Chem. Leipzig* (1971) 248, 49
- [9] PFEIFER, H., 'NMR-Basic Principles and Progress' 55, Springer-Verlag, Heidelberg-New York, 1972
- [10] LOHSE, U., STACH, H., and SCHIRMER, W., *Mber. Dt. Akad. Wiss.* (1970) 12, 819, 828
- [11] BARRER, R. M., and SUTHERLAND, J. W., *Proc. Roy. Soc. A* (1956) 237, 439
- [12] PEINZE, T., FIEDLER, K., STACH, H., and SCHIRMER, W., *Mber. Dt. Akad. Wiss.* (1970) 12, 855, 870
- [13] FIEDLER, K., ORTLIEB, H.-J., and SCHIRMER, W., *Festkolloquium zum 80. Geburtstag von N. N. Semenev, Moscow, 1976* (in press)
- [14] RUTHVEN, D. M., *AIChE. Journal* (1976), 22, 753
- [15] RUTHVEN, D. M., *Nature Phys. Sci.* (1971), 232, 70
- [16] COUGHLAN, B., KILMARTIN, S., McENTEE, J., and SHAW, R. G., *J. Coll. Interf. Sci.* (1975) 52, 386
- [17] RUTHVEN, D. M., *J. Phys. Chem.* (1975) 79, 856
- [18] FIEDLER, K., STACH, H., and SCHIRMER, W., Publication in preparation
- [19] SCHIRMER, W., KOELSCH, P., PETERS, H., and STACH, H., in UYTTERHOEVEN, J. B., 'Proc. III. Internat. Conf. Molecular Sieves', Leuven University Press, 1973, p. 285
- [20] BAKAEV, V. A., *Dokl. AN SSSR* (1967) 167, 369
- [21] FIEDLER, K., STACH, H., and SCHIRMER, W., 'Entwicklung und Testung von statistisch-thermodynamischen Modellen der energetisch heterogenen Adsorption in Zeolithen', Vortrag auf der Chemie-dozententagung der Chem. Ges. der DDR, Freiberg, 1971
- [22] KRETSCHMER, R. G., and FIEDLER, K., *Z. phys. Chem. Leipzig* (in press)

Diffusion in Molecular Sieves: A Review of Recent Developments

DOUGLAS M. RUTHVEN

Department of Chemical Engineering, University of New Brunswick,
Fredericton, N.B., Canada

ABSTRACT

Recent information concerning the diffusion of a range of non-polar molecules in representative types of molecular sieve is reviewed. The general relationships between the pore structure of the sieve, the dimensions of the sorbate molecule and the diffusion behaviour are emphasized. Results of sorption and NMR diffusion measurements are compared.

Introduction

The structural regularity of zeolite frameworks makes possible detailed studies of the relationship between pore geometry and transport properties and this feature has attracted much research. A general review of the information available to 1970 was presented at the Worcester Conference by Barrer⁽¹⁾ and it is the purpose of the present paper to summarize only the more recent developments. The systems selected for discussion are mainly those which we have studied at the University of New Brunswick but these systems are in a general way representative of the systems of industrial interest.

The bidisperse nature of commercial molecular sieve pellets is considered in some detail elsewhere in this conference^(2,3). The present paper deals only with intracrystalline (micropore) diffusion since this is where the relationships between structure and transport properties are observed. Nevertheless it must be emphasized that the rate of sorption in a molecular sieve is not always controlled by intracrystalline diffusion.

Sorption and Chromatographic Measurements

Refinements of the standard gravimetric method⁽¹⁾ for determining diffusivities from transient sorption measurements include the introduction of a correction factor to account for crystal size distribution and the use of small differential steps

to study systems in which the diffusivity is concentration dependent⁽⁴⁾. Of the precautions necessary to obtain reliable results the most important is variation of the sample size or bed configuration, since this provides a diagnostic test both for macro diffusional resistance of the bed and thermal effects⁽⁵⁾.

Chromatographic methods have also been applied to zeolitic systems. The spread of the response peak is determined by the combined effects of mass transfer resistance and axial dispersion. In order to determine micropore diffusivities the effects of macropore and film resistance as well as axial dispersion must either be eliminated or allowed for in the analysis. The method of Eberly⁽⁶⁾ depends on the van Deemter equation⁽⁷⁾ relating plate height (HETP) to gas velocity:

$$\text{HETP} = A + B/u + Cu \quad (1)$$

The constant C which may be determined from the limiting slope of a plot of HETP vs u, is related to the macropore and micropore diffusional time constants. The individual time constants may be separated by using either particles of different size or different carrier gases⁽⁸⁾. The method of moments has also been widely used⁽⁹⁻¹¹⁾. When intracrystalline diffusional resistance is significant the peaks show pronounced tailing making accurate evaluation of the second moment difficult. This difficulty may be avoided by calculating the model parameters (in particular the time constant for intracrystalline diffusion r^2/D) by matching either the Laplace or Fourier transforms⁽¹²⁻¹⁵⁾.

It is generally assumed that the basic assumptions of the chromatographic method (linear isotherm, constant diffusivity) will be fulfilled provided that the sorbate pulse is sufficiently small. However, for certain systems, including those studied chromatographically by Eberly⁽⁶⁾ (Ar-5A, Kr-5A, SF₆-13X), gravimetric studies have shown that even within the Henry's Law region the diffusivity is strongly dependent on concentration^(16,17):

$$D_0 = D'_0/c ; D'_0 = D'_* e^{-E/RT} \quad (2)$$

Within the Henry's Law region $c = Kp$ and K varies with temperature according to a vant Hoff equation ($K = K_0 \exp(q_0/RT)$) so that:

$$D = (D'_*/K_0p) \exp[-(E+q_0)/RT] \quad (3)$$

The precise value of the integral diffusivity determined in a chromatographic experiment will depend on the pulse size but it is clear from eqn. 3 that if the pulse size is kept constant and the temperature varied the apparent energy of activation (E_a) will be given by $E_a = E+q_0$. As may be seen from Table 1, Eberley's chromatographic values of E_a agree well with the values of $E + q_0$ from the gravimetric studies, indicating that the discrepancy arises from the assumption of a constant diffusivity in the analysis of the chromatographic data.

The diffusion of Ar in 4A sieve was studied chromatographically by Sarma and Haynes⁽¹⁴⁾. For this system the assumptions

of a linear isotherm and constant diffusivity are valid and the chromatographic data agree well with the extrapolated sorption data of Eagan and Anderson⁽¹⁸⁾ and Ruthven and Derrah⁽¹⁶⁾. These conditions should also be fulfilled for the diffusion of n-butane in 5A sieve at low concentrations but the chromatographic diffusivities of Hashimoto and Smith⁽¹¹⁾ are several orders of magnitude larger than the gravimetric values⁽¹⁹⁾. The discrepancy may be related to the difficulty of evaluating the second moments of the chromatographic peaks. This problem is compounded by the need to extrapolate the second moment values in order to eliminate the large contributions from macropore resistance.

TABLE I - Comparison of Values of $E + q_0$ with Apparent Activation Energies from Chromatographic Data

System	q_0^* (kcal)	E† (kcal)	$E + q_0$ (kcal)	E_a^\ddagger (kcal)
Ar-5A	3.3	<<1	3.4	3.5
Kr-5A	3.6	2.0	5.6	5.9
SF ₆ -13X	5.0	2.8	7.8	7.5

* Values of q_0 from Eberly⁽⁶⁾ at high temperatures.

† Value of E calculated according to eqn. 2 from gravimetric data.

‡ Apparent activation energy from chromatographic measurements⁽⁶⁾.

The advantage of the chromatographic method lies in the simplicity of the apparatus and the rapidity with which measurements can be made. Macropore diffusivities can be determined with accuracy since variation of particle size and carrier gas provide a simple means of varying macropore resistance but the determination of intracrystalline diffusivities is more difficult.

Corrected Diffusivities and Tracer Diffusivities

From simple thermodynamic considerations it may be shown that the relationship between the Fickian diffusivity (D) and the corrected diffusivity (D_0) defined in terms of a chemical potential gradient driving force, is given by:

$$D = D_0(d\ln a/d\ln c) = D_0(d\ln p/d\ln c) \quad (4)$$

The second of these equations involves the additional assumption of an ideal vapour phase. For liquid phase systems it has been clearly shown that the chemical potential gradient, rather than the concentration gradient, is the true driving force for diffusive transport^(20,21). For zeolitic systems the equilibrium isotherms are, in general, highly non-linear so that the correction factor $d\ln a/d\ln c$ is often large. When considering the variation of diffusivity with the physical properties of the sorbate or sieve it is therefore essential to examine the behaviour of D_0 . Although D_0 is in principle a function of concentration, the

concentration dependence will generally be less pronounced than that of D .

From the principles of irreversible thermodynamics it has been shown by Ash and Barrer⁽²²⁾ that the differential diffusivity measured in a sorption experiment (D) is related to the tracer self diffusivity (\mathcal{D}) by the expression:

$$D = \frac{\mathcal{D}}{(1 - c_A L_{A^*A} / c_A^* L_{AA})} \cdot \frac{d \ln a}{d \ln c} \quad (5)$$

The expression derived by Karger⁽²³⁾ is slightly different due to a difference in the definition of D . In the low concentration limit $d \ln a / d \ln c \rightarrow 1$, $L_{A^*A} \rightarrow 0$ and the tracer diffusivity approaches the limiting diffusivity D_0 . For many zeolitic systems the cross coefficient L_{A^*A} appears to be small even at higher concentration so that eqn. 5 reduces simply to Darken's equation⁽²⁴⁾.

There are only a few systems for which both tracer and self diffusivities have been determined under comparable conditions. For the diffusion of water in several natural zeolites Barrer and Fender⁽²⁵⁾ showed that the concentration dependence of D could be largely accounted for by the activity correction term and $D_0 \approx \mathcal{D}$. Barrer later⁽¹⁾ showed that there is evidence of a small additional concentration dependence arising from the term $c_A L_{A^*A} / c_A^* L_{AA}$ in the denominator of eqn. 5. Tracer diffusivities (\mathcal{D}) for CO_2 in 4A and 5A sieves^(26,27) are in order of magnitude agreement with values of D_0 determined in this laboratory. However, for this system the corrected diffusivity is strongly concentration dependent so detailed comparisons are not possible without more extensive data. The recent tracer data of Quig and Rees⁽²⁸⁾ for C_5 - C_9 alkanes in partially Ca^{++} exchanged 4A sieve are discussed below.

Diffusion in Small Port Zeolites

Two distinct patterns of diffusional behaviour have been observed depending on the relative sizes of the diffusing molecule and sieve window. When the critical molecular diameter is comparable with (or greater than) the free aperture of the sieve window the Fickian diffusivities show a monotonic increase with sorbate concentration, in accordance with equation 4 and the corrected diffusivities are essentially independent of concentration. The temperature dependence of D_0 follows the usual Eyring equation:

$$D_0 = D_* \exp(-E/RT) \quad (6)$$

The activation energies, for a given sieve, show a direct correlation with the critical diameters of the sorbates and the orders of magnitude of the pre-exponential factors are consistent with the predictions of transition state theory. Such behaviour is observed for the diffusion of monatomic and diatomic gases in 4A zeolite⁽¹⁶⁾ and for light hydrocarbons and CF_4 in 4A and 5A sieves

Table II

Systems in which Critical Molecular Diameter is Greater than
or Equal to Window Aperture: Parameters E and D_* giving
Temperature Dependence of Limiting Diffusivity D_0

System	σ (Å)	E (kcal)	Experimental $D_* \times 10^8$ ($\text{cm}^2 \cdot \text{sec}^{-1}$)	Theoretical Values	
				rotating $D_* \times 10^8$	non-rot. ($\text{cm}^2 \cdot \text{sec}^{-1}$)
Ar-4A	3.4	5.8	122	-	103
O ₂ -4A	3.5	4.53	660	132	2.4
Kr-4A	3.6	8.1	9.7	-	13
N ₂ -4A	3.7	6.1	96	266	7.0
C ₂ H ₄ -4A	4.08	8.5	61	3550	5.0
C ₂ H ₄ -5A	4.08	2.75	0.198	132	0.24
C ₂ H ₄ -Erion.	4.08	2.34	0.36	830	1.26
CH ₄ -4A	4.08	7.4	5.8	(172)	(6.22)
CH ₄ -5A	4.08	2.98	7.2	172	6.22
C ₂ H ₆ -4A	4.36	6.24	5.66	-	-
C ₂ H ₆ -5A	4.36	1.28	3.02	332	1.01
C ₂ H ₆ -Erion.	4.36	4.3	6.6	1100	3.1
C ₃ H ₆ -5A	4.95	3.46	0.25	96	0.008
1-C ₄ H ₈ -5A	4.95	3.44	0.18	1660	0.062
tr-2-C ₄ H ₈ -5A	4.95	3.46	0.26	750	0.028
C ₃ H ₈ -4A	5.1	8.7	1.24	(90)	(0.014)
C ₃ H ₈ -5A	5.1	3.5	0.82	90	0.014
*C ₃ H ₈ -Chab.	5.1	4.04	-	-	-
nC ₄ H ₁₀ -4A	5.1	8.5	0.42	(57)	(0.0021)
nC ₄ H ₁₀ -5A	5.1	4.0	0.73	57	0.0021
nC ₄ H ₁₀ -Chab.	5.1	4.16	-	-	-
nC ₅ H ₁₂ -5A	5.1	4.6	0.63	-	-
nC ₅ H ₁₂ -Erion.	5.1	5.0	0.09	-	-
nC ₅ H ₁₂ -Chabz.	5.1	4.95	-	-	-
nC ₇ H ₁₆ -5A	5.1	7.5	15.0	1000	0.0025
cyclo-C ₃ H ₆ -5A	5.2	4.34	1.06	25	0.015
CF ₄ -5A	5.44	9.15	250	192	0.034
cis-2-C ₄ H ₈ -5A	5.58	9.2	151	-	-

The data are correlated according to equation 4 and 6 (D_0 independent of c). The critical diameter σ is defined as the radius of the smallest cylinder which can circumscribe the molecule in its most favourable equilibrium conformation. Window apertures are about 3.4Å for 4A sieve and 4.3Å for 5A. Values for 4A, 5A and erionite are from data obtained in these laboratories (16,29-33). Values for H-chabazite are from Barrer and Davies (34). The calculation of the theoretical values of D_* for CH₄ and CF₄ is discussed in detail by Ruthven and Derrah (29).

(29-32), erionite(33) and chabazite(34). Data for some representative systems are summarized in table II and figure 2. Data for the lighter molecules are consistent with the assumption of a non-rotating transition state while for the larger molecules, which have high moments of inertia, the contribution from rotation or rocking vibrations to the partition function of the transition state becomes increasingly important. The large difference in activation energies between 4A and 5A sieves and the smaller differences between the activation energies for C_2H_6 and C_2H_4 in 5A and erionite are consistent with the differences in the shapes of the windows and the geometry of the sorbate molecules. However the increase in activation energy for the series C_3H_8 , nC_4H_{10} , nC_5H_{12} , nC_7H_{16} in 5A shows that critical molecular diameter is not the only important factor.

Diffusion in partially Ca^{++} exchanged 4A-5A sieves has also been investigated(28,35,36). For less than 25% Ca^{++} exchange the diffusivity is essentially the same as for the pure sodium form (4A). There is a rapid increase in diffusivity at about 30% Ca^{++} exchange corresponding to the composition at which the obstructing Na^+ ions are removed from one third of the windows so that each cell has, on average, two unobstructed windows. When more than two thirds of the Na^+ ions are replaced all windows are open and the diffusional properties become essentially the same as for the Ca^{++} form (5A). The change in molecular sieve properties thus occurs almost entirely over the range 26-67% exchange. A simple theoretical model, based on a random distribution of 'open' and 'closed' windows, has been found to provide a very satisfactory correlation of the experimental data(36). This is illustrated in figure 1. The theoretical curve for nC_6H_{14} is calculated on the assumption that $D_0 = \bar{D}$ using approximate (extrapolated) values of D_0 for the extreme 4A and 5A forms (10^{-17} and 10^{-12} $cm^2 \cdot sec^{-1}$). It is evident that the theory fits the tracer diffusivity data of Quig and Rees(28) well suggesting that the assumption $D_0 \approx \bar{D}$ is at least approximately correct. This is contrary to the conclusions of Quig and Rees but they used values of D_0 estimated from integral diffusivity measurements by the method of Barrer and Clarke(37). When the differential diffusivity is strongly concentration dependent, as with these systems, the method of Barrer and Clarke can lead to large errors in the calculated differential diffusivities. A more detailed analysis requires accurate values of D_0 , determined from differential measurements at low concentration, as well as tracer data for the extreme 4A and 5A forms.

Diffusion in Large Port Zeolites

For systems in which the critical molecular diameter is significantly smaller than the window aperture the pattern of diffusional behaviour is entirely different. At low concentrations within the Henry's Law region, the diffusivity decreases rapidly

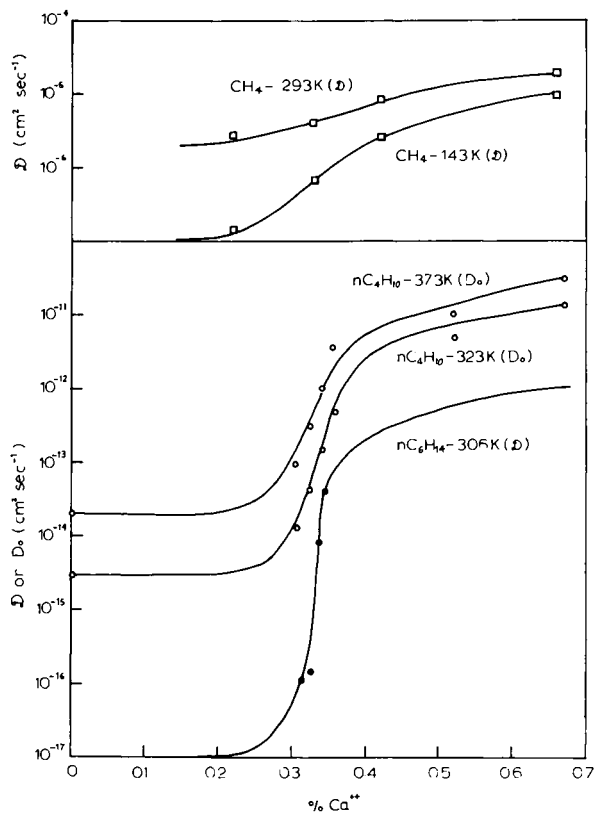


Figure 1. Variation of corrected diffusivities, tracer self diffusivities, and NMR self diffusivities with degree of Ca^{++} exchange in the Na-Ca A zeolites. Theoretical lines are calculated according to the model described in Ref. 36. D_0 values for nC_4H_{10} are from Ruthven (36), D values for CH_4 are from Caro et al. (47), D values for nC_6H_{14} are from Quig and Rees (28).

with increasing sorbate concentration, passing through a minimum and increasing again as the saturation limit is approached. Corrected diffusivities calculated according to equation 4 show an inverse dependence on concentration which may be approximately represented by eqn. 2. Such behaviour is shown by small monatomic and diatomic molecules in the 5A sieve(16) and also by larger hydrocarbon molecules in 13X(38).

TABLE III - Parameters E and D'_* (eqn. 2) for Systems in which Critical Molecular Diameters is Smaller than Window Aperture

System	σ (Å)	E (kcal)	$D'_* \times 10^7$ (molecule.cm ² /cavity.sec.)
Ar-5A	3.4	<<1.0	0.01
Kr-5A	3.6	2.0	0.077
Xe-5A	4.0	3.0	0.15
O ₂ -5A	3.5	1.0	0.026
N ₂ -5A	3.7	1.5	0.052
SF ₆ -13X	6.1	2.77	2.98
nC ₇ H ₁₆ -13X	5.1	6.2	22
C ₆ H ₁₂ -13X	6.5	4.96	10.2
C ₆ H ₆ -13X	6.5	4.9	4.9
C ₆ H ₅ CH ₃ -13X	6.5	6.6	6.6

The data are correlated according to equations 2 and 4. Free aperture of 5A sieve = 4.3Å and of 13X sieve = 7.4Å. Data for 5A are from Ruthven and Derrah(16) and for 13X from Ruthven and Doetsch(17,38).

Representative data are shown in figure 2 and 3 and the parameters for several systems are given in table III.

When the sieve window is large relative to the diffusing molecule the energy barrier between cages is small. Most of the molecules striking a window will pass through and the basic assumption of transition state theory (equilibrium between 'reactants' and transition state) will not be fulfilled. The inverse concentration dependence suggests that, even at low concentrations, the diffusion path is limited by collisions between sorbate molecules. A simple quantitative treatment based on the assumption that the principal contribution to the flux arises from the small fraction of molecules travelling on paths precisely aligned through the centres of successive windows and which can therefore traverse several cages in each flight, can account for the order of magnitude of the experimental diffusivities for monatomic and diatomic gases in 5A sieve(16) and for SF₆ in 13X(17).

The behaviour of the larger molecules such as benzene and toluene in 13X is intermediate between the constant D_0 pattern observed for the small port zeolites and the reciprocal concentration dependence which is observed when the sieve aperture

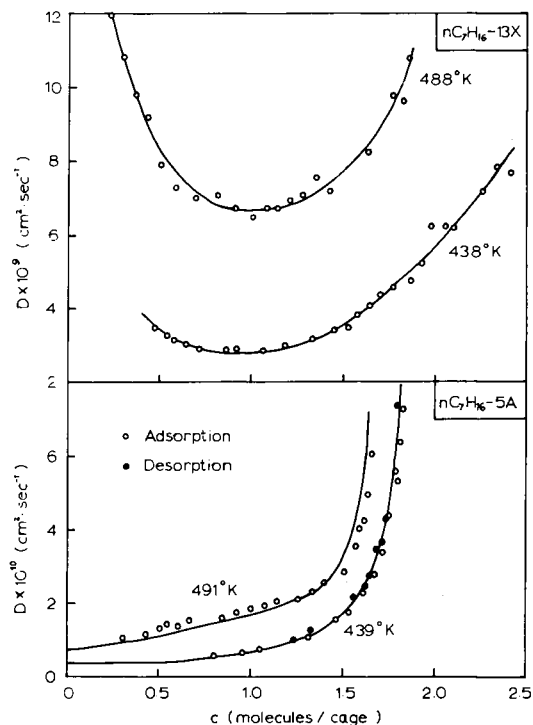
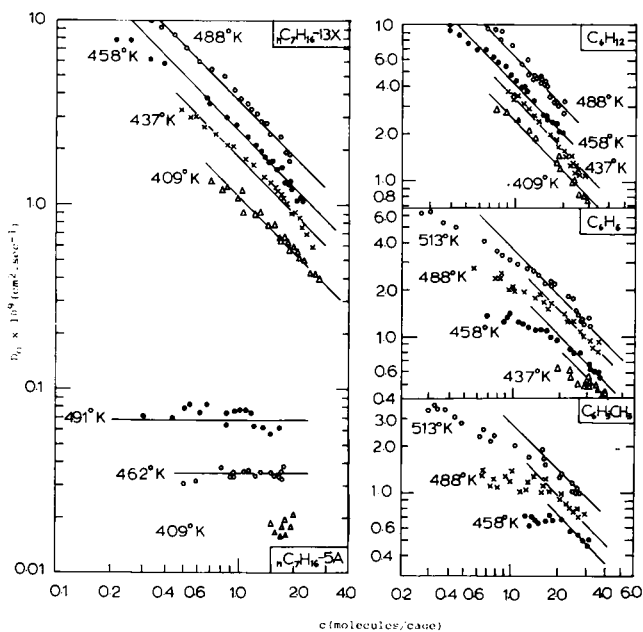


Figure 2. Comparison of diffusivities for nC_7H_{16} in 5A and 13X zeolites



AICHE Journal
Figure 3. Concentration dependence of corrected diffusivity for hydrocarbons in 13X zeolite. Comparative data for nC_7H_{16} in 5A are also shown.

is large. Such behaviour suggests that even larger molecules in 13X may show the constant D_0 pattern.

Comparison of NMR and Sorption Data

Several systems have recently been studied by both NMR and sorption methods and comparative data are presented in table IV. The NMR techniques are of two kinds^(39,40). The relaxation method depends on the determination of the correlation time for molecular motion (τ) and the self diffusivity is then calculated using an assumed mean jump distance (λ):

$$D = \lambda^2/6\tau = \lambda^2 e^{-E/RT}/6\tau_0 \quad (7)$$

In the more recent pulsed field gradient spin-echo method⁽⁴²⁻⁴⁷⁾ the self diffusivity is determined more directly as the measurements yield the mean square distance travelled in a known time interval. For those systems which have been studied by both methods (nC_4H_{10} , nC_7H_{16} , C_6H_{12} in 13X) there is good agreement when λ is taken as the lattice parameter, suggesting that diffusion occurs by jumps between neighbouring cages. The NMR self-diffusivities are however much larger than values of D_0 from sorption measurements and the activation energies are lower but, despite the large difference in numerical values, both NMR and sorption data show similar trends. The relative values of diffusivities for the C_4 hydrocarbons in 5A zeolite fall in the same sequence and, for the 13X systems, D (NMR) and D_0 (sorption) both show a similar inverse dependence on concentration. As illustrated in figure 1 the pattern of variation of both D (or τ) and D_0 with Ca^{++} exchange in NaCaA zeolites can also be quantitatively accounted for in terms of the same theoretical model.

If the adsorbed phase behaves as a set of localized Einstein oscillators with complete rotational freedom, as is suggested by heat capacity measurements⁽⁵⁰⁾, the vibration frequency (ν) may be estimated from the Henry constant:

$$K = K_0 \exp(q_0/RT); K_0/c_s = (kT/e)^{1/2} (2\pi m \nu^2)^{-3/2} \quad (8)$$

For the 13X systems the vibration frequencies are close to the reciprocal NMR correlation times whereas for the 5A systems the reciprocal correlation times are much smaller. This suggests that in the 13X sieve molecular jumps occur predominantly between neighbouring cages whereas in the 5A sieve jumps within a cavity are much more frequent as is to be expected from structural consideration.

Similarly large discrepancies between diffusivities measured by NMR and other methods have been observed for molecular solids^(51,52) but the explanation is uncertain. The pulsed field gradient spin-echo method is free from the obvious object that translational motion may be too slow to dominate the relaxation process and since the r.m.s. distances measured in an experiment are much larger than the lattice parameter, the conclusion that the technique measures molecular motion between cavities seems to

Table IV
Comparison of Results of NMR and Sorption Studies

System	Ref	NMR self diffusion			NMR relaxation			Sorption			Equilibrium	
		$D \times 10^4$ cm ² sec ⁻¹	E kcal	D at 298K cm ² sec ⁻¹	$(1/\tau_0)$ $\times 10^{-11}$ sec ⁻¹	E kcal	D at 298K cm ² sec ⁻¹	E kcal	D at 298K cm ² sec ⁻¹	$K_0 \times 10^{10}$ mol/cage dyne.cm ²	$v \times 10^{-11}$ sec ⁻¹	
SF ₆	(41, 17)	-	-	-	8.8	2.5	3.3×10^{-5}	2.8	2.7×10^{-9}	6.2	8.5	
nC ₄ H ₁₀	(42)	6	2.2	1.5×10^{-5}	8.0	2.2	4.9×10^{-5}	-	-	-	-	
nC ₆ H ₁₄	(43)	8	2.5	1.2×10^{-5}	-	-	-	-	-	-	-	
nC ₇ H ₁₆	(42, 32)	15	3.2	6.7×10^{-6}	5.2	2.9	9.7×10^{-6}	6.2	6.1×10^{-11}	0.54	5.9	
C ₆ H ₁₂	(44, 45, 38)	15	3.0	9.4×10^{-6}	6.7	3.0	1.05×10^{-5}	5.0	2.3×10^{-10}	0.60	6.7	
CH ₄	(46, 29)	0.45	0.9	1×10^{-5}	-	-	-	3.0	4.8×10^{-10}	14.5	7.1	
C ₂ H ₆	(47, 30)	0.1	1.5	1×10^{-6}	-	-	-	3.0	7.8×10^{-11}	3.0	7.5	
nC ₄ H ₁₀	(48, 49, 30)	-	-	-	0.017	2.8	3.7×10^{-8}	4.0	8.3×10^{-12}	6.5	3.8	
1-C ₄ H ₈	(48, 49, 30)	-	-	-	0.09	5.0	4.8×10^{-9}	3.5	5.3×10^{-12}	0.24	11.4	
t-2-C ₄ H ₈	(48, 49, 30)	-	-	-	0.02	4.0	5.9×10^{-9}	3.5	7.4×10^{-12}	0.52	9.2	
cis-2-C ₄ H ₈	-	-	-	-	0.01	5.0	5.5×10^{-10}	9.2	2.6×10^{-13}	-	-	

NMR self diffusion data are for $\theta = 0.2 - 0.3$. D decreases with θ for 13X systems and increases for CH₄ and C₂H₆ in 5A. D for relaxation is calculated from equation 8 with $\lambda = 12.3\text{\AA}$. Values of θ for the relaxation data are SF₆, $\theta = 0.2$; nC₄H₁₀-13X and nC₇H₁₆-13X, $\theta = 0.81$; C₄ hydrocarbons in 5A, $\theta = 0.6 - 0.7$. For 13X systems τ increases with θ corresponding to a decrease in mobility. Sorption values of D_0 are for 1 molecule/cavity which is about $\theta = 0.2 - 0.3$ for the 13X systems.

be justified. Nevertheless, neutron scattering studies of CH_3CN and CH_3OH in 3A sieve, systems in which the sorbate molecules are almost certainly trapped within particular cages, yield jump times $\sim 10^{-11}$ sec and intracavity diffusivities $\sim 10^{-5}$ $\text{cm}^2\cdot\text{sec}^{-1}$ at room temperature (53). These values are close to the NMR diffusivities of Karger and Caro for CH_4 in 5A sieve (46). The NMR diffusivities for 13X zeolite are similar to the values for the pure liquid sorbates whereas the sorption values are of the same order as the diffusivities of molecular solids near the melting point. The latter state seems more consistent with heat capacity evidence (50). Both NMR and sorption data are self-consistent and show the expected trends with changes in sorbate and sieve. The suggestion that sorption rates are controlled by surface resistance rather than by intracrystalline diffusion, even under properly selected conditions, is inconsistent with the form of the uptake curves which show the well known initial dependence on \sqrt{t} , rather than the linear time dependence characteristic of a surface controlled process. The limited diffusivity data obtained from catalytic kinetics under diffusion limited conditions (54,55) are also consistent with the diffusivities from sorption rather than NMR (33) and the recent thermodynamic study of Stroud et al. (56) provides further indirect evidence that, for CH_4 in 5A at low temperatures, the intracrystalline diffusivity is much smaller than the NMR measurements suggest.

Counter Diffusion Studies

The data discussed above refer exclusively to the diffusion of single molecular species either with a net flux, as in a sorption experiment, or with no net flux as in a tracer measurement. Many industrial processes involve a counter-diffusion situation in which one component is diffusing into a crystal while another component is simultaneously diffusing out. It has been shown that in this situation diffusivities may be very much smaller than the diffusivities of the individual components (57-59) but it is not yet certain to what extent such effects arise from the change in the activity correction term ($\partial \ln p / \partial \ln c$) and to what extent they reflect actual changes in the magnitude of the intrinsic diffusivity (D_0 or \bar{D}). From theoretical considerations one would expect that in systems in which the diffusivity is determined primarily by the crystal lattice (i.e. when the molecular diameter is larger in relation to the window aperture) D_0 should not be significantly different under counter diffusion conditions. However, when the collisional diffusion mechanism is dominant a significant difference between the intrinsic diffusivity in a counter diffusion situation, as compared with a single component system, is possible. These hypotheses have not so far been tested experimentally.

Conclusions

The topics covered by this review include only some of the more recent work in this area. The kinetic data in the literature show many apparent anomalies and contradiction but in many cases this seems to be because the pronounced concentration dependence of zeolitic diffusivities and the consequent necessity of making differential rather than integral measurements were not appreciated in much of the earlier work. The more recent data show much greater regularity with a clear correlation between the diffusional behaviour and the relative sizes of sorbate molecule and zeolite window.

Notation

A, B, C	constants in equation 1
a	sorbate activity
c	sorbate concentration
c_s	saturation concentration
D	zeolitic diffusivity
D_0	corrected diffusivity (equation 5)
D^*	pre-exponential factor for D_0 (equation 7)
D'_0	defined by equation 2
D'^*	pre-exponential factor for D'_0 (equation 3)
\bar{D}^*	self diffusivity
E	diffusional activation energy
K	Henry constant (defined by $c = Kp$)
K_0	pre-exponential factor for K ($K = K_0 e^{q_0/RT}$)
L_{AA}, L_{A^*A}	straight and cross coefficients in the irreversible thermodynamic formulation of diffusion
m	mass of sorbate molecule
p	equilibrium sorbate pressure
q_0	limiting heat of sorption
R	gas constant
r	crystal radius
u	gas velocity
θ	fractional saturation (c/c_s)
τ	NMR correlation time for molecular jumps
τ_0	pre-exponential factor in equation 7
λ	jump distance
v	vibration frequency

Literature Cited

1. Barrer, R.M., *Adv. in Chem.* (1971), 102, 1.
2. Lee, L.K., Yucel, H. and Ruthven, D.M. This conference.
3. Dubinin, M.M. This conference.
4. Loughlin, K.F., Derrah, R.I. and Ruthven, D.M., *Can. J. Chem. Eng.* (1971), 49, 66.
5. Ruthven, D.M., *Separation and Purification Methods* (1976) 5, (2).
6. Eberly, P.E., *Ind. Eng. Chem. Fund.* (1969), 8, 25.
7. van Deemter, J.J., Zuiderweg, F.J. and Klinkenberg, A., *Chem. Eng. Sci.* (1956), 5, 271.
8. MacDonald, W.R. and Habgood, H.W., *Can. J. Chem. Eng.* (1972), 50, 462.
9. Ma, Y.H. and Mancel, C., *Adv. in Chem.* (1973), 121, 392.
10. Schneider, P. and Smith, J.M., *A.I.Ch.E.Jl.* (1968), 14, 762.
11. Hashimoto, N. and Smith, J.M., *Ind. Eng. Chem. Fund.* (1973), 12, 353.
12. Mixon, F.O., Whitaker, D.R. and Orcutt, J.C., *A.I.Ch.E.Jl.* (1967), 13, 21.
13. Ostergaard, K. and Michelsen, M.L., *Can. J. Chem. Eng.* (1969), 47, 107.
14. Sarma, P.N. and Haynes, H.W., *Adv. in Chem.* (1974), 133, 205.
15. Gangwal, S.K., Ph.D. Thesis, University of Waterloo, Ontario (1976).
16. Ruthven, D.M. and Derrah, R.I., *J. Chem. Soc. Faraday Trans I* (1975), 71, 2031.
17. Ruthven, D.M. and Doetsch, I.H., *Ibid* (1976), 72, 1043.
18. Eagan, J.D. and Anderson, R.B., *J. Colloid Interface Sci.* (1975), 50, 419.
19. Ruthven, D.M. and Loughlin, K.F., *Chem. Eng. Sci.* (1971), 26, 1145.
20. Haase, R. and Siry, M., *Z. Phys. Chem. (Frankfurt)* (1968), 57, 56.
21. Turner, J.C.R., *Chem. Eng. Sci.* (1975), 30, 1304.
22. Ash, R. and Barrer, R.M., *Surface Sci.* (1967), 8, 461.
23. Kärger, J., *Ibid.* (1973), 36, 797.
24. Darken, L.S., *Trans. A.I.M.E.* (1948), 175 184.
25. Barrer, R.M. and Fender, B.E.F., *J. Phys. Chem. Solid* (1964), 21, 12.
26. Rees, L.V.C. private communication.
27. Sargent, R.W.H. and Whitford, C.J., *Adv. in Chem.* (1971), 102, 155.
28. Quig, A. and Rees, L.V.C., *J. Chem. Soc. Faraday Trans I* (1976), 72, 771.
29. Ruthven, D.M. and Derrah, R.I., *J. Chem. Soc. Faraday Trans I* (1972), 68, 2332.
30. Ruthven, D.M., Derrah, R.I. and Loughlin, K.F., *Can. J. Chem.* (1973), 51, 3514.
31. Ruthven, D.M., Loughlin, L.F., and Derrah, R.I., *Adv. in Chem.* (1973), 121, 330.

32. Doetsch, I.H., Ruthven, D.M. and Loughlin, K.F., *Can. J. Chem.* (1974), 52, 2717.
33. Ruthven, D.M. and Derrah, R.I., *J. Colloid Interface Sci.* (1975), 52, 397.
34. Barrer, R.M. and Davies, J.A., *Proc. Roy. Soc.* (1971), A322, 1.
35. Wolf, F. and Pilchowski, K., *Chem. Techn.* (1971), 23, 672.
Adv. in Chem. (1971), 102, 229.
36. Ruthven, D.M., *Can. J. Chem.* (1974), 52, 3523.
37. Barrer, R.M. and Clarke, D.J., *J. Chem. Soc. Faraday Trans I* (1974), 70, 535.
38. Ruthven, D.M. and Doetsch, I.H., *A.I.Ch.E. J1.* (1976), 22, (5).
39. Resing, H.A. and Murday, J.S., *Adv. in Chem.* (1973), 121, 414.
40. Pfeifer, H., Schirmer, W. and Winkler, H., *Ibid.*, (1973), 121, 430.
41. Thompson, J.K. and Resing, H.A., *J. Colloid Interface Sci.*, (1968), 26, 279.
42. Karger, J., Shdanov, S.P. and Walter, A., *Z. Phys. Chem. Leipzig* (1975), 256, 319.
43. Karger, J., Bulow, M. and van Phat, N., *Z. Phys. Chem. Leipzig* - in press.
44. Karger, J., Lorenz, P., Pfeifer, H. and Bulow, M., *Z. Phys. Chem. Leipzig* (1976), 257.
45. Nagel, M., Pfeifer, H. and Winkler, H., *Z. Phys. Chem. Leipzig* (1974), 255, 283.
46. Karger, J. and Caro, J., *J. Colloid Interface Sci.* (1975), 52, 623.
47. Caro, J., Karger, J., Finger, G. and Pfeifer, H., *Z. Phys. Chem. Leipzig* - in press.
48. Labisch, L., Schollner, R., Michel, D., Rossiger, V. and Pfeifer, H., *Ibid* (1974), 255, 581.
49. Michel, D. and Rossiger, V., *Surface Sci.* (1976), 54, 463.
50. von Basler, W. and Lechert, H., *Ber. Buns. Ges. Phys. Chem.* (1974), 78, 667.
51. Chadwick, A.V. and Sherwood, J.N. in "Point Defects in Solids" et J.H. Crawford and L.M. Slifkin, Plenum Press, New York (1975).
52. Sherwood, J.N., *Surface and Defect Props. of Solids* (1973), 2, 250.
53. Egelstaff, P.A., Downes, J.S. and White, J.W., in "Molecular Sieves", *Soc. Chem. Ind., London* (1968) p. 306.
54. Miale, J.N., Chen, N.Y., Weisz, P.B., *J. Catalysis* (1966), 6, 278.
55. Chen, N.Y. and Garwood, W.E., *Adv. in Chem.* (1973), 121, 330.
56. Stroud, H.J.F., Richards, E., Limcharoen, P. and Parsonage, N., *J. Chem. Soc. Faraday Trans. I* (1976), 72, 942.
57. Satterfield, C.N., Katzer, J.K. and Vieth, W.R., *Ind. Eng. Chem. Fund.* (1971), 10, 478.
58. Satterfield, C.N. and Katzer, J.R., *Adv. in Chem.* (1971), 102, 193.
59. Moore, R.M. and Katzer, J.R., *A.I.Ch.E. J1.* (1972), 18, 816

NMR Studies of Water inside the Sodalite Units of Faujasites with Different Cations

W. D. BASLER

Institute of Physical Chemistry, University of Hamburg,
Laufgraben 24, 2000 Hamburg 13, West Germany

ABSTRACT

Using pulsed NMR, water molecules inside the sodalite units of faujasites could be detected and studied separately from those in the large cavities. The rate of passing into the sodalite units is first order with respect to water activity. The molecules are fixed or rotating, depending on temperature and cation exchange.

Introduction

Some zeolite structures contain different systems of intracrystalline voids and channels, and the accessibility to guest molecules, their behaviour therein and the exchange kinetics between these different sites of sorption may be of interest.

We want to report studies of water sorbed in faujasites. The structure of faujasites is built up by cubooctahedral units (sodalite cages), which are linked by hexagonal prisms, and contains two kinds of intracrystalline voids: The first system are large cavities of 13 Å diameter, interconnected by windows of 8 Å diameter, thus forming a three-dimensional system of channels. The second system consists of the interiors of the sodalite units, more isolated from each other than joined by the hexagonal prisms. The passage from four adjacent large cavities into a sodalite cage is possible through oxygen six-rings of 2.5 Å free diameter, permitting access only of small molecules. The cations which are necessary to compensate the smaller charge of the Al³⁺-ions, are partly localized before or in these six-rings. At room temperature a large cavity can take up 28, a sodalite

unit 4 water molecules(1-5).

In previous NMR-studies(6-12) only water in the large cavities was studied, but recently a second NMR-signal was discovered and attributed to the water inside the sodalite units, independently by two other groups and us(13-15). Further we could show that the water in the large and the small cavities of other zeolites (A-type, ZK 4) can be studied separately by NMR, and that water is sorbed only in the large cavities, if any heating is avoided during sorption, which allowed us to study the kinetics of the water molecules passing through the oxygen six-rings into the sodalite cages(16).

After shortly reviewing the main results of that earlier report(16) we present additional NMR-studies concerning the kinetics (order of reaction) and the behaviour of the water inside the sodalite cages (influence of cation exchange).

Experimental

The zeolites studied were Linde 13X of Union Carbide and faujasites prepared by Kacirek, using newly developed methods of crystallization(17,18). Exchange of cations was performed at 80°C, using a column and 1 n solution of the corresponding chloride. The amount of exchange was determined by chemical analysis of the remaining sodium. The pulsed proton-NMR was done at 60 MHz, using a Bruker B-KR 322s spectrometer, the wide-line-NMR of proton and sodium at 16 and 12 MHz with a Varian DP 60.

Before loading, the zeolite powder was outgassed at 400°C, until the pressure was less 10^{-5} Torr. Checked by pulsed NMR, the outgassed zeolites showed no proton signal after the dead-time of 9 μ s at a detection limit of 1-2 mg water/g zeolite. Sorption was performed using water vapor, the amount was determined by weight.

Results and Discussion

The observation of two-phase-behaviour in pulsed proton-NMR of water in faujasites(13-15) provided a convenient method to detect and to investigate separately the fraction of more mobile water molecules in the large cavities and the fraction in the interior of the sodalite units, more fixed and restricted in translational motion. By this technique, we did some further investigations(16), the main results can be summarized as follows:

1) At low filling the sodalite cages are filled up predominantly and contain half of the water. At higher temperature this equilibrium of sorption is shifted in favour of the large cavities, indicating that the heat of sorption inside the sodalite cages is greater (1 kcal/mol) than in the large cavities.

2) In Na-faujasites the motion of the water molecules in the sodalite units contains at least rotation about one axis and additional tumbling.

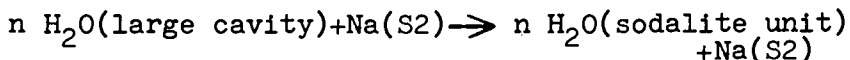
3) If any heating is avoided during the process of sorption, water is exclusively sorbed in the large cavities. In Na-faujasites, where all oxygen six-rings are occupied by cations in sites 2, the rate of passing into the sodalite units is slow (several months at 295 K and 100 mg water/g zeolite). The activation energy is 20-25 kcal/mol for 295-395K. In zeolites with sites 2 not fully occupied the water passes into the sodalite units in less than one hour.

4) Water sorbed in other zeolites containing sodalite cages (NaA, ZK 4) shows the same two-phase-behaviour. The results for water in the sodalite cages are in close agreement with those of water in zeolite sodalite.

5) Studies of another small molecule, ammonia, show essentially the same results.

To get further insight into the mechanism, by which the water molecules pass from the large cavity through the oxygen six-rings into the sodalite cages we looked for the sodium ions, which control the access to the sodalite cages by occupying sites 2. For this we studied the sodium 23-resonance by wide-line-NMR at 12 MHz before and after the water had passed into the sodalite units. The zeolite was Linde 13X with 200 mg water/g and T=295 K. In spite of the difficulties of the interpretation of the whole spectrum(19) a change in the number of mobile sodium ions should be easily detected by the intensity of the sharp central line. As can be seen in Figure 1, no difference is observed. Thus when a sodium ion leaves its site 2 to open the oxygen six-ring for the water molecules to pass, after the passage the site 2 is occupied again.

On the other hand, this can be concluded from the observed slow passage, that means that all sites 2 are occupied, when no water is in the sodalite units, and X-ray-studies, which show fully occupied sites 2, when water is in the sodalite units(20). Therefor we might formulate:



where n is the number of water molecules passing in one step of reaction into the sodalite cage.

To obtain n we determined the rate of this reaction with respect to the activity of the water. We measured the time $t_{1/2}$ needed to fill the sodalite units to half of the equilibrium value. Clearly, a more precise knowledge of the concentration-time-function would give more detailed information, but the limited accuracy (the corresponding signal is only a small part of the total signal) did not allow this. Nevertheless, the approach to equilibrium seemed to be exponential, and the data were analysed using this assumption.

The zeolite was Linde 13X, the temperature 295K and the activity of the water was calculated from the amount of loading, using the sorption isotherm of ref. (14).

Table I. Half-time $t_{1/2}$ of water passing into the sodalite cages of Linde 13X for different loading

Loading(mg/g)	Activity	half-time(hours)
105	0.0004	800
194	0.002	200
255	0.01	100
284	0.04	25
355	0.8	<1

If n water molecules were involved in an elementary step of reaction, it would be expected that

$$\text{rate} = \text{const} \cdot (\text{activity})^n$$

As the half time $t_{1/2}$ is inversely proportional to the rate, the plotting of $\log t_{1/2}$ against \log activity should give a straight line with the slope $-n$. Fig.2 shows that the experimental values are in agreement with $n=1$, the reaction is first order with respect to water.

The results presented above did only give information the rate, by which the water passes into the sodalite cage. The rate of the backward reaction (water leaves the sodalite cage) should be accessible by studying the equilibrium, when exchanges in forward and backward direction are equal. As this can be done by NMR (the two-phase-behaviour vanishes, when the exchange rate is faster than the relaxation rate) we studied all faujasites used before at temperatures up to 475 K. In no case did we observe rapid exchange on the time scale of NMR, approx. 10-100 ms, even in faujasites with open six-rings and full loading. We

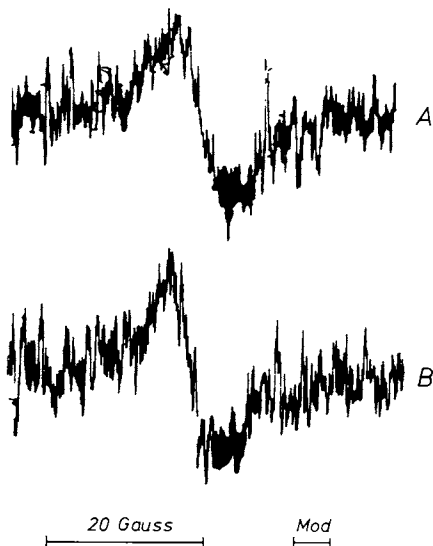


Figure 1. Wide-line NMR of sodium 23, when (A) water is only in the large cavities and (B) the sodalite cages are filled, too. Zeolite Linde 13 X with 200 mg H_2O/g , $T = 295$ K, 12 MHz.

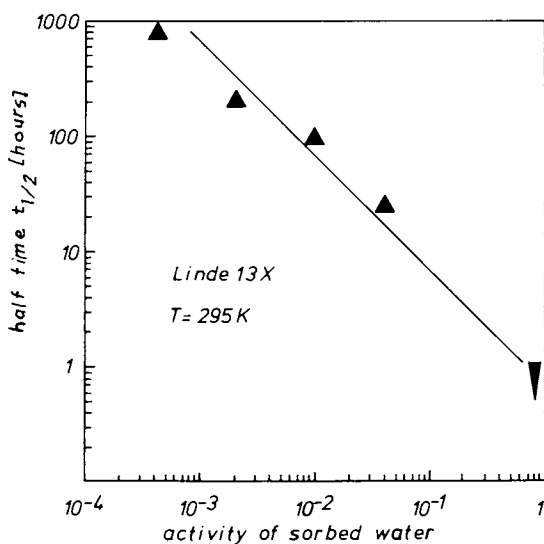


Figure 2. Log-log plot of the half time $t_{1/2}$ to fill the sodalite cages with water against the activity of the sorbed water. Straight line has slope -1 . Zeolite Linde 13 X, $T = 295$ K.

conclude that the water molecules pass more or less rapidly depending on cations in sites 2, into the sodalite cages, but then are strongly bound and fixed there.

To prove this, we more closely examined the free induction decay of the water protons in the sodalite cages of faujasites with different cations. In Fig. 3 are shown the results for NaX (Si/Al=1.18), NaY (Si/Al=2.36), CaY (Si/Al=2.93, 91% exchange), LaY (Si/Al=2.93, 80% exchange) and, to compare, for the immobile water in gypsum.

There is a clear influence of the cations: In Na-faujasites we find rotating and perhaps tumbling water molecules. There is no influence of the Si/Al-ratio, as there are enough sodium ions for the sites inside the sodalite units.

In CaY the water is as immobile as in gypsum. By interaction with the Ca-ions in sites 1' the water molecules are fixed. Passing back into the large cavity is thereby inhibited, and this explains why we do not observe rapid exchange.

In LaY the water molecules make some reorientation with a jump frequency of 10^{-5} s. This weaker sorption, compared with CaY, suggests that the La-ions are in the hexagonal prisms (site 1).

The behaviour at higher temperatures is shown in Fig. 4 and 5: The water molecules in the sodalite cages of LaY and CaY achieve at approx. 400 K the same mobility as those in Na-faujasites have at room temperature.

The influence of washing (1 l distilled water/g zeolite for 24 hours at 295 K) was investigated using Linde 13X. This treatment introduces OH-groups and the NMR-relaxation of the water in the large cavities is strongly influenced by this (14). Whereas we found a ten-fold increase of the transverse relaxation at 375 K, no change of the relaxation or the intensity of the water in the sodalite cages could be observed, in agreement with (13). Thus the integrity of the sodalite units is not affected by washing.

At least we tested the possibility to distinguish the two kinds of water in faujasites by wide-line-NMR. While in pulsed NMR the different parts of the free induction decay are proportional to the different numbers of protons in the sample, in wide-line-NMR the intensity of the signal is additionally roughly inversely proportional to the square of the line-width. Therefore, it is difficult to measure a broad line in the presence of a narrow line, even if the number of protons are comparable. Fig. 6 shows the

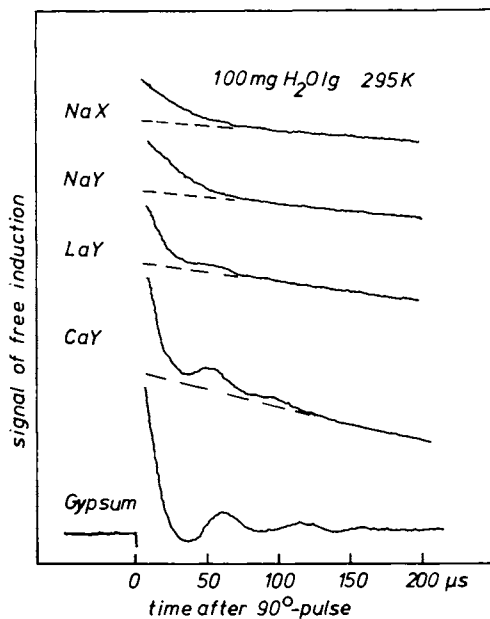


Figure 3. Free induction decay of water protons in the sodalite cages of faujasites with different cations and in gypsum. 100 mg H_2O/g zeolite, $T = 295 K$

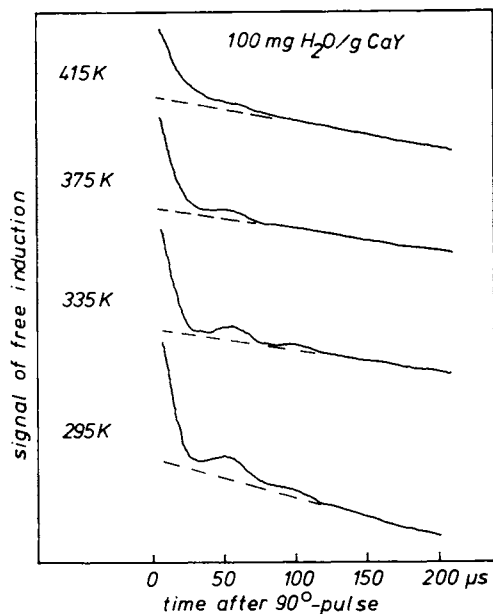


Figure 4. Temperature dependence of the free induction decay of water protons in the sodalite cages of CaY ($Si/Al = 2.93$, 91% exchange)

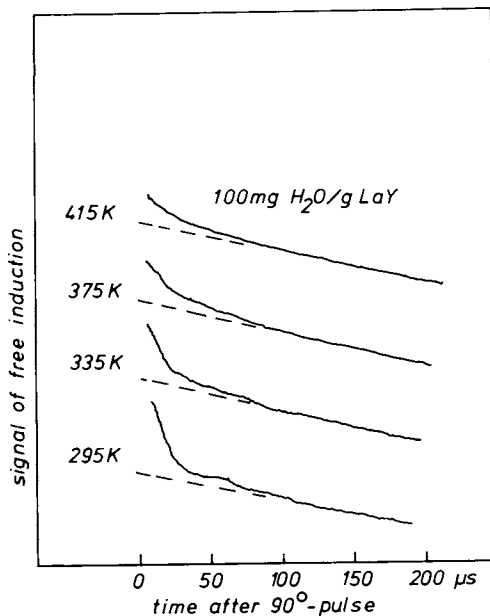


Figure 5. Temperature dependence of the free induction decay of water protons in the sodalite cages of LaY (Si/Al = 2.93, 80% exchange)

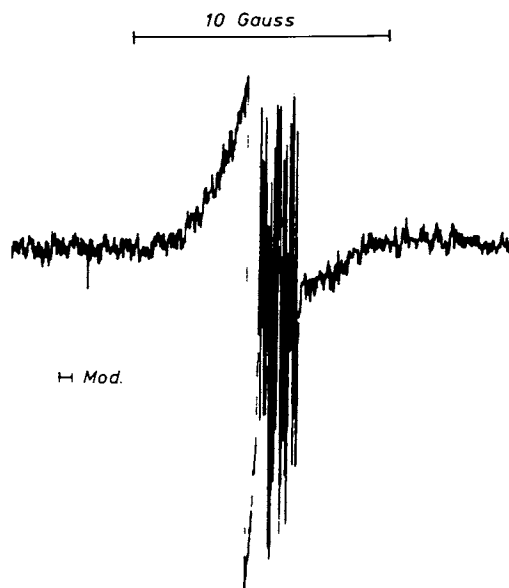


Figure 6. Wide-line NMR of water protons in Linde 13 X. 100 mg H₂O/g, T = 295 K, 16 MHz, 145 scans a 10 min.

result of 145 scans of 10 minutes for a sample of 100 mg water/g Linde 13X at 295 K and 16 MHz. Under the very intense narrow line of the water in the large cavities the broad line of the water in the sodalite cages can be seen with poor signal-noise-ratio: Wide-line-NMR is not suited to distinguish water inside and outside the sodalite cages of faujasites.

Literature Cited

1. Barrer, R. M., *Endeavour* (1964), 23, 122.
2. Fischer, K. F. and Meier, W. M., *Fortschr. Mineral.* (1965), 42, 50.
3. Olson, D. H., *J. Phys. Chem.* (1970), 74, 2758.
4. Mortier, W. J. and Bosmans, H. J., *J. Phys. Chem.* (1971), 75, 3327.
5. Barrer, R. M. and Bratt, C. C., *J. Phys. Chem. Sol.* (1959), 12, 130.
6. Lechert, H. and Henneke, H. W., *Surface Sci.* (1975), 51, 189.
7. Resing, H. A., *8. Coll. NMR-Spectrosc.* (1971), Aachen.
8. Resing, H. A. and Thompson, J. K., *2. Int. Conf. Molecular Sieve a. Zeolites* (1971), Worcester.
9. Pfeifer, H., Przyborowski, F., Schirmer, W. and Stach, H., *Z. Phys. Chem. Leipzig* (1969), 236, 345
10. Pfeifer, H., Gutze, A. and Shdanov, S. P., *Z. Phys. Chem. Leipzig*, in press.
11. Kärger, J., *Z. Phys. Chem. Leipzig*, in press.
12. Pfeifer, H., in *NMR Basic Principles and Progress*, 7, p 53, Springer, Heidelberg (1972).
13. Pfeifer, H., *Surface Sci.* (1975), 52, 434.
14. Murday, J. S., Patterson, R. L., Resing, H. A. Thompson, J. K. and Turner, N. H., *J. Phys. Chem.* (1975), 79, 2674.
15. Basler, W. D., Lechert, H. and Kacirek, H., *Ber. Bunsenges. Phys. Chem.* (1976), 80, 451.
16. Basler, W. D., 172. ACS Nat. Meeting, San Francisco (1976).
17. Kacirek, H., Thesis, Hamburg (1974).
18. Kacirek, H. and Lechert, H., *J. Phys. Chem.* (1975), 79, 1589.
19. Lechert, H., *Habilitation Thesis, Hamburg* (1973).
20. Hseu, K., Thesis, Univ. of Wash. (1972).

Characterization of the Mordenite Sorption Sites by Carbon-13 NMR

M. D. SEFCIK, JACOB SCHAEFER, and E. O. STEJSKAL

Corporate Research Department, Monsanto Co., St. Louis, Mo. 63166

ABSTRACT

Carbon-13 NMR spectra of CO, CO₂, CS₂ and OCS sorbed on a variety of mordenites have been obtained. In the Na⁺-mordenite, lineshape analysis demonstrates the presence of nonrotating molecules sorbed in the side pockets and anisotropically rotating molecules in the main channel. Side-pocket sorption was not observed in the H⁺, K⁺, Cs⁺ and NH₄⁺ exchanged mordenites. Results are presented which suggest that the reduced free aperture in the small-port sieve is not due to occasional stacking faults.

Introduction

The aluminosilicate structure of the Na⁺-mordenite consists of 12-membered rings, opening in the *c*-direction and forming slightly elliptical channels with free apertures of 6.5 x 7.0 Å (1). The elliptical large channels are intersected in the *b*-direction by smaller channels consisting of 8-membered rings with free apertures of 3.3 x 4.7 Å. Rather than interconnecting the large channels, these small channels branch through twisted 8-membered rings, having an aperture of only 2.8 Å, which effectively isolate the large channels and leaves them lined with two rows of side pockets. In the hydrated Na⁺-mordenite, four of the 8 sodium ions per unit cell occupy positions in the center of the twisted 8-membered ring, while the other four are believed to reside near the side pocket entrance and in the large channel (2). Although the large channel is formed by 12-membered rings, only some varieties of mordenite (called large port) have sorption properties consistent with this ring size. A small-port variety sorbs only molecules less than 4 Å in diameter, consistent with a 8-membered ring structure.

It has been suggested that cations, stacking faults or intercalated matter could be responsible for the apparent size

reduction. Sand (3) has shown that mordenites could be converted from one form to the other by chemical treatment.

Many diverse analytical procedures have been applied to the characterization of this sorbent-sorbate system. These techniques, which vary from steady-state x-ray measurements of static properties of the system, to spectrophotometric measurements of the high-frequency properties of the system, do little to enhance an understanding of the dynamic properties of the sorbate under the influence of the sorbent. In many cases, these measurements are sensitive only to gross or average properties of the system which may be misleading in systems which are comprised of a distribution of properties.

We present here results which demonstrate the utility of carbon-13 nuclear magnetic resonance (^{13}C -NMR) in characterizing the motion of molecules sorbed on molecular sieves. This technique offers the advantage of allowing the experimenter to examine a relatively narrow range of sorption sites which are specific for the sorbed species. Since the affinity for a particular molecule for the sorption sites in porous crystals is predictably dependent on the size of the molecule, judicious choice of the probing molecule allows one to examine various sorption sites independently. The probing molecule will be excluded from all sites which are smaller than the molecule itself, and will be only weakly sorbed in sites which are much larger than the molecular dimensions of the sorbate. The greatest concentration of the sorbate will be in sites whose dimensions most nearly match its own. This feature, together with the ability to observe the rotational behavior of sorbed molecules (which is more or less restricted by the size of the sorption site), has enabled us to gain new insight on the sorption properties of mordenite molecular sieves.

Lineshape Analysis

There are three sources of line broadening in the NMR experiment which limit the applicability of this technique in studying sorbent-sorbate interactions. Two of these are dipolar interactions, either between nuclear dipoles or between a nuclear dipole and an electron dipole. The latter is frequently encountered in natural zeolite samples where paramagnetic impurities may be large. The effect of paramagnetic impurities in zeolites on molecular relaxation has been discussed in detail by Resing (4). Paramagnetic broadening was avoided in this study by the use of specially prepared mordenites with low impurity concentrations. Nuclear dipolar interactions may be reduced by using rare-spin NMR and double resonance techniques (5).

While both nuclear and paramagnetic dipolar interactions usually give rise to symmetric broadening of the nuclear magnetic resonance, molecular motions which are slower than about

10^4 Hertz allow a third major source of line broadening, a dispersion of resonance frequencies. The chemical shift or resonant Larmor frequency of a particular nucleus is proportional to the local magnetic field at that nucleus. The local magnetic field is, in the absence of dipolar interactions, dependent on the strength of the applied magnetic field, H_0 , and the very small fields generated by electrons moving about the nucleus. Molecules frequently have an anisotropic distribution of electrons about the nucleus causing a directional dependence in the chemical shift. Theoretical resonance dispersions arising from chemical shift anisotropies (CSA) for nuclei in randomly oriented molecules, such as encountered here, may be calculated for various nuclear site symmetries (6). A cubic or higher nuclear site symmetry results in only one value for the chemical shift, a delta function shown in Figure 1 at σ_1 . (The high frequency molecular motions encountered in liquids and gases effectively increase the nuclear site symmetry of the molecules to spherical, resulting in the narrow lines characteristic of high resolution NMR.) It is worthwhile to note at this point that any interaction between the sorbate and the sorbent which changes the electron density near the observed nucleus will result in a change in the chemical shift, thus providing a mechanism for distinguishing chemi- from physisorption.

Molecules with axial symmetry have two principal values of the chemical shift tensor, one perpendicular to the symmetry axis and one parallel to it (σ_{xx} and σ_{zz} in Figure 1). Figure 1 represents some possible chemical shift dispersions of CO_2 molecules. The linear CO_2 molecule has three possible orientations with respect to the applied magnetic field, two of which have identical chemical shifts. The spectral dispersion which arises from a collection of randomly oriented CO_2 molecules, as in a frozen solid, is a broad line with the doubly degenerate chemical shifts and hence greater intensity on the down-field (7) side, as illustrated by the dashed curve in Figure 1.

If, instead of in a frozen solid, the CO_2 molecules find themselves in an environment where they can execute anisotropic rotation, a very different chemical shift dispersion is observed. As shown by the drawing in Figure 1, rotation about one of the C_2 axes perpendicular to the molecular axis leaves the chemical shift for one orientation unchanged, but averages the other two, producing a narrower spectral dispersion with the degenerate chemical shifts on the up-field solid curve. With rotation about the other C_2 symmetry axis, the CO_2 molecule assumes isotropic or "free" rotation and the chemical shift dispersion collapses to the delta function, as mentioned earlier.

The fourth characteristic CSA lineshape which can be encountered in the NMR of solids is one in which all three orientations of a molecule with respect to the applied magnetic field have unique chemical shifts. This arises from molecules which have lower than axial symmetry (non-symmetric in the

molecular coordinate system) or from an axially symmetric molecule whose anisotropic rotation is not sufficient to average the principal values of the chemical shift tensor. These spectral dispersions are characterized by their "tent" shape having the greatest intensity between the two chemical shift extremes.

Since determination of the molecular motions depends on the careful analysis of the broad spectral dispersions arising from molecular chemical shift anisotropy, every effort should be made to eliminate unwanted sources of line broadening and spectral overlap from molecules which have more than one resonance. Rare-spin NMR has the advantage of minimizing homonuclear dipolar interactions, and the use of isotopically enriched samples may simplify the spectra to that of only one nuclear resonance. As in the work presented here, the carbon-13 NMR of carbon-containing inorganic gases actually provide the most straightforward and accessible experiment since only single resonance experiments need be performed.

Experimental Procedure

A variety of mordenite molecular sieves were compared in this study. Small-port Na⁺-mordenite was prepared from high purity reagents by Leonard B. Sand of Worcester Polytechnic Institute. The X-ray diffraction patterns indicated the samples to be 90-95% mordenite with the remainder as analcime. Paramagnetic impurities ranged from 10 to 170 ppm and had no effect on the lineshape. Hydrogen, K⁺, Cs⁺ and NH₄⁺-mordenites were prepared by cation exchange from excess 1 M chloride solutions at 70°C, repeated three times and washed free of chloride ion. Exchange with HCl was limited to 15 minutes and elemental analysis of the H⁺-form gave a Na:Al:Si ratio of 0.1:1.5:1. Large-port Na⁺ and H⁺-mordenites were obtained from Norton Co., Worcester, Mass. (Lots DZ-23-1 and HB-6E-H, respectively.) A large-port sample was dealuminated by refluxing in HCl until the SiO₂/Al₂O₃ = 70. The small-port samples sorbed less than 2 weight percent neo-pentane while the large-port varieties sorbed 7-9 weight percent neo-pentane at room temperature and one atmosphere.

Approximately 1/2 gram samples of the molecular sieve were placed in 10 mm O.D. NMR tubes and dried in vacuo under a programmed temperature rise to 300°C. The ammonium exchanged sieve was shown to lose ammonia only above 415°C by DTA. After cooling, the sieves were allowed to sorb 90% isotopically enriched ¹³C gases to the desired level. The loading level was defined as a weight percent of the capacity of the sieve at room temperature and 1 atm (300 mm Hg for CS₂). The tubes were sealed with a Teflon plug and Viton O-ring without exposure to the atmosphere and were used reproducibly over several months.

The Fourier transform ¹³C-NMR spectra were obtained on a Bruker spectrometer operating at 22.6 MHz, equipped with a broad-

American Chemical Society
Library

1155 16th St., N.W.

Washington, D.C. 20036

band receiver and quadrature detector (9), with field stabilization provided by an external time-share ^{19}F lock (8). The experiments described here can be performed on any commercial instrument, which is equipped with an external field lock, and which is free from baseline artifacts (9).

Results and Discussion

The ^{13}C -NMR spectra of isotopically enriched $^{13}\text{CO}_2$ sorbed in varying amounts on the Na^+ -mordenite has been presented in a preliminary report of this investigation (10) and are shown in Figure 2. Qualitative analysis of those resonance line-shapes suggested the presence of sorbed CO_2 in at least three distinct states (or a distribution of states), presumably differing in their rotational freedom. The presence of nonrotating, anisotropically rotating and isotropically rotating CO_2 molecules sorbed on the small-pore mordenite are now clearly understood in terms of the thermodynamic interactions between the CO_2 and the sieve and the adsorption site structure.

The energetics of sorption have been discussed in detail by Barrer (11). The major interactions between the zeolite and a sorbed molecule are the dispersion (ϕ_D), short-range repulsion (ϕ_R), polarization (ϕ_P), field-dipole ($\phi_{F-\mu}$), and the field gradient-quadrupole energies (ϕ_{F-Q}). The characteristic initial heat of sorption is then given by

$$\Delta\bar{H} = \phi_D + \phi_R + \phi_P + \phi_{F-\mu} + \phi_{F-Q} .$$

The dispersion and repulsion energies are universal but may vary with the sorbent, while ϕ_P , $\phi_{F-\mu}$, and ϕ_{F-Q} depend on both the heteropolarity of the sorbent and the nature of the sorbate. The dispersion energy dictates that sorbed molecules will have the greatest affinity for sites which offer the highest coordination number (12) or best fit, while short-range repulsions will prevent sorption in sites which are smaller than the van der Waals diameter of the sorbate. The polarization and electrostatic energy components are largest when the sorbate is near the cation centers, decrease with increasing ionic radii, and increase with cation charge. Both the field-dipole and the field gradient-quadrupole interactions are directionally dependent [varying with the $\cos \theta$ in the former and $(3 \cos^2 \theta - 1)$ in the latter, where θ is the angle between the dipole or quadrupole axis and the local field direction], thereby providing an orientational preference of sorbed molecules with permanent dipole or electric quadrupole moments.

The results in Figure 2 can be explained as follows: the first CO_2 molecules sorbed on the small-pore Na^+ -mordenite are attracted to side pockets which line the large channel. Not only are the dispersion energies most favorable here, but, by entering oxygen first, the interaction between the CO_2 quadrupole

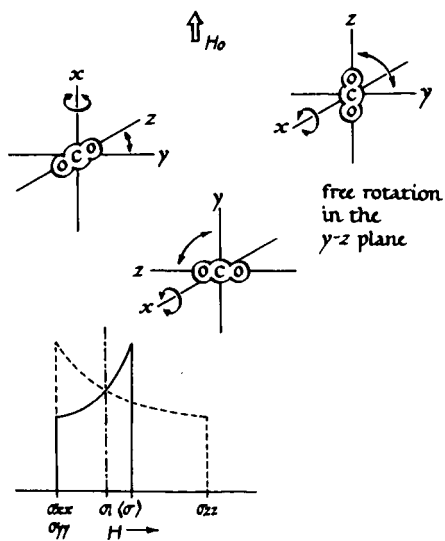


Figure 1. Some theoretical spectra observed in the NMR of sorbed carbon dioxide. A random array of nonrotating molecules (---), anisotropically rotating molecules (—), and isotropically rotating molecules (delta function, broken line). The areas beneath the curves are not shown to scale.

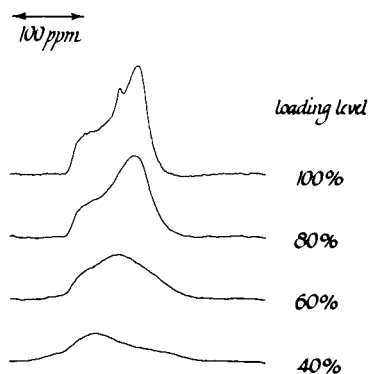


Figure 2. Carbon-13 NMR spectra of CO_2 sorbed on small-pore Na-mordenite as a function of loading level

and the sodium cation located at the end of the side pocket is maximized. The directional dependence of ϕ_{F-Q} and, most importantly, the steric restrictions of the side pocket combine effectively to inhibit rotation of the sorbed CO_2 . Any tendency to rotate in this site would be countered by rapidly increasing repulsive interactions as the CO_2 approaches the walls of the pocket. Strictly speaking, the CO_2 molecules are not rigid but rather execute high frequency "wobbling" in the confines of the side pocket.

As the side pockets are filled, CO_2 molecules will be sorbed next in the large channel, preferentially near the cations (due to ϕ_{F-Q}), and the areas of the large channel which may be partially blocked by intercalated material (due to ϕ_D). While at lower pressures, and in the absence of intermolecular collisions between CO_2 molecules, these sorbed species may remain relatively nonrotating, this behavior gives way to anisotropic rotation at higher loading levels. Rotational movement of about $\pm 60^\circ$ and at a frequency greater than 10^4 Hertz is necessary to average the principal values of the chemical shift tensor. Such motion could arise, for example, during a concerted head-to-tail jump between cation sites (the free end of the oxygen being attracted towards another cation as the previous interaction is weakened), or by collision induced motion of the CO_2 while near a single cation.

At the highest loading level, a small portion of the sorbed CO_2 molecules are isotropically rotating. These, with the least affinity for the mordenite, may be sorbed in areas of the large channel without cations or other blocking atoms and/or sorbed on the external surface in microcracks and pores.

Results from the sorption of CS_2 and OCS (10) (Figure 3) can be explained in similar terms with two important exceptions. Carbon disulfide, which has a critical diameter of 3.6 Å, is excluded from the side pockets as demonstrated by the absence of an NMR spectrum expected for a nonrotating molecule. Carbonyl sulfide, on the other hand, produces this spectral lineshape at all loading levels. The conspicuous absence of anisotropically rotating sorbed OCS may be explained by noting that this asymmetric molecule possesses a permanent dipole moment. Energetically, the field-dipole interaction is expected to increase the heat of adsorption by several Kcal/mole and significant ordering may be induced in the sorbed molecules by dipole-dipole interactions. These factors are apparently sufficient to inhibit any significant anisotropic rotation (some averaging of the chemical shift tensor is indicated by the smoothing of the lineshape at higher loading levels).

The NMR spectra of CO at various loading levels is shown in Figure 4. At all loading levels the spectra are consistent with a nonrotating sorbed species, present only in the side pockets. This result is expected on the basis of the various contributions to the heat of sorption discussed above, with the heat of

sorption dominated by the dispersion and repulsion terms since the polarizability and the dipole and quadrupole moments for CO are much smaller than for the other members of this series. Carbon monoxide has little affinity for the mordenite large-channel where the dispersion forces are much smaller.

The effects of cation exchange on the sorption properties of molecular sieves have also been studied by this NMR technique. Cation exchange to the K^+ , Cs^+ and NH_4^+ forms of the small-port mordenite reduced the sieves sorption capacity for CO and CO_2 . The NMR spectra of CO_2 sorbed at one atmosphere on these cation exchanged sieves were similar to the spectrum of CO_2 fully loaded on the Na^+ -mordenite (top of Figure 2), although lower in intensity by about 40-45%. The spectra of CO sorbed on these sieves, however, differed markedly from spectra observed with the Na^+ -form, Figure 4. While the resonance of CO on the Na^+ -mordenite displayed a chemical shift dispersion of about 130 ppm indicating a nonrotating species, the CO resonance on these cation exchanged forms were symmetric and only about one-third as broad. In fact, these spectra were similar to the spectrum of CO in the gas phase. The integrated areas of the spectra of CO in the gas phase, on the exchanged and on the Na^+ -sieves were 1:1.3:4.6, respectively, consistent with the reduced sorption capacity of the cation exchanged forms of the mordenite.

These results can only be interpreted as evidence of the absence of side-pocket sorption. Cation blockage of the side pockets has been proposed by Rees and Rao (13) in a study of the self-diffusion coefficients of various cations in natural mordenites. More recently, Mortier, Pluth and Smith (14) have initiated a single crystal structural analysis of the position of cations and molecules in zeolites with the mordenite-type framework. The position of the cations in the dehydrated K^+ and Ca^{2+} -mordenites have been identified and in both cases significant occupancy of sites in the side-pockets has been noted. In the dehydrated K^+ -mordenite 3.3 K occupy sites near the back of the side pocket and 3.0 K occupy sites in the opening of the side-pocket (presumably staggered to reduce the electrostatic repulsion between cations). An additional potassium cation was observed in a main channel site. Our results suggest that Cs^+ and NH_4^+ -cations also occupy sites in the side pockets.

Figure 5 shows the NMR spectra of CO_2 and CO sorbed at 1 atm on some of the mordenites studied here. The results from the small-port H^+ -mordenite (Figure 5b) suggest that the internal dimensions of this sieve are smaller than found in the sodium form. That is, the relatively weak symmetric resonance for sorbed CO indicates the absence of side-pocket sorption while the CO_2 spectrum displays only partial averaging of the chemical shift tensor. The restricted access and reduced rotational freedom in the H^+ -mordenite is probably due to steric rather than electrostatic considerations. Barrer (15) has shown that the electrostatic contribution to the heat of sorption of CO_2

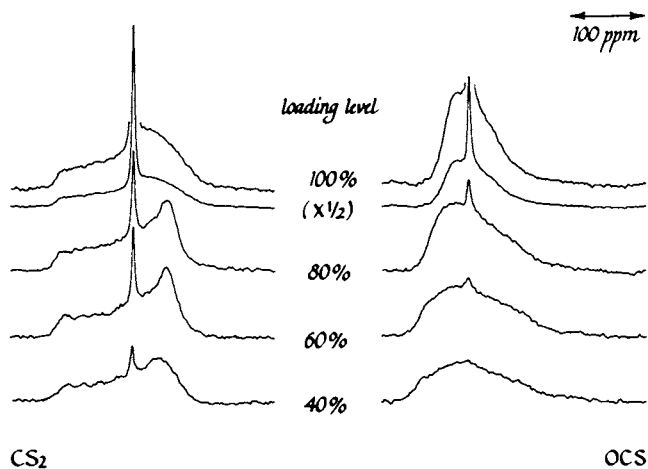


Figure 3. Carbon-13 NMR spectra of CS_2 (left) and OCS (right) sorbed on small-port Na^+ -mordenite as a function of loading level

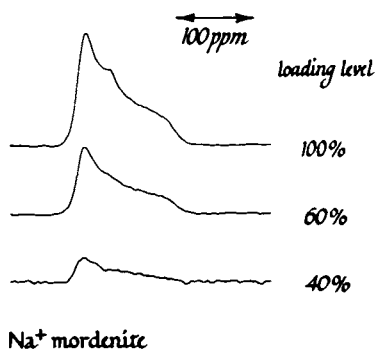


Figure 4. Carbon-13 NMR spectra of CO sorbed on small-port Na^+ -mordenite as a function of loading level

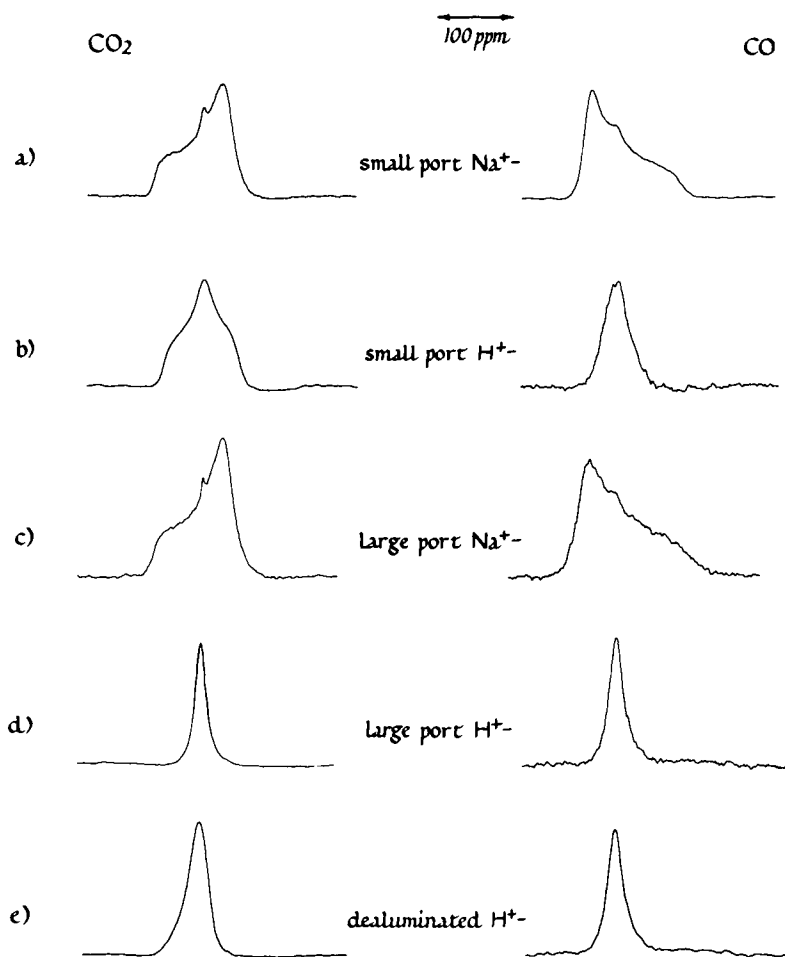


Figure 5. Carbon-13 NMR spectra of CO_2 (left) and CO (right) sorbed on various mordenites at one atmosphere and room temperature. The ordinate scales are chosen arbitrarily for purposes of display.

in the H^+ -mordenite is only about half that in the Na^+ -form.

The inaccessibility of the side pockets to CO sorption in the H^+ -exchanged sieve could be due to blockage of these sites by hydroxyl groups or by aluminum cations which have been leached from the framework during acid treatment. The latter seems unlikely in view of the failure to detect cationic aluminum by the method of Kerr (16). The location of the hydroxyl groups in the H^+ -mordenite has not been established, although it is reasonable to assume that they will be closely associated with the alumina tetrahedra. Based on X-ray crystal analysis, Mortier, Pluth, and Smith (14) have suggested a near statistical distribution of Al in the tetrahedral sites while Meier (17) favors preferential Al occupancy of the tetrahedral sites which form the side pockets. Our results indicate efficient blockage of the side pockets by the hydroxyl groups as well as blockage of the large channel.

Results from a study of large-port mordenites are shown in Figures 5c and 5d. The NMR spectra (over the full range of loading levels) for CO_2 sorbed on the large-port Na^+ -mordenite are similar to those obtained on the small-port variety. This supports our contention that the rotational behavior of sorbed molecules is strongly influenced by electrostatic interactions with the sodium cation. The H^+ -large-port mordenite shows evidence of the same blockage of the side pockets as was observed in the small-port form, but, as determined from CO_2 sorption, significantly different behavior in the large channel. In contrast to the somewhat reduced large-channel dimensions observed in the H^+ -small port, rotational behavior consistent with 12-member ring properties are observed here. Again, the absence of strong electrostatic interactions are noted in the H^+ -form. The aluminum-deficient mordenite gave results similar to the H^+ -large port, although some constriction on the large channel dimensions is indicated by the slight asymmetric broadening of the resonance for sorbed CO_2 . A reduction in sorption capacity for CO_2 at $30^\circ C$ in aluminum-deficient mordenites was also observed by Barrer and Murphy (15).

From the results presented here, some conclusions regarding small- vs large-port behavior in mordenites can be made. The NMR spectra of sorbed CO_2 on the H^+ -mordenites (Figures 5b and 5d) are characteristic only of the large channel properties, since side-pocket sorption does not occur in these samples. If only occasional blockage of the large channel (with cations, stacking faults or intercalated material) accounted for the inability of small-port mordenites to sorb molecules larger than 4 Å, one would expect CO_2 , which could pass the blockage, to behave as it does in the large-port samples. Instead, all of the sorbed CO_2 in the small-port sieve behaves as if it was in a more restricted environment than in the large-port sieve. We estimate that at least 80% of the large channel must be blocked to produce these results. This discounts stacking faults as an explanation for

the cause of large- and small-port properties. Although the presence of cations in the large channel has been established (14), these also cannot be responsible for all the large channel blockage without assuming an unreasonably large radius for the surface hydroxyl groups in the H^+ small-port mordenite. The only source of blockage which is consistent with the results presented here is the random intercalation of excess material, presumably SiO_2 . This explanation is also consistent with the fact that chemical treatment may be used to render large-port behavior in small-port sieves (2).

Conclusion

Carbon-13 NMR of CO_2 sorbed on Na^+ -mordenite indicates the presence of nonrotating, anisotropically and isotropically rotating species, which have been correlated with sorption sites in the side pocket, main channel and the exterior surface, respectively. Each of these sites can be probed independently by choosing sorbates of various sizes and properties. The absence of sorption in the side pockets of the K^+ , Cs^+ and NH_4^+ exchanged mordenites indicates that these large cations occupy sites in the side pockets and do not significantly influence the behavior of molecules in the main channel. By comparison of the behavior of molecules in the main channel of a variety of mordenites, we have shown that the discrepancy between large- and small-port behavior in mordenites is not due to occasional blockage by stacking faults, cations or intercalated material. Rather, over 80% of the main channel must be occluded by intercalated material, probably SiO_2 , in those mordenites which exhibit small-port characteristics.

Literature Cited

1. Meier, W. M., Z. Krist. (1961), 115, 439.
2. Gramlich, V., Diss. No. 4633 - ETH, Zürich (1971).
3. Sand, L. B., "Molecular Sieves," p. 71, Soc. Chem. Ind., London (1968).
4. Resing, H. A., Advan. Molecular Relaxation Processes (1972), 3, 199.
5. Rhim, W-K., Elleman, D. D., and Vaughan, R. W., J. Chem. Phys. (1973), 59, 3740.
6. Bloembergen, N. and Rowland, T. J., Acta Metall. (1953), 1, 731.
7. All of the NMR spectra presented here are displayed with the field strength increasing from left to right.
8. Stejskal, E. O. and Schaefer, Jacob, J. Mag. Res. (1974), 14, 160.
9. Stejskal, E. O. and Schaefer, Jacob, J. Mag. Res. (1974), 15, 173.

10. Sefcik, M. D., Schaefer, Jacob, and Stejskal, E. O., "Symposium on Magnetic Resonance in Colloid and Interface Science," San Francisco (1976).
11. Barrer, R. M., *J. Coll. and Interface Sci.* (1966), 21, 415.
12. de Boer, J. H. and Custers, J. F. H., *Z. Physik. Chem.* (Leipzig), (1934), B25, 225.
13. Rees, L. C. V. and Rao, A., *Trans. Faraday Soc.* (1966), 62, 2103.
14. Mortier, W. J., Pluth, J. J., and Smith, J. V., "Proc. Conf. Nat. Zeolites," Tuscon (1976), in press. See also *Mat. Res. Bull.* (1975), 10, 1037, 1319 and (1976), 11, 15.
15. Barrer, R. M. and Murphy, E. V. T., *J. Chem. Soc. A*, (1970), 2506.
16. Kerr, G. T., *J. Phys. Chem.* (1967), 71, 4155.

Arrangement and Mobility of Li⁺-ions in A-Zeolite and the Influence of Mono- and Divalent Cations and Adsorbed Molecules on It

R. SCHÖLLNER and H.-J. HERDEN

Karl-Marx-University, Department of Chemistry, Leipzig, East Germany

ABSTRACT

The arrangement and mobility of Li⁺-ions in dehydrated NaLiA-zeolites were studied by NMR-line-width measurements. The dependence of the activation energy (E_A) and the correlation time for the thermal motion of Li⁺-ions in A-zeolite on mono (Ag⁺, Tl⁺, K⁺, H⁺) and divalent cations (Mg²⁺, Ca²⁺, Sr²⁺, Be²⁺) and on adsorbed molecules (CH₄, C₄H₁₀, trans-2 C₄H₈) was determined.

Introduction

A great variety of research methods (e.g. IR spectroscopy, x-ray, electrical conductivity, sorption, calorimetry etc.) has been used for the determination of the arrangement of cations and their mobility in A-zeolites. Nuclear magnetic resonance (NMR) represents a particularly efficient method for studying the motion of adsorbed molecules and cations (1).

Taking the works of BARRER (2), REED (3), BROUSSARD (4) and SMITH (5) as a basis a wide range of publications appeared in the last few years on the determination of the structure of cation exchanged A zeolites. Using the single crystal x-ray techniques SEFF et al. studied the structure of TLA, KA, NaCSA and Na(Mn, Co, Ni, Zn) A zeolites (6), (7), (8), (9). Reports on the mobility of cations were given by STAMIREN (10) who used electrical conductivity measurements, and DUBININ et al. (11) and SCHIRMER et al. (12) by means of dielectric studies.

Little has been known so far on the LiA zeolite in the literature. Therefore we used NMR-line-width-

measurements for determining both the position and the mobility of lithium ions in dehydrated NaLiA zeolites. Simultaneously we studied the influence of mono- and divalent cations as well as that of adsorbed molecules on the mobility of lithium ions.

Experimental

We used 4 A Zeosorb in powder form (without binder) in the Na⁺ form as starting material, produced by VEB Chemiekombinat Bitterfeld/Wolfen GDR. The NaOH excess was removed by two washings using distilled water. The ion exchange was carried out by means of aqueous salt solutions considering the thermodynamic and kinetic data from the literature (13), (14).

The level of exchange was determined as the cation content of the exchange solution. The following methods were used:

1. Lithium-, sodium- and potassium-ions were determined using a flame photometer ("Flaphokol" of VEB Carl Zeiss Jena, GDR).
2. Ammonium-ions were determined photometrically by means of Nessler's reagent ("Spectralcolorimeter-Spekol" of VEB Carl Zeiss Jena, GDR).
3. Silver-ions were determined by titration using NH₄SCN solution.
4. Magnesium-, calcium- and strontium-ions were determined by means of EDTA.
5. The thallium-I-ions were determined polarographically.
6. The beryllium content was determined from the difference of the lithium- and sodium-ions in the zeolite before and after the exchange.

The levels of ion exchange of the samples used in the present paper are summarized in Table I.

The zeolites for the NMR studies were activated according to the deep bed method (15). During the period of two hours the samples were heated to 400°C and evacuated for 20 hrs at this temperature (pressure 10⁻⁴ torr).

Table I. Analytical data of the zeolite samples

$$A = \frac{\text{AlO}_2 \cdot \text{SiO}_2}{12}$$

Sample	Degree of ion exchange / % /			Unit cell composition
	Na	Li	Me	
1	68	32	-	Na _{8.2} Li _{3.8} A
2	29	71	-	Na _{3.5} Li _{8.5} A
4	-	100	-	Li ₁₂ A
5	26	67	6	Na _{3.1} Li _{8.1} Ca _{0.4} A
6	21	61	18	Na _{2.5} Li _{7.4} Ca _{1.05} A
16	45	47	8	Na _{5.4} Li _{5.6} Mg _{0.5} A
20	43	49	8	Na _{5.2} Li _{5.9} Be _{0.45} A
21	45	47	8	Na _{5.4} Li _{5.6} Sr _{0.5} A
33	37	43	20	Na _{4.4} Li _{5.2} Ag _{2.4} A
34	35	45	20	Na _{4.2} Li _{5.4} Tl _{2.4} A
37	32	46	22	Na _{3.8} Li _{5.5} K _{2.7} A
38	33	44	23	Na _{4.0} Li _{5.3} (NH ₄) _{2.7} A

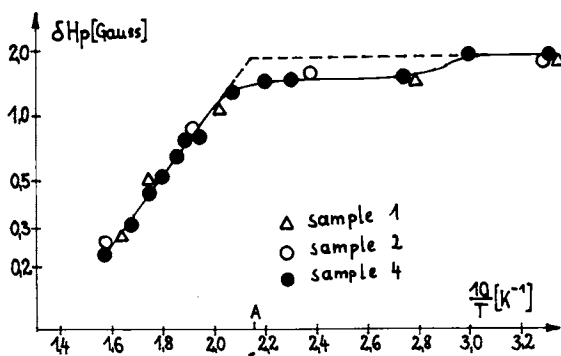


Figure 1. Temperature dependence of the line width ΔH_p of the NMR signal of ${}^7\text{Li}$ in NaLiA-zeolites (sample 1, 2, 4)

Stationary ^7Li -NMR spectra were measured using a wideline spectrometer of the bridge type (KRB 35/62 Akademiewerkstätten Berlin GDR) at 21 MHz.

The pure gases (CH_4 , C_4H_{10} , trans-2 C_4H_8) were adsorbed on a NaLiA sample (see Table II).

Table II. Samples with adsorbed hydrocarbons

Sample	Degree of ion exchange, %/		Adsorbed molecule	Amount adsorbed at 20° C, / molecules per cavity /
	Na	Li		
51	29	71	trans-2 C_4H_8	1.5
52	29	71	n- C_4H_{10}	1.1
53	29	71	CH_4	3.4
55	29	71	CH_4	1.0

The line width δHp of the peak to peak distance of the signal was 1.9 G at room temperature independent on the degree of cation exchange, the nature of cation and the nature of adsorbed molecules. For determining the activation energy (E_A) and the correlation time (τ_c) of the thermal motion of the Li-ions we determined the alteration of the line width as a function of temperature. Figs. 1 and 2. show the development of δHp vs $1/T$ for some samples. From the extrapolated bend points (A) of both the temperature-dependent and the temperature-independent part of the curve correlation times according to (16) can be calculated. From the rise of the temperature-dependent part of the curves the activation energy was determined according to an exponential statement. The values obtained are summarized in Table III.

Discussion

NaLiA and NaLiMe⁺A As has been shown by the spin-echoexperiments (17) the motion process of the Li⁺ ions is caused by a thermal motion of these nuclei from cation position to cation position. The correlation time τ_c of the thermal motion of the Li⁺ ion can thus be considered as the mean life-time of such an ion at a cation position. Fig. 1 shows that the behaviour of the curves δHp vs $1/T$ is the same for the samples 1, 2, 4. The activation energy of the

Table III. Correlation time τ_c and activation energy obtained from the temperature dependence of δ_{Li} .

The second moment for all samples is
 $M_2 = 0.74 \pm 0.07 \text{ G}^2$

Sample	$\tau_c/\mu\text{s}/$ for 200°C	$\tau_c/\text{s}/$ for 20°C	$E_A/\text{kJ}/\text{Mol}/$
1	110	$1 \cdot 10^{-2}$	30
2	110	$1 \cdot 10^{-2}$	30
4	110	$1 \cdot 10^{-2}$	30
5	490	4	58
6	110 at 400°C	-	-
16	460	4	58
20	600	11	63
21	330	2	54
33	180	$4 \cdot 10^{-2}$	34
34	200	$3 \cdot 10^{-1}$	46
37	200	$3 \cdot 10^{-1}$	44
38	200	$3 \cdot 10^{-1}$	45
51	80	$1 \cdot 10^{-3}$	18
52	80	$1 \cdot 10^{-3}$	17
53	70	$8 \cdot 10^{-4}$	16
55	100	$2 \cdot 10^{-3}$	21

thermal motion of the Li^+ -ions in the A zeolite for these samples is 30 ± 3 kJ/mol independent of the degree of lithium exchange. This value is in good agreement with an earlier report (18). The small step at approximately 80°C results from the average to zero of the quadrupolar interaction. For all NaLiA samples we obtained a second moment (M_2) of $M_2 = 0.74 \pm 0.07$ G². The second moment determined by BAKAEV (19) at 13 MHz is in good agreement with the value obtained by us. The second moment found by LECHERT (20) at 16 MHz for NaLiX was $M_2 = 0.49$ G². Thus the position of the Li^+ -ions is not dependent on the Li-exchange degree. According to the equation of van VLECK (21) the mean Li-Al-distance of $r_{\text{LiAl}} = 2.35 \pm 0.03$ Å can be calculated assuming that one Li^+ -ion interacts with one Al-nucleus only. With the assumption that the Li^+ -ion is surrounded by three Al-ions with the same distance the distance increases to $r_{\text{LiAl}} = 2.83 \pm 0.03$ Å. The contribution of the Li-Li interaction to the second moment is smaller than the contribution of the Li-Al interaction as has been shown by (17). It is in the order of magnitude of the measuring accuracy of the second moment. If the Li^+ -ion is on the threefold axis of the six-oxygen ring (as is the Na^+ -ion) we would obtain a second moment of $M_2 = 0.35$ G². The comparison of the second moment determined experimentally with the calculated one leads to the conclusion that the Li^+ -ion cannot be on the threefold axis but is more displaced in the direction of the Al-ion. It deposits asymmetrically in the six-oxygen ring. This result agrees with the NMR measurements made by FREUDE (18). The position of a Li^+ -ion in the A zeolite is shown in Fig. 3.

The isotropic motion mechanism observed by us, in which all Li^+ -ions take part must be a diffusion since the Li-Li interaction too is averaged (17) (not only one motion within the six- or eight-oxygen ring). Assuming that the diffusion of the Li^+ -ions leads from one SI position in the six-oxygen ring to the next SI position via a SII position in the eight-oxygen ring, the motion mechanism observed can be interpreted. The two crystallographic positions cannot be distinguished practically by means of the NMR for the similar Li-Al-distance.

Different monovalent cations (H^+ , K^+ , Ag^+ , Tl^+) reduce the motion of the Li^+ -ions as can be seen from Table III. The activation energy of the mobility of protons (22) in NaHA has been reported to be 42 kJ/mol and that of the Tl^+ -ions in T1A (23) to be 38 kJ/mol.

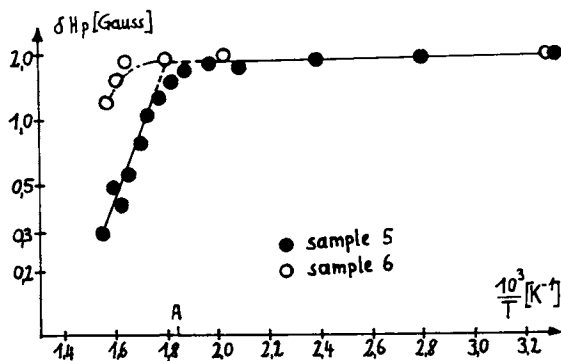


Figure 2. Temperature dependence of the line width δH_p of the NMR signal of ${}^7\text{Li}$ in NaLiCaA-zeolites (sample 5, 6)

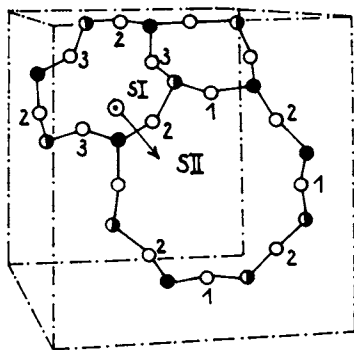


Figure 3. The arrangement of Li⁺ ion in A-zeolite. ●, Al; ◐, Si; ○, O(1,2,3); ⊙, Li.

These values are nearly in agreement with those of the Li motion in the samples 34 and 38. Thus the less movable cations cause a smaller mobility of the Li⁺-ions.

NaLiMe²⁺A Divalent cations (Be²⁺, Mg²⁺, Ca²⁺, Sr²⁺) already reduce the mobility of the Li⁺-ions in the A zeolite at lower Me²⁺ degrees of exchange as can be seen from Fig. 2. and Table III. ESCA studies (24) at a number of NaAgCaA zeolites showed that the condition of binding of the monovalent cations was changed with increasing Ca-content. Thus it can be concluded that the reduced cation mobility is caused by a changed cation lattice interaction, e.g. at the addition of small amounts of divalent cations. The position of the Li⁺-ions is not changed by the divalent cations. An exact determination of E_A and τ_C for sample 6 is not possible yet.

NaLiA hydrocarbons The activation energies and correlation times of the Li⁺-ions in dependence on the adsorbed molecules are given in Table III. It should be noticed that both the adsorbed paraffins and the adsorbed olefin reduce the activation energy and the correlation time. Thus the Li⁺-ions become more mobile as a result of the adsorbed molecules. A specific interaction Li⁺-ion - adsorbed molecule, which would lead to a weakening of the binding Li⁺-ion - zeolite lattice, is not possible for the molecules used (with the exception of trans-2C₄H₆). From the fact that E_A and τ_C for the samples 51-53, 55 are the same within the limits of error it follows that a specific interaction for sample 51 is not the reason for a higher mobility. In our opinion the increase of mobility of the Li⁺-ions could be explained by means of the model of a fluctuant field suggested by TUNG (25), (26) which favours cation jumps into other positions.

Conclusions

The Li⁺-ions are not positioned on the three-fold axis near the six-oxygen ring. They are displaced to the Al-ions (mean Li-Al-distance r_{LiAl} = 2.35 ± 0.03 Å).

Activation energy and correlation time for the thermal motion of Li⁺-ions were affected by the nature of cations and adsorbed molecules.

Acknowledgment

The authors wish to express their thanks to Prof. H. Pfeifer, Dr. D. Freude and Dr. H. Schmiedel, Karl-Marx-University Leipzig, for their comments.

Literature Cited

1. PFEIFER, H. "Nuclear Magnetic Resonance and Relaxation of Molecules Adsorbed on Solids"
"NMR-Basic Principles and Progress"
Vol. 7, pp 53-153, Springer-Verlag, Berlin 1972
2. BARRER, R. M., MEIER, W. M. *Trans. Faraday Soc.* (1958) 54, 1074
3. REED, T. B., BRECK, D.W.J. *Amer. Chem. Soc.* (1956) 78, 5956
4. BROUSSARD, L., SHOEMAKER, D.P. *J. Amer. Chem. Soc.* (1960) 82, 1041
5. SMITH, J.V., DOWELL, L.G. *Z. Kristallogr.* (1968) 126, 134
6. RILEY, P.E., SEFF, K., SHOEMAKER, D.P. *J. Phys. Chem.* (1972) 76, 2593
7. AMARO, A.A., KOVACINY, C.L., KUNZ, K.B., RILEY, P.E., VANCE, T.B., YANAGIDA, R. Y., SEFF, K. *Intern. Conf. Molecular Sieves Zeolites 3rd*, Zürich (1973)
8. LEUNG, P.C.W., KUNZ, K.B., SEFF, K., MAXWELL, I.E. *J. Phys. Chem* (1975) 79, 2157
9. VANCE, T.B., SEFF, K.J. *Phys. Chem.* (1975) 79, 2163
10. STAMIREN, D.N. *J. Chem. Phys.* (1962) 35, 3174
11. GLAZUN, B.A., DUBININ, M.M. *Jzv. Akad. Nauk SSSR, Otd. Khim Nauk* (1966), 392
12. LOHSE, U., STACH, H., HOLLNAGEL, M., SCHIRMER, W. *Z. Phys. Chem. Leipzig* (1971) 247, 65
13. BARRER, R.M., REES, L.V.C., WARD, D.J. *Proc. Roy. Soc. London Ser. A* (1963) 273, 180
14. WOLF, F., FÜRSTIG, H. *Chem. Techn.* (1966) 18, 1
15. KERR, G.T. *J. Catal.* (1969) 15, 200
16. AERAGAM, A. "The Principles of Nuclear Magnetic Magnetism" Oxford Univ. Press (Clarendon) London 1961
17. FREUDE, D., SCHMIEDEL, H., HERDEN, H. to be published
18. FREUDE, D., PRIBYLOV, A., SCHMIEDEL, H. *Phys. Stat. Sol.(b)* (1973) 57 K 73
19. BAKAEV, V.A. Thesis, Moscow (1972)
20. LECHERT, H., BASLER, W.D., HENNEKE, H.W. *Ber. der Bunsengesell.* (1975) 79, 563
21. VLECK, J. *van Physic. Rev.* (1948) 74, 1168
22. OEHME, W. Thesis, Leipzig (1973)
23. FREUDE, D., LOHSE, U., PFEIFER, H., SCHIRMER, W., SCHMIEDEL, H., STACH, H. *Z. Phys. Chem. (Leipzig)*

- (1974) 255, 443 ,
24. FINSTER, J., LORENZ, P., ANGELE, E. to be
published
25. TUNG, S.E. J. Catal. (1968) 10, 166
26. TUNG, S.E., MCININCH, E. J. Catal. (1968) 10, 175

Differential Heat of Adsorption and Isotherms of Carbon Dioxide on Synthetic Mordenite

PIERRE CARTRAUD, ANDRÉ COINTOT, and BERNARD CHAUVEAU

Laboratoire de Chimie-Physique, Université de Poitiers,
40, Avenue du Recteur Pineau, 86022 Poitiers Cedex, France

ABSTRACT

Differential heats of adsorption of carbon dioxide on synthetic mordenite were calorimetrically measured over 10^{-5} atm $< P < 1$ atm and $-77^{\circ}\text{C} < T < +120^{\circ}\text{C}$; adsorption isotherms were determined over 10^{-5} atm $< P < 50$ atm and $-77^{\circ}\text{C} < T < +160^{\circ}\text{C}$. Integral molar entropy, specific heat and density of adsorbed phase were calculated.

Introduction

Differential heats of adsorption of carbon dioxide on synthetic mordenite were calorimetrically measured. Thermal properties give information about adsorbent-adsorbate interactions. Owing to carbon dioxide characteristics, a large range of temperature and pressure can be explored. Consequently, adsorption isotherms were determined from 10^{-5} atm to 50 atm and thermal properties were measured up to 1 atm. Temperatures range from -77°C to $+160^{\circ}\text{C}$.

Experimental

Apparatus. Sorption and thermal measurements were made at the same time between 10^{-2} and 5 torr with a microcalorimeter connected with a classical volumetric system.

Pressure variations were measured, and knowing all different apparatus volumes, adsorbed amounts were calculated using the ideal gas law. We used a differential microcalorimeter devised by Barberi (1) and commercialized by Arion-Electronique.

Thermal effects were also measured up to 1 atm, using known adsorbed amounts which had been thermogravi-

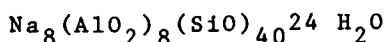
metrically determined. Between 1 and 760 torr, mass variations were measured with a McBain type balance.

A volumetric sorption system is perfected to measure adsorbed amounts from 1 atm up to 50 atm (2). Absolute adsorption was obtained from pressure variations and by measuring gas volumes at atmospheric pressure.

Experimental conditions and evaluations. Before each sorption run, the sample was evacuated by an oil diffusion pump to 10^{-5} torr at $+400^{\circ}\text{C}$ for ten hours. The sample weight was 0.1 g or 0.2 g. The accuracy in the amount adsorbed does not exceed 5% up to 1 atm and 10% above.

With calorimetry the heat quantity ΔQ is measured as a function of the number of moles adsorbed on. The ratio $\Delta Q/\Delta n$ will be closer to the differential of heat adsorption dQ/dn as Δn is smaller. This isothermal technique is such that it has a Δn value of about 10^{-4} mole per gram of anhydrous zeolite, and ΔQ of about 1 cal. The accuracy of these thermal effects measurements is about 10% (3).

Materials. The zeolite we study was synthetic mordenite with the formula:



for a unit cell. It was a powder produced by the CECA Society (4). Its crystal structure has been studied by Meier (5). The structure consists of infinite chains of (AlO_4) tetrahedra, so that a two dimensional channel system appears. The main channels parallel to the c-axis are linked by small channels parallel to the a-axis. These channels have an approximately elliptical opening with a major and minor diameter of 6.95 Å and 5.81 Å for the main channels 4.72 Å and 3.87 Å for the small ones. The volume of these channels is 0.156 cm^3 per gram of anhydrous zeolite. This number was calculated (6) and measured by adsorption of different gases (7).

Differential heats of adsorption

Differential heat curves were plotted against the number of moles adsorbed over the range $-77^{\circ} + 120^{\circ}\text{C}$. Separate curves are obtained for each temperature. They have the same shape with three main features (Figure 1):

- Differential heat has a high value for the initial adsorbed molecules and then decreases.
- it increases again and rises to a maximum.
- then it decreases continuously to a constant value.

Initial range. Interactions between carbon dioxide and the crystal has four components: dispersion and short-range repulsion energies Φ_D and Φ_R , polarization energy Φ_P , and quadrupole energy Φ_{FQ} . Interaction energy between pairs of carbon dioxide molecules may be omitted, because we shall be concerned only with the determination of initial heats (i.e., heats as the adsorbed amount approaches zero).

Barrer and Gibbons (8) have calculated these energies for CO_2 sorbed by ion-exchanged faujasite. Their results indicate that the most important part is played by quadrupole energy Φ_{FQ} . These interactions which seem to be associated more with the quadrupole moment of the CO_2 molecule than with zeolite, may be related to the very high initial values observed. This first range is characteristic of a strong adsorbent-adsorbate interaction. The internal electrostatic field is stronger near sodium ions ensuring crystal-electroneutrality. Consequently these ions may be energetically active centers leading to a strongly localized adsorption.

Taking important relative variations of q_D into account, these curves exhibit a heterogeneous surface character for the initial adsorbed molecules and at the highest temperatures.

Maximum range. When the most energetic centers are occupied, interactions between adsorbed molecules increase, and so does q_D . Curves show very marked maxima. This may be the consequence of increasing interactions leading to a new kind of sorption with different energetic features. Such a pronounced maximum at high temperatures is unusual. However, Kington and MacLeod (9) have also noted it with carbon dioxide sorption by chabazite at 0°C . This range would be typical of strong adsorbate-adsorbate interactions with a new arrangement of adsorbed molecules leading to a new kind of sorption with different energetic features.

In the first range, centers have very different and high energies, whereas after the maximum, centers have lower energies, which are similar to each other. This change in the sorption energetic features can be seen from the important maximum noted on the curves.

Terminal range. In this terminal part of the curve, the differential heat has small variations with increasing amount adsorbed. At any temperature the solid shows a homogeneous surface in this range; q_D values have the magnitude of heats of liquefaction corresponding to the transition of molecules from the

gaseous to the liquid phase. For each temperature, the differential heat tends toward a constant value.

Temperature influence. The important point as evidenced in Figure 1 is that the curves are distinct for each temperature. Few studies gave us informations about temperature influence around the critical point. We can refer to Huang and Zwiebel about CO_2 and SO_2 with H-mordenite (10). For ammonia adsorption by NaA zeolite there are also different curves for each temperature (11). On the other hand indistinguishable curves are found for nitrogen adsorption by silica-gels. However, the temperature variation is small, and the temperature itself is near the adsorbate boiling point (12).

"Initial heat" is frequently obtained by extrapolation of the q_D vs. n curve to $n = 0$. In our case, differential heats show important variations for initial adsorbed molecules, and it is difficult to extrapolate such curves. Qualitatively it appears that the initial value is higher at higher temperatures. This shows that adsorption centers seem to have higher energies at high temperatures, and the surface appears more heterogeneous.

The maximum value of q_D increases as the temperature rises. This behavior is characteristic of strong interactions of the adsorbate-adsorbate type. Thus molecular motion becomes more intense as the temperature increases, limited by the degrees of freedom allowed by adsorption; so interactions are all the stronger.

Instead of plotting differential heats against n , it is possible to plot against degree of coverage $\Theta = n/n_0$. n_0 is the maximum number of adsorbed molecules at temperature T , experimentally determined from isotherms plotted up to 50 atm., where saturation vapor pressure is reached or where adsorption isotherms level out, above critical point.

These maxima are for lower Θ values as the temperature is raised. If we assumed that formation of a condensed phase occurs at the maximum, this would appear at a higher degree of filling at high temperature, i.e. contrary to observations. At the opposite, an energetic distribution of the sites involved by temperature, superposed upon a numerical distribution in relation to their respective energies can explain the initial shape of the curves of differential heats, and their positions in relation with one another.

At temperature T , for a monolayer on a heterogeneous surface the number of sites N_1 of energy E_1 may be

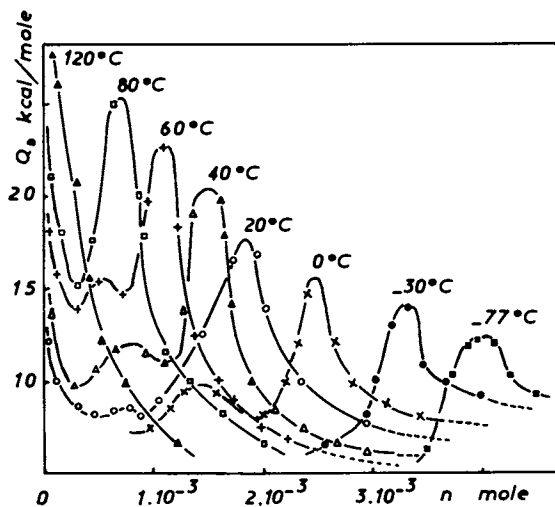


Figure 1. Differential heat of adsorption

an exponential function of this energy (C is a constant) (13):

$$N_1 = C \cdot \exp\left(-\frac{E_1}{RT}\right) \quad (1)$$

A law of distribution where E_1 would also be a function of temperature has not been formulated. In our case heat curves show that increasing temperatures lead to the formation of energy-rich sites. So, initial q_D values would be more important as temperature increases. As the energy of these sites increases, their number decreases according to exponential law of distribution (relation 1). And so, these sites are completely occupied for rather low degrees of filling ($\theta = 0,05$ at $+120^\circ\text{C}$, $\theta = 0,22$ at $+80^\circ\text{C}$) where the maximum appears.

At low temperature the energy of the sites is low and their number much higher. So, the initial values of q_D are lower and the maximum appears for higher values of θ ($\theta = 0,66$ at 0°C , $\theta = 0,83$ at -30°C)

This double distribution of sites allows us to explain the separate curves and their evolution with temperature.

Thermodynamic data for adsorbed phase

Molar integral entropy S_a of adsorbed phase can be calculated (8) from the following relationship:

$$S_a = \frac{1}{n} \int_0^n \bar{S}_a \, dn \quad (2)$$

n is the number of moles adsorbed, \bar{S}_a the molar differential entropy:

$$\bar{S}_a = S_g - \frac{q_{st}}{T} \quad (3)$$

S_g is the molar integral entropy of the gas. Working with a differential calorimetric system according to an isothermal process, isotheric heat q_{st} can be calculated from the experimental values of differential heat q_D :

$$q_{st} = q_D + RT \quad (4)$$

assuming the ideal behavior of the gas (14). Molar integral entropy of adsorbed phase is calculated by graphical integration of the area under \bar{S}_a vs. n curve. These calculations can be made from $+20$ to $+120^\circ\text{C}$ (Figure 2). For initial adsorbed molecules, molar integral entropy is very low in relation to the well-ordered state characteristic of strongly localized adsorption. Then S_a increases and reaches a maximum,

after which the curves approach an approximately constant value which is when the degree of filling becomes important. Barrer and Gibbons (8) have noted maximum and minimum values on integral entropy curves for CO₂ sorption by faujasite. According to them, such curves would be characteristic of heterogeneous surface.

For a given degree of filling Θ , integral entropy decreased as temperature increased. This supports the assumption of the formation of very energy-rich sites at high temperatures in relation to a well-ordered state of adsorbed molecules.

Specific heat C_p of adsorbed phase can be calculated from the relationship:

$$C_p = T \frac{dS_a}{dT} \quad (5)$$

Using integral entropy curves plotted for several temperatures, ratios $\Delta S_a/\Delta T$ are calculated for each couple of similar temperatures and for several degrees of filling (Figure 3). Heat capacity of zeolites is negligible compared with that of the adsorbed phase (15). Specific heat goes through a maximum between +40 and +60°C rising to values much higher than can be attributed to the liquid phase.

Similar curves are found with methane adsorption by CaA (16) and with n-heptane by the same zeolite (11). In the first case, measurements are carried out with a drop calorimeter allowing a direct measurement of the specific heat of adsorbed phase.

Hill (17) suggested that transition between a localized and mobile sorption type could be seen by a maximum of specific heat C_p . He showed that this transition might appear at rather low temperatures (50°K), but was all the higher as the energetic barrier between the sites was large. As we showed that mordenite has a heterogeneous surface from intermediate temperatures (+40°C), the observed maximum near +50°C on specific heat curves could exhibit a similar change in the adsorption. This remark would agree with the illustration of two adsorption ranges on differential heat and integral entropy curves: a first strongly localized type and a second with much less energy-rich sites.

On the other hand, the shape of the curves is the same as the one representing variations of specific heat during the second order Λ transformation. The main character of this transformation is that we never find two phases together; the phenomenon occurs in a single phase where the system goes through an order-disorder transformation.

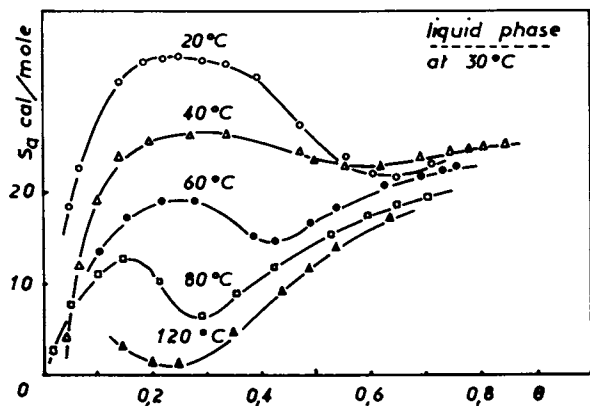


Figure 2. Molar integral entropy of adsorbed phase

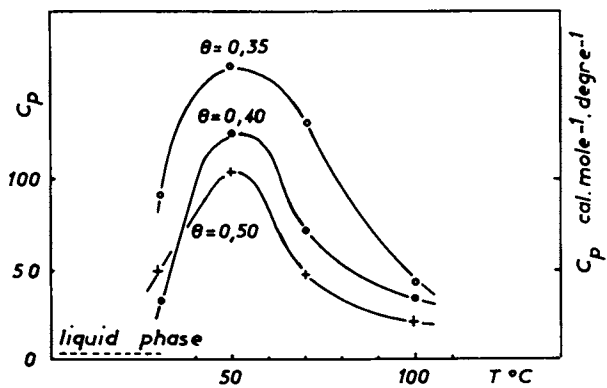


Figure 3. Specific heat of adsorbed phase

Adsorption isotherms

Adsorption isotherms were determined from 10^{-5} atm up to 50 atm and in the range -77 to $+160^{\circ}\text{C}$ with the three experimental techniques described before. The data are plotted in Figure 4. Adsorbed amounts are given in moles per gram of anhydrous zeolite.

Depending on the temperature, isotherms are like sigmoid curves or straight lines in these coordinates, which seems to be a general characteristic for microporous materials (18). However in the usual diagram, these isotherms are like type I of Brunauer *et al.* classification (19). Adsorption and desorption isotherms coincide perfectly.

Isotherms have the same shape on both sides of the critical point; differential heat curves have the same property; this leads us to think that no change appears in adsorption on either side of this temperature (20), (21).

When micropore filling is important, the adsorbed phase is like a condensed phase similar to a liquid from many points of view, even above the critical point (22). This is the reason why we can assume the idea of density in this filling range.

For isotherms plotted up to 50 atm, saturation vapor pressure is reached at $+15^{\circ}\text{C}$. At this pressure, adsorbed amount n_0 represents the whole micropore filling W_0 . Adsorbed phase density is ρ :

$$\rho = M \frac{n_0}{W_0} \quad (6)$$

W_0 was determined earlier (7); M is the molecular weight. Adsorbed amounts on external surfaces of crystallites are negligible compared with that adsorbed in the micropores (23).

Above the critical point, from $+40^{\circ}\text{C}$ to $+120^{\circ}\text{C}$, isotherms level out corresponding to saturation of micropores. The data of ρ vs. temperature are plotted in Figure 5 for No-Mordenite, H-Mordenite, and a 22% strontium exchanged form (24).

The following three remarks can be noted:

- no discontinuity appears in the plot of adsorbed phase density through the critical point.
- above the critical temperature, the adsorbed phase density has the same magnitude as the liquid phase density. However, at the same temperature, the adsorbed phase always appears more dense than the liquid phase. This has often been observed (22), (25).

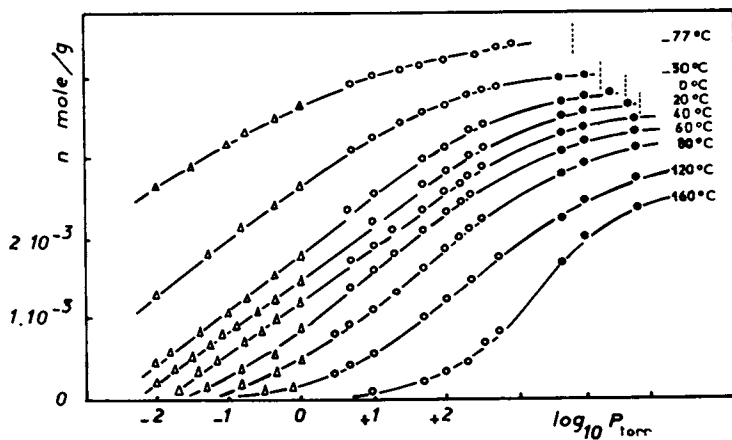


Figure 4. Adsorption isotherms. Data from different experimental techniques. (Δ), volumetry-calorimetry; (\circ), thermogravimetry; (\circ), high pressure volumetry.

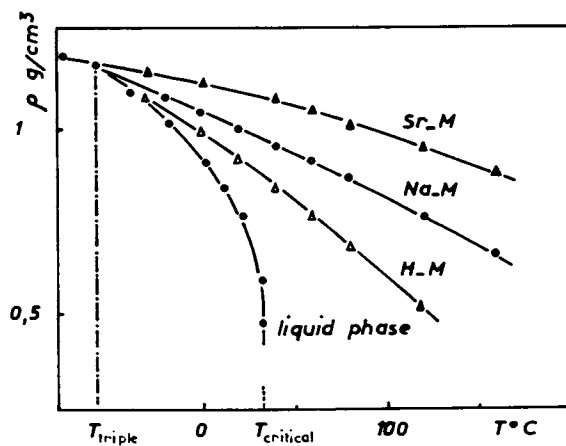


Figure 5. Density variations of adsorbed phases against temperature

- separate curves are obtained for each adsorbent, and each curve is different from the liquid phase curve. This has also been observed previously (26), (27), (28).

Conclusion

Calorimetrically measured thermal properties have given important information about the nature of interactions between carbon dioxide and synthetic mordenite; they are not as simple as theoreticians would like. The data show two adsorption ranges:

- the first relating to a strongly localized adsorption and a heterogeneous surface, which changes with temperature
- a second characterized by sites of identical and low energies.

The temperature dependence of the maxima and of the curves themselves lead to the conclusion that there is a double distribution of sites:

- one, as a function of temperature: its increasing leads to formation of very energy-rich sites.
- the other, as a function of the respective energy of these sites: the most energetic are fewer in number.

Both the shape of the experimental curves of integral entropy and of the specific heat of adsorbed phase, support these assumptions. Adsorption isotherms plotted up to 50 atm allow the adsorbed phase density to be determined experimentally and its condensed nature to be specified.

Literature cited

- 01 Barberi P. Microcalorimètre différentiel miniaturisé. Note C.E.A. N 1623.
- 02 Cartraud P., Cointot A., J. Chim. Phys. (1975), 72, 900.
- 03 Escoubes M., Quinson J.F., Gielly J., Murat M., Bull. Soc. Chim. (1972), 5, 1689.
- 04 CECA. Carbonisations et charbons actifs-78000 Vellizy-Villacoublay, France.
- 05 Meier W.M., Zeit. Krist., (1961), 115, 439.
- 06 Eberly P.E. Jr., J. Phys. Chem. (1963), 67, 2404.

- 07 Cointot A., Cartraud P., Veyssière M.C., Bull. Soc. Chim., (1973), 1, 21.
- 08 Barrer R.M., Gibbons R.M., Trans. Faraday. Soc., (1965), 61, 948.
- 09 Kington G.L., Mac-Leod A.C., Trans. Faraday. Soc., (1959), 55, 1799.
- 10 Huang A.A., Zwiebel I, Adv. Chem. Ser, (1973), 121, 374.
- 11 Sichhart. K.H., Kolsch P., Schirmer W., Adv. Chem., Ser, (1971) 102, 132.
- 12 Grillet Y., Rouquerol F., Rouquerol J., Journées nationales de Calorimétrie, Grenoble, 1975.
- 13 Young D.M., Crowell A.D., Adsorption physique des gaz, p. 251, Presses Universitaires de France, Paris, (1967).
- 14 Young D.M. Crowell A.D, Adsorption physique des gaz, p. 81, Presses Universitaires de France, Paris, (1967).
- 15 Breck D.W. Zeolite molecular sieves, p. 751, John Wiley and Sons, New York, 1974.
- 16 Stroud H.J.F, Parsonage N.G., Adv. Chem. Ser (1971), 102, 138.
- 17 Hill T.L., J. Chem. Phys., (1946), 14, 441.
- 18 Takaishi T, Yusa A., Amakasu F., Trans. Faraday, Soc, (1971), 67, 3565.
- 19 Brunauer S., Deming L.S., Deming W.E., Teller E., J. Am. Chem. Soc., (1940), 63, 1723.
- 20 Coolidge A.S., Fornwalt H.J., J. Am. Chem. Soc, (1934), 56, 561.
- 21 Edwards J., Mass. O., Can. J. Res., (1935), 13B, 133.
- 22 Jones W.M., Isaac P.J., Philipps D., Trans. Faraday. Soc, 1959), 55, 1953.
- 23 Dubinin M.M., Zhukovskaya E.F., Luk'yanovich V.M., Murdmaa K.O Polstyanyov E.F. Senderov E.E. Izv. Akad. Nauk. SSSR, Ser. Khim (1965), 8, 1500.
- 24 Cointot A., Cartraud P., Clavaud C., C.R. Acad. Sc. Paris, Ser C, (1974), 279, 9.
- 25 Menon P.G., Adv. High. Pressure. Res. (1969), 3, 313.
- 26 Cointot A., Cartraud P., Clavaud C., J. Chim. Phys., (1974), 5, 765.
- 27 Cruchaudet J., Simonot-Grange M.H., Cointot A., Bull. Soc. Chim., (1973), 11, 2936.
- 28 Lang J.C., Thèse spécialité, 1975, Grenoble-France.

Multicomponent Sorption Equilibria of Hydrocarbon Gases in 5A Zeolite

K. A. HOLBOROW* and K. F. LOUGHLIN

Department of Chemical Engineering, University of New Brunswick,
P.O. Box 4400, Fredericton, N.B., Canada, E3B 5L1

ABSTRACT

Experimental equilibrium data for three binary pairs in 5A zeolite are reported. The binary propane-cyclopropane has similar molecular volumes, and the system behaves ideally as predicted by a statistical isotherm (8). The binaries ethylene-propane and ethylene-cyclopropane, have significantly different molecular volumes and the systems behave non-ideally. Both the latter systems are azeotropic and it is suggested that this is due to interaction of the molecular volumes of the sorbates in the restricted cavity volume of the zeolite.

Introduction

The problem of predicting multicomponent equilibria from pure component sorption data has attracted considerable attention. Multicomponent sorption models such as the Ideal Adsorbed Solution Theory (IAST) of Myers et al. (1,2), generalized extensions of the Polanyi Potential Theory (3,4), or extended Langmuir equations (5,6,7) have been of limited success for predictive purposes in molecular sieve adsorption. In this paper a multicomponent statistical thermodynamic model, previously successfully applied to predict some existing adsorption data on 5A molecular sieves (8,9), is used to interpret new data obtained in these laboratories (10).

Three binary sorption hydrocarbon mixtures on 5A zeolite are examined. A propane-cyclopropane binary system is considered first and combinations of these gases individually with ethylene are considered subsequently.

Theory

The statistical thermodynamic model of Ruthven (11), for sorption of sorbates in discrete cavities, is based on the assumption that the interaction potential of the occluded molecules in the cavity is independent of the number sorbed. The resulting

*Present Address: New Zealand Steel, New Zealand

isotherm expression is

$$c = \frac{Kp + (Kp)^2(1-2\beta/v)^2 + \dots + (Kp)^m(1-m\beta/v)^m / (m-1)!}{1 + Kp + (Kp)^2(1-2\beta/v)^2/2! + \dots + (Kp)^m(1-m\beta/v)^m/m!} \quad (1)$$

where $m(\text{integer}) \leq v/\beta$ and K is the Henry constant. The corresponding multicomponent isotherm for a cavity containing i molecules component A and j molecules of component B is (8),

$$c_A = \frac{K_A P_A + \sum_i \sum_j (K_A P_A)^i (K_B P_B)^j [1 - (i\beta_A + j\beta_B)/v]^{i+j} / [(i-1)!j!]}{1 + K_A P_A + K_B P_B + \sum_i \sum_j (K_A P_A)^i (K_B P_B)^j [1 - (i\beta_A + j\beta_B)/v]^{i+j} / (i!j!)} \quad (2)$$

$i + j \geq 2 ; i\beta_A + j\beta_B \leq v$

with a similar expression for c_B . Equations (1) and (2) are slightly different from the expressions given previously as an exponential factor, estimated to be of limited importance, has been omitted in order to simplify the expression.

In the derivation of these equations (12,13) the sorbate-sorbent interaction is assumed independent of the number of molecules present within any given cavity, and the effect of the sorbate-sorbate interaction is described by a reduction in free volume due to the finite size of the molecules [the factor $(1-s\beta/v)$].

The correct choice of the molecular volume (β) presents some difficulties. The single component isotherm equation gives the sorbate concentration as a function of two parameters (Kp) and (v/β) and it is therefore possible to derive both the Henry constant and the molecular volume from an experimental isotherm provided that the range of concentration covered extends beyond the Henry Law region (9). The molecular volumes so calculated agree to within $\pm 15\%$ with values obtained by the interpolation method used previously (12,13).

Apparatus and Procedure

Details of the apparatus and procedure followed in this work are presented elsewhere (10,14). The sorbent was pure crystals of Linde 5A zeolite (Lot No. 550043), and the sorbates were Matheson CP grade propane and cyclopropane (purity 99%+), and Linde CP grade ethylene (purity 99.5%+).

Henry Constants and Heats of Adsorption

In previous studies with these sorbates, isotherms, covering the pressure range 30-300 torr and the temperature range 230-423°K, were obtained during kinetic and equilibrium studies in a gravimetric balance (12,13). The data, chiefly high concentration, were successfully modeled using the statistical thermodynamic

isotherm and the Henry constants derived satisfied the van't Hoff equation [$K = K_0 \exp(q_0/RT)$]. In the present work, further data for the 1 to 30 torr region have been obtained and are included in figure 1. The data for both studies are consistent. The Henry constants were re-evaluated and are presented in figure 2. The calculation procedure used was that of Barrer and Lee (15) where appropriate; otherwise the procedure of Ruthven et al. using the parameters in table I was used (12,13). Included also in figure 2 are the originally calculated Henry constants for propane (12), indicating the consistency of both studies. Previous calculated Henry constants for cyclopropane and ethylene (12) are omitted due to molecular volume estimation difficulties for cyclopropane and apparent inapplicability of the statistical thermodynamic model for ethylene.

Values of K_0 and q_0 in the van't Hoff relationship were obtained by regression analysis of the data in figure 2 and the results are presented in table II together with previous estimates of these parameters (12,13,16-20). The q_0 values are approximately 1.5 kcal/mole higher than reported earlier (12,13) but, with the possible exception of propane, are within the range of reported literature values (16-20). The K_0 values are significantly lower (see 12,13) but this may represent a compensation effect, as a small change in q_0 significantly changes the value of K_0 .

The theoretical isotherm plots for propane and cyclopropane calculated using the re-evaluated K_0 and q_0 constants with the parameters in the table I satisfactorily represent the experimental data in figure 1. The theoretical ethylene isotherms are discussed later.

Propane-Cyclopropane Binary

Data for the adsorption of a propane-cyclopropane binary mixture on 5A zeolite at 273K and 8 torr are presented in figure 3. At each experimental point, the gas phase composition (Y_A, Y_B) and the number of moles of each component adsorbed were recorded. Experiments were performed by successively altering the gas phase composition, and the two sets of data points (o,x) presented in figures 3 to 5 result from starting with either gas.

Theoretical plots calculated from equation 2, for c_A and the corresponding expression for c_B , using the parameters derived from the pure component isotherms for propane and cyclopropane, are also shown in figure 3. The agreement between the theoretical model and the data points is excellent for both components. The molar volumes of both species are very similar ($\beta_A \approx \beta_B$), and when this occurs the model postulates that mixing is ideal (8), and this is what is observed in the XY plot where the theoretical and experimental data are symmetric about the diagonal axis. The experimental and theoretical curves, for both the concentration and XY plots, figures 3(a,b), are in excellent agreement at the observed loading of ~75%. Simultaneously matching both plots provides a sensitive test of the theoretical model. In most previous studies of mixture equilibrium in molecular sieves, comparison

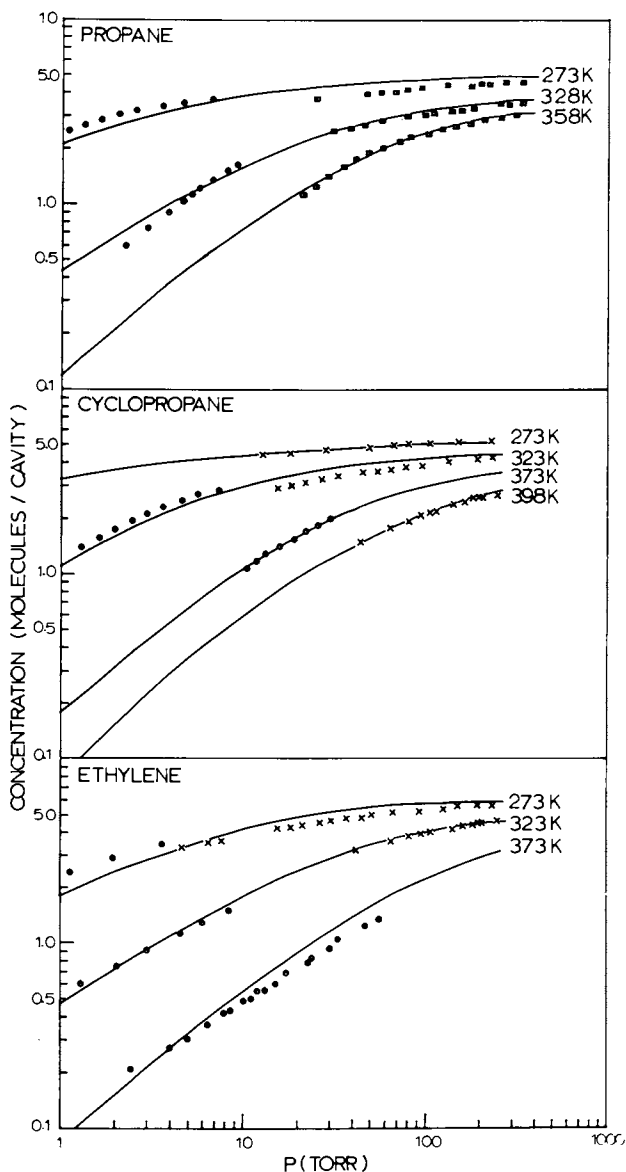


Figure 1. Equilibrium isotherms of propane, cyclopropane, and ethylene on 5A zeolite. Data of Holborow (10) ○, Loughlin (31) ◻, and Derrah (30) ×. Propane and cyclopropane theoretical plots calculated using equation 1 and parameters in Table I. Ethylene theoretical plots using equation 3 and parameters in Table I.

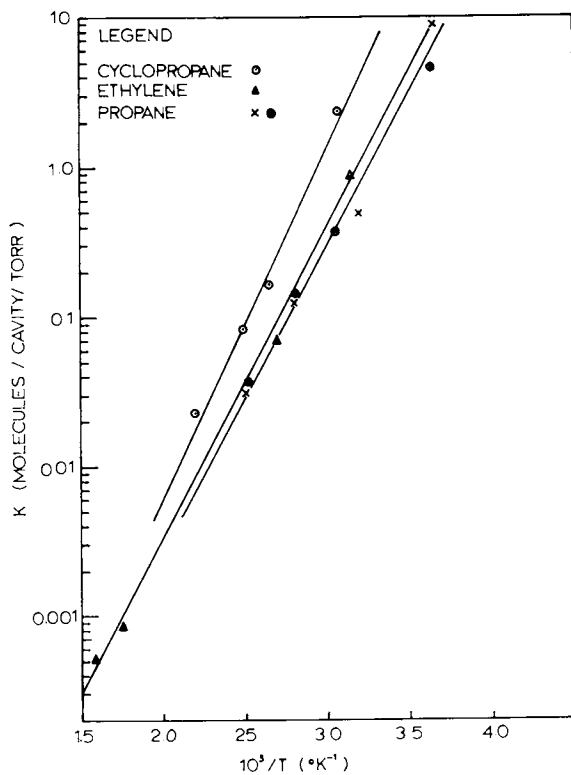


Figure 2. Van't Hoff plot showing temperature dependence of Henry's Law constants for sorption in 5A zeolites. Data of Holborow (10) ○, △, ×; Data Ruthven, Loughlin (12) (×).

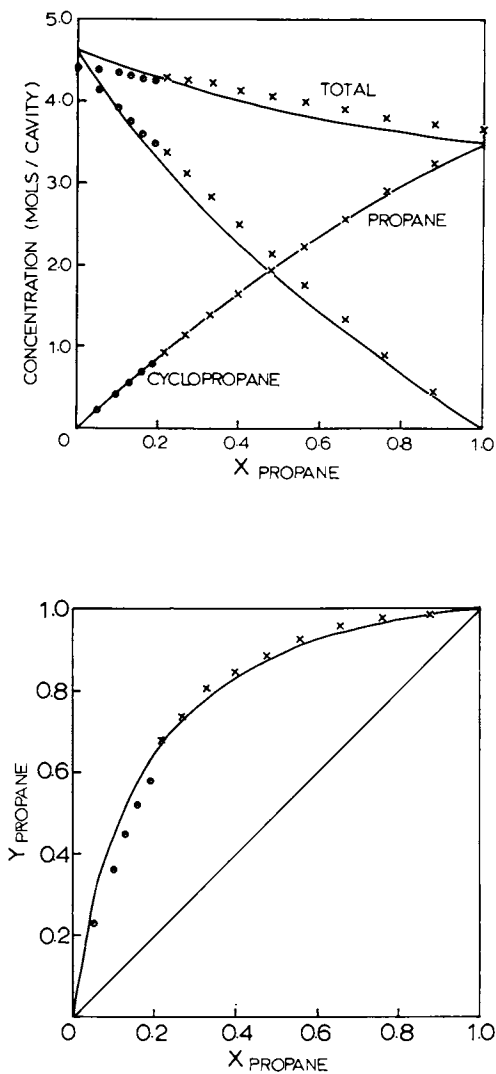


Figure 3. (a) Equilibrium data for sorption of C_3H_8 - C_3H_6 (Δ) mixture in 5A zeolite at $T = 273$ K and $P = 8$ torr. Experimental data of Holborow (10), theoretical curves from equation 2. (b) X-Y diagram for system in (a).

TABLE I - Parameters used in the Calculation of the Statistical Thermodynamic Isotherm

	T_b (22) K	T_c (22) K	V_m (22) $A^{\circ 3}$ mole- cule ⁻¹	$b(22)$ $A^{\circ 3}$ mole- cule ⁻¹	$K_0 \times 10^7$ molecule/cavity torr	q_0 kcal/ mole
C_3H_8	229	370	125	140.2	2.09	9.4
$C_3H_6(\Delta)$	242	397	115 ^a	131(24)	1.53	10.5
C_2H_4	169	283	82.1	94.9	1.78 7.54	9.7 8.2

a) Estimated using the procedure of Ruthven (9)

TABLE II - Henry Constants and Heats of Adsorption

	Exptl. Values this work		Ruthven et al. (12,13) $K_0 \times 10^7$		Kiselev et al. (16,17)	Schirmer et al. (18-20)	
	$K_0 \times 10^7$	q_0	(exptl)	(theor)	q_0	q_0	
C_3H_8	2.09	9.7	12.4	8.0	8.1	8.4-8.8	8.4-8.6
$C_3H_6(\Delta)$	1.53	10.5	25.6	-	8.1	-	-
C_2H_4	1.78	9.4	10.9	11.3	8.0	8.9-9.1	9.1-9.7

Units: K_0 molecules/cavity/torr; q_0 kcal/mole.

between theory and experiment has been restricted to concentration plots (2,25) or the XY diagrams (or the equivalent representation in terms of separation factors) (26,27).

For comparison with the statistical thermodynamic model, the IAST model was calculated using the pure component statistical thermodynamic isotherms developed for propane and cyclopropane in the spreading pressure calculation. Despite the relatively high loadings at the chosen experimental conditions, IAST was found to give almost exactly the same results as obtained for the binary statistical isotherm model and in fact it is not possible to distinguish between the models in figure 3. This confirms the postulate that for sorbates of equal molecular volume, the solution behaves as an ideal mixture (8).

Modified Statistical Isotherm and Modified Binary Isotherm

The Henry constants for the sorption of ethylene were determined using the procedure of Barrer and Lee (15). Calculation of theoretical isotherms with these values and the appropriate parameters in table I give excessive zeolitic concentrations at all concentrations greater than 1 molecule/cavity, revealing the need

to refine the model for this sorbate.

In the original derivation of the statistical thermodynamic isotherm, three assumptions were required in order to define the configuration integral in terms of measurable quantities. The refinement adopted involved changing the second assumption from 'The potential field is uniform throughout the cavity even when more than one molecule is present and the effective volume of the cavity is reduced' to 'The interaction potential throughout the cavity is dependent on s (the number of occluded molecules) and the effective volume of the cavity is reduced'. Physically this is equivalent to having the Henry constant dependent upon s . As this requires excessive experimental data over a wide range of concentrations, a second Henry constant only is introduced. This is taken as an average Henry constant for all $s > 1$. The resulting modified statistical isotherm is

$$c = \frac{K_I P + K_I K_{II} P^2 (1 - 2\beta/v)^2 / 2! + \dots + K_I K_{II}^{m-1} P^m (1 - m\beta/v)^m / (m-1)!}{1 + K_I P + K_I K_{II} P^2 (1 - 2\beta/v)^2 / 2! + \dots + K_I K_{II}^{m-1} P^m (1 - m\beta/v)^m / m!}$$

$$m \leq v/\beta \quad (3)$$

where K_I is the Henry constant for one molecule/cavity and K_{II} is the Henry constant for $s > 1$.

Using the intrinsic Henry constants as K_I , the Henry constants K_{II} were derived from a regression analysis of all the ethylene data. The resulting values for K_{II} followed a van't Hoff temperature relationship with $q_0 = 8.2$ kcal/mole and $K_{O,II} = 7.54 \times 10^{-7}$ molecules/cavity torr. Theoretical plots using these values in equation 3 with the appropriate parameters from Table I indicate satisfactory agreement between the model and the data in figure 1.

The binary isotherm for two Henry constants may be derived by making an analogous assumption to that made for the pure component isotherm. The resulting modified isotherm equations are

$$c_A = \frac{K_{IA} P_A + \sum_j K_A P_A (K_{IIA} P_A)^{i-1} (K_B P_B)^j [1 - (i\beta_A + j\beta_B)/v]^{i+j} / (i-1)! j!}{1 + K_{IA} P_A + K_B P_B + \sum_{ij} K_{IA} P_A (K_{IIA} P_A)^{i-1} (K_B P_B)^j [1 - (i\beta_A + j\beta_B)/v]^{i+j} / i! j!}$$

$$2 \leq i + j; i\beta_A + j\beta_B \leq v \quad (4)$$

with a corresponding expression for c_B .

Binary Systems Involving Ethylene

Data for the adsorption of an ethylene-cyclopropane binary mixture, and for an ethylene-propane binary mixture measured at 323K and 238K at 8 torr are presented in figures (4) and (5).

The sorption behaviour of the binaries are highly non-ideal. Ruthven et al. (8) predicted that for significantly different sorbate molar volumes, pronounced deviations from ideal behaviour are

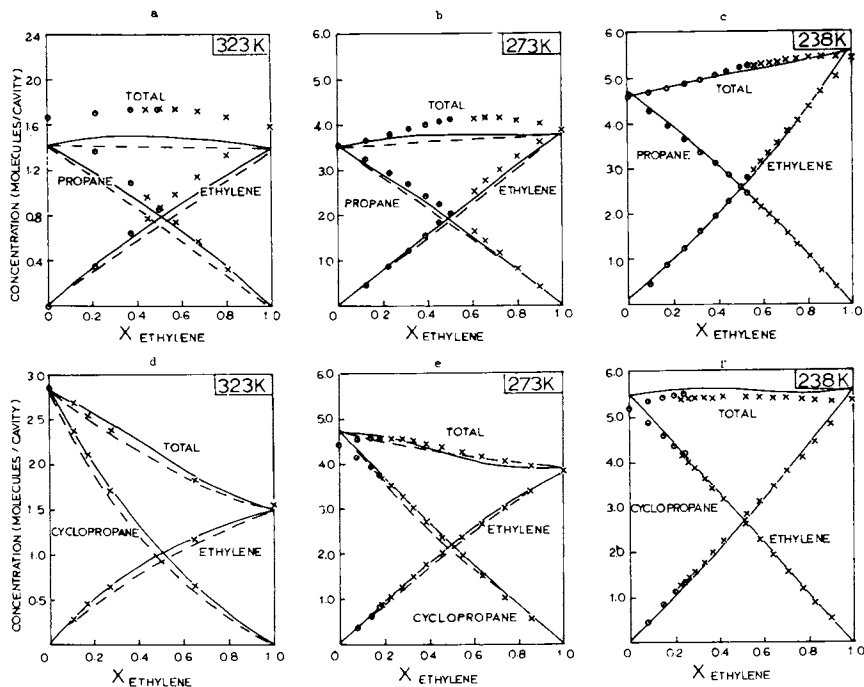


Figure 4. (a,b,c) Equilibrium data for sorption of $C_3H_8-C_2H_4$ mixture in 5A zeolite at $P = 8$ torr and temperature indicated. Experimental data of Holborow (10), (—) theoretical curves from equation 4, (---) IAST model. (d,e,f) Equilibrium data for sorption of $C_3H_6-C_2H_4$ mixture in 5A zeolite at $P = 8$ torr and temperature indicated. Experimental data of Holborow (10), (—) theoretical curves from equation 4, (---) IAST model.

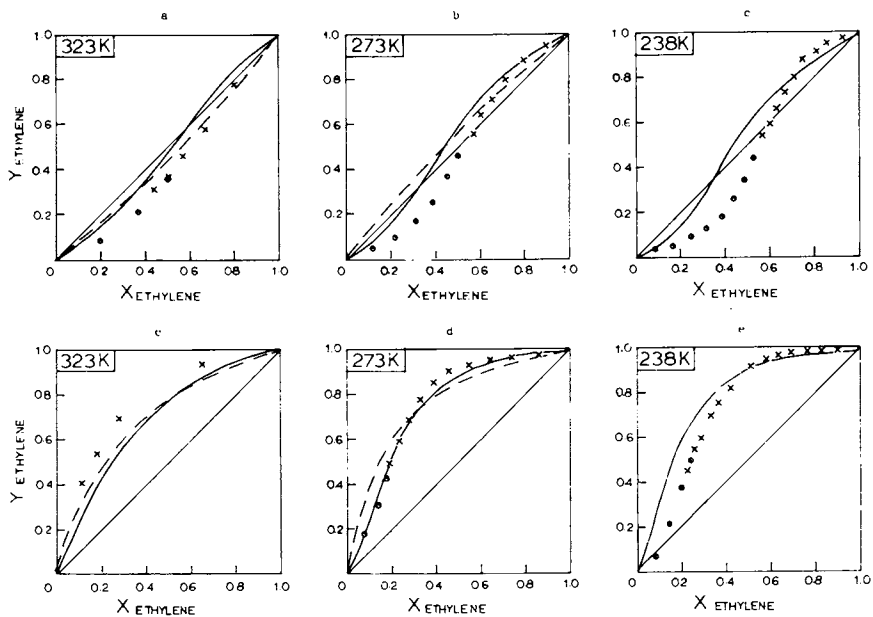


Figure 5. (a,b,c) X-Y diagrams for system presented in Figure 4 (a,b,c). (d,e,f) X-Y diagrams for system presented in Figure 4 (d,e,f).

to be expected in the multicomponent isotherm at sorbate concentrations greater than about one molecule/cavity. This may be observed in the XY diagrams for these binaries both of which have significant molecular volume differences. At low coverage, $\sim 20\%$, the systems behave ideally, figures (5a,d), whereas at high coverage $\sim 90\%$, the XY diagrams are asymmetric and azeotropic, figures 5(c,f). The non-ideal behaviour at high concentrations may be attributed to the volume mixing effect of sorbates of unequal molar volumes.

Theoretical plots, calculated using equation (4) with the parameters noted in table I, are also included in figures (4,5). The agreement between theory and experiment is excellent for the concentration plots of the cyclopropane-ethylene binary, figure 4 (d,e,f) to the extent of even indicating the inflections in the experimental data. The agreement for the propane-ethylene binary is not as good, with the fit at the lowest concentration being poorest, although the shape of the theoretical and experimental plots is exactly similar (figure 5(a)). The fit improves as the loading increases to 85%, converse to that expected, considering the postulated range of applicability of the isotherm ($\sim 75\%$). The poor fit at the low loading could be improved by small changes in the Henry constant, but this would result in using the isotherm as a correlative rather than a predictive mechanism.

The agreement between theory and experiment in the XY plots is not as good, although the general pattern of the sorbate behaviour appear in agreement. The propane-ethylene system is predicted azeotropic at all concentrations but only experimentally observed for the 50 and 85% coverage, figure 5(b,c). Insufficient data at X_{ethylene} of 0.90-0.95 are available to establish the existence of an azeotrope for the 20% loading, figure 5(a). For the ethylene-cyclopropane systems, the theoretical fit is similarly behaved. At low concentrations of 20% (figure 5(d)), sorption behaviour is nearly ideal, and the theoretical model is in qualitative agreement whereas at higher concentrations the XY data become asymmetric as does the theoretical curves. Sorbate behaviour in the zeolite is qualitatively in agreement with the suggested model.

Theoretical binary mixtures were also derived using the IAST model with the spreading pressure calculation estimated using the appropriate sorbate isotherm equation, (1) or (3). The results are included as dotted lines in figures (4,5). The concentration curves for the IAST model in figure (4), are not as good as for the statistical thermodynamic isotherm. The XY theoretical plots are not even qualitatively in agreement except where the behaviour is ideal, figures 5(a,d). This is expected as the sorbates are considered ideal in this model, and consequently the XY plots are symmetric. Where the sorbate behaviour is non-ideal, as occurs for concentrations 50% and over, in these binary systems, predictions of the model are not in agreement with experimental data.

Azeotropes have been observed for both A and Y type zeolites involving the lighter alkanes, alkene, NH_3 and CO_2 (10,27-29). Scherbakova et al. (28) report an azeotrope for the system

$C_2H_4-C_3H_8-CaA$ at $20^\circ C$, atmospheric pressure, arising at a sorbed mole fraction of ethylene of 89%. This system temperature and pressure is approximately equivalent to the 273K, 8 torr case reported here. In this study the existence of an azeotrope, at sorbed ethylene mole fraction 90% was postulated, though not established, indicating both studies are in agreement.

The mechanism of azeotropic formation in molecular sieves may be postulated as due to the filling of a restricted cavity by sorbates of a different size. With significantly different molecular volume species present, the permissible combined molecular volumes of the sorbates present in the restricted space is altered producing azeotropic formation. Lack of quantitative agreement between the theoretical and experimental results suggests the method of addition of the molecular volumes of the sorbates in the isotherm equation should be re-evaluated to derive an improved predictive mechanism for azeotropic systems.

Conclusions

Henry constants and heats of adsorption of propane, cyclopropane and ethylene on 5A zeolite, have been re-evaluated in this work. The values presented here are more accurate as less extrapolation of the data is required to estimate the constants.

It has been shown that the recently developed statistical thermodynamic model (8) gives an excellent representation of the binary equilibrium sorption data for propane-cyclopropane. For this system the molecular volumes are approximately equal, and the system behaves ideally as predicted. The IAST model satisfies these criteria and this model is also satisfactory.

For systems in which the molecular volume differences is substantial, the statistical thermodynamic model predicts the sorption behaviour will be non-ideal and this was observed experimentally. A sorption isotherm for ethylene which could adequately represent the pure component data was postulated based on a principle of sorbate-sorbate interaction different from that selected previously. A binary isotherm, derived for this representation, gave predictions which were qualitatively correct but quantitatively inaccurate.

Acknowledgements

The authors acknowledge many helpful discussions with Prof. Ruthven during this work. The continued financial support of the National Research Council of Canada is gratefully acknowledged.

Notation

A	molecular species A
b	van der Waal's co-volume
B	molecular species B
β	molecular volume of sorbate

c	concentration, molecules/cavity
i, j	integers
K	Henry constants defined by $\lim_{P \rightarrow 0} c = Kp$
K_0	pre-exponential factor
m	saturation limit (molecules/cavity)
p	total, partial pressure, torr
q_0	isosteric heat of sorption kcal/mole
R	gas constant
s	integer
T, T_b, T_c	absolute temperature, normal boiling point critical temperature
v	volume of zeolite cavity (776\AA^3 for type A zeolite).
V_m	molecular volume of sorbate at the boiling point
X	mole fraction sorbed phase
Y	mole fraction gas phase

Literature Cited

1. Myers, A.L., Prausnitz, J.M., A.I.Ch.E.J., (1965), 11, 121.
2. Glessner, A.J., Myers, A.L., Chem.Eng.Prog.Symp.Ser., (1969), 65(96), 73.
3. Dubinin, M.M., Timofeev, D.P., Compt.Rend.Acad.Sci., (1947), 55(4), 327.
4. Lewis, W.K., Gilliland, E.R., Chertow, B., Cadogan, W.P., Ind. Eng.Chem., (1950), 42, 1326.
5. Markham, E.C., Benton, A.F., J.Am.Chem.Soc., (1931), 53, 497.
6. Kemball, C., Rideal, E.K., and Guggenheim, E.A., Trans. Faraday Soc. (1948), 44, 948.
7. Danner, R.P., Wenzel, L.A., A.I.Ch.E.J., (1966), 15, 515.
8. Ruthven, D.M., Loughlin, K.F., Holborow, K.A., Chem.Eng.Sci., (1973), 28, 701.
9. Ruthven, D.M., A.I.Ch.E.J., (1976), 22, 753.
10. Holborow, K.A., Ph.D. thesis, Univ. of New Brunswick, 1974.
11. Ruthven, D.M., Nature, Phys.Sci. (1971), 232(29), 70.
12. Ruthven, D.M., Loughlin, K.F., Faraday Trans., (1972), 68, 696.
13. Derrah, R.I., Loughlin, K.F., Ruthven, D.M., Faraday Trans. (1972), 68, 1947.
14. Loughlin, K.F., Holborow, K.A., Ruthven, D.M., A.I.Ch.E. Symp. Ser., (1975), 71(152), 24.
15. Barrer, R.M., Lee, J.A., Surface Sci., (1968), 8, 354.
16. Kiselev, A.V., Khrapova, E.V., Scherbakoua, K.D., Neftekhimiya (1962), 2, 877.
17. Kiselev, A.V., Chernenkova, Ya, L., Yashin, Ya. I., Keftekhimiya, (1965), 5, 589.
18. Schirmer, W., Meinert, G., Grossman, A., Monats. Deut. Akad. Wiss. Berlin, (1969), 11, 886.
19. Schirmer, W., Chem. Tech., (1971), 23, 98.
20. Bulow, M., Grossman, A., Schirmer, W., Chem.Tech.(1971), 23, 33.

21. Ruthven, D.M., Loughlin, K.F., Derrah, R.I., Adv. Chem.Ser., (1973), 121, 330.
22. Weast, R.C., ed. "Handbook of Chemistry and Physics", 49th Edition, Chem. Rubber Co., Cleveland, 1968.
23. Maxwell, J.B., "Data Book on Hydrocarbons", VanNostrand, Toronto, 1962.
24. Gallant, R.W., Hydrocarbon Proc., (1970), 49(1), 137.
25. Lederman, P.B., Williams, B., A.I.Ch.E.J., (1964), 10, 30.
26. Grossman, A., Schirmer, W., Chem.Tech. (1968), 20, 34.
27. Peinze, T., Bulow, M., Schirmer, W., "Proceedings Third International Conference Molecular Sieves", J.B. Uytterhoeven, Ed., Leuven University Press, Leuven, Belgium, 1973.
28. Shcherbakova, P.R., Byk, S.Sh.,Gazov.Prom.,(1970),15,(1),41.
29. Kamenchuk, I.N., Kel'tsev, N.V., Torochesnikov, N.S., Shevyneva, N.V., Shumyatskii, Yu.I.,Tr.Mask. Khim-Tekhnol. Inst., (1973), 738, 15.
30. Derrah, R.I., Ph.D. thesis, Univ. of New Brunswick, 1974.
31. Loughlin, K.F., Ph.D. thesis, Univ. of New Brunswick, 1970.

CO and CO₂ as Sensitive Probe Molecules for Investigating Migration Effects of Cations in Zeolites

J. A. MICHELENA, G. PEETERS, E. F. VANSANT, and P. DE BIÈVRE

University of Antwerp (U.I.A.), Dept. of Chemistry, Universiteitsplein 1, B-2610 Wilrijk, Belgium

ABSTRACT

Adsorption of CO and CO₂ has been studied on zeolite Y in which Na⁺ ions have been partially exchanged for Ca²⁺ ions. Physisorption of CO and CO₂ indicates that in NaCaY zeolites with a Ca²⁺ loading lower than 35% all the Na⁺ ions initially present in the small cavities as well as the incoming Ca²⁺ ions remain inaccessible for CO and CO₂ molecules. However, a Na⁺ replacement of 35 to 45 % leaves the Ca²⁺ ions unaffected by CO and CO₂ but causes an important migration of inaccessible Na⁺ ions to accessible supercage positions. Further exchange (> 45%) results in Ca²⁺ ions occupying locations exposed to the supercages.

Introduction.

The sorptive properties of the synthetic faujasite depend on the nature and the number of cations present. The distribution of the cations is affected by the lattice charge, valency and dimensions of the cations and by the presence of ligands. The results of X-ray diffraction studies suggest that the exchangeable cations may be found in three different regions of space within the structure of the dehydrated Y zeolite: the hexagonal prisms, the cubooctahedra and the large cavities. The nomenclature adopted in this paper is based on that used by Smith (1).

At room temperature, ion-exchange with polyvalent cations is generally incomplete; however, at higher temperatures, the exchange level increases. Moreover, a dehydration of the zeolite containing polyvalent cations results in a complete redistribution of the cations towards the small cavities (sites I and I').

Because of the specific adsorption of CO and CO₂ on zeolites loaded with divalent cations, a number of workers developed useful spectroscopic and sorptive methods to localize divalent cations in Y-type zeolites (2-10). Egerton et al. (2) observed a specific interaction of CO with polyvalent cations and used this method to detect polyvalent cations exposed to the supercages (site II). Indeed, CO is small enough to enter the supercages

but is too large to enter the sodalite units or hexagonal prisms.

Infrared measurements of Jacobs et al. (4,5) indicate a similar behaviour of CO_2 in calcium and magnesium exchanged X and Y zeolites. In the Y zeolites the asymmetric stretching vibration of CO_2 was found to be cation dependent and suggested that CO_2 was an indicator of the accessible divalent cations at sites II in the zeolite. However, no adsorption study in the Y zeolite was carried out to confirm the specific character of CO_2 towards exchangeable cations. In the zeolite X, intense infrared bands due to carboxylate and carbonate species were observed, but no correlation was found with any structural site. Barrer and Gibbons (13) investigated the adsorption of CO_2 in different exchanged X-zeolites. An important analysis of the total energy of the bond between CO_2 and the zeolites was made.

In order to compare the sensitivities of CO and CO_2 towards accessible cations in the zeolite, detailed CO and CO_2 adsorption experiments were carried out on a number of partially exchanged CaNaY zeolites.

Experimental.

Materials. The synthetic zeolite Y (SK-40, Lot n° 3606-46-8) was supplied by Union Carbide Corporation (France). The anhydrous unit cell composition was $\text{Na}_{55}(\text{AlO}_2)_{55}(\text{SiO}_2)_{137}$. Calcium ions were exchanged in the Y zeolite by a conventional ion-exchange procedure. After the exchange, the zeolite samples were washed several times with distilled water to remove the excess salts and dried at 60°C . Samples with different levels of calcium exchange were prepared and are designated according to the percentage of sodium replaced by calcium. CaY-12 denotes a sample in which 12% of the sodium ions in NaY have been exchanged by calcium ions.

Carbon monoxide and carbon dioxide (J.T. Baker) were stated to have a purity greater than 99% and were used without further purification.

Adsorption experiments. Adsorption isotherms were determined up to 110 Torr in a conventional constant volume system. Adsorption experiments were carried out between 0 and 40°C , the temperature being controlled to within 0.1°C .

The zeolite samples weighed between 0.7 and 1 g. To avoid breakdown of the zeolite structure, special care was taken while raising the temperature during outgassing. The zeolite was activated overnight after heating the sample stepwise from room temperature to 400°C (100°C per hr).

Results.

Figures 1 and 2 show respectively CO and CO_2 adsorption isotherms at 0°C for NaY and samples of partially Ca^{2+} exchanged NaY zeolites. Adsorption equilibrium was reached within 45 minutes, and the isotherms were completely reversible in all cases.

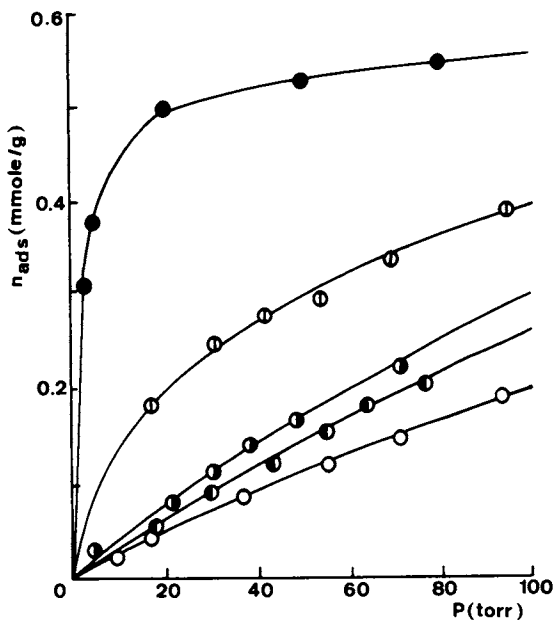


Figure 1. Adsorption isotherms of CO in CaNaY zeolites at 0°C. ●, NaY; ●, CaY-9; ○, CaY-38; ○, CaY-60; ●, CaY-78.

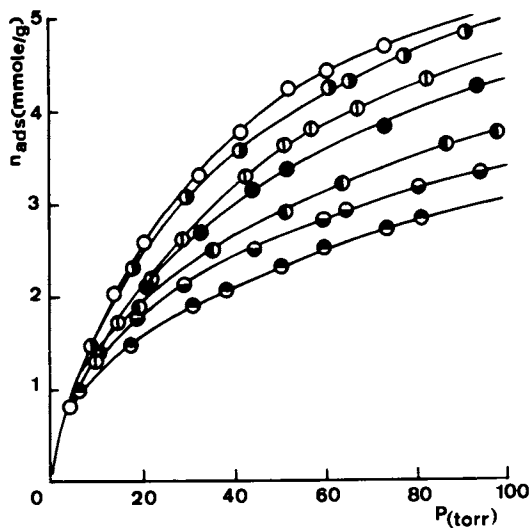


Figure 2. Adsorption isotherms of CO₂ in CaNaY zeolites at 0°C. ○, NaY; ●, CaY-9; ○, CaY-24; ●, CaY-28; ●, CaY-35; ●, CaY-60; ●, CaY-78.

Adsorption experiments at different temperatures were carried out in order to derive the isosteric heats of adsorption from the temperature dependence of the adsorption isotherms.

Figure 3 represents the dependence of the adsorbed quantity of CO and CO₂ at 0°C on the calcium content in the Y zeolite, at an equilibrium pressure of 80 Torr. The adsorption isobar of CO reveals a decrease in adsorption until about 35% of the Na⁺ ions have been replaced. At higher Ca²⁺ contents, an increase in the CO adsorption is observed. The isobar for the CO₂ adsorption however decreases continuously from a pure NaY to a pure CaY.

In order to obtain more information about the specific CO₂-Ca²⁺ interaction, the dependence of the isosteric heat (Q_{st}) on the calcium content is shown in figure 4. This figure indicates a decrease of isosteric heat for a Ca²⁺ content below 35 %, but an increase at higher exchange levels. The isosteric heats are estimated to have an accuracy of 0.7 kcal/mole.

Discussion.

Site occupation in calcium exchanged Y zeolites.

At all temperatures and pressures used, the adsorption of CO and CO₂ is not controlled primarily by the available pore volume, but is dominated by forces between the adsorbate molecules and the adsorbent surface. One can expect a stronger adsorption of CO and CO₂ on calcium exchanged Y compared to the NaY zeolite because of the stronger electrostatic field associated with divalent calcium ions, which causes more pronounced polarization, field-dipole and field gradient-quadrupole interactions. This should be reflected in a higher isosteric heat of adsorption when divalent cations are accessible to the CO and CO₂ molecules. A similar behaviour was found by Barrer et al. (13) in the zeolite X. Table I shows that this is indeed the case in Y zeolite.

Table I : Observed heats of adsorption of CO and CO₂ in NaY and CaY zeolites.

	Heat of adsorption (kcal/mole)	
	CO	CO ₂
NaY	6.3	7.6
CaY	9.3	11.5

X-ray analyses of Ca²⁺ exchanged Y zeolites (1) indicate that, after dehydration, the calcium ions are preferentially localized in the small cavities at the S_I and S_I' positions. The first Ca²⁺ ions to be exchanged occupy inaccessible sites inside the small cavities. This is achieved by a migration, during the dehydration process, of Ca²⁺ ions towards the small cavities. A

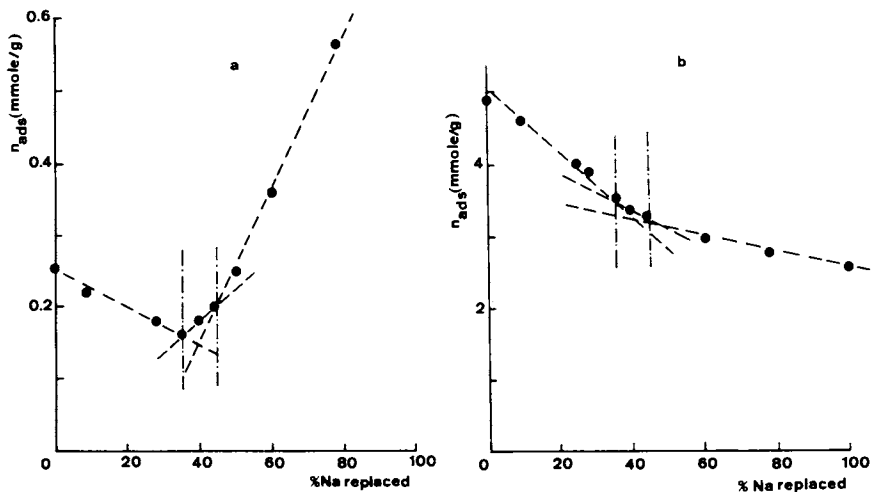


Figure 3. The relationship between the adsorbed quantity at 0°C of CO (a) and CO₂ (b) at an equilibrium pressure of 80 torr

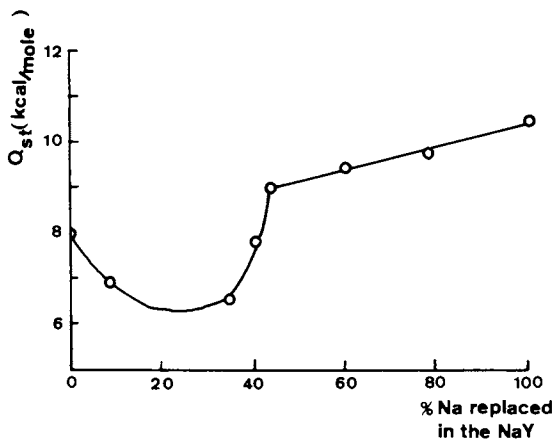


Figure 4. The variation of the isosteric heat of adsorption for the CO₂ adsorption with the calcium content in the Y zeolite

possible replacement of Na^+ ions to supercage positions can be a stoichiometric migration (i.e. 1 Ca^{2+} for 2 Na^+). Apparently below 35% Ca^{2+} , no change in adsorption properties of the large cavities should be expected when the adsorbed gas is cation-specific. However, a decrease in adsorption of CO below a Ca^{2+} content of 35% suggests a preferential migration of Ca^{2+} ions towards sites inside the small cages. This implies a redistribution of initial Na^+ ions inside the small cages and not an intense migration of inaccessible Na^+ ions towards the S_{II} positions. This results in a lower number of exchangeable cations in the supercages compared to those in the pure NaY form and explains the lower adsorbed quantity of CO. This effect should be more pronounced by increasing Ca^{2+} content. Since X-ray studies of CaY zeolites have demonstrated absolute preference of Ca^{2+} ions for the sites I and II', we can suggest that in partially calcium exchanged NaY zeolites, up to a Ca^{2+} content of 35%, the Na^+ and Ca^{2+} ions prefer the exchange positions S_{I} ' and S_{I} respectively.

As far as their effect on the adsorption properties of CO and CO_2 is concerned, two different groups of sites can be considered. The first set of sites are S_{I} , S_{I} ', and S_{II} ', locations inside the small cavities, which have little effect on the adsorption phenomena because the CO and CO_2 molecules are too large to enter these small cages. The second group of sites are the S_{II} positions which are accessible for CO and CO_2 molecules. The influence of cations in the S_{II} positions on the adsorption is uncertain; however, it is not excluded that these cations will interact with CO and CO_2 molecules in the supercages.

a) The adsorption of carbon monoxide (fig. 3a)

The adsorption of CO gradually decreases up to a calcium exchange level of 35%. However, when 35% of the initial Na^+ ions are replaced by Ca^{2+} ions, a change in the adsorption properties of the zeolite occurs. At a Ca^{2+} level of 35%, a sharp increase in the adsorbed quantity is observed. From this Ca^{2+} content, cation positions inside the small cavities apparently start to be disturbed by repulsion forces between cations, which could result in a migration of cations towards the supercages during the dehydration. Up to a Ca^{2+} exchange level of 45%, migration of Na^+ ions into the large cavities dominates. At still higher Ca^{2+} contents, the Ca^{2+} ions, now present in the supercage, are responsible for the higher adsorption.

The linear relationship between the amount of CO adsorbed and the presence of accessible Ca^{2+} ions suggests a strong Ca^{2+} -CO specificity. Interaction energy calculations, which consider dispersion, polarization, field-dipole and repulsion energy effects, have been carried out for NaY and CaY zeolites interacting with CO molecules (12). These calculations indicate that the affinity of CO molecules for Ca^{2+} ions is higher than for Na^+ ions, moreover, a CO/ Ca^{2+} ratio of 2 seems to be energetically favourable in

a Y zeolite.

b) The adsorption of carbon dioxide (fig. 3b).

The CO_2 molecule does not possess a permanent dipole moment, but has a large quadrupole moment which will interact with the field gradient in the zeolite lattice. It might be expected that the cation density in the adsorptive cavities of a zeolite would have effect on the extent of sorption of a quadrupole molecule. This makes CO_2 an excellent indicator for Na^+ and Ca^{2+} ions at accessible positions, because the adsorbed quantity is related to the number of accessible exchangeable cations. The decrement in the adsorption of CO_2 has to be an indication that a smaller number of cations can interact with the CO_2 molecules.

As shown in figure 3b, three different regions can be distinguished in the relationship between the amount of CO_2 adsorbed and the Ca^{2+} content. These three regions correspond exactly to those observed with the adsorption experiments of CO. For a Ca^{2+} content below 35%, a sharp decrease in the CO_2 adsorbed quantity, with increasing Ca^{2+} content, can be explained by a decrease in the Na^+ content in the large cavities. Therefore, at these exchange levels, all the Ca^{2+} ions have migrated during the dehydration process to inaccessible positions inside the small cavities. Therefore, during dehydration, no migration of Na^+ ions from the small cavities towards the large cavities could occur, and they remain inaccessible for the CO_2 adsorption.

Between 45 and 100% Ca^{2+} , a linear decrease in the amount of CO_2 adsorbed in the zeolite is due to a gradual decrease in the number of exchangeable cations in the large cavities. No migration of Ca^{2+} ions towards the small cavities must be assumed, so that the replacement of $2x \text{Na}^+$ ions by $x \text{Ca}^{2+}$ ions decreases the number of cations.

Between 35 and 45%, a migration of Na^+ ions from inaccessible sites into the large cavities explains the less pronounced decrease in the adsorbed quantity of CO_2 .

Furthermore, the change in isosteric heat of adsorption (Q_{st}) with increasing Ca^{2+} content (figure 4), supports this cation localization picture in calcium exchanged Y zeolites. Indeed, between a Ca^{2+} content of 0 and 35%, the isosteric heat decreases due to a decrease in the Na^+ content in the large cavities; however, between 35 and 45%, the isosteric heat increases as a result of an increase in the number of Na^+ ions in the large cavities. From an exchange level of 45%, the isosteric heat changes linearly with the calcium content, which reflects the increase in electrostatic field and the importance of the divalent cation-quadrupole interactions.

In general, the present adsorption results of CO and CO_2 show a high preference of Ca^{2+} ions for inaccessible sites, probably site I, in CaNaY zeolites of low degree of exchange. On the other hand, up till a Ca^{2+} content of 35%, no migration of the Na^+ ions from positions inside the small cavities to the supercages was

observed and they remain probably at S_T positions. These data bring a refinement to the conclusions of Egerton et al. (2) and Jacobs et al. (4,5) with respect to the location of the exchangeable Na^+ as well as Ca^{2+} ions in the CaNaY zeolites. Furthermore, the infrared absorption experiments, as well as interaction energy calculations, establish that a combination of CO and CO_2 is a powerful method for investigating the location of accessible cations in zeolites.

Literature Cited.

- (1) Smith J.V., Adv. Chem. (1971), 101, 171
- (2) Egerton T.A. and Stone F.S., Trans. Far. Soc. (1970), 66, 2364
- (3) Egerton T.A. and Stone F.S., Trans. Far. Soc. (1973), 69, 22
- (4) Jacobs P.A., Van Cauwelaert F.H., Vansant E.F. and Uytterhoeven J.G., J.C.S. Faraday I (1973), 69 1056
- (5) Jacobs P.A., Van Cauwelaert F.H. and Vansant E.F., J.C.S. Faraday I (1973), 69, 2130
- (6) Ward J.W. and Habgood H.W., J. Phys. Chem. (1966), 70, 2420
- (7) Bertsch L. and Habgood H.W., J. Phys. Chem. (1963), 67, 1621
- (8) Angell C.L. and Schaffer P.C., J. Phys. Chem. (1969), 47, 3811
- (9) Angell C.L. and Schaffer P.C., J. Phys. Chem. (1966), 70, 1413
- (10) Rabo J.A., Angell C.L., Kasai P.H. and Schomaker V., Disc. Far. Soc. (1966), 41, 328
- (11) Coughlan B., Ph. D. Thesis, Imperial College of Science and Technology, London (1964)
- (12) Michelena J.A., De Bièvre P. and Vansant E.F., in preparation (1976)
- (13) Barrer R.M. and Gibbons R.M., Trans. Far. Soc. (1965), 61, 948

G. Peeters and J.A. Michelena acknowledge a grant from the EEG (European Economic Community). E.F. Vansant wishes to thank the National Science Foundation (N.F.W.O. - Belgium) for their support.

Kinetics of Sorption, Desorption, and Diffusion of *n*-Butane in Zeolite NaX

H.-J. DOELLE and L. RIEKERT

Institut für Chemische Verfahrenstechnik, der Universität Karlsruhe,
Karlsruhe, West Germany

ABSTRACT

The kinetics of sorption and desorption of *n*-butane in single crystals of zeolite X (crystal diameter = 80 μm) has been studied at 25°C, using a rapid gravimetric apparatus. Intracrystalline diffusion coefficients for sorption and desorption are of the order of 10^{-7} sq.cm sec⁻¹ and independent of the direction of flux. The temperature of the zeolite sample changes significantly in a sorption or desorption run, due to the heat of sorption. Heat transfer is rate limiting in the final approach to equilibrium in unsteady sorption or desorption experiments.

Introduction

Diffusion coefficients of substances sorbed in zeolites have been obtained from rates of sorption and desorption for many systems under the assumption that intracrystalline diffusion is rate determining in these processes. Three peculiarities of the pattern of diffusivities in zeolites, obtained in this way, however, are not easily explained by a random movement of guest molecules in the host lattice as the basic mechanism of diffusion:

- (1) Diffusion coefficients have sometimes been found to depend very strongly on the degree of loading (or concentration of the sorbate) -- with some systems a variation by several orders of magnitude has been observed (1, 2).
- (2) In some cases it follows from the kinetics of sorption

and of desorption that the diffusion coefficient depends rather on the degree of advancement of the process in either direction than on the concentration of the sorbate (3, 4), a relatively high rate (or diffusivity) always being observed at the beginning of sorption or desorption. If the diffusivity decreases with concentration of the sorbate, then the rate of desorption should increase with the advancement of the process, a behaviour that was never observed to our knowledge.

- (3) It was observed in some cases that the diffusivity depends on the direction of the flux, the diffusivity in sorption being much higher than in desorption (5, 6).

These observations taken together can not be explained on the basis of any mechanism of random walk diffusion in a zeolite-crystal (or an ensemble of crystals whose properties and accessibility for the sorbate are identical), even if the diffusivity changes with concentration.

It was the purpose of the work described here to investigate the rate of sorption and desorption of n-butane in zeolite X as an example, different variables in the experiment being carefully controlled in order to establish which factors or processes influence the observed rate.

Experimental procedure, materials

Sorption equilibria and kinetics of sorption and desorption were observed with the apparatus shown schematically in figure 1. The basic equipment of the gravimetric system was a Cahn R 100 electrobalance which proved to be satisfactory after initial difficulties had been overcome. The time constant of the balance and its recording circuitry is of the order of 10^{-1} sec. Temperature of the glass tube with the sample leg was kept constant at $(25 \pm 0,1)^{\circ}\text{C}$ by circulating water. Pressure in the sorption volume ($V_s = 2,79$ l) was monitored by a differential pressure transducer (MKS Baratron Type 77) with 1% accuracy.

Step functions of pressure (symmetrical in sorption and desorption) could be obtained with this apparatus, the time constant of pressure change (0,3 sec) being short compared to the time constant of the resulting mass transfer into or out of the solid. In separate experiments the change in

temperature of the zeolite sample was measured with a thin thermocouple (Pt/PtRh; 0,1 mm ϕ) during sorption runs being exactly identical to those of the gravimetric studies.

Zeolite X was synthesized according to Charnell (7), crystals ranging in size from 10 μm to 100 μm were obtained and a fraction containing only crystals in the diameter range $(80 \pm 10) \mu\text{m}$ was separated by wet sieving and used in the present experiments. The dry composition of the zeolite corresponded to $\text{Na}_2\text{O} \cdot \text{Al}_2\text{O}_3 \cdot 2,25 \text{SiO}_2$; its crystal structure was verified by X-ray diffraction. n-Butane ($\text{CH}_3\text{-CH}_2\text{-CH}_2\text{-CH}_3$) 99,5 vol% pure and no inert carrier gas was used as a sorbate.

Activation of the zeolite crystals in the sample pan was accomplished by evacuating the sample at 300°C to $p < 10^{-4}$ torr until a constant weight reading was recorded by the balance (about 2 hours). Sorption and desorption runs were performed within an approximately linear range of the isotherm, its slope being given as

$$\frac{dn_f(p)}{dp} = K m_z \quad (1)$$

If kinetics are controlled by diffusion into or out of the sample then the evaluation of sorption and desorption experiments should be represented by the appropriate solution of the diffusion equation for the case of "diffusion from a stirred solution of limited volume" (8,9,10), the time dependent boundary condition for this case being identical to the boundary condition for the present case (11, 12).

Results and discussions

Sorption isotherms obtained for n-butane in the zeolite (identical in sorption and desorption) are shown in figure 2. An isosteric heat of sorption $\Delta H_s = -40 \text{kJ mol}^{-1}$ follows from these data. Results of kinetic measurements are presented in figure 3a-3c, where the dimensionless ratio $\Delta n/\Delta n_f$ [fraction of final (positive or negative) uptake] is plotted as a function of \sqrt{t} .

Conditions of the experiments are specified in Table I; the reproducibility of all these results was verified

Table I.—Conditions of experiments presented in figure 3a-3c

No	Type	Zeolite weight $\frac{m_z}{\text{mg}}$	Initial amount of sorbate $\frac{n_0}{\text{m mol}}$	Final amount of sorbate $\frac{n_f}{\text{m mol}}$	Initial pressure $\frac{P_0}{\text{mm Hg}}$	Final pressure $\frac{P_f}{\text{mm Hg}}$
1	Sorption	92	-	$3,97 \cdot 10^{-2}$	0,35	0,112
2	Sorption	39,5	-	$1,63 \cdot 10^{-2}$	0,205	0,108
3	Sorption	18	-	$0,667 \cdot 10^{-2}$	0,165	0,097
4	Sorption	18	$0,88 \cdot 10^{-2}$	$1,47 \cdot 10^{-2}$	0,256	0,198
5	Desorption	18	$1,47 \cdot 10^{-2}$	$0,9 \cdot 10^{-2}$	0,075	0,127
6	Sorption	91	$6,74 \cdot 10^{-2}$	$8,18 \cdot 10^{-2}$	0,327	0,278
7	Desorption	91	$8,17 \cdot 10^{-2}$	$6,74 \cdot 10^{-2}$	0,186	0,234
8	Sorption	92	$3,97 \cdot 10^{-2}$	$8,22 \cdot 10^{-2}$	0,472	0,217
9	Sorption	92	-	$8,19 \cdot 10^{-2}$	0,72	0,215

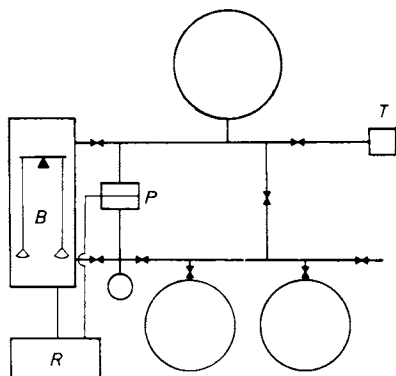


Figure 1. Schematic of the apparatus. B, electrobalance; P, pressure transducer; T, turbomolecular pump.

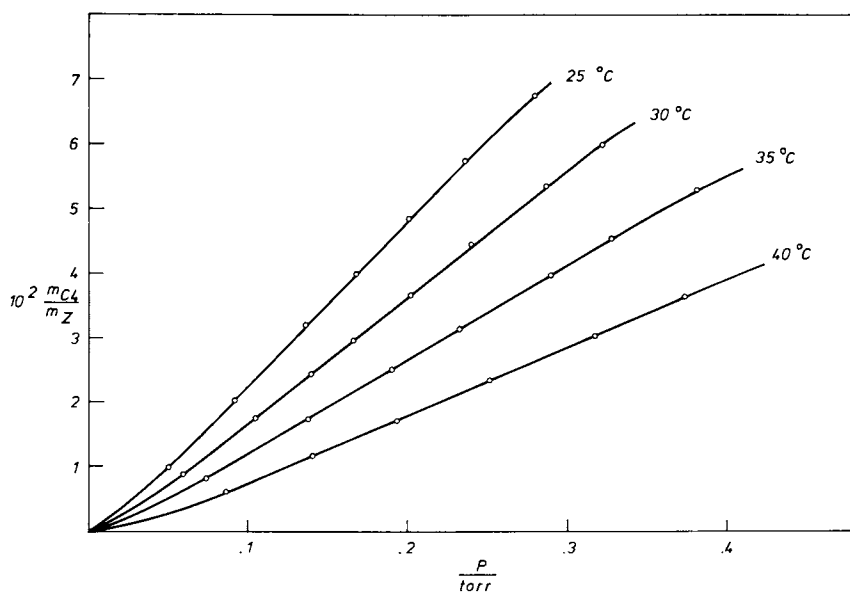
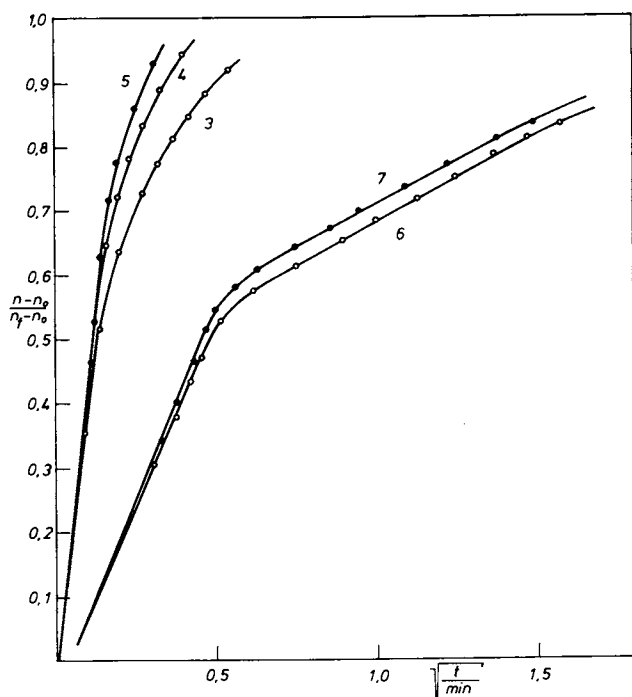
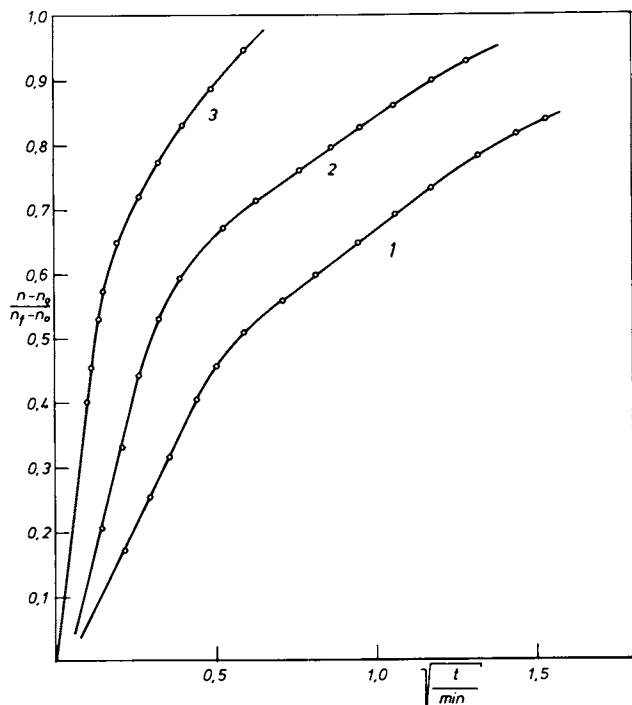


Figure 2. Sorption isotherms of n-butane in NaX: mass ratio of butane and zeolite at equilibrium



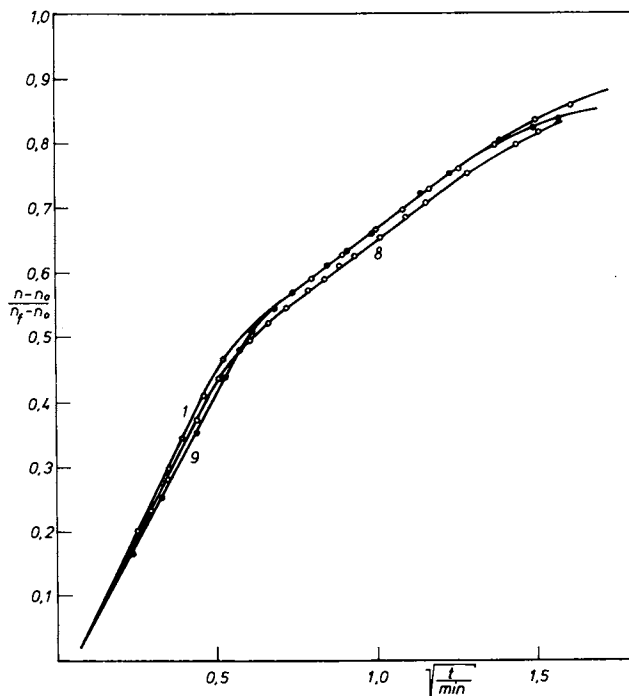


Figure 3. (a,b; left, c; above) Kinetics of sorption (\circ) and desorption (\bullet) of n-butane in NaX. Numbers on curves refer to Table I.

repeatedly.

Three general observations about the rate behaviour are immediately obvious from figure 3a-3c:

- a) The amount Δn of uptake or desorption is initially proportional to \sqrt{t} , the slope being independent of the direction of the flux;
- b) The initial rate of sorption or desorption, resp., decreases with sample-weight;
- c) The rate of sorption or desorption slows down considerably after about 50% of the process is completed: in all cases there is a pronounced bend in the curve of Δn vs. \sqrt{t} .

Observation (a) indicates that a process of diffusive mass transfer controls the rate of sorption or desorption, resp. The zeolite sample consisted of a loose pile (height h) of individual crystals (with diameter d), there are therefore two limiting cases of rate law which can be expected:

- (1) The diffusion of sorbate in the crystals is rate controlling and there is no concentration gradient in the gas phase between the crystals along the height h of the pile. In this case the relative change of the amount of sorbate in the sample must be a function of the dimensionless group $D_c t/d^2$ where D_c is the coefficient of diffusion in the zeolite crystals and t is the time

$$\frac{\Delta n}{\Delta n_f} = f \left(\frac{D_c t}{d^2} \right) \quad (2)$$

the initial slope of $\Delta n/\Delta n_f$ vs. \sqrt{t} being proportional to $\sqrt{D_c}/d$; independent of the sample height h .

- (2) Equilibrium between individual crystals and the gas phase contingent to any crystal is established, depending on gas phase concentration along sample height h . There is then no concentration gradient in the individual crystals, the rate of diffusive mass transfer in the voids between crystals is rate controlling and we must have

$$\frac{\Delta n}{\Delta n_f} = f \left(\frac{D_{app} \cdot t}{h^2} \right) \quad (3)$$

the initial slope of $\Delta n/\Delta n_f$ vs. \sqrt{t} being proportional to $\sqrt{D_{app}/h}$, dependent on sample height h . D_{app} will be given by

$$D_{app} = \left(\frac{D_{eff}}{KRT \rho_{sample} + \epsilon} \right) \quad (4)$$

where D_{eff} is the effective diffusivity in the void spaces of the sample, K the slope of the isotherm (equ. (1)) and ϵ the void fraction in the sample pile (13).

As can be seen from figure 3a, the slope of $\Delta n/\Delta n_f$ vs. \sqrt{t} decreases almost linearly with the inverse of the weight m_z of the sample

Expt. no.	1	2	3	
m_z	92	39,5	(18)	mg
$\lim_{t \rightarrow 0} \frac{d}{d\sqrt{t}} \frac{\Delta n}{\Delta n_f}$	1.1	2.0	(4.3)	min ^{-1/2}

It can thus be concluded that the second case, equ. (3), was approximated, mass transfer in the voids between crystallites strongly influencing the rate in experiments no. 1 and 2 with the larger samples.

In order to obtain the diffusivity D_c of *n*-butane in the zeolite-crystals the mass transfer resistance in the voids between the crystals had therefore to be avoided. This was achieved by using a small sample ($m_z=18$ mg) spread evenly over a surface of 2 cm² on a special sample-pan made from aluminum foil. The sample consisted thus of less than a monolayer of crystals (about 65%); no resistance to mass transfer in the gas phase is possible with this arrangement, whereas in experiments no 1 and 2 a smaller sample pan and thus a pile of approximately 16 or 37 monolayers of crystals was used. Rate data for the monolayer-case are shown as runs no 3,4,5 in figure 3b. It can be seen that the amount of uptake or desorption is initially proportional to \sqrt{t} also in this case where it then must be represented by equ. (2).

From the solution of the diffusion equation for spherical geometry follows a lower limit for the diffusion coefficient D_c of n-butane in NaX at 300 K of

$$D_c \geq 2 \cdot 10^{-7} \text{ cm}^2 \text{ sec}^{-1}.$$

This value is given as a lower limit since in this case 50% of $\Delta n / \Delta n_f$ was reached at $t \approx 0.75$ sec, which is close to the response-time of the equipment.

Interestingly this value of D_c comes close to intracrystalline diffusion coefficients that have been observed in zeolites by NMR spin-echo techniques (14, 15). The variation of $\Delta n / \Delta n_f$ with time is independent of the direction of the flux, the diffusivity D_c obtained for sorption is equal to the value which characterizes desorption. This result was obtained by observing the relaxation of sample weight and pressure in a closed system after the volume of the system had been expanded at $t = 0$ in a step-like fashion. The desorbing gas was not removed from the system by pumping, because in that case the rate of desorption would have been influenced by the pumping-rate, which is always finite.

The change of $\Delta n / \Delta n_f$ was always linear in \sqrt{t} up to $\Delta n / \Delta n_f \approx 0.5$, afterwards a decrease in the slope was observed in all cases which is much more pronounced than could possibly be explained on the basis of the diffusion-equation. This bend can also not be due to a concentration dependent diffusion coefficient since it occurs in desorption in exactly the same way as in sorption. Furthermore it was also observed in experiments no. 1, 8, 9 where the rate was mainly controlled by gas-phase diffusion between crystals, the apparent diffusion coefficient D_{app} being constant in the linear range of the isotherm according to equ. (3). The phenomenon can therefore not be explained by any peculiarity of diffusive mass-transfer. However, since the sorption of n-butane is exothermic ($\Delta H_S = -40 \text{ kJ mol}^{-1}$), the sample cannot remain at strictly constant temperature in any sorption or desorption run, as has been pointed out by Wicke (16). It's average temperature T will be given by a heat balance

$$\frac{dT}{dt} = \frac{-\Delta H_S}{h_T} \frac{dn}{dt} + \frac{T_0 - T}{\tau_T} \quad (5)$$

where $h_T = m_z (c_p)_z + n (c_p)_s + m_p (c_p)_p$ is the combined heat capacity of zeolite (z), sorbate (s) and sample-pan (p), and τ_T is the time-constant of temperature-equilibration with the surroundings at T_0 . Since sorption or desorption is very rapid initially - following \sqrt{t} - the first term on the right hand side of equ. (5) will be more important than the second in the early stages of a run, the sample being then approximately adiabatic. The amount n of sorbate at equilibrium decreases with pressure and with temperature, the equilibrium point will therefore be reached earlier under adiabatic than under isothermal conditions. The combination of the mass and heat balances is illustrated schematically for the case of sorption ($\Delta n > 0$) in figure 4, assuming that the sample is adiabatic up to point B, where the actual uptake Δn becomes equal to the equilibrium value Δn^* . At this point the system is in equilibrium with respect to mass transfer, but not with respect to heat transfer. After point B has been reached the temperature difference $T - T_0$ will decrease exponentially with time constant τ_T . The equilibrium uptake $\Delta n^*(T, p)$ will now increase accordingly and so will the actual uptake Δn if the sample remains close to equilibrium with respect to mass transfer. This rather simple model predicts a change of the rate law at point B (n_B^* , b); it's location can be calculated from the heat balance and from the equilibrium data presented in figure 2. E. g. for the conditions of experiment no. 1 point B should be reached before $\Delta n / \Delta n_f$ equals 0.7; the change of the rate law being more gradual in the actual system than in the simplified model which neglects gradients of temperature or concentration in the sample.

The variation of temperature with \sqrt{t} obtained by T -measurements in the zeolite sample is shown in figure 5 together with the sorption kinetics under identical conditions; the maximum of T occurs at the same time as the bend in $\Delta n / \Delta n_f$. After this point the temperature increment $T - T_0$ decreases exponentially with time and so does the distance ($n_f - n$) of the amount n of butane in the zeolite from the amount n_f at final equilibrium, the time constant being $\tau_T = 1.8$ min in both cases as shown in figure 6. We may thus safely conclude that the rate of sorption or desorption after the bend in the curves of $\Delta n / \Delta n_f$ is essentially controlled by heat transfer and not relevant with respect to diffusion in the zeolite.

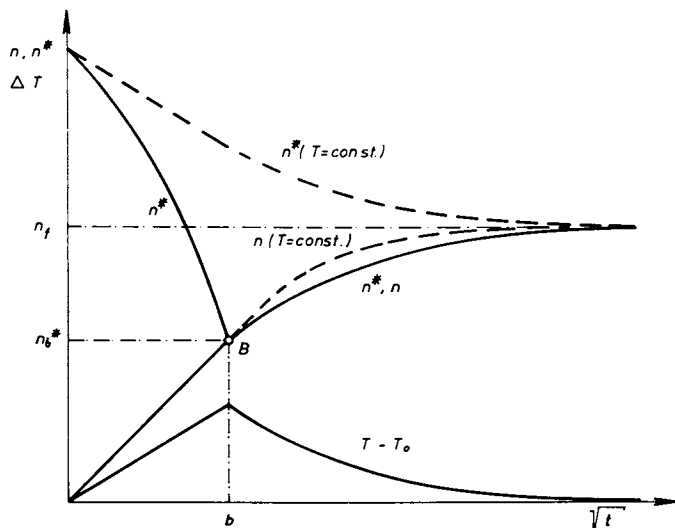


Figure 4. Variation of Δn , temperature, and Δn^* (p, T) with \sqrt{t} if sample behaves nearly adiabatic up to point (n_b^*, b) (schematic); (· · ·), isothermal case

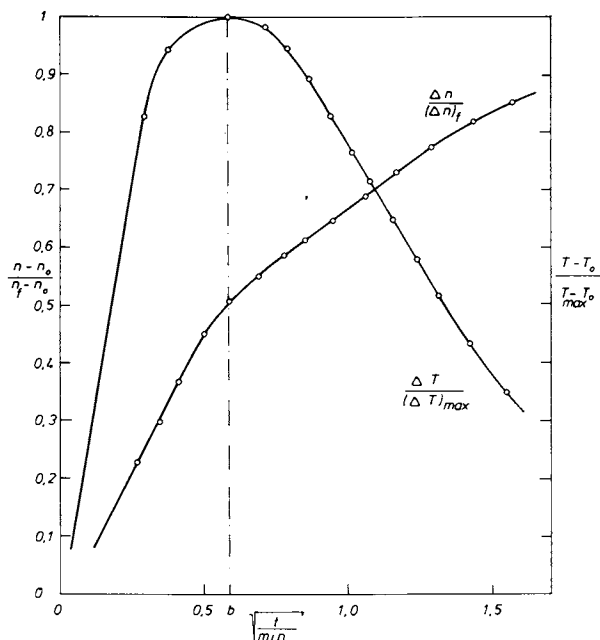


Figure 5. Variation of sample temperature from thermocouple measurements and sorption kinetics under identical conditions

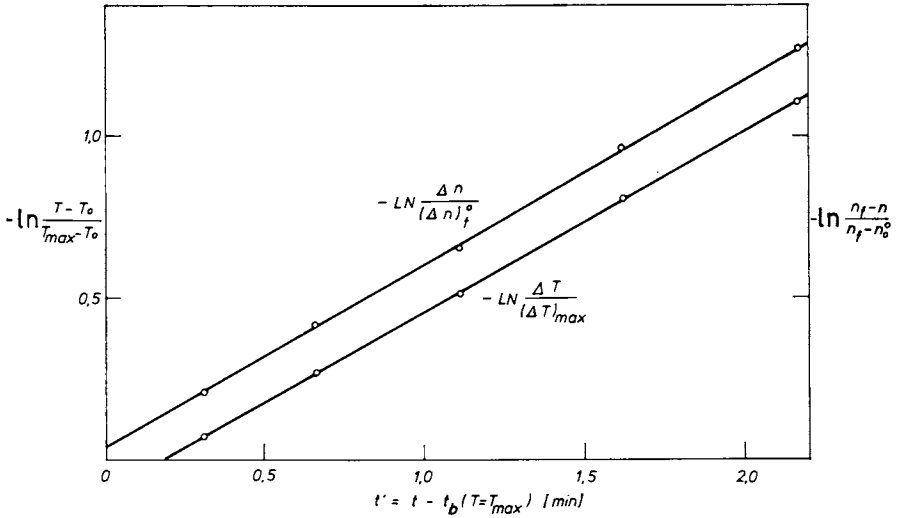


Figure 6. Approach of temperature T and sorbed amount n to final equilibrium (T_0, n_f) after change of rate law

It also follows that sorption during the initial uptake does not take place in a strictly isothermal system. The coefficient of intracrystalline diffusion obtained from the initial rate of sorption or desorption in a monolayer of crystals has hence to be considered as an average for the respective temperature interval of approximately 10 K.

Conclusions

Three conclusions can be drawn from these results:

- a) Sorption and desorption of *n*-butane in individual crystals of NaX is controlled by diffusion, the diffusivity being at least $2 \cdot 10^{-7} \text{ cm}^2 \text{ sec}^{-1}$ at 300 K, independent of the direction of the flux.
- b) The time constant of diffusion in the crystals $\tau_D = d^2/4 D_c \pi^2$ is of the order of magnitude of only 8 sec with the relatively large crystals ($d=80 \mu\text{m}$) used here and it will be shorter for smaller crystals. Diffusion in the gas phase between crystals will then be likely to control the rate of sorption or desorption in agglomerates.
- c) Unsteady sorption or desorption can never be strictly isothermal; the final approach to equilibrium is controlled by heat transfer.

Acknowledgement

We are indebted to H. Pütow who synthesized zeolite NaX in large crystals. Financial support of our work from the Fonds der Chemie is gratefully acknowledged.

Notation

- c_p Heat capacity at constant pressure, $\text{J g}^{-1} \text{ K}$
 D_c Diffusion coefficient of butane in zeolite crystals, $\text{cm}^2 \text{ sec}^{-1}$
 D_{eff} Effective diffusion coefficient of butane in the voids between crystals, $\text{cm}^2 \text{ sec}^{-1}$

D_{app}	Apparent diffusivity, $\text{cm}^2 \text{sec}^{-1}$
ΔH_S	Heat of sorption, J mol^{-1}
K	Slope of the equilibrium isotherm, $\text{mol Pa}^{-1} \text{g}^{-1}$
m_z	Mass of the zeolite sample, g
n	Amount of sorbate in the sample, mol
p	Pressure, Pa
R	Gas constant = $8.32 \text{ J mol}^{-1} \text{K}^{-1}$
T	Absolute temperature, K
t	Time, sec

Subscripts

- o Value at the beginning of experiment ($t=0$)
- * Value at equilibrium with respect to mass transfer
- f Final value at equilibrium with respect to mass and heat transfer

Literature Cited

- 1 Loughlin, K.F., Derrah, R.J., Ruthven, D.M., *Can.J.Chem. Eng.* (1971) 49, 66
- 2 Ruthven, D.M., Loughlin, K.F., Derrah, R.I., *Advan.Chem. Ser.* (1973) 121, 330
- 3 Satterfield, C.N., Margetts, W.G., *A.I.Ch.E.J.* (1971) 17, 295
- 4 Brandt, W.W., Rudloff, W., *J. Phys.Chem.Solids* (1964) 26, 741
- 5 Satterfield, C.N., Frabetti, A.S., *A.I.Ch.E.J.* (1967) 13, 731
- 6 Karge, H.G., Klose, K., *Ber.Bunsenges.phys.Chem.* (1975) 79, 454
- 7 Charnell, J.F., *J.Cryst.Growth* (1971) 8, 291
- 8 Berthier, G., *J.Chim.Phys.* (1952) 49, 527
- 9 Carman, P.C., Haul, R.A.W., *Proc.Roy.Soc.A* (1954) 222, 109
- 10 Crank, J., *The Mathematics of Diffusion*, Oxford Univ. Press 1970
- 11 Barrer, R.M., *Trans. Faraday Soc.* (1949) 45, 358
- 12 Riekert, L., *A.I.Ch.E.J.* (1971) 17, 446
- 13 Weisz, P.B., *Trans. Faraday Soc.* (1967) 63, 1801

- 14 Resing, H.A., Murday, J.S., *Advan.Chem.Ser.* (1973) 121, 414
- 15 Pfeifer, H., Schirmer, W., Winkler, H., *Advan.Chem.Ser.* (1973) 121, 430
- 16 Wicke, E., *Kolloid-Zeitschrift* (1939) 86, 167

Kinetics of Sorption in Biporous Molecular Sieves

L. K. LEE, H. YUCEL, and D. M. RUTHVEN

Department of Chemical Engineering, University of New Brunswick,
Fredericton, N.B., Canada

ABSTRACT

A mathematical model is developed to describe kinetics of sorption in a bi-porous adsorbent pellet for systems which exhibit a highly favourable (rectangular) adsorption isotherm. The theoretical uptake curves differ significantly from the predictions of a linear dual resistance model. The theory is used to analyze experimental data for sorption of cis-2-butene in a 5A molecular sieve pellet at 273°K.

Introduction

Commercial molecular sieve adsorbents consist of small microporous zeolite crystals formed into a macroporous pellet, sometimes with the aid of a clay binder. The kinetics of sorption are therefore determined by the combined effects of two distinct diffusional resistances: macropore and micropore. The relative importance of these resistances varies greatly depending on the particular system and the conditions. The sorption behaviour can be properly described by a simple diffusion model only when one or other of the resistances is negligible (the extreme cases of micropore or macropore control). For many systems, under practically important conditions, both resistances are significant and to provide a realistic kinetic model for such systems requires solution of the coupled diffusion equations.

Hitherto such solutions have been obtained only for systems with a linear equilibrium isotherm. A numerical solution was given by Sargent and Whitford⁽¹⁾ and a more elegant analytical solution was obtained by Ruckenstein et al.⁽²⁾. This was used by Ma and Ho⁽³⁾ to interpret kinetic data for sorption of allene and methyl acetylene in Linde 13X sieve. The linear model is appropriate for the exchange of isotopically tagged species studied by Sargent and Whitford⁽¹⁾ but for most systems, including those studied by Ma and Ho⁽³⁾, the assumption of linearity is a severe approximation. The equilibrium isotherms for many systems of practical importance are highly non-linear and in order to

increase our understanding of the behaviour of such systems we consider here a system in which the isotherm is rectangular (irreversible). This is the extreme limit of highly favourable type I isotherm for which the curve approaches a step function:

$$q^* = 0, c = 0; q^* = q_m, c > 0 \quad (1)$$

Mathematical Model

As an idealized representation we consider a macroporous spherical pellet composed of an assemblage of small uniform spherical microporous crystals. Transport within both micropores and macropores is assumed to occur by diffusion with the coefficients D_z and D_p independent of concentration. Neglecting accumulation with the macropores which, for molecular sieve adsorbents is generally small in comparison with the capacity of the zeolite crystals, the kinetics of sorption may be described by a pair of coupled differential equations:

$$\frac{1}{n^2} \cdot \frac{\partial}{\partial n} \left(n^2 \frac{\partial \bar{Q}}{\partial n} \right) = \frac{\beta}{3} \cdot \frac{\partial \bar{Q}}{\partial \tau} \quad (\text{macropore diffusion}) \quad (2)$$

$$\frac{1}{\gamma^2} \cdot \frac{\partial}{\partial \gamma} \left(\gamma^2 \cdot \frac{\partial Q}{\partial \gamma} \right) = \frac{\partial Q}{\partial \tau} \quad (\text{micropore diffusion}) \quad (3)$$

where $\bar{Q}(n, \tau)$ is the dimensionless adsorbed phase concentration averaged over a crystal:

$$\bar{Q} = \frac{\bar{Q}}{q_m} = 3 \int_0^1 Q(n, \gamma, \tau) \gamma^2 \cdot d\gamma \quad (4)$$

The appropriate initial and boundary conditions, assuming a step change in adsorbed phase concentration at the particle surface at time zero, are:

$$x(n, 0) = 0; \quad x(1, \tau) = 1 \quad (5)$$

$$\bar{Q}(n, 0) = Q(n, \gamma, 0) = 0; \quad Q(n, 1, \tau) = Q^* \quad (6)$$

$$\left. \frac{\partial Q}{\partial \gamma} \right|_{n, 0, \tau} = 0 \quad (7)$$

For the case of linear isotherm ($q^* = Kc$, $Q^* = Kc/q_m$) this set of equations is formally similar to the model of Ruckenstein et al. (2)

A rectangular isotherm implies that the equilibrium absorbed phase concentration approaches saturation for any finite fluid

phase concentration. Under conditions of macropore diffusion control sorption therefore proceeds from layer to layer through the pellet in a manner similar to the shrinking core model of a gas - solid reaction^(4,5). The uptake curve is then given by:

$$\tau_{\text{macro}} = 9 \tau/\beta = \frac{3}{2} - \frac{3}{2}(1-\bar{Q})^{2/3} - \bar{Q} \quad (8)$$

or

$$\bar{Q} = 1 - \left[\frac{1}{2} + \text{Cos} \left\{ \frac{\pi}{3} + \frac{1}{3} \text{Cos}^{-1} \left(1 - \frac{36\tau}{\beta} \right) \right\} \right]^3 \quad (9)$$

For the other extreme case of micropore control the uptake curve is given by the well known solution of eqn. 3 for a step change boundary condition:

$$\bar{Q} = \frac{M_t}{M_\infty} = 1 - \frac{6}{\pi^2} \sum_{n=1}^{\infty} \frac{1}{n^2} \exp[-n^2\pi^2\tau] \quad (10)$$

In order to describe the coupled diffusion problem which arises when both macropore and micropore resistances are significant we note that, for a rectangular isotherm, the progress of the concentration front penetrating the pellet can be represented as a time dependent step function:

$$Q(\eta, 1, \tau) = S[\tau - \tau_f(\eta)] \equiv \begin{cases} 0, & \tau < \tau_f(\eta) \\ 1, & \tau \geq \tau_f(\eta) \end{cases} \quad (11)$$

$$x(\eta_f, \tau_f) = 0 \quad (12)$$

A material balance at the concentration front gives:

$$-\beta \frac{d\eta_f}{3 d\tau_f} = \frac{\partial x}{\partial \eta} \Big|_{\eta=\eta_f} \quad (13)$$

$$\text{with } \eta_f = 1, \tau_f = 0 \text{ at } \tau = 0. \quad (14)$$

Since a crystal at the radial position η in the pellet is subjected to a step change in surface concentration at time $\tau_f(\eta)$ the uptake curve and the rate of sorption at that point are given by:

$$\bar{Q} = 1 - \frac{6}{\pi^2} \sum_{n=1}^{\infty} \frac{1}{n^2} \exp[-n^2\pi^2(\tau - \tau_f(\eta))] \quad (15)$$

$$\frac{\partial \bar{Q}}{\partial \tau} = 6 \sum_{n=1}^{\infty} \exp \left\{ -n^2 \pi^2 [\tau - \tau_f(\eta)] \right\} \equiv 3F[\tau - \tau_f(\eta)] \quad (16)$$

so that eqn. 2 becomes:

$$\frac{1}{\eta^2} \cdot \frac{\partial}{\partial \eta} \left(\eta^2 \frac{\partial x}{\partial \eta} \right) = \beta F[\tau - \tau_f(\eta)] \quad (17)$$

The relationship between τ_f and η_f must be found by simultaneous solution of eqns. 13 and 17 subject to the initial and boundary conditions expressed by eqns. 5, 12 and 14. Once this relationship is established the uptake curve is easily calculated by direct integration:

$$\frac{M_t}{M_{\infty}} = \bar{Q}(\tau) = \frac{\bar{q}}{(1-\epsilon)q_m} = 3 \int_0^1 \left\{ 1 - \frac{6}{\pi^2} \sum_{n=1}^{\infty} \frac{1}{n^2} e^{-n^2 \pi^2 [\tau - \tau_f(\eta)]} \right\} \eta^2 \cdot d\eta \quad (18)$$

Method of Solution

The substitution $y = (\eta - \eta_f)/(1 - \eta_f)$ was employed in order to reduce the moving boundary problem (eqns. 13 and 17) to a fixed boundary value problem:

$$-\frac{\beta}{3} \frac{d\eta_f}{d\tau_f} = \frac{1}{(1-\eta_f)} \cdot \frac{\partial x}{\partial y} \Big|_{y=0} \quad (19)$$

$$\frac{1}{(1-\eta_f)^2} \cdot \frac{\partial^2 x}{\partial y^2} + \frac{2}{(1-\eta_f)[y(1-\eta_f) + \eta_f]} \cdot \frac{\partial x}{\partial y} = \beta F[\tau - \tau_f(y)] \quad (20)$$

$$x(1, \tau) = 1 \quad ; \quad x(0, \tau) = 0 \quad (21)$$

These equations were then solved by orthogonal collocation since, in the solution of non-linear boundary value problems this method has been shown to be more efficient than the finite difference approach^(6,7). In accordance with usual collocation procedure the form of the trial function is chosen to satisfy automatically the boundary conditions:

$$x(y, \tau) = y + y(1-y) \sum_{n=1}^N a_n(\tau) \cdot P_{n-1}(2y-1) \quad (22)$$

where P_{n-1} is the shifted Legendre polynomial of order $(n-1)$. Substitution of the trial function (eqn. 22) in eqn. 20 yields a

set of N algebraic equations, one for each collocation point. The solution of this set of equations yields the values of the N coefficients $(a_n(\tau))$ so that $(\partial x/\partial y)|_{y=0}$ may be evaluated as a function of η_f for any particular value of τ with β as a parameter. Eqn. 19 is thus reduced to an ordinary differential equation of the form $(d\eta_f/d\tau_f) = f(\eta_f)$ which may be integrated directly by any standard routine such as Runge-Kutta to yield the required relation between η_f and τ_f . Since eqn. 19 is singular at the surface of the particle ($\tau_f = 0$, $\eta_f = 1$) the numerical integration was started from a value of η_f slightly less than unity (usually 0.95). Corresponding values of τ_f for the initial region were then obtained by assuming that in this region the coefficients a_n in the trial function are independent of time. This assumption is reasonable when η_f is close to unity. Convergence of the solution was established by increasing the number of collocation points. For $N > 4$ the uptake curves showed very little change.

Theoretical Uptake Curves

A family of theoretical uptake curves is shown in figure 1. For small values of β (< 0.1) the curves approach the limiting curve for complete micropore control (eqn. 10). As β is increased the shape of the curve changes but the limiting form for macropore control (eqn. 9) is approached only when β is very large ($\beta > 10^4$). For intermediate values of β the uptake curves cannot be properly represented by a single resistance diffusion model. Matching uptake curves of this form to eqn. 9 (or eqn. 10) will lead to apparent diffusivities which vary with fractional uptake. Such trends have been reported in the literature^(8,9) and this is one possible explanation. As the two diffusional resistances are not strictly in series the assumption of linear additivity, introduced by Roberts and York⁽¹⁰⁾ cannot be justified. Such an assumption cannot account for the changing shape of the uptake curves.

In figure 1 uptake curves for the present system (rectangular isotherm, dual resistance model) are also compared with curves calculated from the modified linear dual resistance, Ruckenstein model⁽¹¹⁾. For the rectangular isotherm there is a distinct concentration front which penetrates the pellet and crystals behind the front attain immediately the final saturation concentration at their surfaces. For a linear system the sorbate penetrates the pellet more rapidly although the concentration in the central region is low. The initial rate of uptake is faster for a linear system as more crystals are in contact with the sorbate. However as sorption proceeds uptake by the rectangular system becomes relatively more rapid due to the effect of the higher sorbate concentration at the surface of the crystals. The qualitative difference in the shapes of the curves can be understood on this basis.

isotherms were essentially the same ($D_0 \approx 2.5 \times 10^{-14} \text{ cm}^2 \cdot \text{sec}^{-1}$ as compared with $6 \times 10^{-14} \text{ cm}^2 \cdot \text{sec}^{-1}$ from extrapolation of high temperature data obtained with the larger Linde 5A crystals⁽¹⁴⁾). The theoretical lines in figure 4 are back calculated from eqn. 23 and it is evident that the differences in the differential coefficients (D_z) are due mainly to the differences in the isotherms.

The values of D_z determined from the integral experiments ($4.2, 5.0$ and $6.0 \times 10^{-14} \text{ cm}^2 \cdot \text{sec}^{-1}$) are somewhat higher than the limiting values of D_0 . This is to be expected since the integral diffusivity should correspond to an average value of D_z calculated over the range $0 \rightarrow q_m$:

$$\bar{D}_z = \frac{1}{q_m} \int_0^{q_m} D_z \cdot dq \quad (24)$$

Pellet diameter 0.387 cm. Crystal diameter 0.7 micron. Experimental pellet density $1.12 \text{ gm} \cdot \text{cm}^{-3}$. Porosity, calculated assuming solid density $1.57 \text{ gm} \cdot \text{cm}^{-3}$ $\epsilon = 0.29$. Mean macropore radius $\sim 450 \text{ \AA}$. Values of K from slopes of experimental isotherm.

Integration of the curve of figure 4 yields values of D_z close to the experimental values and showing the observed increasing trend with increasing pressure.

The importance of considering both macropore and micropore resistances may be seen by examining the sorption curves for the differential runs which, in the initial region, are almost linear in \sqrt{t} . The time constants calculated from the initial slopes of these curves, assuming only a single diffusional resistance (either micropore or macropore as in eqn. 9 or 10), are compared in table II with the values derived from the linear dual resistance model. It is evident that, under these conditions, the assumption of a single resistance will lead to large errors in the calculated diffusivities. Since a bed of zeolite crystals can act like a macroporous pellet the possible intrusion of secondary diffusional resistance is a factor which should always be considered in the analysis of transient sorption curves.

Conclusions

In the analysis of the single resistance diffusion problem it has been shown that, for systems in which the diffusivity increases with sorbate concentration, the form of the uptake curve differs

TABLE II - Comparison of Diffusion Time Constants Calculated from Single Resistance and Dual Resistance Models (sec^{-1})

Run	Calculated From Linear Dual Resistance Model		Calculated from Single resistance Models	
	$(D_z/r_z^2) \times 10^4$	(D_p/R_p^2)	Eqn. 8 $(D_z/r_z^2) \times 10^4$	Eqn. 9 (D_p/R_p^2)
D-1	2.1	0.20	0.5	0.061
D-2	2.9	2.21	0.57	0.055
D-3	4.1	0.063	0.46	0.031

Comparison of Theory and Experiment

Experimental isotherms for cis-2-butene in Davison 5A sieve (crystals and binderless pellet at 273°K are shown in figure 2. The isotherms are highly favourable and at this temperature sorption is slow and approximately isothermal. In an integral adsorption experiment the requirements of the rectangular isotherm bipore model are therefore approximately fulfilled whereas in a differential experiment the system will be approximately linear. Under differential conditions adsorption and desorption curves are identical but desorption measurements are experimentally easier. The experimental values of β and D_z/r_z^2 (Table I) were determined by matching the experimental uptake curves to the appropriate family of dimensionless theoretical curves (rectangular or linear model). The difference between differential and integral curves is evident in figure 3. Deviations between theoretical and experimental curves are more pronounced for the integral curves but this is to be expected since the assumption of a constant diffusivity is a more severe approximation in the integral case. Furthermore, the lower value of β implies greater influence of micropore resistance and under these conditions deviations in the tail of the curve are to be expected due to crystal size distribution⁽¹²⁾. Also given in Table I are the values of β calculated a priori assuming a tortuosity factor of 6^(11,13). Knudsen diffusion in the macropores is dominant but at the higher pressures molecular diffusion is also significant. Although the theoretically estimated values of β are smaller than the experimental values there is order of magnitude agreement.

Micropore diffusivities calculated from the differential runs are shown in figure 4 which includes also the values obtained from differential experiments with unaggregated crystals (β_{so}). The differential diffusivities show the usual strong concentration dependence arising from the non-linearity of the equilibrium isotherm:

$$D_z = D_0(\text{d}lnc/\text{d}lnc) \quad (23)$$

For both sizes of crystal and for the pellet the values of D_0 calculated from eqn. 23 using the values of $(\text{d}lnc/\text{d}lnc)$ from the

TABLE I - Details of Experiments and Calculated Parameters

	$P \rightarrow P_2$		From Curve Matching		Estimated Values	
	(torr)	K	$10^4(D_z/r_z^2)$ (sec ⁻¹)	β	β	D_p/R_p^2 (sec ⁻¹)
Differential						
D-1	4.2-2.9	505	2.1	4	2	0.4
D-2	7.5-4.2	390	2.9	4	2.1	0.4
D-3	8.6-7.5	210	4.1	8	1.6	0.4
Integral	$q_m(\text{mmoles.cm}^{-3})$					
I-1	0-51	3.31	0.34	1	0.75	0.38
I-2	0-99	3.46	0.41	1	0.5	0.35
I-3	0-199	3.55	0.52	1	0.4	0.3

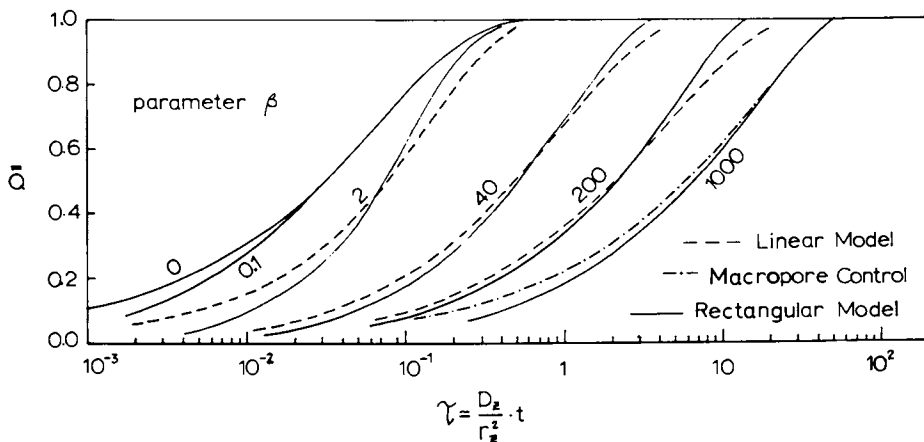


Figure 1. Comparison of theoretical uptake curves calculated from linear and rectangular isotherm dual resistance models. The line for macropore control (equation 9) is plotted for $\beta = 10^4$ on the micropore time scale.

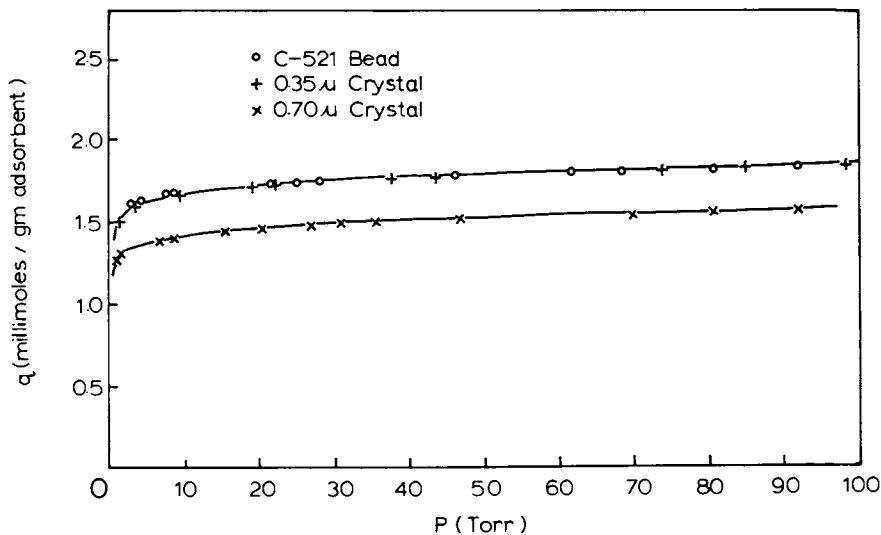


Figure 2. Experimental isotherms for sorption of cis-2-butene at 273°K in Davison 5A sieve. 0.7 micron crystals, \times ; 0.35 micron crystals, $+$; pellet, \circ .

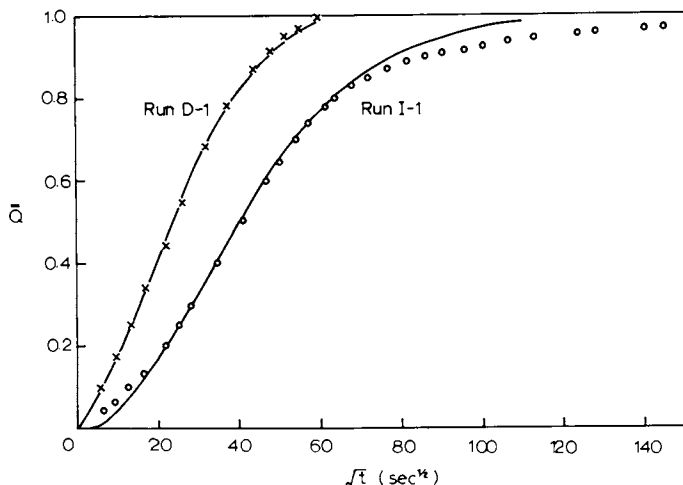


Figure 3. Comparison of theoretical and experimental sorption curves. Theoretical curves for run D-1 from linear dual resistance model and for run I-1 from rectangular dual resistance model. Parameters are given in Table 1.

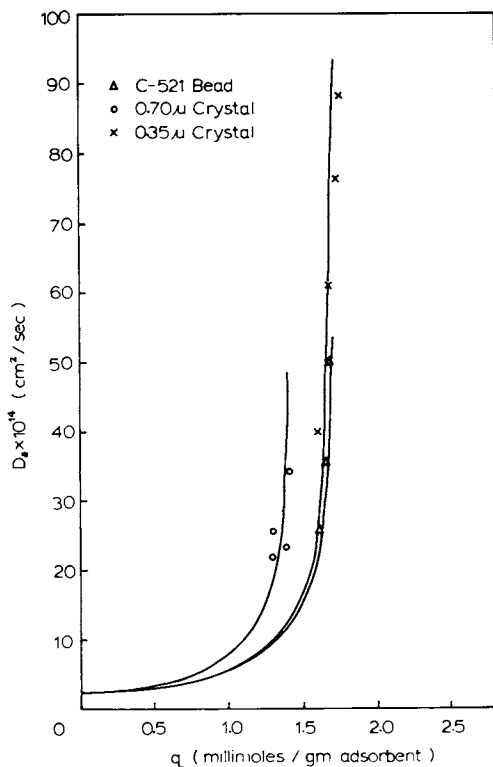


Figure 4. Variation of micropore diffusivity with sorbate concentration. Pellet, Δ ; 0.7 micron crystals, \circ ; 0.35 micron crystals, \times . Theoretical curves are from equation 23 with $D_0 = 2.5 \times 10^{-14} \text{ cm}^2 \cdot \text{sec}^{-1}$.

only slightly from the constant diffusivity case⁽¹⁵⁾. The assumption of a constant effective micropore diffusivity may therefore be an acceptable approximation in the present model although in a rigorous analysis the concentration dependence would have to be considered.

The theoretical uptake curves for an irreversibly adsorbed species in a bi-porous molecular sieve pellet differs significantly from the equivalent curves for a linear system. The proposed model provides a satisfactory interpretation of experimental integral uptake curves for cis-2-butene in Davison 5A sieve at 273°K since for this system, under the experimental conditions, the assumption of a rectangular isotherm is a reasonable approximation. By contrast, in differential experiments, the system can be considered as linear and the sorption curves conform to the predictions of the linear dual resistance model. For more complete confirmation of the validity of the theoretical analysis further experiments with pellets of different size are desirable.

Notation

c	fluid phase concentration of adsorbate
c_o	fluid phase concentration at external surface of pellet
D_z	diffusivity of sorbate in zeolite crystal
D_p	macropore diffusivity (based on pore area)
q	adsorbed phase concentration (moles/unit solid volume)
q_m	saturation capacity of adsorbed phase
q^*	equilibrium adsorbed phase concentration
\bar{q}	adsorbed phase concentration averaged over a crystal
$\bar{\bar{q}}$	adsorbed phase concentration averaged over the pellet
r	radial coordinate for crystal
r_z	equivalent radius of zeolite crystal
R	radial coordinate for pellet
R_p	equivalent radius of pellet
t	time

Dimensionless Variables

K	dimensionless equilibrium constant for linear system
m_t/m_∞	fractional uptake by a crystal
M_t/M_∞	fractional uptake by pellet as defined by eqn. 20
Q	q/q_m
\bar{Q}	\bar{q}/q_m
$\bar{\bar{Q}}$	$\bar{\bar{q}}/(1-\epsilon)q_m$
Q^*	q/q_m
η	R/R_p
η_f	value of η at concentration front
γ	r/r_z
x	c/c_o
α	$(D_z/r_z^2)/(D_p/R_p^2)$
τ	$D_z t/r_z^2$
τ_f	value of τ at concentration front (η_f)
β	$3\alpha(1-\epsilon)q_m/\epsilon c_o$
ϵ	void fraction of pellet

Literature Cited

1. Sargent, R.W.H., Whitford, C.J., *Adv. in Chem.* (1971), 102, 155.
2. Ruckenstein, E., Vaidyanathan, A.S., Youngquist, G.R., *Chem. Eng. Sci.* (1971), 26, 1305.
3. Ma, Y.H., Ho, S.Y., *A.I.Ch.E. J.* (1974), 20, 279.
4. Levenspiel, O., "Chemical Reaction Engineering", 2nd. Ed. Wiley, New York, p. 366, (1972).
5. Vermeulen, T., *Adv. in Chem. Eng.* (1958), 2, 147.
6. Villadsen, J., "Selected Approximation Methods for Chemical Engineering Problems", Reproset, Copenhagen, (1970).
7. Yoshida, K., Kunii, D., Shimizu, F., *J. Chem. Eng., Japan*, (1975), 8, 417.
8. Satterfield, C.N., Katzer, J.R., *Adv.Chem.* (1971), 102, 193.
9. Schirmer, W., Fiedrich, G., Grossman, A., Stach, H., "Molecular Sieves", p. 276, *Soc. Chem. Ind., London* (1968).
10. Roberts, P.V., York, R., *Ind. Eng. Chem. Process Design Develop.* (1967), 6, 516.
11. Ruthven, D.M., Loughlin, K.F., *Can.J.Chem.Eng.* (1972), 50, 550.
12. Ruthven, D.M., Loughlin, K.F., *Chem.Eng.Sci.* (1971), 26, 577.
13. Ruthven, D.M., Derrah, R.I., *Can.J.Chem.Eng.* (1972), 50, 743.
14. Ruthven, D.M., Loughlin, K.F., Derrah, R.I., *Adv.Chem.* (1973), 121, 330.
15. Crank, J., "Mathematics of Diffusion", p. 280 Oxford University Press, (1956).

Effects of Exchangeable Cations on Diffusion in Faujasite Pellets

TING YUEH LEE and YI HUA MA

Chemical Engineering Department, Worcester Polytechnic Institute,
Worcester, Mass. 01609

ABSTRACT

Intracrystalline diffusion coefficients of n-butane, isobutane and 1-butene in Na-, Ca- and La-form of synthetic faujasite were measured in a constant volume, well-stirred system. The diffusion coefficient decreases in the following order for all three hydrocarbons: $D_i(\text{LaX}(\text{Na})) > D_i(\text{CaX}(\text{Na})) > D_i(\text{NaX})$. The activation energy for diffusion ranges from 4 to 11 kcal/g-mole.

Introduction

Sorption rates of different molecules are sensitive to the ionic radii of, and the interaction with, the exchangeable cations. By base exchange of the molecular sieve, it is possible to modify the characteristics of the cavities of the sieves leading to potential applications in purification and separation processes. Barrer and his co-workers (1,2,3) studied the diffusion and equilibrium properties of Kr, Ar, N₂, O₂ and H₂ in Li, Na, K, NH₄, Ca and Ba ion-exchanged mordenites. It was found that the energy of activation for diffusion depends upon the ionic radius and the polarizing power of the interstitial cation. A series of crystalline sorbents, in which the framework charge and cation density were progressively reduced by reacting the zeolite with acid solution, had been studied and characterized by sorption of CO₂ and Kr. They found that the extent of decationization altered the molecular sieve character and affinity for CO₂ but to a lesser extent for Kr. The dipole, quadrupole, dispersion, repulsion and polarization contribution to the isosteric heat were also discussed. Habgood (4) studied the sorption properties of n-alkanes in LiX, NaX, and KX and found that the radii and positions of the cations affected the heat of adsorption. Bosacek (5) investigated the effects of various contents of K⁺ and Ca⁺⁺ cations on adsorption and chromatographic selectivity of X-type zeolites. He found that K⁺ preferentially occupied the

SIII positions and Ca^{++} occupied S_1 positions. Smith (6) summarized the X-ray diffraction studies on H_2O -, SO_2 -, Kr-, Xe-, I_2 -, and Br_2 -complexes of Linde A sieve, on H_2O -, Cl_2 -, and Br_2 -complexes of chabazite and on H_2O -complexes of many zeolites with various pore sizes. He concluded that the exchangeable cations often moved in response to the sorbed molecules.

In the present study, the effects of cations upon the diffusion of n-butane, iso-butane and 1-butene were investigated. NaX and its ion-exchanged forms of CaX(Na) and LaX(Na) were chosen for the study due to the industrial importance of the zeolites.

Apparatus and Procedure

A well-stirred constant volume sorption system was employed for the diffusion study. Spherical sorbent pellets (about 1g) were placed in two baskets which were rotated at 3,300 rpm in a constant volume sorption chamber shown in Figure 1. A measured amount of sorbate gas was injected into the reactor through an injection port. Gas samples were withdrawn through the sampling loop and the gas phase concentration was analyzed by gas chromatograph. A detailed description of the apparatus and the procedure can be found in (8).

Helium and C₄-hydrocarbon gases are research grade obtained from the Matheson Company. They were passed through columns packed with 5A sieve pellets to remove trace quantity of water. Zeolite X was provided by Davison Chemical Division of W.R. Grace Company. Ion exchange of the NaX was done by contacting the zeolite with calcium acetate solution and lanthanum nitrate solution at room temperature. X-ray fluorescence analysis was employed to determine the extent of completion of the ion exchange. The completion of exchange for CaX(Na) was about 85% and for LaX(Na) was about 75%. Twenty weight percent Georgia kaolinite clay was then added as a binder for the formation of spherical pellets. It has been shown (9) that the effect of the inert binder upon diffusion is negligible. The average radius of the particles is 0.230 cm and the average crystal size as measured by an electron microscope is 108 μm .

Results and Discussion

The mathematical model developed by Ma and Lee (8) is employed for the determination of the micropore diffusion coefficients. If one considers N spherical particles immersed in a reservoir of well-stirred fluid of volume V, mass balances in both macropores (intercrystalline pores) and micropores (intra-crystalline pores) give

$$\frac{D_a \epsilon_a}{r_a^2} \frac{\partial}{\partial r_a} \left(r_a^2 \frac{\partial C_a}{\partial r_a} \right) - \frac{3(1-\epsilon_a)}{R_i} D_i \left(\frac{\partial C_i}{\partial r_i} \right)_{r_i=R_i} = \frac{\partial C_a}{\partial t} \epsilon_a \quad (1)$$

$$D_i \left(\frac{\partial^2 C_i}{\partial r_i^2} + \frac{2}{r_i} \frac{\partial C_i}{\partial r_i} \right) = \frac{\partial C_i}{\partial t} \quad (2)$$

Material balance in the fluid gives

$$V \frac{dC}{dt} = - N \epsilon_a 4\pi R_a^2 D_a \left(\frac{\partial C_a}{\partial r_a} \right) \quad (3)$$

The assumptions involved in deriving Equations (1), (2) and (3) and the appropriate initial and boundary conditions necessary for the solution of these equations can be found in (8). Once the solution is obtained, one can easily get an expression for the ratio $\frac{C(t)}{C^0}$, which is the normalized form of the change of sorbate concentration in the bulk phase and can be measured experimentally. The experimental data were then fitted with the theoretical curves to determine the intracrystalline diffusion coefficient (8). A typical comparison between theoretical results and experimental data is shown in Figure 2 which shows good agreement between theoretical and experimental values.

Diffusion measurements were made for three hydrocarbons, n-butane, iso-butane and 1-butene, on NaX(Na) and LaX(Na) at three temperatures, 5°C, 35°C and 60°C. The results of these measurements are tabulated in Table I, II and III together with the constants used for the determination of the intracrystalline diffusion coefficients. It should be noted that these constants were determined independently. In particular, Henry's law constant, K, is obtained from independent adsorption equilibrium studies (10). A typical Arrhenius plot of the intracrystalline diffusion coefficients as a function of temperature for NaX pellets is shown in Figure 3. The activation energies calculated from the Arrhenius plots are listed in Tables I, II, and III.

From the results shown in Table I, II and III, it is evident that the intracrystalline diffusion coefficient decreases in the following order for all three hydrocarbons:

$$D_i(\text{LaX(Na)}) > D_i(\text{CaX(Na)}) > D_i(\text{NaX})$$

This is caused by the fact that one Ca cation replaces two Na cations and one La cation replaces three Na cations due to their differences in valences. The cation sites are different in the framework of the zeolite and thus offer different resistances to sorbate diffusion. It appears that the channels of the Ca⁺⁺ and La⁺⁺ exchanged forms of the X zeolite were opened up somewhat due to a lesser number of cations present. This is consistent

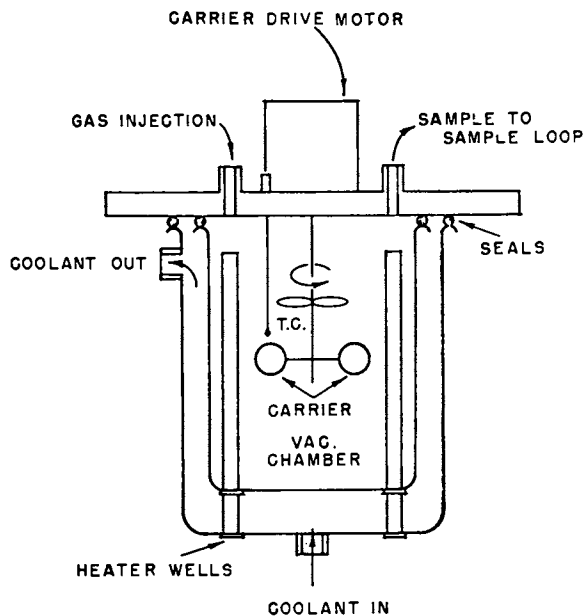


Figure 1. Constant volume sorption chamber

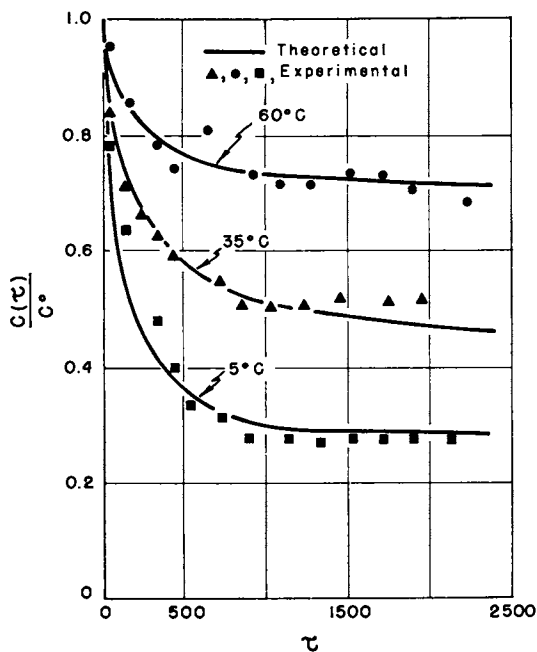


Figure 2. Diffusion of iso-butane in $\text{LaX}(\text{Na})$ pellets

Table 1. Diffusion Results in NaX Pellets

	N-Butane			Iso-Butane			1-Butene		
	5	35	60	5	35	60	5	35	60
Temp. °C									
Initial amount m moles	2.22	1.93	1.99	1.99	1.94	1.86	2.22	2.12	1.92
E _i Kcal/g-mole		10.34			9.27			11.27	
K	403,000	106,200	21,200	154,600	50,800	15,200	637,900	22,200	61,000
R _a cm		0.2302			0.2302			0.2302	
R _i cm		1.08x10 ⁻⁴			1.08x10 ⁻⁴			1.08x10 ⁻⁴	
D _a cm ² /s	0.0465	0.0517	0.0558	0.0421	0.0472	0.0511	0.0438	0.0496	0.0537
D _i cm ² /s	0.383	0.402	0.418	0.383	0.402	0.418	0.389	0.410	0.426
D _j cm ² /s	1.700 x 10 ⁻¹⁴	0.432x 10 ⁻¹³	3.584x 10 ⁻¹³	1.470x 10 ⁻¹³	1.038x 10 ⁻¹²	2.248x 10 ⁻¹²	9.014x 10 ⁻¹⁵	4.903x 10 ⁻¹⁴	2.714x 10 ⁻¹³
ε _a		0.5			0.5			0.5	
Tortuosity factor		4.5			4.5			4.5	

Table II. Diffusion Results in CaX(Na) Pellets

	N-Butane			Iso-Butane			1-Butene		
	5	35	60	5	35	60	5	35	60
Temp. °C									
Initial amount m moles	1.95	1.88	1.89	1.93	1.90	1.95	2.48	1.81	1.88
E ₁ Kcal/g-mole		7.01			3.56			7.49	
K	85,700	31,500	9,816	60,900	18,000	6,851	94,600	81,900	40,600
R _a cm		0.2302			0.2302			0.2302	
R _i cm		1.08x10 ⁻⁴			1.08x10 ⁻⁴			1.08x10 ⁻⁴	
D _a cm ² /s	0.0465	0.0517	0.0558	0.0421	0.0472	0.0511	0.0438	0.0496	0.0537
DK cm ² /s	0.383	0.402	0.418	0.383	0.402	0.418	0.389	0.410	0.426
D _i cm ² /s	1.096x	2.226x	9.503x	8.104x	1.803x	2.298x	4.824x	9.704x	4.885x
	10 ⁻¹³	10 ⁻¹³	10 ⁻¹³	10 ⁻¹³	10 ⁻¹²	10 ⁻¹²	10 ⁻¹⁴	10 ⁻¹⁴	10 ⁻¹³
ε _a			0.5		0.5			0.5	
Tortuosity factor			4.5		4.5			4.5	

Table III. Diffusion Results in LaX(Na) Pellets

	N-Butane			Iso-Butane			1-Butene		
	5	35	60	5	35	60	5	35	60
Temp. °C									
Initial amount m moles	1.91	1.87	1.91	1.90	1.86	1.87	2.30	1.79	
E _i Kcal/g-mole		4.93			3.76			8.66	
K	48,600	13,500	3,511	35,500	11,200	3,149	144,000	65,600	
R _a cm		0.2302			0.2302		0.2302		
R _i cm		1.08x10 ⁻⁴			1.08x10 ⁻⁴		1.08x10 ⁻⁴		
D _a cm ² /s	0.0465	0.0517	0.0558	0.0421	0.0472	0.0511	0.0438	0.0496	
D _K cm ² /s	0.383	0.402	0.418	0.383	0.402	0.418	0.389	0.410	
D _i cm ² /s	4.043x 10 ⁻¹²	1.211x 10 ⁻¹¹	1.713x 10 ⁻¹¹	1.894x 10 ⁻¹²	2.996x 10 ⁻¹²	5.744x 10 ⁻¹²	1.204x 10 ⁻¹³	5.463x 10 ⁻¹³	
ε _a		0.5			0.5			0.5	
Tortuosity factor		4.5			4.5			4.5	

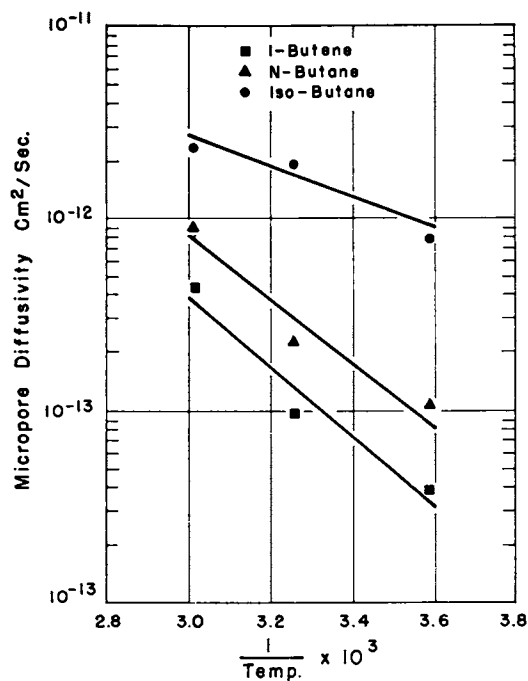


Figure 3. Arrhenius plot of intracrystalline diffusion coefficient for NaX pellets

with the order of increase in activation energies for diffusion.

$$E(\text{LaX}(\text{Na})) \cong E(\text{CaX}(\text{Na})) < E(\text{NaX})$$

This indicates that low diffusion coefficients are associated with high activation energies. This is consistent with the fact that a low diffusion coefficient means a high diffusional resistance and thus the molecules encounter higher energy barriers.

The magnitudes of the intracrystalline diffusion coefficients for CaX(Na) and NaX are in the following order for the three gases: iso-butane > n-butane > 1-butene. Comparison of the overall molecular sizes of three gases would be reasonable for the present case as the pore openings are relatively larger than the sizes of the molecules. An estimate of the effective sizes of these three molecules by considering the bond length, bond angle, relative orientation of the atoms, and carbon-carbon bond rotation indicates that iso-butane is somewhat smaller than n-butane and 1-butene and thus can diffuse faster than the other two gases.

It is interesting to note that the order of the values of the intracrystalline diffusion coefficients for iso-butane and n-butane is reversed for LaX(Na). This might be caused by the larger ionic radius of the La cation. The electrostatic or induced or dispersed forces of the similar sized Na^+ (0.98Å) and Ca^{++} (1.06Å) ions acting on the incoming molecules appear to be approximately equivalent in this system. On the other hand, the La^{+++} cation has a somewhat larger ionic radius of 1.28Å and the positions of the La^{+++} cations are, in general, much farther displaced into the supercages from the pore wall (i.e., in sites III and IV as discussed by Breck (7)). The interaction between the more or less spherical iso-butane molecules and La^{+++} cations is probably larger than that of the long n-butane molecules and La^{+++} cations. Consequently, iso-butane molecules diffuse slower than n-butane molecules in LaX(Na).

The diffusion coefficient for 1-butene is the lowest in all three ion-exchanged forms of the X zeolite. This is caused by a greater interaction existing between the cation and 1-butene molecules due to the presence of a double bond. Such a strong interaction would certainly slow down the molecular movement and give a low diffusion coefficient.

The intracrystalline diffusion coefficient is between 10^{-11} cm^2/s and 10^{-15} cm^2/s . These values are somewhat lower than those previously reported by Ma and Ho (11) for diffusion of allene and methylacetylene in X zeolite but higher than those reported by Riekert (12) on similar systems (10^{-13} to 10^{-18} cm^2/sec for zeolite T). The relatively low value of diffusion coeffi-

cients may also be due to the presence of the "inert" gas helium. The activation energy for diffusion ranges from 4 Kcal/g-mole to 11 Kca/g-mole which are quite reasonable for the systems reported here.

Conclusions

The effects of cations in X zeolite upon intracrystalline diffusion coefficients were investigated. Three ion-exchanged forms of the zeolite were employed in the study: NaX, CaX(Na) and LaX(Na). The intracrystalline diffusion coefficients were determined at three temperatures, 5°C, 35°C and 60°C for all three ion-exchanged forms of faujasite. The diffusion coefficients were found to decrease in the following order for all three hydrocarbons (n-butane, iso-butane, 1-butene):

$$D_i(\text{LaX(Na)}) > D_i(\text{CaX(Na)}) > D_i(\text{NaX})$$

This is caused by the replacement of Na^+ cations by one third the number of La^{+++} cations or one-half the number of Ca^{++} cations which have different sites in the zeolitic framework and offer different resistances to sorbate diffusion. This is consistent with the order of increase in activation energies for diffusion.

$$E(\text{LaX(Na)}) \cong E(\text{CaX(Na)}) < E(\text{NaX})$$

The magnitudes of the intracrystalline diffusion coefficients for CaX(Na) and NaX are in the following order for three gases:

$$\text{iso-butane} > \text{n-butane} > \text{1-butene}$$

The order of iso-butene and n-butane is reversed for LaX(Na) and is probably caused by the stronger interaction between the La^{+++} cation and the diffusing molecules.

Acknowledgments

This investigation was supported by the National Science Foundation under Grant GK-33351. The molecular sieve was provided by W.R. Grace and Co., Davison Chemical Division.

Notation

C = concentration of sorbate, m moles cm^{-3}
 D = diffusion coefficient, cm^2s^{-1}
 D_K = Knudsen diffusion coefficient, cm^2s^{-1}
 E = activation energy, Kcal mole^{-1}

K = equilibrium constant
N = number of adsorbent particles
R = radius, cm
r = radial distance, cm
t = time, s
T = temperature, °K
V = volume of reactor, cm³

Greek Letters

$\tau = D_{at}/R_a^2$
 $\epsilon = \text{void volume}$

Subscripts

i = micropore
a = macropore

Literature Cited

1. Barrer, R.M., Trans. Farad. Society, 40 (1948) 358.
2. Barrer, R.M. & Breck, D.W., Trans. Farad. Society, 49 (1953) 1049.
3. Barrer, R.M. & Coughlan, B., Molecular Sieve, Society of Chemical Ind., London, (1968) p. 141.
4. Habgood, H.W., Chemical Engineering Progress Symposium Series, Series 73, Vol. 63 (1967) 45.
5. Bosacek, V., Molecular Sieve, Society of Chemical Ind., London, (1968) p. 164.
6. Smith, J.V., Molecular Sieve, Society of Chemical Ind., London (1968) p. 28.
7. Breck, D.W., "Zeolite Molecular Sieve", John Wiley & Sons (1974).
8. Ma, Y.H. and Lee, T.Y., AIChE J. 22 (1976) 147.
9. Tamboli, J.K., "SO₂ Adsorption Properties and Acid Stability of Molecular Sieve Zeolites", M.S. Thesis, Worcester Polytechnic Institute, Worcester, MA (1970).
10. Lee, T.Y., "Single and Multicomponent Diffusion in Faujasite Pellets", Ph.D. Thesis, Worcester Polytechnic Institute, Worcester, MA (1976).
11. Ma, Y.H., and Ho, S.H., AIChE J., 19 (1973) 1055.
12. Riekert, L., AIChE J., 17 (1971) 446.

Inter- and Intraparticle Diffusion of Ions in Zeolites

G. T. KOKOTAILO, S. L. LAWTON, and S. SAWRUK

Mobil Research and Development Corp., Paulsboro, N.J. 08066

ABSTRACT

Ion migration in and between different cationic forms of the crystalline zeolites A and X has been monitored by x-ray diffraction. The mobility of the ions is dependent on their state of hydration and temperature. The relative order of rates of inter-crystalline ion exchange was determined.

Introduction

In the determination of zeolite structures it is difficult if not impossible to locate all the cations. This is thought to be due to the low occupancy of certain sites by these cations or to their mobility. For example, in the structure determination of ZK-5(1), it was found that a lower R factor could be obtained for x-ray diffraction data obtained from a sample at 150°C than for that at room temperature. This is consistent with a reduction in diffuse scattering by removal of water and by a more rigid binding of cations to the framework.

Nuclear magnetic studies (2) of hydrated and out-gassed NaX and NaY zeolites have shown that the sodium ions are mobile, with the speed of motion being a function of water content. The temperature dependence of the cation resonance, and the very narrow proton resonance line width at temperatures above -20°C indicating almost complete freedom of motion of water molecules in the zeolite cavities, has been found (3).

Hirst(4) has reported that the ^{23}Na NMR spectra of water loaded NaA and NaX indicated motional narrowing by $^{23}\text{Na}^+$ translational jumps.

The mobility of the cations in zeolites and their migration across contact boundaries between adjacent crystals may be studied using x-ray diffraction by observing the rate of change of lattice parameter. In zeolites the cation jumps will be dominated by the size of the cavities, openings to cavities, periodicity in the crystalline electrostatic fields and contact of crystals with each other.

In this paper we report on the inter- and intracrystalline migration of cations in LiA-NaA, LiA-CaA, LiA-NH₄A, LiX-NaX, LiX-NH₄X, & LiA-NaX mixtures as a function of hydration and temperature.

LiX and LiA zeolites were chosen in this study primarily because of their large differences in lattice parameters from those of other cation forms. By making use of this fact, changes in ion content may be readily monitored by means of x-ray diffraction techniques.

The study of the mobility of ions in zeolites is of interest in structure determination and in solid state ion exchange.

Experimental

The zeolites used were Linde 13X (NaX), Lot 187832; Linde 10X (CaX), Lot 109; Linde 4A (NaA), Lot 4353; and Linde 5A (CaA), Lot 5104. Samples of LiX and LiA were prepared by aqueous ion exchange with reagent grade LiCl at 90°C. The ion exchanges were repeated until no further change in lattice parameter was observed. The samples were washed with hot water and dried, and 92% of the Na cations were replaced by Li in NaA and 95% in NaX. Samples of NH₄X and NH₄A were prepared by exchanging the sodium forms with NH₄NO₃ at room temperature, washing and drying.

In the hydrated mixture studies the component zeolites were first equilibrated at room temperature with an atmosphere at a relative humidity of 50%. The mixed systems were then prepared by placing 0.2 gm of

each component in a plastic vial, together with a plastic sphere, and mixing with a Wiggle Bug for two minutes. The Wiggle Bug describes a figure 8 motion with 100 vibrations per second. This action gives a high degree of mixing and particle-to-particle contact without introducing any appreciable grinding action. X-ray diffraction patterns were obtained immediately after mixing. In the dehydrated mixture studies the individual components of equal weight were first calcined for six hours at 500°C in ambient air, then mixed hot and calcined further. Samples were withdrawn at various time intervals and immediately scanned by an x-ray diffractometer.

The x-ray diffraction patterns were obtained using a Norelco x-ray diffractometer and nickel filtered copper radiation. Patterns were obtained within the angular range $2\theta \leq 36^\circ$ at a scanning rate of $1/2^\circ$ per minute. Owing to the observed interparticle ion migration which takes place the instant two hydrated zeolites of dissimilar cations are physically mixed, reference patterns of the mixed systems (*viz.*, LiA-NaA, LiX-NaX, LiA-NaX, etc.) prior to ion migration were obtained by superimposing separate diffraction scans of the component zeolites on the same chart paper.

Results

LiA-NaA System. The superimposed x-ray diffraction patterns of LiA and NaA are shown in Figure 1. The doublet nature of the pattern shows the large difference in lattice parameters. Mixing equal weights of the hydrated zeolites for two minutes in a Wiggle Bug produced a large ion migration indicated by the almost complete disappearance of the doublets in the x-ray pattern (Figure 1). The peaks are not Gaussian and are due to a two phase system of nearly equal composition, and intermediate lattice parameter.

When the two zeolites are precalcined for 6 hrs. at 500°C and mixed hot in a 1:1 ratio, an x-ray pattern (run immediately after mixing with no equilibration) is generated which indicates the occurrence of virtually no ion migration. This is evident by a comparison of the subsequent doublet pattern with that of the super-

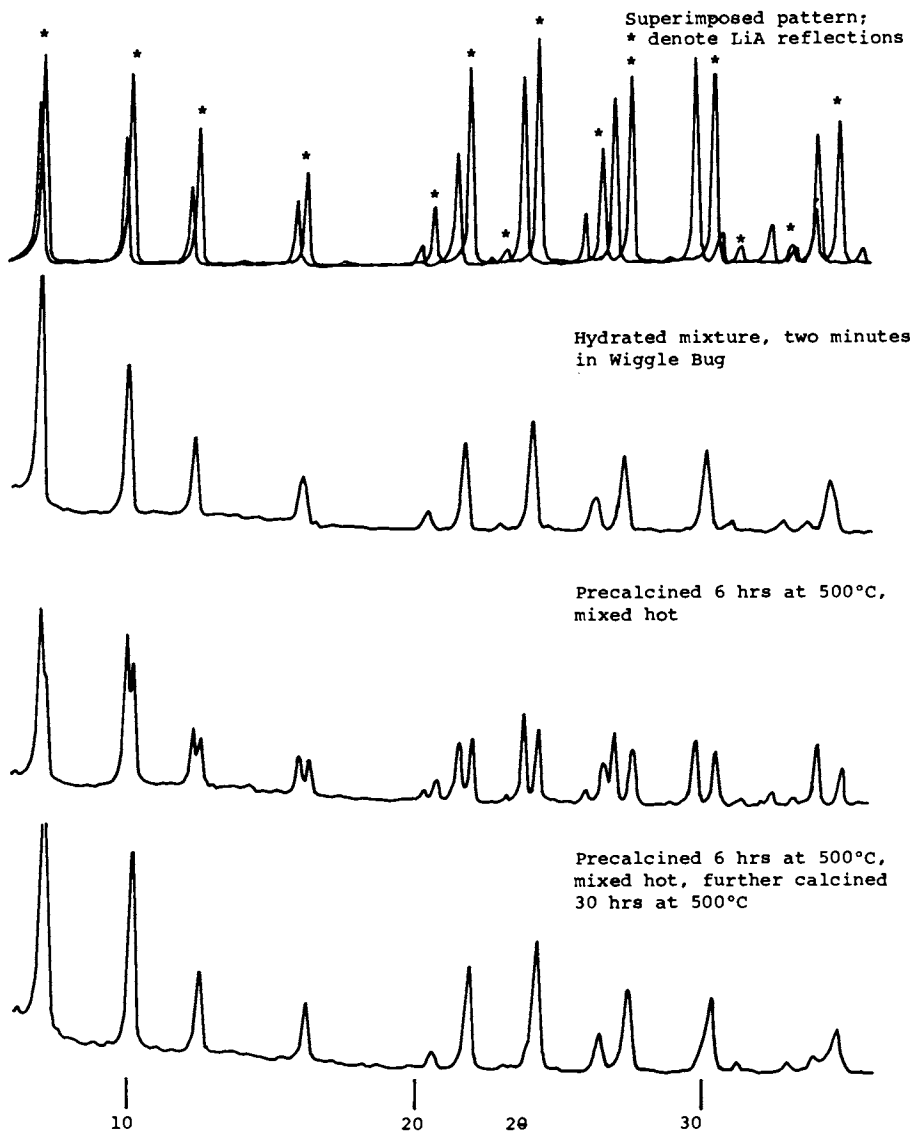


Figure 1. X-ray diffraction patterns of LiA-NaA system

imposed patterns (Figure 1). An x-ray diffraction pattern of the mixture calcined for thirty hours at 500°C is essentially the same as that of the two minute mixed hydrated sample, indicating that considerable inter- and intracrystalline ion migration had occurred at this elevated temperature.

LiA-NH₄A System. The two minute Wiggle Bug mixing of equal weight hydrated components yields an x-ray diffraction pattern showing a sharp singlet pattern with an intermediate lattice parameter, indicating a single phase LiNH₄A zeolite similar to LiNaA.

LiA-CaA System. The x-ray diffraction pattern of the two minute Wiggle Bug mixture of hydrated components shows very little shifting of diffraction lines as compared to the superimposed patterns (Figure 2), indicating very little interparticle migration of Li⁺ and Ca⁺⁺ ions. The precalcined (6 hours at 500°C) zeolites mixed hot and further calcined 48 hours at 500°C remains a two phase mixture but with a decrease in lattice parameter of both components (Figure 2). Further heating for 406 hours at 500°C results in a three phase system (Figure 2). The predominantly LiA phase has an expanded lattice while the predominantly CaA phase is split into two phases, one with a larger and the other with a smaller lattice parameter. Since the Linde 5A (CaA) is a CaNaA the redistribution of both Li and Na ions in the CaA structure may be responsible for the three phase system.

LiX-NaX System. A mixture of equal weights of hydrated components shows a single phase system with an intermediate lattice parameter as compared to the superimposed patterns (Figure 3). When the zeolites are precalcined for 6 hours at 500°C and mixed hot, the doublet nature of the resulting diffraction pattern indicates a two phase system with no change in lattice parameter when compared to the superimposed patterns. Calcination of the mixture for 14 hours shows a trend toward a single phase LiNaX system (Figure 3) with an intermediate lattice parameter.

LiX-NH₄X System. A mixture of the 1:1 hydrated components yields a single phase LiNH₄X system with

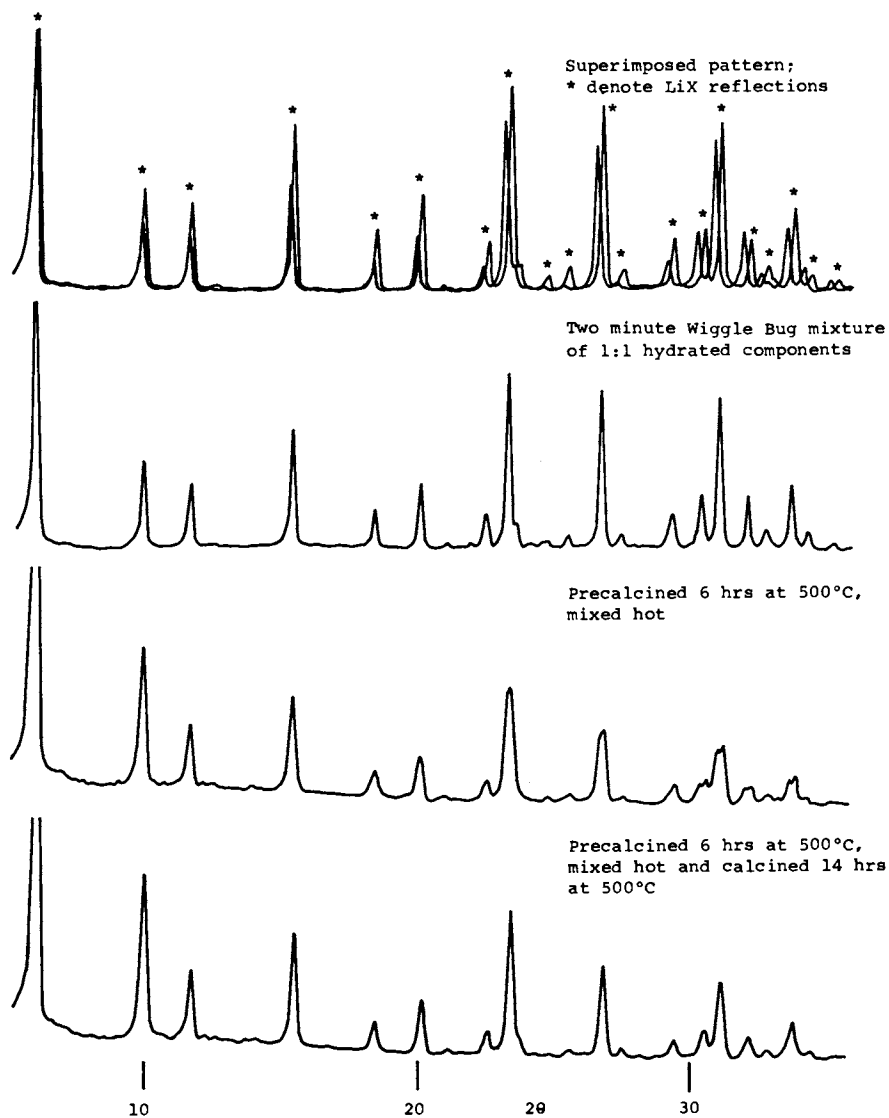


Figure 3. X-ray diffraction patterns of LiX-NaX system

an intermediate lattice parameter similar to LiNaX.

LiA-NaX System. A mixed hydrated system shows a decrease in the lattice parameter of the NaX phase and an increase in the parameter of the LiA phase, indicating the two homogeneous phases LiNaA and LiNaX (Figure 4).

The x-ray diffraction pattern of the precalcined (6 hours at 500°C) LiA and NaX mixed hot and calcined 18 hours at 500°C shows a small change in the lattice parameters of the two phases, indicating some inter-crystalline cation migration. Calcination for 98 hours at 500°C changes the lattice parameters further and after 208 hours at 500°C a homogeneous two phase system LiNaA and LiNaX had been obtained.

Discussion

The structure of Linde A is well known (5-8). It has 4.1Å openings and all the cations occupy sites in the large cavity; none have been found in the sodalite cages. The Linde X structure has a large cavity 13Å in diameter and windows of about 7.4Å in diameter (9,10). The large cavities and openings in Linde X should make ion and water migration more facile than in Linde A. The results of NMR studies (3) of cations and water in zeolites indicate that cations form a kind of cation solution with adsorbed water and the anionic framework.

The intersite motion of cations would thus be facilitated by the presence of water. All the cations are situated on the surface of the alumino-silicate framework. This ion migration would then be a surface rather than bulk phenomenon. Barrer (11) reported that surface diffusion coefficients are much larger than bulk. The very fast inter- and intraparticle migration of lithium, sodium and ammonium ions in the hydrated case confirms this. The hydrated ionic radii, and the number of water molecules associated with a fully hydrated ion indicated in parentheses, of Li⁺, Na⁺, K⁺, and NH₄⁺ are 3.82 (2.8), 3.58 (1.2), 3.31 (0.9) and 3.31Å(0.5), respectively, compared with the dehydrated ionic radii 0.60, 0.95, 1.33 and 1.48Å (12). The smaller ions become more hydrated and their large radii reduce the rate of migration. The large ions such as

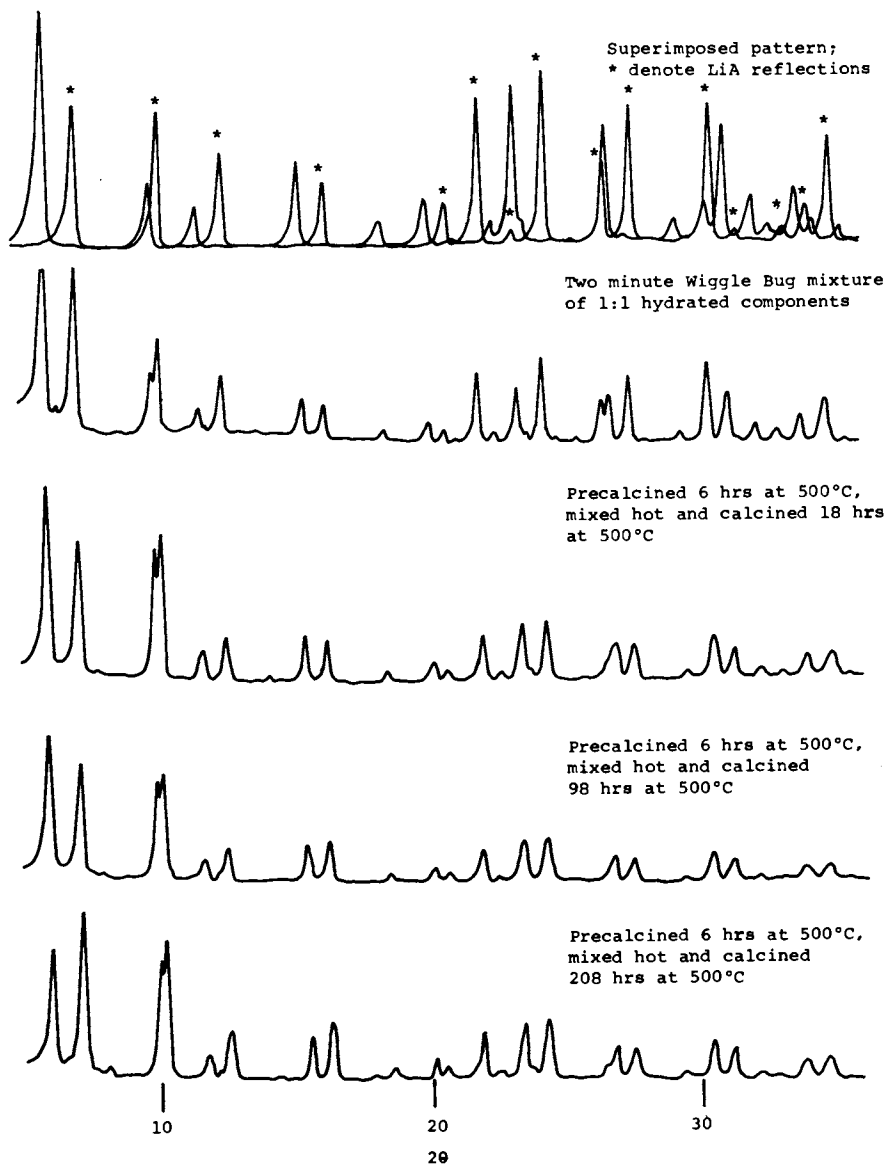


Figure 4. X-ray diffraction patterns of the LiA-NaX system

American Chemical Society
Library
1155 16th St., N.W.
Washington, D.C. 20036

K^+ and NH_4^+ are essentially bare or unhydrated and their mobility is greater because of their smaller hydrated radii (12).

The increased rate of inter-migration of ions in the $Li^+ - NH_4^+$ over the $Li^+ - Na^+$ system is consistent with the higher mobility of ions with smaller hydrated radii. Of course, the cations in the zeolite systems studied may not be fully hydrated and may have smaller hydrated radii with lower mobility.

The lack of intraparticle diffusion of ions in the hydrated $Li^+ - Ca^{++}$ zeolite system is probably due to the difference in valence state of the cations. The hydrated and dehydrated ionic radii of Ca^{++} are 4.12 and .99A, indicating a high degree of hydration. This should reduce its mobility somewhat but not completely.

The large decrease in this rate of migration at elevated temperatures (500°C) confirms the part that water plays. Of course, there was considerably greater contact of zeolite crystals in the room temperature case.

Partial dehydration of NaY and faujasite zeolites, which have essentially the same structure as NaX but differing in the Si/Al ratio and cation content, cause some of the cations to move into site 1 (the double six-membered ring). Bennett and Smith (13) have reported that in dehydrated calcium-exchanged faujasite, this site was fully occupied. This was also reported by Baur (14).

Calcium ions show a large preference for water molecules and in the hydrated zeolite structure are loosely bound to the anionic framework. When the calcium ion loses its water of hydration, it wants to surround itself with oxygen ions and therefore buries itself into the anionic framework with a preference for small cages, such as the double six-membered rings. It now becomes more tightly bound and its ease of migration to other sites is considerably retarded. Rehydration will allow it to migrate from site 1 to other sites in the structure. The very slow inter- and intraparticle migration of calcium ions is, in part, due to this tighter binding of calcium ions on dehydration. It is also partially due to the replacement of one calcium ion by two lithium ions in this

random walk process. Sodium also shows a tendency to migrate to site 1 on dehydration, as seen in the NaY case (15). The occupancy is much lower and it rehydrates much more readily.

The migration of ions from one zeolite crystal to another and their redistribution within the crystal is at least a two step process. The ion must first migrate across a contact boundary between two crystals, then an intersite migration within the crystal. Intersite migration will depend to a large extent on the degree of hydration. In the case of zeolite X, cations in the small cages will be more tightly bound than those in the large cages and ion migration in and out will be retarded not only due to this tighter binding but by the small windows to the small cages. It is difficult to separate the inter- and intracrystalline rates of diffusion as in the hydrated case the rate is very rapid and in the high temperature case the intracrystalline migration becomes more complex.

The crystals in the zeolite A and X samples used were 1 - 5 μ . There are 4.9×10^{10} cations in 2 μ LiA and NH₄A crystals. In the mixing process using a Wiggle Bug, each crystal will contact six other crystals, if there is close packing, 100 times per second since the probability of a LiA crystal contacting another LiA crystal is .5. In the hydrated LiA - NH₄A system, where a single phase LiNH₄A system is formed after a two minute mixing in a Wiggle Bug, 4.1×10^9 Li⁺ and 4.1×10^9 NH₄⁺ ions migrate across a crystal face in this time interval. The cation content of the unit cell outer layer of a 2 μ zeolite A crystal is 3.7×10^8 . The average rate of cation migration across a crystal face contact is 3.4×10^6 per second over a two minute period. This is a qualitative picture of the high rate of intraparticle diffusion of cations in mixed cation zeolite systems. The rate of intraparticle diffusion is much greater than that of interparticle diffusion.

If more than two cations are involved in a mixture of two zeolites, the number of phases increases and the complexity of the distribution of ions increases.

In the Linde A case, the intraparticle diffusion is fairly straightforward since the cations are all in the large cages (truncated cubo-octahedra) and the windows to these large cages are all eight-membered rings (4.1Å). Dehydration results in a strong binding of the cations to the anionic framework thereby reducing the rate of intersite migration.

Literature Cited

1. Meier, W. M., and Kokotailo, G. T., *Z. Kristallogr.* (1965), 121, 211.
2. Knappwost, A., Gunsser, W., and Lechert, H., *Z. Naturforsch.* (1966), 21a, 1200.
3. Knappwost, A., Lechert, H., and Gunsser, W., *Z. Phys. Chem.* (1968), 58, 278.
4. Hirst, R. C., private communication.
5. Broussard, L., and Shoemaker, D. P., *JACS* (1960), 82, 1041.
6. Reed, T. B., and Breck, D. W., *JACS* (1956), 78, 5972.
7. Howell, P. A., *Acta Crystallogr.* (1960), 13, 737.
8. Gramlich, V., and Meier, W. M., *Z. Kristallogr.* (1971), 133, 134.
9. Bergerhoff, G., Baur, W. H., and Nowacki, W., *Neues Jb. Miner. Mh.* (1958), 9, 193.
10. Meier, W. M., *Soc. Chem. Ind. (London)* (1968), 10.
11. Barrer, R. M., "Diffusion in and Through Solids", The University press, Cambridge, Eng., 1941.
12. Nightingale, E. R., *J. Phys. Chem.* (1959), 63, 1381.
13. Bennett, J. M., and Smith, J. V., *Mat. Res. Bull.* (1968), 3, 633.
14. Baur, W. H., *Am. Mineral* (1964), 49, 697.
15. Eulenberger, G. R., Shoemaker, D. P., and Kiel, J. G., *J. Phys. Chem.* (1967), 71, 1812.

Acidic and Catalytic Properties of Zeolites

DENISE BARTHOMEUF

Laboratoire de Catalyse Organique, L.A. CNRS n° 231, Ecole Supérieure de Chimie Industrielle de Lyon, 43, boulevard du 11 novembre 1918, 69621 Villeurbanne, France

ABSTRACT

In the first part a review of zeolite acidity is presented. The concepts of proton and cation mobilities which become more widely considered these last years, are emphasized. The dynamics of zeolite systems appears also in the second part related to correlations between catalytic and acidic properties. A model based on the comparison of zeolites with polyacids in solution is presented.

Recent reviews in the field of catalysis with zeolites have been published (1-5). They point out that the major applications of zeolites in catalytic systems are related to their acidic properties.

A - ZEOLITE ACIDITY

A - I Acidity Models. The first reports on the catalytic properties of zeolites X and Y (6,7) were soon followed by works which noted the presence of acid centers and hydroxyl groups in these catalysts (6,8-10). The acidity measurements methods already used for the study of the amorphous silica-alumina catalysts gave progressively a large amount of results and interestingly pointed out differences between these materials and zeolites. In contrast with silica-alumina, zeolites completely exchanged with polyvalent cations hold concomitantly a large number of protonic sites (8). Besides, the importance of the cations was postulated in determining the strength of the acidity. In 1963 Hirschler (9) suggested that "the polarizing action of the field of the cation tends to free (make acidic) a proton of a hydroxyl group attached to an adjacent silicon or aluminum atom, or a proton of a water molecule adsorbed on the cation itself. The greater the field strength of the cation, the stronger would be the resultant acidity". A few years later some more elaborated models were presented. Richardson (11) considered that increasing the ionic potential (e/r) of the cation results in a shift of electron charge

distribution toward the vicinity of the cation via a conduction band model. This weakens the OH bonds on the surface of the surface making them more acidic. The large number of possible environments for the hydroxyl groups induce a wide acid strength distribution. Only a small number of hydroxyl are sufficiently acidic to be active in catalysis. This fraction depends on the ionic potential of the cation. The results of Ward (12) over MgHY zeolites are explained on that basis. A second parameter which may increase the acid strength is the dehydroxylation (13,14). Lunsford (13) proposed that defect sites due to dehydroxylation act inductively on local hydroxyl groups to form strong protonic acids. Recently Jacobs and al. (15,16) suggest an alternative explanation which imply the formation of ultra active Brönsted sites during heat treatment of zeolites. Tung and McIninch (17) have discussed a different type of mechanism for the modification of acid strengths. Movements of the cations in the framework generate changes in the surface field strength and consequently in the strength of protonic sites. Freude and al. (18) apply the idea of these authors to the mobility of protons and consider a time fluctuating Brönsted acidity. The correlation between the acid strength distribution and the site environment was considered by Dempsey (19) who described a structural model to explain why close to 35% of the aluminum and sodium atoms are associated to weak acidity in Y zeolites (20,21). He relates the weak acid sites to protons associated, through O_1H hydroxyls, with the aluminum atoms of the square faces carrying two aluminum atoms in the sodalite cages.

The various models proposed belong to one of the two types, static or dynamic. In spite of the fact that the static approach has been able to explain a large number of acidity results, one must consider that the real acid sites (protonic sites) are moving continuously in the structure, the life time of a proton on a site being between 10^{-2} and 10^{-7} seconds. Hence the mean population of protons at each site results from a kind of equilibrium between the occupancy factors at the various oxygen atoms. These considerations imply that the acidic properties will be influenced both by the chemical environment of the framework oxygen atoms and by the intrinsic proton mobility. This is rather important to consider when acidity models are used in relation with catalytic properties which of course imply dynamics of the system.

As to the number of acid centers in zeolites, in the case of polyvalent exchanged materials, there is, for a large number of cations, a linear relationship between the protonic acidity concentration and electrostatic field of the cations (22,23). In a series of X and Y zeolites, it was shown that only a fraction of each acid site could be titrated (24). This allowed an efficiency of sites to be defined.

A - II - Acidity Measurement Methods. The ideal method of acidity measurement should give information on several parameters,

the nature, number, strength, location, environment and mean life time of acid sites. Hence it should be able to characterize acid centers enough precisely to differentiate which type is responsible for the selective transformation of a reactant molecule. In fact each method gives information but none fully describes the acid sites.

Spectroscopic methods have been widely used. Certainly, i.r. spectroscopy is the more usual and it has given a large number of results related to hydroxyl characterization and to Brønsted and Lewis acidity (25,26). A large number of works will be described in the next paragraphs. Acid site concentrations are generally determined semi-quantitatively. Quantitative evaluations have been recently performed (15,27). Pyridine and to a lesser extent NH_3 are the bases commonly used. Recently 2-6 dimethylpyridine was suggested as a base specific for protonic centers since steric hindrance of the nitrogen atom prevents its coordination to aluminum atoms (28). It has been employed with faujasite (29). UV spectroscopy was used to study the adsorption of various molecules on zeolites (30,31). In the case of pyridine on X zeolite with sodium cations (31) three kinds of adsorbed species characterized respectively the interactions with cations, protons and Lewis sites. It was noted that UV method have the advantage to be very sensitive but it is difficult to distinguish the positions of the respective peak maxima. Optical electronic spectroscopy was also used to differentiate protonic and non protonic sites (32). Besides the study of redox properties of zeolites (33) ESR has been applied to study atomic hydrogen formed on γ irradiation and relates it to protonic acidity (34). Relaxation and linewidth studies in NMR have been employed to characterize the proton mobility and interactions with cations (18,35-38). These studies afford a further insight into the nature of protonic acidity. It is proposed that the higher is the jump frequency (inverse mean life time at lattice oxygen atoms), the higher is the strength of the proton (18,36). It is shown that an adsorbed base such as pyridine increases (up to 60 times at 200°) the proton mobility probably because during pyridinium ion formation and decomposition a hydroxyl proton must be first attached to the pyridine molecule and then given back to another oxygen atom. It is hence suggested that investigations of proton mobility can lead to conclusions on acidity only if the study is made in the presence of basic molecules (18). NMR measurements also permits the computation of an elementary "proton capture probability" by the acceptor molecule diffusing upon the surface. This probability decreases from 1 to 0.06 after a long outgassing performed between 0° and 300°C (36) (for NH_3).

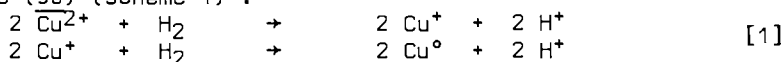
Besides the spectroscopic methods several approaches have been used to characterize acidic properties. Minachev, Bremer et al. performed several works using H_2 - D_2 exchange to study the proton mobility (39-41). The concentration of exchangeable OH groups (40,42) could also be determined. Several thermal methods have been used to study the interactions of bases with acid sites [DTA (43), calorimetry and chromatography (44-46)]. It was shown that

NH_3 or butylamine give a small heat of adsorption on cations. The distribution of the strengths of acid sites could be obtained from the heat of adsorption of benzene on progressively pyridine poisoned samples (45). A method based on the determination of the amount of oxygen used for the oxidation of NH_3 in the ammonium forms of zeolites has been described to measure the number of acid centers. It distinguishes between Brønsted and Lewis acidities (47). After the early work of Hirschler (9), titration with butylamine and colored indicators has been used (20,23,24,48,49). The method allows an easy determination of acid site concentration and strength to be done but it does not give information on the precise nature of acid centers. The question arises also as to the size of the reactants may modify the results. In fact in Y zeolites, the number of acid sites determined in this way is close to that deduced from i.r. experiments using pyridine (15). The results performed with various bases, indicators and zeolites suggest that with regard to the aperture of the zeolite channels, the size of the base molecule is more critical than that of the indicator. Assuming that at the equilibrium the base, small enough to move in the channels, neutralizes the same fraction of acid sites wherever they are located (inside or outside the particles), the large indicator molecules may detect the end of neutralization from the reaction with the only accessible sites.

Among all these methods the one which has brought the newest ideas is the NMR which demonstrated the proton mobility even in the absence of adsorbed molecule. At first the proton mobility affords a new definition of acid strength from the jump frequency values. This approach seems very interesting with regards to the changes upon heating or ultrastabilization (36). Nevertheless it is not known if the numerical value depends only on the acid strength. For example the increase in jump frequency upon pyridine adsorption is related to the help of pyridine which improves the proton migration (18). This might be compared to the high proton mobility in aqueous solutions. Secondly the proton mobility is a rather new fact which is in agreement with the idea that zeolite framework have some properties of electrolytes (50). The question arises as to whether it will be possible to proceed the analogy with acidic solutions. A third aspect of proton mobility is that it may explain some phenomena such as an unusual dehydroxylation which will be mentioned further. Among the other methods, infrared spectroscopy is the most powerful since it gives a very large number of informations on the acid sites. However the difficulty to correlate precisely infra-red results with other properties such as catalytic behavior, points out the fact that the characterization of static and definite hydroxyl groups is not precise enough to explain which protons act in the dynamic catalytic processes.

A - III Generation of Acid Sites. Acid centers are generated in various ways. 1) The thermal decomposition of ammonium exchanged zeolites yields the hydrogen form (51). Deamination in anhy-

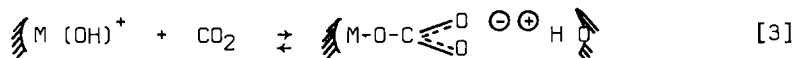
drous conditions of alkylammonium, piperidinium or pyridinium Y zeolites produces a stoichiometric hydrogen zeolite only in the case of primary alkylammonium ions. With other cations a considerable dehydroxylation is observed producing a so-called dehydroxylated zeolite with Lewis acid sites (52). This dehydroxylation effect is also observed during the adsorption of amines, particularly with pyridine (53,54). One can wonder whether the high proton mobility in the presence of pyridine (18) does not facilitate the dehydroxylation phenomena. ii) The Brønsted acidity due to the water ionization on polyvalent cations (2,25,55) already well described has been studied by various methods. NMR was applied to the calculation of the interproton distance (d_{H_2O}) in water coordinately bonded to the cations (56). In various polyvalent Y zeolites, several (up to 6) types of OH groups were found (40) differing by their concentration, acid strength and thermal stability. iii) The reduction by hydrogen of transition metal cations in zeolites was supposed to form a hydrogen zeolite (57,58). Such Brønsted acidity has been observed in an i.r. study of a hydrogen reduced $Cu^{2+}Y$ zeolite (59) (scheme 1) :



The reduction of Cu^{2+} cation with CO (59) or its self-reduction (60) gives cuprous ions and Lewis acidity. The concentration of OH groups of Y zeolites containing Ni, Co or Cu was noted to increase by reduction with hydrogen at 250-450° and to increase with the rise of the reduction temperature (61). A reduction by hydrocarbons of cations to metals with formation of protonic acidity has been shown in the case of Ni, Fe and Co zeolites during the cumene cracking. A similar reduction is postulated with Cr and Cd zeolites (62) :



iiii) Brønsted acid sites are also generated in bivalent cation-containing Y zeolites on exposure at room temperature to halide compounds (63) or at 150-400°C to CO_2 (64). In the case of n-propyl halide, acid halide is formed. The halide is fixed to the cation and H^+ is attached to an oxygen of the zeolite to give a hydroxyl group (63). In the second case, CO_2 reacts reversibly with $M(OH)^+$ resulting from water hydrolysis on Mg or Ca cations and gives an unidentate carbonate species while the hydrogen atom forms an acidic OH group with a framework oxygen atom giving i.r. bands at 3640 and 3550 cm^{-1} (64) (scheme 3) :



The various and independent ways of acid site generation show that the experimental conditions of zeolite pretreatments or acidity measurements could modify greatly the intrinsic acidity. Further this suggests that zeolite acidity may be changed by the presence of catalytic reagents (dehydroxylation by reactants, reduction of reducible cations by hydrocarbons, reaction with acidic compounds). Hence independently of aging effects, there may be

large differences in acidity between the fresh and the actual catalyst.

A-IV- Acid Site Number and Strength. The number of acid sites has been investigated by various methods (2,25,65). The method based on changes in acidic OH groups concentration has been widely and successfully used (25). Jacobs et al. (53) studied the adsorption of different amines on Na-hydrogen X and Y zeolites. They showed that adsorption involves the reaction with acidic hydroxyls, the residual sodium ions and the dehydroxylated sites. They conclude that the decrease of the integrated absorbance of amines cannot be used to determine the apparent integrated intensity of OH bands. In slightly different conditions, Bielanski et al. (27) were able to evaluate extinction coefficient of OH bands and the approximate concentrations of both types of OH groups. Irrespective to the value of Si/Al ratios and providing 50 % at least of the cations have been exchanged, the highest concentration of the 3650 cm^{-1} OH groups is equal to about 16 OH groups per unit cell, i.e. one OH group on average per hexagonal prism. Similar values were obtained by Jacobs et al. by quantitative i.r. spectroscopy (16). The same authors obtained higher values using reaction with pyridine which is postulated to titrate supercages acidic OH vibrating at 3650 cm^{-1} . They found close to 35 OH groups per unit cell for a hydrogen Y sample 80 % exchanged and heated at 400°C . The number of hydroxyls depends on the Si/Al framework ratio. Brönsted acidity deduced from i.r. bands of pyridinium ions showed similar values (15).

The titration with amine and colored indicators showed that close to 30 % of the acid sites are weak (20) in hydrogen Y zeolites. They are related to the 30 % of weakly bonded aluminum atoms easily removable upon dealumination or particular heating (20,51). The number of acid sites of the so-called aluminum-deficient, deep-bed or ultrastable zeolites has been evaluated. The comparison with hydrogen Y is not easy since simultaneously when the aluminum framework content is decreased, the thermal stability is increased and generally the sodium content is lowered. Jacobs, Uytterhoeven et al. (15) found that their deep-bed samples are less acid than HY while Topchieva et al. (49) showed that dealuminated and ultrastable samples they studied are more acidic than Y zeolite. The ratio strong/weak acidity concentration increases upon dealumination (20,46). Beaumont et al. (66) showed moreover that their dealuminated samples contain stronger Brönsted and Lewis sites than the parent hydrogen form. A higher jump frequency of protons, i.e. a higher acid strength in deep-bed Y zeolites has also been noted (36).

Other kinds of zeolites modifications imply acidity changes. With regard to decationization, Bielanski et al. (67) observed a rise in Brönsted acidity strength at exchange levels higher than 70 %. The mobility of protons was also reported to be the highest with highly exchanged HNaY zeolites (39). The decationization also leads to a reinforcement of the electron-accepting properties of

the surface (68). Changes upon steaming were noted for a number of zeolites. With rare earth X and Y zeolites there is a decrease in the number of strong acid sites while the number of sites with intermediate and weak acid strength remains unchanged (48). With Y zeolites of various Si/Al ratios the acid site concentration is also decreased (69,70). The presence of Brönsted and Lewis acidity is maintained in La zeolites even after steaming at 820°C (71). Dehydroxylation of Y zeolites upon heating increases the electron affinity of Lewis centers (72).

Hence the strength and the mobility of protons increase upon dealumination and high exchange of cations. Moreover the Lewis acidity strength is also increased by dehydroxylation. If these strength changes during decationation and dehydroxylation are logical, the increase due to dealumination and the decrease related to steaming are more difficult to be predicted. Especially in the case of steaming the reactions are complex, involving chemistry of the solid state and it would be very exiting to find a model describing the results.

The acidity determination of zeolites with rather small pores is of course complicated by the accessibility of sites particularly with pyridine. Hence Detrekoy and al. (73) showed that only 10 % of the OH groups of clinoptilolite react with pyridine. They conclude that only 10 % of the lattice OH are on the external surface. In the case of L zeolites (74) the acidity decrease at exchange levels higher than 50 % is explained in terms of a proton migration toward hidden sites in cages made free of cations by exchange. With mordenite, the restriction for pyridine reaction with the acid sites in the channels parallels the ionic radius : $H < Be < Ca < Ce$ (75). Mordenite has stronger (44,76,77) and thermally more stable (75) protonic sites than faujasite. The acidity of dealuminated mordenite measured by NH_3 chemisorption decreases roughly linearly with Al content (78).

A-V- Hydroxyl Groups in Zeolites. Assignments and Acid-Base Properties. The hydroxyl groups of faujasite type are now well described (25,26). The new information which appeared are mainly related to the refinements of the assignments of the i.r. bands and to the characterization of the hydroxyl acid and basic properties. Jacobs and Uytterhoeven (79) broke down into six different components the spectra of hydroxyls in X and Y materials. The narrow band at 3650 cm^{-1} is assigned to O_1H hydroxyl groups while the broad and asymmetric band at 3550 cm^{-1} contains components due to O_2H , O_3H and O_4H groups. In hydrolyzed zeolites (deep-bed) non acidic OH bands around 3680 and 3600 cm^{-1} are due to surface OH groups near Al defect location. The non acidic OH bands in synthetic faujasite exchanged with polyvalent cations (i.e. La) are explained on the same basis. Peri (80) reported that in ultrastable faujasite a 3700 cm^{-1} band was eliminated by NH_3 adsorption but bands at 3750 cm^{-1} and 3620 cm^{-1} , accessible to NH_3 , were relatively unaffected. Scherzer and Bass (71) studied low-soda lanthanum

Y zeolites thermally and hydrothermally treated and showed that steaming produces dealumination. The bands at 3650 and 3600 cm^{-1} are acidic (reaction with NH_3 , pyridine, NaOH) whereas the band at 3700 cm^{-1} is non acidic. The band at 3540 cm^{-1} is acidic in low-La Y zeolites but is practically non-acidic in high-La zeolites. The bands at 3700, 3650 and 3540 cm^{-1} are generated primarily by O_4 , O_1 and O_3 framework atoms respectively. The 3540 cm^{-1} band is also generated by OH groups attached to La ions. The results presented by these authors show some discrepancies which cannot be explained on the basis of very simple models. This suggests that parameters such as the thermal treatments might be as important or even more important than the chemical composition in determining the hydroxyls properties. Moreover it has been now clearly demonstrated that protons are mobile. This dynamic property may render too simple the static model of hydroxyls proposed for zeolites. One might suggest that jumping from oxygen to oxygen the protons would prefer some of these atoms for energetic reasons. Hence whatever their sources, protons could give rise to the same i.r. band, the frequency of which would be determined by the type of framework oxygen involved. Since a definite i.r. band is broad enough to include a small range of frequencies each of these bands would characterize a variety of hydroxyls with different chemical properties (acidic or non acidic) determined by the various micro-environments of the oxygen atom involved. Besides the case of these thermally treated faujasite, new results have been reported on other zeolites. In the case of non reduced Ni-hydrogen Y, Ward (81) reported a band at 3680 cm^{-1} assigned to NiOH and two bands at 3635 and 3540 cm^{-1} analogous to those observed in hydrogen Y zeolites. Deamination of NH_4X and PdNH_4X zeolites gives bands at 3660, 3625 and 3560 cm^{-1} (82). The 3625 cm^{-1} band which is not often observed increases with the extent of exchange. It is assigned to OH groups in the supercage. As to basic properties, Bielanski et Datka (83) indicated a reaction of the OH vibrating at 3660 cm^{-1} and 3565 cm^{-1} in Y zeolites with acidic compounds such as formic, acetic and benzoic acids. This points out an amphoteric property of these hydroxyls. The non acidic bands in Mg and Ca hydrogen Y zeolites, vibrating at 3685 and 3675 cm^{-1} respectively were shown to react reversibly with CO_2 . The increase in band intensity which parallels the cation content and the reversible formation of an unidentate carbonate suggest that these basic OH are linked to the cation (64) (scheme 3). The OH groups of mordenite were studied by means of i.r. spectroscopy. Two OH bands occur in NH_4 mordenite at 3637 cm^{-1} and 3740 cm^{-1} and are shifted to 3612 cm^{-1} and 3715 cm^{-1} respectively upon heating (84). Karge noted in H mordenite an acidic band at 3610 cm^{-1} and a non acidic OH band at 3640 cm^{-1} (85).

A-VI- Base Cation Interactions. Acidity of Transition Metal Zeolites. The simplest molecule adsorbed, water, is known to generate acidity through the dissociation of water on polyvalent

ions and to induce cation movement (86). In 1964, Baur (87) pointed out that in zeolites the water molecules and cations act as a mobile electrolyte solution. In fact it has now been shown that cations may also move easily in the presence of molecules other than water. It has been found that cations interact with pyridine (25) or aromatics (11). Leith et al. (88) report a copper migration after treatment of the zeolite with but-1-ene. Gallezot et al. showed very accurately that several molecules could modify the cation location and form organometallic complexes in CuY (89) and NiY (90) zeolites. A nickel ion migration in NiX zeolite has also been reported (54,91).

Due to the importance of the interactions and migrations, these effects have to be considered in determining the acidic properties of zeolites with transition metal cation. They render the evaluation of the number of base molecule reacting only with the acid sites difficult. The correlations with catalytic activity would have also to consider that cation location may differ in acidity and catalytic measurements.

Only a few works have been reported on the acidity measurements of transition metal cation zeolites (25). The protonic acidity of a series of NiHY zeolites (81) determined from the concentration of pyridinium ions follows very closely the population of the 3635 cm^{-1} hydroxyl groups. No Lewis acid sites were observed. The reduction of transition metal cation creates a new acidity as evidenced with a copper Y zeolite containing 6.5 % cupric ions (12 cations per unit cell) (59). Steinberg et al. (61) also pointed out that the concentration of OH groups of Y zeolites with Ni, Co and Cu cations is increased upon reduction with hydrogen and upon increase of reduction temperature. However with noble metals, the usual contents in catalysts will render this acidity change very small. Studies of CaHY with 0.5 % of Pt, i.e. close to 0.3 cations per unit cell, did not show any measurable acidity modifications due to the reduction of platinum with hydrogen (92). In PtY materials with a high Pt content of 6 to 14 %, Gallezot et al. (93) showed a strong NH_3Pt interaction for Pt-agglomerates 10 Å in diameter. They suggest a competitive adsorption between platinum and Brønsted sites for NH_3 .

To conclude this chapter one may first point out again the importance of pretreatments conditions and the modifications introduced by the base in the ion (cation or proton) location and mobility. Secondly the existence of basic OH groups in polyvalent forms of zeolites suggest that such basic hydroxyls might exist in other zeolites, for example US or dealuminated materials which have several non acidic OH groups near 3600 and 3700 cm^{-1} .

B - CORRELATIONS BETWEEN ACIDITY AND CATALYTIC ACTIVITY

B-I- General Comments. The research of correlations between the acidic and catalytic properties of acidic oxides has been a matter of interest for a very long time. The new field of zeolites has provoked an increase in the number of works related to the

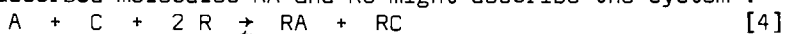
subject and very interesting results have been described (2,25). Trying to refine the description of active sites in terms of acidity, it soon appeared that the quite well defined zeolite structure did not allow in fact a rapid answer to the problem as it was expected. At the present time the published works point out the difficulty to find a direct and general correlation between acidity and activity. Besides the fact that acidity studies are performed on fresh catalysts while, often, catalytic measurements referred to aged materials, some other points which may account for this difficulty will be considered.

B-I-a- Proton Mobility. In reactions such as cracking for instance it is generally admitted that protons are active centers (15). The difficulties then arise from the proton properties themselves, particularly the proton mobility which depends on various factors : zeolite pretreatment, adsorbed species, coverage, temperature... (18,36-38). The proton motion involves two facts. At first protons in inaccessible cavities may be attracted in large cages. Secondly the jump frequency depends on the reactant. Hence it will not be easy to find a basic molecule to titrate acidity which reacts, with regard to these two parameters, in the same way than the reacting molecule. In the case of hydroxyl studies where no basic molecule is implied, correlations have been observed between OH groups concentration and activity. However, Richardson (11) suggests that only the more acidic fraction of the hydroxyls is active in cumene cracking. This fraction, up to now not easily measurable, would be increased upon the influence of parameters such as the ionic potential of the cation. Studying a series of various hydrogen or cationic forms of Y zeolites, Jacobs and al. (15) also showed that only a part of the hydroxyls act as active sites. They are "superactive sites". The authors extend the hypothesis in considering that due to "the high mobility of protons in the temperature range required for cracking, it is not possible to correlate the cracking activity with definite hydroxyl groups as observed in the infrared spectrum".

B-I-b- Number of Active Sites. While acidity measurements provide values close to 10^{20} , 10^{21} sites per g, in agreement with the number of potential acid sites, activity studies give results near these values only when complete poisoning with bases are used (2,10,11,15). The values obtained from poisoning of the more active sites are 10^2 times lower (15) while those deduced from kinetic studies are $\sim 10^6$ times lower (11). Such differences had already been reported for amorphous silica-alumina catalysts. The question arises as to whether the various measurements methods are questionable, or, if the number of active sites being actually very low, the values given by poisoning must be regarded as upper limits only.

B-I-c- Competitive Adsorption on Cation and Acid Centers. Adsorption and catalytic results suggest that there is a competi-

tive adsorption of a reactant R on the uncovered cationic (C) and acidic (A) sites of a zeolite (94). The following equilibrium with the adsorbed molecules RA and RC might describe the system :



The total rate r of the transformation of a reactant is the sum of the rates on acid and cationic sites (r_A and r_C respectively). It may be written :

$$r = r_A + r_C = k RA + k' RC \quad [5]$$

The higher the adsorption on cations (high RC) the smaller will be RA, hence also the rate r_A on acid sites. Catalysis on acid sites may then be dependent of the adsorption on cations.

The three points of these general comments suggest that in order to reach a better understanding of the correlations acidity-activity the dynamics of the system should be considered in addition to the usual "static" parameters used to define the acid centers (nature, strength, concentration, OH type). This conclusion is reinforced when one consider the facilities of cation movements in the structure.

B-II- Accessibility of Sites and Cavities. A growing number of fundamental research seems to be devoted to mordenite catalysts. Weeks et al. (84) pointed out that amorphous alumina deposits formed in the channels upon heating may considerably modify catalytic activity. Steric effects due to the pore size are noted in t-butylalcohol dehydration (95), benzene alkylation with ethylene and propylene (96), toluene disproportionation and o-xylene isomerization (75). Yashima et al. (75) conclude that due to steric hindrance, alkylbenzene reactions parallel the protonic acidity measured with pyridine but not with NH_3 . A correlation pyridine-acidity and catalytic activity is also observed with clinoptilolite in but-1-ene isomerization (73). Due to the "cage effect" in erionite, the observed rate of reaction parallels the rate of reactant diffusion through the zeolite. This implies a unique selectivity (97) (selectoforming).

B-III- Proton Catalysed Reactions. A very large number of reactions have been described. In many cases the activity is related to hydroxyl groups (15,16,73,96). With MgHY zeolites Ward (98) showed that the activity and acidity maxima occur before dehydroxylation, which differs from hydrogen Y. The difference may arise from the greater thermal stability of Mg materials. Independently of the hydroxyl stability, Jacobs et al. (15) conclude that several factors (Lewis acidity, Na^+ ions, extra-lattice aluminum) are influencing the activity per hydroxyl group. The activity in various reactions is increased in the presence of CO_2 (3,99,100). A large amount of work has been done in toluene disproportionation by Minachev et al. (3,99). Studying isooctane cracking, Mirodatos et al. (64) relate the reversible rise in catalysis to the formation of protonic hydroxyls in CO_2 atmosphere. As to the strength of sites, Jacobs et al. (15) showed that ultra-active hydroxyls

are acting in cumene cracking and toluene disproportionation. The second reaction requires hydroxyl groups with higher acidity. Moscou and Mone (48) related the increased cracking selectivity of rare earth zeolites upon steaming to the loss of strong acidity. The high o-xylene isomerization activity of MgHY materials with low sodium levels is related to the hypothesis of very strong acidity (12). It has been shown previously that acidity generation may depend on several parameters. Accordingly the catalysis could also be influenced by the nature of the charge and that of the carrier gas. There may be formation of new acid centers, dehydroxylation by reactants, cation migration, change in proton strength and location... These factors render more difficult the understanding of catalytic properties.

B-IV- Other Catalytic Sites. The Lewis acidity is often involved in catalytic processes. It may increase the protonic acid strength via an inductive effect (12) or act as active site. The alkylation of benzene with ethylene over LaY zeolites showed (101) that benzene is adsorbed on Lewis acid sites to form a charge transfer complex while ethylene is adsorbed on Brønsted acid sites to form carbonium ions. In the conversion of propylene to acetylene and butadiene (102), the catalytic activity is related to the Lewis acidity and also depends on the cations. Only few examples are known which imply basic sites in catalysis with zeolites. However zeolites, like amorphous silicas-aluminas, may contain such sites. The basic and acidic sites may then act jointly or concurrently. For example basic centers are implied in toluene alkylation with methanol and formaldehyde over X and Y zeolites (103). The side chain alkylation, poisoned by HCl gives styrene and ethylbenzene and is related to basicity (K and Rb X zeolites). The ring alkylation giving xylene, poisoned by a basic reagent such as aniline, is related to the weak acidity (Li zeolites). The basic sites are also implied in the decomposition of 2-propanol over alkali cation exchanged Y zeolites (104). Over Li or Na zeolites there is only dehydration while over K, Rb and Cs samples both dehydration and dehydrogenation occurs. The dehydration and dehydrogenation are selectively depressed by the addition of a basic reagent (pyridine) and an acidic reagent (phenol) respectively. Hence K, Rb or Cs zeolites have both basic and acid sites. As to hydrogenation-dehydrogenation reactions, unsaturated compounds may be hydrogenated over cationic zeolites (105,106). A large number of patents and papers have been published on the activity of noble-metal containing zeolites (4,57). Recent studies are concerned with the properties of unusual small agglomerates stabilized in the cages of Y zeolites (57,93,107). The electron deficiency of the clusters is suggested to explain their catalytic properties and their behavior toward poisons such as NH_3 or sulfur compounds (93, 107,108).

B-V- Miscellaneous Catalytic Studies. The large variety of reactions catalyzed by zeolites has already been described in de-

tails (1-5). The more recently mentioned are reported here. The n-hexane dehydrocyclisation activity of Te Na X catalysts has been studied. The active sites has been well described as a Te^{2-} cation in the supercage, coordinated with Na ions (109). Neale et al. (110) described the interest of the synthesis of n-isopropylidene-methylamine over ZnY zeolite and ascribed the catalytic activity to the Zn^{2+} cation. Poncelet et al. (111) report the reaction of CO and NH_3 over CaY, NH_4Y and Fe^{2+} X zeolites to give urea and aminoacids which may be related to origin of life. A very important practical reaction implies the methanol conversion to higher carbon number hydrocarbons over ZSM-5 zeolite (112). The C_5^+ hydrocarbon yield is maximized by incorporating a limited amount of a Brönsted or Lewis base. Barrer et al. (113) formed polymer-zeolite composites by the polymerization of various vinyloethers over H-mordenite and Y zeolite. Dimerization of ethylene to n-butenes proceeds selectively on Y zeolites containing zerovalent Ni and Rh highly dispersed in the framework (114). Over CrY high polymerization of ethylene occurs. Ethylene is also converted to C_5 and higher hydrocarbons over a CaNaY zeolite containing 1 % Pd introduced by ion exchange (115). The catalytic activity is sharply reduced by treatment with hydrogen or helium.

B-VI- Catalytic Properties of Aluminum-Deficient, Deep-Bed or Ultra-Stable Zeolites. Such studies have been reported for faujasite or mordenite materials (4,51). Acid leached mordenite has a high selectivity for isomerization and a low deactivation rate (116). Over aluminum-deficient Y, Beaumont et al. (21) observed no change in isooctane cracking if aluminum loss is less than ~ 35 %. Beyond, the cracking rate is decreased. The changes quite parallel the number of strong acid sites measured with colored indicators (21) or atomic hydrogen formed under γ irradiation (34). Jacobs et al. (15) found no good correlation between DH concentration and cracking or disproportionation activities for different stabilized catalysts (deep-bed, ultrastable or Al-deficient). In butene isomerization turn over numbers calculations based on poisoning experiments indicate that hydroxyl groups are more heterogeneous in hydrolyzed zeolites than in Y materials (16). Ward obtained very active and stable catalysts in aromatics isomerization and disproportionation upon defined treatments of NH_4Y (117).

It was mentioned above that the acidity (A-IV) and OH (A-V) studies of such modified zeolites made by various authors did not give exactly similar results. Discrepancies are also observed in catalytic studies. A very clear paper was presented on the chemistry of aluminum migration and removal in Y zeolites (51). It seems that in fact several modifying effects may occur simultaneously very easily. Then slight changes in experimental conditions from one laboratory to the other may result in samples with various aluminum atoms locations. The catalytic properties will be certainly better explained when the precise location of aluminum atoms will be possible.

B-VII- Catalytic Activity of Transition Metal Complexes Ions Zeolites. The chemistry and catalytic properties of transition metal complexes in zeolites has recently received considerable attention (118,119). These complexes appear to offer new reaction pathways which are in many ways more similar to catalysis by metal complexes in homogeneous media than to conventional heterogeneous catalysis. Reactions implying the cations as active centers have been early mentioned (1,2). In order to investigate the specific catalytic properties of metal ions alone it is desirable to poison the acid sites. Reactions implying ammonia which may form complexes with some transition metal cations and poison the acid centers have hence been especially successful. The formation of aniline from ammonia and chlorobenzene was shown to be closely related to the order of electronegativity or ammine complex formation constant of metal cations (120). Over CuY zeolite, the ring transformation of γ -butyrolactone and NH_3 to 2-pyrrolidinone could be related to the coordination of the reactant to the metal cation (121). Lunsford et al. (118,122) studied the role of the copper ammonia complex $[\text{Cu}(\text{NH}_3)_4]^{2+}$ in the oxidation reaction of ammonia by oxygen. It was also shown (118,123) that $[\text{Co}(\text{NH}_3)_n\text{NO}]^{2+}$ within a Y type zeolite catalyzed the reduction of NO by NH_3 at temperatures higher than 50°C . In the cyclotrimerization of acetylene over Y zeolites it was shown (124) that the active cations are those with an even number of half-filled d orbitals (Ni^{2+} , Co^+ , Fe^{2+} , Cr^{2+}). The decomposition of H_2O_2 has been used to study the activity of various Y zeolites with transition metal ions (125). The activity pattern is correlated with the transition metal redox potentials in basic solutions.

C - CONCLUSION

In the case of protonic acidity, the difficulty to find good correlations between acidity and catalytic properties suggest that the models used for the characterization of the sites may be too simple. The method consisting in the very careful definition of acid sites has not been able to explain all the catalytic properties. Hence one can wonder whether a more global approach might not be considered. The literature results suggest some remarks on the subject. Considering the proposal that zeolites behave like electrolytes (50) one may suppose that the electrolyte could be made of the atoms of the solid framework themselves and of the spaces in cavities where ions such as protons and cations are moving. Keeping in mind the idea of electrolyte some analogies between the properties of acid solutions (126) and what is known of the protonic acidity in zeolites are very striking. A first effect which is well known in acid solutions is the change in acid strength with the substituents in the acid structure. It is already well known in solid acids that for example Cl or F atoms introduced in aluminas or silicas-aluminas increase greatly their acid strength i.e. decrease the strength of the bond proton-surface. Such examples are not usual in zeolites but it is well known that polarizing

cations may increase the acid strength. The explanations of Hirschler (9) and Richardson (11), for polyvalent cations, which involve charge displacements are very similar to those involved in solutions. A second example of structure effect is related to the acid strength of polyacids in solutions. Due to interactions between negatively charged anions the strength of acidity functions decrease as the successive acidities are implied. Applied to zeolite this can explain on the same basis the existence of a scale of acidity strengths. Secondly solvent effects modify greatly acidity scale. This is due to chemical interactions between basic solvents and the proton and for a part to electrostatic interactions related to the dielectric constant of the solvents. Results on proton mobility depicted by Freude et al. (18) and Mestdgah et al. (36) show that the proton mobility is greatly dependent on the molecule carrying the proton. Besides the acid-base reaction implied, Freude et al. (18) note that pyridine induces a very higher mobility than toluene. It is the same order than the dielectric constants. Accordingly one might suggest that pyridine, besides its basic action, is acting as a dielectric which decreases the strength of the bond zeolite-H⁺. Such a "solvent effect" might be important in catalysis depending on the dielectric constant of the reactant and that of the "coke" deposit. Thirdly the proton mobility just mentioned and the cation movement are very similar to ion displacement in solutions. Of course, especially for cations, the usual mean path is certainly less than in the liquid phase. Fourthly the acid properties of solutions and kinetics of acid catalyzed reactions are also changed by salt effects. The salt effects linked to ionic strength of the solution modify the concentration of free protons in solution. The question arises as to whether an ionic strength in zeolite could not be defined and a salt effect could not be considered to explain a peculiar influence of cation concentration on activity results (94).

These three remarks suggest the hypothesis that zeolites may be considered as solids acting more or less like protonic polyacids in solution. In contrast with other solid acids, the protons, like protons in solutions, may go inside and through the zeolite framework and be in close contact with the structure atoms. This is due to the large void space and to the fact that each framework atom is also a surface atom. Moreover due to the small size of cavities (less than usual pores in oxides) the influence of the walls is very high. According to this hypothesis one suggest that the acid properties and the acid catalysis might then be described using an approach deduced of that used for solutions. The very fine description of interactions modifying the acid site which have been performed up to now might be included in activity coefficients in a manner similar to the case of activity coefficients in ion-exchange in zeolites. This model can explain on the one side a large part of the acid properties of zeolites and on the other side the difficulty to correlate catalytic results with very defined acidic sites. The basic properties of some zeolites may also be included in the model. Moreover, independently of the model pre-

sented, the results described here show that zeolites cannot be considered as static systems but that one should take into account the dynamics of their properties.

LITERATURE CITED

1. VENUTO, P.B., Adv. Chem. Ser. (1971), 102, 260.
2. RABO, J.A., POUTSMA, M.L., Adv. Chem. Ser. (1971), 102, 284.
3. MINACHEV, Kh.M., ISASKOV, Ya.I., Adv. Chem. Ser. (1973), 121, 451.
4. LEACH, H.F., Ann. Rep. Progr. Chem., Sect. A (1971) (publ. 1972), 68, 195.
5. ZEN'KOVICH, I.A., TOPCHIEVA, K.V., Sovrem. Probl. Fiz. Khim. (1975), 8, 166.
6. RABO, J.A., PICKERT, P.E., STAMIRE, D.N., BOYLE, J.E., Proc. Intern. Congr. Catalysis, 2nd, Paris (1960), 2055.
7. WEISZ, P.B., FRILETTE, V.J., J. Phys. Chem. (1960), 64, 382.
8. NORTON, C.J., Proc. Intern. Congr. Catalysis, 2nd, Paris (1960), 2073.
9. HIRSCHLER A.E., J. Catal. (1963), 2, 428 and (1968), 11, 274.
10. BORESKOVA, E.G., TOPCHIEVA, K.V., FIGUZOVA, L.I., Kin. i Kat. (1964), 5, 1115.
11. RICHARDSON, J.T., J. Catal. (1967), 9, 172 and 182 ; (1968), 11, 275.
12. WARD, J.W., J. Catal. (1972), 26, 470.
13. LUNSFORD, J.H., J. Phys. Chem. (1968), 72, 4163.
14. HOPKINS, P.D., J. Catal. (1968), 12, 325.
15. JACOBS, P.A., LEEMAN, H.E., UYTTERHOEVEN, J.B., J. Catal. (1974), 33, 17 and 31.
16. JACOBS, P.A., DECLERCK, L.J., VANDAMME, L.J., UYTTERHOEVEN, J.B., J.C.S. Faraday I (1975), 71, 1545.
17. TUNG, J.E., McININCH, E., J. Catal. (1968), 10, 166 and 175.
18. FREUDE, D., OEHME, W., SCHMIEDEL, H., STAUDTÉ, B., J. Catal. (1974), 32, 137.
19. DEMPSEY, E.J., J. Catal. (1974), 33, 497 and (1975), 39, 155.
20. BEAUMONT, R., BARTHOMEUF, D., J. Catal. (1972), 27, 45.
21. BEAUMONT, R., BARTHOMEUF, D., J. Catal. (1973), 30, 288.
22. WARD, J.W., J. Catal. (1968), 10, 34.
23. KLADNIG, W., J. Phys. Chem. (1976), 80, 262.
24. BEAUMONT, R., BARTHOMEUF, D., J. Catal. (1972), 26, 218.
25. WARD, J.W., Adv. Chem. Ser. (1971), 101, 380.
26. HUGHES, T.R., WHITE, H.M., J. Phys. Chem. (1967), 71, 2192.
27. BIELANSKI, A., BERAK, J.M., CZERWINSKA, E., OATKA, J., DRELINKIEWICZ, A., Bull. Acad. Pol. Sci. Ser. Sci. Chim. (1975), 23, 445.
28. BENESI, H.A., J. Catal. (1973), 28, 176.
29. JACOBS, P.A., HEYLEN, C.F., J. Catal. (1974), 34, 267.
30. KISELEV, A.V., KITIASHVILI, D.G., LYGIN, V.I., Kin. i Kat. (1971), 12, 1075 and (1973), 14, 262.
31. YOSHITERU KAGEYAMA, TAKAO YOTSUYANAGI, KAZUO AOMURA, J. Catal. (1975), 36, 1.

32. ZHDANOV, S.P., KOTOV, E.I., *Adv. Chem. Ser.* (1973), 121, 240.
33. FLOCKHART, B.D., MEGARRY, M.C., PINK, R.C., *Adv. Chem. Ser.* (1973), 121, 509.
34. ABOU KAIS, A., VEDRINE, J., MASSARDIER, J., DALMAI-IMELIK, G., *J. Catal.* (1974), 34, 317.
35. DEROUANE, E.G., FRAISSARD, J., FRIPIAT, J.J., STONE, W.E.E., *Catalysis Rev.* (1972), 7, 121.
36. MESTDAGH, M.M., STONE, W.E.E., FRIPIAT, J.J., *J. Catal.* (1975), 38, 358 and *J.C.S. Faraday I* (1976), 1, 154.
37. PIONTKOVSKAYA, M.A., EREMENKO, A.M., DENISENKO, G.I., NEIMARK, I.E., *Adsorbtsiya Adsorbenty, Respub. Mezhvedom SB* (1972), 1, 71 - CA 80 41178.
38. DEININGER, D., REIMANN, B., *Z. Phys. Chem. (Leipzig)* (1972), 25, 353.
39. MINACHEV, Kh.M., BREMER, H., OMITRIEV, R.V., STEINBERG, K.H., ISAKOV, Ya.I., OETIYUK, A.N., *Izv. Akad. Nauk. SSSR, Ser. Khim.* (1974), 2, 289.
40. STEINBERG, K.H., BREMER, H., HOFMANN, F., MINACHEV, Kh.M., OMITRIEV, R.V., OETIYUK, A.N., *Z. Anorg. Allg. Chem.* (1974), 404, 129 and 142.
41. HEYLEN, C.F., JACOBS, P.A., *Adv. Chem. Ser.* (1973), 121, 490.
42. KIKUCHI, E., HIROGORI, R., KIMURA, T., MORITA, Y., *Bull. Jap. Petrol. Inst.* (1973), 15, 129.
43. STEINBERG, K.H., BREMER, H., FALKE, P., *Z. Chem.* (1974), 14, 110.
44. BRUEVA, T.R., KLACHKO-GURVICH, A.L., MISHIN, I.V., RUBINSHTEIN, A.M., *Izv. Akad. Nauk. SSSR, Ser. Khim.* (1974), 6, 1254 and (1975), 4, 939.
45. NAVALIKHINA, M.O., ROMANOVSKII, B.V., TOPCHIEVA, K.V., *Kin. i Kat.* (1971), 12, 1062.
46. HUO SHI THUONG, TOPCHIEVA, K.V., ROMANOVSKII, B.V., *Kin. i Kat.* (1974), 15, 1053.
47. HILOEBRANDT, R.A., SKALA, H., *J. Catal.* (1968), 12, 61.
48. MOSCOU, L., MONE, R., *J. Catal.* (1973), 30, 417.
49. TOPCHIEVA, K.V., HUO SHI THUONG, *Zh. Fiz. Khim.* (1973), 47, 2103.
50. RABO, J.A., *Progr. Solid State Chem.* (1975), 9, 1.
51. KERR, G.T., *Adv. Chem. Ser.* (1973), 121, 219.
52. JACOBS, P.A., UYTTERHOEVEN, J.B., *J. Catal.* (1972), 26, 175.
53. JACOBS, P.A., THENG, B.K.G., UYTTERHOEVEN, J.B., *J. Catal.* (1972), 26, 191.
54. GUILLEUX, M.F., TEMPERE, J.F., DELAFOSSE, O., *J. Chim. Phys.* (1974), 6, 963.
55. PLANCK, C.J., *Proc. Intern. Congr. Catalysis, 3rd Amsterdam* (1964), 1, 727.
56. GVAKHARIYA, V.G., KULIVIDZE, V.I., TSITSISHVILI, G.V., *Dokl. Akad. Nauk. SSSR* (1975), 223, 273.
57. RABO, J.A., SCHOMAKER, V., PICKERT, P.E., *Proc. Intern. Congr. Catalysis, 3rd, Amsterdam* (1964), 2, 1264.
58. BRECK, D.M., CASTOR, C.R., MILTON, R.M., *U.S. Pat.* 3,013,990 (1961).

59. NACCACHE, C.M., BEN TAARIT, Y., J. Catal. (1971), 22, 171.
60. JACOBS, P.A., DE WILDE, W., SCHOONHEYOT, R.A., UYTTERHOEVEN, J.B., BEYER, H., J.C.S. Faraday I (1976), 72, 1221.
61. STEINBERG, K.H., MINACHEV, Kh.M., BREMER, H., OMITRIEV, R.V., DETYUK, A.N., Z. Chem (1975), 15, 372.
62. TSUTSUMI, K., FUJI, S., TAKAHASHI, H., J. Catal. (1972), 24, 8.
63. ANGELL, C.L., HOWELL, M.V., J. Phys. Chem. (1970), 74, 2737.
64. MIRODATOS, C., PICHAT, P., BARTHOMEUF, O., J. Phys. Chem. (1976), 80, 1335.
65. TURKEVICH, J., Catalysis Rev. (1967), 1, 1.
66. BEAUMONT, R., PICHAT, P., BARTHOMEUF, O., TRAMBDUZE, Y., Hightower, "Catalysis", 1, 343, North Holland Publish.Co., Amsterdam (1973).
67. BIELANSKI, A., DATKA, J., J. Catal. (1975), 37, 383.
68. RATOV, A.N., KUBASOV, A.A., TOPCHIEVA, K.V., ROSOLOVSKAYA, E.N., KALININ, V.P., Kin. i Kat. (1973), 14, 1024.
69. ZUL'FUGAROV, Z.G., ZUL'FUGAROVA, L. Sh., KAKHRAMANOVA, Ch.G., MURADOVA, S.A., ANNAGIEV, M.Kh., ASKEROV, A.G., OZHAFAROVA, E.M., OZHAFAROVA, S., YUSIFOVA, Sh.A., Mech. Hydrocarbon React. Symp. (1975), 379.
70. TOPCHIEVA, K.V., HUO SHI THUONG, Vestn. Moskov. Univ. Khim. (1974), 15, 239.
71. SCHERZER, J., BASS, J.L., J. Phys. Chem. (1975), 79, 1200.
72. BEN TAARIT, Y., NACCACHE, C., IMELIK, B., J. Chim. Phys. (1973), 70, 728.
73. DETREKOY, E.J., JACOBS, P.A., KALLO, D., UYTTERHOEVEN, J.B., J. Catal. (1974), 32, 442.
74. FRANCO PARRA, C., BALLIVET, O., BARTHOMEUF, D., J. Catal. (1975), 40, 52.
75. TATSUAKI YASHIMA, NOBUYOSHI HARA, J. Catal. (1972), 27, 329.
76. KARGE, H., KLOSE, K., Z. Phys. Chem. (1973), 83, 100.
77. HUO SHI THUONG, TOPCHIEVA, K.V., Dokl. Akad. Nauk. (1973), 211, 870.
78. THAKUR, D.K., WELLER, S.W., Adv. Chem. Ser. (1973), 121, 596.
79. JACOBS, P.A., UYTTERHOEVEN, J., J.C.S. Faraday I (1973), 69, 359 and 379.
80. PERI, J.B., Hightower, "Catalysis", 1, 329, North Holland Publ. Co., Amsterdam, (1973).
81. WARD, J.W., J. Catal. (1975), 38, 351.
82. GUILLEUX, M.F., DELAFOSSE, D., J.C.S. Faraday I (1975), 71, 1777.
83. BIELANSKI, A., DATKA, J., J. Catal. (1974), 32, 183.
84. WEEKS, T.J., HILLERY, H.F., BDLTON, A.P., J.C.S. Faraday I (1975), 10, 2051.
85. KARGE, H.G., Z. Phys. Chem. (1975), 95, 241.
86. SMITH, J.V., Adv. Chem. Ser. (1971), 101, 171.
87. BAUR, W.H., Am. Mineralogist (1964), 49, 697.
88. LEITH, I.R., KEMBALL, C., LEACH, H.F., J.C.S. Chem. Comm. (1971), 8, 407.
89. GALLEZOT, P., BEN TAARIT, Y., IMELIK, B., J. Catal. (1972), 26, 295.

90. GALLEZOT, P., IMELIK, B., *J. Phys. Chem.* (1973), 77, 652 and 2556.
91. YOKO SENDOOA, YOSHIO ONO, TOMINAGE KEII, *J. Catal.* (1975), 39, 357.
92. TOPCHIEVA, K.V., DOROGOCHINSKAYA, V.A., HUO SHI THUONG, *Zh. Fiz. Khim.* (1974), 48, 182.
93. GALLEZOT, P., DATKA, J., MASSARDIER, J., PRIMET, M., IMELIK, B., 6th Intern. Congr. Catalysis, London 1976, paper A-11.
94. BEAUMONT, R., HA, B.H., BARTHOMEUF, D., *J. Catal.* (1975), 40, 160.
95. IGNACE, J.W., GATES, B.C., *J. Catal.* (1973), 29, 292.
96. BECKER, K.A., KARGE, H.G., STREUBEL, W.D., *J. Catal.* (1973), 28, 403.
97. CHEN, N.Y., GARWOOD, W.E., *Adv. Chem. Ser.* (1973), 121, 575.
98. WARD, J.W., *J. Catal.* (1972), 26, 451.
99. MINACHEV, Kh.M., ISAGULYANTS, G.V., ISAKOV, Ya.I., USACHEV, N.Ya., ROZHDESTVENSKAYA, N.N., *Izv. Akad. Nauk. SSSR, Ser. Khim.* (1974), 1, 42.
100. FRILETTE, V.J., MUNNS, G.W. Jr., *J. Catal.* (1965), 4, 504.
101. MORITA YOSHIRO, MATSUMOTO HIROSHIGE, KIMURA TAKAYOSHI, KATO FUMIYOSHI, TAKAYASU MASAMI, *Bull. Jap. Petrol. Inst.* (1973), 15, 37.
102. MŌCHIOA ISAO, IKEDA YOSHIMASA, FUJITSU HIROSHI, TAKESHITA KENJIROU, *Chem. Lett.* (1975), 12, 1213.
103. TATSUAKI YASHIMA, KEIICHI SATO, TOMOKI HAYASAHARA, NOBUYOSHI HARA, *J. Catal.* (1972), 26, 303.
104. TATSUAKI YASHIMA, HISAKI SUZUKI, NOBUYOSHI HARA, *J. Catal.* (1974), 33, 486.
105. TOPCHIEVA, K.V., ROSOLOVSKAYA, E.N., SHAKHNOVSKAYA, O.L., *Sovrem. Problem. Fiz. Khim.* (1975), 8, 199.
106. MINACHEV, Kh.M., KHDDAKOV, Yu.S., SAVCHENKO, B.M., NESTEROV, V.K., *Izv. Akad. Nauk. SSSR, Ser. Khim.* (1975), 8, 1722 and references therein.
107. DALLA BETTA, R.A., BOUDART, M., Hightower "Catalysis", 2, 1329, North Holland Pub. Co., Amsterdam (1973).
108. FIGUERAS, F., GOMEZ, R., PRIMET, M., *Adv. Chem. Ser.* (1973), 121, 480.
109. SILVESTRI, A.J., SMITH, R.L., *J. Catal.* (1973), 29, 316.
110. NEALE, R.S., ELEK, L., MALZ, R.E. Jr., *J. Catal.* (1972), 27, 432.
111. PONCELET, G., VAN ASSCHE, A.I., FRIPIAT, J.J., *Origins of life* (1975), 6, 401.
112. CHANG, C.D., LANG, W.H., U.S. 3,899,544 (1975).
113. BARRER, R.M., OEI, A.T.T., *J. Catal.* (1973), 30, 40 and (1974), 34, 19.
114. TATSUAKI YASHIMA, YOSHIHISA USHIDA, MIKIO EBISAWA, NOBUYOSHI HARA, *J. Catal.* (1975), 36, 320.
115. LAPIDUS, A.L., MAL'TSEV, V.V., GARANIN, V.I., MINACHEV, Kh. M., EIDUS, Ya.T., *Izv. Akad. Nauk. SSSR, Ser. Khim.* (1975), 12, 2819.

116. BIERENBAUM, H.S., PARTRIDGE, R.D., WEISS, A.H., Adv. Chem. Ser. (1973), 121, 605.
117. WARD, J.W., U.S. 3,887,630 (1975).
118. LUNSFORD, J.H., Catal. Rev.-Sci. Eng. (1975), 12, 137.
119. KELLERMAN, R., KLIER, K., Surf. Defect. Prop. Solids (1975), 4, 1.
120. KOU HATADA, YOSHIO ONO, TOMINAGA KEII, Adv. Chem. Ser. (1973), 121, 501.
121. KOU HATADA, MASATOSHI SHIMADA, YOSHIO ONO, TOMINAGA KEII, J. Catal. (1975), 37, 166.
122. WILLAMSON, W.B., FLÉNTGE, D.R., LUNSFORD, J.H., J. Catal. (1975), 37, 258.
123. WINDHORST, K.A., LUNSFORD, J.H., J.C.S. Chem. Comm. (1975), 20, 852.
124. BESOUKHANOVA, T., PICHAT, P., MATHIEU, M.V., IMELIK, B., J. Chim. Phys. (1974), 5, 751.
125. MOCHIDA ISAO, TAKESHITA KENJIRO, J. Phys. Chem. (1974), 78, 1653.
126. BELL, R.P., "The proton in chemistry", Chapman and Hall, London (1973).

Transition Metal Complexes in Zeolites

JACK H. LUNSFORD

Department of Chemistry, Texas A&M University, College Station, Tex. 77843

ABSTRACT

Transition metal complexes may either be synthesized within the zeolitic cavities or exchanged in as complex cations. Complexes with metal ions of the first transition series are reviewed.

Introduction

Transition metal complexes in zeolites have long been proposed as reactive intermediates in heterogeneous catalysis; however, detailed studies of such complexes have been carried out only in recent years. A number of different complexes have now been characterized by various types of spectroscopy and by X-ray diffraction techniques. At least four review articles have been devoted to complexes in zeolites, with each article emphasizing a particular aspect of the problem (1-4). In the present review an attempt will be made to draw together much of the spectroscopic, structural and reaction data for transition metal complexes in zeolites. We will restrict our attention to those complexes in which at least one ligand other than water or an oxide ion is present. Furthermore, only the first transition series will be considered here, although a limited amount of work has been done on complexes of ruthenium (5), osmium (5) and silver (6,7).

In the formation of these complexes the zeolite framework may function as a ligand, an anion and a solvent. Usually the zeolite plays two or even three of these roles, simultaneously. One of the more surprising features of this work has been the ease with which neutral molecules may replace the oxide ions of the lattice as ligands, forming more stable complexes. In order to accommodate the larger ligands the metal ion may move at moderate temperatures to sites in or on the surface of the large cavities where there is adequate volume for complex formation.

Furthermore, metal ions in the zeolite offer an opportunity to form complexes which have unusual symmetries and coordination numbers. Besides having significance in inorganic chemistry such complexes, coupled with other restraints in zeolites, offer some interesting possibilities as catalysts for reactions involving small molecules. In other cases the added ligand may fully coordinate with the metal ion, forming complexes very similar to those observed in more conventional solvents.

Most of the complexes studied up to this time have been synthesized by adding a ligand to a dehydrated zeolite; however, it has also been demonstrated that a cationic complex may first be formed in solution and subsequently exchanged into the zeolite. The stability of the complex in the zeolite may be significantly altered with respect to its stability in a more conventional solvent such as water. This has a marked effect on the ion exchange equilibria as shown in a communication by Pleysier and Cremers (8), which was presented at the 3rd International Conference.

In the following sections the complexes will be treated according to the metal ion involved. Emphasis on complexes with copper and cobalt ions reflects the distribution of papers on the subject.

Copper Complexes

Copper(II) Ammine Complexes. In aqueous solution Cu^{2+} ions form at least three ammine complexes, $[\text{Cu}(\text{II})(\text{NH}_3)_4]^{2+}$, $[\text{Cu}(\text{II})(\text{NH}_3)_5]^{2+}$, and $[\text{Cu}(\text{II})(\text{NH}_3)_6]^{2+}$ of which the tetraammine is the most stable. In a dehydrated Y-type zeolite the Cu^{2+} ions prefer site I', according to X-ray diffraction data (9), and even at low exchange levels at least two different forms of the copper may be detected by epr spectroscopy. Upon the addition of excess ammonia to a CuNaY zeolite, the pale green color changes to the characteristic blue color of the copper-ammine complex and the epr spectrum indicates that at low exchange levels all of the copper is present as the square planar $[\text{Cu}(\text{II})(\text{NH}_3)_4]^{2+}$ ion in the zeolite.

In such a complex the unpaired electron is expected to be in a $d_{x^2-y^2}$ orbital. The four equivalent ammonia molecules in the x,y plane of the molecule give rise to the nitrogen superhyperfine structure as depicted in Figure 1 (10). Ammonia molecules in the 5th and 6th coordination sites would not be expected to give additional superhyperfine lines, although the g values and copper hyperfine splitting would be expected to change if one or two additional ligands were added. The ir spectrum of the copper ammine system provides additional evidence that with stoichiometric or excess NH_3 the square planar complex is formed (10).

Most investigators now agree that the square-planar tetraammine complex is formed in the presence of excess ammonia, but

its location in the zeolite remains open to debate. Since the sodalite cage has a free diameter of 6.6 Å, and the longest distance across the square-planar complex is approximately 5.5 Å, it is conceivable that the complex is in the sodalite cage. We believe, however, that the experimental evidence favors the formation of most of the complexes in the large cavities. The strongest piece of evidence which indicates this viewpoint is the "decoupling" of the exchange-coupled Cu^{2+} ions as indicated by epr data (10). For such decoupling to occur upon adsorption of ammonia, the copper ions must move apart from one another and at least a part of the complexes must reside in the large cavities.

Similar results have been obtained with copper(II) in an X-type zeolite, except that not all of the Cu^{2+} was complexed upon addition of excess NH_3 (11). Furthermore, the g values of g_{\parallel} for the complex in the X zeolite is somewhat greater than the value observed for the complex in the Y zeolite, as indicated in Table I, but the difference is within the range observed for tetrammines having different anions.

Even with less than a stoichiometric amount of NH_3 the $[\text{Cu}(\text{II})(\text{NH}_3)_4]^{2+}$ complex is formed, provided the adsorption is carried out near 36°C. A linear increase in both the epr and the ir spectra was observed up to the stoichiometric amount of NH_3 . At this point the intensity of the spectra ceased to increase with the addition of excess ligand (10).

Vedrine *et al.* (15) have studied the temperature dependence of the hyperfine coupling for copper ammine complexes in a Y-type zeolite. They used epr data to calculate $[\nu(\text{Cu-N})]$, the stretching frequency of the copper-nitrogen bond. The calculated frequencies agreed well with the frequencies observed in their infrared experiments, although the calculated frequencies range from 100 to 300 cm^{-1} below $[\nu(\text{Cu-N})]$ observed in the analogous inorganic salts. Hydrogen bonding of the ammonia molecule with lattice oxygens was given as the primary reason for such large shifts in frequency. The frequency for the copper-nitrogen stretch was greater for a sample with excess ammonia present than for a sample in which the excess had been removed. The authors reason that when larger amounts of ammonia are present the complex is located in the supercage, while at lower ammonia coverage the complex is located in the sodalite cages where the hydrogen bonding becomes a factor.

Gallezot *et al.* (9) have used X-ray diffraction techniques to study the migration of cupric ions upon adsorption of various ligands. A sample was equilibrated with an excess of ammonia, and then the excess ammonia was removed by pumping at room temperature for an unspecified period of time. Analysis of this sample indicated that most of the copper was in site S_{11} , as observed for the dehydrated zeolite. The authors point out that ammonia molecules can enter the sodalite cages to coordinate with cupric ions; however, they suggest that upon addition of a

Table I. Spectroscopic Parameters for Copper Amine Complexes in Zeolites.

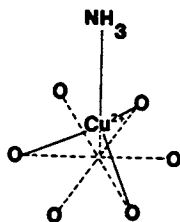
Complex	g Values		Hyperfine Structure ^a				Infrared Bands ^b	Optical Bands ^c	Ref.
	g	g _⊥	A _{Cu} A	A _{Cu} A _⊥	A _N A	A _N A _⊥			
[Cu(II)NH ₃] ²⁺ Y	2.01-2.04	2.24-2.25	141				1260		<u>12,13</u>
[Cu(II)(NH ₃) ₄] ²⁺ Y	2.23-2.25	2.002-2.04	168-175 ^d	14-15	14		1275, 311		<u>10,12-15</u>
[Cu(II)(ND ₃) ₄] ²⁺ Y	2.236	2.035	172 ^e , 184 ^f	20	12.4	9			<u>10</u>
[Cu(II)(NH ₃) ₄] ²⁺ X	2.284	2.02	154						<u>11</u>
[Cu(II)(me) ₄] ²⁺ Y ^g	2.23	2.02	167						<u>13</u>
[Cu(II)(et) ₄] ²⁺ Y ^h	2.22-2.23	2.02	170						<u>13</u>
[Cu(II)(en) ₂] ²⁺ Y ⁱ							15,300		
[Cu(II)(en) ₂] ²⁺ X (hyd)	2.268	2.053	165	14			15,300		<u>16</u>
[Cu(II)(en) ₂] ²⁺ X (dehyd)	2.239	2.047	173	23			15,300		<u>16</u>
[Cu(II)(en) ₂] ²⁺ Y	2.194	2.035	190	30			18,300		<u>16</u>
[Cu(II)(en) ₂] ²⁺ X	2.176	2.034	199	40			18,300		<u>16</u>
[Cu(II)(en) ₃] ²⁺ Y	2.206	2.043	172	18			16,200		<u>16</u>
[Cu(II)(en) ₃] ²⁺ X	2.209	2.046	168	25			16,800		<u>16</u>

<u>Complex</u>	<u>g Values</u>	<u>Hyperfine Structure^a</u>	<u>Infrared^b Bands</u>	<u>Optical^c Bands</u>	<u>Ref.</u>
[Cu(II) (py) ₄] ²⁺ yj	g 2.24-2.25 g _⊥	A Cu I AN I A N	309		<u>12,14,15</u>
[Cu(II) (py) ₄] ²⁺ x	2.253	2.002-2.03 176-187 ^d 16-17			<u>11</u>

a in units of gauss; b in units of cm⁻¹; c in units of cm⁻¹; d hyperfine splitting is a function of temperature and exchange level; e ⁶³Cu; f ⁶⁵Cu; g me = monoethylamine; h et = monoethylamine; i en = ethylenediamine; j py = pyridine.

large excess of ammonia the cupric ions migrate toward the supercages.

Upon desorption of ammonia at 100°C two groups (12,13) have observed that an inversion of the values for g_{\parallel} and g_{\perp} occurs (Table I). This inversion of g values was attributed by Vansant and Lunsford (13) to the change in symmetry from square planar to distorted tetrahedral in which the copper ion is coordinated to one ammonia molecule and three O_2 or O_4 lattice oxygens (I). Adsorption data indicated that there was approx-



(I)

imately one ammonia molecule per cupric ion in the sample.

Copper(II) Amine and Pyridine Complexes. Monomethylamine (me) and monoethylamine (et) molecules also react with Cu^{2+} ions in a Y-type zeolite, forming complexes with magnetic parameters listed in Table I, which are similar to those observed for $[Cu(II)(NH_3)_4]^{2+}$ (13). Because of size limitations these copper (II)-amines must be located in the large cavities of the zeolite. Only part of the copper ions react with the amines. Furthermore, it was observed that the covalency of the Cu^{2+} ligand bond and the density of the unpaired electron on the nitrogen increased with increasing ligand size.

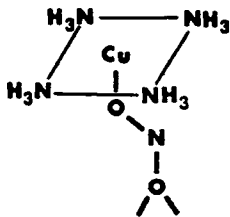
In contrast to the previous work in which the amine ligand was added from the gas phase to a CuY zeolite, one may also form a complex in solution and exchange it into the zeolite. $[Cu(II)(en)_2]^{2+}$ (en = ethylenediamine) complexes have been exchanged into both X- and Y-type zeolites and studied by epr and reflectance spectroscopy (16). At low exchange levels the $[Cu(II)(en)]^{2+}$ complex was stable only in the X zeolite, but at higher loadings it was also stable in the Y zeolite. The $[Cu(II)(en)_3]^{2+}$ complex was formed by adsorption of excess en at 100°C.

Several groups (11,12,14,15) have studied the formation of the $[Cu(II)(py)_4]^{2+}$ (py = pyridine) complex in zeolites. Due to steric considerations this complex must also be located in the supercage. The epr spectrum of the complex has a large number of well-resolved hyperfine lines in the high-field region of the spectrum due to the hyperfine splitting of the Cu and the superhyperfine splitting of the N nuclei. An analysis of the spectra indicates greater covalent bonding of the Cu^{2+} with py than with NH_3 in the Y zeolite, but the reverse was noted in the X

zeolite. Gallezot *et al.* (9) observed by X-ray diffraction that py induced a significant migration of copper ions from S_I and S_{II} sites, presumably to the supercages where they interact with adsorbed molecules. These authors suggest that the formation of the organometallic complex is accompanied by a proton transfer to the framework oxygen atoms, which they believe is necessary to neutralize the negative charge on the zeolite.

Copper(II) Complexes with Nitric Oxide. Naccache and co-workers (17) have noted that Cu^{2+} ions in a dehydrated zeolite react with NO molecules to form a complex which may be described as $[Cu(I)NO^+]^{2+}$, where it is assumed that the copper ion also is coordinated to the zeolite. The nitric oxide stretching vibration occurred at 1918 cm^{-1} , which is characteristic of coordinated NO^+ . As expected because of spin-spin interaction, the Cu^{2+} epr signal intensity decreased as NO was adsorbed on the zeolite at room temperature. Desorption of the NO restored the Cu^{2+} spectrum.

While studying the activity of the CuY zeolites as catalysts for the reduction of NO by NH_3 , Williamson and Lunsford (18) noted that the addition of NO to $[Cu(II)(NH_3)_4]^{2+}$ complexes within a zeolite did not result in the formation of a nitrosyl ligand. This is consistent with the observation of Enemark and Feltham (19) that no d^9 or d^{10} metal nitrosyl complexes with C_{4v} symmetry have been observed. The addition of 50 torr of NO to a zeolite containing $[Cu(II)(NH_3)_4]^{2+}$ resulted in the formation of weak ir bands at 1240 and 1330 cm^{-1} , suggesting that either a nitrite ion or a bridging nitro ligand may be formed between the square planar complex and the zeolite as depicted in II (18). A symmetric epr signal with $g_{iso} = 2.120$ was observed



(II)

after addition of NH_3 and NO to a CuY zeolite, followed by brief evacuation of the gas phase (the evacuation of NH_3 being the critical factor). The sample turns from blue to green as this species is formed. A tetrahedral complex is believed to be formed in which Cu^{2+} is bonded to three NH_3 ligands and a NO_2^- ion. The NO_2^- ion apparently lifts the copper ammine away from the walls of the zeolite supercage, and thus gives rise to motional averaging which would result in the symmetric signal.

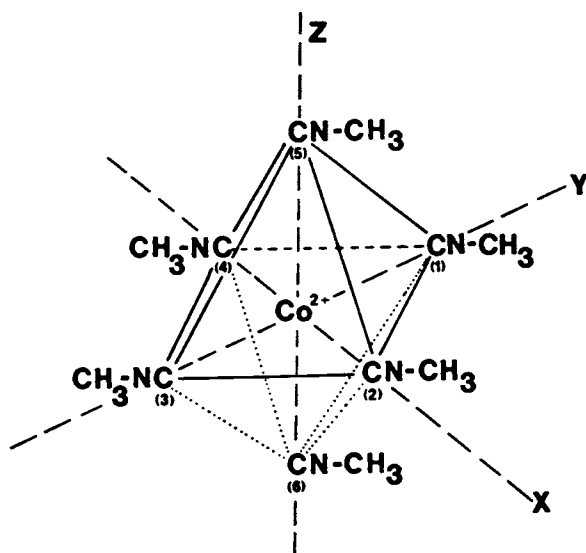
Copper(I) Complexes with Nitric Oxide and Carbon Monoxide.

Copper(II) may be reduced to copper(I) in a Y-type zeolite by heating the material in CO at 500°C. The resulting Cu^+ forms a weak complex with NO at temperatures below 150°K. The epr spectra of the complex was independently reported by Chao and Lunsford (20) and by Naccache, Che, and Ben Taarit (21). In the latter paper a value of $g_{||} = 1.74$ was incorrectly assigned. As indicated in Table II, the copper hyperfine splitting suggests considerable spin density on the metal ion, and the epr spectrum has been interpreted by assuming partial localization of the unpaired electron in a $3d_{z^2}4s$ orbital.

Unlike the case with NO, copper(I) forms a more stable complex with CO as observed by Huang (26). This complex is characterized by a very strong infrared band at 2160 cm^{-1} which is at a considerably higher wave number than normally found in copper(I) carbonyls. The Cu^+ ions are believed to be located at sites in the zeolite, where σ bonding with the lone pair on the carbon is allowed, but back donation through π bonds is prevented by the oxide ions. Prior adsorption of ammonia pulls the copper out into the supercage, where the more usual type of backbonding is allowed, thus a band at 2080 cm^{-1} is observed.

Cobalt Complexes

Cobalt(II) Complexes with Methylisocyanide. Both the penta- and hexacoordinated methylisocyanide complexes (IV) have been



(III)

Table II. Spectroscopic Parameters for Nitrosyl Complexes in Zeolites.

<u>Complex</u>	<u>g Values</u>		<u>Copper Hyperfine Structure^a</u>		<u>Infrared Bands^b</u>	<u>Ref.</u>
	$g_{ }$	g_{\perp}	$A_{ }$	A_{\perp}		
[Cu(I)NO] ⁺ Y	1.89	2.01	240	190		<u>20,21</u>
[Cu(I)NO ⁺] ²⁺ Y					1918	<u>21</u>
[Co(II)(NO) ₂] ²⁺ Y					1910,1830	<u>22</u>
[Co(II)(NH ₃)(NO) ₂] ²⁺ Y					1880,1800	<u>22</u>
[Co(III)(NH ₃) _n NO ⁻] ²⁺ Y					1710	<u>12</u>
[Cr(I)NO ⁺] ²⁺ Y	1.917	2.000			1780-1760	<u>23</u>
[Cr(II)(NO) _x] ²⁺ Y					1896,1780-1760	<u>23</u>
[Ni(I)NO ⁺] ²⁺ Y	2.41, 2.15, 2.33	2.16			1892	<u>23,24</u>
[Fe(I)NO ⁺] ²⁺ Y(S=3/2)	2.003	4.07			1890	<u>25</u>
[Fe(I)NO ⁺] ²⁺ Y(S=1/2)	2.015, 2.055, 2.089				1778	<u>25</u>
[Fe(II)(NO) ₂] ²⁺ Y					1930,1822	<u>25</u>

^a in units of gauss; ^b in units of cm⁻¹.

formed in Y-type zeolites (27). These complexes have characteristic epr spectra which allow an unambiguous identification. The $[\text{Co}(\text{II})(\text{CH}_3\text{NC})_6]^{2+}$ complex is formed by adsorption of excess methylisocyanide from the gas phase. Desorption of excess methylisocyanide at 100°C results in the loss of one ligand, and the formation of the penta- complex. These complexes inside the zeolite cavities have essentially C_{4v} symmetry and are very stable. Apparently the unoccupied sixth coordination site of the $[\text{Co}(\text{II})(\text{CH}_3\text{NC})_5]^{2+}$ complex interacts with the zeolite, making it inaccessible for other ligands. The magnetic parameters for the penta- and hexacoordinated complexes in a zeolite and other solvents are compared in Table III.

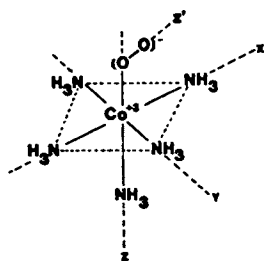
From this study one may conclude that it is possible to form fully coordinated complexes within the large cavities of a zeolite, and that the framework oxygens need not be in the first coordination sphere of the metal ion. The resulting complex is apparently able to effectively balance the charge in

Table III. Magnetic Parameters for Some Cobalt(II) Isocyanide Complexes

<u>Complex</u>	<u>Solvent</u>	g_{\perp}	g_{\parallel}	a_{\perp}, G	a_{\parallel}, G	<u>Ref.</u>
$[\text{Co}(\text{CH}_3\text{NC})_5]^{2+}$	Zeolite	2.163	2.003	89	-32	27
$[\text{Co}(\text{CH}_3\text{CH}_2\text{NC})_5]^{2+}$	Methylene Chloride	2.127	2.006	80	-50	28
$[\text{Co}(\text{CN})_5]^{3-}$	Water	2.161	2.005	89	-30	28
$[\text{Co}(\text{CH}_3\text{NC})_6]^{2+}$	Zeolite	2.087	2.007	67	-73	27
$[\text{Co}(\text{CH}_3\text{CH}_2\text{NC})_6]^{2+}$	Ethyl Isocyanide	2.089	2.005	64	-70	28

the zeolite, and at low exchange levels there is no reason to expect that the ligands ionize or dissociate to form protons.

Cobalt(II) Amine Oxygen Adducts. Monomeric 1:1 cobalt oxygen adducts have been stabilized in solution by using macrocyclic polydentate ligands, but with smaller ligands the complexes rapidly dimerize. Because of the restriction to motion in a zeolite, it has been possible to synthesize these complexes using simple amines as ligands. Lunsford and coworkers (29-31) have demonstrated the reversible formation of low-spin $[\text{Co}(\text{III})\text{L}_n\text{O}_2]^{2+}$ adducts within the large cavities of a $\text{Co}(\text{II})\text{Y}$ zeolite, where $\text{L} = \text{NH}_3$, CH_3NH_2 , $n\text{-CH}_3\text{CH}_2\text{CH}_2\text{NH}_2$ and $\text{H}_2\text{NCH}_2\text{CH}_2\text{NH}_2$ (en). For all but the latter ligand n is probably equal to 5 and for en n is equal to 2. The structure of the ammine complex is believed to be (29):



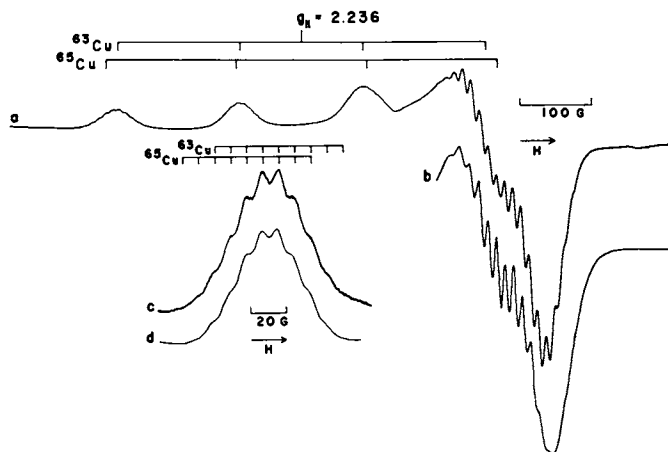
(IV)

This complex was formed by the adsorption of excess ammonia at 25°C into a dehydrated Co^{II}Y zeolite, followed by exposure to about 10 torr of oxygen at -78°C. The epr spectrum of the complex indicates almost complete transfer of an electron from Co²⁺ to the oxygen moiety. As depicted in (IV) the two oxygens are nonequivalent. Brief evacuation at 25°C caused immediate removal of the oxygen adduct, but the complex was restored by further exposure to oxygen at -78°C.

Even in the zeolite there is sufficient motion of the complexes at 26°C to allow the formation of the dimeric μ -superoxo $[L_xCo(III)O_2Co(III)L_x]^{5+}$ adducts with ammonia and monomethylamine ligands, but not with n-propylamine or ethylenediamine ligands (30). The en is stable in the presence of O₂ at temperatures up to 70°C. Concentrations up to nearly one complex per large cavity have been achieved (31).

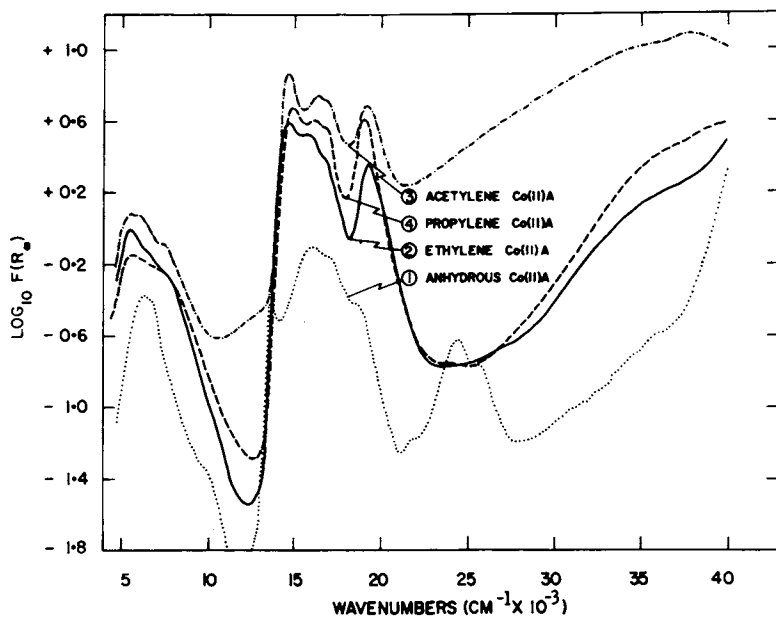
Cobalt(II) Complexes with Olefins and Acetylene. Cobalt(II) ions form well defined π -bonded complexes with simple olefins and acetylenes in A-type zeolites (32). Adsorption isotherms at 23°C indicate that one ethylene molecule is complexed to each cobalt ion. The optical spectra of the complexes shown in Figure 2 indicates the formation of a tetrahedral-type complex with a perturbation which lowers the symmetry from T_d to C₁. The cobalt is bonded to three oxide ions of the zeolite at the base of a trigonal pyramid, with the C-C internuclear axis being perpendicular to the C₃ axis of the oxygen ring. The spectra indicate that the ethylene molecule is rapidly rotating around this C₃ axis. Propylene, cis-2-butene, trans, 2-butene and acetylene form similar complexes to ethylene; however, the methyl groups tend to sterically hinder the π bonding of the olefin to the Co²⁺ ion. The spectrum of complexed acetylene also indicates extensive charge transfer and a more complex bonding than observed with the simple olefins.

Similar complexes with acetylene have also been observed by X-ray diffraction for NaA (33), Mn(II)A (34) and Co(II)A (34) zeolites and with ethylene for Co(II)A (35). These results also demonstrate that the cation moves toward the adsorbed mole-



Journal of Physical Chemistry

Figure 1. Epr spectrum of CuY with 350-torr ND_3 . (a), Experimental spectrum; (b), simulated spectrum in the perpendicular region; (c), low-field component with the receiver gain three times the value of spectrum a; (d), simulated spectrum of the low-field component (10).



Journal of Chemical Physics

Figure 2. The diffuse reflectance electronic spectra of anhydrous Co(II) -exchanged zeolite 4A (1) and of the ethylene (2), acetylene (3), and propylene (4) zeolitic Co(II)A complexes. The ordinates represent the experimental absorption intensities (32).

cule, thus entering a distorted tetrahedral symmetry. Seff attributes the bond to the polarization of the π -orbitals of the hydrocarbon by the cation in the zeolite.

Cobalt(II) Complexes with Nitric Oxide. In a Y-type zeolite Co^{2+} ions react to form a dinitrosyl complex which is characterized by infrared bands at 1830 and 1910 cm^{-1} (22); whereas, in an A-type zeolite a mononitrosyl complex is formed, having νNO at 1860 cm^{-1} (35). Seff (4) has used X-ray diffraction techniques to determine the geometric structure of the latter complex. As depicted in Figure 3 the CoNO angle is approximately 140° and the bond lengths are 2.4 Å for Co-N and 1.5 Å for N-O. The Co^{2+} ion is located only slightly out of the plane of three oxygens in the six-membered ring. Seff has proposed the formation of a $[\text{Co(III)NO}]^{2+}$ complex.

The dinitrosyl complexes in the Y-type zeolite are unreactive with molecular oxygen, which indicates that they are located within the sodalite unit (22). The formation of these two significantly different complexes with NO illustrates the dramatic role which may be played by the zeolite framework, provided the oxide ions are involved as ligands.

The addition of one NH_3 molecule per Co^{2+} ion in a Y-type zeolite, followed by the adsorption of NO resulted in the formation of a $[\text{Co(II)(NH}_3)(\text{NO})_2]^{2+}$ complex with infrared bands at 1800 and 1880 cm^{-1} (22). The shift to lower wave numbers may be explained in terms of an increase in electron density on the nitrosyl ligand. The addition of excess ammonia, followed by nitric oxide, led to the formation of a mononitrosyl complex described as $[\text{Co(III)(NH}_3)_n\text{NO}]^{2+}$ with an ir band at 1710 cm^{-1} . Here n is either 4 or 5. The intramolecular reaction of NO with NH_3 in both of these complexes leads to the formation of N_2 and H_2O at 25°C. These cobalt ammine nitrosyl complexes are effective catalysts for the reduction of NO by NH_3 (37).

Cobalt(II) Complexes with Carbon Monoxide. From X-ray diffraction data a $[\text{Co(II)CO}]^{2+}$ complex has been accurately described by Riley and Seff (38). Upon addition of excess CO to a Co(II)A zeolite the Co^{2+} ion moves from nearly trigonal-planar symmetry to more tetrahedral symmetry with linear coordination to the CO molecule. The relatively long Co^{2+} to C bond distance of 2.29 Å implies a weak interaction, presumably because the d orbitals of the metal ion are contracted and the π back-bonding is eliminated. These results and the previous work of Huang (26) on copper(I) carbonyls suggest that the absence of π back-bonding may be common to carbonyl complexes in zeolites.

Chromium Complexes

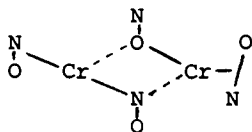
Chromium(II) Complexes with Oxygen. After dehydration Cr^{2+} ions in an A-type zeolite are believed to be coordinated to

three oxygen atoms (D_{3h} symmetry) in the six-membered ring which connects the sodalite unit with the large cavity. Klier and co-workers (39) have shown that molecular oxygen coordinates reversibly with this metal ion, presumably by the transfer of an electron as described earlier for the cobalt(II)-oxygen complexes. The adsorption isotherm is depicted in Figure 4. At room temperature the magnetic moment decreases from 5.0 to 3.7 BM, indicating spin pairing between the chromium ion and the oxygen radical anion. The electronic spectrum is interpreted as a transformation from a d^4 ion in D_{3h} symmetry to a d^3 ion in C_{1v} symmetry.

At 150°C oxygen or nitrous oxide react with anhydrous Cr(II)A to produce a complex which is believed to be $[Cr(IV)O^-]^{2+}$ where the chromium ion is also coordinated to three oxygens of the zeolite framework. This complex can be reduced to the original Cr(II)A complex by carbon monoxide at 300°C with the liberation of carbon dioxide, thus providing a pathway for the catalytic oxidation of carbon monoxide.

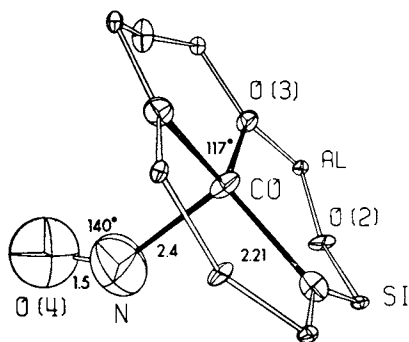
Chromium(II) Complexes with Nitric Oxide. According to Naccache and Ben Taarit (23) chromium(II) ions may be formed in zeolite Y and mordenite by the exchange of Cr^{3+} , followed by dehydration and reduction at 500°C in hydrogen. Adsorption of NO at room temperature results in the formation of a strong epr signal which has been attributed to $[Cr(I)NO^+]^{2+}$. The d^5 chromium(I) is apparently in the low spin $S = 1/2$ state, and the nitric oxide is effectively present as a nitrosonium ion. Naccache and Ben Taarit (23) assign part of an infrared band in the 1760-1780 cm^{-1} region to NO^+ . This might seem to be a rather low wave number for coordinated NO^+ ; however, in low-spin transition metal nitrosyls the stretching frequency is commonly shifted to lower wave numbers.

In the same zeolites two other ir bands were observed at 1896 and at 1786-1760 cm^{-1} . The authors (23) attribute these two bands to terminal and bridging NO ligands in a complex depicted as



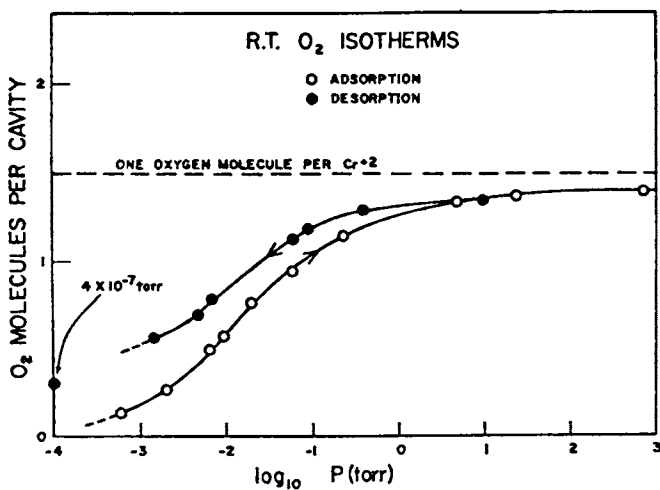
V

In view of the pair of bands observed at 1910 and 1830 cm^{-1} for the $[Co(II)(NO)_2]^{2+}$ complex in the Y-type zeolite it appears likely that a similar complex may be formed with Cr^{2+} ions. This hypothesis could be checked by using a mixture of ^{14}NO and ^{15}NO isotopes.



Accounts of Chemical Research

Figure 3. A six-oxygen window in CoA, showing the coordination of NO to the cobalt ion (4)



Journal of the American Chemical Society

Figure 4. A room-temperature isotherm for O_2 adsorbed on Co(II)A zeolite (39)

It was interesting to note that neither the epr spectrum nor the ir spectrum was affected by the addition of molecular oxygen (23). A similar $[\text{Cr}(\text{I})\text{NO}^+]^{2+}$ complex on the surface of alumina reacted rapidly with O_2 at room temperature (40). It is likely, therefore, that the chromium nitrosyl complexes are located in the sodalite cages of the faujasite and in the small cavities of the mordenite, where they are inaccessible to oxygen molecules.

A Chromium(I) Complex with Benzene. Dibenzenechromium(I) cations have been exchanged into Y-type zeolites from an aqueous solution or a 1:1 mixture of methanol/benzene. For purposes of comparison the complex was also supported on silica gel. The bis- π -arene complex is sufficiently small (<8 Å across) to allow motion through the 9 Å twelve-membered ring of the zeolite. Up to one complex per large cavity was exchanged into a NaY zeolite from the methanol/benzene solvent. The epr signal of the complex began to decay upon evacuation of the silica gel at 25°C; however, it was reasonably stable up to 80°C in the zeolite. At this temperature benzene was evolved from the sample. Attempts to reform the π -arene cation by adding back benzene were unsuccessful. Furthermore, it was not possible to form new π -arene complexes by reacting $[\text{Cr}(\text{I})(\text{C}_6\text{H}_6)_2]^+$ with mesitylene, deuterated acetylene, methylacetylene, or dimethylacetylene. From the epr parameters it is evident that the surface does not significantly affect the bonding within the complex.

Nickel Complexes

Nickel(II) Complexes with Nitrous Oxide, Cyclopropane, Ethylene, Propylene and Acetylene. One of the earliest studies on transition metal complexes in zeolites was carried out by Klier and Ralek (42) on NiA. As with CoA the Ni^{2+} ions are trigonally coordinated to oxide ions of the lattice in the dehydrated zeolite. Adsorption of nitrous oxide, cyclopropane, ethylene, propylene or acetylene resulted in a change in color of the zeolite from yellow to pink and an optical spectrum which indicated a transition from D_{3h} to an effective C_{3v} symmetry. With the exception of acetylene all of these gases were reversibly adsorbed at room temperature. No decomposition of nitrous oxide or isomerization of cyclopropane was observed.

A Nickel(II) Complex with Nitric Oxide. Nitric oxide reacts with Ni^{2+} ions in NiY zeolites, forming a complex which has been identified as $[\text{Ni}(\text{I})\text{NO}^+]^{2+}$ (23). Kasai (24) first noted this electron transfer from NO to Ni^{2+} ions by observing the characteristic epr spectrum of a d^9 ion. Actually two overlapping spectra, as shown in Figure 5, indicate the presence of the complexes at two different sites in the zeolite. The NO stretching mode leads to a sharp, strong ir band at 1892 cm^{-1} ,

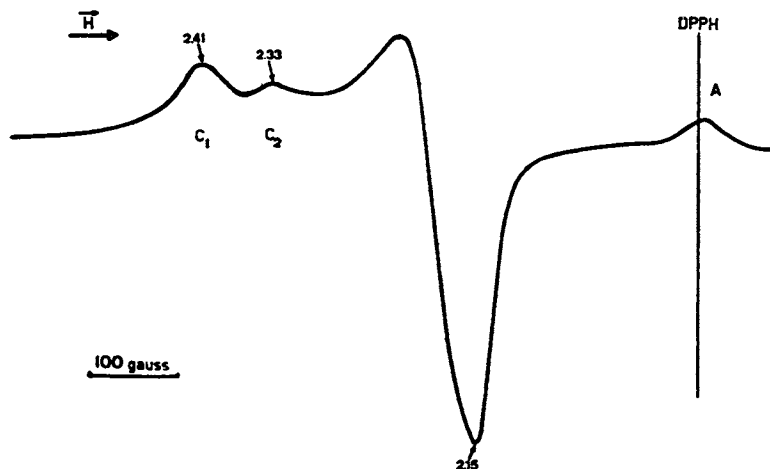
which is a more reasonable position for an NO^+ moiety. Based on X-ray diffraction data it has been suggested that there may be three NO molecules coordinated to a single Ni^{2+} ion; however, this evidence is questionable because of the large errors associated with the occupancy factors.

Iron Complexes

Iron(II) Complexes with Nitric Oxide. The formation of nitrosyl complexes in Fe(II)Y zeolites has been studied by epr and ir spectroscopy (25). Upon adsorption of small amounts of nitric oxide a high-spin ($S = 3/2$) complex identified as $[\text{Fe}(\text{I})\text{NO}^+]^{2+}$ was observed. This complex is characterized by an epr spectrum with $g_{\perp} = 4.07$ and $g_{\parallel} = 2.003$ and by an infrared band at 1890 cm^{-1} . Upon addition of excess NO additional infrared bands were observed at 1822 and 1930 cm^{-1} , and it is now believed that these bands are due to the formation of a dinitrosyl complex. After keeping the sample under vacuum for several hours, these dinitrosyl bands decreased in intensity as shown in Figure 6, and a new epr signal was observed, having $g_{xx} = 2.015$, $g_{yy} = 2.055$ and $g_{zz} = 2.089$. The growth of this spectrum is accompanied by an infrared band at 1778 cm^{-1} . This complex has been identified as the low-spin ($S = 1/2$) complex $[\text{Fe}(\text{I})\text{NO}^+]^{2+}$ which is believed to be formed by the partial dissociation of the dinitrosyl. As mentioned previously in the discussion of the $[\text{Cr}(\text{I})\text{NO}^+]^{2+}$ complex, the wave number for the stretching mode is somewhat low for coordinate NO^+ ; however, the g values favor the identification as a low-spin d^7 ion, rather than a d^5 ion. Apparently the $[\text{Fe}(\text{I})\text{NO}^+]^{2+}$ complexes are in two different sites in the zeolite, and the local symmetry affects the degree of spin pairing.

Conclusions

It is evident from the number of different complexes described here that zeolites serve as a fertile medium for carrying out inorganic and organometallic synthesis. The problem of constructing these complexes in a zeolite has been likened to building a model ship within a bottle; nevertheless, the constraints offered by the zeolite and the role of the framework atoms themselves, offer an environment for some novel chemistry. Several studies have demonstrated the unusual catalytic behavior of these complexes in zeolites, and it is anticipated that practical applications may be made of these materials in the removal of nitric oxide from fixed sources. The effect of complexing on ion-exchange equilibria likewise shows promise for the removal of trace quantities of metal ions from effluent streams. Most of the effort up to the present time has been devoted to the synthesis and characterization of new complexes in zeolites; however, it is anticipated that



Journal of the Chemical Society, Faraday Transactions 1

Figure 5. Epr spectrum at 77°K of NO adsorbed on NiY dehydrated at 200°C (23)

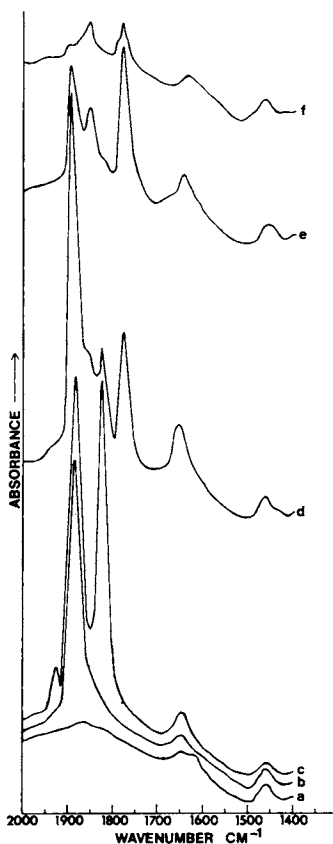


Figure 6. Infrared spectrum of Fe(II)Y. (a), Before addition of NO; (b), 1 torr of NO; (c), 10 torr of NO, evacuated 15 sec; (d), sample under vacuum 4 hr at 25°C; (e), sample under vacuum 1 hr at 50°C; (f), sample under vacuum 1 hr at 100°C.

future work will largely be directed toward understanding the role of these and other complexes in intrazeolitic reactions.

Literature Cited

1. Mikheikin, I. D., Zhidomirov, G. M. and Kazanskii, V. B., *Russian Chem. Rev.*, (1972), 41, 468. Engl. Trans.
2. Lunsford, J. H., *Catal. Rev.*, (1975), 12, 137.
3. Kellerman, R. and Klier, K., in "Surface and Defect Properties of Solids", Vol. 4, The Chemical Society Burlington House, London, pp. 1-33.
4. Seff, K., *Accts. Chem. Res.*, (1976), 9, 121.
5. Laing, K. R., Leubner, R. L. and Lunsford, J. H., *Inorg. Chem.*, (1975), 14, 1400.
6. Chao, C. C. and Lunsford, J. H., *J. Phys. Chem.*, (1974), 78, 1174.
7. Huang, Y. Y., *J. Catal.*, (1974), 32, 482.
8. Pleysier, J. and Cremers, A., *Proceedings of the Third International Conference on Molecular Sieves, Zurich, Sept. 1973*, p. 206.
9. Gallezot, P., Ben Taarit, Y. and Imelik, B., *Compt. Rend.*, (C), (1971), 272, 261; *J. Catal.*, (1972), 26, 295.
10. Flentge, D. R., Lunsford, J. H., Jacobs, P. A. and Uytterhoeven, J. B., *J. Phys. Chem.*, (1975), 79, 354.
11. Leith, J. R. and Leach, H. F., *Proc. Roy. Soc. Lond. A.*, (1972), 330, 247.
12. Naccache, C. and Ben Taarit, Y., *Chem. Phys. Lett.*, (1971), 11, 11.
13. Vansant, E. F. and Lunsford, J. H., *J. Phys. Chem.*, (1972), 76, 2860.
14. Turkevich, J., Ono, Y. and Soria, J., *J. Catal.*, (1972), 25, 44.
15. Vedrine, J. C., Derouane, E. G. and Ben Taarit, Y., *J. Phys. Chem.*, (1974), 78, 531.
16. Peigneur, P., Lunsford, J. H., DeWilde, W. and Schoonheydt, R. A., to be published.
17. Naccache, C., Che, M. and Ben Taarit, Y., *Chem. Phys. Lett.*, (1972), 13, 109.
18. Williamson, W. B. and Lunsford, J. H., to be published.
19. Enemark, J. H. and Feltham, R. D., *Coord. Chem. Rev.*, (1974), 13, 339.
20. Chao, C. C. and Lunsford, J. H., *J. Phys. Chem.*, (1972), 76, 1546.
21. Naccache, C., Che, M. and Ben Taarit, Y., *Chem. Phys. Lett.*, (1972), 13, 109.
22. Windhorst, K. A. and Lunsford, J. H., *J. Amer. Chem. Soc.*, (1975), 97, 1407.
23. Naccache, C. and Ben Taarit, Y., *JCS Faraday Trans. I*, (1973), 69, 1475.
24. Kasai, P. H. and Bishop, R. J., *J. Amer. Chem. Soc.*, (1972),

- 94, 5560.
25. Jermyn, J. W., Johnson, T. J., Vansant, E. F. and Lunsford, J. H., *J. Phys. Chem.*, (1973), 77, 2964.
 26. Huang, Y. Y., *J. Amer. Chem. Soc.*, (1973), 95, 6636; *J. Catal.*, (1973), 30, 187.
 27. Vansant, E. F. and Lunsford, J. H., *JCS Chem. Commun.*, (1972), 830; *JCS Faraday Trans. II*, (1973), 69, 1028.
 28. Maher, J. P., *J. Chem. Soc., A*, (1968), 2918.
 29. Vansant, E. F. and Lunsford, J. H., *Adv. in Chem. Series*, (1973), 121, 441.
 30. Howe, R. F. and Lunsford, J. H., *J. Amer. Chem. Soc.*, (1975), 97, 5156.
 31. Howe, R. F. and Lunsford, J. H., *J. Phys. Chem.*, (1975), 79, 1836.
 32. Klier, K., Kellerman, R. and Hutta, P. J., *J. Chem. Phys.*, (1974), 61, 4224.
 33. Amaro, A. A. and Seff, K., *J. Phys. Chem.*, (1973), 77, 906.
 34. Riley, P. E. and Seff, K., *Inorg. Chem.*, (1975), 14, 714.
 35. Riley, P. E., Kunz, K. B. and Seff, K., *J. Amer. Chem. Soc.*, (1975), 97, 537.
 36. Hutta, P. J., Lin, M. J., Windhorst, K. A. and Lunsford, J. H., unpublished results.
 37. Windhorst, K. A. and Lunsford, J. H., *JCS Chem. Commun.*, (1975), 852.
 38. Riley, P. E. and Seff, K., *Inorg. Chem.*, (1974), 13, 1355.
 39. Kellerman, R., Hutta, P. J. and Klier, K., *J. Amer. Chem. Soc.*, (1974), 96, 5946.
 40. Shelef, M., *J. Catal.*, (1969), 15, 289.
 41. Kippenberger, D. J., Vansant, E. F. and Lunsford, J. H., *J. Catal.*, (1974), 35, 447.
 42. Klier, K. and Ralek, M., *J. Phys. Chem. Solids*, (1968), 29, 951.
 43. Gallezot, P., Ben Taarit, Y. and Imelik, B., *J. Phys. Chem.*, (1973), 77, 2556.

Reduction and Reoxidation of Silver-Mordenites

HERMANN K. BEYER

Central Research Institute for Chemistry, Hungarian Academy of Sciences,
Budapest II, Pusztafazeri ut. 57/69, Hungary

PETER A. JACOBS

Centrum voor Oppervlaktischekunde en Colloidale Scheikunde, Katholieke
Universiteit Leuven, De Croylaan 42, B-3030 Heverlee, Belgium

ABSTRACT

The reduction and reoxidation of silver exchanged Na-zeolon has been followed volumetrically. Isothermal and temperature programmed methods, together with in situ infra-red spectroscopy and X-ray spectrometry have been applied to investigate the stoichiometry and the kinetic behaviour of the chemical reactions involved. The results have been compared with the AgY system.

Introduction

Silver metal-containing zeolites prepared by hydrogen reduction of silver ions are found active and selective in the gasphase oxidation of ethylene (1). Silver ions in Y type zeolites upon reduction also form bulky metal clusters outside the zeolite structure (2). However, the silver metal whether it is located inside or outside the Y zeolite can be reoxidized to the original silver cation containing zeolite (3,4).

Recently, we reported on the reducibility of Ag⁺ ions in Y zeolite (4). The location of the cations at different sites mainly determines the reducibility. The Ag⁺ ions in the supercages are reducible at lower temperatures and as a result the formation of a highly dispersed metal phase containing unreduced silver has been advanced. The Ag⁺ ions located in the hexagonal prisms are only reduced at temperatures at which considerable sintering has occurred already. The migration of the ions away from the hidden sites becomes rate limiting (4).

In this work, we tried to generalize the concepts derived for Y zeolites using a completely different

molecular sieve structure. The stoichiometry of the reduction of Ag ions in mordenite and the kinetic mechanism of the reduction has been derived.

Unfortunately the exact location of exchangeable cations in mordenite is only known for K^+ (5) : 3.34 K^+ ions are located in the "side pockets" of the structure (site II) and are coordinated to oxygens belonging to a 8-membered ring and to an oxygen atom across a small channel. The other possible cation locations (sites IV and VI) are in the big pores and contain 3.04 and 0.91 cations respectively. The ions in the former sites are located in a 8-membered ring of oxygen ions, the latter in a distorted 6-membered ring.

Experimental

Materials. A commercial sample of Na-zeolon from Norton Company has been used. It was purified by treating with several NaCl solutions and was then exchanged with $AgNO_3$ solutions. Exchange in an excess of a 0.05 mol dm^{-3} solution repeated several times produced the samples with the following unit cell composition :

NaAgZ ^z -75	Na _{1.92}	Ag _{5.69}	Al _{7.62}	Si _{40.4}	O ₉₆
NaAgZ-84	Na _{1.20}	Ag _{6.42}	Al _{7.62}	Si _{40.4}	O ₉₆
NaAgZ-94	Na _{0.15}	Ag _{7.5}	Al _{7.62}	Si _{40.4}	O ₉₆

The original Na-zeolon (Z) contained 1.6 % by weight of Fe_2O_3 . After several extractions with dithionite (6) a zeolite Z^z containing only 0.74 % by weight of Fe_2O_3 is obtained. The samples are dehydrated under vacuum at 673 K for several hours, then oxygen is admitted to re-oxidize Ag^0 possibly formed by a photochemical process (4) and the sample is outgassed again.

Methods. The volumetric uptake of hydrogen and oxygen is measured either in the isothermal or temperature programmed mode. The detailed instrumentation has been described elsewhere (4). Also the infra-red spectroscopic measurements and the X-ray diffraction techniques have been described earlier (4).

Results and Discussion

Stoichiometry of hydrogen and oxygen uptake.

Volumetric results. Gas uptake measurements of dry NaAgZ mordenite at different temperatures are shown in table I. Already at 195 K hydrogen is taken up by the solid, only 41 % of which is held irreversibly at that temperature. This indicates that a considerable amount of H₂ is held in the zeolite via a physisorption process. At ambient temperature the amount of hydrogen consumed has decreased by 25 %, but more gas is held irreversibly by the zeolite. Below 423 K, there is no further progress of the degree of reduction. However, at this temperature almost 96.0 % of the hydrogen can be titrated with oxygen and is removed from the system as water. At higher reduction temperatures (643 K), the silver ions can be reduced completely, the ratio of hydrogen to oxygen and of water to oxygen uptake is close to 2. Reoxidation is almost complete under these conditions, while during a second redox cycle the system can be brought closely to its original state with respect to the gas uptake values.

Infra-red evidence. The appearance of deuteroyl groups in the zeolite channels upon reduction was proved by infra-red spectroscopy (Figure 1.). Under mild conditions (Figure 1.b) a band appears at 2650 cm⁻¹. This band shows acidic behavior towards ammonia gas. The 2650 cm⁻¹ OD band increases upon reduction at higher temperatures, while new bands around 2690 and 2750 cm⁻¹ also appear (Figure 1.c,d). Deuteroyl bands have been observed at the same frequency in earlier work (7). They correspond to OH bands with the following frequencies (7) : 3610, 3650 and 3735 cm⁻¹. The latter band has been assigned to amorphous SiO₂ inclusions (8) and the 3610 cm⁻¹ band to acidic OH groups in the main pores (7-9); the presence of the 3650 cm⁻¹ band depends upon the pretreatment or the sample preparation (8). Upon oxygen treatment of a reduced AgNaZ sample (Figure 1.e,f), the 2690 cm⁻¹ is not completely eliminated. The ultimate presence of this band together with the slight irreversibility as observed from the volumetric data, indicates that irreversible structural changes occur to a limited extent, most probably of the same nature (= "deep bed" effects) as described earlier (8).

The presence of Ag⁺ ions in the zeolite channels has been probed with carbon monoxide. It seems that

TABLE I.- Gas uptake of NaAgZ mordenite.

Sample	Treatment	Adsorption temp. (K)	gas uptake (mmole g ⁻¹)		reduction %	reoxidation %		
			(H ₂)	(H ₂ O) ⁽¹⁾ (O ₂)				
NaAgZ-84	H ₂	195	0.633	0.00				
	outg. 195K + H ₂	195	0.371	0.00	(11.3)	(2)		
	H ₂	295.4	0.463	0.00				
	outg. 295.4K + H ₂	295.4	0.010	0.00	(13.9)	(2)		
NaAgZ*-75	H ₂	423	0.500	0.00	0.225	0.480	14.0	96.0
NaAgZ*-75	1st redox cycle	643	0.830	0.00	0.386	0.71	98.2	93.0
	2nd redox cycle	643	0.750	0.00	0.365	0.63	97.2	97.3

(1) H₂O formed after reduction (r) or reoxidation (o);

(2) apparent degree of reduction.

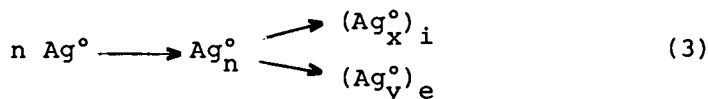
the 2175 cm^{-1} band, reflecting the interaction of Ag^+ with CO, decreases upon reduction (Figure 1.a,b,c,d), and is restored upon oxygen treatment (Figure 1.e,f) remaining slightly below its original intensity (Figure 1.a,f). This also is indicative of the slight irreversibility of the system after a redox cycle.

X-ray diffraction data. X-ray diffraction lines of the zeolon structure and of possible external phases are shown in Figure 2. The relative intensity of the diffraction lines changes to a minor extent upon hydrogen reduction (Figure 2,a,b,c) but even after several redox cycles the material remains highly crystalline (Figure 2.a,e). At increasing reduction temperatures, the intensity of the (111) diffraction of crystalline silver external to the zeolite increases, while X-ray line broadening techniques show that the average particle size of the Ag crystallites also increases. Upon oxidation at sufficiently high temperatures the external silver phase disappears (Figure 2.f). After a second redox cycle at 643 K, a relatively small amount of silver remains located between the zeolite crystallites (Figure 2.g). This again is indicative for the slight irreversibility of the system.

Stoichiometry of the redox reactions. From the amount of gases taken up or evolved during a redox cycle, from the appearance of OH groups and disappearance of Ag^+ ions after reduction and from the opposite behavior upon oxygen treatment, the following overall stoichiometry appears straightforward :



The X-ray evidence suggests that metal agglomeration occurs during reduction, the system remaining reversible to a major extent :



where $y \gg x$ and the suffix i and e stands for metal agglomerates internal and metal crystallites external to the zeolite. Almost complete reversibility of the system appears during oxidation :

Figure 1. Infrared investigation of the reduction and reoxidation of NaAgZ-94 in the OD region ($2800\text{--}2500\text{ cm}^{-1}$) and after CO physisorption ($2300\text{--}2100\text{ cm}^{-1}$). (a), After outgassing and oxygen treatment at 673 K; (b), after D_2 treatment for 1 hr at 313 K; (c), after reduction with D_2 at 423 K for 1 hr; (d), after D_2 treatment at 623 K for 1 hr; (e), after oxygen treatment at 623 K for 1 hr; (f), after D_2 treatment at 573 K and oxygen treatment at 623 K.

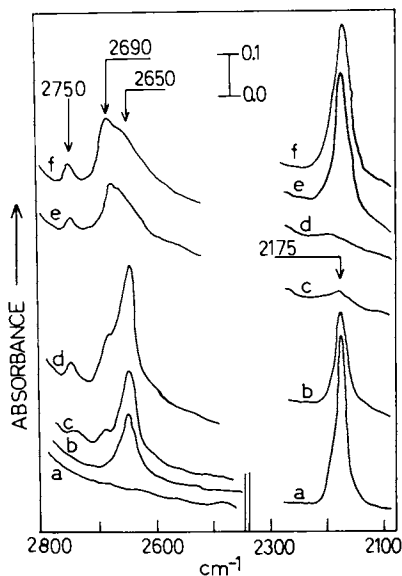
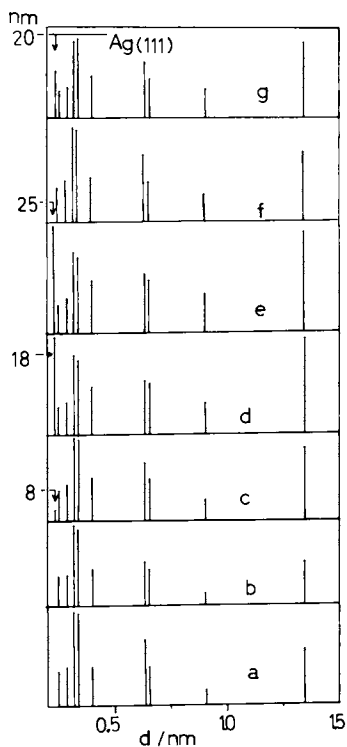
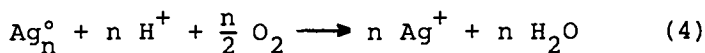


Figure 2. X-ray diffraction lines of NaAgZ*-75 upon various redox treatments. (a), Dehydrated zeolite; (b), H_2 reduction at 432 K; (c), at 571 and (d), at 643 K; (f), O_2 treatment of (d) at 571 K; (g), after one more redox cycle at 643 K.





Essentially the same behavior has been observed for the AgY system (3,4). However, upon repeated redox cycles, a slight degree of irreversibility is observed most probably due to dealumination or "deep bed" effects.

In contrast to other transition ion zeolites such as copper (10), in no case has an external oxide phase been detected. The presence of the latter phase would exclude the reversibility of the system (10).

The hydrogen uptake at low and ambient temperatures, already suggests that reduction has taken place. However, at 195 K no reduction of Ag^+ ions could be derived from infra-red methods. At ambient temperatures, a fast chemisorption of hydrogen occurs, while Ag° metal is formed at a much slower rate. This is illustrated in Figure 3, where the degree of reduction deduced from the hydrogen uptake, the amount of OD groups formed and the decrease of the concentration of the $\text{Ag}^+\dots\text{CO}$ complex has been compared. The chemisorption of hydrogen is related to the presence of Ag^+ ions since no uptake occurs over NaZ, and to the mordenite structure since also no chemisorption has been observed on AgY, Ag-stilbite or Ag-chabasite. The present data however do not allow to advance a hypothesis concerning the chemical nature of the chemisorption site.

Kinetic study of the redox behavior. The kinetic curves of the hydrogen uptake of NaAgZ-84 mordenite at different temperatures are shown in Figure 4. At high temperatures (> 473 K) the rate of uptake does not depend on the hydrogen pressure in the pressure region from 3.99 to 53.2 kNm⁻². The reaction is first order with respect to the amount of unreduced silver. The activation energy is the same for the three samples, differing by their degree of ion exchange and by their iron content and is equal to 103.0 ± 0.50 kJ mol⁻¹. This is close to the value required for the reduction of silver ions located in the hexagonal prisms of the Y faujasite (4). The amount of Ag^+ involved in the high temperature reduction process is equal to 2 Ag^+ ions per unit cell for sample NaAgZ-84. If it is assumed that the ion exchange of Ag^+ for Na^+ occurs preferentially in the big pores and that only when the latter sites are filled up exchange in the side pockets occurs, this amount corresponds very closely to the reduction of the Ag^+ ions located in the side pockets (3.3-1.2 ions per unit cell). All these arguments are in favor of the hypothesis that the reduction at high tempera-

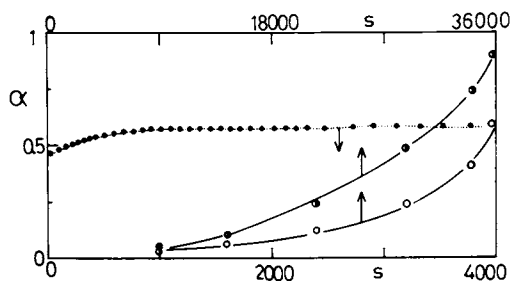


Figure 3. Degree of reduction (α) with time of NaAgZ*-75 at 318 K. (●), from hydrogen uptake; (○), from the intensity of the OD stretching band at 2650 cm^{-1} ; (●), from the intensity of the CO stretching vibration (2175 cm^{-1}) of the complex $\text{Ag}^+ \dots \text{CO}$.

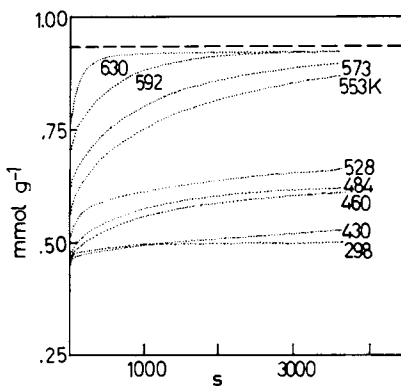


Figure 4. Hydrogen uptake with time of NaAgZ-84

tures involves the migration of silver ions from the "side pockets" of the structure (Site II).

The reduction is a catalyzed process : hydrogen most probably is activated on iron impurity centers present in the zeolite. Indeed, in Figure 5 it is clearly shown that the rate of reduction strongly depends on the iron content of the structure. Indeed, on the deironized material, the rate of reduction of the silver ions in the "side pockets" of the structure shows a 5-fold decrease, while the reduction mechanism remains unchanged as deduced from the slope of the Arrhenius plots.

A kinetic study of the reduction at lower temperatures (< 473 K) cannot be carried out since overlapping exists with the chemisorption process observed at low temperatures. However, the uptake curves of Figure 4 at temperatures below 510 K show initially very fast rates of hydrogen uptake, while this rate gradually decreases at longer reduction times. From identical observations on AgNaY (6), the conclusion was derived that some of the silver ions associate with reaction products, agglomerating preferentially to Ag_3^+ species which are more difficult to reduce. In the present case, the reduction rate only starts to decrease when 80 % of the Ag^+ ions available in the big pores (sites IV and VI) are reduced. This means that Ag_5^+ species are formed preferentially upon hydrogen treatment under mild conditions.

Dispersion of Ag^0 in the mordenite pores. Reoxidation of Ag^0Z zeolites at 523 K is only complete when reduction is carried out under mild conditions (below 523 K). In a temperature programmed oxidation (TPO) experiment the rate of oxygen uptake is maximum around 423 K (Figure 6.a). After reduction at higher temperatures and longer contact times, a second maximum in the reoxidation rate is observed slightly below 573 K (Figure 6.b,c). Comparison with X-ray diffraction results, shows always the concomitant presence of the second maximum and big Ag^0 crystallites. This is a general observation for other metal loaded zeolites (11). The first maximum is therefore assigned to the oxidation of metal agglomerates in the zeolite pores, while the second maximum corresponds to the oxidation of bulky metal crystallites at the outside of the zeolite structure. Under these assumptions 100, 75 and 40 % of the reduced silver remains highly dispersed in the zeolites under the reduction condition described sub a, b and c respectively (Figure 6).

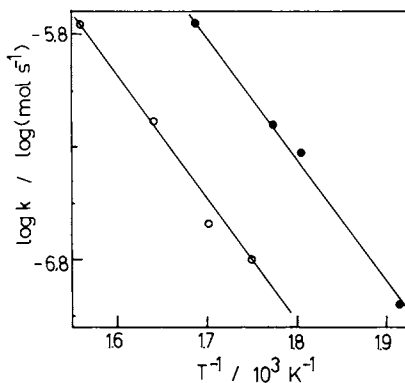


Figure 5. Rate of reduction of Ag^+ ions in NaAgZ*-75 (\circ) and NaAgZ-85 (\bullet). Arrhenius plot of the rate constants.

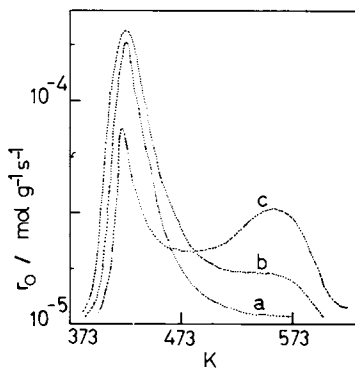


Figure 6. Temperature-programmed oxidation of Ag^0 mordenite: rate of oxygen uptake (r_o) at different temperature. (a), After reduction at 473 K for 1 hr; (b), at 523 K for 1 hr; (c), at 673 K for 1 hr.

Conclusion

The reduction and subsequent reoxidation of silver ions in mordenite are reversible processes. During repeated redox cycles only a slight irreversibility is observed due to deep bed effects. The kinetic laws of the reduction are essentially the same as for the AgY system. The reduction of Ag^+ ions in the inner sites is most difficult, while there is kinetic evidence that upon mild reduction the ions in the main pores agglomerate as Ag_5^+ .

The activation of hydrogen occurs by activation on the iron impurities in the zeolite. Since silver particles inside and outside the zeolite are oxidized at a distinct rate, their repartition may be determined easily.

Acknowledgments

P.A.J. acknowledges a research position as "Aangesteld Navorsers" from N.F.W.O. (Belgium).

Literature Cited

1. Giordano, N., Montelatici, S., and Zen, C., "Molecular Sieves", p. 449, J.B. Uytterhoeven, ed., Leuven University Press, 1973.
2. Tsutsumi, K., and Takahashi, H., Bull. Chem. Soc. Japan, (1972), 45, 2332.
3. Riekert, L., Ber. Bunsenges. Phys. Chem., (1973), 73, 331.
4. Beyer, H., Jacobs, P.A., and Uytterhoeven, J.B., J.C.S. Faraday I, (1976), 72, 674.
5. Mortier, W.J., Pluth, J.J., and Smith, J.V., Proc. Conf. Natural Zeolites, Tucson, Pergamon Press, to be published, 1976.
6. Derouane, E., Mestdagh, M., and Vielvoye, L., J. Catalysis, (1974), 33, 169.
7. Karge, H., Zeitschr. Phys. Chem. N.F., (1971), 76, 133.
8. Karge, H., Zeitschr. Phys. Chem. N.F., (1975), 95, 241.
9. Karge, H., and Klose, H., Zeitschr. Phys. Chem. N.F., (1973), 83, 100.
10. Herman, R.G., Lunsford, J.H., Beyer, H., Jacobs, P.A., and Uytterhoeven, J.B., J. Phys. Chem., (1975), 79, 2388.
11. Jacobs, P.A., and Beyer, H., J.C.S. Faraday I, to be published.

Isomerization of *n*-Hexane and *n*-Pentane over Various Bifunctional Zeolitic Catalysts

I. Influence of the Structure Parameters of the Catalysts on the Activity and Selectivity

G. BRAUN, F. FETTING,* and H. SCHOENEGER

Institut für Chemische Technologie, TH Darmstadt, West-Germany and
E. Gallei, BASF AG., 6700 Ludwigshafen, West-Germany

ABSTRACT

H-mordenite and CaY-zeolite loaded with various noble and transition metals were tested. The bifunctional catalysts containing platinum or palladium were demonstrated to be the most active. The H-mordenite catalysts showed high activity and selectivity at temperatures as low as 573 K. The isomerization of *n*-hexane and *n*-pentane over Pt/CaY are possibly "structure sensitive" reactions. Kinetic studies showed that intraparticle mass transfer limitations in the secondary pore system were significant for Pt/CaY but not for Pt/H-mordenite catalyst.

Introduction

The requirements for unleaded high octane gasolines have led to research efforts, both industrial and academic, in the area of paraffin isomerization and other reforming reactions. Because of the regulations regarding the emissions of hydrocarbons, carbon monoxide, nitrogen oxide and lead compounds from internal combustion engines, lead alkyl concentrations will have to decrease, resulting in an increased need for light hydrocarbons with high octane numbers, e.g. isomers of *n*-hexane and *n*-pentane. In former studies we investigated the dehydrocyclization of *n*-hexane over commercial bifunctional catalysts (1,2). The structure parameters of these industrial catalysts were not completely available, so a detailed statement concerning the correlations between the structure of the catalysts and their activity was not possible. In addition, the information from the literature about reforming reactions over zeolitic catalysts is scanty regarding the relations between activity and selectivity and structural parameters of the employed catalysts (3-10). However, such correlations are important for catalyst optimization.

*To whom correspondence concerning this paper should be addressed.

Therefore, in this work the influence of the catalyst structure parameters, especially of the state of the metallic phase, on the activity and selectivity for the isomerization of *n*-hexane and *n*-pentane was investigated.

As testing reactions, the isomerization reactions of *n*-hexane and *n*-pentane were selected mainly for two reasons: first, their low heats of reaction prevent high temperature profiles in the catalyst bed and second, all reaction products can be quantitatively analyzed. This facilitated evaluation of the kinetic data, which was carried out along with investigations regarding mass transfer limitations on the external (gas to particle) and internal surface (intraparticle) of the catalyst pellets.

Experimental

Materials: Starting materials for the catalysts were NaY zeolite powder (Linde SK-40) and a commercial H-mordenite powder (Norton Zeolon 100). Both materials were free of clay binder. CaY zeolite was prepared from NaY by exchanging part of the Na-ions (75%) by Ca²⁺. The chemical compositions and the structural parameters of the zeolites are given in Table I.

zeolite parameter		NaY	CaY	H-mordenite
chemical composition [wt %]	SiO ₂	64.3	65.0	87.9
	Al ₂ O ₃	21.9	22.1	10.6
	Na ₂ O	13.8	3.5	1.5
	CaO	—	9.4	—
specific surface area [m ² /g]		1250		500
pore volume [ml/g]	primary pores	0.60 ± 0.06		0.57
	secondary pores	0.30 ± 0.03		0.37
mean pore diameter [Å]	primary pores	9		7-8
	secondary pores	4000		10000
crystal size [μ]		1.2		6

Table I. Chemical analysis on anhydrous basis and structure parameters of zeolites

Some of these zeolites were loaded with 0.5% by weight of various transition and noble metals (11) by ion exchange or impregnation at room temperature. Noble metal loaded zeolites were reduced at 573 K and zeolites containing Ni^{2+} ions at 773 K. The structure parameters, e.g. specific surface area of the zeolites and the pore structure were determined by gas sorption methods and mercury penetration (12). The composition of the zeolite surface regarding the functional groups was investigated by means of infrared spectroscopy (13).

Measurement of the Dispersion of the Metallic Phase. The structural parameters of the metallic phase, for example the dispersion of the metal on the carrier, the metal crystallite size and the specific surface area of the supported metal have been determined by chemisorption of hydrogen for nickel and platinum and of carbon monoxide for palladium, using a modified Perkin-Elmer Shell Sorptometer model 212 B. The pulse flow adsorption method was employed.

For all catalysts good agreement was obtained between this pulse technique and electron microscopy determinations of the structural parameters of the metallic phase (14).

Catalytic Activity Measurements (Reactor). Isomerization of *n*-hexane and *n*-pentane was performed in a flow apparatus with a fixed bed reactor operated under isothermal and plug-flow conditions and differential conversions (<10%). The downflow tube reactor had an inner diameter of 20 mm and a length of 165 mm. The maximum liquid feed for fluid hydrocarbons and hydrogen gas was 200 ml/hr and 1500 NL/hr, respectively. The catalyst pellets (3 x 3 mm) were contained in the middle of the reactor tube. Inert spheres were placed above and under the catalyst bed to obtain better mixing. Before measuring the activity and selectivity, the catalyst pellets were activated for 12 hours with hydrogen (2 NL/hr) at 623 K and at 1 bar.

Feed mixtures of hydrogen and hydrocarbons were preheated to the reactor temperature before entering the bed. Merck "analytical grade" liquid hydrocarbon was dosed by a "Burdosa" microdosing pump into a heated stream of hydrogen controlled by a flowmeter.

Beyond the catalyst bed a partial stream of products was removed and directly transferred to a gas chromatograph equipped with a 100 m squalane capillary and a FID. This design allowed a continuous quantitative analysis of the products. The main product stream was cooled down and conducted into a separator and decompression vessel.

Catalytic Activity Measurements (Procedure). The testing procedure was dependent on the various problems to be solved and varied in the following range:

Temperature T	: 473 - 773 K
Pressure P	: 5 - 30 bar
Ratio H ₂ /HC	: 2 - 20 mole/mole
Weight of catalyst W	: 0,5 - 2,5 gram
Liquid feed F	: 0,2 - 1,2 ml/min.

Results and Discussion.

At first the zeolitic catalysts had to be tested regarding their activity and selectivity for the isomerization of n-hexane and n-pentane. As a measure for the activity was defined the temperature dependency of the conversion and for the selectivity the fraction of the isomers of the total conversion. Thereby had to be kept in mind, that the chemical equilibrium between n-paraffins and iso-paraffins is shifted to the isomers at low temperatures. Therefore valuable catalysts should show high activity and selectivity already at fairly low temperatures.

Bifunctional Catalysts. For the preparation of the bifunctional catalysts the active zeolites CaY and H-mordenite had been employed as supports. The characteristic properties of the carriers were not changed during metal loading, as determined by infrared spectroscopy and mercury penetration (12,15). The results obtained for the conversion of n-hexane over various bifunctional catalysts are shown in Figure 1 and the corresponding data are listed in Table II.

catalyst	activity [mole %]	selectivity
Re / CaY	40,6	0,01
Ir / CaY	25,0	0,24
Pt / CaY	20,7	0,83
Pd / CaY	36,2	0,86

Table II. Activity and selectivity for the conversion of n-hexane over various bifunctional catalysts with CaY zeolite as support at 673 K.

Almost no isomerization activity was found for the catalysts with Ni, Ru and Rh as metallic components and CaY-zeolite as carrier. The isomerization selectivity of the Ir/CaY catalyst was moderate and that of the Re/CaY was even lower (see Table II). However, The Ru, Rh and Ni containing catalysts revealed a high hydrocracking activity yielding preferentially methane as product; and a rapid deactivation was observed. The results for isomerization of n-hexane over catalysts with H-mordenite as support and Ni, Pd, or Pt as metallic components are illustrated in

Figure 2 and Table III.

catalyst	activity [mole %]	selectivity
Ni/H-mordenite	51,9	0,20
Pd/H-mordenite	11,9	0,97
Pt/H-mordenite	25,4	0,90

Table III. Activity and selectivity of bi-functional catalysts with H-mordenite as support at 573 K.

Contrary to the catalysts with CaY-carriers, Pt/H-mordenite shows a higher activity than Pd/H-mordenite. The catalyst Ni/H-mordenite is very active for hydrocracking as already reported for Ni/CaY. Differences, however, arise in the products produced over the Ni/H-mordenite or the Ni/CaY catalyst. Whereas over Ni/CaY methane is produced as main product over Ni/H-mordenite the *n*-hexane conversion yields propane and butane as already reported in literature (16). It should be emphasized the low temperatures (493-573 K) at which the catalysts with H-mordenite supports show already high activity. For a comparison of the activity and selectivity of one metal component on different carriers in Figure 3 are plotted the conversions and selectivities as a function of the temperature for the catalysts Pt/CaY and Pt/H-mordenite. From Figure 3 it is shown, that the high activity and selectivity for Pt/H-mordenite, which is already observed at temperatures between 523 and 583 K is reached with Pt/CaY first between 613 and 693 K. The same results were obtained for the *n*-pentane conversion.

Influence of the Dispersion of the Metal Phase. For a closer insight into the catalytic properties of the metallic components, the influence of the metal dispersion on the conversion for the *n*-hexane and *n*-pentane isomerization was investigated.

The characteristic structure parameters are as already mentioned the dispersion *R*, the specific metal surface area *S*, and the mean metal particle diameter \bar{d} . The dispersion *R* is defined as the ratio of free metal atoms on the surface to the total metal atoms on the carrier.

A comparison of the methods of loading, e.g. impregnation or ion-exchange for the catalyst Pt/CaY resulted in metal dispersions of *R* = 0.62 and 0.81, respectively. The testing of these catalysts in the reactor yielded a higher activity for the ion-exchanged catalyst, that means activity and metal dispersion are in this range proportional to each other. More detailed information regarding the dispersion should be obtained by systematic studies of sintering of the metal phase followed by testing of these catalysts for the *n*-hexane isomerization activity. Sintering

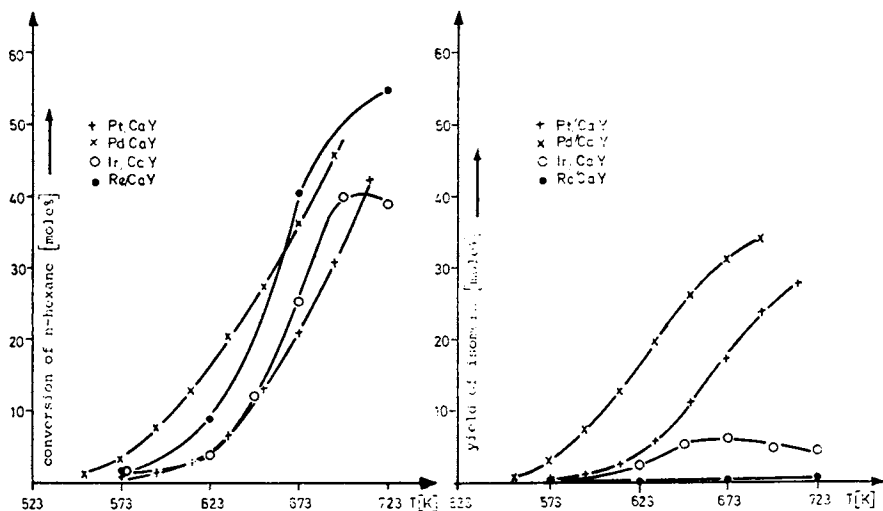


Figure 1. Conversion of n-hexane and yield of isomers as function of temperature for bifunctional catalysts with CaY as support

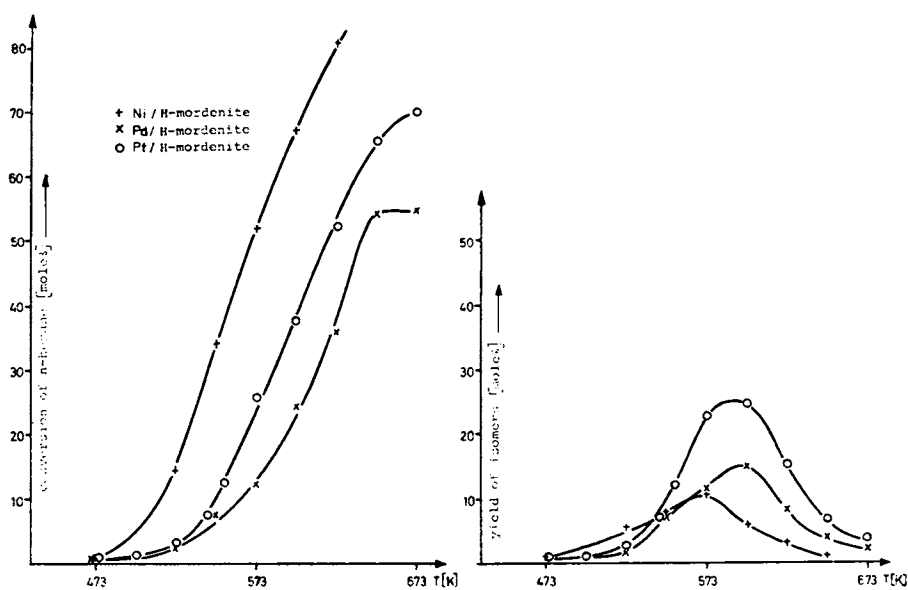


Figure 2. Conversion of n-hexane and yield of isomers as functions of temperature for bifunctional catalysts with H-mordenite as support

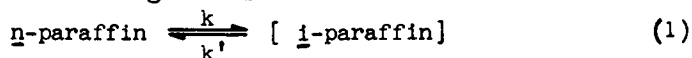
of the metal phase decreases the specific metal surface area and simultaneously increases the mean metal particle size. The crystalline structure of the zeolitic supports was not damaged by the sintering procedure as checked by x-ray analysis. The hydroxyl group concentration is mainly a function of the activation temperature and had a constant value for all catalyst samples as determined by ir-spectroscopy. The structure parameters of a Pt/CaY sample sintered at 973 K for different times are listed in Table IV.

catalyst	sintering	$S[\frac{m^2 Pt}{gr Pt}]$	\bar{d} [Å]
Pt/CaY	-	189,0	11
Pt/CaY	2 hrs, 973 K	39,0	60
Pt/CaY	5 hrs, 973 K	25,0	95
Pt/CaY	16 Hrs, 973 K	14,0	163

Table IV. Structural parameters of the metallic phase after sintering at 973 K for different times.

By normalizing the obtained activities for the various sintered catalysts to the corresponding specific surface area S the specific activity can be calculated. If the specific activity is plotted against the mean metal crystallite diameter \bar{d} , the curves shown in Figure 4 are obtained for the isomerization of n -hexane. Identical results were obtained for the isomerization of n -pentane. The graphs have a maximum for the specific activity at metal particle diameters between 80-100 Å. These results lend mild support to the conclusion that the isomerization of n -hexane and n -pentane is a "structure sensitive" reaction; the possible migration of the cations in the zeolite lattice during the sintering steps could also have slightly influenced the specific activity. The concept of "structure sensitive or insensitive reaction" has been proposed previously in connection with relations, between catalytic activity and structure of metallic phase (17). For a "structure sensitive" reaction the conversion of n -hexane or n -pentane becomes dependent on the arrangement of metal atoms in the individual metal crystal faces. Such relations are not yet known in literature for n -hexane and n -pentane isomerization over Pt/CaY catalysts.

Kinetics. A first order kinetic model with k and k' , the forward and reverse reaction rate constants, respectively, was based on the following reaction



The rate of reaction, expressed as moles of i -hexanes or i -pentanes produced per hour, per gram catalyst is represented by

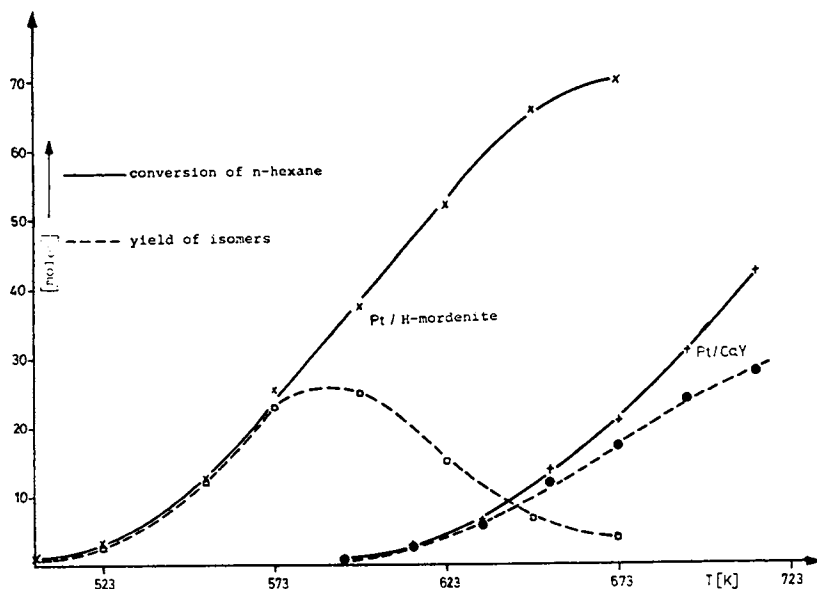


Figure 3. Conversion of n-hexane and yield of isomers as function of temperature for bifunctional catalysts with Pt as metallic component on CaY and H-mordenite support

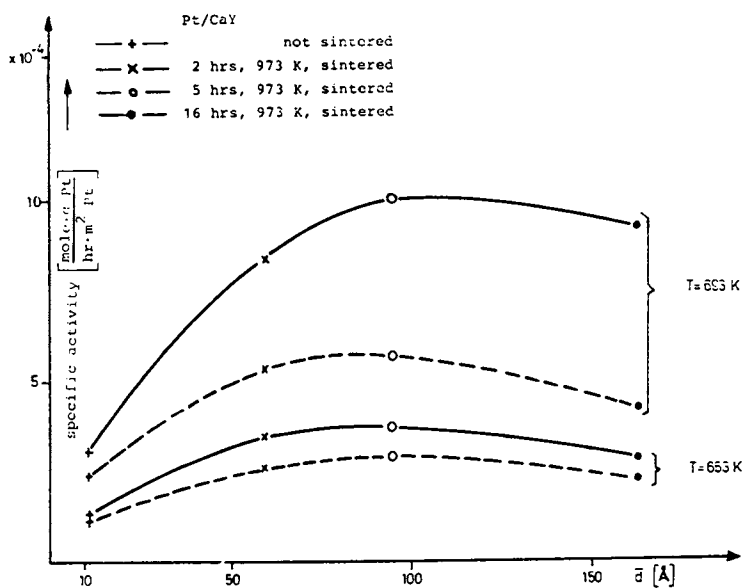


Figure 4. Specific activity as function of mean metal crystallite diameter for the isomerization of n-hexane

$$r = k_{\text{eff}} \left(1 - \frac{x_{1-\text{hexanes}}}{x_{1-\text{hexanes}}} \right) \quad (2)$$

where $[x_{1-\text{hexanes}}]$ stands for the mole fraction of all isomers of n -hexane and x_1 for the corresponding mole fraction at equilibrium.

After integration equation 2 can be used to determine values for k_{eff} . The dependency of k_{eff} on the temperature is used to evaluate the activation energies. Each set of data was linearly regressed to obtain k_{eff} and the activation energies. The obtained kinetic data are "overall" values which are evaluated for a coupled reaction system. Before the evaluation of the kinetic data the influence of gas-to-particle mass transfer and intraparticle diffusion on the overall rate had to be investigated. It was shown, that gas-to-particle mass transfer was an insignificant resistant to the overall rate for both Pt/CaY and Pt/H-mordenite confirmed by the criterion of Mears (18). The influence of intraparticle diffusion in the secondary pores was studied by systematic variation of the catalyst pellet size. A small influence of intraparticle mass transfer limitation was found for Pt/CaY but not for Pt/H-mordenite. The importance of micropore diffusion was not determined and the kinetic rates include any effect of diffusional rates in micropores. The experimentally determined values for

catalyst	pellet size d=H[mm]	effectiveness factor η_{exp}	$E_A \left[\frac{\text{kJ}}{\text{mole}} \right]$	$k_{\text{eff}} \left[\frac{\text{mole}}{\text{hr} \cdot \text{gr cat.}} \right]$
		$T=633 \text{ K}$		
Pt/CaY	4	0.60	66.9 ⁺ 7	7.66 x 10 ⁻³
Pt/CaY	3	0.73	76.1 ⁺ 8	9.52 x "
Pt/CaY	0.7	1.00	97.0 ⁺ 10	13.23 x "
Pt/CaY	0.5	1.00	97.0 ⁻ 10	13.25 x "
		$T=543 \text{ K}$		
Pt/H-mord.	4	0.90	115.0 ⁺ 11	1.67 x 10 ⁻²
Pt/H-mord.	3	0.94	115.0 ⁺ 11	1.89 x "
Pt/H-mord.	0.7	1.00	120.0 ⁺ 12	2.06 x "
Pt/H-mord.	0.5	1.00	120.0 ⁺ 12	2.02 x "

Table V. Results of intraparticle mass transfer limitation

effectiveness factors and the corresponding rate constants and activation energies are listed in Table V. The almost constant values of the activation energies and effectiveness factors for Pt/H-mordenite catalysts indicate that no significant mass trans-

fer limitation occurs. However, with Pt/CaY catalyst a continuous increase of effectiveness factors and activation energies is observed if the catalyst pellets are broken up into small pieces. These results indicate the occurrence of intraparticle diffusion limitation in the secondary pore system that means in the space between the zeolite crystals. Additional support is given by the structural parameters of the secondary pores of Pt/CaY and Pt/H-mordenite (Table I). The average diameter of the secondary pores of Pt/CaY has a value of 4000 Å and makes the diffusion limitation much more probable than the appropriate pore diameter for Pt/H-mordenite which is 2,5 times higher (10 000 Å).

Similar effects concerning mass transfer limitations have been obtained for the isomerization of n-pentane.

Conclusions.

The most active bifunctional isomerization catalysts are composed of zeolitic support like H-mordenite or CaY and noble metals like Pt or Pd. The catalysts with H-mordenite as support show already at temperatures as low as 573 K very high activity and selectivity for the isomerization. The investigation about the relations between the structural parameters of the metallic phase and the activity revealed that the isomerization of n-hexane and n-pentane over Pt/CaY catalysts is possibly "structure sensitive". Kinetic studies showed a slight intraparticle mass transfer limitation for Pt/CaY, but not for Pt/H-mordenite.

Acknowledgement.

The authors want to thank H.Litterer und C.P.Hälsig for experimental assistance and helpful discussions. They are also indebted to the "Deutsche Forschungsgemeinschaft" and the "Bundesministerium für Forschung und Technologie" for substantial financial support.

Literature Cited.

1. Cristoffel, E., Vierrath, H., Fetting, F., 5th European, 2nd Int. Symp. Chem. Reaction Engng., Amsterdam, (1972) 2-49
2. Christoffel, E., Fetting, F., Vierrath, H., J. Catal. (1975) 40, 349
3. Hopper, J. R., Voorhies, A., Jr., Ind. Eng. Chem. Proc. Des. Develop. (1972), 11, 294
4. Garanin, V. J., Minachev, Kh. M., Isakova, T. A., Neftekhimiya (1972), 12, 501
5. Beecher, R., Voorhies, A., Jr., Ind. Eng. Chem. Proc. Des. Develop. (1969) 8, 366
6. Minachev, Kh. M., Garanin, V. J., Piguzova, L. I., Vitukhina, A. S., Izv. Akad. Nauk SSSR, Ser. Khim. (1966), 6, 1001
7. Rabo, J. A., Pickert, P. E., Mays, R. L., Ind. Eng. Chem. (1961), 53, 773
8. Kouwenhoven, H. W., Adv. Chem. Ser. (1973), 121, 529
9. Lanewala, M. A., Pickert, P. E., Bolton, A. P., J. Catal. (1967), 9, 95
10. Bolton, A. P., Lanewala, M. A., J. Catal. (1970), 18, 1

11. Gallei, E., Eisenbach, D., Ahmed, A., *J. Catal.* (1974), 33, 62
12. Eisenbach, D., Gallei, E., *Chem. Ing. Techn.* (1973), 45, 1261
13. Gallei, E., Eisenbach, D., *J. Catal.* (1975), 37, 474
14. Braun, G., Ph.D. Thesis, TH Darmstadt, in preparation
15. Eisenbach, D., Ph.D. Thesis, TH Darmstadt, West-Germany, (1975)
16. Burbridge, B.W., *Advan. Chem. Ser.* (1971), 102, 400
17. Boudart, M., *Advan. Catal. Rel. Subj.* (1969), 20, 153
18. Mears, D.E., *Ind. Eng. Chem. Proc. Des. Develop.* (1971), 10, 541

Deactivation of Pd-H-Mordenite Catalyst during *n*-Hexane Isomerization

D. J. CHICK, J. R. KATZER, and B. C. GATES

Department of Chemical Engineering, University of Delaware, Newark, Del. 19711

ABSTRACT

Rates of reaction of *n*-hexane catalyzed by Pd-H-mordenite were measured at H₂ partial pressures near 1 atm and temperatures near 250°C. The rate of cracking decreased sharply as the Pd content increased to about 0.7 wt%, whereas the rate of isomerization increased gradually with increasing Pd content. The rate of catalyst deactivation increased with the rate of cracking and the associated deposition of coke in the pore mouths.

Introduction

Processes for paraffin isomerization to give gasoline components with high octane numbers require a catalyst with high activity and good stability to take advantage of the relatively high equilibrium conversions at low temperatures (1). Such a process using a noble-metal-containing H-mordenite catalyst has been introduced commercially (2,3,4,5).

The literature indicates that much industrial research has been devoted to characterization of the activities of metal-containing zeolite catalysts in this class. The *n*-C₆ isomerization activity (at 24-26 hr on stream) of RE-NH₄-Y, for example, has been found to increase linearly with Pt (or Pd) content up to 0.4 wt% and then become constant (6). The Pd-H-Y catalyst has been reported to be more active than Pt-H-Y (7); Pd-H-mordenite is typically found to be more active than Pd-H-Y (8,9,10,11), but these two catalysts have similar activities if their Na⁺ contents are extremely low (12). Paraffin isomerization activity of H-mordenite appears to be independent of noble metal content (9,13) or to increase somewhat with metal incorporation (8). Metal incorporation reduces cracking activity (8,9,12).

Catalyst stability is no less important than activity, but the literature provides little quantitative information about deactivation rates. Qualitative results show that metal-free H-mordenite deactivates very rapidly, and application of high hydro-

gen partial pressures or addition of metal stabilizes the catalyst (2,3,4,5,12,14). Slow deactivation has been reported for Pd-Y and for Pt-Y in paraffin isomerization (6,7).

The objective of this work was to provide a quantitative characterization of the Pd-H-mordenite isomerization catalyst. The desired data were rates of *n*-hexane conversion to isomerization and cracking products and rates of catalyst deactivation as a function of Pd content, reaction temperature, and reactant composition. Relatively severe reaction conditions were chosen to give high rates of deactivation and allow experiments to be completed rapidly.

Experimental Methods

Apparatus. Catalyst pretreatment and reaction were carried out in a conventional continuous-flow, packed-bed microreactor (15). An aluminum cylinder surrounding the reactor and held in a thermostatted Lindberg electric furnace provided reaction temperatures which varied only $\pm 0.2^\circ\text{C}$. Hydrogen and helium feeds flowed to the reactor through columns containing reduced copper catalyst and molecular sieve to remove O_2 and H_2O . Normal-hexane flowed from a Sage syringe pump through a vaporizer to a tee where it was mixed with hydrogen. The well-mixed vapor stream passed through a heated line to the reactor. Oxygen for catalyst calcination flowed through a separate line. Product vapors from the reactor passed through a heated line to a heated gas sampling valve, which allowed periodic injection of samples into a gas chromatograph. A 2-m by 3.2-mm *n*-octane on Porasil C column separated all the hydrocarbon products except CH_4 , which appeared with H_2 , and $\text{C}_2^=$, which appeared with C_2 .

Procedure. Zeolite powder (0.1 to 0.7g) was weighed onto a 5-cm by 10-cm layer of glass wool, which was rolled into a 10-cm long cylinder and inserted lengthwise into the reactor. Glass wool filled the space downstream of the catalyst section, and 3-mm diameter glass beads filled a 16-cm long preheater section upstream of the catalyst. The zeolite was calcined in flowing O_2 ($\sim 100 \text{ cm}^3/\text{min}$) as it was heated from 25 to 346°C at $2^\circ\text{C}/\text{min}$ then held for 3.0 hr at 346°C (16,17). The catalyst was cooled in flowing O_2 , then it was purged with He and reduced in flowing hydrogen ($\sim 60 \text{ cm}^3/\text{min}$) by heating at $2^\circ\text{C}/\text{min}$ to 397°C and holding for 3.1 hr. Typical run conditions were as follows: temperature, 247°C ; pressure, 1.35 atm; hydrogen flow rate 0.039 moles/hr; and *n*-hexane feed rate, 0.0063 moles/hr (giving a H_2 :*n*- C_6 molar ratio of 6.1). The first sample was taken 10 min after initiation of hexane flow; subsequent samples were taken at 35-min intervals, the time required for analysis. Total run time was typically 6 hr.

Materials. All chemicals were at least of reagent grade

purity (15). Catalysts were prepared from H-mordenite (Zeolon 100 H powder from Norton Company; 0.35 wt% Na₂O; SiO₂:Al₂O₃ = 12.5). The mordenite was converted to the NH₄⁺ form by slow addition of aqueous 1.0 N NH₄OH until the pH was 7.8 (18). The slurry was filtered, and the zeolite was washed then dried at 102°C for 12 hr. The resulting base material was used for preparation of catalysts containing 0.106, 0.249, 0.505, 0.711 and 1.47 wt% Pd. The mordenite was slurried in a 1 N NH₄NO₃ solution having a pH of 10. The desired amount of Pd(NH₃)₄Cl₂ (Matthey Bishop), dissolved in 1 N NH₄NO₃ solution, was added dropwise over a 1-hr period to the stirred slurry (2,8), then the slurry was held for 96 hr before filtering, to allow distribution of metal throughout the mordenite pore structure. (Pd removal from the solution was complete within a few minutes of Pd addition, as indicated by atomic absorption analysis.) The Pd-containing mordenite was filtered and washed until no Cl⁻ could be detected; no Pd losses were observed.

Details of the experimental methods are given elsewhere with a complete compilation of the results (15).

Results

In the absence of catalyst, there was no hexane conversion at temperatures as high as 350°C. When catalyst was present, a variety of cracking and isomerization products were observed. For each product, a plot of conversion against inverse space velocity gave a straight line passing through the origin, demonstrating differential reactor behavior for total conversions of at least 15%. Consequently, the conversion data provided reaction rates directly. Figure 1 shows how the total isomerization rate depended on time on stream and gives an indication of run-to-run reproducibility of the data. These results are similar to those obtained by plotting rates of isomerization and cracking to give each of the individual products (15).

Since the rate of each reaction evidenced a nearly exponential decrease with time, all the data have been summarized in a set of equations of the form

$$R_i = R_{i,0} e^{-\frac{t}{Y_i}} \quad [1]$$

This expression has been frequently observed for deactivating catalysts (e.g., 19,20), and it suggests that the rate of deactivation was directly proportional to the number of catalytic sites (21). Eq. [1] was fitted to the rate data for each product with least squares linear regression, then Chauvenet's criterion (22) was used to reject data points deviating too far from the mean, and expression [1] was refitted to the remaining points. The full set of results has been summarized in terms of initial rate ($R_{i,0}$), the time constant for deactivation (Y_i), and deviation at the 90% confidence limits; some of these data appear in the accompanying

figures and tables, and all of them are given in a thesis (15).

The rate of cracking in the presence of metal-free H-mordenite was initially high and decreased rapidly with time; for example, conversion of *n*-hexane at 247°C after 10 min was 60.6% (54.1% cracked and 5.7% isomerized); after 43 min, the total conversion had fallen to 15.7% (11.6% cracked and 4.2% isomerized). In the presence of 0.106 wt% Pd-H-mordenite under the same conditions, the total conversion of *n*-hexane after 10 min was 15.7% (9.9% cracked and 5.8% isomerized), and that after 40 min was 8.3%. For each of these catalysts, the two earliest points fell significantly above the line fitted to the remaining points, and the early points were excluded from the final fitting, so that the extrapolated initial rates are low for these two catalysts. For catalysts with higher Pd contents, no such systematic deviation from the general pattern was observed, and the extrapolated initial rates are considered to be good estimates of the true values (Figure 1).

The data summarizing the initial rates of formation of each saturated cracking product are shown in Figure 2. Each rate decreased markedly with increasing catalyst Pd content up to 0.7 wt%, but it did not decrease further with further increases in Pd content. In the presence of metal-free H-mordenite, a significant amount of propylene was produced; with 0.106 wt% Pd-H-mordenite, a small amount was produced; and with higher Pd contents, no olefinic products were detected.

The initial rate data representing formation of each C₆ isomerization product are summarized in Figure 3. The rate of formation of each product except 2,2-dimethylbutane generally increased with increasing Pd content, in contrast to the cracking results. An increase in Pd content exerted a greater relative influence on production of dimethylbutanes than methylpentanes, leading to a marked shift in selectivity toward the methylpentanes-dimethylbutanes equilibrium.

The ratio of the total isomerization rate to the total cracking rate increased with increasing Pd content (Figure 4). Only for Pd contents greater than about 0.4 wt% was the total isomerization rate greater than the total cracking rate.

The rates of deactivation represented by $1/Y_1$ for each of the isomerization products are collected in Figure 5, and the comparable data for the cracking products are shown in Figure 6. The rate of deactivation for each cracking and isomerization reaction decreased markedly with increasing catalyst Pd content up to 0.5–0.6 wt%, beyond which value little further decrease and even a small increase occurred. The initial rates of deactivation observed with the metal-free H-mordenite and with the 0.106 wt% Pd-H-mordenite were higher than indicated because the rapid initial deactivation was not represented by the fitting technique; the deviation is especially significant for cracking. The important result is the similarity in deactivation behavior for cracking and isomerization reactions.

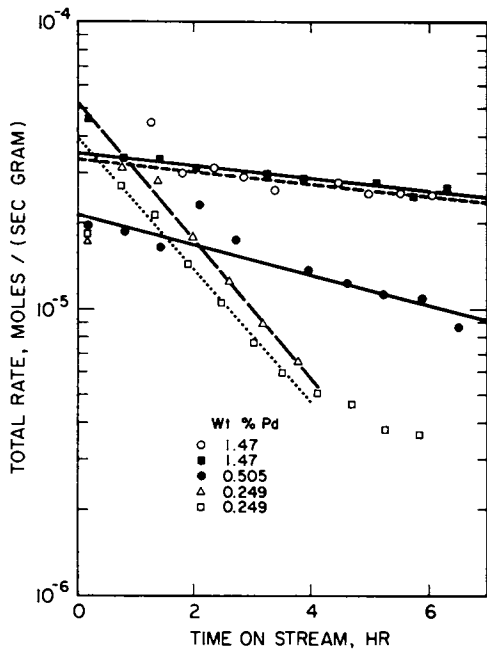


Figure 1. Total n-hexane isomerization rate catalyzed by 0.249, 0.505, and 1.47 wt % Pd-H-mordenite at 247°C

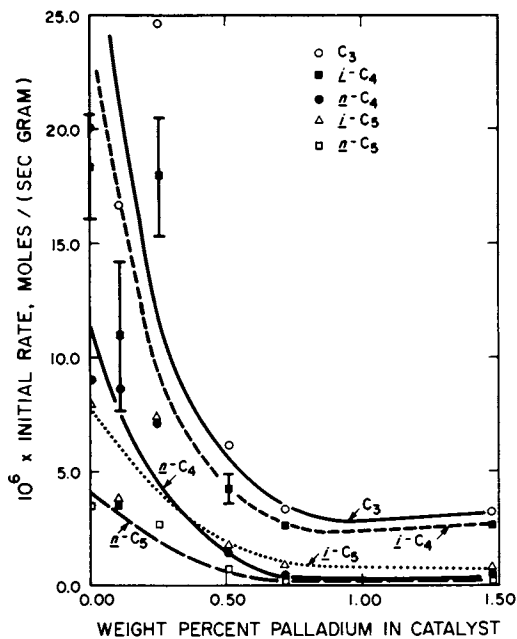


Figure 2. Effect of Pd content of H-mordenite on initial rate of formation of cracking products at 247°C

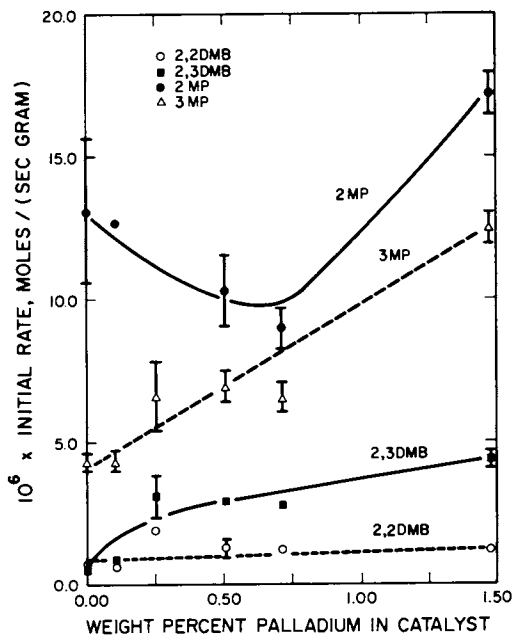


Figure 3. Effect of Pd content of H-mordenite on initial rate of formation of C₆ isomers at 247°C

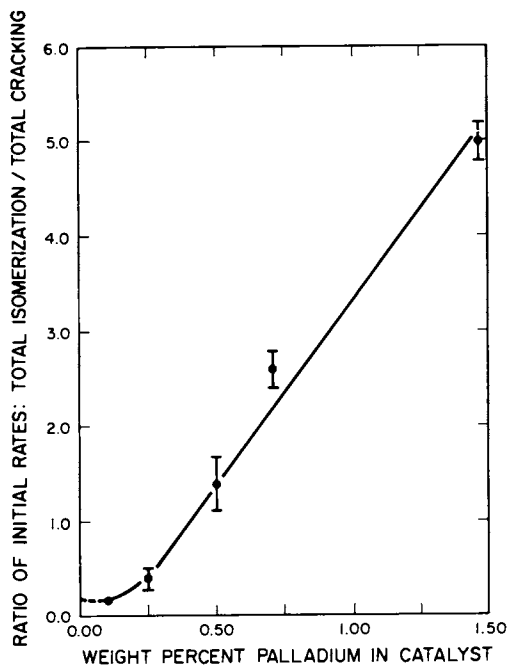


Figure 4. Effect of H-mordenite Pd content on ratio of total isomerization to total cracking rate at 247°C

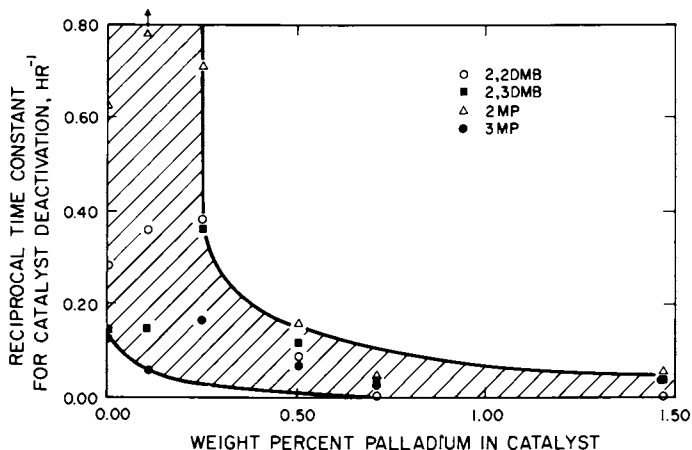


Figure 5. Effect of H-mordenite Pd content on the rate of deactivation for formation of isomerization products at 247°C

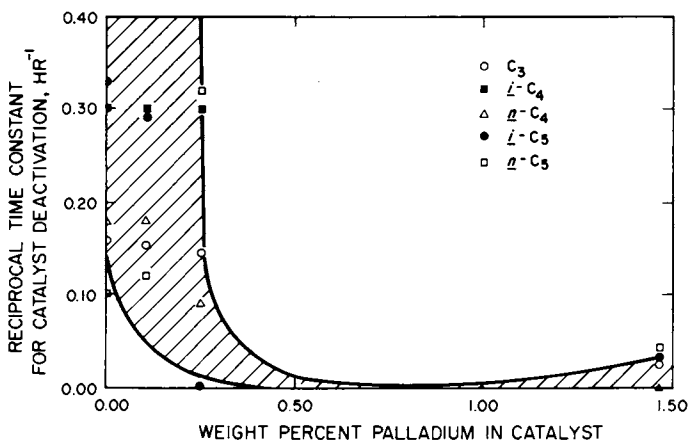


Figure 6. Effect of H-mordenite Pd content on the rate of deactivation for formation of cracking products at 247°C. The catalysts containing 0.505 and 0.711 wt % Pd had deactivation rates for total cracking which were indistinguishable from zero. The catalyst containing 1.47 wt % Pd, however, had a measurable deactivation rate which was well reproduced in three runs.

The apparent activation energies for the formation of each of the products catalyzed by the 0.505 wt% Pd-H-mordenite were calculated from the initial rate data and are given in Table I. Activation energies for isomerization were typically 34 kcal/mole, about 20 kcal/mole less than for cracking. The literature reports values of 31-38 kcal/mole for *n*-pentane isomerization catalyzed by Pd-H-mordenite (9,13,23,24). The activation energy for acid-catalyzed *n*-hexane cracking is typically 30 kcal/mole (25,26), but in the presence of H₂ and a catalyst with 0.5 wt% Pd, we found it to be about 55 kcal/mole, which is consistent with the literature value of 54-55 kcal/mole reported for *n*-hexane cracking catalyzed by 0.5 wt% Pd-H-mordenite at 51 atm (10).

The time constants representing loss of the total isomerization activity were 27.8, 8.30, and 3.37 hr⁻¹ at 234, 246, and 267°C, respectively. The apparent activation energy of this deactivation process calculated from the slope of a plot of ln($\frac{1}{Y}$) vs. ($\frac{1}{T}$) was 34 kcal/mole. Because of the very low rate of activity loss for cracking in the presence of the 0.505 wt% Pd-H-mordenite catalysts, a good estimate of the corresponding activation energy could not be obtained.

TABLE I. Activation Energies and Pre-Exponential Factors for Cracking and Isomerization of *n*-Hexane Catalyzed by 0.505 Wt% Pd-H-Mordenite^a

Product	$\frac{A}{b}$	E_a , kcal/mole
C ₁ +C ₂ ^c	3.2 x 10 ⁸	35.8
C ₃	4.1 x 10 ¹⁸	56.9
<i>i</i> -C ₄	4.9 x 10 ¹⁶	52.6
<i>n</i> -C ₄	3.5 x 10 ²⁰	63.5
<i>i</i> -C ₅	1.8 x 10 ¹⁶	52.5
<i>n</i> -C ₅	5.9 x 10 ¹⁵	52.9
2,2DMB	1.1 x 10 ¹¹	40.4
2,3DMB	2.2 x 10 ⁸	33.0
2MP	2.2 x 10 ¹⁰	36.5
3MP	3.9 x 10 ⁷	30.4
$\Sigma(C_2-C_5)$ ^d	1.9 x 10 ¹⁸	55.3
$\Sigma(i-C_6)$ ^d	6.1 x 10 ⁹	34.4

^aReaction conditions: temperature range = 234 to 267°C; total pressure = 1.36 atm; H₂:*n*-C₆ molar ratio = 6.0; total conversion less than 15%.

^bPreexponential factor, moles/(g sec).

^cImprecise since only small amounts of these products were formed.

^dCalculated by summing the initial rates at each temperature and then performing the least-squares analysis.

Decreasing the H₂:*n*-C₆ molar ratio from about 6.2 to 2.8 with the 1.47 wt% Pd-H-mordenite catalyst resulted in a doubling of the initial total cracking rate and a marked increase in the rate of deactivation for cracking (Y decreased from 27 to 6.2 hr). The

isomerization rate increased by only about 40%, but the rate of deactivation for isomerization increased considerably (Y decreased from 25 to 6.2 hr).

Discussion

Metal-free H-mordenite is an extremely active cracking catalyst (25), but it undergoes rapid deactivation, probably caused by blocking of its narrow pores by deposited coke. The observed absence of significant amounts of olefins in the cracking products indicates that there was significant coke deposition, since cracking produces olefins and their saturation must be accounted for in the overall hydrogen balance. Direct hydrogenation of olefins at our conditions in the absence of metal is probably unimportant.

Addition of Pd to the catalyst leads to a sharp decrease in the rate of cracking (Figure 2) and in the rate of deactivation (Figures 5 and 6). The results of these figures are the first quantitative data substantiating the generally accepted conclusion that added metal stabilizes the isomerization catalyst (3,4,5,7,12,27). The rate of deactivation is clearly correlated with the rate of cracking (Figures 2,5, and 6), and this result suggests that the cracking reactions lead directly to catalyst deactivation through coke formation, as olefins formed in cracking are polymerized and as hydrogen is transferred from unsaturated species to olefins.

The isomerization reactions occur in parallel with the cracking reactions, and it is inferred that they take place independently of them, since the isomerization rate, in contrast to the cracking rate, increases with increasing Pd content. Since the catalyst deactivation for both cracking and isomerization is correlated directly with the rate of cracking reactions, it is suggested that deactivation is related to pore blocking by coke. This suggestion does not account for all the deactivation data, however, since isomerization and cracking reactions experience different patterns of deactivation at the higher metal contents (Figures 5 and 6). The loss of isomerization activity observed in the range for which cracking activity loss was immeasurably small (\sim 0.6-1.0 wt% Pd) may be interpreted as an indication of poisoning of the isomerization sites.

The important suggestion is that the stabilization by Pd in the catalyst is associated much more with a reduction of the cracking activity than with hydrogenation of coke or coke precursors or the establishment of more favorable olefin-paraffin-carbonium ion ratios (3,12).

The literature indicates that small metal crystallites and uniform dispersion of the metal are preferred (2,3,4,5,8,12), and therefore the above preparation procedures were chosen to assure maximum metal dispersion (12,16,17). X-ray diffraction examination of the 1.47 wt% Pd-H-mordenite gave no indication of Pd crystallites large enough to produce line broadening (\geq 3.0 nm)

and confirmed that the metal was well dispersed. In H-mordenite containing 0.5 wt% Pd there is expected to be about one Pd atom per 18 nm of pore length, provided that there is no clustering. Catalysts with lower Pd contents could have had significant fractions of their pores which lacked Pd atoms (or clusters) for distances of several 10's of nm into the pore. Such pores are expected to behave as though they were metal-free H-mordenite, which has a high cracking activity and a high deactivation rate. Only when so much Pd is present that almost all the pore mouths contain Pd, is the rapid cracking and rapid deactivation expected to be lacking. We suggest that this condition prevails for Pd contents in excess of 0.5 wt%; then deactivation rates are low and, like cracking rates, they are almost independent of metal content.

To test this suggestion, mordenite containing 0.506 wt% Pd was prepared in the usual way, except that all contacting times were reduced to minimize the migration of Pd atoms from the pore mouths toward the interior regions. Only three hours elapsed between the first contacting of mordenite with Pd and the start of its calcination in the reactor. The catalyst prepared in this way evidenced an initial isomerization rate, an initial cracking rate, and a rate of deactivation characteristic of standard catalysts with higher Pd contents (Table II). These results are in agreement with the earlier suggestion of the importance of the fraction of the pore mouths having Pd atoms near them.

Under the conditions of this study and in the absence of a metal, isomerization and cracking both occur by carbonium ion mechanisms. Activation of paraffins requires hydride abstraction by Lewis acid sites (27) or protonation by "super acid" groups (13,28,29), probably those adjoining a Lewis acid site (30). Lewis acid sites are produced in H-mordenite under the pretreatment conditions used in this work (31). Therefore, the suppression of cracking and of catalyst deactivation by added Pd is inferred to result from a reduction in the number and/or strength of Lewis acid sites, perhaps as these sites combine with monohydrogen species spilling over from the Pd onto the zeolite surface (30). Complete suppression of 2,3-dimethylbutane cracking by H₂ in the presence of Pd-H-Y has been reported (30); the cracking appeared to require Lewis acidity. Suppression of cracking and of deactivation might alternatively result from a reduction in the carbonium ion lifetime associated with a greater reactivity of hydrogen in the presence of Pd. But this suppression is not simply the result of the occupation of Lewis acid sites by Pd, since an increased H₂:n-C₆ ratio led to reduced rates of cracking and of deactivation and to increased rates of isomerization.

H-mordenite is a good monofunctional paraffin isomerization catalyst, provided that the hydrogen partial pressure is high enough to suppress cracking and to reduce deactivation (9,12,13,14). Pd appears to have much the same effect as high hydrogen partial pressure. The observed increase in isomerization activity

TABLE II. The Effect of Metal Contacting Time on the Catalytic Properties of Pd-H-Mordenite

Metal Content, Wt%	$10^6 \times$ Initial Rate ^{a,b}		Isomerization Deactivation Time Constant, hr
	Isomerization	Cracking	
0.506 ^c (short prep. time)	27.4	8.6	21.6
0.505	21.4	15.0	8.3
0.711	19.4	7.6	25.9
1.47	35.1	7.0	20.6
1.47	33.5	6.8	20.7

^aRate in moles (total isomerized or total cracked) per gram of catalyst per second.

^bReaction conditions: Temperature = 247°C; total pressure = 1.36 atm; WHSV = 1.5-1.8; H₂:n-hexane molar ratio = 6.0-6.2.

^cTotal catalyst preparation time was 3 hr; all other catalysts were prepared by the standard procedure described in the text.

(both absolute and relative to cracking) with increasing Pd content is inferred to result from a shift in the relative proportion of site types and site strengths. This suggestion is supported (1) by the observation that the total initial rate of reaction decreased about twofold and the isomerization rate increased about threefold as the Pd-content increased over the range studied and (2) by the observation that at higher pressures the addition of Pd affects the isomerization slightly (8) or not at all (9,13,14).

Literature reports (3,4,5,12) indicate that increasing the Pd content of H-mordenite from 0 to 0.003 wt% led to a 13-fold increase in the rate of isomerization of n-pentane at 20 hours onstream time. The present data suggest that this result primarily reflects the effect of Pd on the extent of catalyst deactivation, rather than on the intrinsic catalytic activity for isomerization.

A bifunctional reaction mechanism, involving olefin formation catalyzed by the metal, has been proposed for isomerization in zeolites (3,4,5,9,12,13,14,23,24), as has a mechanism involving bimolecular cyclohexane ring formation (32). In contrast to the former suggestion, no C₆-olefins were detectable in the product, although equilibrium concentrations could have been easily determined. Nonetheless, strong preferential adsorption of olefins may have prevented their escape into the product stream (33). In contrast to the suggestion of a bimolecular cyclohexane ring formation mechanism, no hydrocarbons with more than six carbon atoms could be detected in the liquid product. Nor were cyclic products such as benzene and methylcyclopentane formed.

Although our results do not rule out the bifunctional reaction mechanism in the presence of Pd, they give no evidence

suggesting that it plays a role. Nor did we find evidence of a mechanism involving a bimolecular cyclohexane ring intermediate. The data are explained by the simple suggestion that deactivation is a direct result of cracking, and the reduction of the rate of deactivation with increased catalyst Pd content results more from the reduction in the rate of cracking than from the hydrogenation of coke precursors and coke. Our results suggest that Pd plays the role of controlling the surface acid properties in the H-mordenite pore structure and thereby altering the catalyst selectivity.

Acknowledgment

We thank G.C.A. Schuit for helpful discussions, the Norton Company for providing the mordenite, and Matthey-Bishop, Inc., for providing the Pd salt.

Nomenclature

- A = preexponential factor, moles/g of catalyst/sec
E_a = activation energy, kcal/mole
R_i = rate of formation of species i, moles/g cat/sec (R may also represent total isomerization rate or total cracking rate)
R_{i,0} = initial rate (at t = 0) of formation of species i, moles/g cat/sec
t = time on stream, hr
WHSV = weight hourly space velocity, g n-C₆/g cat/hr
Y_i = time constant for catalyst deactivation for formation of component i, hr

Literature Cited

1. Douslin, D. R., Preprint 23-71, A.P.I. Division of Refining (May, 1971).
2. Kouwenhoven, H. W., and van Helden, H.J.A., British Patent 1,189,850 (April 29, 1970).
3. Kouwenhoven, H. W., and van Zijll Langhout, W. C., "Shell Hydro-Isomerization Process for C₅/C₆ Fractions," 68th AIChE National Meeting, Houston (1971).
4. Kouwenhoven, H. W., and van Zijll Langhout, W. C., Chem. Eng. Prog. (1971), 67, (4), 65.
5. Kouwenhoven, H. W., and van Zijll Langhout, W. C., Petrol. and Petrochem. Inter. (1971), 11, (11), 64.
6. Lanewala, M. A., Pickert, P. E., and Bolton, A. P., J. Catal. (1967), 9, 95.
7. Rabo, J. A., Pickert, P. E., Stamires, D. N., and Boyle, J. E., "Actes Congr. Intern. Catalyse, 2^e Paris," (1960), 2, 2055, Editions Technip, Paris (1961).
8. Benesi, H. A., U.S. Patent 3,527,835 (Sept. 8, 1970).

9. Voorhies, A., and Bryant, P. A., *AIChE J.* (1968), 14, 852.
10. Voorhies, A., and Hatcher, W. J., Jr., Preprint 20A, 61st AIChE Annual Meeting, Los Angeles (1968).
11. Barbridge, B. W., Keen, I. M., and Eyles, M. K., *Advan. Chem. Ser.* (1971), 102, 400.
12. Kouwenhoven, H. W., *Advan. Chem. Ser.* (1973), 121, 529.
13. Minachev, K. H., Garanin, V., Isakova, T., Kharlamov, V., and Bogomolov, V., *Advan. Chem. Ser.* (1971), 102, 441.
14. Bryant, P. A., Ph.D. Thesis, Louisiana State University (1966).
15. Chick, D. J., "Catalyst Deactivation During *n*-Hexane Isomerization Catalyzed by Pd-H-Mordenite," M.Ch.E. Thesis, University of Delaware, Newark, Del. (1974).
16. Dalla Betta, R. A., and Boudart, M., "Proc. 5th Intern. Congr. Catal.," ed., J. W. Hightower, (1972), Vol. 2, p. 1329, North-Holland, Amsterdam (1973).
17. Shell International Research Mij, British Patent 1,189,850 (April 20, 1970).
18. Kimberlin, C. N., Jr., U.S. Patent 3,259,564 (July 5, 1966).
19. Nolley, J. P., and Katzer, J. R., *Advan. Chem. Ser.* (1973), 121, 563.
20. Nace, D. M., *Ind. Eng. Chem. Product Res. Develop.* (1969), 8, 24, 31.
21. Tan, C. H., and Fuller, O. M., *Canad. J. Chem. Eng.* (1970), 48, 174.
22. Young, H. D., "Statistical Treatment of Data," McGraw-Hill Book Co., New York (1962).
23. Hopper, J. R., and Voorhies, A., *Ind. Eng. Chem. Prod. Research Develop.* (1972), 11, 294.
24. Voorhies, A., and Beecher, R. G., "Hexane Isomerization over a Zeolite Catalyst," Preprint 20B, 61st AIChE Annual Meeting, Los Angeles (1968).
25. Miale, J. C., Chen, N. Y., and Weisz, P. B., *J. Catal.* (1966), 6, 278.
26. Chen, N. Y., "Proc. 5th Intern. Congr. Catal.," ed., J. W. Hightower, Vol. 2, p. 1343, North-Holland, Amsterdam (1973).
27. Goble, A. G., and Lawrance, P. A., "Proc. 3rd Intern. Congr. Catal.," Amsterdam (1964), 1, 320, North-Holland, Amsterdam (1965).
28. Olah, G. A., *J. Amer. Chem. Soc.* (1972), 94, 808.
29. Bickel, A. F., *et al.*, *Chem. Commun.* (1967), 634.
30. Turkevich, J., and Ono, Y., "Advances in Catalysis," Vol. 20, eds., D. D. Eley, H. Pines, and P. B. Weisz, p. 135, Academic Press, New York (1969).
31. Karge, H., *Z. Physik. Chem.* (1971), 76, 133.
32. Bolton, A. P., and Lanewala, M. A., *J. Catal.* (1970), 18, 1.
33. Thomas, C. L., and Barmby, D. J., *J. Catal.* (1968), 12, 341.

Properties of the Metallic Nickel in Reduced NaNiY Zeolite Catalysts

K. H. BAGER, F. VOGT, and H. BREMER

Department of Chemistry, Technical University "Carl Schorlemmer"
Leuna-Merseburg, Merseburg, West Germany

ABSTRACT

The reducibility of the Ni^{2+} cations, the dispersion and location of the metallic phase and the catalytic dehydrogenation activity were investigated on zeolites NaNiY (~ 4 wt. % Ni) modified by mono, two and trivalent cations (NH_4^+ , Ca^{2+} , Ce^{3+}).

The metallic nickel is localized on the external surface as well as in the zeolite cages depending on the temperature of reduction and the nature of the second-cation.

Introduction

Zeolite catalysts which contain cations of group VIII b exhibit bifunctional properties after reduction. Therefore most zeolite catalysts used for hydrocracking, hydroisomerization and selectoforming contain noble metals like Pt, Pd or the cheaper nickel as hydrogenation/dehydrogenation components.

For optimal hydrogenation/dehydrogenation properties the content, the dispersion and the location of the metal are of essential importance. It should be possible to modify these properties to a certain extent by choice of the pretreatment conditions, the degree of cation exchange and a controlled directional effect on the Ni^{2+} ion location, e. g., by exchange of a second-cation with different site selectivity.

The reducibility of Ni^{2+} ions in faujasite type zeolites and characterization of the metal by X-ray, electron microscopy, magnetic, chemisorption and catalytic methods have been the subject of many investigations (1-14). Most authors agree that after reduction the nickel migrates to the external surface where it deposits yielding large agglomerates. Nevertheless there is little information on which conditions of pretreatment and of reduction lead to the reduced nickel remaining within the zeolite cages and on what its properties are. The site-directing influence of a

second-cation on the properties of the reduced nickel zeolites has not been investigated. The present work deals with these problems.

Experimental

Materials. The zeolites studied are summarized in Table I. The samples were prepared by a consecutive ion exchange (2 h) at 70°C with 0.1 N nitrate solutions of the Ni²⁺, NH₄⁺, Ca²⁺ and Ce³⁺ ions, respectively. The degree of exchange was determined by analyzing the solid for the amount of remaining sodium and exchanged cations.

Table I.- Zeolites Studied

Sample	SiO ₂ /Al ₂ O ₃ Mole Ratio	Exchange Degree	
		equ. % of Ni ²⁺	equ. % of Second cation
NaY	5.2	0	0
Na 0.30NiY	5.2	30	0
0.30CaNa 0.31NiY	5.2	31	30
0.47CeNa 0.32NiY	5.2	32	47
0.49NH ₄ Na 0.32NiY	5.2	32	49

Pretreatment of Samples. All samples were reduced with hydrogen (4 l/h) for 2 h at temperatures between 300 and 500 °C after drying at 110 °C. For comparison parts of the dried samples were reduced after pretreatment (15 min.) at 500 °C in a stream of argon (4 l/h) and air (4 l/h), respectively.

Experimental Technique. The degree of reduction of nickel was determined by an iodimetric titration. The metallic nickel was solved by an acid 1.0 M K₂Cr₂O₇ solution (15). XPS investigations were carried out on an A.E.I. spectrometer, ES-100 with AlK_α-radiation (E= 1486.6 eV). The samples were pretreated at 400 °C in vacuum (5·10⁻⁶ torr) and for 2 h in a hydrogen atmosphere, followed by a vacuum treatment for 2 h (16)^a. The electron ferromagnetic resonance (EFR) spectra were recorded by ESR spectrometer ER 9 (VEB Carl Zeiss Jena) in the region of 600-5000 Oe. After reduction samples were evacuated (10⁻³ torr)

^a These investigations were carried out at the Academy of Sciences of USSR, Institute of Organic Chemistry, Moscow, in the laboratory of Prof. Dr. Kh. M. Minachev.

for 2 h at 250°C and sealed under vacuum. Chemisorption of oxygen was carried out at 0°C by a pulse chromatographic method. For electron microscopy we used a microscope of type SEM 3/2 (VEB Werk für Fernsehelektronik Berlin). The reduced samples were investigated by means of coal replica techniques. Catalytic activity in cyclohexane dehydrogenation was measured at 280–320°C by a pulse technique.

Results

In Figure 1 the degree of reduction is given as function of reduction temperature for all unpretreated samples and for the pretreated NaNiY. For all reduction temperatures the same sequence of degree of reduction ($\text{Ni}^0/\text{Ni}^0 + \text{Ni}^{2+}$, %) was observed: $\text{CaNaNiY} > \text{NaNiY} > \text{NH}_4\text{NaNiY} > \text{CeNaNiY}$. Three different regions of temperature can be clearly distinguished for the reduction of Ni^{2+} ions, especially in the case of the zeolites CaNaNiY and NaNiY. Until about 350°C the degree of reduction strongly increased with temperature, followed by only slight changes in the reduction degree. Above 420°C a further increase of the amount of reduced nickel was observed. For NH_4NaNiY and CeNaNiY a significant reduction of the nickel occurs only at temperatures above 420°C. In Figure 1 the influence of pretreatment on the degree of reduction for NaNiY is also shown. The typical reduction behavior remains unchanged, but the dehydration before reduction diminished the extent of reduction. The distinct differences existing at lower temperatures are no longer present at reduction temperatures of 500°C.

The degree of reduction determined by XPS after 2 h of reduction at 400°C is summarized in Table II. For comparison the values for the reduction degrees as measured by the chemical method are given in parenthesis.

Table II.— Degree of Reduction of Nickel (XPS)

Sample	Degree of Reduction ($\text{Ni}^0/\text{Ni}^0 + \text{Ni}^{2+}$ %)	
	after Vacuum Treatment (400°C, 16 h)	after Air Treatment (500°C, 5 h)
CaNaNiY	58 (42)	38 (28)
NaNiY	49 (28)	35 (20)
CeNaNiY	32 (6)	18–20 (6)
NH_4NaNiY	27 (18)	10–11 (12)

The values obtained by XPS are higher than those measured by the chemical method. While XPS is only sensitive to the nickel in the external surface layers the chemical method determines the integral value for surface and bulk. In spite of these differences the sequence of reduction degrees in the samples examined is the same with both methods (exception: CeNaNiY).

From the EFR spectra we got the line intensity (I_{REL}), the line with (ΔH) and the g-values (17). The change of these parameters with temperature of reduction is shown in Figure 2 for the unpretreated NaNiY (CaNaNiY shows an analogous behavior) and NH_4NaNiY . These differences in the reduction behavior in the case of CaNaNiY and NaNiY on the one hand and in the case of NH_4NaNiY and CeNaNiY on the other hand are reflected in the I_{REL} -values. While the ΔH - and g-values for the NaNiY, CaNaNiY and CeNaNiY are constant with increasing reduction temperature, both parameters for the NH_4NaNiY sample are characterized by a maximum value at reduction temperatures of 450 °C. The $I_{REL, Ni}$ -values (I related to the amount of nickel) for all unpretreated samples and a sample of NaNiY which were thermally treated (vacuum, 580 °C, 50 h) after the reduction are shown in Figure 3. The curve course for all samples was similar with the exception of NH_4NaNiY . For reduction temperatures up to 400 °C the $I_{REL, Ni}$ -values are essentially unchanged. Above 400 °C they decrease. At 450 °C for the NH_4NaNiY a significant maximum is evident. Up to 400 °C the sequence of $I_{REL, Ni}$ -values is: CeNaNiY > NaNiY (580 °C, 50 h) > CaNaNiY > NaNiY >> NH_4NaNiY .

Figure 4 shows for all unpretreated samples the results obtained in the oxygen chemisorption as function of reduction temperature. The F-value characterizes the proportion of the nickel surface atoms (available for oxygen) to the total number of nickel atoms. For the calculation of the average particle size from the chemisorption data the edge distance of regular octahedrons was taken as particle diameter (d_{Ni}). An adsorption stoichiometry of Ni:O=1:1 and an effective Area of 7,2 Å² Ni per oxygen atom were assumed. NH_4NaNiY shows the highest F-values and corresponding the lowest Ni particle sizes (1-30 Å) changing strongly with increasing reduction temperature. For the other samples the Ni particle sizes (60-300 Å) nearly independent of reduction temperature.

Results of the electron microscopy of the airpretreated samples and the specific nickel surface area of the unpretreated samples are summarized in Table III. This table shows that with increasing reduction temperature the crystallites at the external surface of the NaNiY and CaNaNiY increase. The nickel in CeNaNiY at high temperatures tends to migrate and crystallize at the external zeolite surface upon reduction. For NH_4NaNiY at all reduction temperatures no nickel crystallites were detectable at the surface. Although the NH_4NaNiY and CeNaNiY exhibit comparable degrees of reduction of nickel, the specific nickel surface area

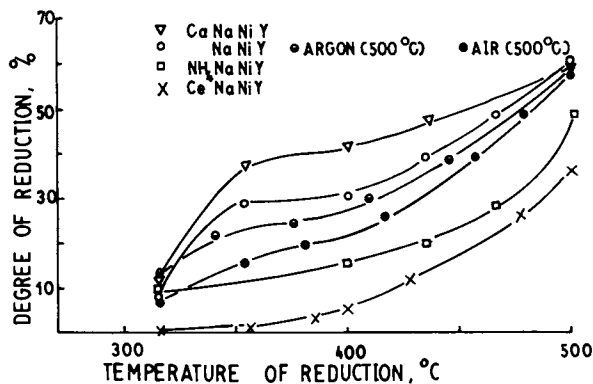


Figure 1. Temperature dependence of the degree of nickel reduction for unpretreated samples and pretreated NaNiY

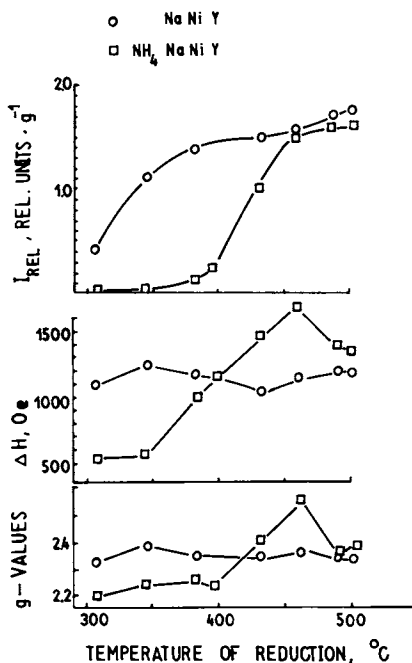


Figure 2. Temperature dependence of the EFR parameters for the NaNiY and NH_4NaNiY

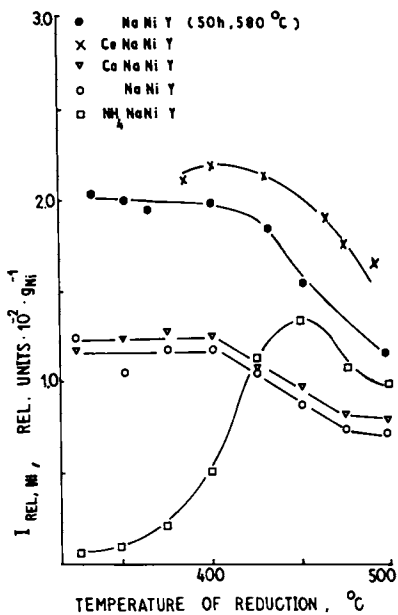


Figure 3. EFR line intensity ($I_{REL, Ni}$) as a function of reduction temperature

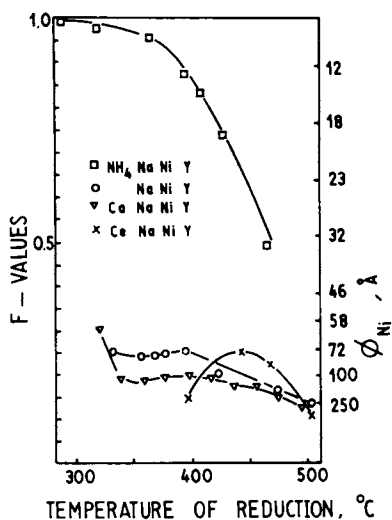


Figure 4. Dependence of crystallite size (ϕ_{Ni}) and F-value on the temperature of reduction

differs by threefold. For all samples there is a maximum of the specific nickel surface area at a reduction temperature of about 450 °C.

Table III.- Sizes of the Nickel Crystallites, ϕ_{Ni} (Electron Microscope) and Specific Nickel Surface Area, S_{Ni} (Oxygen Chemisorption)

Sample	ϕ_{Ni} , Å		S_{Ni} , m ² /gNi		
	after Reduction at		after Reduction at		
	386 °C	486 °C	400 °C	450 °C	500 °C
NaNiY	50	135	2.2	2.6	2.4
CaNaNiY	160	260	2.4	2.6	2.4
CeNaNiY	-	260	0.8	1.8	1.6
NH ₄ NaNiY	-	-	4.2	4.8	4.6

Based on critical molecular diameter the dehydrogenation reaction of cyclohexane to benzene should occur on the metallic nickel on the external zeolite surface as well as on the finely dispersed nickel in the supercages. The apparent (per g catalyst) and specific (per m² Ni) constants of reaction rate (calculated according to the equation of Basset and Habgood (18) from the degrees of conversion determined at 290°C) are shown in Figures 5 and 6 for the untreated samples as a function of the reduction temperature. NH₄NaNiY reduced between 350–400°C has the highest dehydrogenation activity despite the extremely low degree of reduction. With the exception of CeNaNiY all the other samples have their maximum catalytic activity after reduction at 350–400°C. The NaNiY has a second maximum at the reduction temperature at which also the maximum catalytic activity of the CeNaNiY occurs (460 °C).

For NaNiY the specific catalytic Ni activity decreases only slightly with increasing reduction temperature; it decreases more significantly for the other samples (Figure 6). Reduced NaNiY have the highest specific dehydrogenation activity of all samples investigated.

Discussion

Nickel zeolite carrier catalysts exhibit good hydrogenation/dehydrogenation properties when they have a large and accessible metallic surface. The catalytically effective metallic surface is determined by the amount, the dispersion and the location of the metal in zeolite cages.

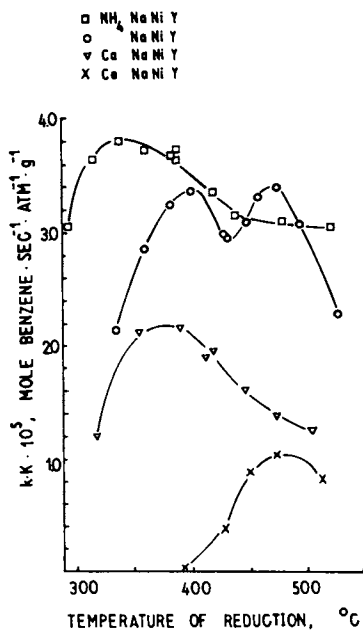


Figure 5. Apparent reaction rate constants as a function of reduction temperature

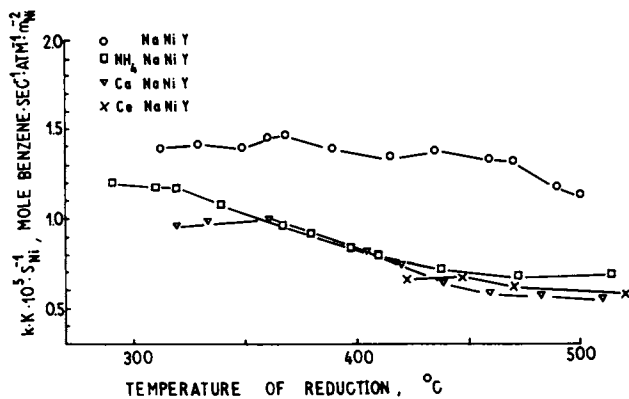


Figure 6. Influence of reduction temperature on specific reaction rate constants

Figure 1 clearly illustrates that the amount of nickel reduced between 300–500 °C increases considerably. While at 500 °C the differences in the extent of reduction of the samples are not large; for lower temperatures significant differences are observed. From this it follows that at reduction temperatures below 400 °C (Figure 1) the Ni^{2+} ions in the supercages are reduced and that only at higher temperatures does reduction of Ni^{2+} in the small cages take place. While cations which support the Ni^{2+} location in the small cages (S_I , $\text{S}_{I'}$, S_{II}) decrease the nickel reducibility (NH_4^+ , Ce^{3+}), Ca^{2+} cations (high S_I -selectivity) cause an increased reducibility.

By the choice of the cation present not only nickel reducibility but also the dispersion of the metal formed can be influenced. In the case of CaNaNiY and NaNiY the reduction leads to relatively large metal crystallites (Figure 2 and 3) which have superparamagnetic and ferromagnetic properties, respectively. Metal crystallites with these properties may only be formed at the external surface. The oxygen chemisorption measurements and the electron microscopic investigations (Figure 4 and Table III) confirm the migration and the location of the nickel at the external surface. A remarkable reduction of CeNaNiY begins only at temperatures above 400 °C and leads to the formation of only a few but relatively large nickel crystallites at the external surface (Figure 3 and 4, Table III).

On the other hand the reduction of the nickel in NH_4NaNiY below 400 °C results in the formation of very small nickel particles expressed by relatively small values of I_{REL} , ΔH and g (Figure 2 and 3). The high stability of the metal dispersion is probably due to a strong interaction of the nickel with defects of the zeolite lattice. For reduction temperatures above 400 °C the nickel increasingly agglomerates in the supercage, forms clusters and the size of the active metal surface decreases (Figure 5). But on the other hand the reduction of the nickel in the small cages begins. Both procedures are reflected by a maximum of $I_{\text{REL, Ni}}$ at a reduction temperature of 450 °C (Figure 3).

The decrease of $I_{\text{REL, Ni}}$ at reduction temperatures above 400 °C indicates in all samples an increase in the amount of finely dispersed nickel as a consequence of further reduction. Even a vacuum treatment (50 h) at 580 °C of reduced NaNiY did not alter this curvature which is characteristic for all samples (Figure 3) and confirms the high stability of the reduced nickel remaining in the small cages.

Amount, dispersion and location of the metallic nickel correspond well with the catalytic properties of the samples examined (Figure 5 and 6). The dehydrogenation activity increases with increasing reduction temperature and is caused by the increasing amount of accessible nickel. At temperatures above 400 °C the process of metal agglomeration predominates. This process as well as the formation of metallic nickel in the small cages decrease the accessible nickel surface and decrease the catalytic

activity. The optimum conditions with respect to the accessibility and catalytic activity of the metal surface are realized in the NaNiY sample.

Literature Cited

1. Yates, D.J.C., *J. Phys. Chem.* (1965) 69, 1676
2. Rabo, J.A., Angell, C.L., Kasai, P.H., Schomaker, V., *Disc. Faraday Soc.* (1966) 41, 328
3. Rubinshtein, A.M., Minachev, Kh.M., Slinkin, A.A., Garanin, V.I., Ashavskaya, G.A., *Izv. Akad. Nauk SSSR, Ser. Khim.* (1968) 786
4. Riekert, L., *Ber. Bunsenges. Phys. Chem.* (1969) 73, 331
5. Lawson, J.D., Rase, H.F., *Ind. Eng. Chem., Prod. Res. Develop.* (1970) 9, 317
6. Richardson, J.T., *J. Catalysis* (1971) 21, 122
7. Romanovski, W., *Roczniki Chem. [Ann. Soc. Chim. Polon.]* (1971) 45, 427
8. Bredichina, T.N., Evdokimov, V.B., *Zh. Fiz. Khim.* (1967) 41, 2975
9. Brooks, C.S., Christopher, G.L.M., *J. Catalysis* (1968) 10, 211
10. Schmidt, F., Gunsser, W., Knappwost, A., *Ber. Bunsenges. Phys. Chem.*, (1973) 77, 1022
11. Herd, A.C., Pope, C.G., *J. Chem. Soc., Faraday Trans. I* (1973) 5, 833
12. Selenina, M., *Z. anorg. allg. Chem.* (1972) 387, 179
13. Vogt, F., Forner, Ch., Bremer, H., Becker, K., Weber, M., *Chem. Techn.* (1975) 27, 460
14. Minchev, H., Steinbach, F., Penchev, V., *Z. Phys. Chem. (Frankfurt am Main)* (1976) 99, 223
15. Bremer, H., Bager, K.H., Vogt, F., *Z. Chem.* (1974) 14, 199
16. Minachev, Kh.M., Antoshin, G.V., Shpiro, E.S., *Izv. Akad. Nauk SSSR, Ser. Khim.* (1974) 1012
17. Slinkin, A.A., *Usp. Khim.* (1968) 8, 1531
18. Bassett, D.W., Habgood, H.W., *J. Phys. Chem.* (1960) 64, 769

Platinum Catalysts Supported on Zeolite. Hydrogenation of Cyclopropane and Hydrogenolysis of Ethane

C. NACCACHE, N. KAUFHERR, M. DUFAUX, J. BANDIERA, and B. IMELIK

Institut de Recherches sur la Catalyse, 79, boulevard du 11 Novembre 1918, 69626, Villeurbanne Cédex, France

ABSTRACT

Pt-zeolite catalysts were prepared by ion exchange technique. Hydrogen chemisorption and electron microscopy have been employed for measurements of metal dispersion and particle size. 10 Å metal aggregates were found on zeolites calcined in oxygen at 623°K and 15-20 Å size metal crystallites on zeolites calcined at 773°K. Comparison of the catalytic activity for ethane hydrogenolysis over Pt-zeolite and Pt-SiO₂ showed a minor effect of the carrier. In contrast, the patterns of catalytic activity for cyclopropane hydrogenation indicated a high promoting effect of the zeolite which was interpreted in terms of the electrostatic field.

Introduction

Since the importance of metal dispersion in the efficient use of metal catalysts has been well established, extensive research has been carried out to develop methods of preparation that produce finely dispersed metal catalysts. Several reports have been published on the use of zeolites as carriers. Rabo et al. (1) who prepared supported Pt-zeolites suggested that the metal was almost atomically dispersed. Lewis (2) found that platinum in zeolites was present as two sizes, particles of 10 Å size, small enough to fit inside the zeolite cages and of 60 Å size on the external surface. Kubo et al (3) concluded from H₂ chemisorption and electron microscopy studies that the platinum particle size was strongly dependent on the calcination temperature of Pt exchanged zeolite before H₂-reduction. Dalla Betta and Boudart (4) have suggested that small platinum clusters which contained less than 6 atoms were formed in the supercages. More recently, Imelik and coworkers (5) (6) showed that depending on the calcination temperature, either Pt-agglomerates (10 Å size) or Pt-crystallites (20 Å size) were present in Y-zeolites.

Although the behaviour of these small metal particles in hydrogen and oxygen chemisorption has interested several authors, less attention has been paid to their catalytic properties. Kubo et al. (7) found a good correlation between the amount of hydrogen ad-

sorbed and the catalytic properties of the zeolite supported platinum. However they did not mention a particular behaviour for these catalysts. Dalla Betta and Boudart (4) reported that small Pt clusters possessed catalytic activities for hydrogenation of ethylene or neopentane hydrogenolysis an order of magnitude higher than Pt supported on silica. Imelik and co-workers (5) found that Pt-crystallites in zeolites have an enhanced catalytic activity. In view of these previous results it was thought of interest to further investigate the catalytic properties of small platinum particles supported on zeolites for carbon-hydrogen and carbon-carbon bond activation in order to determine the significant influence of the zeolite support.

Experimental

Sodium and ammonium forms of Linde Y zeolite ($\text{Si}/\text{Al} = 2.43$) were exchanged with $(\text{Pt}(\text{NH}_3)_4)^{2+}$ solutions. Samples were then filtered, thoroughly washed and dried at 313°K . Pt contents as determined by chemical analysis were in the range 0.5 - 10 wt %. To form the platinum metal catalysts the samples were given the following treatments : about 0.1 g of the exchanged zeolite was introduced either into the cell used for hydrogen adsorption or into the catalytic reactor. The standard pretreatment was to purge with pure oxygen at 298°K and then to raise the temperature up to 623°K at $0.5^\circ\text{C min}^{-1}$ while oxygen was continuously circulated through the sample. This treatment removed NH_3 ligands without significant reduction of Pt^{2+} ions. Furthermore, at 623°K NaY was almost dehydrated and NH_4Y decomposed to the HY form. Hydrogen reduction was carried out at 623°K for at least 3 hours. A series of samples were calcined in oxygen up to 773°K and then H_2 -reduced at 673°K . Dispersion is defined as the percent of platinum atoms at the surface. The number of surface platinum atoms was determined by the hydrogen adsorption technique in a volumetric apparatus. The metal surface was calculated from $s = 6/\rho d$ where ρ is the platinum density and d the mean particle diameter. Particle sizes were further determined by electron microscopy using the same procedure as in (6) ; catalytic activities were measured in a glass fixed-bed differential continuous flow reactor at atmospheric pressure. Ethane hydrogenolysis catalytic measurements were made in the temperature range $573 - 673^\circ\text{K}$ at a flow rate of 6 l h^{-1} .

The activity of the catalysts decreased with time. Hence to obtain reproducible data, the samples were regenerated between each gas chromatography analysis by the procedure proposed by Yates and Sinfelt (8). Cyclopropane hydrogenation was carried out between 293°K and 313°K at a flow rate of 18 l h^{-1} .

Results

The electron micrographs revealed that the platinum particles supported on zeolites varied in their size as a function of the

calcination temperature in oxygen. On almost all the zeolite samples oxygen-treated at 623°K and then reduced at the same temperature the metal particles were around 10 Å size, while they were about 15 - 20 Å size on the zeolites that were oxygen-treated at 773°K. Figure 1 shows the size distribution of platinum crystallites in NaY and NH₄Y zeolites derived from electron micrographs.

In tables II, III, IV, V are collected particle sizes obtained from electron microscopy, platinum dispersion values calculated from hydrogen adsorption.

Catalytic studies

The rate equation for ethane hydrogenolysis was determined over the pressure ranges 30 - 100 torr for ethane and 190 - 450 torr for hydrogen. Table I summarizes the change of the orders of reaction with temperature.

TABLE I.- Orders for ethane hydrogenolysis, $r = kP_{C_2H_6}^n P_{H_2}^m$

Catalyst	T°K reaction	P _{H₂} torr	P _{C₂H₆} torr	n	m
Pt/NaY d = 10 Å	578	30 - 100	190 - 450	1	- 2.5
	637	"	"	0.9	- 1.1
	663	"	"	1	- 1
Pt-SiO ₂ d = 15 Å	599	30 - 100	190 - 450	1	- 1.8
	631	"	"	1	- 1.2
	643	"	"	0.9	- 1.1

From the kinetic data it appeared that there were little changes in the orders of reaction over the temperature range 633-663°K for all the samples examined in the present study. Thus the specific activity for ethane hydrogenolysis was determined at a standard set of conditions : P_{H₂} = 317 torr, P_{C₂H₆} = 33 torr, T = 663°K. The apparent activation energies were calculated in the temperature range 633-663°K. The results are collected in table II.

The activities of Pt-NH₄Y and Pt-SiO₂ for hydrogenolysis of propane were also studied under standard conditions over the temperature range 473-533°K. The results are shown in table III. Values for the apparent activation energies shown in table III are very similar for the two catalysts. The hydrogenolysis of propane over these catalysts resulted in the formation of methane and ethane with a CH₄/C₂H₆ ratio of 1. The specific activity for propane hydrogenolysis was determined at standard conditions :

P_{H₂} = 317 torr, P_{C₃H₈} = 33 torr, T = 533 K.

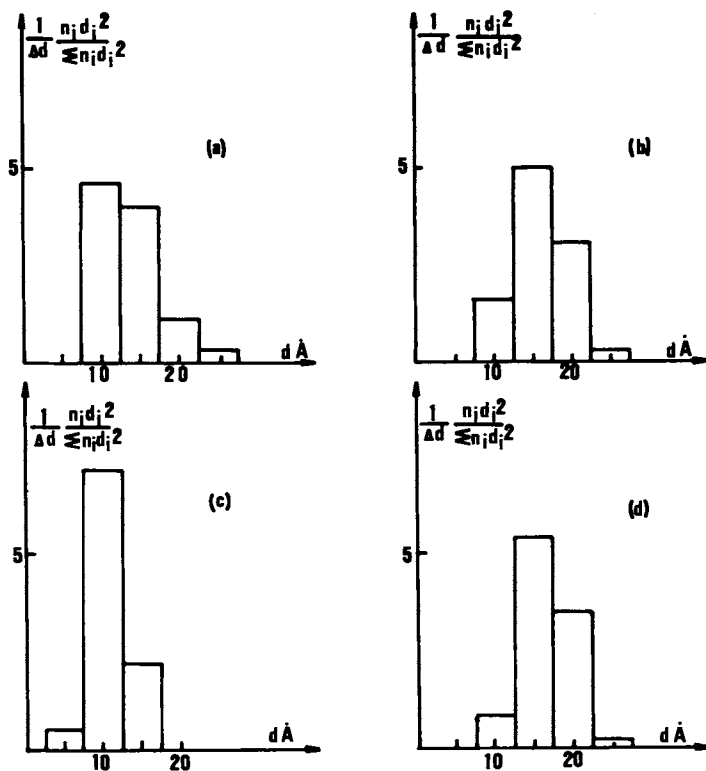


Figure 1. Size distribution of platinum particles. (a), PtNaY 3.8% wt Pt O₂ 350°C-H₂ 350°C; (b), PtNaY 3.8% wt Pt O₂ 500°C-H₂ 400°C; (c), PtNH₄Y 10.8% wt Pt O₂ 350°C-H₂ 350°C; (d), PtNH₄Y 10.8% wt Pt O₂ 500°C-H₂ 400°C.

TABLE II. - Hydrogenolysis of ethane ;

Catalyst	°K		Dispersion % H ₂	d _A EM	rate ₂ mole/h m ² Pt x 10 ⁴	E _{ap} Kcal mole
	Treatment O ₂	H ₂				
Pt-NaY	623	623	100	10	50	60
3.8 %	773	673	16	15	13	58
Pt-NH ₄ Y	623	623	62	13	32	53
3.5 %	773	673	22	20	6	54
Pt-NH ₄ Y	623	623	78	10	60	56
10.8 %	773	673	30	15	17	54
Pt-SiO ₂	623	623	72	15	14	44
2.6 %	773	673	40	40-60	3	50

TABLE III. - Hydrogenolysis of propane ;

Catalyst	d _A EM	E _{app} Kcal mole ⁻¹	rate x 10 ⁴
			mole/h ¹ m ² Pt
Pt-NH ₄ Y	10	36	60
10.8 %	15	36	17
Pt-SiO ₂	15	29	14
2.6 %	40 - 60	29	2.8

Cyclopropane hydrogenation

The reaction of cyclopropane with hydrogen was studied in the temperature range 273 - 313°K. The orders of reaction in hydrogen and cyclopropane were respectively 0 and 0.6 for all the catalysts examined. The temperature dependence of the reaction rates at constant hydrogen and cyclopropane pressures gave an apparent activation energy of about 12 kcal.mole⁻¹. The specific activities were then determined at standard conditions : T reaction = 295°K, P_{C₃H₆} = 11 torr, P_{H₂} = 327 torr. Table IV summarizes the results obtained for platinum catalysts supported on NaY, Ce-Y, Al₂O₃ and SiO₂ carriers. The data given in table V have been computed from the results obtained with Pt-NH₄Y catalysts.

In order to provide some evidence that cyclopropane hydrogenation

tion can or cannot proceed by a dual-functional mechanism on the platinum supported on acidic carriers the reaction of isomerization of cyclopropane to propene over Pt-HY zeolites and Pt-NaY was investigated. At room temperature no significant isomerization reaction occurred ; propylene appeared as a product only at about 473°K.

Furthermore the acceptor properties of Pt-NH₄Y zeolites activated at 773°K as a function of platinum content were studied following the procedure by Figueras et al. (9) which consisted of determining the number of radical cations formed by adsorption of anthracene. The data obtained indicate that the increase of platinum content produced a decrease in the acceptor properties of the carrier. When the platinum content reached a value of about 1.9 wt %, Pt-NH₄Y activated at 773°K showed the same very low Lewis acidity as Pt-NaY zeolite.

TABLE IV : Hydrogenation of cyclopropane over Pt-NaY, Pt-SiO₂ and Pt-Al₂O₃

Catalyst Treatment	°K		Dispersion % H ₂	d _A EM	rate x 10 ³ mole/h.g	N h ⁻¹ x 10 ⁻²
	O ₂	H ₂				
Pt-NaY 1.1 %	623	623	85	-	160	35
	773	673	11	-	13	21
Pt-NaY 3.8 %	623	623	100	10	653	34
	773	773	16	15 - 20	140	45
Pt-NaY 7.9 %	773	673	18	-	154	37
Pt-CeY 1.1 %	623	623	100	-	556	89
Pt-Al ₂ O ₃ 1.7 %	773	673	77	13	2.1	0.32
Pt-Al ₂ O ₃ 10 %	773	673	27	>40	4.0	0.30
Pt-SiO ₂ 2.6 %	623	623	72	15	9	0.90

TABLE V : Cyclopropane hydrogenation over Pt-NH₄Y

Catalyst	°K		Dispersion % H ₂	d _p Å EM	rate x 10 ³ mole/h.g.	N h ⁻¹ x 10 ⁻²
	O ₂	H ₂				
Pt-NH ₄ Y 0.5 % ⁴	623	623	65	-	90	56
Pt-NH ₄ Y 0.95 % ⁴	623	623	62	-	187	62
	773	673	29	-	80	57
Pt-NH ₄ Y 1.9 % ⁴	623	623	67	-	342	54
	773	673	24	-	83	36
Pt-NH ₄ Y 3.5 % ⁴	623	623	62	10	486	42
	773	673	22	15 - 20	143	37
Pt-NH ₄ Y 10.8 % ⁴	773	673	22	20	396	33

DISCUSSION

The results of this work, in agreement with previously published data, have shown that exchanged platinum ions yielded on reduction highly dispersed platinum metal. The satisfactory agreement between the results from the hydrogen chemisorption and electron microscopy indicates that in zeolites oxygen-calcined at 623°K before reduction, the metallic phase is made up of small particles of 8-10 Å size and homogeneously dispersed inside the supercages. Once formed the particles are too large to escape through the small 7.2 Å port windows. Thus the zeolite framework would increase the stability of the metal particles to sintering and allows obtaining a relatively high metal loading without substantial increase of the metal particle size. The results obtained with platinum loaded zeolites oxygen treated at 773°K showed considerable discrepancies among the particle size calculated from the chemisorption of hydrogen and electron microscopy. In Pt²⁺Y zeolites calcined at 773°K a large number of Pt²⁺ ions are located in the sodalite cages (5, 6). Upon H₂-reduction Pt²⁺ form Pt (0) atoms, a part of which being stabilized inside the sodalite cages. Platinum atoms which escape through the 2.2 Å cage windows agglomerate in the supercages and form platinum aggregates (8 - 10 Å size) or crystallites (15 - 20 Å). As the electron micrographs have shown the platinum crystallites were also embedded within the zeolite, one could suggest that during the metal aggregation part of the zeolite framework around the crystallite was destroyed thus enlarging the supercage size (6). Following this analysis the apparent discrepancy between H₂ chemisorption and electron microscopy can be understood if one suggest that atomically dispersed Pt(0) atoms have little ability to adsorb hydrogen (3, 5). Hence only an "apparent disper-

sion" would be measured by hydrogen chemisorption for Pt-loaded zeolites calcined at 773°K.

Striking effects of the zeolite carrier, close to those reported by earlier workers (4, 5) have been obtained for cyclopropane hydrogenation. Tables IV and V show that zeolite-supported platinum catalysts were more active for cyclopropane hydrogenation than Pt-SiO₂ or Pt-Al₂O₃ at all states of platinum dispersion. From tables IV and V the following orders of reactivity for cyclopropane hydrogenation were found (table VI).

TABLE VI.- Orders of specific activity for C₃H₆ hydrogenation

Catalyst	Pt-CeY	Pt-HY or LY	Pt-NaY or neu- tralized acidic zeo- lite	Pt/conventional carrier Al ₂ O ₃ or SiO ₂
Electros- tatic field	strong	medium	low	-
Turnover Number N h ⁻¹	89	56	36	0.03, 0.1

The enhanced hydrogenating properties of small platinum clusters supported on zeolite was previously interpreted in terms of electron transfer between the metals clusters and the zeolite, thus the platinum clusters behaving more like iridium (4). However, this interpretation cannot account for the results on cyclopropane hydrogenation for the following reasons: (i) it is reasonable to expect that the metal-carrier interaction would have a higher effect on the electronic properties of small clusters than on large crystallites, thus the specific activity for hydrogenation should be higher for small platinum clusters. In contrast the observed specific activities for 10 Å aggregates and 20 Å crystallites supported on NH₄Y zeolite were about the same (table V). (ii) In a study of cyclopropane hydrogenation on group VIII metals Sinfelt and co-workers (12) observed that the specific activity of platinum was about 2 orders of magnitude higher than that of iridium. Thus if electron transfer between small Pt aggregates and the zeolite carrier had occurred, one would have observed a decrease of the specific activity for cyclopropane hydrogenation from Pt-SiO₂ to Pt-zeolite catalysts. In sharp contrast our results indicate that zeolite-supported platinum catalysts are 100 times more active for cyclopropane hydrogenation than Pt-SiO₂ or Pt-Al₂O₃. On the basis of the above analysis the major role of the zeolite carrier in the enhancement of the hydrogenating properties Pt-zeolite catalysts would be better described in terms of the effect of the electrostatic field, present inside the zeolite cavities, on the reactants

rather than on the metal. Cyclopropane undergoes hydrogenation reactions which are characteristic of molecules possessing a carbon-carbon double bond, thus suggesting that the molecule has a pseudo olefinic character. However in contrast with ethylene, recent molecular orbital calculations (11) have shown that the lowest unoccupied molecular orbital in cyclopropane has a σ -type structure which favors more linear geometries. The addition of a negative charge in this σ -orbital increases the equilibrium angle of the cyclopropane thus favoring the ring opening. Therefore one might suggest that the electrostatic field in the zeolite acts as a negative charge which removes the stabilization of the strained cyclopropane ring thus increasing its reactivity. The 3-fold increase of the turnover number from Pt-NaY to Pt-CeY catalysts is probably due to the higher electrostatic field in rare earth exchanged zeolite. Recently it has been shown that the heat of adsorption of hydrogen on CaY is larger than on NaY, the increase was attributed to the higher electrostatic field in CaY zeolite (13). Finally a dual function mechanism for hydrogenation of cyclopropane over Pt-zeolite catalysts is less likely to occur as it has been shown that no cyclopropane isomerization occurred on these catalysts up to about 473°K.

Our results on ethane hydrogenolysis provide further arguments for rejecting the direct effects of platinum-zeolite interaction on the catalytic properties of the metal. The catalytic hydrogenolysis of ethane has been extensively used to investigate the catalytic properties of metals (10). In considering the pattern of the catalytic activities for the hydrogenolysis of ethane it has been shown that both the electronic structure of the metal (10) and to a lower extent, the metal particle size (8) played an important rôle. The results of the present study on platinum are similar to those found by Yates and Sinfelt on rhodium (8). The specific activity for ethane hydrogenolysis decreases with the increase of the platinum particle size, the catalysts containing particles of 10 Å size having the highest specific activity. Furthermore, table II shows that the specific activity is almost independent of the nature of the carrier. For platinum supported on non acidic and acidic zeolites in which the metal particles are 10 Å size, approximately identical specific activities were found ($50-60 \cdot 10^{-4}$ mole/h m^2). The specific activities in the hydrogenolysis reaction on 15 Å size platinum crystallites supported on NaY, NH_4Y or SiO_2 , although lower, were also nearly constant ($13, 17, 14 \cdot 10^{-4}$ mole/h m^2). Moreover, table II shows that the apparent activation energy remains approximately the same for all the catalysts studied, the average value of 54 kcal/mole is in good agreement with previously reported values for platinum catalysts (10). The enhancement of the catalytic activity for neopentane hydrogenolysis over zeolite supported small platinum clusters was interpreted in terms of partial electron transfer from the Pt cluster behaving more like iridium (4). Our results, at least for ethane and propane hydrogenolysis, are not consistent with these

suggestions. In fact it has been shown (10) that specific catalytic activity, at standard conditions, for hydrogenolysis of ethane over iridium was about 5 orders of magnitude higher than over platinum. Furthermore the apparent activation energy decreased from 54 kcal/mole for Pt to 36 kcal/mole for Ir (10). More recently Yermakov et al. (14) pointed out, from their ESCA results on (W + Pt) SiO₂, a decrease in the electronic density of the platinum. Simultaneously the apparent activation energy for ethane hydrogenolysis decreased from 54 kcal/mole for pure platinum catalyst to 28 kcal/mole for (W + Pt)/SiO₂. Hence the constant value of the apparent activation energy for ethane hydrogenolysis on Pt-zeolite and Pt-SiO₂ provided further evidence that the zeolite carrier has a relatively minor effect upon the electronic structure of the supported encaged platinum aggregate or Pt crystallites. Indeed if the 10 Å size platinum aggregates were more like iridium on should have observed a significant decrease in the apparent activation energy and also a much higher value of their specific activity, in contrast with our results.

In conclusion this work has shown that hydrogenolysis of ethane over supported platinum is strongly dependent on particle size, the smallest particles being the most active. Although other works have indicated that small metal particles are electron deficient (which means more acidic, thus giving stronger metal-carbon bonds with dehydrogenated ethane), it appears from this work that this property does not vary significantly from one carrier to another but is mainly an intrinsic property of small metal clusters. In contrast cyclopropane hydrogenation, which is a "nondemanding" reaction, was found to be highly sensitive to the particular carrier employed. The patterns of variation of catalytic activity from zeolites to conventional carriers seems to be a consequence of the important polarizability properties of the zeolite.

ACKNOWLEDGMENTS

The authors are grateful to Dr. Dalmai-Imelik G. for assistance with the electron microscopy study and thank Mr. Urbain who performed the chemical analysis.

Literature Cited

1. Rabo, J.A., Schomaker, V. and Pickert, P.E., Proc. Int. Congress Catalysis 3d, 1964, North Holland Pub. Company, (1965), Vol. 2, 1264.
2. Lewis, P.H., J. Catalysis, (1968), 11, 162.
3. Kubo, T., Arai, H., Tominaga, H., Kunugi, T., Bull. Chem. Soc. Japan (1972), 45, 607.
4. Dalla Betta, R.A. and Boudart M., Proc. Int. Congress Catalysis 5th, North Holland Pub. Company (1973), 2, 1329.
5. Gallezot, P., Datka, J., Massardier, J., Primet, M., Imelik, B. Proc. Int. Congress Catalysis 6th,
6. Gallezot, P., Mutin, I., Dalmai-Imelik, G., Imelik, B., J. Microsc. Spectrosc. Electron (1976), 1, 1.

American Chemical Society
Library

1155 16th St., N.W.
Washington, D.C. 20036

7. Kubo, T., Arai, H., Tominaga, H., Kunugi, T., Bull. Chem. Soc. Japan, (1972), 45, 613.
8. Yates, D.J.C. and Sinfelt, J.H., J. Catalysis (1967), 8, 348.
9. Figueras, F., Menciaer, B., De Mourgues, L., Naccache, C., and Trambouze, Y., J. Catalysis, (1970), 19, 315.
10. Sinfelt, J.H. and Yates, D.C., J. Catalysis, (1967), 8, 82.
11. Buenker, R.J. and Peyrimhoff, S.D., J. Phys. Chem., (1969), 73, 1299.
12. Dalla Betta, R.A., Cusumano, J.A. and Sinfelt, J.H., J. Catalysis, (1970), 19, 343.
13. Benson, J.E. and Boudart, M., J. Catalysis, (1967), 8, 93.
14. Loffe, M.S., Kuznetsov, B.H., Ryndin, Yu. A. and Yermakov, Yu. I., Proc. 6th. Internat. Cong. Catalysis, London (1976), paper A5.

Modification in the Nature of Active Sites of Zeolites A by Co^{2+} Exchange

EMIL DETREKÖY and DÉNES KALLÓ

Central Research Institute for Chemistry of the Hungarian Academy of Sciences,
Budapest, Hungary

ABSTRACT

The isomerization of 1-butene to 2-butene and the oligomerization of 2-methyl-propene were investigated on K-A, Ca-A, Co,K-A, Co,Ca-A. Brönsted acidic sites associated with partly dehydrated bivalent cations are active in both reactions. The difference in the catalytic behaviour of the fully dehydrated Co^{2+} and Ca^{2+} forms in both reactions can be attributed to the effect of 3d electrons of Co^{2+} on the coordinated olefin molecules.

Introduction

Earlier studies showed that several zeolites exchanged with bi- or trivalent cations contain structural acidic hydroxyl groups generated from water molecules coordinated to the cation by the electrostatic field of the latter (1). The presence of OH groups and their acidity in transition metal containing Y zeolites was showed by Ward (2). Riley and Seff (3) obtained crystallographic evidence for the existence of OH groups in the hydrated, partially cobalt(II)-exchanged zeolite A.

The catalytic activity of the zeolites containing bivalent cations is explained by their structural hydroxyl groups (1) and by the polarizing effect of the cation on the reactant molecule (4).

If a zeolite containing transition metal cations is chosen, the role of the free coordination sites available for complexing of the reactant can be significant.

For the investigation of the different effects resulting from the catalytic activity of the transition metal ion exchanged zeolites, a comparative catalytic study of K^+ , Ca^{2+} and Co^{2+} containing zeolites A seemed

to be advantageous. The three metals are situated in the same row of the periodic table of the elements and the electron system around the Co^{2+} cation differs only in the presence of the $3d^7$ electrons from that of the Ca^{2+} ion.

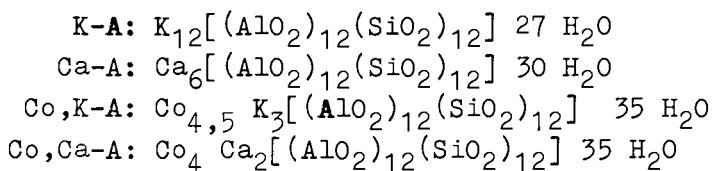
The cation positions in the lattice of the zeolite A and their change upon dehydration is nearly the same for both the Co^{2+} and Ca^{2+} cations and both derivatives are stable in their completely dehydrated forms (5-8).

In this study the formation and disappearance of different types of active sites of partially and fully dehydrated K^+ , Ca^{2+} and Co^{2+} exchanged zeolites A are traced in the isomerization of 1-butene and in the oligomerization of 2-methyl-propene.

The effects observed are related to the outer surface of the zeolite, which is supposed to represent the active sites of the intracrystalline pores. This approximation seems to be correct according to our present investigations. Our preliminary experiments and calculations showed that even in the case of n-butenes the mass transport in the pores is negligibly small compared to the rate of conversion observed, i.e., the effect of active sites in the intracrystalline pores can be neglected.

Experimental

Synthetic Linde A zeolite was used in its original and Co^{2+} -exchanged forms. The unit cell composition of the samples investigated corresponds approximately to the following formulas:



The 1-butene and 2-methyl-propene used were Fluka purum grade. Pyridine of uvasol quality was from Merck A. G. and dried with Linde 4A molecular sieve.

The isomerization of 1-butene and the reduction with hydrogen were performed in a closed static circulation system. The samples of 0,01-1 g were pretreated by heating for 1 hour at given temperatures in a vacuum of 10^{-3} Torr "in situ" in the reactor. The temperature of the isomerization was 200 °C, and the initial pressure of 1-butene 100 Torr. The rates (in $\frac{\text{mol}}{\text{g}_{\text{cat}} \text{s}}$) of con-

version of 1-butene to cis-2-butene and 1-butene to trans-2-butene, r_{12} and r_{13} , respectively, were determined.

The 2-methyl-propene oligomerization experiments were carried out in a conventional flow reactor. The pretreatment of the catalyst samples of 2-10 g was performed "in situ" in the reactor, passing a hydrogen flow of 400 ml/min for 1 hour at given temperatures. The moles per gramme feed of the monomer unconverted, n_A , and that of the dimer and trimer formed, n_B and n_C , respectively, were determined as a function of the reciprocal space velocity, W/F , given in $\frac{\xi_{cat}^S}{\xi_{feed}}$. The main

products of transformation are 2,4,4-trimethyl-pentene-1, 2,4,4-trimethyl-pentene-2 (dimers) and double bond isomers of 2,2,4,6,6- and 1,3,3,5,5-pentamethyl-heptenes (trimers).

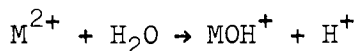
The water treatment of the samples preceding the isomerization of 1-butene was carried out for 5 minutes at 200 °C in a flow of nitrogen saturated with water vapour at room temperature.

The pyridine treatment was performed by introducing pyridine onto the catalyst bed at reaction temperature in an amount far above the surface chemisorption capacity of the sample.

Results and Discussion

Attempted Reduction of Co^{2+} Exchanged A-Zeolite. Co,K-A after dehydration at 350 °C and 10^{-3} Torr was kept for 1 hour in hydrogen stream at 300—600 °C and 760 Torr in a closed recirculation apparatus. No-consumption of hydrogen could be observed indicating that Co^0 was not formed.

Partly Dehydrated Co^{2+} Exchanged Zeolites A. In the case of partly dehydrated transition metal ion exchanged zeolites Y Ward (2) showed that the concentration of the Brönsted acidic sites increases linearly with the increasing ionization potential of the cations similarly as experienced with alkaline-earth zeolites (2a). The effect was attributed to the different strength of the electrostatic fields of the cations resulting in a different degree of fission of adsorbed water according to the following scheme:



No simple relationship was observed, however, between

the concentration of acid sites and catalytic activity (2)

It was shown for partially dehydrated Co,Na-A zeolite (3) that one Co^{2+} ion per unit cell resides in the sodalite unit while the other three are distributed at about equivalent sites on unit cell three fold axes and the latter cause the fission of the adsorbed water molecules. We have found that the partly dehydrated Ca-A, Co,K-A and Co,Ca-A samples were active both in 1-butene isomerization (Figure 1) and in 2-methyl-propene oligomerization (Figure 3) while K-A was inactive in both transformations.

As cited before (1-3), the catalytic activity in both reactions can be attributed to the Brønsted acidic OH groups in the partly dehydrated A zeolites containing bivalent cations.

The Effect of Dehydration and Rehydration. The 1-butene isomerization activity of the Ca-A sample decreases with dehydration and becomes zero for the completely dehydrated sample (Figure 1). It can be concluded that interaction between the charge of Ca^{2+} and the dipole induced in the 1-butene molecule is not sufficient for the activation of the latter.

The same kind of interaction results, however, in the activation of the 2-methyl-propene molecule as shown by the activity of the totally dehydrated Ca-A in the oligomerization reaction (Figure 3). The difference in activity of the dehydrated forms can be explained by a slight change in the position of the Ca^{2+} ion, moving along the three fold axis nearer to the centre of the sodalite cage and so becoming less accessible to the reactant.

The behaviour of samples containing Co^{2+} differs substantially from that of the Ca-A. While the activity of the Ca-A zeolite decreases both in 1-butene \rightarrow trans-2-butene and in 1-butene \rightarrow cis-2-butene transformations with increasing degree of dehydration, in the case of the Co^{2+} ion exchanged derivative the latter transformation seems to be independent of the dehydration between 200-600 °C (Figure 1). This phenomenon suggests that a reaction mechanism involving a common surface intermediate (carbonium ion) which is probable on the acidic forms is not dominating on the Co-forms. The two transformations may involve different surface intermediates which arise either on the same sites or on different sites. Since the activities of the Co-forms are independent of dehydration both in 1-butene \rightarrow cis-2-butene conversion and in 2-methyl-propene oligomerization, the two reactions may take place on the same active sites.

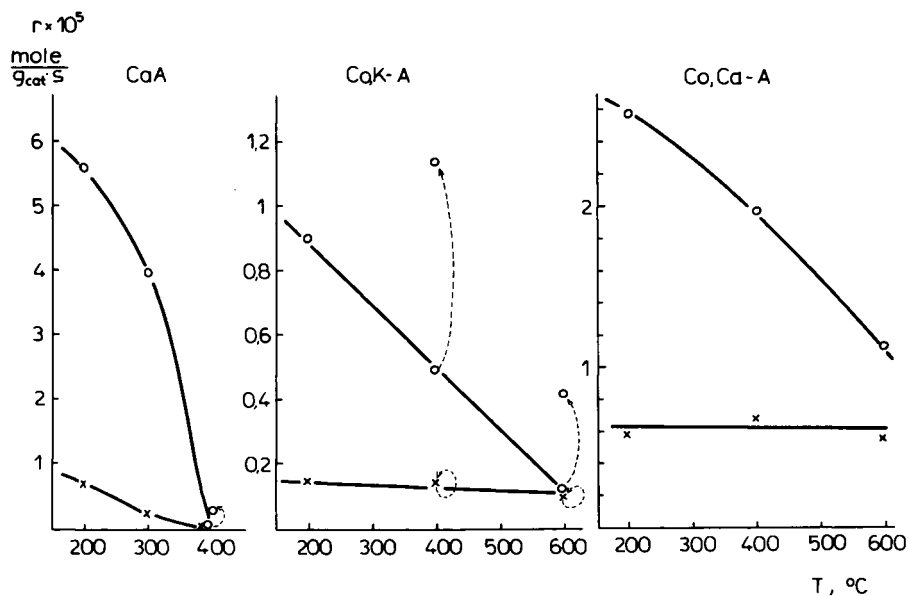


Figure 1. The rates of 1-butene \rightarrow cis-2-butene, r_{12} (\times), and 1-butene \rightarrow trans-2-butene, r_{13} (\circ), transformations on Ca-A, Co,K-A, and Co,Ca-A zeolites as a function of the pre-treatment temperature. Dotted arrows show the effect of water readsorption on r_{12} and r_{13} .

It seems likely that the Co^{2+} ions are not equivalent. Some of them have the same position and the same degree of hydration or dehydration between 200 and 600 °C. It is also possible that hydrated as well as dehydrated Co^{2+} ions exhibit the same activity in these reactions.

Upon rehydration at 200 °C the 1-butene isomerization activities of the Ca-A and Co,K-A samples increase indicating a regeneration of the OH groups (Figure 1). The extensive rehydration of the Co,K-A in a 5 minutes period can be attributed to the high reactivity of the three-fold coordinated Co^{2+} ions similarly to that observed by Trifiro and coworkers (9) for the dehydrated Co,Na-A zeolite. Because of the relatively lower rate of rehydration of Ca-A, several hours were needed for the complete regeneration of the activity in the 2-methyl-propene oligomerization. This difference in the rate of rehydration is in agreement with the difference of the ionization potential of Ca and Co.

The Effect of Adsorbed Pyridine. Pyridine adsorption at 200 °C on Brønsted acidic hydroxyls decreases the catalytic activity in 1-butene isomerization of Ca-A, Co,K-A and Co,Ca-A (Figure 2), the oligomerization activity of Ca-A (Figure 4) while it does not influence the oligomerization activity of Co,K-A, independently of its dehydration (Figure 4). The lack of poisoning effect of pyridine indicates that 2-methyl-propene and its oligomers are adsorbed at 200 °C on the active sites stronger than pyridine, so that the Co^{2+} -cation — 2-methyl-propene interaction cannot be regarded as a simple Lewis acid-base interaction. It seems likely, therefore that the poisoning effect of pyridine in 1-butene \rightarrow cis-2-butene transformation may be attributed to the adsorption of pyridine on Co^{2+} cation, which is stronger than the adsorption of 1-butene.

The Kinetics of the Oligomerization on the Dehydrated Ca^{2+} and Co^{2+} Ions. Our earlier results (10) show that the mechanism of the 2-methyl-propene oligomerization on partially dehydrated Ca-A zeolite is of Rideal-Eley type and proceeds probably via carbonium ions like that observed in the same reaction on a Brønsted acidic synthetic ion exchange resin (11) where similarly a larger adsorption coefficient of the monomer than of the dimer was found.

The course of the reaction is quite different on partially dehydrated Ca-A and on fully dehydrated Co,K-A as can be seen in Figure 5. The product retardation on Co,K-A may be evidenced in contrast to Ca-A, where the

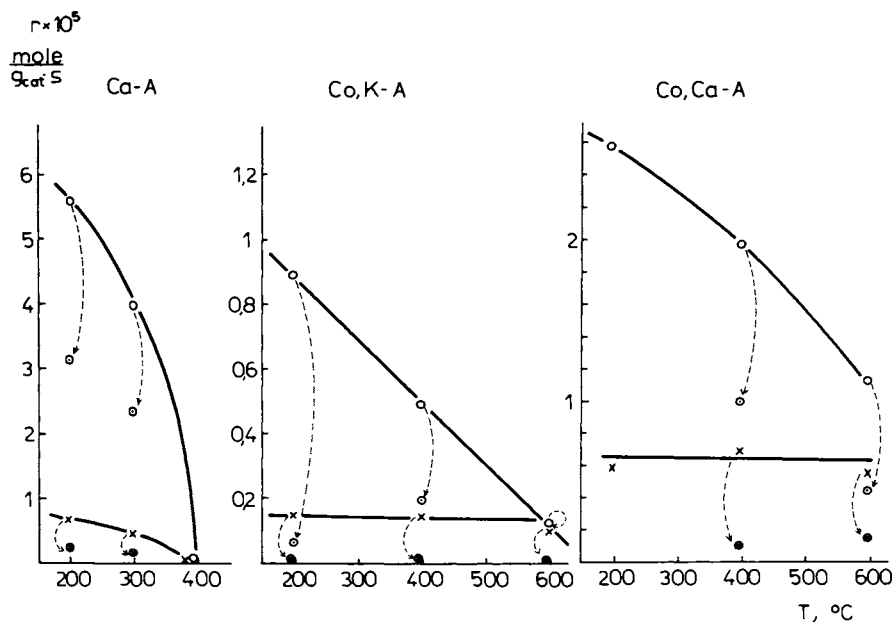


Figure 2. The effect of pyridine adsorption at 200°C on the 1-butene isomerization activity of Ca-A, of Co,K-A, and of Co,Ca-A zeolites. (\times), r_{12} before pyridine adsorption; (\otimes), r_{12} after pyridine adsorption; (\circ), r_{13} before pyridine adsorption; (\odot), r_{13} after pyridine adsorption.

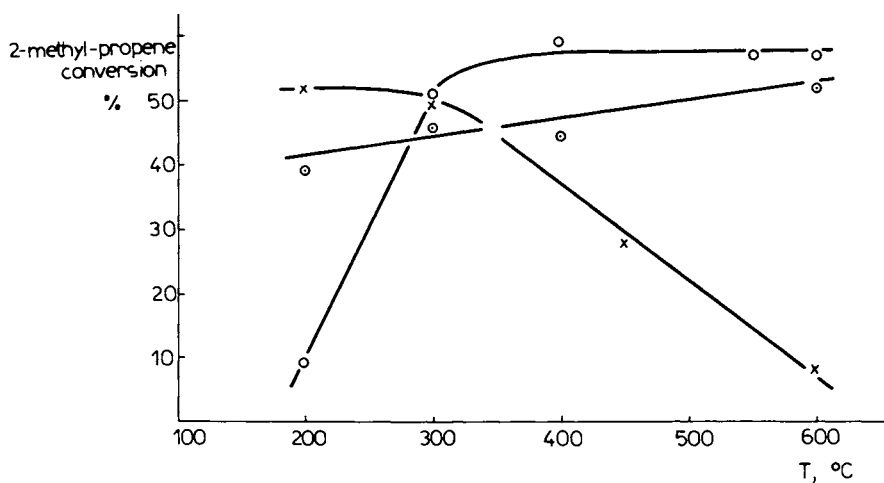


Figure 3. Conversion of 2-methylpropene at 200°C as a function of the pretreatment temperature on (\times), Ca-A; (\odot), Co,K-A; and (\circ), Co,Ca-A zeolites; $W/F = 2.5 \cdot 10^3$ g_{cat} s g⁻¹ feed.

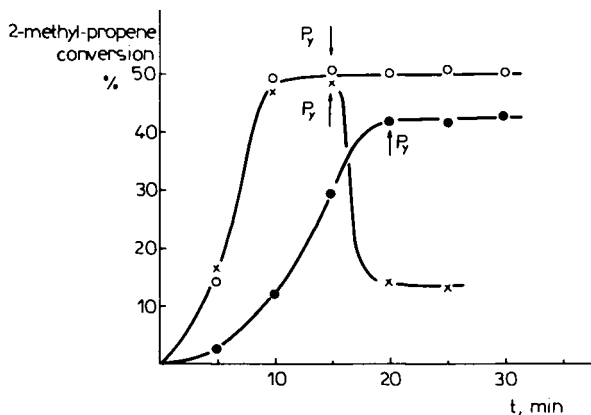


Figure 4. The effect of pyridine on the 2-methylpropene oligomerization activity of Co,K-A pretreated at 600°C (○), of the Co,K-A pretreated at 220°C (●), and of the Ca-A pretreated at 300°C (×). The temperature of the oligomerization 200°C. $W/F = 2.5 \cdot 10^3 \text{ g}_{\text{cat}} \text{ s g}_{\text{feed}}^{-1}$.

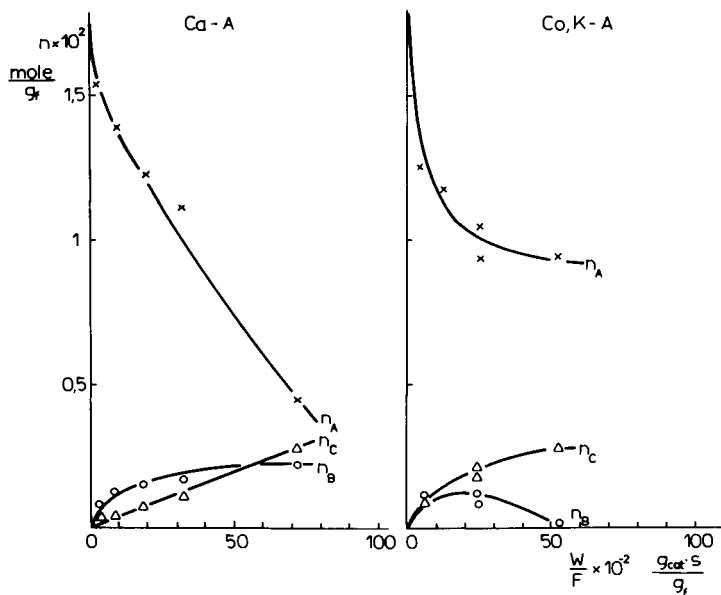


Figure 5. Conversion curves of 2-methylpropene oligomerization at 150°C on Ca-A pretreated at 300°C and on Co,K-A pretreated at 450°C; (×), n_A , moles of the monomer; (○), n_B , moles of the dimer; (△), n_C , moles of the trimer in 1 g of feed.

adsorption of the monomer is predominant.

The disappearance of the dimer from the gas phase at longer contact times on Co,K-A shows that the trimer forms from gas phase dimer and adsorbed monomer, too. From the rates of formation of the products it can be concluded that the higher the molecular weight, the stronger the adsorption.

Conclusions

It is known that the ability of a cation for complexing ligand molecules depends on its charge and size. In the fourth row of the periodic system the sequence of ionic radii is $K^+ > Ca^{2+} > Co^{2+}$.

Because of its small charge and big ionic radius the K^+ ion can neither dissociate the neighbouring water molecule nor form a reactive complex with olefin molecules and so can neither indirectly nor directly be a source of catalytic activity as it was in fact found for both reaction studied.

The difference in Ca^{2+} and K^+ ions both in ionic radius and in charge is significant, hence Brönsted acidic surface hydroxyls can be found in partly dehydrated Ca-A zeolite which proves catalytically active in the reactions investigated. Corresponding to its enhanced ability for complexing, the Ca^{2+} ion is able to activate olefin molecules of higher reactivity (2-methylpropene).

The complexing ability of the Co^{2+} is even higher. Its position in the framework of zeolite A is similar to that of the Ca^{2+} ion. In addition to the water fission, however, it is able to activate the less active olefins (e.g. 1-butene), too.

The replacement of Ca^{2+} ions by K^+ , results in the non-dissociation of the adsorbed water molecules, and a decrease in the catalytic activity. The catalytic activity in the isomerization is the sum of the activities of hydrated Ca^{2+} and Co^{2+} ions.

In the case of the totally dehydrated samples, both dehydrated K^+ and dehydrated Ca^{2+} ions are inactive by themselves. Surprisingly, in spite of this, a large difference was found between the 1-butene isomerization activities of the Co,K-A and Co,Ca-A derivatives although their Co^{2+} content was nearly the same. The possible unequal cation distribution cannot explain the high difference observed in the catalytic activities.

The supposed sources of the catalytic activity, the dehydrated Co^{2+} cations, are situated in S_{III} positions where the surrounding ligand field of D_{3h} symmetry of oxygen atoms has presumably a strong effect on

the complexing $3d^7$ electron system of the ion. This ligand field is probably significantly influenced by the nature of the neighbouring cations (K^+ , Ca^{2+}).

Literature Cited

1. Eberly, P. E., J. Phys. Chem. (1968), 72, 1042.
2. Ward, J. W., J. Catalysis (1971), 22, 237.
- 2a. Ward, J. W., J. Catalysis (1969), 14, 365.
3. Riley, P. E. and Seff, K., J. Phys. Chem. (1975), 79, 1594.
4. Pickert, P. E., Rabó, J. A., Dempsey, E. and Shomaker, V., "Proc. 3rd. Intern. Congr. Catalysis, Amsterdam 1964". Vol I. p. 714, Wiley, New York (1965).
5. Breck, D. W., Eversole, W. G., Milton, R. M., Reed, T. B. and Thomas, T. L., J. Am. Chem. Soc., (1956), 78, 5963.
6. Seff, K., "Account of Chemical Research" Dep. of Chem. Univ. of Hawaii, Honolulu, Hawaii (1975).
7. Amaro, A. A., Kavacini, C.L., Kunz, K. B., Riley, P. E., Vance, T. B., Jr, Yanagida, R. Y. and Seff, K., "Mol. Sieves Proceedings on the Third Intern. Conf. on Molecular Sieves 1973". p. 113, Zurich, Switzerland, Leuven Univ. Press (1973).
8. Seff, K. and Shomaker, D.P., Acta Cryst. (1967), 22, 162.
9. Hoser, H., Krzyzanowski, S. and Trifiro, F., J. Chem. Soc. Faraday Transactions, I. (1975), 71, 665.
10. Detrekóy, E. and Kalló, D., Third Intern. Conf. on Heterogeneous Catalysis, 1975, Varna, Bulgaria
11. Haag, W. O., Chem. Eng. Progress, Symposium Series (1967), 63, 140.

NO Reduction and CO Oxidation over Zeolites Containing Transition Elements

KH. M. MINACHEV, G. V. ANTOSHIN, YU. A. YUSIFOV, and E. S. SHPIRO
Zelinsky Institute of Organic Chemistry of U.S.S.R. Academy of Sciences, Moscow

ABSTRACT

NO reduction with CO and CO oxidation with O₂ over zeolites containing transition elements were studied in parallel with XPS measurements of transition elements state in zeolites. Zeolites are active catalysts for these reactions at temperatures above 150°C. The valence and physical states of the transition elements are the most important factors determining the catalytic activity of zeolites.

Introduction

Catalytic reduction of NO is of great practical importance with a view to automobile exhaust purification. Literature data (1-3) show that catalytic reduction of NO with H₂, CO, NH₃ and some hydrocarbons proceeds over transition metals and their oxides.

The purpose of this work was to study the catalytic properties of some transition metals (Ni, Co, Cu and Cr) in Y zeolites that catalyze the reduction of NO with CO and the oxidation of CO with oxygen. The influence of the reducing and redox pretreatments of the catalysts on their activity was also investigated. It is known that transition elements in zeolites can change their valence and physical state in the course of pretreatment of the catalysts as well as in the course of catalytic reactions. To follow such changes X-ray photoelectron spectroscopy was used in this work.

Experimental

Zeolites containing transition elements were

prepared by means of cationic exchange between NaY and aqueous solutions of corresponding cation salts. The description of samples preparation and analysis was published earlier (4,5) as well as the method of preparation of the gases used (5). The characterizations of samples are shown in table 1.

TABLE 1.- Characteristics of zeolite catalysts studied

Zeolite	Degree of substitution of Na ⁺ by cation (%)	Salts for ionic exchange
NiNaY	33	Ni(NO ₃) ₂
CoNaY	33	Co(NO ₃) ₂
CuNaY	26	Cu(CH ₃ COO) ₂
CrNaY	31	Cr(CH ₃ COO) ₂
CoNiNaY	32(Co), 31(Ni)	Co(NO ₃) ₂ , Ni(NO ₃) ₂
CuNiNaY	30(Cu), 29(Ni)	Cu(CH ₃ COO) ₂ , Ni(NO ₃) ₂
CrNiNaY	28(Cr), 34(Ni)	Cr(CH ₃ COO) ₂ , Ni(NO ₃) ₂

The samples after cationic exchange were dried at room temperature or at 120°C in air and then treated in vacuum or in gases in static conditions (p= 5-50 torr) before measurements of catalytic activity and the recording spectra. The treatment of the samples with the gases was carried out in special chamber connected to the spectrometer. To obtain spectra of adsorbed species the samples were cooled in gases to room temperature, evacuated to p=10⁻⁶- 10⁻⁷ torr and then introduced into the working chamber of spectrometer under vacuum.

Three series of the samples were studied:

1. Cationic forms prepared by dehydration of zeolites in air and O₂ at 550°C.
2. Metal-zeolites prepared by reduction of dehydrated samples with H₂ at 500°C.
3. "Oxidized" forms obtained by subsequent treatment of dehydrated samples with H₂ and O₂ at 500°C.

The catalytic reactions were studied in circulatory static unit at initial pressure of stoichiometric mixtures of 10+ 20 torr. Kinetics of the reactions was observed by pressure drop due to CO₂ removal in the trap which was kept at -140°C. The composition of the products was analyzed by gas chromatography.

The values of initial rates (W₀) for all catalysts studied were measured by tangent to pressure-time curves at zero time, the sample size being the

same (0.1 g).

X-ray photoelectron spectra were recorded by means of an A.E.I. ES-100 spectrometer with Al and Mg anodes. The procedure of recording spectra and calibration was described elsewhere (6,5).

Results

1. NO reduction with carbon monoxide. Since there was no information in literature on the catalytic properties of zeolites in reaction of NO reduction with CO, first of all it was necessary to find out the conditions of catalysis. It was shown that zeolites reveal catalytic activity for this reaction in the temperature range 200-500°C.

Figure 1 shows the dependences of pressure change of stoichiometric mixture of NO with CO on time of the reaction over various cationic forms of zeolites at 350°C. It should be noted that the activity of all zeolites at this temperature is reproducible in the series of subsequent runs. These data show that CuNaY and CrNaY are more active than other monoforms. The introduction of the second transition element into zeolite results in considerable increase of the activity of the catalysts. The most pronounced effect was observed in the case of CoNiNaY. Ni- and Co-monoforms are inactive in temperature range of 250-450°C, whereas mixed CoNiNaY was the most active sample among the cationic forms studied.

The kinetic regularities of NO reduction over some samples were studied in detail. Figure 2a presents as an example the kinetic dependences of pressure change of NO and CO mixture on time at different temperatures and at $p=10$ torr for CuNiNaY. It is seen from this figure that at low temperatures ^{reduction} does not proceed to complete conversion. The degree of conversion (X) in the first run at 250°C is not higher than 35-40%. After four subsequent runs under the same conditions the deactivation of the catalyst is apparent. The conversion and initial rates drop drastically. The increasing the temperature increases the rate and X. The catalyst activity becomes reproducible at 300°C. Further rise of the temperature up to 350-400°C results in the achievement of complete conversion of the reactants and stable catalyst activity. After reaction at 350-400°C and cooling the sample to 250°C the activity is the same as in the first run at 250°C. Similar regularities were also observed for other zeolites.

It should be noted that incomplete conversion at

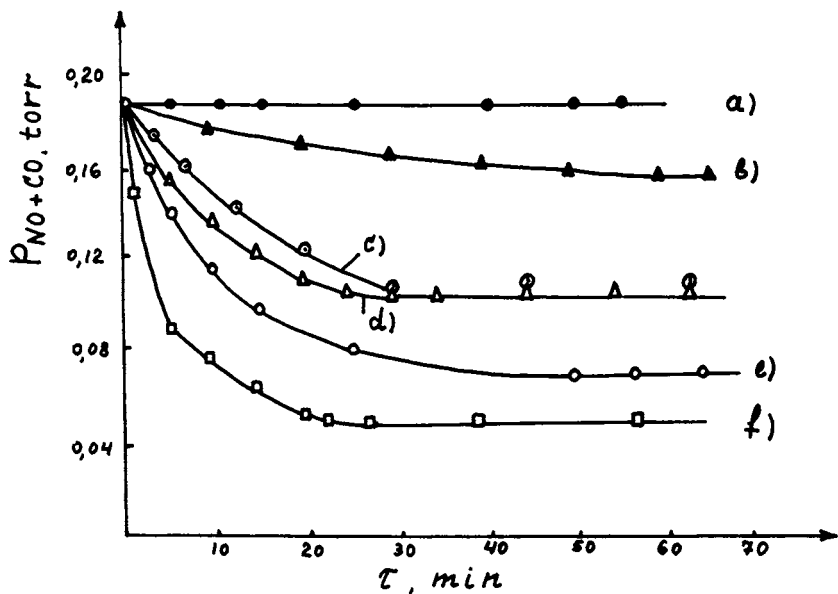


Figure 1. The dependences of pressure change of stoichiometric mixture of NO with CO on time of the reaction over various cationic forms of zeolites at 350°C. (a), NiNaY and CoNaY; (b), CuNaY; (c), CrNaY; (d), CrNiNaY; (e), CuNiNaY; (f), CoNiNaY.

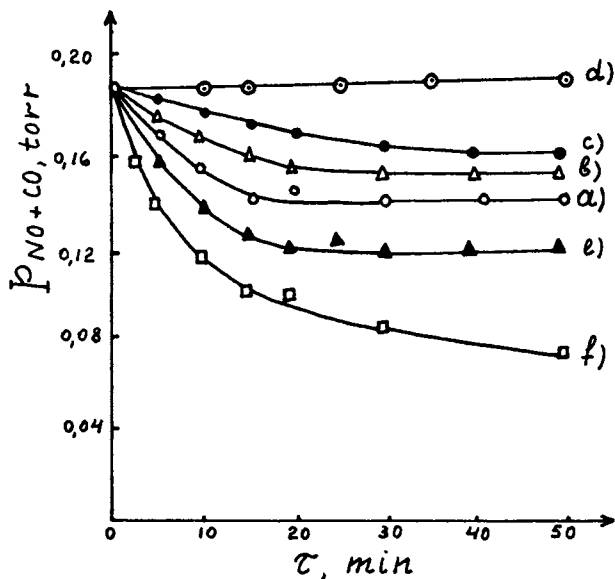


Figure 2a. The kinetic dependences of pressure change of NO and CO mixture on time at different temperatures and at $p = 10$ torr for CuNiNaY. (a), 250°C, 1 run; (b), 250°C, 2 run; (c), 250°C, 3 run; (d), 250°C, 4 run; (e), 300°C; (f), 350°C.

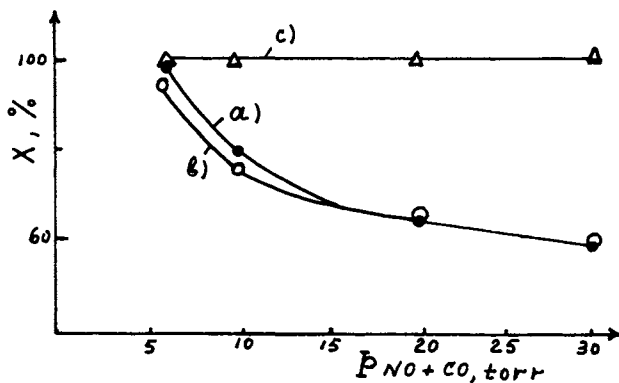


Figure 2b. The dependence of $X(\%)$ on the pressure of stoichiometric mixture of NO with CO over CuNiNaY. (a), 300°C, 6-30 torr; (b), 300°C, 30-6 torr; (c), 400°C.

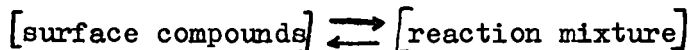
low and intermediate temperatures is a characteristic feature of the reaction kinetics over zeolites.

Thus one can conclude that there are three temperature ranges at least in which regularities of NO reduction over zeolites are different:

a) Low temperature range (200+300°C). The catalyst activity is not stable, and after series of the runs without intermediate treatment of the catalysts the complete deactivation of the latter occurs. To obtain additional information on the nature of this deactivation the influence of pretreatment of the catalysts with various mixtures of starting substances and some reaction products on the activity was studied. CuNiNaY was treated for 30 min at 250°C, i.e. in low temperature range, at working pressures with the following gases: CO + NO, CO₂+O₂, CO+N₂O, CO₂+N₂O, N₂+CO, CO₂+NO, H₂+N₂O, N₂+CO₂, CO, NO, CO₂ and N₂O. The sample was then evacuated at 250°C and its activity was measured. Treatment of the catalyst with the NO+CO mixture decreased the initial reaction rate by a factor of 2. Treatment with NO by itself also caused a decrease in reaction rate, although the activity reduction by a factor of 1.6 was less than observed for the NO+CO pretreatment. In all other cases the pretreatment did not produce noticeable change of the activity. These data probably suggest that the surface compounds responsible for catalyst deactivation at low temperatures are formed in the course of catalytic reaction, and some of these compounds are in equilibrium with starting substances.

b) Intermediate temperature range (300+350°C). Incomplete conversion is also a characteristic of this range. The increase of the pressure at constant temperature results in the decrease of the conversion. Evacuation of the samples at experiment temperature restores their activity.

Figure 2b shows the dependences of X on the pressure of stoichiometric mixtures at 300 and 400°C. It follows from these data that the decrease of X is observed at 300°C only whereas at 400°C the conversion at all pressures is about 100%. Thus one can conclude that the deactivation of the catalysts in intermediate temperature range is reversible and is due to the formation of unstable surface compounds. The latter are decomposed under the evacuation and exist only in equilibrium with starting substances:



The increase of the reaction mixture pressure results

in the shift of the equilibrium to the left side and in the decrease of X.

c) High temperature range (350+450°C). In this temperature range the reaction proceeds to complete conversion and the activity of the catalysts is stable and reproducible.

It was of interest to elucidate the influence of the pretreatment of zeolites with typical reducing and oxidizing agents such as H_2 and O_2 , correspondingly, on the activity of zeolites in relation to NO reduction.

Some data of such experiments are presented in table 2. As it follows from these data, reducing or redox treatments of the samples results in the increase of the activity of zeolites (increasing of the initial rates and conversions and decreasing of the temperature of the beginning of the reaction). The most active metal-zeolites are bimetallic catalysts. As for "oxidized" catalysts CoNaY shows high activity as well as mixed forms.

The analysis of the reaction products shows that on the samples of the first series (cationic forms) at low temperatures (200-250°C) a small amount of N_2O is present along with N_2 and CO_2 . N_2O was also observed in the products of the reaction over CrNaY and CrNiNaY after reducing and redox pretreatments. In all other cases N_2 and CO_2 were the only products.

It was of interest to compare the catalytic properties of the zeolites containing transition elements with the catalytic properties of corresponding transition element oxides and with catalysts, containing the elements of the VIII group which are known to be the effective catalysts of NO reduction. For this purpose the following oxides were studied: CuO , Cr_2O_3 and NiO as well as a Rh-containing zeolite of the X type. Some data for these catalysts are also presented in table 2. The comparison shows that the oxides are more active catalysts than zeolites containing the corresponding elements. The RhX catalyst is the most active among the catalysts studied. However, it should be noted that NO reduction over RhX in this temperature range proceeds mainly to N_2O .

2. CO oxidation.

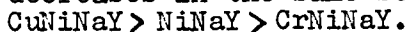
The data of the table 3 show that NiNaY and CuNiNaY cationic forms are active in this reaction. But the pattern of the kinetic curves which were obtained in the first runs at low temperatures suggests that catalyst "formation" takes place under action

Table 2.- NO reduction

Serie	Sample	Temperature range(°C)	W _o (350°C) (min)	X (%)
1.	RhX	200+300	4.6	60+100
	CoNiNaY	200+300	4.5	40+100
	CuNiNaY	250+350	2.5	40+90
	CrNiNaY	250+450	1.7	20+100
	CrNaY	250+450	1.3	40+100
	CuNaY	350+450	0.3	20+50
	CoNaY	100+500	neglig.	-
	NiNaY	100+500	neglig.	-
	NaY	100+500	neglig.	-
2.	RhX	150+250	5.0	80+100
	CoNiNaY	200+400	4.5	30+60
	CuNiNaY	250+350	3.5	80+100
	CrNiNaY	200+350	3.3	40+70
	CoNaY	200+350	2.3	30+80
	CuNaY	100+350	2.0	10+80
	CrNaY	250+450	1.5	40+100
	NiNaY	250+400	0.8	20+60
3.	Co-NaY	150+250	4.8	30+80
	RhX	150+250	4.2	60+100
	CuNiNaY	250+350	3.5	60+90
	CrNiNaY	250+450	3.5	40+100
	CoNiNaY	200+300	2.8	30+60
	CuNaY	250+400	2.0	50+100
	CrNaY	250+450	1.3	40+100
	NiNaY	250+500	0.3	20+70
oxides	CuO	100+200	7.0	80+100
	Cr ₂ O ₃	150+300	4.0	60+100
	NiO	200+350	2.2	60+90

of reaction mixture. In the subsequent runs the activity of these catalysts is stable and reproducible. CrNiNaY and NaY are inactive.

The activity of the catalysts studied increases as a result of redox pretreatments: the initial rates increase 1-2 orders of magnitude, the apparent activation energies (E_a) decrease c.a. two times, the temperature of the beginning of the reaction decreases 100-150°C. The activity of "oxidizing" zeolites was of the same order of magnitude as the activity of metal-zeolites and was higher than the activity of cationic forms. For all three series of the catalysts the activity decreases in the same sequence:



In all series the mutual influence of transition elements on the activity was observed. Cu promotes the activity of Ni-containing zeolite whereas Cr produces the opposite effect.

Table 3.- CO oxidation

Serie	Sample	Temperature range (°C)	W_0 (350°C) (min)	E_a (kcal/mole)
1.	CuNiNaY	200+400	3.2	19
	NiNaY	350+450	1	33
	NaY	100+550	neglig.	-
	CrNiNaY	100+550	neglig.	-
2.	CuNiNaY	100+180	15	10
	NiNaY	180+250	10	24
	CrNiNaY	180+280	8	11
3.	CuNiNaY	80+160	40	7
	NiNaY	180+250	13	21
	CrNiNaY	180+280	5	21

3. The state of transition elements in zeolites

The spectra of figure 3 show the changes of valence and physical state of Ni in zeolite as the result of interaction of zeolite with CO+NO and CO+O₂ reaction mixtures and with the separate components of these mixtures. Spectrum "a" consisting of the main and satellite lines, corresponds to Ni²⁺ ions in dehydrated zeolite. The treatment of the sample with CO under catalysis conditions leads to the appearance of two new lines (spectrum "b"). The line with lower

binding energy (852 eV) corresponds to metal nickel and the other line which occupies intermediate position between metal nickel and Ni^{2+} cations in zeolite lines can be attributed to Ni^+ . A part of Ni remains in the form of cations Ni^{2+} (zeol.). The subsequent treatment of the sample with NO results in back shift of Ni 2p_{3/2} spectrum ("c"). The treatment of the starting sample with NO+CO mixture does not produce any significant change in spectrum.

As the result of interaction of NO and NO+CO with NiNaY and NiCuNaY the lines of adsorbed NO appear in N 1s spectrum (figure 4). The line with lower binding energy probably may be attributed to the surface nitrosyl complex whereas high energetic peak corresponds to N in nitrate ions (7,8). The spectrum characterizes the forms of strongly chemisorbed NO, since the intensities of the lines are high enough after evacuation of the samples at 350°C.

Taking this into account, one can suggest that the treatment of the zeolite with NO+CO results in the reduction of a portion of nickel and the formation of a strong surface compound of the nitrate type between adsorbate and metal which produces the positive effective charge on the Ni and a back shift of the Ni lines in spectrum. When cationic Ni-forms are treated with CO+O₂ mixture under reaction conditions, a portion of nickel² is reduced to metal. However, it should be noted that the energetic resolution of Ni⁰ and Ni^{2+} (zeol.) lines after treatment of the samples with CO+O₂ mixture is lower than in the case of the samples² treated with hydrogen (9,10). It may be due to the presence of a portion of nickel in intermediate form of Ni^+ in case of zeolite treatment with CO+O₂ mixture. One cannot the possibility that reduced² nickel can be partially oxidized to the Ni^{2+} (oxide) form, the line position in spectrum of the latter being different from Ni^{2+} (zeol.) one.

Some samples (CoNaY, CoNiNaY, NiNaY) prereduced with H₂ were treated with CO+NO mixture. After such treatment the lines of Co²⁺(oxide) and Ni^{2+} (oxide) were observed in Co 2p and Ni 2p spectra. In addition a portion of Ni and Co in zeolites remains in metallic state. Similar treatment of "oxidized" zeolites did not produce noticeable changes in Co 2p_{3/2} and Ni 2p_{3/2} spectra.

Conclusions.

Thus the results of this work show that zeolites containing transition elements (Co, Cu, Ni, Cr) are ac-

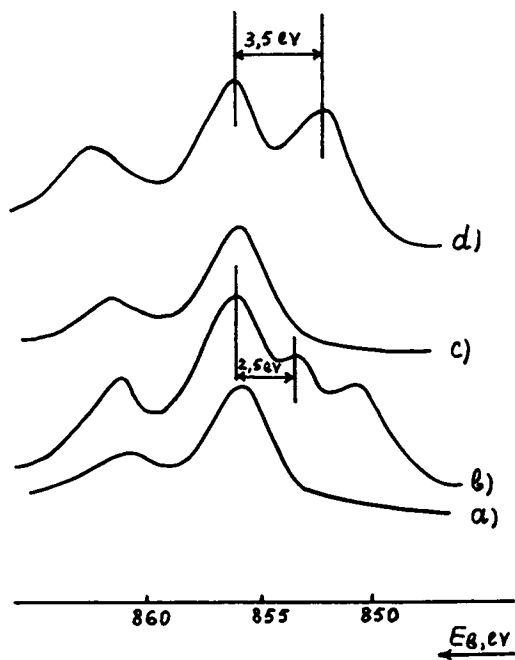


Figure 3. XPS Ni $2p_{3/2}$ spectra of 0.33 NiNaY zeolite. (a), Dehydrated sample; (b), 350°C, CO; (c), 350°C, NO, after CO at 350°C; (d), 400°C, CO + O₂.

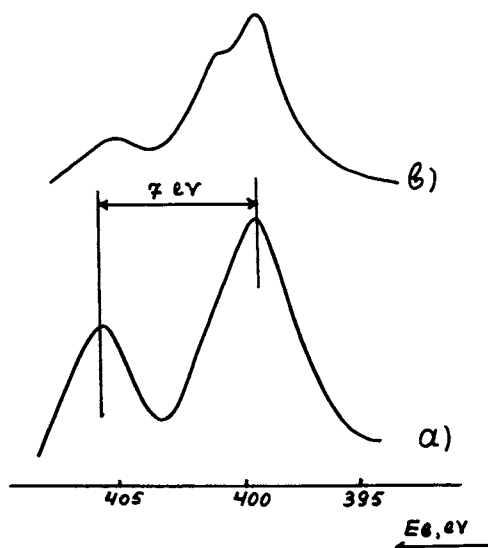


Figure 4. XPS N 1s spectra of 0.33 NiNaY zeolite with adsorbed gases. (a), NO + CO adsorption at 400°C; (b), NO adsorption at 400°C.

tive catalysts for NO reduction with CO and CO oxidation with O₂ in the temperature range between 100 and 450°C. Reducing and redox treatments increase the activity of zeolites which were active in cationic forms and cause samples which did not catalyze this reaction when used in cationic forms to become active.

XPS data showed that valence and physical state of transition elements after such pretreatments is drastically different from the state in the starting material. After reduction the formation of metal phases on the external surface of zeolites occurs, whereas after redox pretreatment oxide phases and amorphous oxides are formed in the zeolite cavities. In the cases of polycationic CoNi-, CrNi-, and CuNi-forms of zeolites the mutual influence of transition elements on their ability for reduction and migration was observed (5). The effects may cause the observed changes in catalytic activity.

Treatment of the catalysts with CO+O₂ under catalysis conditions causes a modification of surface layer of the catalysts to occur, in particular, Ni²⁺(zeol.) is reduced to metal and intermediate Ni⁺ states. A part of the Ni is present in an oxide form. The "formation" of the "active" catalyst is probably due to the changes of the transition element state under action of the reaction mixture. Such changes were not observed in case of NO reduction with CO over zeolite catalysts. As it mentioned above it may be due to the formation of stable surface compounds. For instance, in case of nitrates formation which was observed in N 1s spectrum the effective charge on Ni should be very close to effective charge on Ni in zeolite. The formation of nitrates or other stable surface compounds (11,12) may be the reason for catalyst deactivation under the action of the reaction mixture.

It is evident that the catalytic activity of zeolite for NO reduction will depend on the stability and reactivity of surface compounds along with the physical and valence state of the transition elements.

It should be noted that the results on kinetics of NO reduction over zeolites which were obtained up to now should be considered as preliminary results and further investigation is necessary to elucidate the mechanism of this reaction.

Literature cited

1. M. Shelef, Otto K., Gandhi H., J. Catalysis, (1968), 12, 361

2. Otto K. and Shelef M., *J. Phys. Chem.*, (1972), 76, 37
3. Shelef M., *Catalysis revs.*, (1975), 11, 1
4. Minachev Kh.M. and Isakov Ya.I., Preparation, activation and regeneration of zeolite catalysts CNIITENeftekhim, Moscow (1971)
5. Minachev Kh.M., Antoshin G.V., Shpiro E.S. and Yusifov Ya.A., *Proceed. VI Int. Cong. on Catalysis*, B2, London (1976)
6. Minachev Kh.M., Antoshin G.V., and Shpiro E.S., *Problemy kinetiki i kataliza*, (1975), 16, 189
7. Kishi K. and Ikeda Sh., *Bull. Chem. Soc. Japan*, (1974), 47, 2532
8. Hendickson D.N., Hollander J.M. and Jolly W.L., *Inorg. Chem.*, (1969), 8, 2462
9. Minachev Kh.M., Antoshin G.V. and Shpiro E.S., *Izvest. Akad. Nauk S.S.S.R., Ser. khim.*, (1974), 1015
10. Minachev Kh.M., Antoshin G.V., Shpiro E.S. and Isakov Ya.I., *Izvest. Akad. Nauk S.S.S.R., Ser. khim.*, (1973), 2131
11. Unland M.L., *J. Catalysis*, (1973), 31, 459
12. Unland M.L., *Science*, (1972), 179, 567

Catalytic Active Centers in Cerium-Exchanged Faujasite Zeolites

HANNA HOSER, ANDRZEJ DĄBROWSKI, and STANISLAW KRZYŻANOWSKI
Institute of Organic Chemistry, Polish Academy of Sciences, 01-224 Warsaw, Poland

ABSTRACT

The catalytic activity of cerium-exchanged zeolites for *n*-butene isomerization depends upon the Si/Al ratio, the extent of cation exchange, the temperature and method of activation. All these factors have the influence on the character and "concentration" of the catalytic active centres in the zeolites.

Introduction

Our earlier study (1) on the isomerization of olefins catalyzed by cobalt-exchanged X zeolites allowed one to conclude that the reaction involves a carbonium cation intermediate, and that acidic zeolite hydroxyl groups are the active centres responsible for the course of the reaction. IR spectral studies (2-4) disclosed that if trivalent cation-exchanged zeolites are subjected to thermal dehydration the number of the resulting acid hydroxyl groups is higher than that produced in bivalent cation-exchanged zeolites. This fact allows us to propose that cerium-exchanged zeolites should be highly active catalysts for olefins isomerization. On the other hand, numerous investigators (5-8) have long reported that certain zeolites, including rare earth-exchanged zeolites, when brought into contact with unsaturated hydrocarbons, are capable of generating organic radicals at room temperature.

Studies on CuNaX zeolite-catalyzed isomerization of butenes have led Dimitrov and Leach (8) to postulate a radical mechanism for the reaction on the ground of an induction period observed. However, Keii *et al.* (9), who also have demonstrated formation of organic

radicals during isomerization of butenes on CeNaX and especially CeNaY, have rejected the radical mechanism because they found the reaction to proceed at a faster rate than did the radical formation.

One of the present authors(10,11) who studied the mechanism of organic radicals formation during adsorption of olefins on cerium-exchanged zeolites, showed that both the rate of radical formation and concentration are greatly affected by the activating pretreatment and that number of radicals can be considerably enhanced if appropriate conditions of activation are used. Therefore, it was deemed advisable to study whether activation of cerium-exchanged zeolites under strictly similar conditions would also result in modification of their catalytic activity. Isomerization of but-1-ene was chosen as the test reaction because its mechanism has been well recognized for various types of active centres operative in the catalysts employed.

Experimental

Materials. Series of cerium-exchanged zeolites were prepared by ion exchange. The starting material was a 13 NaX zeolite (the Inowroclaw Soda Works, Matwy, Poland), Si/Al=1.27+.02, NaY (Institute of Industrial Chemistry, Warsaw), Si/Al=2.37+.02 and dealuminated NaY (Institute of Catalysis, Lyon, France), Si/Al=4.14+.02, all used as a powder containing no clay-binders.

The exchange procedure was done at pH=6.2 to prevent precipitation of cerium hydroxides. This procedure in the case of X-type zeolites caused not only the exchange but also partly replacement of sodium by hydronium ions. The hydrolysis degree was not the same for all samples. It was ca 15% for the samples of the exchange ratio lower than 56% of cerium. In the case of the highest extent of the exchange, the hydrolysis degree was much lower, e.g. for CeNaX-68 it was ca 5%. In comparison, for NaX alone (the blank test), the hydrolysis degree was 13.6%. In the case of Y type zeolites the hydrolysis degree was rather low (1-2.5%) and in the case of dealuminated zeolites it was negligible. The ion-exchange procedure and the analysis have been described in details elsewhere(1).

Pure-grade but-1-ene (Fluka) was degassed and purified by repeated vacuum bulb-to-bulb distillation.

Apparatus and procedure. A 235-ml glass reactor was used, operated in conjunction with a conventional

vacuum apparatus which enabled catalysts to be preliminarily outgassed and activated in a dry oxygen or argon atmosphere and reactants to be added in predetermined amounts. For each experiment a fresh portion of a hydrous-form catalyst₂ was weighed, 0.100g. The catalyst was outgassed (10^{-5} Torr) initially at room temperature, and later the reactor with the catalyst was placed in a thermostated electrical oven and heated to a required temperature. Afterwards, the zeolite catalyst, activated in vacuum for 3 h, was cooled to 50°C and used directly for the reaction. The second series of catalysts after activation for 2 h in vacuum was reactivated at the same temperature for 30 min in a dried and purified oxygen atmosphere (ca p=250 Torr). The oxygen excess was then removed and the catalyst was outgassed for 30₅ min at an identical temperature until a vacuum of 10^{-5} Torr was achieved. In a few cases the catalysts were activated in dry argon.

After having been activated, the catalyst was cooled to 50°C (the thermostated oven was changed), and used for the reaction immediately after the conditions become established.

The isomerization was carried out in static system at 50°C. Argon-born but-1-ene (14 mole %) was admitted to the reactor by opening a greaseless valve which led to a part of the apparatus (equipped with a manometer) calibrated so as to produce a pressure of 200 Torr in the reactor. Reaction time was recorded from the moment of valve opening. The reactor was then closed and samples for analysis were withdrawn through a rubber septum at 15 or 30-sec intervals. The samples were stored in gas-tight syringes and then injected into a dimethylsulpholane (20% by wt./chromosorb P) column, 3m long, operated at room temp.

The IR spectra of tested zeolites have been recorded with UR-20 (Jena, GDR) and Perkin-Elmer 325 spectrometers applying the method described by Pichat(12). The pure zeolite disks for IR measurements were activated in vacuum quartz-glass cells at the same temperatures and atmosphere as the samples for catalytic tests.

The EPR measurements have been described in details elsewhere(11).

Results

But-1-ene was isomerized selectively to n-butenes over each of the investigated catalyst. A deposit

ca. 10%, was found to occur on the catalyst. The experimental rate constants for the disappearance of but-1-ene, which was assumed to be a first-order reaction(1), were used as a measure of catalyst activity. The kinetic equation, $\log(X_e - X) = -kt + \log X_e$, proved to be a good fit up to about 75% of the equilibrium conversion. In this equation, X and X_e stand for the conversions recorded after a period of time t and at the equilibrium set up at a given reaction temperature, respectively.

The catalytic activity of the zeolites is related to the Si/Al ratio, the extent of cation exchange, and the temperature and mode of activation.

As the ratio Si/Al is increased, the activity rises as may be seen from Table I.

TABLE I.- Effect of Si/Al ratio

Zeolite [§]	Ce ³⁺ /unit cell	But-1-ene disappearance rate constant $k \times 10^{17}$ (molecules $dg^{-1} s^{-1}$)
NaX	0	inactive
NaY	0	inactive
NaY dealum.	0	0.00987
CeNaX-68	19.23	0.986
CeNaY-67	12.51	3.21
CeNaY dealum.-70	5.54	4.30

[§] -each catalyst examined was activated in vacuum at 400°C.

Effect of exchange extent. The plots in Fig. 1 show the zeolite activity to be closely related to Ce³⁺ ion content. The NaX, NaHX-13.6, and CeNaX (below 30% of exchange) proved to be practically inactive. As the cerium ion content is raised above 30%, the zeolite activity rises only slightly, but, at contents exceeding 45%, it rises quite rapidly. Whether below or above 45%, the rise is almost rectilinear.

Figure 2 shows IR spectra of the zeolites. As cerium ion content is increased, the band at ca. 3640 cm^{-1} rises in intensity and the absorption maximum shifts itself to lower frequencies. With the zeolites more than 40% Ce-exchanged, a new band is produced at ca. 3520 cm^{-1} , which becomes more intense as the Ce³⁺ is further increased (curves d - f). The degree of hydrolysis was practically constant at ca. 15% (curves b - g).

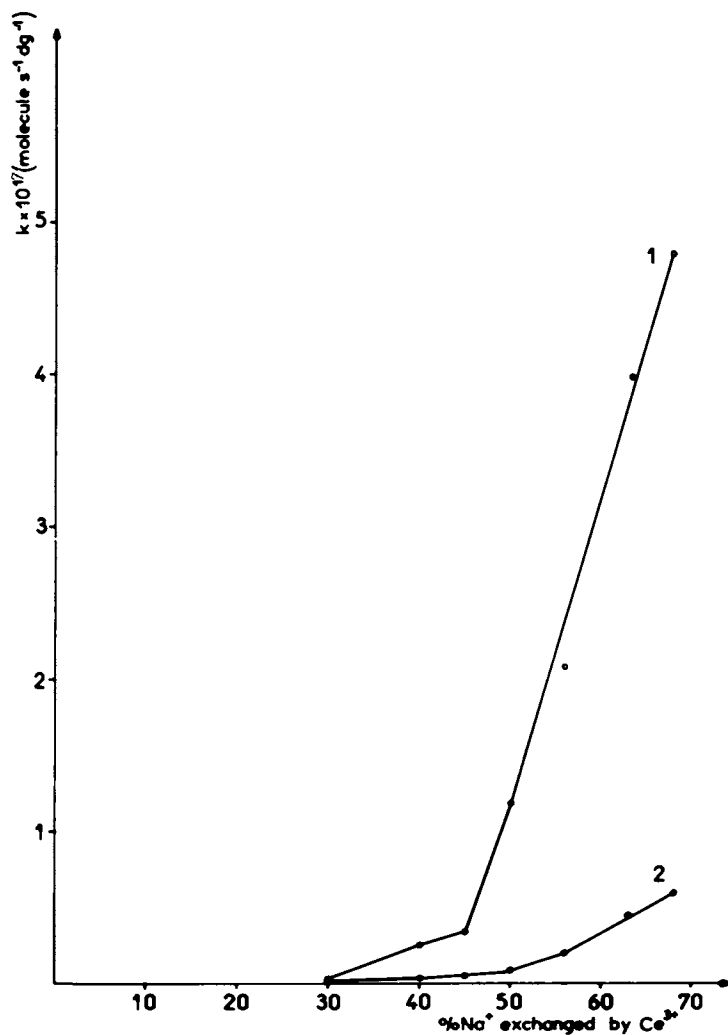


Figure 1. The effect of the degree of exchange of Na^+ for Ce^{3+} ions in X zeolites on the catalyst activity in isomerization of but-1-ene at 50°C. (1), Activated at 300°C; (2), activated at 500°C.

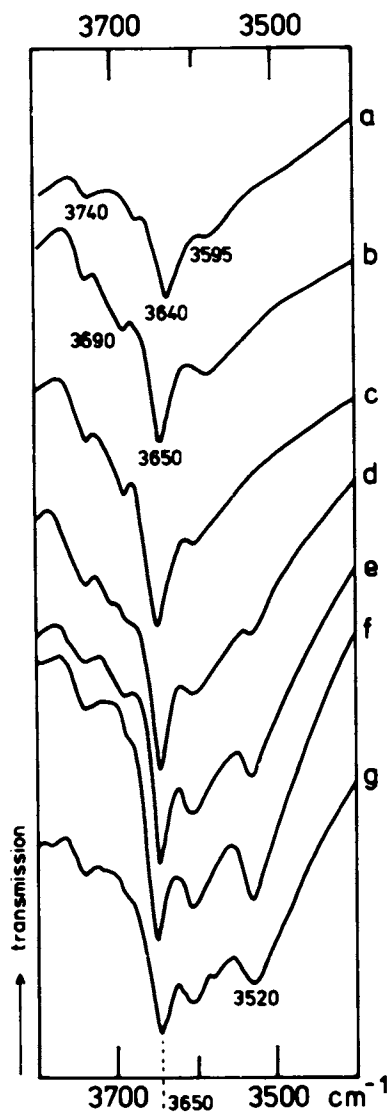


Figure 2. IR spectra of X type zeolites activated in vacuum at 300°C. (a), NaHX-13.6; (b), CeNaX-20; (c), CeNaX-30; (d), CeNaX-40; (e), CeNaX-56; (f), CeNaX-63; (g), CeNaX-68.

Table II. Kinetic data on isomerization of but-1-ene over cerium-exchanged zeolites

Catalyst	Activa- tion temp., °C	Rate constants of but-1-ene disappearance $k \cdot 10^{17}$ molecule dg ⁻¹ s ⁻¹	
		Activation in: vacuo	oxygen
CeNaX-68	200	2.43	2.78
	300	4.79	3.89
	400	0.986	4.09
	500	0.599	3.91
CeNaY-67	200	3.28	3.44
	300	5.28	4.44
	400	3.21	3.89
	500	1.30	2.38
CeNaY-dealum-70	300	6.83	5.05
	400	4.58	5.50
	500	2.05	2.45

Effect of activation temperature. With the zeolites activated in vacuum at 200 - 500°C (Table II), the catalytic activity rises as the outgassing temperature is increased, attains maximum at 300°C and, at still higher temperatures, falls rapidly. With the CeNaY and CeNaY dealuminated, this fall is much smaller than that observed with CeNaX. Again, at activation temperatures higher than 300°C, the intensity of the the 3500 - 3700 cm^{-1} bands attributable to hydroxyl groups vibrations becomes considerably reduced. The maximum changes occur with the zeolite X (cf. curves a in Fig. 3A, 3B and 3C).

Effect of activation mode. Reactivation of Ce-exchanged zeolites in oxygen has resulted in considerable modification of the catalytic activity of the vacuum-activated specimens (Table II). Except for the specimens vacuum-activated at 300°C, the oxygen-reactivated zeolites are the more active. Those reactivated at still higher temperatures, and especially the zeolite X, exhibited the most pronounced changes. As the vacuum activation temperature is raised to 400°C, the activity of each zeolite rises and past this temperature falls. This activity fall is, however, less pronounced than that observed with the specimens activated only in vacuum.

Reactivation in oxygen (especially of the zeolite X at the higher temperature) has also a distinct effect on the product ratios observed at the initial reaction stages. The cis/trans mole ratio evaluated from the data obtained at low conversions was plotted as a function of but-1-ene conversion. The ratios evaluated at zero conversion are listed in Table III.

TABLE III.- Effect of temperature and mode of activation on cis/trans but-2-ene ratio

Catalyst	Temperature of activation °C	Product ratio	
		Activation carried out in Vacuum	Oxygen
CeNaX-56	200	1.23	1.19
	300	1.39	1.00
	400	1.44	0.94
	500	1.50	0.89
CeNaX-68	200	1.11	1.08
	300	1.38	1.06
	400	1.43	0.92
	500	1.52	0.88

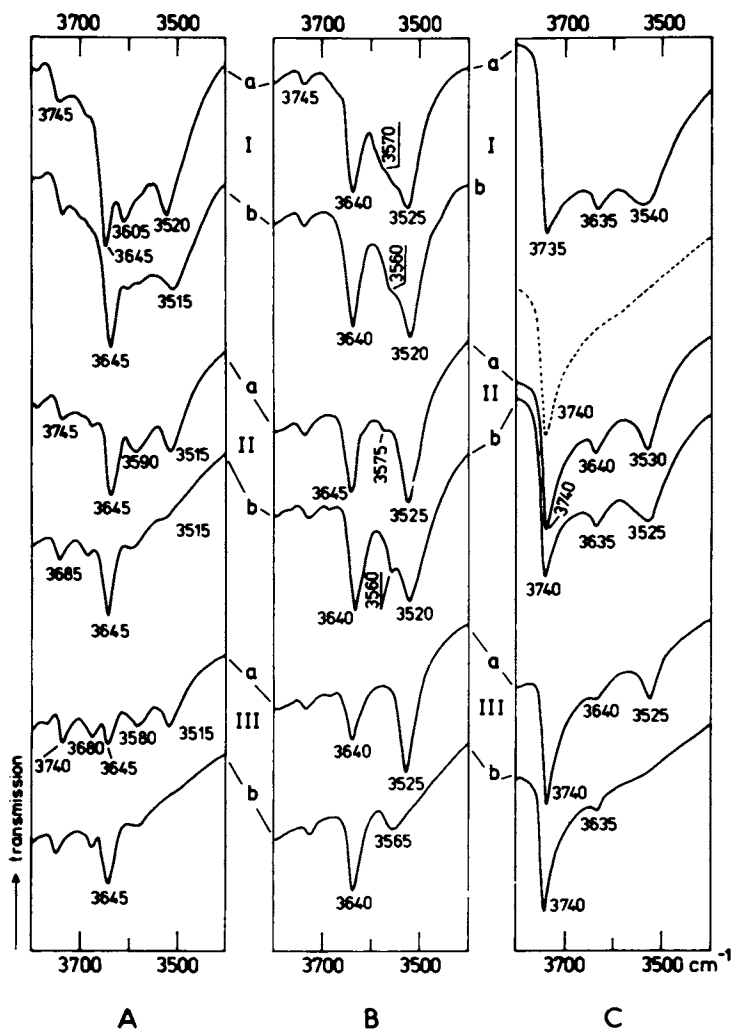


Figure 3. IR spectra of zeolites. (A), CeNaX-63; (B), CeNaY-dealuminated-70, activated: (a), in vacuum; (b), in oxygen at the temperature: (I), 300°C; (II), 400°C; (III), 500°C. (---), NaY-dealuminated activated at 400°C.

Again, reactivation has considerably affected the IR spectra of zeolites (Fig. 3). With the zeolites reactivated at 400°C and 500°C, the ca. 3640 cm^{-1} band rises in intensity whereas the ca. 3520 cm^{-1} band diminishes to nil.

Discussion

Active centres in vacuum-activated cerium-exchanged zeolites. Comparison of the activity data (Fig. 1) with the IR spectral evidence (Fig. 2) indicates the following conclusions: The initial increase in the Ce^{3+} ion content (up to 40% exchange) while resulting in a much higher intensity of ca. 3640 cm^{-1} band (rise of hydroxyl group concentration in the zeolite), only slightly enhances the catalytic activity of the zeolites. On the other hand, a further increase in the Ce^{3+} ion content while leading to progressively high ca. 3640 cm^{-1} band intensities and resulting in a new and increasingly intense band at ca. 3520 cm^{-1} , does at the same time rapidly enhance the catalytic activity of the zeolites. This fact may be regarded as typical, because analogous relationships were found by the authors (13) in the study of isomerization of butenes over CoNaY zeolites and by Ward (14) in the isomerization of *o*-xylene over variously Na^+ -exchanged NaHY zeolites. To interpret Ward's data, Dempsey (15) has postulated the occurrence of hydroxyl groups differing in acid strength but occupying identical lattice sites. According to Dempsey, the acidic properties of the resulting hydroxyl groups are affected by the number of Al ions present in the adjacent lattice element. Dempsey believes, that at low Na^+ for H^+ exchange, there are formed weakly acidic hydroxyl groups responsible for the ca. 3640 cm^{-1} band, whereas at higher exchange degrees, strongly acidic hydroxyl groups are formed responsible for the ca. 3640 cm^{-1} and 3540 cm^{-1} bands. The order of the increasing acid strength assumed for the hydroxyl group formation to follow the progress in the exchange of Na^+ ions for protons in a zeolite Y is consistent with the present data concerning CeNaX zeolites. Therefore, the zeolite active centres responsible for isomerization appear to involve acidic hydroxyl groups which are formed in the CeNaX after a suitable degree of cerium ion exchange has been achieved.

Dempsey's interpretation (14) provides an easy explanation for the commonly observed rise in the catalytic activity of the zeolites with the increase in the Si/Al ratio. The fall in the Al ion proportion in

the zeolite lattice gives rise to a reduced number of weakly acidic hydroxyl groups per unit cell.

The activity fall observed in cerium-exchanged zeolites activated at temperatures exceeding 300°C is associated with progressive dehydroxylation which is evident from the diminishing intensity of the ca. 3520 and 3640 cm^{-1} absorption bands in the IR spectrum (cf curves a in Fig. 3A, 3B and 3C). In the case of the CeNaX preactivated at 500°C the bands are barely visible.

Active centres in Ce-exchanged zeolites reactivated in oxygen. The activity of the reactivated zeolites is seen (Table II) to vary a great deal with particularly high differences occurring for CeNaX activated at the higher temperatures. Reference to the IR spectral evidence (Fig. 3) hardly assists in explaining these variations. Reaction at 400°C and especially at 500°C gives rise to a considerably more intense ca. 3640 cm^{-1} band and at the same time to a considerably less intense ca. 3520 cm^{-1} band as compared with those recorded upon vacuum activation of the specimens (Fig. 3). Our earlier EPR studies on Ce-exchanged oxygen-reativated zeolites (10, 11) have shown that under these conditions radical oxygen centres are formed, representing both paramagnetic (O_x^-) and diamagnetic (O_x^{2-}) adsorbed oxygen species ($x = 1, 2$). The nature of the arising oxygen centres is related primarily to the temperature of zeolite activation.

Confronting the earlier (10, 11) with the present results reveals a correlation to exist between the number of radical oxygen species in zeolites and their catalytic activity in isomerization of but-1-ene. Changes observed in the initial cis/trans but-2-ene product ratios (Table III) suggest that radical centres participate in the isomerization, which would thus account for the enhanced catalytic activity of the oxygen-reativated zeolites. Modified radical-generating capacities of various faujasite-type zeolites (CeNaX > CeNaY dealum. > CeNaY) may also be responsible for the changes observed in the catalytic properties of the zeolites reactivated in oxygen at higher temperatures.

Summing up, we believe that, on being activated, cerium zeolites produce at least two types of active centres which are responsible for the course of isomerization, viz., ionic centres associated with the presence of strongly acidic hydroxyl groups and radical centres associated with the presence of adsorbed oxygen species. The application of suitable conditions

for the activation of zeolites results in a higher or lower "concentration" of a given type of centres. In vacuum activation as well as in oxygen reactivation, though only at lower temperatures, the ionic centres predominate in Ce-exchanged zeolites, whereby the isomerization proceeds mainly through a carbonium cation as an intermediate stage. On the other hand, reactivation in oxygen, especially of CeNaX at higher temperatures, increases the concentration of the acidic sites but also gives rise to a considerably higher number of radical centres, which in our opinion results in at least partial modification of the reaction mechanism toward the radical mode.

Literature Cited

1. Hoser, H., Krzyżanowski, S., *J. Catal.* (1975), 38, 366.
2. Jacobs, P.A., Uytterhoeven, J.B., *J. Chem. Soc., Faraday Trans. I.* (1973), 69, 359, 373.
3. Smith, J. V., *Advances in Chemistry Series No 101, Molecular Sieve Zeolites-I, Chapter 15*, p 171, ACS (1971).
4. Ward, J.W., *J. Catal.* (1969), 14, 365.
5. Hirschler, A.E., Neikam, W.C., Barmby, D.S., James R.L., *J. Catal.* (1965), 4, 628.
6. Raseev, G., *J. Catal.* (1971), 20, 120.
7. Krzyżanowski, S., *J. Chem. Soc., Chem. Commun.* (1974), 1036.
8. Dimitrov, Chr., Leach, H.F., *J. Catal.* (1969), 14, 337.
9. Suzuki, J., Honda, Y., Ono, Y., Keii, T., *Proceedings of Vth Intern. Congress on Catalysis, Palm Beach, (1973), Vol 2*, p 1377.
10. Krzyżanowski, S., *Bull. Acad. Polon. Sci., Ser. Sci Chim.* (1976), 24, 165, 231.
11. Krzyżanowski, S., *J. Chem. Soc., Faraday Trans. I.* (1976), 72, 1573.
12. Pichat, P., Chapter in "Spectroscopies Infrarouge et Raman", *Monographies du Centre d'Actualisation Scientifique et Technique de l'INSA, No 9*, Masson et Cie, Éditeurs, Paris (1974), p 240.
13. Hoser, H., Dąbrowski, A., Krzyżanowski, S., to be published.
14. Ward, J.W., Hansford, R.C., *J. Catal.* (1969), 13, 364.
15. Dempsey, E., *J. Catal.* (1975), 39, 155.

Infrared Spectroscopic and Catalytic Studies on Mordenite-like Zeolites

HELLMUT G. KARGE

Fritz-Haber Institut der Max-Planck Gesellschaft, 1 Berlin 33, Faradayweg 4-6, Germany

ABSTRACT

Hydrogen forms as well as ion-exchanged forms of synthetic mordenite-like zeolites have been studied by means of the IR technique and used as catalysts in the alkylation of benzene and the cracking of ethylbenzene. These zeolite catalysts have been investigated with special attention given to active sites, life-time and shape selectivity.

Introduction

The zeolite mordenite shows certain structural and chemical properties which make it a useful catalyst for specific reactions. Thus, due to the high silicon content and to the predominant role of 5-rings in the structure, mordenites are usually very stable with respect to high temperatures and chemical agents such as strong acids (1). The diameter of the pores is close to the larger diameter of a benzene molecule. One would therefore expect a pronounced "shape selectivity" for instance in benzene alkylation and similar reactions. Because of their special properties the mordenites have created great interest, which in turn has produced during the last few years an increasing number of papers concerned with the behavior of these zeolites in catalysis as well as in adsorption and diffusion. This article summarizes results which were obtained during our systematic investigation of hydrogen mordenite and cation-containing mordenites. During the course of this work we have studied the IR spectra of the zeolites as well as of certain zeolite/adsorbate systems. The IR results were correlated with studies of the catalytic alkylation of

benzene and cracking of ethylbenzene over the mordenite-like zeolites.

Experimental

The cation-containing zeolites (NH₄M, BeM, MgM, CaM, SrM, BaM, LaM) were prepared in the usual manner by ion exchange, starting with the commercially available sodium form from the Norton Comp., Mass. (Na-Zeolon: 78.3 SiO₂, 14.3 Al₂O₃, 7.4 Na₂O in wt %, Si/Al = 4.7). In order to prepare beryllium mordenite (BeM) it proved to be very important to use solutions of sufficiently high pH, e. g. pH = 3 - 4. Otherwise a direct substitution of Na⁺ by H⁺ occurred and the resulting samples were very similar to the hydrogen form containing practically no Be at all.

TABLE I. - Extent of Ion Exchange

No.	1	2	3	4	5	6	7	8	9
Zeolite	HM	NH ₄ M	NaM	BeM	MgM	CaM	SrM	BaM	LaM
Degree of Exchange [%]	95	99,6	0	55	59	68	78	90	64

Hydrogen mordenite (H-Zeolon: 87.3 SiO₂, 12.3 Al₂O₃, 0.4 Na₂O in wt %, Si/Al = 6.0) was supplied by the Norton Comp., Mass., or prepared via NH₄-mordenite (NH₄M). The IR spectra were recorded with Perkin Elmer spectrophotometers type 225 and 325. (For technical and experimental details of the IR investigations see Ref. 2.) The alkylation and cracking was carried out in a flow-reactor in which 0.2 - 1.0 g of the catalyst powder could be prepared under nearly the same conditions as were used in the IR experiments. A Perkin Elmer gas chromatograph type F 20 or 3920 equipped with an apiezon or a benton 34 + di-n-decylphthalate column was used to analyze the reaction products. Under the experimental conditions all the products were gaseous. During the run they were directly fed into the gas chromatograph in short intervals. The catalytic test conditions were as follows: a) feed gas: ethylene (7 torr) + benzene (80 torr) + helium (720 torr) and ethylbenzene (10 torr) + helium (790 torr), respectively b) flow rate: 30 ml per minute, c) mass of catalyst: 0.5 g, d) height of the catalyst bed: 20 mm, e) volume of the catalyst: 1 ml, f) both activation and reaction temperature: 450° C.

Results

Structural OH Groups. Figure 1 shows the OH region of the IR spectra of the various mordenites. The OH band at 3740 cm^{-1} is not relevant to the catalytic process and most probably corresponds to OH groups of amorphous inclusions of silica (3). Brønsted sites of stronger acidity, which are possibly active centers, are indicated by the OH band with its center near 3600 cm^{-1} . This band is very prominent in the spectra of HM, BeM, MgM, and LaM. Assuming that acid OH groups play a significant catalytic role, one would expect pronounced catalytic activity particularly with these four mordenite-like zeolites. In the case of BeM the intensity of this band was measured as a function of the degree of exchange. As one would expect, the intensity increases as the BeO content is increased. However, this relationship is obviously not linear as can be seen from Figure 2.

Adsorption of Bases (Ammonia, Pyridine). Only upon adsorption of ammonia ($p = 30$ torr) did the OH band near 3600 cm^{-1} disappear completely, while pyridine merely weakened it in intensity. Even after a two hour adsorption of pyridine ($p = 4.3$ torr) on BeM (No. 4) at 200° C the intensity of the 3605 cm^{-1} band only decreased by about 5%. This means that only a small part of the acid OH groups of BeM is accessible to the relatively large pyridine molecules under these conditions. The corresponding figure for HM is 70%. However, in every case the adsorption of pyridine by mordenites containing acid OH groups gave rise to the well-known IR bands of adsorbed pyridine, especially to that at 1542 cm^{-1} . This band is indicative of pyridinium ion formation at Brønsted acid centers (4). If the commercial hydrogen form (HM, No. 1, dehydrated at 450° C under high vacuum) was used as adsorbent a further strong band appeared at 1452 cm^{-1} , due to pyridine coordinately bonded on Lewis sites (4). It can thus be concluded that the commercial form of HM contained Lewis acid centers even before dehydroxylation which begins at temperatures around 450° C (2, 5). In this characteristic property it differs significantly from hydrogen mordenite prepared via the ammonium form (HM, No. 2) and from the corresponding hydrogen forms of faujasite-like zeolites such as HY (6). On the other hand, only in the case of HM did the expected 1452 cm^{-1} band appear upon pyridine adsorption after dehydroxylation. With dehydroxylated ion-exchanged mordenites (BeM, LaM) however, no new bands could be detected ascribable to newly formed

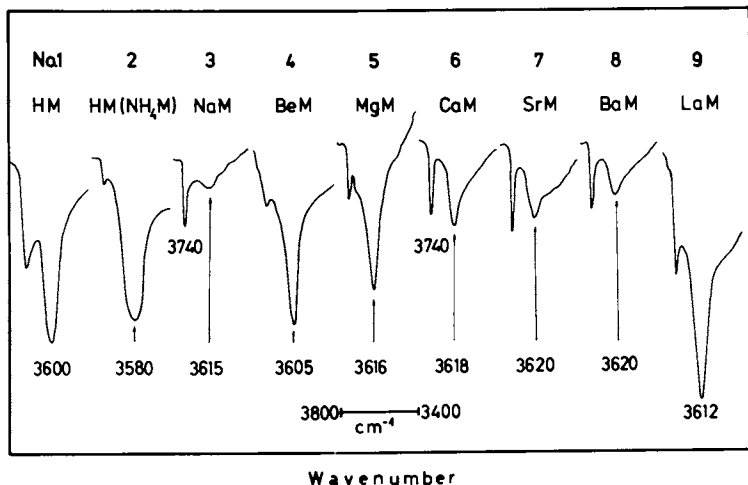


Figure 1. OH stretching bands of the various mordenites (No. 1-9, see Table I). The samples were of nearly equal thickness, 12-14 mg/cm² and calcined under HV at either 300°C (BeM) or 450°C (all the others).

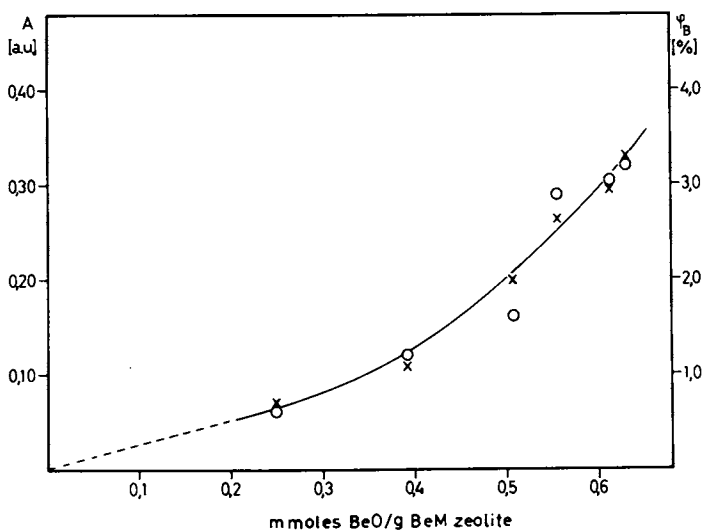


Figure 2. (A), Maximum absorbance of the OH band of beryllium mordenite as a measure of OH group concentration (X); ϕ_B , conversion of benzene (alkylation) over beryllium mordenite (O). Both A and ϕ_B as a function of BeO content.

Lewis centers, although the OH bands had been completely eliminated. The only bands which could be observed both before and after dehydroxylation and subsequent pyridine adsorption were those characteristic of pyridine bonded to the respective cation (NaM: 1441,8 cm^{-1} , BeM: 1452,8 cm^{-1} , MgM: 1448,5 cm^{-1} , CaM: 1444,5 cm^{-1} , SrM: 1443,5 cm^{-1} , BaM: 1443,0 cm^{-1} , LaM: 1442,8 cm^{-1}).

Adsorption of Benzene. One effect of benzene adsorption on the OH groups of HM was a small shift of the OH band from 3600 to 3589 cm^{-1} . Furthermore, a broad plateau developed around $\tilde{\nu} = 3400 \text{ cm}^{-1}$, most probably due to hydrogen bonding (Figure 3). Besides the CH fundamental vibrational band at 3088 cm^{-1} (ν^{CH}) and the combination bands at 3068 and 3032 cm^{-1} the¹² very intense band at 1478 cm^{-1} (ν_{13}^{CC}) appeared (7, 8). Complete dehydroxylation reduced the amount of benzene adsorbed practically to zero in the case of hydrogen mordenite (HM, No. 1 and No. 2). The adsorbed benzene could be easily removed by merely pumping at the temperature which the sample attained in the IR beam (ca. 100° C, abbreviated with "B. T.").

In comparison with HM, the interaction between benzene and the OH groups of the cation-containing mordenites (e.g. BeM, LaM) was significantly less pronounced (Figure 3). In contrast to the HM it turned out that the adsorption of benzene by the cation-containing mordenites is favored by higher temperatures. The adsorption was not reversible, e.g. only about 70 % of the benzene adsorbed on BeM at B. T. could be desorbed by merely pumping at the same temperature.

Adsorption of Ethylene. The take-up of ethylene by HM was completely irreversible, even at room temperature. The OH band was very strongly affected (Figure 4). The new bands appearing in the CH region upon exposure to ethylene exclusively belong to aliphatic species (e.g. ν^{CH_3} : 2950 cm^{-1} , ν^{CH_2} : 2930 cm^{-1} , $\nu_{\text{s}}^{\text{CH}_3}$: 2860 cm^{-1} , and a broad $\delta_{\text{as}}^{\text{CH}}$ band at 1468 cm^{-1}). The original spectrum could not be restored by pumping. On the other hand, the OH groups of the exchanged mordenites NaM, MgM, CaM, SrM, BaM, and LaM remained practically unaffected by ethylene. The IR spectra of the samples exposed to 100 torr ethylene exhibited only olefinic CH bands (e.g. ν^{CH} : 3080 cm^{-1} , $\nu_{12}^{\text{CH}_2}$: 1442 cm^{-1}). Upon desorption into high⁹vacuum the adsorbate bands immediately disappeared, i.e. the adsorption was quite reversible.

Beryllium mordenite (BeM) was intermediate between hydrogen mordenite and the other zeolites under in-

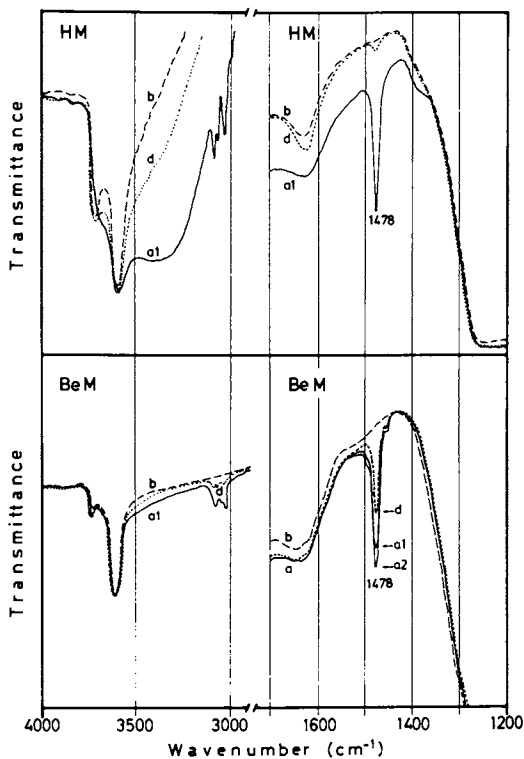


Figure 3. Adsorption of benzene ($p = 24$ torr) on hydrogen mordenite (HM, No. 1), activated at 450°C under HV and on beryllium mordenite (BeM, No. 4), activated at 300°C under HV. (b), IR base spectrum (---); (a), IR spectrum after adsorption (—); (1), at B.T.; (2), at 200°C ; (d), IR spectrum after desorption (· · ·).

vestigation. During ethylene adsorption a broad band at 3250 cm^{-1} developed, probably indicating hydrogen bonding or π -complex formation. This band grew with increasing pressure (Figure 4). At first the ethylene was reversibly adsorbed as was the case with the other cation-containing mordenites. The CH bands which were exclusively ascribable to olefinic species could be readily removed by pumping. During continued exposure, bands of saturated hydrocarbons started to develop. The same occurred when the adsorption temperature was increased to $100 - 150^\circ\text{ C}$. After desorption of those species which had remained olefinic in character, the newly formed bands of aliphatic hydrocarbons were still present in the spectrum (Figure 4).

Alkylation of Benzene. In the case of HM, the OH group concentration of the catalyst was systematically varied by increasing the calcination temperature, i.e. by increasing the degree of dehydroxylation. The result was a distinct correlation between the activity and the concentration of OH groups and Brønsted centers, measured by the intensity of the corresponding pyridine band at 1542 cm^{-1} (see Ref. 2 and 9). The presence of Lewis acid centers alone was obviously not a sufficient condition for catalyzing the alkylation process. After dehydroxylation at 650° C the concentration of such Lewis sites was high (0.18 mmole g^{-1}) as determined via the 1452 cm^{-1} band, but the activity had dropped to zero.

Among the cation-containing mordenite-like zeolites only BeM and LaM turned out to be active enough to render quantitative measurements possible. Over MgM only slight traces of alkylbenzene were produced. In the case of BeM a systematic variation of the OH group concentration was obtained by increasing the degree of ion exchange. Figure 2 demonstrates that the increase of OH group concentration of BeM corresponded to the increasing alkylation activity of this zeolite (10). In further agreement with the results obtained with HM (9), the complete dehydroxylation at $650 - 700^\circ\text{ C}$ removed also any catalytic activity from BeM and LaM.

The comparison between HM, BeM, and LaM showed that under identical conditions the initial activity of HM is by far the highest. On the other hand, the HM catalyst was poisoned much faster than BM and LaM (see Figure 5). Table II gives a typical example of product distribution. One realizes that the selectivity of BeM and LaM is evidently superior to that of HM.

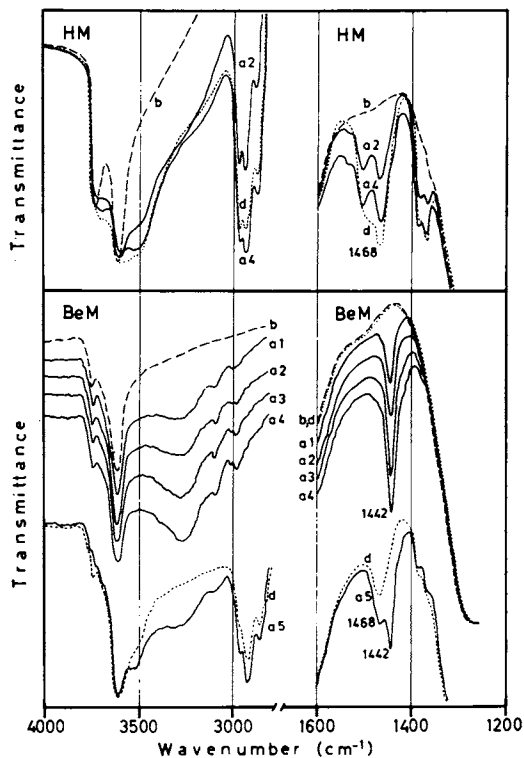


Figure 4. Adsorption of ethylene on hydrogen mordenite (HM, No. 1) activated at 450°C and beryllium mordenite (BeM, No. 4) activated at 300°C. (b), IR base spectrum (---). (a), IR spectrum after adsorption at B.T. (—); (1), 13 torr; (2), 20 torr; (3), 50 torr; (4), 100 torr, all 1 hr; and (5), 100 torr, 20 hr. (d), IR spectrum after desorption (· · ·).

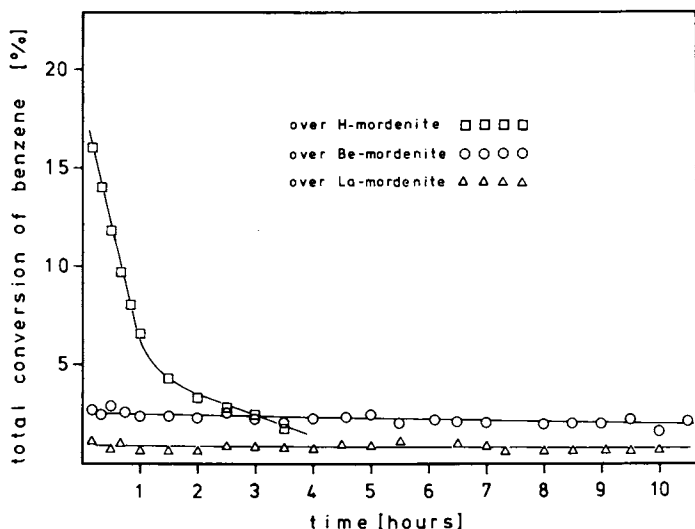


Figure 5. Alkylation of benzene (both activation temperature and reaction temperature 450°C) over HM (No. 1), BeM (No. 4), and LaM (No. 9).

TABLE II. - Distribution of Alkylation Products in Percent

Products	H - mordenite			Be-mordenite			La-mordenite		
	time 10	[min.] 120	[min.] 180	time 10	[min.] 120	[min.] 180	time 10	[min.] 120	[min.] 180
Ethyl- benzene	11,4	53,8	50,0	64,7	71,4	71,4	100	100	100
Toluene	82,3	38,5	38,9	35,3	28,6	28,6	-	-	-
m-Xylene	1,3	-	-	-	-	-	-	-	-
Ethyl- toluene	2,5	7,7	11,1	-	-	-	-	-	-
Diethyl- benzene	2,5	-	-	-	-	-	-	-	-

Activation and reaction temperature: 450° C.
For further experimental details see text.

Cracking of Ethylbenzene. The ion-exchanged mordenites BeM and LaM also showed with respect to the inverse reaction, i.e. the cracking of ethylbenzene, a significant longer life-time than HM. Table III shows an example of the product distribution.

TABLE III. - Distribution of Cracking Products in Percent

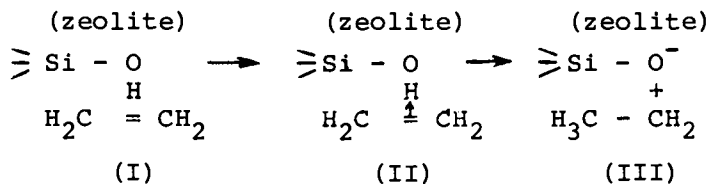
Products	H - mordenite			Be-mordenite			La-mordenite		
	time 10	[min.] 120	[min.] 180	time 10	[min.] 120	[min.] 180	time 10	[min.] 120	[min.] 180
Ethylene	38,0	32,9	32,0	45,1	44,1	44,2	46,1	38,9	37,0
Benzene	43,4	51,8	56,0	48,5	49,2	50,4	34,9	43,6	47,7
Toluene	13,3	12,0	10,0	4,1	4,8	4,0	7,8	10,6	10,0
m-Xylene	1,4	1,0	-	-	-	-	-	-	-
Ethyl- toluene	4,0	2,3	2,0	2,3	1,9	1,4	11,2	6,9	5,3

Activation and reaction temperature: 450° C.
For further experimental details see text.

The hydrogen mordenite exhibited a characteristic behavior in that it catalyzed even the cracking of benzene. When, under the same reaction conditions as used in the cracking of ethylbenzene, a mixture of benzene vapor ($p = 198$ torr) and helium ($p = 602$ torr) was contacted at 450° C with the HM catalyst, 5 % of the benzene reacted. The main products were toluene and ethylene.

Discussion

Because of the good correlation between concentration and activity in benzene alkylation it may be concluded that the acid OH groups of the active mordenites are the catalytically relevant centers. Ethylene interacts with the OH groups of all the mordenites under investigation (see Figure 4). The IR results from the ethylene adsorption suggest that an activation of the olefin by a Brønsted acid center may be the important initial step. Probably this occurs through π -complex formation or through formation of carbonium ions:



However, while ethylene is adsorbed in the olefinic state (I) both on NaM and on most of the ion-exchanged mordenites, the structure (III) appears to be preferred in the case of HM. This leads to a high activity in the beginning of the alkylation reaction but also favors the rapid poisoning due to formation of saturated-type adsorbates (polymerisation) and subsequent coking, since polymerisation will also occur via a carbonium ion mechanism. The irreversible adsorption of olefins (especially hexene) on acid faujasite type zeolites giving rise to saturated species has been previously reported by Eberly in his pioneering work (11). Weeks and Bolton (12) have reached similar results and conclusions in their study of the role of butene/HY intermediates in the catalytic alkylation of benzene. With BeM (and LaM) the state II seems to be mainly produced and subsequently changes only slowly to structure (III). The initial activity is thus lower than that of HM, but on the other hand, the poisoning due to polymerisation is much less important.

Clearly, the OH groups of the hydrogen mordenites

(both commercial and prepared via NH_4M) are also relevant with respect to the adsorption of benzene. When the HM samples are completely dehydroxylated, the extent of benzene adsorption turns out to be nearly zero. This cannot be explained by a partial collapse of the lattice, since the X ray patterns did not show any structural change and, furthermore, the dehydroxylated samples were still able to adsorb the nearly identically shaped pyridine molecules.

The situation obviously is quite different with the ion-exchanged mordenites. Here the benzene does not interact with the OH groups to a detectable extent, but rather the benzene molecules are strongly bonded by the cations themselves. In comparison with HM, the sorption and desorption of benzene in the cation-containing mordenites is markedly slower and these processes must be thermally activated. This is most probably one of the reasons for the fact that the alkylation of benzene over BeM and LaM needs much higher reaction temperatures than over HM. The selectivity of BeM and LaM with respect to alkylation of benzene is better than that of HM. The higher yield of toluene over HM is mainly due to the cracking of benzene, catalyzed by this zeolite. One further reason may be the presence of other intermediates, produced by the simultaneously occurring olefin polymerisation over HM. In any case, formation of monoalkylbenzenes is evidently favored due to the geometric conditions within the zeolitic pores, which influence the identity of the nascent products ("shape selectivity"). Csicsery (13, 14) has pointed out that the very same explanation applies to the shape selectivity of HM in trans-alkylation and disproportionation of alkylbenzenes.

Acknowledgements

The author wishes to thank Mrs. E. Popović for valuable assistance during the experimental work. He is also grateful to Prof. Dr. K. A. Becker and Prof. Dr. J. H. Block for helpful discussions and critical revision of the manuscript. The financial support of this work from the Deutsche Forschungsgemeinschaft is gratefully acknowledged.

Literature Cited

1. Zoltay, T., and Bürger, M. J. Z., Z. Krist. (1960), 114, 1.
2. Karge, H. G., Z. physik. Chem. Neue Folge (1971), 76, 133.

3. Karge, H. G., *Z. physik. Chem. Neue Folge* (1975), 95, 241
4. Basila, M. R., Kantner, Th. R., and Rhee, K. H., *J. Phys. Chem.* (1964), 68, 3197.
5. Lefrancois, M., and Malbois, G., *J. Catalysis* (1971), 20, 351.
6. Ward, J. W., *J. Catalysis* (1967), 9, 225.
7. Galkin, G.A., Kiselev, A.B., and Lygin, V.I., *J. Phys. Chem. English Transl.Russ.*(1962), 36, 851.
8. Abramov, V.N., Kiselev, A.B., and Lygin, V.I., *J.Phys.Chem.English Transl.Russ.*(1965), 37, 613.
9. Becker, K. A., Karge, H. G., and Streubel, W.-D., *J. Catalysis* (1973), 28, 403.
10. Ladebeck, J., private communication
11. Eberly jr., P.E., *J.Phys.Chem.*(1967), 71, 1717
12. Weeks, T. J., and Bolton, A. P., *Proc. 3rd Int.Conf.on Molecular Sieves, Zurich 1973* Paper No.162, publ. in "Molecular Sieves" (Ed. J. B. Uytterhoeven), 1973, p. 426.
13. Csicsery, S. M., *J. Catalysis* (1970), 19, 394.
14. Csicsery, S. M., *J. Catalysis* (1971), 23, 124.

Ring Transformation of Tetrahydropyran into Piperidine over Dealuminated L-Zeolites

YOSHIO ONO, ANAND HALGERI, MASAMICHI KANEKO, and KOU HATADA

Department of Chemical Engineering, Tokyo Institute of Technology, Meguro-ku, Tokyo, Japan 152

ABSTRACT

The reaction of tetrahydropyran with ammonia to give piperidine has been studied over L-zeolites. Dealumination of the zeolite enhanced the ring conversion. The reaction kinetics was determined and the reaction mechanism was proposed. The effects of dealumination on the thermal stability and the acidic property were also studied.

Introduction

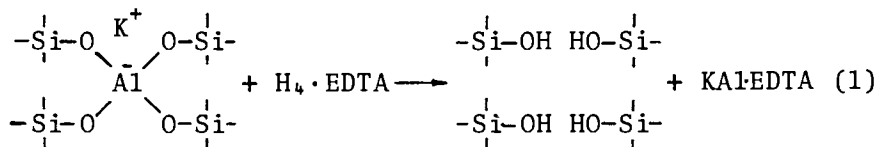
Recently, we have reported that synthetic zeolites are very effective catalysts for the ring conversion of lactones and cyclic ethers into the corresponding lactams and cyclic imines in the presence of ammonia (1-5). It should be noted that the hydrogen form of L-zeolite(HL) shows higher selectivity than the hydrogen form of Y-zeolite(HY) for the conversion of cyclic ethers into imines. For examples, tetrahydrofuran is converted into pyrrolidine over HL at 350°C with a yield of 53 % and at a selectivity of 91 % (4). However, the yield and the selectivity for the conversion of tetrahydropyran into piperidine was not very satisfactory (4).

Here, we report that the dealumination of L-zeolite enhances the catalytic activity and the selectivity for the ring transformation of tetrahydropyran into piperidine. The kinetics of the reaction is studied and a reaction mechanism is proposed. The thermal stability of dealuminated L-zeolites are studied by means of X-ray and infrared spectroscopy. The acidic properties of dealuminated NH_4L are also studied by infrared spectroscopy and by the use of

Hammett indicators.

Experimental

Materials. The starting zeolite is KL zeolite from the Linde Division of Union Carbide Corp. The chemical analysis of the zeolite gave the composition of $K_{8.4}Al_{8.4}Si_{27.6}O_{72} \cdot 20H_2O$. Ion exchange was performed with aqueous solutions of ammonium chloride. Dealumination of KL was carried out in a following manner. KL (20 g) was added to 300 ml of aqueous H_4EDTA of various concentration and the mixture was refluxed. The part of the supernatant liquid was dried up and the residue was calcined at $600^\circ C$ to get white powder of alumina, which was then dissolved in nitric acid. Aluminum content of the solution was determined as the oxine complex by measuring the absorbance at 380 nm. The potassium extracted was determined by flame photometry. The amount of the aluminum extracted and that of the potassium extracted were almost equivalent. Thus, the chemical reaction involved in the dealumination may be written by a following equation.



The dealuminated KL was exchanged with aqueous ammonium chloride to obtain dealuminated NH_4KL zeolites.

Catalytic Reaction. Reaction of tetrahydrofuran and ammonia was carried out in a fixed bed type reactor under continuous flow conditions at atmospheric pressure. Prior to reaction, the catalysts were heated in an air stream at $460^\circ C$ for 180 min and then in an ammonia stream at reaction temperature for 30 min. Tetrahydropyran (THP) was pumped into preheating zone of the reactor by a microfeeder. The products were collected in a cold trap maintained at $-100^\circ C$. The main product separated by fractional distillation was piperidine, since the infrared spectrum agreed with that of the pure compound. The reaction products were analyzed by a gas chromatograph with a hydrogen flame ionization detector. The analytical column was a 4 mm x 2 mm stainless steel tubing packed with PEG-6000

on Shimalite F. Identification of byproducts was not attempted.

Infrared Spectrum. Infrared measurements were conducted in a previously described manner(6), allowing the thin sample wafers to be heated under vacuum or equilibrated with pyridine vapor. The samples were compressed under 600 kg/cm^2 into 20 mm-diameter disks. Spectra were recorded after cooling the sample to room temperature. For measurements in the lattice vibrations ($400\text{-}1400 \text{ cm}^{-1}$), the Nujol method was used.

Acidity Measurement. The acidic character of the zeolites was determined by the Benesi method by use of n-butylamine as a titer and Hammett indicators. Zeolites were heated for 2 hr at 500°C prior to the measurements.

Results and Discussion

Effect of Dealumination on Ring Conversion. In Table 1, the activity and the selectivity for the ring conversion of tetrahydropyran into piperidine of the original and the dealuminated zeolites are summarized. Like the initial zeolite, the dealuminated KL which does not have some cation exchange of K^+ with NH_4 is inactive for this ring transformation. Dealuminated HL

Table 1 Effect of dealumination on activity and selectivity for the ring conversion of tetrahydropyran into piperidine

<u>catalyst</u>	<u>Si/Al</u>	<u>total conversion(%)</u>	<u>piperidine yield (%)</u>	<u>selectivity (%)</u>
KL	3.2	11	0	0
KL	4.8	15	0	0
HL	3.2	24	14	58
HL	6.0	25	20	80
HY	2.4	15	5	33
HY	4.7	26	17	65

and dealuminated HY are more active than the original HL and HY, respectively. In the case of HL, a selectivity of 80 % can be attained. As described in a previous paper (4), non-crystalline solids like alumina or silica-alumina give much less selectivity. Since dealuminated HL gave a reasonably good selectivity, an effort was made to find the optimum reaction conditions with use of dealuminated HL as a catalyst.

Time Course of the Reaction. Figure 1 shows a typical time course of the reaction over dealuminated HL. The reaction conditions are as follows; reaction temperature 350°C, catalyst weight 3.5 g, $\text{NH}_3/\text{THP}=7$, $\text{W/F}=26$ g-cat·hr/mole. At these reaction conditions, a piperidine yield of 22 % with a selectivity as high as 80 % was obtained. Further, it is note worthy that there is no sign of deactivation of the catalyst within 7 hr.

Effect of Reaction Temperature. The effect of the reaction temperature on the catalytic activity of dealuminated HL was examined and the results were illustrated in Figure 2. The total conversion of tetrahydropyran increases with the reaction temperature, while the yield of piperidine increases with the reaction temperature up to 350°C, but falls down over 370°C. It can be concluded that the optimum reaction temperature lies around 350°C. The selectivity to piperidine remains as high as 80 % at this temperature.

Kinetics of the Reaction. Reaction kinetics was examined in the temperature range of 310-350°C in a low W/F condition (13.8 g-cat·hr/mole). Figure 3 shows the effect of the partial pressure of ammonia (P_{NH_3}) on the reaction rate. It is clear that the reaction rate is the first order with respect to the partial pressure of ammonia. The dependence of the rate on the partial pressure of tetrahydropyran (P_{THP}) is shown in Figure 4. The rate depends markedly on P_{THP} when $P_{\text{THP}} < 0.2$ atm, but is almost independent of P_{THP} when $P_{\text{THP}} > 0.2$ atm. In this region, the rate (r ; mole/hr·g-cat) can be expressed as follows,

$$r = k P_{\text{NH}_3} \quad (P_{\text{THP}} > 0.2 \text{ atm}) \quad (2)$$

The values of the first order rate constant, k , calculated from the slope of Figure 3 are 0.52, 1.02 and 2.02 mole/hr·g-cat at 310, 330 and 350°C, respectively. From the dependence of the rate constant on reaction

Figure 1. Variation of the conversion of tetrahydropyran (Δ), the yield of piperidine (\circ), and the selectivity (\square) with time on stream

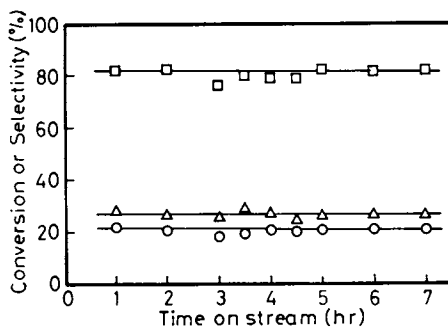


Figure 2. Variation of the conversion of tetrahydropyran (Δ), the yield of piperidine (\circ), and the selectivity (\square) with reaction temperature. $W/F = 26$ g-cat-hr/mole $P_{NH_3}/P_{THP} = 7$.

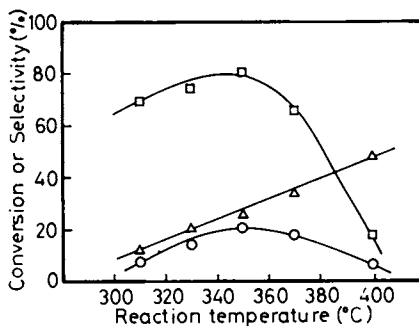
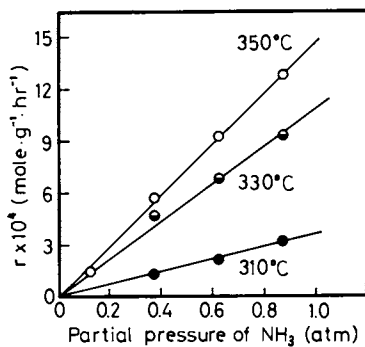


Figure 3. The dependence of the reaction rate on the partial pressure of ammonia, $P_{THP} = 0.125$ atm



temperature, the activation energy was calculated to be 24.7 kcal/mole. Essentially the same expression has been obtained for ring conversion of tetrahydrofuran into pyrrolidine, though the activation energy to tetrahydrofuran is 17 kcal/mole.

Effect of KL on its Thermal Stability. The change in the structure of KL with dealumination was studied by infrared spectroscopy and X-ray diffraction. A new OH band at 3700 cm^{-1} appears after dealumination and the intensity of the band increases with increasing dealumination. The OH band is considered to be due to the Si-OH groups formed by the reaction (1).

Pichat et al. (7) showed that the 608 cm^{-1} band due to the vibration of double D-6 rings was a good measure for the crystallinity of the zeolites. The intensity of 608 cm^{-1} band decreases with increasing dealumination. Thus, the dealumination of L-zeolite leads to the destruction of zeolite framework. The same conclusion is also drawn from the X-ray diffraction. The intensities of diffraction lines decrease with dealumination. Calcination of the samples at 460°C for 1 hr leads to further decay of the crystal structure.

Adsorption of Pyridine on Dealuminated KL.

Pyridine was adsorbed at 100°C for 1 hr on dealuminated KL. The ir band due to the pyridine molecule interacting with potassium cations was observed around 1440 cm^{-1} . But, no bands of pyridine adsorbed on acidic centers are observed. The OH band at 3700 cm^{-1} does not react with pyridine. Thus, the OH groups formed by reaction (1) have no acidic character.

Acidic Properties of Dealuminated NH_4L . The infrared spectrum of the NH_4 form of dealuminated L-zeolite ($\text{NH}_{43.0}\text{K}_{2.3}\text{Al}_{5.2}$) was investigated as a function of the evacuation temperature. The desorption of water and ammonia takes place in almost the same manner as in the case of ordinary NH_4L zeolite, which has been reported previously (7). The sample evacuated at 460°C showed bands at 3640, 3280 and 2600 cm^{-1} , which are quite similar to those observed in ordinary NH_4L (7). The only difference between dealuminated and ordinary NH_4L is the presence of 3700 cm^{-1} band in the former, which is ascribed to SiOH groups formed by the reaction (1).

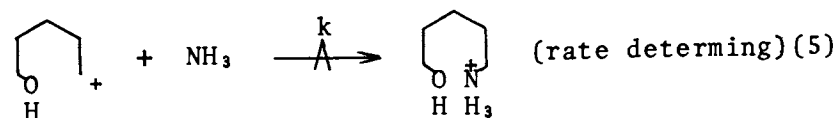
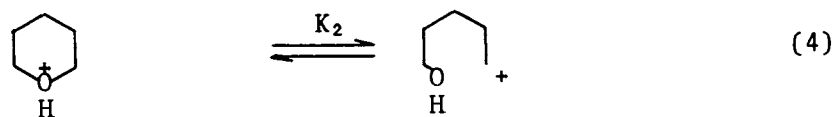
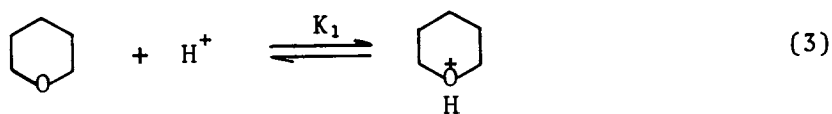
After the sample was evacuated at 460°C , it was exposed to pyridine vapor at 100°C for 30 min, and then evacuated at 200°C for 1 hr. Then, the bands at 3640, 3280 cm^{-1} disappeared, but the band at 3700 cm^{-1}

remained, indicating that the former OH group are acidic and that the latter is not. The presence of the band at 2600 cm^{-1} shows that the pyridinium ions thus formed are hydrogen-bonded with lattice oxygen.

Adsorption of pyridine leads to the appearance of a band at 1550 cm^{-1} , indicative for pyridinium ions. The intensity of the band is plotted as a function of the exchange degree by NH_4^+ per unit cell for ordinary and dealuminated zeolites (Figure 5). The intensity of 1550 cm^{-1} band of the dealuminated NH_4L is stronger than that of ordinary NH_4L if samples of the same exchange level are compared.

The increase in the number of acid centers by dealumination is also demonstrated by titration with n-butylamine. Hammett indicators with H_0 values of 3.3, 1.5 and -3.0 are used. The results are given in Figure 6. In the case of ordinary NH_4L , only part of H^+ ions introduced is effective as acidic centers. Though the same can be said also of dealuminated NH_4L , the fraction of H^+ ions effective for the adsorption of n-butylamine is much larger than that found for NH_4L . The extent of the increase is more pronounced for centers of stronger acidity ($H_0 = -3.0$). This increase in acidity and the strength of acid might be responsible for the enhanced catalytic activity for ring conversion of tetrahydropyran into piperidine.

Reaction Mechanism. In previous papers (3,4), we have proposed a mechanism for the reaction of tetrahydrofuran and ammonia, including Bronsted acids as active centers. Since essentially the same kinetics was found also for the ring conversion of tetrahydropyran, we assume the following reaction mechanism is operative for the reaction.



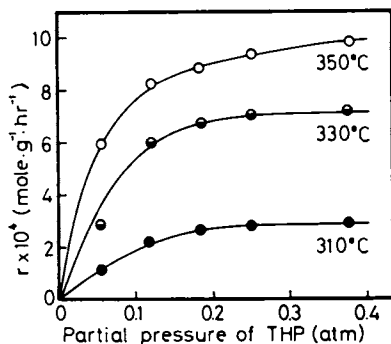


Figure 4. The dependence of the reaction rate on the partial pressure of tetrahydropyran, $P_{NH_3} = 0.625$ atm

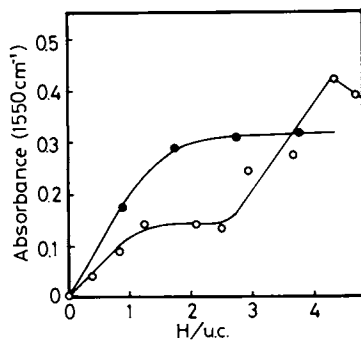


Figure 5. The change in the absorbance of 1550 cm^{-1} band with H^+ content per unit cell. Ordinary HL, (○); dealuminated HL, (●).

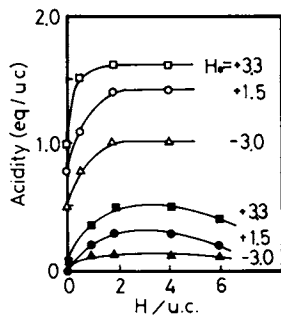
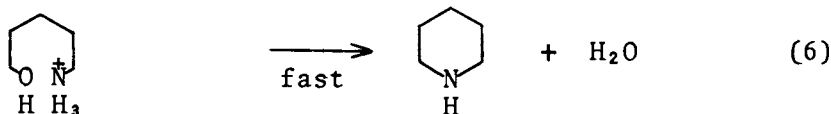


Figure 6. The change in the acidity with H^+ content per unit cell. Solid marks for ordinary HL and open marks for dealuminated HL.



Ammonia may react with Bronsted sites;



From the above mechanism, the following rate expression is obtained,

$$r = \frac{k K_1 K_2 C_{\text{H}^+}^{\circ} \cdot P_{\text{THP}} P_{\text{NH}_3}}{1 + K_1 (1 + K_2) P_{\text{THP}} + K_3 P_{\text{NH}_3}} \quad (8)$$

where $C_{\text{H}^+}^{\circ}$ is the surface concentration of Bronsted sites effective for the reaction. If $K_1 (1 + K_2) P_{\text{THP}} \gg 1 + K_3 P_{\text{NH}_3}$, Eq.(8) is reduced to

$$r = \frac{k K_2 C_{\text{H}^+}^{\circ}}{1 + K_2} P_{\text{NH}_3} \quad (9)$$

Eq.(9) agrees with observed rate expression. Comparison of Eq.(1) with Eq.(9) gives the following relation.

$$k_{\text{obs}} = \frac{k K_2 C_{\text{H}^+}^{\circ}}{1 + K_2} \quad (10)$$

If one assumes $K_2 \ll 1$, Eq.(10) yields the following relation.

$$k_{\text{obs}} = k K_2 C_{\text{H}^+}^{\circ}$$

Thus, the observed activation energy is the difference between the activation energy of step (5) and the heat of reaction (4). Though the activation energy of step (4), which is the reaction of a carbonium ion with ammonia, hardly depends on the ring size of the original ether, the heat of the reaction (4) should markedly depend on the ring size of the ether. Since a five-membered ring is more strained than a six-membered ring, the heat of the ring opening may be larger in the former case. This explains the difference in activation energy between the conversion of tetrahydrofuran and that of tetrahydropyran.

According to the suggested mechanism, dealumination of the catalyst increases the rate by increasing the number of effective site, C_H^+ .

Literature Cited

1. Hatada, K., Simada, M., Fujita, K., Ono, Y., and Keii, T., *Chem. Lett.*, (1974), 439.
2. Fujita, K., Hatada, K., Ono, Y., and Keii, T., *J. Catal.*, (1974), 35, 325.
3. Hatada, K., Shimada, M., Ono, Y., and Keii, T., *J. Catal.*, (1975), 37, 166.
4. Ono, Y., Hatada, K., Halgeri, A., and Keii, T., *J. Catal.*, (1976), 41, 322.
5. Ono, Y., Takeyama, Y., Hatada, K., and Keii, T., *Ind. Eng. Chem., Prod. Res. Dev.*, in printing.
6. Ono, Y., Kaneko, M., Kogo, K., Takayanagi, H., and Keii, T., *J. Chem. Soc., Faraday I*, (1976), 72, 2150.
7. Pichat, P., Franco-parra, C., and Barthomeuf, D., *J. Chem. Soc., Faraday I*, (1975), 71, 991.

n-Butenes Isomerization over Protonated Germanic near Faujasite and X and Y Molecular Sieves

G. PONCELET and M. L. DUBRU

Groupe de Physico-Chimie Minérale et de Catalyse, Université Catholique de Louvain, Place Croix du Sud 1, B-1348 Louvain-la-Neuve, Belgium

P. A. JACOBS

Centrum voor Oppervlaktescheikunde en Colloïdale Scheikunde, Katholieke Universiteit Leuven, de Croylaan 42, B-3030 Heverlee, Belgium

ABSTRACT

n-Butenes isomerization has been studied in the temperature range 150–350°C. The kinetic parameters over the Ge-faujasite are in agreement with a mechanism which implies the formation of the sec.-butyl-carbonium ion. The activation energies, the 2:1 product ratios and the frequency of the OH stretching vibration show that the average acidity of the active sites increases with the Si(Ge)/Al ratio.

Introduction

n-Butene isomerization was chosen to evaluate the catalytic properties of a partially ammonium exchanged germanium near faujasite.

The protonated form of the Y sieve develops high activity in reactions involving the formation of carbonium ions. In most cases, the occurrence of secondary reactions results in more or less rapid deactivation of the catalyst (1–3).

On such catalysts, the *n*-butene isomerization reaction proceeds via the formation of a common intermediate, the sec.-butyl-carbonium ion (3,4).

In aluminium deficient and ultrastable faujasite-type zeolites, it has been shown that the acid site efficiency in the supercages decreases with increasing Al content of the zeolites (5).

This study reports the results of *n*-butene isomerization over a germanic near faujasite with Ge:Al ratio equal to 1. The isomerization activity of this zeolite was compared to the activities of X and Y ammonium exchanged zeolites with higher Si:Al ratios.

Experimental

Materials. A germanic near faujasite zeolite, and X and Y Linde sieves were used in this study.

The germanic zeolite was synthesized at 90°C from Al-Ge gels according to the procedure described elsewhere (6). Some surface and catalytic properties of this zeolite have been reported in a previous study (7).

The NaY^x zeolite was obtained from the parent NaY zeolite by H₄EDTA extraction, following the method described by Kerr (8).

The four zeolites were partially exchanged with NH₄⁺, using diluted solutions of ammonium acetate. The unit cell compositions are as follows :

HNaY ^x	(Na) _{12.6}	(NH ₄) _{29.4}	(AlO ₂) ₄₂	(SiO ₂) ₁₉₂
HNaY	(Na) _{16.5}	(NH ₄) _{38.5}	(AlO ₂) ₅₅	(SiO ₂) ₁₃₇
HNaX	(Na) _{42.5}	(NH ₄) _{42.5}	(AlO ₂) ₈₅	(SiO ₂) ₁₀₇
HNaGeX	(Na) _{75.8}	(NH ₄) _{20.2}	(AlO ₂) ₉₆	(GeO ₂) ₉₆

n-Butene isomers with Baker's purity (99.5%) were treated using the freeze-thaw procedure. Pyridine was uvasol grade from Merck, and was distilled in vacuo before use.

Method. A U-shaped quartz reactor was loaded with 0.12 g of zeolite. The sample was pretreated as follows: after outgassing at room temperature, the reactor was slowly heated to 300°C, and was further evacuated at this temperature for two hours. The cell was then cooled to the reaction temperature. The procedure for the HY zeolites has been described elsewhere (3).

The experiments were carried out in an all-glass circulation apparatus consisting mainly of a reactor, a gas-circulation pump, a mercury manometer and 1 liter glass bulb. The total volume of the system was approximately 1.5 liter. In the working conditions, the circulation speed of the pump was about 2 liter min⁻¹.

A 6-way sampling valve was connected to a Hewlett-Packard gas-chromatograph equipped with a thermal conductivity detector. The valve was outgassed before sampling. The separation of the butene isomers was achieved at 30°C on a 20 ft long column (1/4" o.d.) packed with 20% tributylphosphate on 30-60 mesh chromosorb P.

The deactivation of the catalysts was followed in a conventional flow reactor, using helium as carrier gas (3).

Procedure. The isomerization of the three n-butene has been investigated mainly on a 20% NH_4 -exchanged sample in the temperature range 150-350°C, using initial pressures between 10 and 75 torr. A few experiments were performed on 4%, 29% and 43% NH_4 exchanged samples.

From the conversion vs time plots, the apparent rate constants were established according to the equation :

$$\ln(x_0 - x_e) - \ln(x_t - x_e) = kt$$

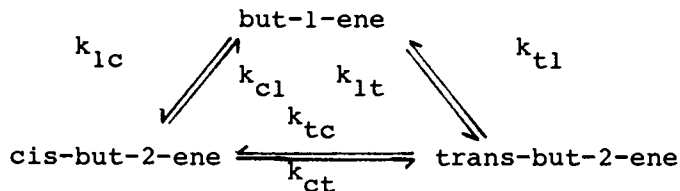
where x refers to the concentration at zero time (x_0), at time t (x_t) and at equilibrium (x_e). The latter values were taken from Kallo and Schay (9).

Results and Discussion

Isomerization over germanic near faujasite. Figure 1(a) shows that the reaction proceeds following first order kinetics for the three isomers through the whole reaction period investigated. These linear relationships indicate that no appreciable deactivation occurs over a 3 1/2 hour period, i.e. when the conversion of the isomers is near equilibrium (Figure 1b).

From experiments performed on the silicic HY sieve under similar conditions, Jacobs et al. (3) observed that the first order law is followed only during the first 6 minutes of reaction. Afterwards, the departure from linearity increases with time. IR spectroscopy could not reveal the presence of bands at 1580 and 1530 cm^{-1} , indicating that no appreciable deactivation due to secondary reactions occurs. These bands, more developed on HY than on HX (10) are indicative of adsorbed diene type species (3).

The first order kinetics for the three butene isomers being established, the rate constants of the parallel, reversible reactions



should verify the following equations :

$$k_{cl} \cdot k_{lt} \cdot k_{tc} = k_{ct} \cdot k_{tl} \cdot k_{lc} \quad (1)$$

$$\text{or} \quad \frac{\text{trans}}{1} \times \frac{1}{\text{cis}} \times \frac{\text{cis}}{\text{trans}} = 1 \quad (2)$$

The experimental values for equation (2) are given in Table I.

TABLE I. Product ratios and selectivity products at different temperatures

Temp. (°C)	cis/trans	1/cis	trans/1	Product of selectivity ratio
200	1.03	1.06	0.66	0.72
250	0.83	0.90	0.97	0.72
300	0.76	0.76	1.65	0.96
350	0.72	0.79	1.61	0.92

Values close to 1 are observed for the experiments carried out at 300 and 350°C. The lower values obtained at 200-250°C might be accounted for by preferential adsorption of cis- to trans-2-butene during 1-butene isomerization.

The numerical values of the relative rate constants were calculated, taking k_{lc} equal to unity. The values are given in Table II.

TABLE II. Relative rate constants

Temp. (°C)	k_{lt}	k_{tl}	k_{lc}	k_{cl}	k_{tc}	k_{ct}
200	0.97	0.23	1	0.59	0.22	0.39
250	1.2	0.37	1	0.69	0.41	0.67
300	1.32	0.51	1	0.62	0.67	1.03
350	1.39	0.67	1	0.76	0.84	1.22

The apparent activation energies were established from the first order rate constants in the 200-300°C temperature range. This has been done at different pressures between 11 and 75 Torr. The values remain virtually unchanged, which clearly indicates that working conditions are within the linear part of the adsorption isotherm. Independently, the difference in activation energies between two parallel paths were determined from the temperature dependence of the initial selectivity ratios. The energy profiles for the three isomers are shown in Figure 2.

A few experiments were carried out on NaNH_4GeX

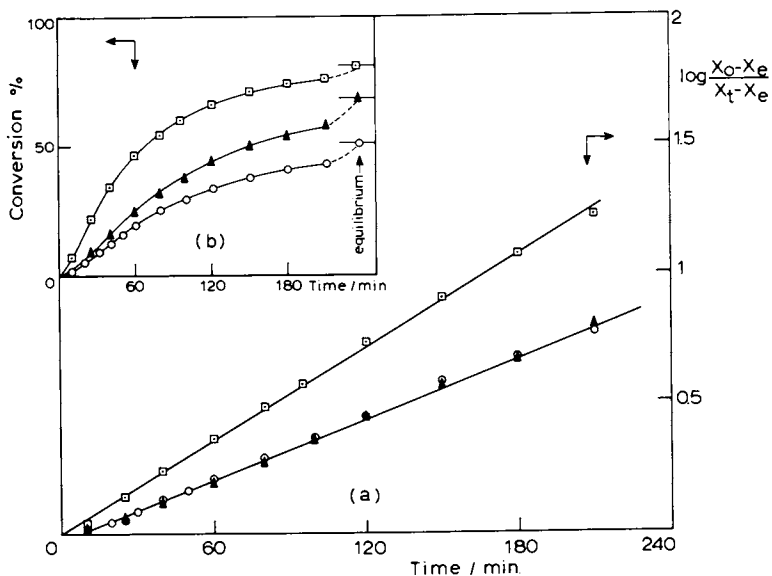


Figure 1. First-order plots (a) and conversion percentages (b) for *n*-butenes isomerization over HGeX at 300°C ($p_{init.} = 30$ torr). □, 1-butene; ○, trans-but-2-ene; △, cis-but-2-ene.

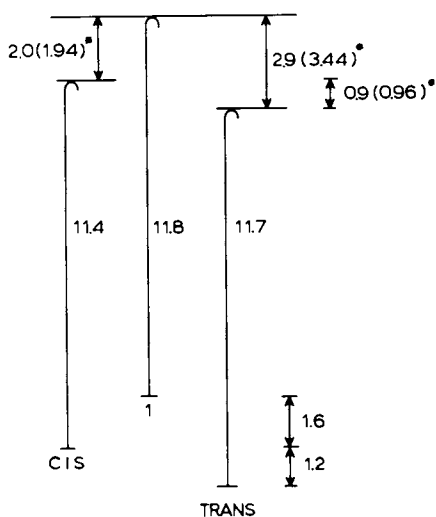


Figure 2. Energy profile for *n*-butene isomerization. Values between brackets were obtained from \log (selectivity) = $\Delta E_a/RT$

with different NH_4 contents, e.g. 4, 20, 29 and 43 %. X-ray diffraction showed that appreciable lattice breakdown occurred for the highest exchanged catalysts. The linear relationship of Figure 3 indicates that the reaction rate is dependent upon the number of OH groups. That the slope of the line is smaller than unity would mean either that only a part (about half) of the hydroxyl groups takes part in the reaction, or that, as the OH content increases, the degree of lattice collapse also increases. Germanic near faujasite structure is more fragile than the silicic homologues (6).

Addition of pyridine to a 21% NH_4 exchanged sample resulted in a decrease in the isomerization activity. Almost 80% of the activity was lost after addition of 0.64 molecule of pyridine per OH group.

The following arguments indicate that *n*-butene isomerization over germanic near faujasite occurs via a common carbonium intermediate: the sec.-butyl-carbonium ion. Firstly, there exists a relation between the rate constant and the proton content. Secondly, such a mechanism is able to predict the experimentally observed selectivities: the reaction is first order in each of the isomers; the product of the selectivity ratios is equal to 1 and there is agreement between the experimental and the calculated temperature dependency of the product ratios; finally the overall activation energies and the difference in activation energy between two parallel paths fit into the same energy diagram. Besides, the kinetic parameters for this system, i.e. 2:1 selectivity ratio and activation energies are similar to those reported for other acidic catalysts where the existence of the C^+ intermediate has been thoroughly investigated (4,11-13).

Influence of the aluminium content of the faujasite (GeX , X and Y) on the isomerization reaction. Figure 4 shows the loss in activity as a function of the reaction time for HY, HX and HGeX sieves.

The HY zeolites, with the highest initial activities, exhibit the most pronounced deactivation with time. HX zeolite also deactivates, but less markedly. HGeX, which shows the lowest activity, does not deactivate appreciably, as observed from repeated reactions carried out on the same sample, after five runs of 3 hours each. A drop of less than 10% in the conversion was observed. A general rule emerges from Figure 4: the higher the Al content of the faujasite, the shorter on-stream time necessary to reach steady state activity.

Curve a of Figure 5 shows the relationship between the position (in cm^{-1}) of the high frequency OH band as

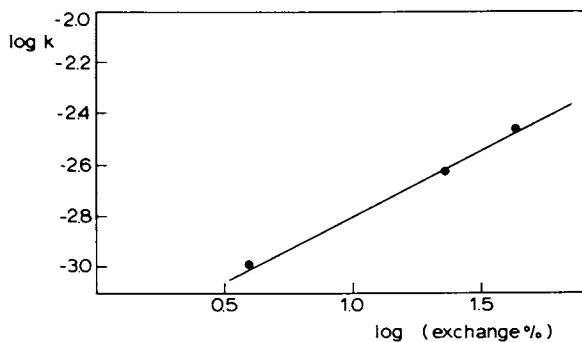


Figure 3. Logarithmic relationship between the rate constant and the exchange percentage for HGeX at 300°C ($P_{init.} = 30$ torr)

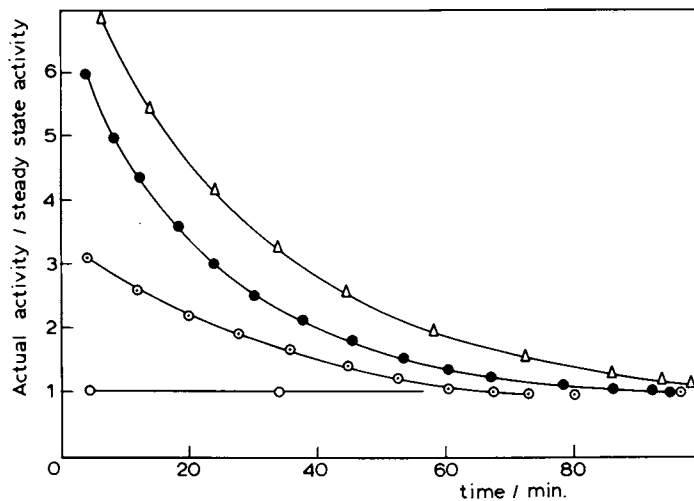


Figure 4. Deactivation observed for the different zeolites. (Δ), HY; (\bullet), HY at 160°C; (\odot), HX at 190°C; (\circ), HGeX at 200°C.

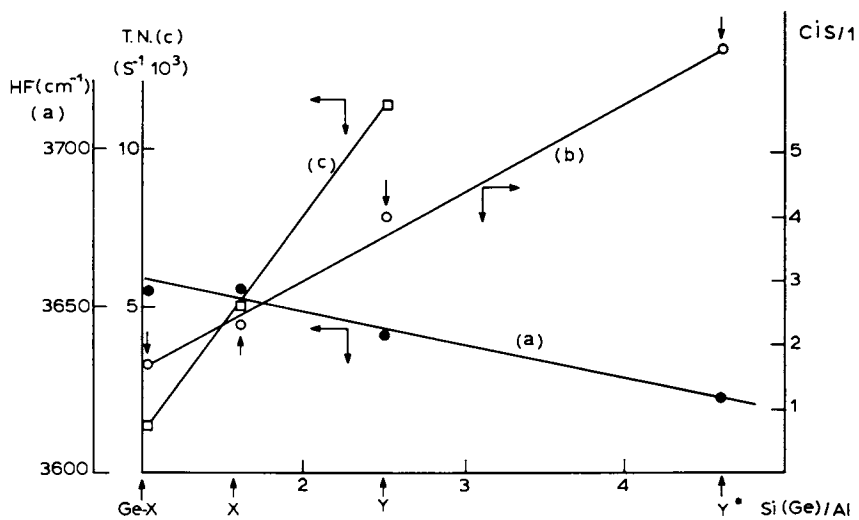


Figure 5. Plots of the IR absorption frequency of the supercage OH groups, *cis*:1 ratio and turnover number (T.N.) vs. Si(Ge):Al ratios of the zeolites

a function of the Si(Ge):Al ratio. The frequency of this band decreases as the Si(Ge):Al increases. Since this band is assigned to the OH groups located in the supercages (14,15), this relationship reflects the increase in average acidity with the Si(Ge):Al ratio. If the initial cis:1 ratio for the isomerization of the trans-but-2-ene (at 200°C) is plotted against the Si(Ge):Al ratio, an almost linear relationship is observed (curve b of Figure 5). Changes in the 2:1 product ratio reflect changes in selectivities from preferential double bond shift (low 2:1 ratios) towards preferential geometrical isomerization (high 2:1 ratios). For the catalysts under consideration, it has been found that the same isomerization mechanism occurs. As a consequence, as the overall acidity of the supercage OH groups decreases, the reaction will appear more concerted and double-bond isomerization will occur preferentially. This statement experimentally proved in this work, was first advanced by Lombardo et al. (4).

A similar correlation between 2:1 selectivity and acid strength was reported by Misono et al. (16) using supported metal sulphates catalysts, and also for liquid phase homogeneously catalyzed isomerization and olefin forming eliminations (17,18). This emphasizes the fact that such a relationship is quite general.

Finally, curve c of Figure 5 refers to the turnover number calculated for the reaction of 1-butene at 150°C. The values were calculated from the initial rates, assuming that only the OH groups of the supercages are involved in the isomerization process. Here again, the linear relationship which is obtained, indicates that, when the average acidity in the supercage increases, the catalytic efficiency of the OH also increases.

The proportionality between the efficiency of the supercage acid sites and the Al content was advanced earlier by Beaumont and Barthomeuf (5).

Conclusion

Germanium near faujasite appears to be a selective catalyst for the isomerization of the n-butene, as compared to the X and Y zeolites. No deactivation was observed with the former, whereas deactivation is more pronounced as the Si:Al ratio increases.

As for the silicic sieves, the isomerization proceeds via a common intermediate, the sec.-butyl carbonium ion, as supported by the kinetic and energetic data.

The relationship between the absorption frequency

Diffusion Effects on the Catalytic Behavior of Ca, Na-Y-Zeolite

J. VELEZ, E. A. CORNEJO, and E. A. LOMBARDO*

Facultad de Ingenieria Quimica, Universidad del Litoral, Santa Fe, Argentina

ABSTRACT

The isomerization of both *cis*-2-butene and 1-butene were studied between 130° and 200°. The data obtained are diagnostic of diffusion limitations. The Wei treatment was used to calculate the effective diffusivities. The pressure dependency was studied in both the chemical and the diffusion limited regimes. A Langmuir-Hinshelwood model applies in the first regime but not in the second.

Introduction

It is thought that the small openings of the zeolite crystals introduce diffusion limitations when these solids act as catalysts. As early as in 1966 Weisz, *et al.* (1) have demonstrated the effect of intracrystalline diffusion in zeolite catalysis. Moreover, in most hydrocarbon reactions catalyzed by molecular sieves, "residues" are formed (2-5) which further impair the movement of reacting molecules within the crystal. Butt, *et al.* (4,5) have recently investigated the effect of coking on the diffusivity of reacting molecules in mordenites.

Chutoransky and Dwyer (6) have studied the liquid phase isomerization of xylenes over a zeolite containing catalyst available in two different particle sizes. This allowed them to study the effect of intracrystalline diffusion. Using the kinetic analysis of Wei and Prater (7,8) they have shown that their system was diffusion limited when the particle size of the zeolite catalyst was 2 to 4 μ .

The goal of the study reported herein is to show the role of diffusion limitations on the kinetic

behavior of even a relatively inactive Y-Zeolite catalyst. The isomerization of the n-butenes provides an adequate model reaction for this purpose. Furthermore, the reaction mechanism for this system on similar zeolite catalysts has been thoroughly studied and reported elsewhere (3,9,10).

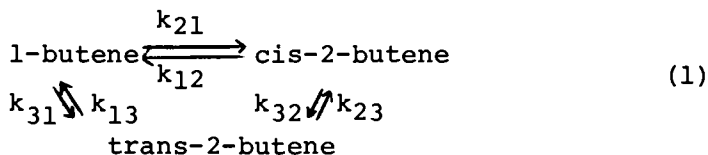
Experimental

Reactants. The n-butenes were Matheson research grade and contained less than 0.2% impurity of the other isomers.

Catalyst and Pretreatment. The starting material was a Linde Na-Y-Zeolite (lot 1280-133) whose chemical analysis is given elsewhere (11). This material was purified by successive exchange with sodium acetate followed by washing with slightly alkaline water. The chemical analysis showed that the purified zeolite contained only 0.02% Ca^{2+} . This corresponds to 0.3% of Na^+ replaced by Ca^{2+} . An aliquot of this parent catalyst was back exchanged with calcium acetate until 6% of the Na^+ was replaced by Ca^{2+} . Before each run an aliquot of this material was treated with oxygen at 1 atm and 400° followed by overnight evacuation to 10^{-5} torr at the same temperature.

Reactor. A 300 cc static reactor, described elsewhere (9), containing 100 mg of catalyst was used. The reactor temperature was electronically controlled to ± 0.5 . The same aliquot of catalyst was used throughout the experiments reported here. No modification in activity was observed when the catalyst was pretreated as described above.

Treatment of Data. The rate constants are defined as follows.



The diffusivities of the three isomers were assumed to be equal. They were calculated from the kinetic data using the treatment of Wei (8) which is summarily described below.

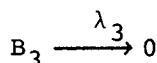
A complex system of first order reactions can be

described by the matrix equation

$$d\vec{\alpha}/dt = K\vec{\alpha} \quad (2)$$

where $\vec{\alpha}$ is the composition vector and K is the rate constants matrix. Wei and Prater (7) have shown that this highly coupled system can be converted into an equivalent uncoupled system of species B_i with rate constants $\lambda_1=0$, and λ_2 and λ_3 related to the k_{ij} constants of the real system.

B_1 does not change



Wei has further shown (8) that in a system with pore diffusion limitations equation (4) applies

$$d\vec{\alpha}/dt = K^+\vec{\alpha} \quad (4)$$

where K^+ is now made up of the diffusion-disguised rate constants. This system can also be uncoupled with the new disguised rate constants being $\lambda_1^+=0$, λ_2^+ , and λ_3^+ . If the diffusivities of the reacting species are all equal, there is a simple relationship between λ_i and λ_i^+

$$\lambda_i^+ = \eta_i \lambda_i \quad (5)$$

$$\eta_i = 3\phi_i^{-2} (\phi_i \coth \phi_i - 1) \quad (6)$$

$$\phi_i = R \sqrt{\frac{\lambda_i}{D_{ef}}} \quad (7)$$

where η_i is the effectiveness factor, ϕ_i the Thiele modulus, R the particle radius and D_{ef} the effective diffusivity.

To calculate the effective diffusivity for the n-butenes a computer program was written. The data input consisted of the diffusion-disguised rate constants and the extrapolated real rate constants. The particle equivalent spherical radius was taken to be 1 micron, based on average crystal sizes of synthetic Y-Zeolites. Given these data the computer calculated the values of λ_i and λ_i^+ and then used equations (5)

through (7) to calculate the effective diffusivity.

Results

Temperature Dependency. Two series of experiments were performed using either 1-butene or cis-2-butene as reactants at temperatures ranging from 130° to 200°. In every case 2H₂O/cage were added as co-catalyst. At all temperatures studied the reactions were first order. The rate constant ratios k_{21}/k_{31} and k_{12}/k_{32} calculated from these data were plotted against $1000/T$ in Fig. 1. These plots obey the Arrhenius law up to a certain critical temperature beyond which they show a definite curvature. The same behavior for different Ca, Na-Y-Zeolite compositions was reported elsewhere (3,11,12). Moreover the critical temperature decreased as the catalytic activity increased. Similar results were obtained when n-pentenes were isomerized on the same catalysts (13).

The individual rate constants were calculated from the activity and selectivity data and the equilibrium constants. The Arrhenius plot for each rate constant also showed a definite curvature at higher temperatures, diagnostic of pore diffusion limitations.

The kinetic data were processed as explained in the preceding section to calculate the effective diffusivities at different temperatures. The results are given in Table I.

TABLE I.- Effective Diffusivities of n-Butenes in Ca, Na-Y-Zeolite Calculated Under Reaction Conditions (1)

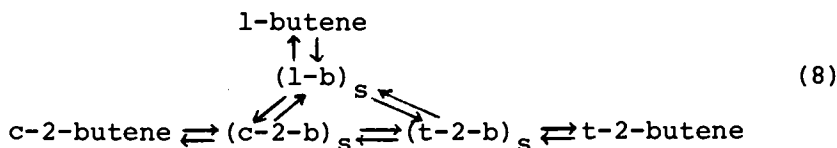
<u>Temperature</u>	D_2	D_3	\bar{D}_{ef}
	$\text{cm}^2/\text{sec} \times 10^{11}$		
180	9.1	9.7	9.4
190	3.9	6.5	5.2
200	1.6	2.8	2.2

(1) The diffusivities of the n-butenes were assumed to be equal. D_2 and D_3 were given by the computer, \bar{D}_{ef} is the average value.

Pressure Dependency. Two temperatures were chosen to study the effect of pressure, one in the chemical regime and the other in the interval when

intracrystalline diffusion effects are limiting.

i) Chemical Regime. The runs were performed at pressures of *cis*-2-butene ranging from 50 to 150 mm Hg at 150°. The rate constant values ($k_{12}+k_{32}$) are given in Table II. When plotted against $1/P$ the shape of the curve is consistent with the following mechanism.



Assuming that the rate determining step is the surface reaction and that the three isomers will compete for the adsorption sites, the following equation applies for the initial disappearance of any of the isomers and particularly for the *cis*-2-butene

$$r = (k_{12}^S + k_{32}^S) \frac{K_C P_C}{1 + \sum K_i P_i} \quad (9)$$

where k_{ij}^S are the rate constants for the surface reaction, K_i and P_i are the adsorption equilibrium constant and the partial pressure of the i isomer, respectively. If the K_i 's are assumed to be equal, then

$$r = (k_{12}^S + k_{32}^S) \frac{K P_C}{1 + K P_T}; \quad P_T = \sum P_i \quad (10)$$

therefore,
$$k_{12} + k_{32} = (k_{12}^S + k_{32}^S) \frac{K}{1 + K P_T}$$

Based on the same model it is predicted that the selectivity ratios should be pressure independent. The selectivity ratios shown in Table II are in fact fairly constant.

ii) Diffusion Limited Regime. Essentially the same experiments were repeated now at 200°. The data is no longer consistent with the Langmuir-Hinshelwood model given above. Table II shows that the catalytic activity increases with pressure, while the selectivity decreases with this variable.

TABLE II.- Pressure Effects on Activity and Selectivity of Cis-2-Butene Isomerization Over Ca, Na-Y-Zeolite

<u>Chemical Regime</u>			T=150°+0.5
<u>P (mm Hg)</u>	<u>(k₁₂+k₃₂)x10³ (min⁻¹g⁻¹)</u>		<u>k₁₂/k₃₂</u>
49	1.4		2.5
62	1.2		2.5
77	1.2		2.6
152	0.7		2.4
<u>Diffusion Limited Regime</u>			T=200°+0.5
<u>P (mm Hg)</u>	<u>(k₁₂+k₃₂)x10² (min⁻¹g⁻¹)</u>		<u>k₁₂/k₃₂</u>
60	1.3		2.2
81	2.0		1.7
160	2.3		1.3

To check these results a similar set of experiments was performed with the parent catalyst. Due to its lower activity higher temperatures were required. Otherwise its behavior was the same as reported here for the Ca, Na-Y-Zeolite.

Discussion

The plots of Fig. 1 are diagnostic of diffusion limitations. The calculated effective diffusivities are low if compared to the scarce data available for the diffusion of gases in zeolites. No data have been found for n-butenes diffusing into Y-Zeolites. Therefore in Table III data are shown for comparison of n-butenes, propylene and ethylene diffusing into smaller pore zeolites. It is expected that n-butenes diffusing in Y-Zeolites with larger pore openings will have a diffusivity two or three orders of magnitude larger. However, the calculated value of D_{ef} included for comparison in Table III shows that this is not the case.

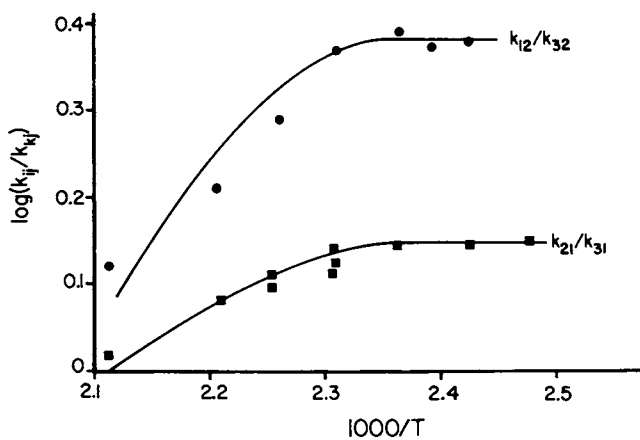


Figure 1. Temperature dependency of selectivity ratios

TABLE III.- Diffusivities of C₂-C₄ Mono-Olefins in Zeolites (1)

Adsorbant	Adsorbent	E kcal/mol	D.10 ¹¹ 200°	References
C ₂ H ₄	5A	2.75	10.7	} Ruthven, <u>et al.</u> (14)
C ₃ H ₆	5A	3.46	6.3	
1-C ₄ H ₈	5A	3.44	4.6	
t-2-C ₄ H ₈	5A	3.46	6.5	
c-2-C ₄ H ₈	5A	9.2	8.5	
n-butenes	Na-Y-Z		D _{ef} =2.2	Table I McGrath, B.Sc. Thesis cited in (14)

(1) Limiting diffusivities calculated from data given in the literature.

A possible explanation for this discrepancy might be the formation of residues which further reduce the diffusion ability of the n-butenes. It is well documented that residues form during most hydrocarbon reactions. Particularly, Lombardo and Hall (3) have shown that small amounts of residues form even in a less active catalyst (5.2×10^{-2} mmole/g of Na-Y-Zeolite). Another fact that is consistent with this picture is the decrease in D_{ef} as temperature increases as shown in Table II. Butt, et al. (4,5) have recently reported the effect on D_{ef} of coke deposition in mordenites. His levels of residues, however, were much higher than ours. Another possible interference with the movement of the n-butene molecules is the presence of water added as co-catalyst since water is known to modify the diffusivities of several gases.

Tempère, et al. (14) have reported similar results when studying 1-butene isomerization using a series of different zeolite catalysts in a flow system. They reported a wide range of selectivity values in going from large pore zeolites (X or Y) to the A type having smaller windows. They interpreted the ten-fold increase in cis/trans ratio in terms of the much smaller diffusivity of the cis-2-butene in the A-Zeolite (15). Tempère, et al. (14) also show in Fig. 3 of their paper Arrhenius plots for Na-X and Y-Zeolites which became curved at higher temperatures, as reported here.

It is expected that the pressure dependency of the reaction can be accounted for by the Langmuir-Hinshelwood mechanism shown above since the same model applies for the isomerization of n-butenes on other acidic catalysts (16,17). Although a different behavior is expected when diffusion limitations exist, the activity and selectivity behavior seem to be contradictory. The increase in activity with pressure can be interpreted in terms of the results reported by Ruthven, *et al.* (18). They have found that the diffusivity increased with increasing pressure for different hydrocarbons in smaller pore zeolites. Based on these results Ruthven (19) has shown that the effectiveness factors should increase with increasing pressure. What is at variance with this interpretation, however, is the variation in selectivity with pressure. If the diffusivity goes up with pressure, so should too the selectivity ratio, but this is not the case as shown in Table II.

In summary, it has been shown that diffusion effects are present even in a system involving a relatively inactive zeolite and small hydrocarbon molecules. The reason for this might be the formation of residues. Perhaps the presence of water could also play a role. Note that the most common test to detect pore diffusion limitations, namely the use of different particle sizes, might not be readily available for some zeolites. Therefore, other alternative diagnostic tests can be used when trying to detect diffusion effects on zeolites.

Literature Cited

1. Miale, J. N., Chen, N. Y. and Weisz, P. B., *J. Catal.* (1966), 6, 278.
2. Venuto, P. B., *Advan. Chem. Ser.* (1971), 102, 260.
3. Lombardo, E. A., Hall, W. K., *Proc. Int. Congr. Catalysis*, 5th (1973), 2, 1365.
4. Butt, J. B., Delgado-Diáz, S., Munro, W. E., *J. Catal.* (1975), 37, 158.
5. Butt, J. B., *J. Catal.* (1976), 41, 190.
6. Chutoransky, P., Jr., Dwyer, F. G., *Advan. Chem. Ser.* (1973), 121, 540.
7. Wei, J., Prater, C. D., *Advances in Catalysis* (1962), 13, 203.
8. Wei, J., *J. Catal.* (1962), 1, 526.
9. Lombardo, E. A., Hall, W. K., *AIChE J.* (1971), 17, 1229.

10. Lombardo, E. A., Velez, J. *Advan. Chem. Ser.* (1973), 121, 553.
11. Lombardo, E. A., Sill, G. A., Hall, W. K., J. *Catal* (1971), 22, 54.
12. Velez, J., Lombardo, E. A., Unpublished results.
13. Lombardo, E. A., Velez, J., Cornejo, E., *Acta Cientifica Venezolana* (1973), 24, 160.
14. Tempère, J. F., Kermarec, J., Imelik, B., *Bull. Soc. Chim. de France* (1970), 11, 3808.
15. Tempère, J. F., Imelik, B., *Bull. Soc. Chim. de France* (1970), 12, 4227.
16. Forni, L., Zanderighi, L., Carra, S., *J. Catal.* (1968), 12, 298.
17. Ballivet, D., Barthomeuf, D., Trambouze, I., *J. Catal.* (1974), 34, 423.
18. Ruthven, D. M., Loughlin, K. F., Derrah, R. I., *Advan. Chem. Ser.* (1973), 121, 330.
19. Ruthven, D. M., *J. Catal.* (1972), 25, 259.

Polymerization of Ethylene over Cr-Y Zeolite

TATSUAKI YASHIMA, JUN-ICHI NAGATA, and YUJI SHIMAZAKI

Department of Chemistry, Faculty of Science, Tokyo Institute of Technology,
Ookayama, Meguro-ku, Tokyo 152, Japan

NOBUYOSHI HARA

Department of Engineering Chemistry, Faculty of Engineering, Tokyo University
of Agriculture and Technology, Naka-machi, Koganei-shi, Tokyo 184, Japan

ABSTRACT

The polymerization of ethylene over a Cr-Y catalyst without solvent was studied at relatively low reaction temperature. It was found that the polyethylene thus produced showed a high melting point and linear chain molecules without branches. It was then concluded that the active sites on Cr-Y were composed of divalent chromium ions.

Introduction

It has been found that transition-metal cations are stably supported on zeolites by the ion-exchange procedure and promote some reactions just like complex catalysts or metal oxide catalysts. Transition-metal cation exchanged zeolite catalysts have recently been used for the oxidation of hydrocarbons at a relatively low reaction temperature(1-3), and in the amination of chlorobenzene with ammonia(4). We have found that over Ni-Y, Rh-Y, and Ru-Y the dimerization of ethylene to n-butenes proceeds selectively at relatively low reaction temperature, 0-100°C(5). We have concluded by infrared and ESR studies that the active sites on Ni-Y and Rh-Y for the ethylene dimerization are zero valent Ni and Rh, respectively, which are highly dispersed in the zeolite framework(5). On the other hand, we have found that over the Cr-Y catalyst the polymerization of ethylene proceeds, and the polyethylene produced has a high melting point, high molecular weight, high density, and linear chain structure without branches. In this paper, the polymerization of ethylene over the Cr-Y catalyst and some properties of the polyethylene are studied, and the characteristics of the active sites on the catalyst are discussed.

Experimental Methods

Material. Ethylene, having a purity of over 99.8%, was obtained from a commercial source.

Catalyst. Cr-Y was prepared by a conventional cation exchange procedure using Linde SK-40 and 0.2N aqueous solution of CrCl_3 (pH:3.7) at 70°C. The exchanged Cr-Y was washed by pure water, dried at 100°C, pelleted without a binder, crushed and sized in 14-20 mesh. The Cr-Y catalyst used had an ion exchange of 76% determined by atomic absorption spectrophotometry, that is, the atomic ratio obtained was Na : 3Cr : Al=24 : 76 : 100. The specific surface area of this Cr-Y was 870 m^2/g , which was measured by BET method.

Apparatus and procedure. The experiments for polyethylene synthesis were carried out in a stainless steel autoclave (200ml). The catalyst (0.5g) was placed in an electrically heated quartz tube, activated at various temperatures under evacuation, and was sealed in a glass tube to make an ampoule. The ampoule was put into the autoclave and heated at the various reaction temperatures after evacuation. The reaction started when the ampoule was broken by the pressure of ethylene and it proceeded under constant ethylene pressure without a solvent. The polyethylene formed was put into water to separate it from the broken pieces of glass, and an HF aqueous solution was added to dissolve the catalyst. The polyethylene was then washed by a mixture of methanol and HCl aqueous solution, followed by washing with acetone, and was dried at room temperature. The polyethylene was then used as a sample for measurements of melting point, density, and infrared spectra.

The experiments for the observation of the effect of the calcination atmosphere and the effect of additives fed into the reaction system were carried out in a fixed bed type apparatus. The catalyst (0.8g) was placed in an electrically heated quartz reactor, and calcined at various temperatures in various atmospheres, such as oxygen, hydrogen, CO as well as in a vacuo. Then the reactor was kept at a given reaction temperature using a water bath. Ethylene was fed at 200 Torr after the catalyst had adsorbed various amounts of water, NO, CO, or oxygen in a gaseous state and ethylene was circulated through the catalyst bed. The rate of pressure drop was measured with a mercury manometer.

Infrared measurement. The sample films of polyethylene were made by pressing with hot plates. The sample wafers of the catalyst were prepared in a self-supporting form by pressing the fine powder at 200 kg/cm^2 . The wafers were electrically heated at various temperatures and various atmospheres in an infrared cell. After the evacuation, the wafers were exposed to NO at

40 Torr for 30 min followed by evacuation at room temperature. All the infrared spectra were recorded at room temperature.

ESR measurement. The Cr-Y catalysts were electrically heated at various temperatures and various atmospheres in a quartz tube. After evacuation, the samples were exposed to NO at 200 Torr for 30 min followed by evacuation at room temperature. All the ESR measurements were carried out at -196°C with an X-band spectrometer.

Reflective visible measurement. All visible measurements were made with Cr-Y in the same form as the sample of infrared measurement. After evacuation, the wafers were exposed to water, NO, ethylene, and ammonia at 40 Torr in a quartz cell. All the spectra of the wafers were recorded at room temperature.

Results and Discussion

Synthesis of polyethylene. The catalyst with the higher exchange degree of Cr ion showed the higher activity for the polymerization of ethylene. However, the maximum degree of ion exchange was 76% when our ion exchange procedure was used.

Table 1 (Run No. 1-5) shows the effect of evacuation conditions on the catalyst activation. It was found that more than 200°C was needed for the evacuation temperature, and the optimum temperature was 350°C . These results show that the water in the zeolitic cage depresses the polymerization, and on the other hand, at higher evacuation temperatures the crystallinity of Cr-Y is decreased by the destruction of zeolitic structure; the BET surface area has decreased from 870 to $820\text{ m}^2/\text{g}$ at 550°C of evacuation temperature. One hour evacuation at 350°C was sufficient to activate the Cr-Y catalyst for polymerization.

Table 1 (Run No. 2,6-11) shows the effect of reaction conditions on the polyethylene yield. It was found that the polymerization proceeded at relatively low reaction temperatures, and the optimum temperature was $50-70^{\circ}\text{C}$. Even at 0°C , the polyethylene could be formed after 5 hr of reaction time. The yield of polyethylene increased linearly with the pressure of ethylene in the range from 5 to 50 atm, and increased linearly with the reaction time up to 10 hr. However, the increase of polyethylene yield gradually reached a ceiling after more than 10 hr of reaction time. When 34.5 g/g-cat. of the yield (after 10 hr of reaction time) was reached, the catalyst surface was sufficiently covered by the polyethylene produced. The step in which ethylene diffused through the polyethylene layer to the active sites on the catalyst seems to have some part in determining the rate of polymerization. In the case of hydrogen addition at 10 atm to the reaction system, the yield of polyethylene did not change. However, the addition of benzene as a solvent decreased the yield of polyethylene. The benzene

Table 1. Effect of activation and reaction conditions on yield and melting point of polyethylene

Run No.	Activation conditions		Reaction conditions		Polyethylene yield(a) (g/g-cat.)	Melting point (°C)
	Evacuation temperature(°C)	Time (hr)	Temperature (°C)	Ethylene pressure(atm)		
1	200	3.0	50	40	4.6	138
2	350	3.0	50	40	13.8	140
3	500	3.0	50	40	7.2	140
4	350	0.5	50	40	8.7	140
5	350	1.0	50	40	13.6	140
6	350	3.0	0	40	2.5	142
7	350	3.0	110	40	4.7	134
8	350	3.0	50	10	3.0	140
9	350	3.0	50	50	16.4	140
10(b)	350	3.0	50	40	13.1	135
11(c)	350	3.0	50	40	3.8	140

(a): The values after 5 hr of reaction time. (b): The addition of hydrogen at 10 atm into the reaction system. (c): The addition of 30 ml of benzene as solvent into the reaction system.

used was purified by the addition of Na metal followed by distillation, but might possibly still contain some impurities.

Some properties of polyethylene. The melting points of all polyethylene samples are shown in Table 1. The polyethylene produced at lower reaction temperature showed the higher melting points; 142, 140, and 134°C at 0, 50, and 110°C, respectively. In the case of addition of hydrogen into the reaction system, the melting point of the polyethylene produced was 135°C. These low melting points would be related to the degree of branching of the polyethylene. The infrared spectra of the polyethylene samples are shown in Figure 1. Absorption bands were observed at 1303, 1353, and 1369 cm^{-1} , and a small shoulder band was observed at 1375 cm^{-1} in the range between 1300 and 1400 cm^{-1} . The absorption bands at 1303, 1353, and 1369 cm^{-1} were attributed to the CH_2 group in the linear chain of polyethylene and the band at 1375 cm^{-1} was attributed to the CH_3 group of the branch(6). The very small absorption band at 1375 cm^{-1} shows very little branching in the linear chain polyethylene. However, the spectra of polyethylenes produced at 110°C and produced under the presence of hydrogen showed a rather larger absorption at 1375 cm^{-1} . These results suggest that these polyethylenes had a small amount of branching in the linear chain polymer.

The density of polyethylene produced was 0.962 g/cm^3 , and it was not changed by the change of reaction conditions. This value shows that the polyethylene produced over Cr-Y catalyst has high crystallinity. The molecular weight of the polyethylene samples could not be measured, because the gelation of the polyethylene occurred in p-xylene as a solvent. We estimate that the molecular weight of all polyethylene samples is more than 2 million.

Nature of active sites. It is suggested that the properties of the polyethylene produced by this work are similar to those of the polyethylene produced by the Phillips Process using chromium oxides as a catalyst. In the study on the Phillips catalyst, many papers have reported on the active sites, especially on the valence state of chromium in the active center. Recently, Kazanskii et al.(7) have concluded that the exposed Cr^{3+} ions in low coordination state are the active centers. On the other hand, Krauss et al.(8,9) and Ermakov et al.(10) proposed that Cr^{2+} ions were contained in the active centers. We present some information on the nature of active sites of Cr-Y catalyst for the polymerization of ethylene.

After activation under evacuation at 350°C for 3 hr, the catalyst was calcined in oxygen at 350°C for 10-60 min followed by evacuation for 1 hr. The calcined catalyst showed lower activity than the uncalcined catalyst, and the longer the catalyst was oxidized, the lower the activity. On the other

hand, the catalysts which were calcined in hydrogen or CO at 350°C for 10-180 min, showed lower activity than the uncalcined catalyst. The Cr-Y activated under evacuation was the most active catalyst. These results suggest that the valence state of chromium ions which compose the active sites is neither higher than trivalent nor completely reduced metal.

Figure 2 shows that the addition of water and NO decreases the catalytic activity of Cr-Y. The poisoning effect of water was relatively small, though NO remarkably poisoned the active sites. The addition of oxygen and CO remarkably decreased the catalytic activity, but after some period the activity recovered. The length of this inactive period related to the amount of additives (Figure 3). It is shown that NO strongly interacts with the active sites.

The infrared spectra of NO adsorbed on Cr-Y activated under evacuation at 350°C for 3 hr were measured. The absorption bands were observed at 1780 and 1900 cm^{-1} . These absorption bands could not be found in the case of Cr-Y evacuated up to 200°C which had no catalytic activity for ethylene polymerization. These results show that these absorption bands can be attributed to the interaction between the active sites on the catalyst and NO. These bands gradually decreased with the evacuation temperature after adsorption, but held their absorption up to 100°C. Naccache et al. (11) attributed these bands to the nitrosyl complex formed by NO with Cr^{2+} on the zeolite.

An ESR signal was observed on the untreated Cr-Y. This signal (g -value=1.97, width=500G) can be attributed to Cr^{3+} . When the Cr-Y was activated under evacuation at 350°C for 3 hr, only a broad signal was observed. This signal would be a background of the zeolite, because the same signal was observed on Na-Y. When NO was added into the system in which Cr-Y has been activated under evacuation, a new ESR signal was observed; g_{\parallel} =1.999, g_{\perp} =1.918. This signal is caused by $(3d^5)\text{Cr}^+$ in the linear nitrosyl complex of Cr^{2+} , and was reported by Naccache et al. (11) and Shelef et al. (12). On the other hand, when Cr-Y was calcined in oxygen at 350°C, a clear ESR signal was observed, and was attributed to Cr^{5+} by the data of g -value=1.98 and width=50G. On the Cr-Y reductively treated by hydrogen, a weak and broad signal was observed, but it could not be attributed to any valence state of chromium, because this signal overlapped with the background.

Figure 4 shows the reflective visible spectra of Cr-Y treated under various conditions. The absorption bands on untreated Cr-Y were observed at 410 and 580 nm. These bands show that the state of chromium ions in the zeolite is trivalent and coordinates with six water molecules (13). When the Cr-Y was activated under evacuation at 350°C, one absorption band was observed at 750 nm, and did not shift by the addition of water, NO, or ethylene. However, the addition of ammonia in this system shifted the absorption band to 630 nm. These phenomena were

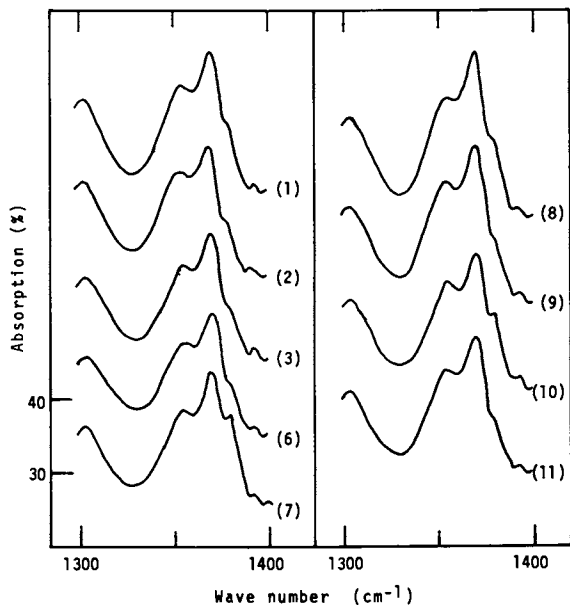


Figure 1. Infrared spectra of polyethylene. The numbers in the figure correspond to the run numbers in Table I.

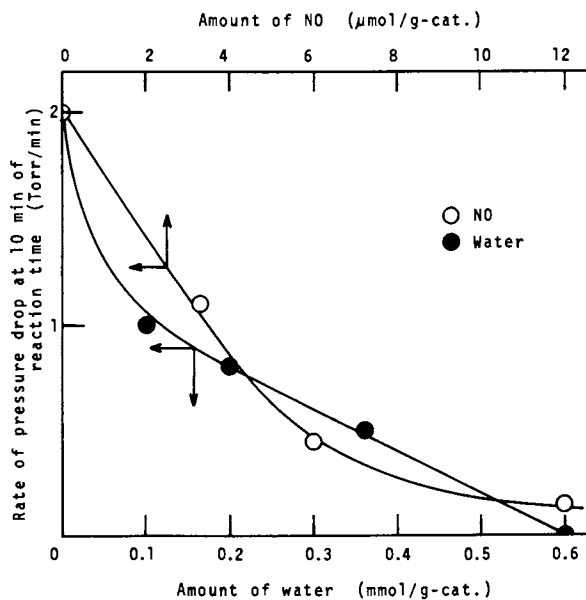


Figure 2. Effect of addition of NO and water. Reaction conditions: catalyst, Cr-Y activated under evacuation at 350°C for 3 hr; reaction temperature, 60°C; ethylene initial pressure, 200 torr.

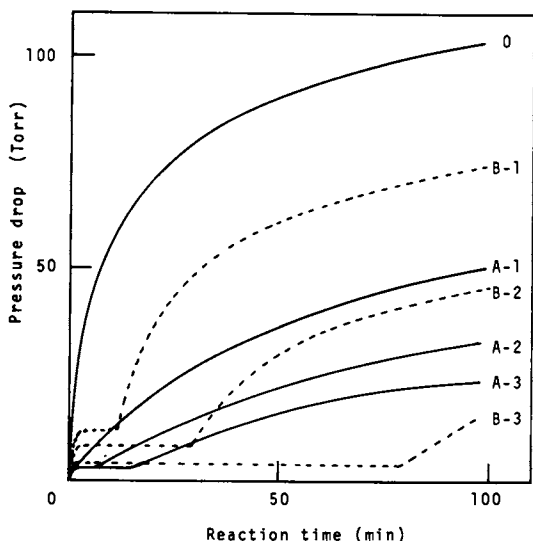


Figure 3. Effect of addition of CO and oxygen. (0), no additives. (A), CO addition; (1), $1.6 \mu\text{mol/g-cat.}$; (2), $3.3 \mu\text{mol/g-cat.}$; (3), $6.5 \mu\text{mol/g-cat.}$ (B), oxygen addition; (1), $0.5 \mu\text{mol/g-cat.}$; (2), $1.0 \mu\text{mol/g-cat.}$; (3), $1.5 \mu\text{mol/g-cat.}$ Reaction conditions: catalyst, Cr-Y activated under evacuation at 350°C for 3 hr; reaction temperature, 60°C ; ethylene initial pressure, 200 torr.

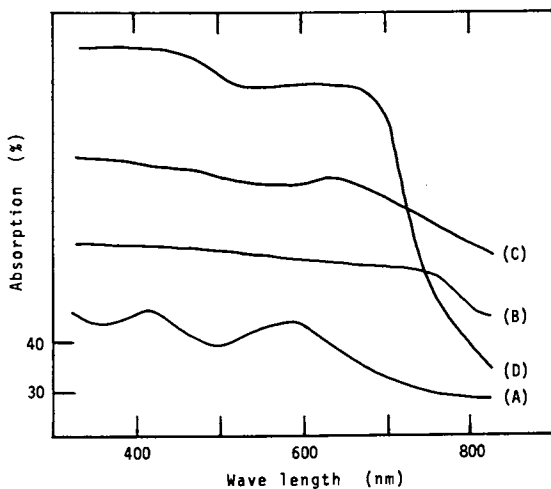


Figure 4. Visible spectra of Cr-Y catalyst. (A), uncalcined; (B), activated under evacuation at 350°C for 3 hr; (C), ammonia adsorbed on (B); (D), calcined (B) in oxygen at 350°C for 1 hr.

characteristics of divalent Cr ion(7). Thus, it is suggested that the divalent Cr ions are formed by the activation. In consequence, it is concluded that the active sites of Cr-Y catalyst are composed by divalent Cr ions which are stably supported on the zeolite.

Literature Cited

- (1) Van Sickle, D. E., and Prest, M. L., *J. Catal.*, (1970), 19, 209.
- (2) Mochida, I., Hayata, S., Kato, A., and Seiyama, T., *J. Catal.*, (1969), 15, 314; (1970), 19, 405; (1971), 23, 31.
- (3) Kubo, T., Kumada, F., Tominaga, H., and Kunugi, T., *Nippon Kagaku Kaishi*, (1972), 1972, 1621.
- (4) Hatada, K., Ono, Y., and Keii, T., *Advan. Chem. Ser.*, (1973), 121, 501.
- (5) Yashima, T., Ushida, Y., Ebisawa, M., and Hara, N., *J. Catal.*, (1975), 36, 320.
- (6) Krimm, S., Liang, C. Y., and Sutherland, G. B. B. M., *J. Chem. Phys.*, (1956), 25, 549.
- (7) Przhivalskaya, L. K., Shvets, V. A., and Kazanskii, V. B., *Kinet. Katal.*, (1970), 11, 1310; *J. Catal.*, (1975), 39, 363.
- (8) Krauss, H. L., and Stach, H., *Inorg. Nucl. Chem. Letters*, (1968), 4, 393.
- (9) Krauss, H. L., and Schmidt, H., *Z. Anorg. Allg. Chem.*, (1972), 392, 258.
- (10) Druzhkov, V. N., Zakharov, V. A., and Ermakov, Yu. I., *Kinet. Katal.*, (1973), 14, 998.
- (11) Naccache, C., and Taarit, Y. B., *Faraday Trans. I*, (1973), 69, 1475.
- (12) Shelef, M., *J. Catal.*, (1969), 15, 289.
- (13) Anderson, J. H. Jr., *J. Catal.*, (1973), 28, 76.

Molecular Sieve Adsorbent Applications State of the Art

R. A. ANDERSON

Union Carbide Corp., Molecular Sieve Department,
Tarrytown Technical Center, Tarrytown, N.Y. 10591

ABSTRACT

The use of molecular sieves as a highly versatile means of performing difficult separations has become firmly established. In addition to a review of both regenerative and non-regenerative applications, it is shown that the invention of new molecular sieves, tailored to provide an almost limitless variety of product performance characteristics, promises the continued discovery and development of new and exciting separation applications.

Introduction

The purpose of this paper is to review the impact of zeolite molecular sieve adsorption technology upon the commercial world in which we live. This unique family of materials has gained broad acceptance and brought the unit operation of adsorption to maturity. A comprehensive review of the range of adsorptive separations being performed on a commercial scale in the world today will be provided along with some quantitative market information. To begin, it is usually appropriate to describe the phenomena of adsorption, the unit operation as practiced today, and to describe zeolite molecular sieves.

Adsorption is a phenomenon whereby molecules in a fluid phase spontaneously concentrate on a solid surface without any chemical change. Adsorption takes place due to unsatisfied forces in a surface which attract and hold the molecules of the fluid surrounding the surface. The adsorption energy determines the strength with which any given molecule is adsorbed relative to other molecules in the system. The range of separations practiced covers gases from gases, liquids from liquids, and solutes from solutions.

Adsorbents have been developed for a wide variety of separations. Commercial materials are usually provided as pellets, granules or beads, although powders are occasionally used. The adsorbent may be used once and discarded, or, as is more common, it is employed on a regenerative basis and used for many, many cycles. They are generally used in cylindrical vessels through which the stream to be treated is passed. In the regenerative mode, two or more beds are usually employed with suitable valving, etc., with at least one bed being in the regeneration mode to allow for continuous processing. Regeneration can be car-

ried out by means of a thermal cycle, a pressure cycle, a displacement purge cycle, an inert purge stripping cycle or combinations of these. The selection of the appropriate regeneration cycle is an important factor in the design of any system. Adsorbents are used in applications requiring from a few ounces to over a million pounds in one plant. These applications are all based on the unique adsorptive properties of the crystalline zeolites.

Adsorption is unique in a number of respects. In some cases, the separation performed involves the accomplishment of hundreds of mass transfer units. In others, the properties of the adsorbent allow the selective removal of one component from a mixture, based on molecular size differences, that would be nearly impossible to perform by any other means. In addition, removal of contaminants from fluid streams can be performed which achieves virtually undetectable levels of the impurity in the product. The advent of zeolite molecular sieves has brought adsorption to the forefront as a major tool of the chemical processing industry. This unit operation has undergone a major development in the last 15 to 20 years and the future growth of this unique operation is unquestioned.

Molecular Sieves are a unique class of synthetic zeolites which are characterized by a highly ordered, uniform crystal structure. They are basically hydrated crystalline metal aluminosilicates and are characterized by uniformly small sized pores leading from the exterior surface to an internal three-dimensional cagework formed of interconnecting silica and alumina tetrahedra. Essentially all of the adsorption takes place internally as opposed to the amorphous sorbents which sorb on their external surface. In some cases, molecules which are small enough to pass through these pores and be adsorbed, can be separated from larger molecules, which are too big to pass through—hence, the name Molecular Sieves. Molecular Sieves have a strong affinity for polar or polarizable molecules. This property combined with the internal adsorption characteristics allows for purifications and separations to be performed that were not even considered 20 years ago. In addition, the synthetic zeolites can be altered still further by ion exchange to provide a nearly limitless variety of products and potential uses.

The commercial application of Molecular Sieve adsorbents has grown into two major areas: Purification and Bulk Separation. This paper will discuss the range of Molecular Sieve adsorbent applications along these two major lines.

Purification

The major gas and liquid purification processes utilizing Molecular Sieves can be classified by either the type of stream requiring purification or by the type of impurity removed. Because much of the technology centers upon the impurity to be removed (adsorbate) and because of the large varieties of streams processed in the petroleum, petrochemical and chemical industry, the discussion of the applications in terms of the adsorbate is logical.

A) Water. The first industrial gas purification applications for Molecular Sieves were dehydration of natural gas and dehydration of air. Because of their high adsorptive selectivity and high capacity at low water partial pressures, Molecular Sieves were an obvious processing choice for total front-end water removal for cryogenic extraction of helium from natural gas and cryogenic air

separation of oxygen, nitrogen and the rare atmospheric gases. The process design aspects of dry bed Molecular Sieve dehydration were easily adapted to existing silica gel and activated alumina systems. In fact, many systems originally designed around other adsorbents were converted to Molecular Sieves for increased drying efficiencies when Molecular Sieves were first made commercially available in the late 1950's. Today, all of the major helium recovery plants in the United States use Molecular Sieves to dehydrate a total of over 3.5 billion SCFD of natural gas. Additional units are under construction elsewhere in the world to increase that figure by 50%.

Total dehydration for cryogenic processing continues to be a major market for Molecular Sieves today. Two recent cryogenic applications which represent significant potential in the years ahead are associated with natural gas processing. First, Molecular Sieve dehydration is now used almost exclusively in the cryogenic production of liquified natural gas (LNG), for both the relatively small peak demand type storage facilities found throughout the United States, and the giant base load facilities currently under very active development around the world. The base load units provide the LNG being shipped in super tankers from the gas producing countries to the major industrial nations. Molecular Sieves dehydrate over six billion cubic feet of natural gas per day in this one area alone. A typical LNG "train" will employ about 60 tons of Molecular Sieve to dehydrate 300 MMSCFD.

Secondly, the trend toward deep ethane recovery from natural gas, utilizing the cryogenic turboexpander process, has necessitated low dew point dehydration of the feed gas. While several of the earlier plants have used methanol injection, high efficiency glycol systems or dry bed silica gel, Molecular Sieves have proven to be the most popular and effective dehydration route. It is expected that the majority of all future cryogenic ethane recovery plants will be designed with front-end Molecular Sieve dehydration. Currently over 7-1/2 billion SCFD of natural gas being fed to cryogenic liquids recovery processes are being dried with Molecular Sieves.

Another area in which Molecular Sieves have found widespread use in recent years is the dehydration of cracked gases prior to low temperature fractionation in ethylene plants for olefin production. In this application, the small pore Type 3A Molecular Sieve crystal was developed which is selective for water molecules and will not co-adsorb the larger olefin molecules. As a result, many of the problems associated with the use of non-selective activated aluminas, including hydrocarbon "hold-up" and coking (causing loss of dehydration capacity), have been effectively reduced or eliminated. While activated alumina has been used in this application for a number of years, current industry trends indicate Molecular Sieve as the preferred desiccant. At present, there are over 55 Molecular Sieve dehydration systems operating in olefin service. Molecular Sieves are also employed for drying finished product ethylene, propylene, and acetylene following salt dome or conventional storage. New grass roots ethylene plants typically employ about 150 tons of Molecular Sieve.

An interesting application which is somewhat specific, but which demonstrates the unique features of Molecular Sieves as dehydration agents, is the removal of water from natural gas streams containing high percentages of Acid Gases, (i.e., hydrogen sulfide and carbon dioxide). While other dry bed adsorbents degrade rapidly in highly acidic environments, special acid-resistant Molecular Sieves have been developed which maintain their dehydration ca-

capacities over long periods of on-stream use. Acid-resistant Molecular Sieves are also used to dehydrate various industrial gas and refinery gas streams which contain corrosive components like chlorine, sulfur dioxide, and hydrogen chloride.

A flow sheet of a typical Molecular Sieve dehydrator appears in Figure 1. After physical separation of entrained solids and liquids, the inlet gas is simply passed through a tower containing the adsorbent. When the Molecular Sieve approaches saturation, the inlet stream is switched to a second tower, while the adsorbent in the first is regenerated by flowing heated, dry gas counterflow to the direction of the stream that was being dried. After leaving the tower, the warm, moist regeneration gas is cooled and much of the water is condensed, separated and removed from the system. The regeneration gas is then either mixed with the wet inlet gas to the adsorbing tower (closed cycle operation), or returned to a lower pressure distribution line (open cycle operation). Once regenerated, the tower must be cooled by a flow of cool, dry gas before being placed back in service.

Molecular Sieves have also found wide use in dehydration of liquid phase streams. Both batch type and continuous processes have been developed for drying a variety of hydrocarbon and chemical liquids including alkylation feed, isomerization feed, natural gas condensates, absorber oil, kerosine, solvents, alcohols, aromatics and halogenated hydrocarbons. The processing is essentially the same as for gas phase operation except for the necessary draining and filling steps.

There are, of course, a number of other less general Molecular Sieve dehydration applications in industrial use today. The advantages and features of using Molecular Sieve for all low dew point dehydration applications include: low system pressure drops, no liquids carryover or make-up, simple unattended operation, and low operating costs.

Non-regenerative drying employing Molecular Sieves is also practiced. In this case, the Molecular Sieve unit is sized to last for the lifetime of the unit. A typical example in this area is in refrigerant drying and purification. The refrigerant system has two problems: water, the first, some of which will be present upon initial filling and, of course, that which will inevitably diffuse in; the second is the decomposition products of the refrigerant. The former can result in system failures due to freeze-ups in the expansion valve (or capillary). The latter will cause corrosion of the hardware. A suitably sized cartridge of the proper Molecular Sieve, installed in the circulating refrigerant stream, will adequately protect the refrigeration system for the life of the unit by adsorbing these impurities.

Another non-regenerative drying application for Molecular Sieve is its use as a desiccant and solvent adsorbent for dual-pane insulated glass windows. In this case, the proper Molecular Sieve is loaded into the spacer frame used to separate the panes. Once the window has been sealed, the Molecular Sieve will maintain extremely low hydrocarbon and water dew points within the enclosed space for the lifetime of the unit. Consequently, no condensation or fogging will occur within this space which would foul the window.

The technology has been developed and commercially proven to allow the design of gas and liquid dehydrators employing Molecular Sieves to provide product gas streams of <1 ppm(v) water and product liquid streams routinely to <10 ppm(v) of water. Applicable pressure ranges are from sub-atmospheric to

several thousand psi. Designable temperatures range from below zero to several hundred °F. The higher temperatures (> 100° - 120°F range) are of considerable importance since the amorphous adsorbents rapidly lose water adsorption capacity at elevated temperatures. Design technology includes mass transfer rate information as a function of temperature, pressure, mass flow rate, viscosity, water content, and carrier composition. Regeneration technology covers the same range of conditions.

B) Carbon Dioxide. Molecular Sieves are commonly used to purify gas streams containing carbon dioxide in cryogenic applications where freeze-out of CO₂ would cause fouling of low temperature equipment. Like dehydration, one of the earliest CO₂ removal applications for Molecular Sieves was for cryogenic air separation plants. The unique adsorption features of Molecular Sieves were exploited by using one front-end purifier unit for simultaneous removal of both water and CO₂, thus eliminating the need for complex and less efficient purification systems. Product gas purities of less than 1 ppm CO₂ and 0.1 ppm H₂O have been easily attained using a properly designed Molecular Sieve system. Today, there are over 40 such units installed and operating worldwide in air separation plants.

Peakshaving natural gas liquefaction is employed by utilities to store-up LNG during the summer for use during the winter. These plants also utilize Molecular Sieve for front-end feed purification. Here again, Molecular Sieve units are designed for both water and CO₂ removal. Carbon dioxide in its free state forms a solid at -109°F. It is only slightly soluble in liquid methane and must, therefore, be removed to satisfactory levels to prevent crystallization and plugging of the cryogenic equipment. Inlet natural gas typically contains from 0.5 to 2 volume percent CO₂ in addition to up to 7 pounds of water/mmscf (~150 ppmv). The required reduction of carbon dioxide is based on the measured solubility limits CO₂ in methane. At -260°F and 100-400 psia, the solubility limit is ≤ 350 parts per million by volume. Safe operating practice, however, usually requires CO₂ removal to below 50 parts per million by volume. Of the over 55 LNG peakshaving plants operating or under construction, over 90% utilize Molecular Sieve for feed purification.

While removal of CO₂ from natural gas feed for base load LNG plants is dominated by the conventional liquid scrubbing processes, recent development work on Molecular Sieve based large volume CO₂ removal processes is expected to find commercial acceptance in the near future. Two units of this size are already in commercial operation in front of cryogenic liquids recovery units.

The process consists of essentially the same equipment and the same operation of an ordinary dry desiccant dehydrator (Figure 2). Incoming gas flows downward through one tower filled with Molecular Sieve. Water is removed in the upper section of the adsorbent bed and carbon dioxide is removed in the lower section. Effluent natural gas typically contains from less than one to up to 50 parts per million by volume CO₂ and less than 0.1 part per million by volume H₂O. The adsorber towers are designed for relatively short cycle times of 2 hours or less with automatic switching valves for unattended operation. Depending on such factors as the particular cycle and the location of the liquefaction plant, regeneration of the second tower may be effected at essentially the same pressure as adsorption (e.g., pipeline pressure), or at some lower

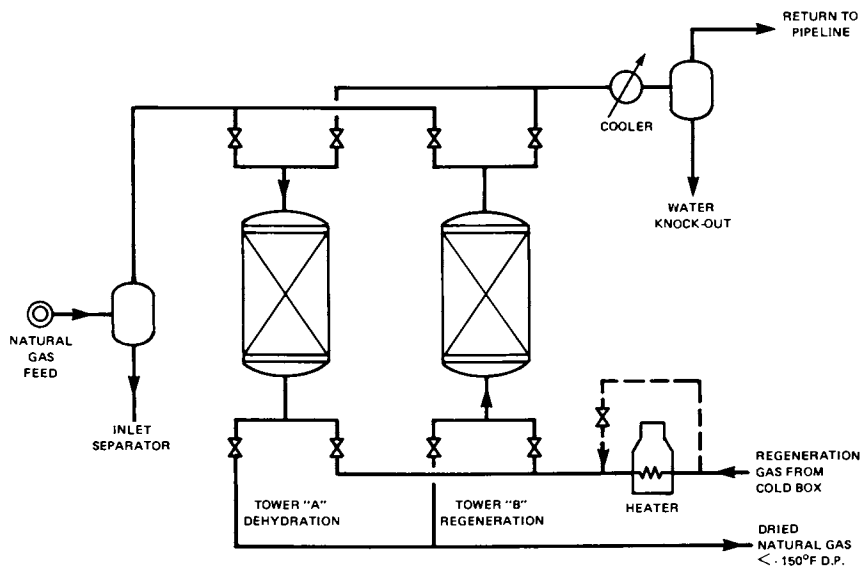


Figure 1. Molecular sieve natural gas dehydrator

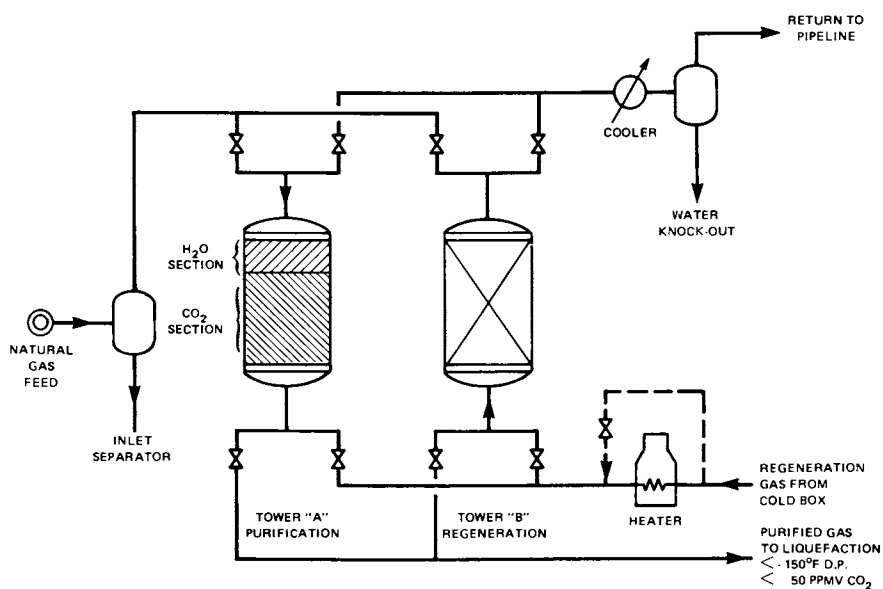


Figure 2. Molecular sieve system for combined natural gas dehydration and CO₂ removal

pressure (e.g., the distribution system pressure). Regeneration gas passes through a heater and into the regenerating tower in an upflow direction to remove (desorb) both CO_2 and H_2O . Exit gas passes through a cooler/knockout combination and then back into the pipeline. After sufficient heating and desorption, the inlet gas heater is by-passed and the bed is cooled.

Multiple vessel Molecular Sieve purification processes have also been designed for more efficient integration with certain liquefaction cycles. For example, an expansion cycle requires more dry gas than is used for liquefaction. In this case, a four-tower Molecular Sieve system is utilized - two towers for removing water from the total inlet natural gas stream, and two towers for removing carbon dioxide from the portion of gas being liquefied. Resulting equipment and utility costs are substantially reduced when compared to a larger system which removes H_2O and CO_2 from the total inlet stream (Figure 3).

Molecular Sieve treating capacities for carbon dioxide removal range from about 800-1500 pounds of Molecular Sieve per mmscf processed gas. Design parameters are strongly affected by feed gas conditions - temperature, pressure, CO_2 and water concentrations, and by the treating cycle time. Adsorber vessels are designed such that the pressure drop during treating is usually on the order of only 1-2 psi. The CO_2 rich regeneration stream is re-injected into a transmission line eliminating the problem of disposal or further treatment.

High purity polymerization grade ethylene is treated for CO_2 and trace water removal by Molecular Sieve in over 10 domestic ethylene plants. While feed CO_2 levels vary from 10 to over 3000 ppm(v), Molecular Sieve treated ethylene is produced with 1 ppm(v) or less CO_2 . Simple, clean operation has been the key to success for Molecular Sieves in this application area.

There are currently six (6) Molecular Sieve units in commercial operation removing CO_2 from mixtures of ethane and propane. CO_2 levels are reduced from approximately 0.5 to 1.0 mole percent to below a 1000 ppm(v) specification following extraction and fractionation of the $\text{C}_2\text{-C}_3$ from natural gas. The treated stream is sold as a premium cracking feed to olefins producers who enjoy improved compression train efficiencies when the feed gas has low CO_2 concentrations.

The removal of CO_2 from synthesis gases has been commercialized for quite a few years - although it has not been practiced on as large a scale as the applications previously mentioned. However, the design technology has been developed for the range of synthesis gas compositions encountered in industry today.

The design capability and proven commercial performance has been established for the removal of CO_2 from air, natural gas, ethylene, ethane-propane mix (EPM), and synthesis gases. Wide ranges of pressure and temperature have been studied as well as composition, mass flow rate, viscosity, etc. Likewise, full regeneration design capabilities have been developed.

C) Sulfur Compounds. There are several streams which are treated by Molecular Sieves to remove various sulfur compound contaminants. A prime example is wellhead natural gas sweetening for selective removal of H_2S and low molecular weight mercaptans. This application has matured within the past six years to the extent that over 3 billion scf of natural gas is now sweetened daily via Molecular Sieves and an additional 2 billion scf is scheduled for start-up in the near future.

Unlike most of the conventional liquid scrubbing processes, Molecular Sieves remove the sulfur compounds, but do not remove carbon dioxide. While this may at first seem contradictory based on the above commercial processes for CO₂ removal, Molecular Sieves have a greater affinity for certain sulfur compounds than for CO₂. As a result, Molecular Sieve based processes for selective sulfur compound removal are possible. The advantages of Molecular Sieve natural gas sweetening over liquid scrubbing processes lie in both decreased equipment sizing, because the "acid gas" load is smaller, in production economics because there is no gas "shrinkage" by leaving CO₂ in the residue gas, and in the fact that the gas is also fully dehydrated -- so there is no need for a downstream dehydration unit.

The area of applicability for Molecular Sieve natural gas sweetening is dictated not by the performance limits for efficient adsorption systems, but by the ability of natural gas producers and transmitters to balance and/or blend-off higher CO₂ content gases with lower CO₂ content gases to meet minimum/maximum BTU fuel value requirements. There are Molecular Sieve units in operation today which sweeten natural gases with as little as .1% or as much as 50% CO₂ and with hydrogen sulfide levels ranging from < 1 grain/100 scf to over 400 grains/100 scf. All units provide pipeline quality natural gas with less than 1/4 grain H₂S per 100 scf (4 ppmv). Plants processing as little as 1/2 MSCFD and up to > 1 billion SCFD are in operation.

The operation of a Molecular Sieve natural gas desulfurizer is somewhat different from the previous applications discussed. Specifically, the regeneration gas must be processed since in essence, the Molecular Sieve process has provided a concentrating device--that is, the sulfur compounds have been concentrated in the regeneration gas stream but have not been rejected. Thus, the Molecular Sieve system is usually integrated with a liquid scrubbing system to clean up the regeneration gas. A typical integration of the two systems is shown in Figure 4. In this case, a CO₂ rich gas was chosen to illustrate the benefits of desulfurizing with Molecular Sieve. The Molecular Sieve adsorption process is a conventional two-bed thermal cycle system, similar to those discussed in previous applications. Here, however, the regeneration gas is processed through an amine scrubber. As can be seen, an additional 6 mmscfd of gas meeting the pipeline specifications is available versus using a total amine system. Furthermore, the Molecular Sieve system removed only the H₂S -- thus, 6 mmscfd of CO₂ did not need to be scrubbed out via amine, thus reducing the operating costs substantially. The effluent from the amine scrubber is a suitable feed for a Claus unit for ultimate sulfur rejection.

An extension of the natural gas desulfurization technology employing Molecular Sieves has allowed the desulfurization of de-ethanizer overhead streams. More of these are being encountered as natural gas/liquid processing modes evolve.

A further extension of this gas treating technology has permitted the offering of Molecular Sieve based processes for total desulfurization of natural gas wherein the natural gas is used as feed for steam-methane reforming for ammonia synthesis. In this application, commercial experience has demonstrated that Molecular Sieves are effective in removing the trace quantities of mercaptans, carbonyl sulfide and organic sulfides which are present in most all natural gas feedstocks. Historically, activated carbons have been used in this service. However, studies have shown carbons to be inadequate for effective total removal of

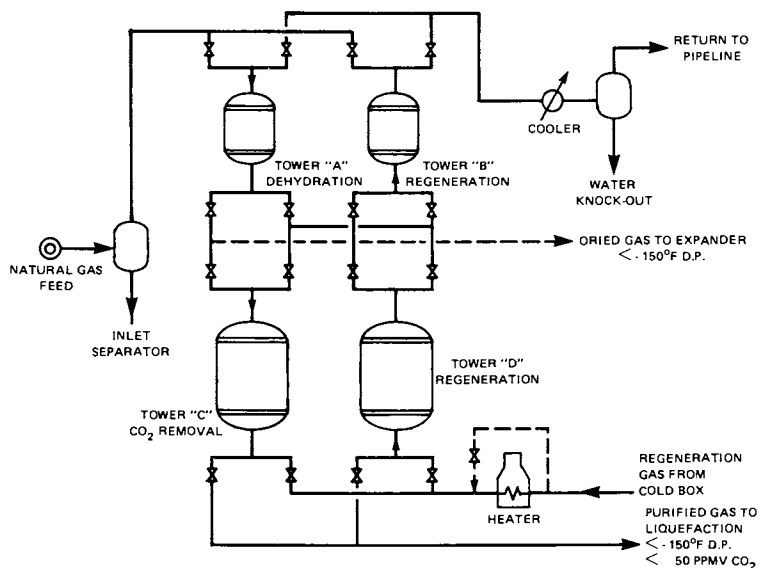


Figure 3. Four-tower molecular sieve system for natural gas dehydration and CO_2 removal adapted for expander liquefaction cycle

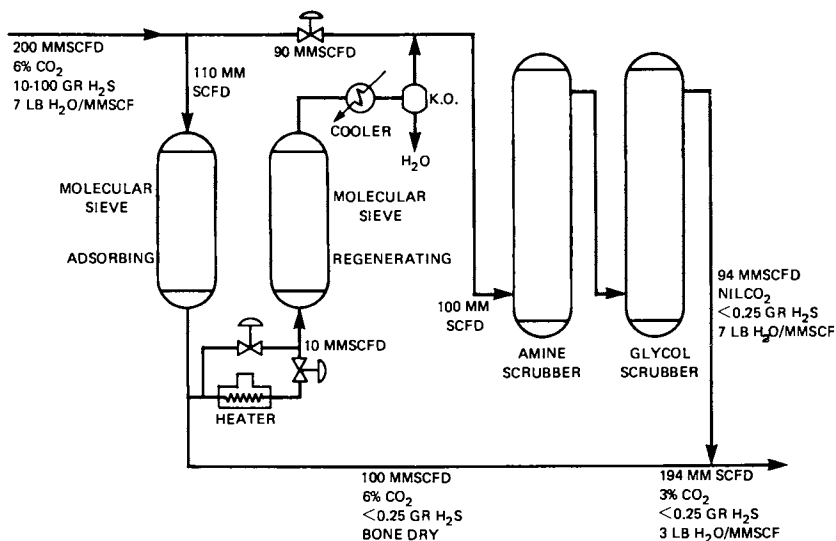


Figure 4. Typical CO_2 -rich natural gas desulfurization unit integration of molecular sieve with amine scrubbing of the regeneration gas

all sulfur contaminants. Noticeable improvement in the life of sulfur sensitive low temperature shift catalysts has been demonstrated when Molecular Sieves are employed for front-end feed purification.

In addition to natural gas desulfurization, Molecular Sieves are being used to treat refinery hydrogen streams containing ppm quantities of hydrogen sulfide. A single Molecular Sieve unit may be designed to remove trace water and H_2S in the recycle hydrogen loop of a catalytic reformer to protect the sulfur and water sensitive catalyst from poisoning. During catalyst regeneration, the same Molecular Sieve unit acts as a drier for treating the inert gas used to periodically regenerate the reforming catalyst. This application represents an interesting example of the versatility of Molecular Sieve for treating more than one stream for more than one contaminant using a single purification unit.

One of the most popular uses of Molecular Sieves in the natural gas industry is liquified petroleum gas (LPG) sweetening. There are over 200 Molecular Sieve installations processing propane, butane and mixed LPG streams to provide low sulfur content products. The problems associated with the handling and disposal of caustic solutions via conventional scrubbing processes are avoided. Additionally, Molecular Sieve treating combines both sweetening and dehydration into one unit eliminating the need for separate equipment for each processing step. The regeneration medium is typically a natural gas and this can be scrubbed with amine systems for subsequent sulfur rejection. The process cycle is similar to those already described with the addition of draining and filling steps. In LPG liquid sweetening, not only H_2S , but mercaptans, sulfides, disulfides, and carbonyl sulfide can be removed. Recently, the technology to treat light refinery streams ($< C_4$), containing considerable quantities of olefins has been developed. A broad range of adsorption data is available covering nearly all the types of typical sulfur compounds encountered in refineries. A proprietary process/product technique is available to prevent the fouling of the adsorbent bed by polymers, which is typical when processing olefin containing streams on a thermal cycle basis. Commercial plants are processing as little as a few hundred barrels per day (BPD) to over 50,000 BPD of LPG streams.

The technology and proven commercial performance has been established for the removal of a wide range of sulfur compounds from gas and liquid streams, from hydrogen through butane. Purifications to exacting specifications can be achieved even with extremely sour feed streams. The regeneration technology is available as well as information regarding the integration of the regeneration gas with liquid scrubbing systems.

D) "PURASIV" Systems. Three additional commercially proven adsorptive purification processes have been developed in the area of pollution abatement. Due to the complexity of integrating these systems with the chemical plant involved, they are sold on a proprietary package basis.

The first to be discussed is for the removal of mercury from chlor-alkali plant vent streams (H_2 and seal air). The process has been called PuraSiv Hg and provides effluent vent streams containing Hg in the 10-20 ppbv range. The system employs a closed loop regeneration scheme which results in the rejection of the Hg in liquid form. Commercial scale operation is now approaching 5 years.

The next is called PuraSiv N and is designed to remove nitrogen oxides

(NO_x) from nitric acid plant tail gas. The regeneration system is integrated with the NO_x absorber tower so that not only is a low ppm vent gas produced, but increased acid yields are realized. The process employs a proprietary product and proprietary processing technology. Current effluent design specifications are for 50-250 ppm(v) of NO_x. Commercial experience has passed the 3-year mark.

The third system is called PuraSiv S and is aimed at cleaning up the vent gases from sulfuric acid plants. As in the previous case, the sulfur oxides (SO_x) are recycled and integrated into the acid plant such that acid yield is increased. Currently, design specifications for the effluent vent gas run from 50-250 ppm(v) SO_x. Commercial operation now covers 4 years.

Bulk Separations

The separation of process streams into two or more major components, as opposed to purification, has been termed bulk separation. Usually, the components to be separated range from 20/80 mixtures to 50/50 mixtures. The development of both the processes and the products employed are extremely complex and expensive. Consequently, they have all become proprietary and are purchased as a complete package with various royalties, etc. High purities and yields are achievable due to the unique products and process techniques employed. The commercial processes will be reviewed separately.

A) Normal/Iso Paraffin Separation. The separation of normal paraffins from mixed refinery streams was one of the first major commercial applications of Molecular Sieves. By using a Molecular Sieve of the proper pore size, the n-paraffins can be adsorbed and the branched and/or cyclic hydrocarbons are rejected. During the adsorption step, the effluent contains non n-paraffins. During the desorption step, the n-paraffins are recovered. Isothermal operation is typical due to short cycle times. The upper limit is < 800° F to avoid cracking.

The regeneration is carried out by one of two methods. For a process separating light hydrocarbons (< C7), a pressure swing process can be employed. For heavier streams, a displacement desorption employing other selected n-paraffins is employed. These can then be easily separated by subsequent distillation. If high purities are required, a displacement step is employed between the adsorption and desorption steps to sweep non-normal paraffins from the voids before carrying out the desorption of the n-paraffins.

Seven commercial processes are available at the present time. They are Union Carbide's IsoSiv process, Texaco's T.S.F. process, Shell's process, B.P.'s process, Exxon's Ensorb process, VEB Leuna Werke's process, and U.O.P.'s Molex process. The first six operate in the vapor phase. One, the Molex process employed by U.O.P., is unique in two ways: First, it operates liquid phase, and secondly, the unit simulates the operation of a moving bed. In this case, the adsorption unit consists of one vessel segmented into multiple sections with separate inlet and outlet ports. Flow to the various segments is accomplished by means of a rotary valve which allows each bed segment to proceed sequentially through all of the adsorption/desorption steps.

The normal paraffins produced are employed as raw materials for the manufacture of biodegradable detergents, plasticizers, alcohols, and synthetic proteins. In the case of gasoline upgrading, the removal of the n-paraffins yields a large improvement in the octane number of the non-normal fraction.

American Chemical
Society Library
1155 16th St., N.W.

Molecular Sieves—II, 636, J.;
Washington, D.C. 20036

B) Xylene Separation. The separation of para-xylene from mixed xylenes and ethyl benzene is accomplished by means of U.O.P.'s Parex process. A proprietary adsorbent and process cycle are employed in equipment similar to that discussed previously; namely, a simulated moving bed system. High purity para-xylene can be produced. The para-xylene is used as a raw material for polyester production.

C) Olefin Separation. Two processes are available for the separation of olefin-containing streams. Union Carbide's OlefinSiv process is used mainly to separate n-butenes from iso-butenes. High purity levels are achieved. U.O.P.'s Olex process is for separating olefins from mixed feedstocks.

D) Oxygen From Air. In the last few years a demand has developed for oxygen in modest amounts, about 50 tons per day or less. A good number of these involve the use of the oxygen in biological waste water treatment plants. For this plant size, the use of pressure swing Molecular Sieve adsorption processing is competitive with the conventional cryogenic separation route. At least six (6) processes are known; developed by Union Carbide, Esso Research and Engineering, W. R. Grace, Air Liquide, Bayer-Mahler, and Nippon Steel. The differences involve the number of vessels, specific zeolites employed, and the processing steps. Oxygen of 95% purity can be obtained with the major impurity being the inert gases found in air (e. g., Argon). Over 50 such units are in operation today. The trouble-free operation of an adiabatic pressure swing system assures the continued growth of this application.

Capsule Summary

The use of Molecular Sieve adsorbents as a highly versatile means of performing difficult separations and purifications has become firmly established in the chemical process industries. The advantages of clean dry bed processing combined with high flexibility, especially in regard to turn-down ratios have proven to be valuable assets welcomed by chemical processors. The ability to tailor Molecular Sieve adsorbents to provide a wide variety of product performance characteristics, promises the continued discovery and development of new and exciting separation applications. The process development and design techniques are sound and their implementation is commonly practiced by those involved in this technology. In addition, the almost continuous development of new zeolite types ensures continued expansion and diversification of this unique separation method.

Literature Cited

1. Thomas, T. L., and Clark, E. L., Molecular Sieve Process Development and Their Impact on the Natural Gas Industry, Proc. 46th Annual Conv., Nat. Gas Process. Assn.
2. Lukchis, G. M., Adsorption Systems Parts I, II and III, Chem. Eng., June 11, 1973, July 9, 1973 and August 6, 1973.
3. Mantel, C. L., Adsorption, McGraw-Hill, New York, 1951.
4. Weyermuller, G. L., and Harlan, J. D., Molecular Sieves Keep Helium Plant on-Stream, Chem. Eng. Progr., 37, (1966).

5. Emery, W. B., II et al., "Alaskan Liquefaction Plant to Supply Gas for Japanese Use", *Oil Gas J.*, **66**: (1968).
6. Turnock, P. H., and Gustafson, K. J., *Advances in Molecular Sieve Technology for Natural Gas Sweetening*, Presented at 22nd Annual Gas Conditioning Conference, Norman, Oklahoma, April, 1972.
7. Lee, M. N. Y., and Collins, J. J., *Ammonia Plant Feed Desulfurization with Molecular Sieves*, Presented at Air and Ammonia Plant Symposium, Tripartite A. I. Ch. E. Meeting, Montreal, Canada, September 25, 1968.
8. Greenfield, B. E., and Bond, G. E., *Mix Processes for Sour Gas, Hydrocarbon Process.*, August, 1973.
9. Breck, D. W., *Zeolite Molecular Sieves*, Wiley Interscience, 1974.
10. *Molecular Sieves, First International Conference Proceedings*, The Society of Chemical Industry, London, 1968.
11. *Molecular Sieve Zeolites, Advances in Chemistry Series 101*, Vol. 1, Gould, R. F., Ed., American Chemical Society, U.S.A., 1971.
12. *Molecular Sieve Zeolites, Advances in Chemistry Series 102*, Vol. 2, Gould, R. F., Ed., American Chemical Society, U.S.A., 1971.
13. Canjar, L. N., and Camp, D. T., Eds., *Developments in Physical Adsorption*, Chemical Engineering Progress Symposium Series 96, A. I. Ch. E., New York, 1969, 65.
14. Lee, M. N. Y., and Zweibel, I., *Adsorption Technology*, Chemical Engineering Progress Symposium Series, 117, A. I. Ch. E., New York, 1971.
15. Conviser, S. A., *Removal of CO₂ from Natural Gas With Molecular Sieves, Proceedings of the Gas Conditioning Conference*, University of Oklahoma, 1964, 1F.
16. Griesmer, G. J., Avery, W. F., and Lee, M. N. Y., *Separate n-Paraffins With IsoSiv*, *Hyc. Proc. Petr. Ref.*, 44 (6), 147, 1965.
17. Cooper, D. E., Griswold, H. E., Lewis, R. M., and Stokeld, R. W., *The Texaco Selective Finishing Process*, *CEP*, 62 (4), 69, 1966.
18. Carson, D. B., and Broughton, D. B., *The Molex Process*, *Pet. Ref.*, 38 (4), 130, 1959.
19. *A New Generation in Hydrogen Cleanup Units*, *Chem. Eng.*, 74 (26), 30, 1967.
20. *Examine These Ways to Use Selective Adsorption*, *Petr. Ref.*, 36, 136, 1957.
21. Grotz, B. J., *Syngas Purifier Cuts Ammonia Costs*, *Hyc. Proc. Petr. Ref.*, 46 (4), 197, 1967.
22. Harris, T. B., *Natural Gas Treating With Molecular Sieves*, *Pipeline and Gas Journal*, June and August, 1972.

Zeolite Cracking Catalysts—an Overview

JOHN S. MAGEE

W. R. Grace & Co., Davison Chemical Division, Washington Research Center,
7379 Rt. 32, Columbia, Md. 21044

ABSTRACT

The introduction and rapid commercial utilization of zeolite cracking catalysts in the early 1960's effectively caused a re-birth of interest in the cracking process as an efficient means of obtaining high yields of valuable petroleum products. Intensive research and engineering efforts were quickly instituted to optimize the catalytic properties of the catalysts and their usage in commercial cracking units. This paper presents an overview of the results of these efforts.

Introduction

By the end of 1975, worldwide, there were over 50,000,000 barrels per day of petroleum processed in over 750 refineries. Of this quantity, approximately 7.5 million barrels per day can be catalytically cracked at full refinery capacity. In the more gasoline oriented economies of the Western Hemisphere, a significantly higher percentage of the crude oil can be cracked than indicated by the worldwide figures. In the United States, for example, 30% of the crude capacity of over 15.5 million barrels per day can be catalytically cracked at full capacity (1, 2, 3).

These processing quantities require the production of approximately 150,000 tons per year of zeolite cracking catalyst worth nearly \$100,000,000 - one of the largest produced and most valuable catalysts of all times. Valuable, because in a time of critical energy usage, these catalysts have acted as "capacity expanders", capable of expanding refinery output by giving previously unheard of increases in yield and selectivity to gasoline and light olefins with no increase in coke yield, all this with no physical expansion of the refinery units. The importance of higher yields, other than for avoiding capital expenditures for expansion, was also recently emphasized by crude oil price increases instituted in 1973 by the Organization of Petroleum Exporting

Countries (OPEC) when crude oil prices were, in less than a year, increased by 350% (4). Furthermore, since OPEC controls 69% of the world's known petroleum reserves of 716 billion barrels, it is not likely that this financial incentive will diminish without a policy change on the part of OPEC (5). In addition, high energy usage will not diminish through 1990, since at least one forecast (6) calls for an increase of from 68 to 155 million barrels per day crude oil equivalent energy demand between 1977 and 1990. Nearly 50% of this demand will be derived from petroleum. While not forecasting the exact refinery configuration at this time (petrochemical or fuel oriented), it is not difficult to imagine that significant, if not increased, zeolite catalyst usage will be seen.

The present paper attempts to give an overview, rather than a review, of the effects that zeolite cracking catalysts have had on the petroleum industry and catalyst manufacturers. The contributions that these groups in turn have made to the understanding and full realization of the potential of these catalyst systems will be described.

A very recent publication (7) has described in detail such areas as the nature of active sites in zeolites, the kinetics and mechanisms of cracking reactions over zeolites, shape selective transformations using faujasites, diffusion considerations of reactions over faujasite, and the preparation and performance of zeolite cracking catalysts. Thus, from the standpoint of the present paper, an overview of the catalysts themselves, the factors which affect their activity and selectivity, and what will be demanded of them in the future seems appropriate.

The choice of references used in this overview of zeolite cracking catalysts was dictated by the constraints that the author placed on the objectives of the paper, and in no way should be interpreted as representing all of the significant and careful work done in this area. Rather, the above chapter references may be used as a source of details for items of interest to the present readers.

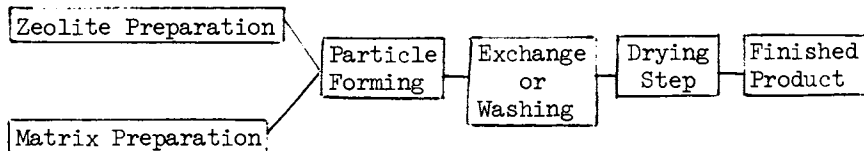
Preparation of Zeolite Cracking Catalysts

Commercially used zeolite catalysts consist of a mixture of synthetic faujasite in a matrix which is relatively catalytically inactive compared to the zeolite portion itself. Zeolite content has been increased substantially since 1964 from an average of ~8-10 wt.% to the present level of approximately 14-16 wt.%. This means that catalyst manufacturers are now producing over 22,000 tons/year of synthetic faujasite for use in zeolite cracking catalysts plus substantial additional quantities for use in hydrocracking.

A summary of the catalyst grades available from the principal catalyst suppliers is given in Table I. Since all contain synthetic faujasite, either X or Y type, the table was divided into

classifications based on the three main matrix types available — clay, synthetic or semi-synthetic.

A generalized scheme for the preparation of a zeolite cracking catalyst is given below:



Many variations of this generalized procedure have been reported and are summarized in some detail elsewhere (8). Several of the steps are of sufficient importance in subsequent discussions in the present paper to be described further here.

Zeolite Preparation

As described by Breck (9) and others (10, 11), zeolites X and Y are prepared by digesting a mixture of silica, alumina, and caustic near the boiling point of the mixture for several hours until crystallization occurs. Commercially, it has been found desirable to seed such mixtures with zeolite precursors to enhance both crystallization time and product purity (12). Both X and Y type faujasite generally are used in a mixed rare earth ion exchanged form in commercial cracking catalysts. The extent of ion exchange and the actual composition of rare earths in the exchange solution are dependent upon the rare earth source. In general, however, the starting faujasite of approximate formula $\text{Na}_{58}(\text{AlO}_2)_{58}(\text{SiO}_2)_{134}(\text{H}_2\text{O})_{250}$ (Type Y) is exchanged so that from 80 - 97+% of the Na_2O is replaced with equivalent amounts of rare earth ions (usually consisting mainly of lanthanum, neodymium, and cerium mixtures). The similarity of rare earth distribution on the faujasite after exchange compared with the ion distribution in solution indicates that no preferential exchange of one ion over the other takes place.

All of the zeolites formed for commercial catalyst usage, REX, REY and HY, are strongly acidic and ultimately protonic (13). The extraordinary amount of this acidity and the unique crystalline structure which incorporates it is the ultimate basis for the unique catalytic differences between zeolite and amorphous cracking catalysts.

With few exceptions, the matrices of the catalysts in commercial usage today (Table I) are prepared from silica/alumina or alumina gel procedures. The importance of the colloid chemistry of these materials as they relate to the relatively high surface area nature of these materials has been described in numerous references (14, 15, 16, 17). Suffice it to say that these matrices were the active portion of the catalysts of the 1950's, and that the colloidal basis of the matrix enables the combination zeolite/

Table I

Summary of Commercially Marketed Grades of
Fluid Zeolite Cracking Catalyst^{1,2,3}

<u>Matrix Type</u>	<u>Manufacturing Co.^{4,5}</u>	<u>Grade Designation</u>	<u>Type Zeolite⁶</u>
Silica/alumina gel based generally with clay diluent	Davison	XZ-25, 36, 40	REX
		DZ-5, 7, 8	REY
		AGZ-50, 200, 290 ⁺	REY
		CBZ-1, 2, 3, 4	REY
		CCZ & PCZ	REY
	Akzo Chemie	DM-1	REY
		MZ-1, 2, 3	REY
	Joseph Crosfield	Same as Davison Grades	
	Clay based	Davison	DHZ-15
CCZ-22			REY
PCZ-22			REY
Houdry/M&C		HFZ-20, 23, 28, 33	HY
		HFZ-77	REHY
		HEZ-55	-
Clay-gel based	Filtrol	F-700, 800,	REY, REMgY
		900, 950	"
		AR-10, 20, 30	REMgY
		75-F	REMgY
		HS-7, 10	REMgY

- Moving bed catalyst is manufactured by Mobil Oil Corp. under the trade name Durabead. Houdry Process and Chemical Co. manufactures moving bed catalyst HZ-1 at this time.
- The combined total of ~190,000 tons/yr. includes ~40,000 tons/yr. of amorphous (non-zeolite containing) catalyst.
- The wide variety of grades available differ from one another primarily in cracking activity and physical properties.
- C&CI produces catalysts designated SZC and SZH which are apparently REY contained in gel based matrices with the former containing clay, the latter all synthetic.
- Catoleum grades are presumed similar to previously prepared Nalco Chemical Corp. grades; i.e., REY contained in gel based matrices with and without added clay.
- For clarity, no attempt was made to differentiate between the wide variety of compositions possible between REX and REMgY. A wide variety of silica/alumina ratios, exchange levels, etc., are in use in the commercial preparation of zeolite catalysts.

matrix to be formed into the final particle shape used for refinery operation.

Evaluation of Zeolite Cracking Catalysts

Composite zeolite cracking catalysts of commercial importance are subjected to a wide variety of chemical, physical and catalytic tests before being marketed (19-22). The zeolites themselves are exhaustively tested to determine their structure, stability and catalytic properties independently of the composite catalyst, and a survey of these procedures has been given elsewhere (18).

Activity and Selectivity Testing of Catalysts

Nearly everyone involved in zeolite catalyst research or usage has his own specific test unit for evaluating catalysts. These tests range in product output of from a few milliliters per hour to several barrels per day. However, widely used at the present time for the rapid screening of catalyst cracking activity and product selectivity is the microactivity unit originally designed by Atlantic-Richfield (23, 24). This unit is extremely efficient and is in wide use by all catalyst suppliers and many refiners. Furthermore, the equipment and testing procedures are currently under study (25) by the American Society of Testing Materials for possible usage as a recommended standard for zeolite catalyst evaluation and comparisons.

Factors Affecting Activity and Selectivity

Our discussions to this point have been aimed at obtaining a general overview of how zeolite cracking catalysts are made and tested. However, the question of what makes them operate as they do, so much more active and with improved gasoline and coke selectivity compared with their amorphous predecessors, has hardly been touched. A formidable array of literature (26-30) has been addressed at illustrating the important factors which make zeolite catalysts of all types different from nonzeolite catalysts.

From an industrial catalytic standpoint, it has been important to determine what chief factors, which can be readily controlled, affect activity and selectivity. From this search, it was eventually found (31) that by far the dominating control was zeolite content of the catalyst - that which was available to the oil molecules after deactivation. However, numerous more subtle influences are present; influences that will surely become more and more important and ultimately lead to complete selectivity control in future catalysts.

Studies done throughout the catalytic world to determine the controlling activity and selectivity parameters have been done on a wide variety of catalysts - both composite catalysts and pure

zeolites. The following sections will summarize principle areas of study.

The Effects of Zeolite Concentration on the Activity and Selectivity of Composite Catalysts

A continuing survey has been made in the Davison laboratories of the cracking activity and selectivity of virtually every commercially available zeolite cracking catalyst which has appeared since 1964 and of thousands of experimental catalysts. From this survey, it was concluded (32) that the major selectivity and activity changes observed could be attributed primarily to increases in cracking catalyst zeolite content.

The major selectivity and activity characteristics observed as a function of catalyst zeolite content for experimentally prepared zeolite catalysts of varying zeolite content are summarized below.

- As zeolite content (active site concentration) was increased in a catalyst system regardless of matrix type; the first effects observed, at constant conversion, were lower coke formation, lower dry gas yields, and higher yields of gasoline and light cycle oil.
- At high zeolite contents, C₃ and C₄ olefins disappeared at a much faster rate than would be expected as a result of acid activity only. It was speculated that they may be undergoing a type of conjunct polymerization (33) to form saturates and aromatics in the light cycle oil range and coke.
- Reactor residence time began to play a more important role than acid activity in catalysts of very high zeolite content. High yields of light cycle oil could not be obtained since the long contact times required to convert the heavy gas oil to lighter hydrocarbons inevitably led to overcracking of light cycle oil and, to a lesser degree, of gasoline.

Matrix Effects on Yield and Selectivity

Evaluation of all available commercial catalysts and hundreds of exploratory laboratory samples, as in the preceding section, has shown only slight differences in pilot unit product yield distributions caused by varying matrix composition, at equivalent catalyst activity levels. The main exception to the lack of yield response with matrix compositional changes was observed with the silica-magnesia (SiO₂/MgO) matrix which acts to reduce light hydrocarbon yields, while enhancing gasoline selectivity and significantly increasing light cycle oil (430 to 640°F boiling range) yield and quality (34).

It has also been shown (35, 36) that certain matrices can have a beneficial effect on both activity and stability of the zeolite present by acting as "soda sinks" which effectively act to lower the sodium ion concentration in the zeolite. The dele-

terious effect of sodium ion on activity and stability of zeolites under cracking conditions has been shown in many studies (37, 38), but in the present case sodium in the zeolite is visualized as undergoing a solid state exchange with ordinary matrix components, thus: $RENaY+H$ or Al gel \longrightarrow $RE(H$ or $Al)Y$ + Na -gel.

Effects on Zeolite Catalyst Activity and Selectivity Caused by Variations in the Zeolite Itself

Since it has now been shown that a large proportion of the activity and selectivity differences between various zeolite cracking catalysts are caused by the amount of zeolite present in the catalyst, it becomes of prime importance to describe what the controlling chemical or physical properties are which make one zeolite totally alike or different from another, so that equal activity at equal concentration can be obtained. Many of these properties have been exhaustively studied due to their undeniable importance in commercial applications of zeolite catalysts. Chief among such properties for zeolite X and Y are:

Silica/Alumina Ratio. In their study of cumene cracking, Tsutsumi and Takahashi showed (39) that cracking activity using Y faujasite exchanged to varying extents with La^{3+} , NH_4^+ , or Ca^{2+} increased with the degree of exchange and the silica/alumina ratio of the zeolite. The increased activity at high ratio was attributed to the increased stability of the more active Bronsted acid sites to conversion to less active Lewis sites. Furthermore, it was shown in this study and elsewhere (40) that reconversion of Lewis sites to Bronsted in the presence of water vapor could be accomplished with higher ratio (more stable) materials. Many of the silica/alumina ratio effects on activity and selectivity are, however, shown to be directly related to the increased hydrothermal stability of type Y over type X so that when tested at equal concentration, equivalent product distributions are attained as shown in Figure 1 (41).

Nature and Extent of Ion Exchange. The importance of removing Na_2O and its replacement by rare earth or hydrogen ions to obtain high catalytic activity is shown in Table II (42). Shown in the table are relative activities of various ion-exchanged zeolites indicating activities of up to 10,000 times being obtained for fully rare earth exchanged faujasites with low Na_2O content compared with amorphous silica/alumina catalyst. Catalysts prepared by ion exchange with hydrogen or rare earth ions are the only types which have become commercially important (43). However, partial exchange with transition metal ions has been reported to give substantially changed yields of light gases, olefins, aromatics and coke (44, 45, 46).

Nature of the Active Sites. This topic has been the subject

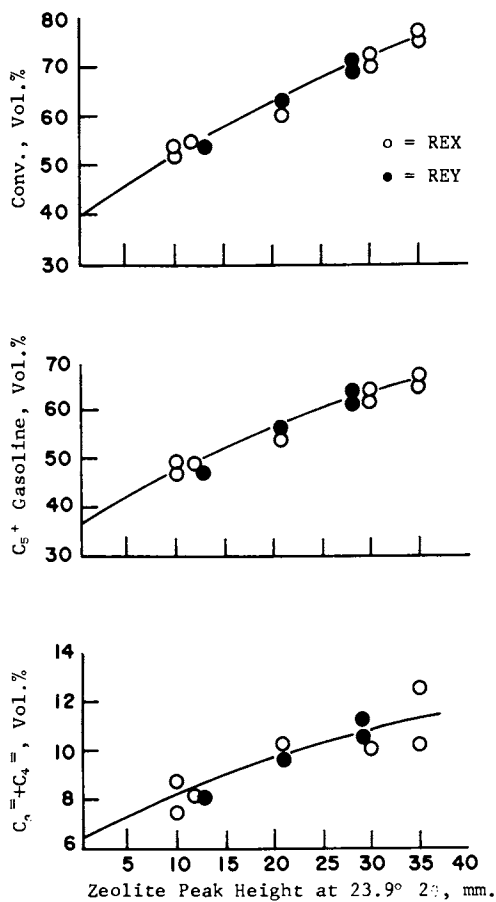


Figure 1. Effect of faujasite on product yields and selectivity at varying zeolite inputs

of considerable investigation since zeolite catalysts were introduced (47, 48, 49), and the consensus at this time appears to be that the sites themselves are strongly acidic and of a protonic (Bronsted) nature (50, 51, 52). While there are probably electrostatic effects (53) superimposed on the Bronsted acidity, the similarity in product yields and mechanism of cracking strongly suggest active sites similar in nature to those found in amorphous silica-alumina (54). Many papers (55-65) discussing the nature of these active sites have been published.

Type of Zeolite Present. The molecular sieving aspects of zeolite cracking selectivity were among the earliest aspects reported by Frilette, Weisz and Golden (66) showing the amount of cracking of n-hexane and 3-methyl pentane over sodium and calcium type A and X zeolites. Their results clearly showed that geometric access into the zeolite was required for cracking. More recently, a summary of "shape selective" catalysts has been given by Csicsery (67), but to date no industrial catalysts have become available for cracking which take advantage of this information. The use of natural zeolites in catalysis has recently been reviewed by Vaughan (68); but, again, no important zeolite cracking catalysts have appeared at this time containing such materials.

Kinetic Considerations of Zeolite Catalyst Activity and Selectivity

The chief reason for studying the kinetics of hydrocarbon conversion by zeolite cracking catalysts is to determine overall conversion rates and to generate data which will allow the quantitative prediction of reaction products under a variety of reaction conditions. All of this is done in the presence of a catalyst which is contributing to the reaction velocity but is itself being deactivated as the reaction proceeds. From an overall standpoint, kinetic studies of zeolite cracking have correlated well with the observed extraordinary activity of the zeolites, their excellent gasoline and coke selectivities and the loss of product olefins. Methods by which optimum product selectivities can be obtained have been formulated, and mathematical models to predict changes in refinery operation are in current use based on the substantial amount of kinetic data thus far obtained. A comprehensive review of this entire area has recently been published (69).

Metals and Coke Effects on Zeolite Cracking Catalyst Activity and Selectivity

The effect of metals normally present in cat cracker feed on catalyst activity and selectivity has been the subject of investigations long before the introduction of zeolite catalysts (70, 71, 72). However, a recent study by Cimbalò, Foster and Wachtel (73) updated the older studies (without substantially changing earlier conclusions) with the emphasis on zeolite catalysts. Early studies

have shown that under normal operating conditions cracking catalysts become contaminated with Ni, V and Fe which occur in the feed to the cat cracker (though most are removed in distillation prior to cracking). Characterization of the effectiveness of metals has shown Ni to be about four times as effective for promoting undesirable dehydrogenation reactions as vanadium. Iron is substantially less effective than vanadium; but when present as "tramp iron" or magnetic oxide stripped from reactor walls, it also has the most undesirable property of catalyzing the highly exothermic oxidation of CO to CO₂ in the regenerator dilute phase which can cause excessively high catalyst temperatures. Even though alternate oxidation and reduction reactions in cracking and regeneration rapidly reduce the ability of the transition metals to catalyze light gas and coke formation, "effective" metals level will persist which will be a function of catalyst makeup rate. As shown in the above study, an increase in "effective" metals of from 180 to 1130 ppm caused conversion to decrease from 79.0% to 75.6% with a corresponding loss in gasoline yield.

It has also been shown that zeolite cracking catalysts are less susceptible to transition metal poisoning as a result of the lower catalyst/oil contact times which can be used with these catalysts (74, 75) without appreciable yield penalty. It is speculated that under these conditions (2-5 seconds contact time is not uncommon), the extent of dehydrogenation of compounds to materials which are potentially condensable to coke over metals, metal oxides or sulfides on the catalyst surface is not substantial before the catalyst is removed from the reactor zone to be stripped and regenerated. Indeed, data obtained by Davison on a wide selection of equilibrium catalysts over the years of zeolite catalyst usage has shown that metals levels have increased from ~130 to ~260 ppm Ni and ~300 to ~450 ppm V from 1964-1975 (76). During this time, the average conversion as measured by the Davison microactivity test has increased from 33% to 68%. Thus, refiners are attaining far higher conversion levels with zeolite catalysts than with amorphous, even with increased metals loadings on the catalysts.

Coke

Coke is a carbonaceous product of cracking of low hydrogen content long known for its deleterious effects on amorphous and zeolite containing cracking catalysts (77). It has been stated (78) that since cracking units operate to a coke limitation of about 6%, amorphous cracking catalysts were limited to conversion levels of 46-55%, but that the superior coke selectivity of the zeolite catalysts allowed, even in the initial stages of their development, for conversion increases of at least 12%.

The quantitative potential of zeolite catalysts to improve product yields by minimizing the carbon-on-regenerated catalyst (CRC) has recently been described (79).

Data illustrated in Figures 2 and 3 and presented in Table III

Table II

Cracking Activity of Zeolites

Catalyst	Composition Wt. %					Temp. °C ⁽¹⁾	α ⁽²⁾
	SiO ₂	Al ₂ O ₃	Na	Ca	RE		
Si/Al	90.0	10.0				540	1.0
Faujasite-Ca	47.8	31.5	7.7	12.3		530	1.1
Faujasite-NH ₄	75.7	23.1	0.4	-		350	6,400
Faujasite-RE	-	-	0.39	-	28.8	<270	>10,000
CaA	42.5	37.4	7.85	13.0		560	0.6
Mordenite-Ca	(≈77)		1.01			520	1.8
Mordenite-H	80.1	13.4	0.3	1.54		300	2,500
Mordenite-NH ₄			0.1			<270	>10,000

(1) Temperature for ≈5-20% n-hexane conversion.

(2) Relative activity after 5 minute run time.

Table III

Comparison of CRC and Severity Effects

Catalyst: AGZ-50		
Deactivation: 1520°F, 20% Steam, Fluid Bed		
Pilot Unit Conditions: 40 WHSV, 920°F, WTGO Feed		
C/O Ratio:	8.0	4.0
CRC: W% of Catalyst	0.45	<0.1
<u>Conversion:</u>	72.5	71.0
Total C ₃ 's: V% FF	8.7	7.4
C ₃ = : "	6.9	5.7
Total C ₄ 's: V% FF	15.8	11.8
C ₄ = : "	6.5	4.7
C ₅ ⁺ Gasoline: V% FF	60.0	61.5
C ₅ ⁺ Gaso./Conv.	0.83	0.87
Octane No.		
RON	89.3	86.3
MON	78.3	76.8
Bromine No.:	72	62
Aniline Pt.: °F	85	93
<u>Light Cycle Oil:</u> V% FF	8.9	9.3
<u>Coke:</u> W% FF	4.6	3.6

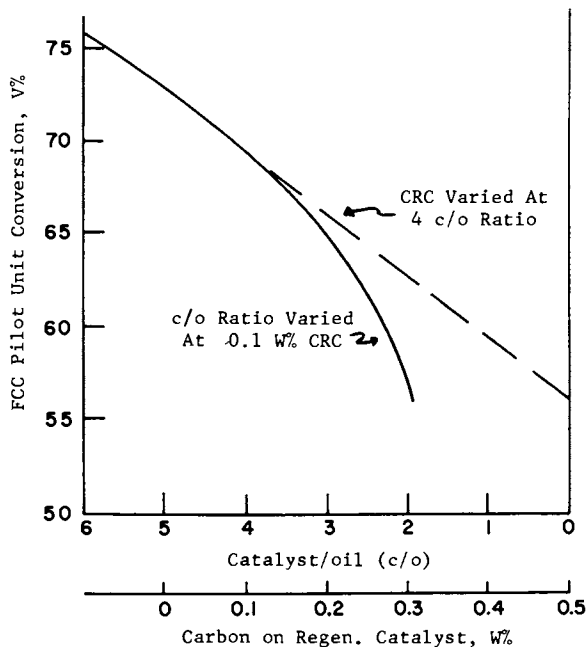


Figure 2. Effect of CRC on conversion (compared with *c/o* ratio)

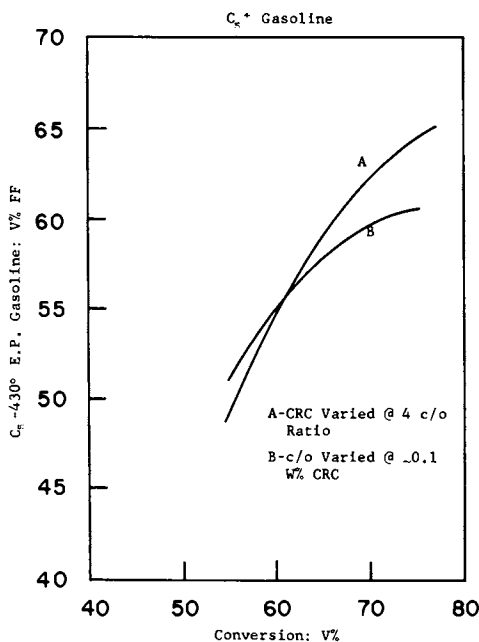


Figure 3. Comparison of yield changes effected by changes in CRC and *c/o* ratio

show the beneficial effects of operations at low CRC on activity in Figure 2, on gasoline selectivity in Figure 3, and also the problems of operating at high cat/oil ratio in lieu of low CRC. It may be seen that conversion varies nearly linearly with changes in CRC at constant cat/oil ratio, but that varying the cat/oil ratio to maintain activity at constant CRC can lead to substantial activity losses. The same effect is seen with gasoline yield in Figure 3, where at high conversion losses in gasoline selectivity are seen even at low CRC's. Table III again shows such losses with high CRC, and in addition indicates that yields from catalysts with low CRC compared to the same catalyst at high CRC appear similar to catalysts containing more zeolite. Thus, coke and gasoline selectivity are improved at low CRC and olefin content is lowered. Low olefin losses can be restored, however, with catalysts of low CRC by raising reactor temperature with no other adverse effects.

While the above valuable effects of operating zeolite catalysts at low CRC are caused more by processing changes than catalyst changes, a recent zeolite catalyst development appears to have inherent capability for producing the same desired effect. This new zeolite catalyst system was designed to promote the combustion of CO to CO₂ in the regenerator dense bed, thus minimizing high temperature in the dilute phase of the regenerator and eliminating the possibility of afterburning which can collapse catalyst pore structure. A report of the benefits of operation of these catalysts was presented at the American Petroleum Institute Meeting in Los Angeles in May, 1976 (80). As in the case of high temperature regeneration operations, the complete combustion of CO to CO₂ liberates sufficient heat to effectively lower the CRC level, thus optimizing zeolite performance as previously described.

Effect of Feedstock Type and Feed Hydrotreating on Zeolite Cracking Catalyst Activity and Selectivity

While zeolite catalysts are inherently active enough to selectively crack nearly any type gas oil, it was early recognized that feeds which were composed of mainly paraffinic molecules operated most satisfactorily (81). Subsequent studies, reported above, showed that these effects are related to the amount of coke formed on or near the zeolite.

Feedstock improvement by hydrotreating has long been known (82, 83) as a partial remedy for the problems of coke formation with consequent loss in activity and selectivity. This effect is mainly due to the fact that hydrotreating reduces sulfur and nitrogen contents of the feed, saturates the difficult to crack polynuclear aromatics to easily cracked naphthenes, reduces the Conradson carbon residue and reduces the metals present. It was shown that the beneficial effect of higher conversion, higher quality products and lower coke make, were even more advantageous for zeolite catalysts than for amorphous catalysts, and that the advan-

tages increased with increasing severity of the hydrotreatment procedure.

Even though only 10% of the feed to cat crackers in the United States is hydrotreated today, large increases can be expected as SO_x and NO_x restrictions increase and as the use of high metals, low K factor feeds (residual feeds) becomes more commonplace (84).

Refinery Operational and Equipment Changes

Soon after the commercial introduction of zeolite cracking catalysts in 1962, it was learned that operational and equipment changes could advantageously affect product yields and quality. The indications were that zeolite catalysts operated best at low catalyst/oil contact times in the reactor, when the carbon on regenerated catalyst was low and when light, paraffinic feeds were used. As seen before, these changes are those which minimize coke formation on the catalyst.

Thus, the first refinery changes made were regenerator modifications to improve coke burning (improved catalyst/air mixing, increased regenerator bed height to diameter, installation of new alloys to allow higher regenerator temperatures), reactor modifications to lower catalyst/oil contact time and back mixing, and the use of segregated feed risers which allowed separate reactors for fresh feed and recycle (85).

Virtually all of the major U.S. refiners have redesigned their units to operate within the above design or operational change procedures (86, 87). Because of increasingly stringent pollution control regulations, the refiners and equipment and catalyst manufacturers are also concerned that the operational and equipment changes also help minimize particulate emissions from the cat cracker and also lower or eliminate gaseous emissions of CO, SO_x and NO_x .

The Future for Zeolite Cracking Catalysts

The 1970's have been a decade in which a re-awakening of an appreciation for energy usage and energy supply was realized. Surveys are regularly made to indicate changes in the energy supply/demand picture, but all are in agreement that oil will supply more energy than any other single energy source up to at least the beginning of the 21st century. Since zeolite cracking catalysts have established themselves as "capacity expanders", it is logical to assume they will maintain a dominant role in petroleum conversion processes.

However, they will be asked to play a role not restricted only to their ability to effectively crack light feeds at low coke yield. Instead of such feeds, and partly because of the uncertainty in world petroleum supplies and prices from the OPEC nations, petroleum industry trends will be to use zeolite cracking

catalysts for cracking heavy residual oils or even crudes high in metals content and for operating at higher conversion levels. Higher conversion level operation will be possible even under conventional commercial cracking conditions since cat crackers can accept slightly lower coke yields while still maintaining heat balance (88). Also, as reported by Montgomery (89), a large spread (approximately 14 numbers in conversion) exists between the mean activity values and the high value reported throughout the refining industry in their cat crackers. Naturally, all crackers will not be able to operate at the high level, but distinct improvement in the average appears possible.

Projections made by the Pace Company (90) show that if high energy demands exist worldwide in 1990, a usage of over 150 million barrels/day crude oil equivalent (COE) will be required, and 49.3% of the COE requirement will be derived from petroleum (the remainder being composed of energy from solid fuel, natural gas, hydro/geothermal and nuclear sources). Assuming that the percentage of cat cracking capacity remains approximately as today's, the amount of zeolite cracking catalyst produced could increase by >50,000 tons/year. The second largest petroleum process using zeolites is hydrocracking, and healthy increases in this process are forecast (91).

It is not completely clear whether future refiners will consist of cat cracker/hydrocracker facilities or, as has been suggested, cat cracker/hydrotreaters to obtain high yields of high quality (low S and N) products in combination with reforming and alkylation processes, but the increased high usage of zeolites in cat cracking and hydrocracking appears assured.

What then of the catalysts themselves? In light of the preceding discussions, projections of future zeolite catalysts should include:

- Higher activity FCC catalysts
- High stability
- Improved selectivity
- Pollution control

Thus, until the use of other energy forms supersedes petroleum in its primary role, it appears probable that a challenging and important future awaits zeolite cracking catalysts in future petroleum refinery operations.

Summary

From an overview of the effects that zeolite cracking catalysts have had on the scientific and industrial communities, one must come away with the picture that these catalysts have demonstrated exceptional activity/selectivity advantages. They have become "capacity expanders" - materials that in industry have allowed increased production of petroleum products without the necessity of increasing the physical plant size.

A survey of the preparation and characterization of zeolite

cracking catalysts indicates a large worldwide production capability of nearly 150,000 tons/year of zeolite cracking catalyst containing about 14 wt.% (22,000 tons) of zeolite. All zeolite used is synthetic faujasite, predominately type Y but with some type X still produced.

The preparation, analysis, and evaluation of zeolite catalysts were thus described but with the principle emphasis on the important factors which affect the catalysts' cracking activity and selectivity. While many of the factors were found to be interrelated, the chief variable found to affect activity and selectivity was the amount of zeolite of a specific type present in the catalyst under cracking conditions which was stable and accessible to feed molecules.

Moderating activity/selectivity influences can and do evolve from the type of matrix used with the zeolite, from changes in zeolite composition or type, from differences in rates of deactivation and rates of hydrogen transfer, but these changes are small compared to concentration effects. The ability of zeolite catalysts to operate more effectively under more severe conditions than amorphous catalysts, in the presence of contaminant metals and sulfur and nitrogen, is indicative of their substantially greater number of acid sites. At the same time, the similarity in cracking reaction paths based on a carbonium ion mechanism indicates that the active sites are basically the same in the two catalysts.

Yields and selectivity of zeolite catalysts are, however, more substantially improved by feed hydrotreatment, short catalyst/oil contact times, and better regeneration (lower carbon on regenerated catalyst) than are amorphous catalysts.

Finally, the use of petroleum as one of the primary energy sources through the remainder of the 20th century should ensure the continued substantial and important usage of zeolite catalysts in the petroleum industry.

Literature Cited

1. International Petroleum Encyclopedia, 1974, The Petroleum Publishing Co., Tulsa, Okla. 74101, 342-64.
2. International Petroleum Encyclopedia, 1975, The Petroleum Publishing Co., Tulsa, Okla. 74101, 310-28.
3. Aalund, L. R., *Oil Gas J.* (1976), 74, (13), 55-57.
4. Ref. 2, p. 7.
5. Ref. 2, p. 6.
6. Pace Company Report, "Energy and Petrochemicals in the United States to 1990" (1976), Vol. II, pp. 107-8. The Pace Consultants & Engineers, Inc., Houston, Tex. 77052.
7. Rabo, J. A., Ed., "Zeolite Chemistry and Catalysis", ACS Monograph 171, Pub. by American Chemical Society, 1976.
8. Ref. 7, pp. 617-32.
9. Breck, D. W., US Patent 3,130,007 (1964).

10. Milton, R. M., US Patents 2,882,243 and 2,882,244 (1959).
11. Breck, D. W., Flanigan, E. M., "Synthesis and Properties of Zeolites X, Y and L", 1st Molecular Sieve Conf., (London) 1967, p. 47.
12. Maher, P. K., Albers, E. W., McDaniel, C. V., US Patent 3,671,191 (1972).
13. Venuto, P. D., Hamilton, L. A., Landis, P. S., J. Catal. (1966), 5, 484-493.
14. Plank, C. J., J. Colloid Sci. (1947), 2, 399-427.
15. Plank, C. J., Drake, L. C., J. Colloid Sci. (1947), 2, 299.
16. Iler, R. K., "The Colloid Chemistry of Silica and Silicates", Cornell U. Press, Ithaca, N. Y., (1955), 26.
17. Dobres, R. M., Rheume, L., Ciapetta, F. G., Ind. & Eng. Chem., Product R&D (1966), 5, 174.
18. Ref. 7, pp. 635-639.
19. Bondi, A., Miller, R. S., Schlaffer, W. G., Ind. Eng. Chem., Process Design & Dev. (1962), 1, 196.
20. Viland, C. K., Petrol. Processing (1950), 5, 830.
21. Ref. 7, pp. 639-640.
22. Letzsch, W. S., Ritter, R. E., Vaughan, D. E. W., Oil Gas J. (1976), 74, (4), 130-44.
23. Ciapetta, F. G., Henderson, D. S., Oil Gas J., (1967), 65, (42), 88-93.
24. Montgomery, J. A., Letzsch, W. S., Oil Gas J. (1971), 69, (47), 60-63.
25. ASTM Committee D-32 on Catalysts, 1916 Race St., Phila., Pa., 19103.
26. Venuto, P. B., Hamilton, L. A., Ind. Eng. Chem., Product R&D (1967), 6, 190.
27. Pickert, P. E., Rabo, J. A., Dempsey, E., Schomaker, V., Proc. Intern. Congr. Catal., 3rd., Amsterdam, 1964, 714.
28. Beaumont, R., Barthomeuf, D., Trambouze, Y., Molecular Sieve Zeolites - II, Adv. in Chem. Series 10, Am. Chem. Soc., Wash., D. C. (1971), 327 ff.
29. Rabo, J. A., Poutsma, M. L., Molecular Sieve Zeolites - II, Adv. in Chem. Series 10, Am. Chem. Soc., Wash., D. C. (1971), 327 ff.
30. Cimbalo, R. N., Foster, R. L., Wachtel, S. J., 37th Midyear Mtg., API Div. of Ref., 1972.
31. Magee, J. S., Blazek, J. J., Ritter, R. E., "Catalytic Cracking - New Catalyst Developments", ACS Div. of Pet. Chem., Preprints, Symposia - Group 1, New York, N. Y., B63.
32. Ref. 31, pp. B52-65.
33. Thomas, C. L., Barmby, D. S., J. Catal. (1968), 12, 341.
34. Ref. 7, p. 656.
35. Plank, C. J., Rosinski, E. J., US Patent 3,391,088 (1968).
36. Plank, C. J., Rosinski, E. J., US Patent 3,462,377 (1969).
37. Mialet, J. N., Chen, N. Y., Weisz, P. B., J. Catal. (1966), 6, 278.
38. Ref. 7, p. 636.

39. Tsutsumi, K., Takahashi, H., *J. Catal.* (1972), 24, 1-7.
40. Benesi, H. A., *J. Catal.* (1967), 8, 368-374.
41. Baker, R. W., Maher, P. K., Blazek, J. J., *Hydro. Processing* (1968), 47, 125-130.
42. Eastwood, S. C., Plank, C. J., Weisz, P. B., 8th World Petrol. Congr. Proc. (1971), 4, 246.
43. Ref. 7, pp. 621-622.
44. Scherzer, J., Albers, E. W., US Patent 3,867,307 (1975).
45. Dolbear, G. E., Magee, J. S., US Patent 3,830,725 (1974).
46. Dolbear, G. E., Magee, J. S., US Patent 3,835,032 (1974).
47. Plank, C. J., *Proc. Intern. Congr. Catal.*, 3rd. (1965), 1, 727.
48. Benesi, H. A., *J. Catal.*, (1967), 8, 368.
49. Venuto, P. B., Wu, E. L., Cattanack, J., *Soc. Chem. Ind., Conf. Mol. Sieves, London*, (1967).
50. Ward, J. W., *J. Catal.* (1969), 13, 321, 364.
51. Scherzer, J., Bass, J. L., *J. Phys. Chem.* (1975), 79, 1204.
52. Ref. 39, p. 5.
53. Pickert, P. E., Bolton, A. P., Lanewala, M. A., *Chem. Eng. Progr. Symp.* (1967), 63, 50-55.
54. Ref. 42, p. 246.
55. Moscou, L., Mone, R., *J. Catal.* (1973), 30, 417-22.
56. Ref. 39, p. 6.
57. Ref. 48, p. 373.
58. Olson, D. H., Kokotailo, G. T., Charnel, J. F., *J. Colloid Interface Sci.* (1968), 28, 305.
59. Hunter, F. D., Scherzer, J., *J. Catal.* (1971), 20, 246.
60. Bennett, J. M., Smith, J. V., *Mater. Res. Bull.* (1968), 3, 865 (1969), 4, 7, 77, 343.
61. Rabo, J. A., Angell, C. L., Schomaker, V., *Proc. Int. Congr. Catal.* 4th, Moscow, 1968.
62. Smith, J. V., Bennett, J. M., Flanigen, E. M., *Nature* (London), (1967), 215, 241.
63. Ref. 58, p. 313.
64. Ref. 59, p. 257.
65. Scherzer, J., Bass, J. L., Hunter, F. D., *J. Phys. Chem.* (1975), 79, 1194-99.
66. Frilette, V. J., Weisz, P. B., Golden, R. L., *J. Catal.* (1962) 1, 301.
67. Ref. 7, pp. 680-713.
68. Vaughan, D. E. W., "Properties of Natural Zeolites", *International Conference on Natural Zeolites, ZEOLITE '76*, Tucson, Ariz., 1976.
69. Ref. 7, pp. 475-483, 514-515.
70. Eckhouse, J. G., Keightley, W. A., *Petrol. Eng.* (1954), 26, C96.
71. Connor, J. E., Rothrock, W. J., Birkhimer, E. R., Leum, L. N., *Ind. Eng. Chem.* (1957), 49, 276.
72. Meisenheimer, R. G., *J. Catal.* (1962), 1, 356.
73. Ref. 30.

74. Grave, H. R., Connor, J. E., Masologites, G. P., *Petrol. Ref.* (1961), 40, 168.
75. Ref. 7, p. 675.
76. Stuart, H. V., private communication, Davison Catalagram data.
77. Weekman, V. W., Nace, D. M., *A.I.Ch.E. J.* (1970), 16, 398.
78. Masologites, G. P., Jacobs, H. E., *World Petrol. Congr.* Tokyo, Japan, *Oil Gas J.* (1975), 73, (21), 94-96.
79. Ritter, R. E., *Oil Gas J.* (1975), 73, (36), 41-43.
80. Ritter, R. E., Rheaume, L., Blazek, J. J., Montgomery, J. A., "Controlled CO Emission from FCC Units - Theoretical and Commercial Aspects", 41st Midyear Mtg. API, Los Angeles, Calif., 1976, API Preprint No. 52-76.
81. Bulletin; Davison Technical Service, "Comments on Questions Frequently Asked about Cracking Catalysts", Davison Chemical, Charles & Baltimore Sts., Baltimore, Md. 21203, p. 11.
82. Eberline, G. R., Wilson, R. T., Larson, L. G., *Ind. Eng. Chem.*, (1957), 49, 661.
83. Bailey, W. A., Jr., Nager, M., *World Petrol. Congr. Proc.* 7th, (1967), 4, 185-192.
84. Ritter, R. E., Blazek, J. J., Wallace, D. N., *Oil Gas J.* (1974), 72, (41), 99-111.
85. Ref. 7, p. 664.
86. Ref. 7, pp. 666-673.
87. Ref. 7, pp. 674-675.
88. Ref. 78, p. 96.
89. Montgomery, J. A., *Oil Gas J.* (1972), 70, (50), 81-86.
90. Ref. 6, pp. 107-109.
91. Doshier, J. R., *Chem. Eng.* (1970), 77, 103-106.

Systems Approach to Molecular Sieve Applications in Natural Gas Processing/Liquid Hydrocarbons Recovery

E. S. HOLMES

Union Carbide Corp., Molecular Sieve Department,
Tarrytown Technical Center, Tarrytown, N.Y. 10591

ABSTRACT

A study is presented of the technical considerations and design alternatives used in providing an integrated molecular sieve adsorption system for producing sulfur-free propane and butane, pipeline specification natural gas, and dried natural gas liquids from a hydrocarbon-rich natural gas feedstock. The liquid products are then available for use as petrochemical feedstocks, LPG fuels and liquid fuel.

Introduction

The lead sentence in a recent Oil and Gas Journal article states that "Petrochemical markets will triple worldwide by 1985", (1) representing an increase from a 1974 Petrochemical Industry volume of \$106 billion to a 1985 sales volume of \$350 billion, excluding inflation. This development, together with other recent changes in the worldwide energy supply and demand situation (2) are providing new opportunities for the application of molecular sieve adsorbents in the natural gas industry. As these changes occur, the need for more sophisticated treatment and recovery systems has emerged. The following is a study of a typical case in which an integrated molecular sieve adsorption system is used in producing sulfur-free propane and butane, pipeline specification natural gas, and dried natural gas liquids from a hydrocarbon rich natural gas feedstock. The propane, butane and natural gas liquids are then available for use as petrochemical feedstocks, LPG fuels and liquid fuel.

To insure that the optimal integrated process package is obtained, it is essential that the adsorption unit designs are considered by the producer or primary contractor in the early stages of project planning. If this is not done, decisions based on limited information may be made which do not take

advantage of the combined advantages of the integrated process package. Generally, the producer, based on his own preliminary engineering analysis will present an initial hydrocarbon recovery scheme such as that presented in Figure 1. The percentage recovery of each product is determined by the type of hydrocarbon recovery system that is used, such as lean oil absorption, cryogenic separation, or fractionation, and does not fall within the scope of this paper. In addition to the feedstock and product definitions, the producer will generally make the decision as to the number of processing trains which are to be used. At this point, the involvement of the adsorption systems engineer becomes vital.

Let us consider that the decision has been made to process the typical feedstock in two identical trains, one of which is shown schematically in Figure 1. Final product impurities which must be controlled are identified in both the product streams and the feed stream. Initially, let us briefly examine the product specifications. Note that the butane product has specifications on both the amount of hydrogen sulfide (H_2S) and the total sulfur including mercaptans (RSH) and carbonyl sulfide (COS). The propane product has similar specifications, while the natural gas and natural gas liquids streams have specifications on both water content and carbonyl sulfide content. For the dehydration units, the specifications refer to bulk feed streams prior to hydrocarbon recovery, while specifications on the propane and butane apply to the actual finished products. For the typical case, consideration is now made of the individual adsorption units that are included in the overall process scheme. These units, as identified in Figure 1, are a natural gas dryer, a natural gas condensate dryer, a propane treater, a butane treater, and possibly a natural gas desulfurizer (treater) as indicated by the dotted block in Figure 1.

Adsorbent Performance Requirements

Natural Gas Dehydrator. Dehydration of natural gas by the use of solid desiccants, particularly molecular sieves, is a well established practice. (3)(4)(5) During the past two decades, the application has evolved from a simple two-bed unit typically utilizing a few thousand pounds of molecular sieves to dehydrate 10 to 20 MMSCFD of natural gas feed to the point where it is common to have multiple bed systems wherein several hundred thousand pounds of molecular sieves are used in the dehydration of several hundred MMSCFD of natural gas. Thus, in terms of bulk size, the typical case which is now being considered is not abnormal. However, there is a non-standard requirement for the current case, that is, the necessity to minimize carbonyl sulfide in the dryer effluent streams. The significance of this requirement will be briefly examined at this point.

U.S. pipeline specifications require that pipeline natural

gas contain no more than $\frac{1}{4}$ grain of H_2S /100 cubic feet, or about four ppm(v). This H_2S level minimizes the corrosion effect on the pipelines and their auxiliary equipment. Some molecular sieves used for the desulfurization of natural gas can promote the reaction between hydrogen sulfide and carbon dioxide to form carbonyl sulfide plus water.(6) If the product gas is then stored, hydrolysis of the COS can occur, forming H_2S , resulting in natural gas which is again highly corrosive. The molecular sieve products which are normally used for H_2S removal, have a much lower affinity for carbonyl sulfide. Thus, in systems where minimal final sulfur contamination is a requirement, it is essential that the reaction of H_2S and CO_2 be minimized. By re-design of the molecular sieve products, this reaction can be minimized.(6) Furthermore, residual water on the molecular sieves can also reduce the magnitude of the reaction.(7) However, this is not generally a consideration in natural gas dehydration units.

In the current case, minimization of COS formation in the dehydrators will decrease the sulfur load (and thus unit size) in the downstream treaters since H_2S will tend to separate with the ethane (lights) fraction, while any COS present will concentrate in the propane fraction.

Natural Gas Condensate Dehydrator. In defining the molecular sieve adsorbent product to be used for the liquids dehydration, the same considerations for water adsorption and COS minimization apply as in the case of the gas drying unit. However, in the liquids dryer, which will contain significant amounts of the heavier hydrocarbons, hydrocarbon fouling of the zeolite with possible deleterious effects on dehydration, must be considered. Thus, in these units the adsorbent chosen should have high water adsorption capacity and minimize formation of COS and hydrocarbon fouling.

Propane Treater. The adsorbent used in the propane unit must obviously possess sufficient sulfur capacity to yield a product meeting the required specification. However, in achieving this end, consideration must again be given to the presence or formation of COS.

An additional factor which must be considered in designing the propane treater is the overall effect of sour gas regeneration on the unit's performance. Typically, in units of this type, the regeneration fluid has been a low sulfur content gas such as pipeline quality natural gas which contains less than four ppm(v) of H_2S , or vaporized product which contains less than one ppm(v) of H_2S . The dried residue gas which is to be used for regeneration in the present case will contain 200 ppm(v) of H_2S , a much higher level than that normally encountered. This level of H_2S may affect unit performance in three different ways: 1) Hydrogen sulfide remaining on the

adsorbent bed at the end of regeneration may be stripped off, resulting in off-specification propane product in the subsequent adsorption stroke; 2) The residual H_2S may reduce the unit capacity during the subsequent adsorption stroke, thus decreasing the adsorption cycle time; or, 3) The use of hot acid gas as the heating medium may result in crystal damage to the adsorbent. All of these factors must be evaluated in choosing an adsorbent product for this application.

Butane Treater. Considerations in defining the adsorbent for use in the butane unit are essentially the same as those for the propane unit, with two exceptions. Since H_2S and CO_2 in the butane feed stream are at very low initial levels, there is little possibility of carbonyl sulfide formation over the adsorbent bed. Secondly, the possible presence of heavier mercaptans in the butane stream may require the use of a different adsorbent than that used in the propane treater.

Regeneration Gas Treater. As indicated previously the use of sour gas for regeneration of the propane and butane treaters presents a potential problem. If, upon further analysis, this is indeed a real problem, then one solution is the installation of a natural gas desulfurization unit which will produce the required quantity of low sulfur gas for regeneration of the propane treater and the butane treater. If it is decided that this unit is essential, the adsorbent used would be a standard desulfurization grade product type which has been used for several years in this service.

Adsorbent Selection/Design Considerations

Having defined the required performance characteristics for the various adsorbents to be used, the following sections provide an overview of the key data obtained in selecting the specific products used, together with a summary of the molecular sieve inventories and operating conditions for each unit. Due to the broad scope of the overall project and the length constraints for this paper, only the most pertinent features of each unit are discussed. It should be noted that the design concepts applied for all of the units are similar to those presented in Collins' "The LUB/Equilibrium Section Concept for Fixed Bed Adsorption" (8) and Lukchis' "Adsorption Systems", (9) which have become standard industry practice.

Natural Gas Dehydrator. As indicated, a controlling requirement of the product used in the natural gas dehydrator is a minimum carbonyl sulfide formation tendency. Using the work of Turnock together with additional unpublished data as a basis, a series of screening runs were carried out on products known to have a high probability of possessing the required

characteristics. Test conditions are presented in Figure 2, together with a brief comparison of the results obtained at the standard conditions. As a result of these tests, Product 2 was chosen for further studies. In these studies, Product 2 was preloaded to known levels of residual water and again subjected to testing at the standard conditions shown in Figure 2. From these data, a plot of COS formation activity as a function of residual water level for Product 2 was established (Figure 3 shows the typical shape). Applying the data obtained to the typical design case conditions, it was established that Product 2 maintained at a controlled residual water level, when used as the adsorbent in the natural gas dehydrator, would yield an effluent product meeting the required COS formation level.

Having defined the product needed, together with the operating control required, a standard dynamic drying run similar to that described by Collins was carried out to confirm that Product 2 could provide the required drying performance. Following this experiment, the results of which were positive, sizing of the natural gas dehydrator was completed, utilizing a three-bed unit as shown in Figure 4. The regeneration cycle uses dried residue gas as the process fluid. Each adsorber vessel contains over 30 tons of molecular sieves. The complete design involves consideration of other factors such as heat balances, hydraulics, bed L/D ratios, and physical characteristics of the product.

Natural Gas Liquids Dehydrator. As previously discussed, the adsorbent used in the liquids dehydration unit must possess COS formation characteristics similar to that of the adsorbent used in the natural gas dehydrator. However, the product chosen must be able to provide the required dehydration performance in the presence of liquid hydrocarbons which have a potential of fouling the zeolite, with the possibility of reduced water adsorption capacity and reduced water mass transfer efficiency. Using a zeolite of the same type as the natural gas dehydration Product 2 but modified for liquid service, a standard dynamic liquid drying test to define dehydration performance, as well as the COS formation, was carried out, again yielding positive results. Data obtained in this test was then used directly in sizing the natural gas liquids dehydrator for the typical case.

The natural gas liquids dehydrator is a two-bed system using over 20 tons/bed of molecular sieves. A schematic diagram of this unit is also included in Figure 4.

After dehydration, the natural gas and natural gas liquids are re-combined and sent to the hydrocarbon recovery section. The liquid products recovered include a propane fraction, a butane fraction, and a C₅+ heavy fraction. The propane and butane streams must be desulfurized prior to their sale as

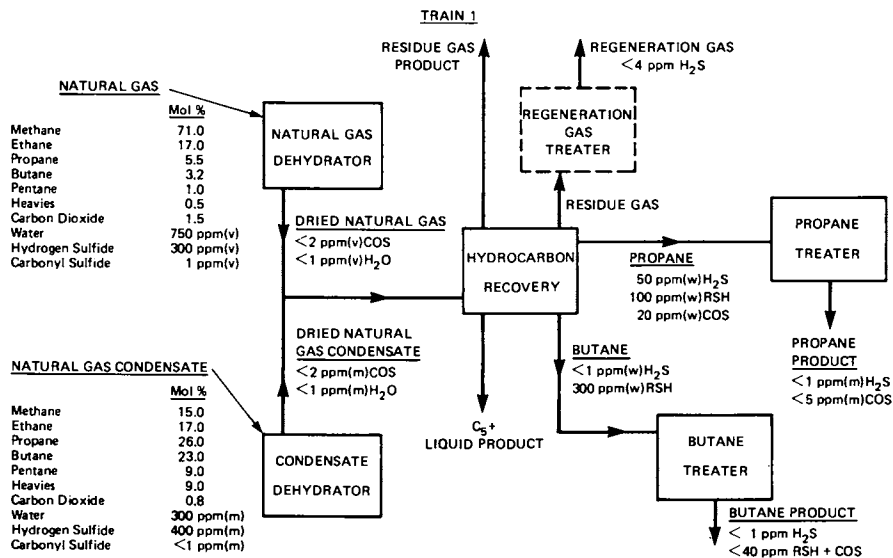


Figure 1. Natural gas liquids recovery system

TEST CONDITIONS

Temperature	75°F
Pressure	550 psia
Flow Rate	120 SCFH N ₂
H ₂ S Inlet Concentration	410-440 ppm(v)
CO ₂ Inlet Concentration	1.5 volume %
Cross Section	0.006 ft ²

Adsorbent Product No.	App. ΔX H ₂ S Wt. %	Max. COS ppm(v)	Avg. Conv. %
1	0.73	20	4.9
2	1.07	<1	<.25
3	0.96	280	51.5
4	1.39	<1	<.25
5	3.33	<1	<.25

Figure 2. COS formation over miscellaneous adsorbents

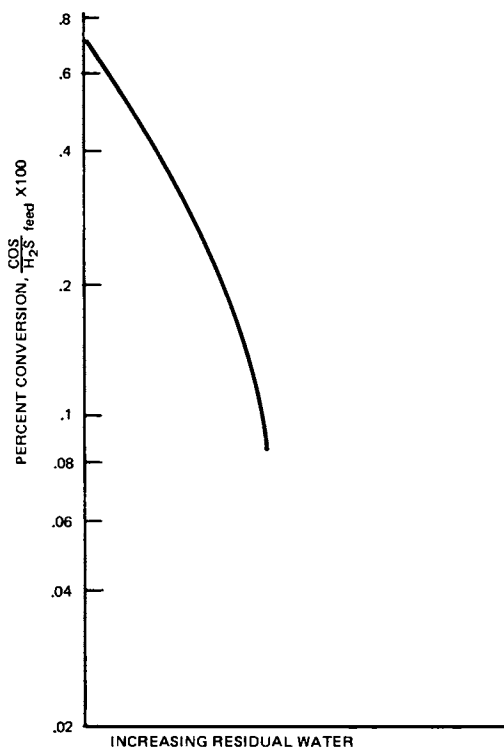


Figure 3. COS formation as a function of residual water product number 2

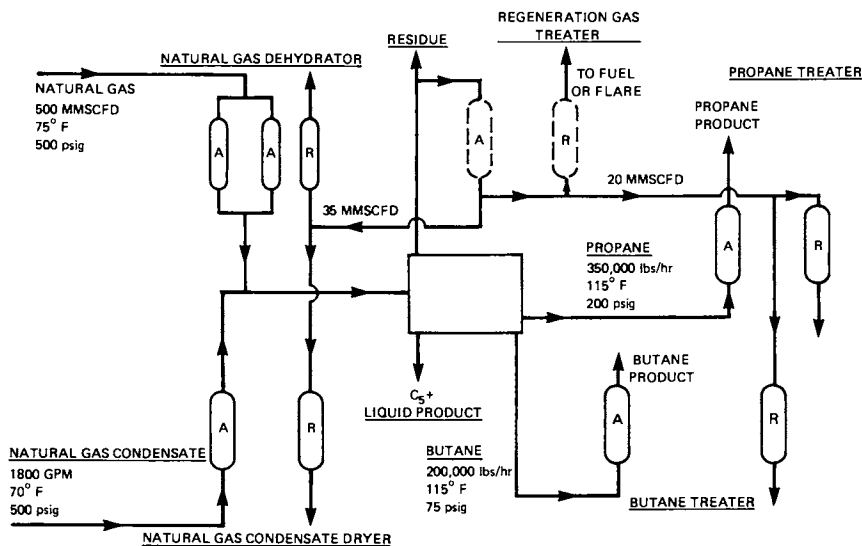


Figure 4. Natural gas liquids recovery system/adsorption units

petrochemical feedstock and fuel. The pentane and heavier fraction may be sent as is to a gasoline refining operation. For the present case, the propane and butane treaters will now be defined.

Propane Treater. In the propane treater, essentially total removal of the H_2S must be achieved with partial removal of the RSH and COS that is present in the feed together with any COS that may be formed during the propane treating operation. A molecular sieve product possessing these required adsorption characteristics has recently been discussed in a technical paper by M. B. Mick. (10) Thus, the testwork required to confirm that this product is satisfactory for use in the typical case was an evaluation of its ability to withstand repeated regenerations with a moderately sour gas regeneration fluid. A cyclic test scaled from the projected commercial unit sizing was set up to simulate the repeated adsorption and regeneration steps. At periodic intervals, the adsorbent in the cyclic unit was subjected to dynamic regeneration and adsorption "Product Specification" runs. Data from one of these tests carried out after 150 cycles of operation is presented in Figure 5. This 150-cycle time period represents about one year of cyclic operation. As shown in the upper curve in Figure 5, during regeneration a typical breakthrough curve for H_2S was obtained, nearly approaching the feed H_2S level. The CO_s level in the effluent regeneration gas started at a moderately high level and then quickly dropped off to less than 25 ppm by volume. The decrease in the amount of H_2S and CO_2 reacting to form COS is apparently due to the near depletion of CO_2 and H_2S in the adsorbed phase.

Following the heating step, the bed was cooled and subsequently propane was fed to the unit at conditions indicated in Figure 5. As shown, no H_2S appeared in the effluent stream, while an initial level of one to two ppm(v) COS was detected, which quickly diminished. This small level of COS may be the result of some combination of H_2S , CO_2 , and possibly COS left on the adsorbent bed at the end of regeneration. A short purge with purified product propane at the end of heating can be effectively used to remove this trace contamination.

Using the existing design basis for the product to be used in the propane sweetener and with experimental capacity tests which confirmed that the product did not degrade significantly when regenerated with sour gas, the propane treating unit for the typical case under consideration was designed. This unit utilizes a two-bed system, with each bed containing over 60 tons of molecular sieves, treating the design feed rate. Regeneration is accomplished in a series of steps including a drain step, a heating step using the sour natural gas followed by a short purge of sweet vaporized product propane which, as mentioned above, is included to insure that essentially all of the sulfur

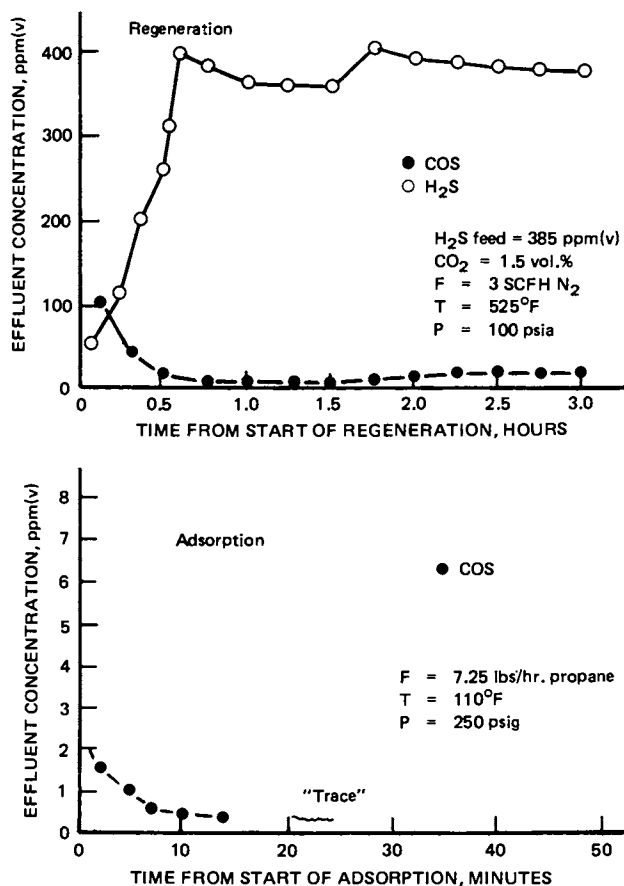


Figure 5. Propane treating molecular sieve sour gas regeneration product quality test after 150 cycles

compounds are removed from the effluent end of the bed during heating. The unit is then cooled and filled with product propane. This unit is shown schematically in Figure 4.

Butane Treater. The practice of treating (or desulfurizing) butane as well as propane and mixed LPG's by the use of molecular sieve adsorbents is a well known industrial practice. The product used in the typical case has been used successfully for several years. Again, as in the case of the propane treater, a key question for this molecular sieve adsorbent was its ability to withstand the effect of sour gas regeneration. Thus, cyclic studies similar to those performed for the propane system were carried out for the butane treater adsorbent. Regeneration/adsorption experiments were carried out after 300 cycles, or the equivalent of about two years of operation.

Results of the tests performed are presented in Figure 6. Note that the COS formation characteristic of this material is significantly different than that of the propane treater product, with a COS level of 50 ppm(v) or 25% of the H₂S feed concentration being present after three hours of the heating step. However, after cooling, when butane feed was introduced to the adsorber, there was no H₂S or COS detectable in the effluent stream. Again, results obtained in these cyclic studies confirmed that the molecular sieve adsorbent used in the butane treater could indeed withstand the use of sour gas regeneration.

The butane treater design presented in Figure 5 includes two beds of molecular sieves, each containing over 40 tons of product, treating the butane feed. The regeneration scheme for this unit is similar to that for the propane treater.

As described in the preceding sections, the test program carried out confirmed that the adsorbents to be used in the propane and butane treaters held up well during cycling with sour gas heating.

Regeneration Gas Treater. In some systems where an extra margin of safety is desired, a molecular sieve natural gas desulfurization unit treating only as much gas as required for regeneration of the propane and butane treaters could provide this margin of safety. Such a unit, based on the studies by Turnock referred to earlier, is included in Figure 4, and uses a total of 20 tons of molecular sieve product. Note that when compared to the large molecular sieve inventories contained in the main process units, this natural gas treater with its small molecular sieve inventory appears to be an extremely reasonable means of providing an increased margin of safety both in insuring that effluent product specifications will be met, and that the adsorbent bed will be subjected to relatively mild dynamic conditions during heating.

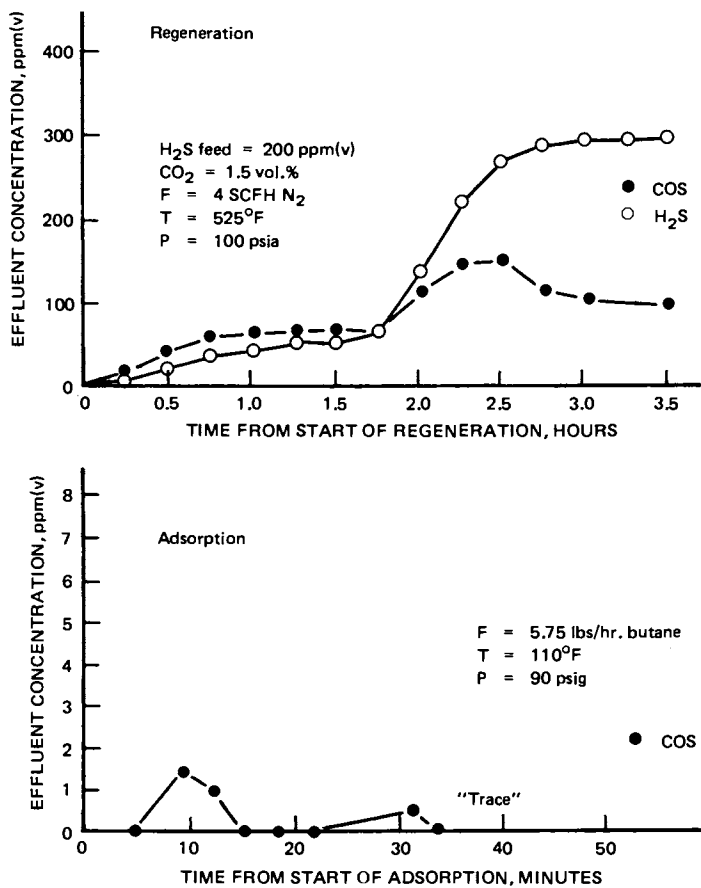


Figure 6. Butane treating molecular sieve sour gas regeneration product quality test after 300 cycles

Summary

The preceding discussion contains an examination of the adsorbent characteristics required, highlights of an experimental test program and individual unit sizes for the five separate adsorption units in the typical case. These units, shown in Figure 5, are:

- 1) The natural gas dehydrator;
- 2) The natural gas condensate dehydrator;
- 3) The sulfur from propane unit;
- 4) The sulfur from butane unit; and,
- 5) The auxiliary natural gas desulfurizer.

In linking up the individual molecular sieve adsorption units into the integrated package as shown in Figure 4, it is seen that a SYSTEM is presented in which over four billion pounds per year of LPG products, and 30,000 gallons per hour of natural gas C₅+ liquids are recovered from 500 million standard cubic feet per day of natural gas, with a relatively lean by-product residue gas stream which may be reinjected into the oil or gas field for later recovery, or following further treating, may be used as either liquid or vapor phase natural gas. Finally, the overall project utilizes over 350 tons of molecular sieve adsorbents.

Literature Cited

1. _____, Oil and Gas Journal (1975), 73, (No. 38), 64.
2. Winton, John M., Chemical Week, (1974), July 24, 31 ff.
3. Kessock, A., and Fris, J. P., Hydrocarbon Processing and Petroleum Refiner, (1965), 44, (no. 4), 123, 124.
4. Young, Philip L., presented at the A.G.A. 1968 Distribution Conference, Houston.
5. Rosenzweig, Mark D., Chemical Engineering, (1970), 77, January 12, 74 ff.
6. Turnock, Phillip H., and Gustafson, Kenneth G., presented a
a at the 22nd Annual Gas Conditioning Conference, The University of Oklahoma, (April, 1972), Norman, Oklahoma.
7. Sherman, J. D., and Katsaros, A. T., West German OFS 2,356,551.7, (January, 1976).
8. Collins, John J., Chemical Engineering Progress, Symposium Series No. 74.
9. Lukchis, George M., Chemical Engineering, (1973), 80 (June 11, July 9, August 6).
10. Mick, M. B., presented to the Gas Processors Association, San Antonio, Texas, March 24, 1976.

Pneumatic System Air Drying by Pressure Swing Adsorption

J. P. AUSIKAITIS

Molecular Sieve Department, Linde Division, Union Carbide Corp.,
Tarrytown, N.Y. 10591

ABSTRACT

Removing water from air is the most basic application for molecular sieves. Regeneration of molecular sieves by the use of a pressure swing cycle and incorporating additional isothermal purge to the depressurization step adds a degree of complexity to the application. This paper describes the incorporation of this cycle in small-to-moderate size pneumatic systems, develops the pertinent design theory and equations, defines the key process parameters, and demonstrates their effect on drying performance.

Introduction

All equipment requiring compressed air is susceptible to the problems of corrosion and damage of air actuated components by the passage of moisture, oil and dust. More severe damage can occur in cold weather when moisture in the compressed air may condense and result in freeze-ups. The term air precleanup is used to include the removal and rejection of all the previously mentioned contaminants from the compressed air system. The benefits of this precleanup step are: (a) minimizing the frequency of repair, (b) reduction of routine maintenance, and (c) most importantly, to decrease downtime losses.

Source of Problem

As the temperature of air increases it can subsequently contain more water vapor before it becomes saturated. The opposite is true for increasing pressures. As air is compressed above atmospheric pressure, it will hold less water at saturation. Figure 1 shows the effects of pressure on the saturated water content of air.

Most pneumatic equipment requires air at 100 to 150 psi to operate air actuated components. A single-stage compressor is

often used to provide the compressed air. This compression is done in an adiabatic manner; and the compressed air usually passes to a primary reservoir exposed to ambient temperatures. The compressed air may only approach ambient temperature to within 20 to 50°F before entering the reservoir. The hot compressed air could carry-over all of the water as vapor and, as the air cools, liquid water will accumulate in the primary reservoir. The significant ambient conditions which affect the magnitude of this water accumulation are ambient temperature and relative humidity. Routine maintenance such as "blowing down" the primary reservoir will not circumvent this problem. Furthermore, this procedure cannot limit downstream condensation if the compressed air is subsequently used in pneumatic equipment at temperatures below those of the reservoir.

Conventional Drying Devices

In recent years, the pneumatic equipment user has been supplied with numerous types of precleanup equipment, each claiming to do all or part of the total precleanup job required. These devices can be classified as mechanical separators, centrifugal separators, heat exchangers, and/or aftercoolers. Although these devices may be called by one particular name, all take advantage of heat exchange and mechanical separation to partially condense and separate entrained water, oil and dust. Units employing these two precleanup classifications can achieve moisture removal to levels no lower than ambient temperature dew points at pressure, even operating at 100% efficiency. Such devices are loosely termed as dryers. However, can any of the previously mentioned dryers even be classified as dryers at all? Or, are they simply devices which hasten the rate at which the compressed air seeks its new equilibrium condition. Thus the ultimate performance of any of these units is only that final condition that the compressed air would have obtained by itself given time. These mechanical devices are not useless of course because the air system is usually operating in a dynamic mode and therefore entrainment will occur along with condensation of water in the air lines. These devices are adequate for reducing the amount of liquid water that will reach the primary reservoir.

Pressure Swing Desiccant Dryers

The usual drawback of using pressure swing for dehydration is that very low dew points are difficult to attain. In addition, the energy requirement per pound of water removed is unfavorable when compared to a long cycle thermal swing process. However, bone dry air is not required in many pneumatic applications. The only requirement is that the air system be completely free of liquid water which inevitably is a result of condensation. Since such equipment is exposed to the environment, the compressed air

will have a maximum temperature change imposed by normal daily temperature cycles. Therefore, if the dew point of the compressed air is far below the existing ambient temperature, no condensation will occur when the ambient temperature falls. Depending upon the geographic location, this dryness requirement may be quantified as a 20 to 60°F dew point depression. To attain this degree of dryness it is necessary to remove water vapor in addition to entrained and condensed liquid water. This is where a pressure swing desiccant dryer takes over where other devices leave off. A desiccant dryer can take full advantage of the normal intermittent service of air compressors by regenerating the desiccant immediately after the completion of the duty cycle. In addition, this type of dryer has the physical size and, when the proper desiccant is used, the mechanical strength required for use on equipment which imposes rigorous demands on such units.

Figure 2 shows the relative performance of a desiccant dryer operating at a 60°F (Point A) and a 30°F (Point B) dew point depression versus the performances of an aftercooler which attains a 20°F approach to ambient temperature (Point E) and a heat exchanger which attains a 10°F approach to ambient temperature (Point D). As can be seen from the figure, if the compressed air temperature falls back to ambient temperature (Point C) from Point E or D, there is still potential for further water to condense. The performance is based on the total percentage of inlet water to the compressor rejected versus several ambient relative humidities at a temperature of 75°F and a total pressure of 125 psi.

Operation of a Pressure Swing Desiccant Dryer

Figure 3 is a functional diagram of the internals of a typical desiccant dryer. When the pressure in the primary reservoir falls below its minimum allowable level, the compressor engages and begins to pump up the reservoir. Air from the compressor enters the annular section of the concentric cylinders which is made up of an external housing and the internal desiccant chamber. Air swirls around and down along the cool surface of the external housing, condensing water and coalescing oil droplets in the process. While the liquid water and oil are collected in the sump, the air changes direction 180 degrees and begins to flow upflow through the bed of desiccant. The air passes through the bed and is dried on the way. Dried air exits the top of the dryer and flows to the primary reservoir. While the primary reservoir is being pumped up with dry air, a fraction of this air is diverted and saved for the purge volume. When the primary reservoir is pumped up to its maximum operating pressure, the compressor disengages. The compressor unloading actuates the blowdown valve and the pressure within the desiccant chamber is rapidly reduced to

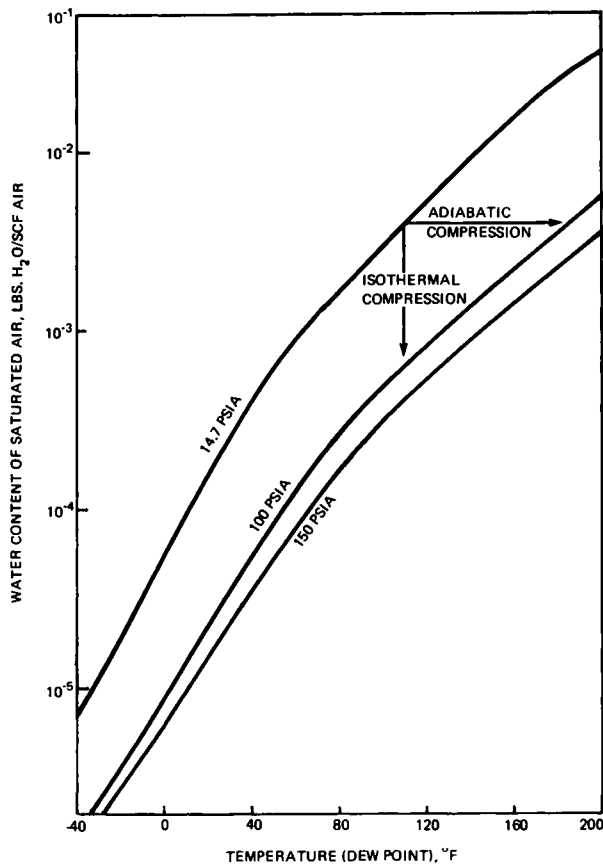
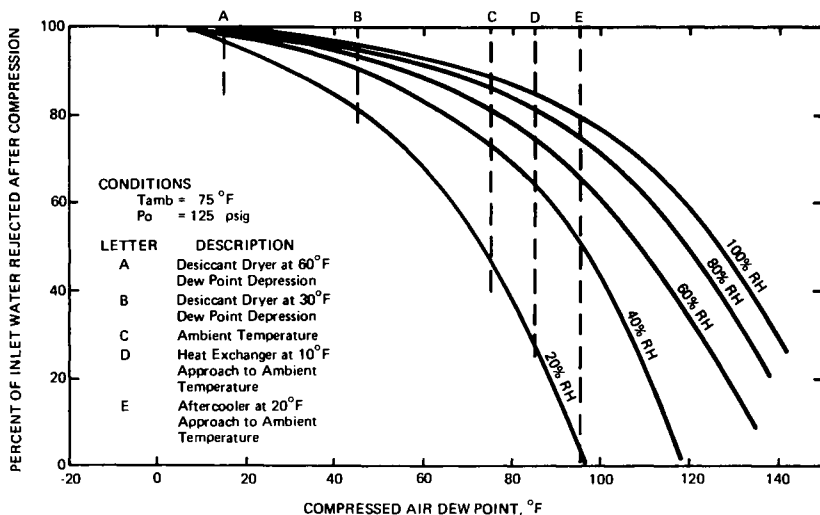


Figure 1. (right) Water content of saturated air vs. temperature at various total pressures

Figure 2. (below) Relative performance of a pressure swing desiccant dryer vs. a heat exchanger and an aftercooler as a function of relative humidity



atmospheric pressure. The air from the purge volume is expanded through a restriction, such as an orifice, in a direction countercurrent to adsorption. This dried purge air flows over the desiccant and picks up water until it exits the dryer as wet air via the blowdown valve in the sump. As compressed air is used, the air pressure in the reservoir begins to fall until the lower pressure limit is reached, at which time the compression and drying cycle repeat.

Basic Pressure Swing Theory

A pressure swing adsorption process adsorbs water at high total pressures and desorbs water at low total pressures. In so doing, adsorption is carried out at the highest water partial pressure, resulting in higher loadings; and desorption is carried out at the lowest water partial pressure, resulting in lower loadings. Water is carried out of the bed by using a fraction of the dried higher pressure product air expanded to the lower desorption pressure. Because air has a higher saturated water content at the lower pressures, only a fraction of the dried compressed air needs to be used to remove an equivalent amount of water from the adsorbent.

A typical pneumatic air system might require 600 SCFH of dry air at 125 psig. To provide this volume of air an additional volume of dried air must be produced for purging during the desorption step. In addition, the compressor is operating intermittently which allows for the desorption step. Therefore, a 24 SCFM compressor would be suitable to provide the required volume of air. Typically, this system would operate on approximately one minute cycles, during which the compressor would operate 60% of the time. The compressor would thus deliver 14.4 SCF of compressed air per cycle. To dry this air a two pound bed of molecular sieve is adequate. Saturated at 75°F and 125 psig, this volume of air would contain only 0.00216 pounds of water. Therefore, the available adsorption capacity for the two pounds of molecular sieve would need to be 0.108 weight percent based on equilibrium considerations. Thus the displacement involved along the isotherm is very small. Therefore it might be expected that the shape of the isotherm may not be nearly as important to the overall performance of the desiccant dryer as the mass transfer resistance of the adsorbent. In fact, it is the mass transfer zone that controls the ultimate product dew point that the dryer will achieve. The function of the adsorbent, which is in excess of the mass balance requirements, is containing the mass transfer zone. Figure 4 depicts the characteristic shape of a mass transfer zone. The cross-hatched area between the adsorption mass transfer front and the desorption mass transfer front is the differential amount of water rejected per cycle. Instead of the small differential amount of water being rejected instantaneously by a small amount

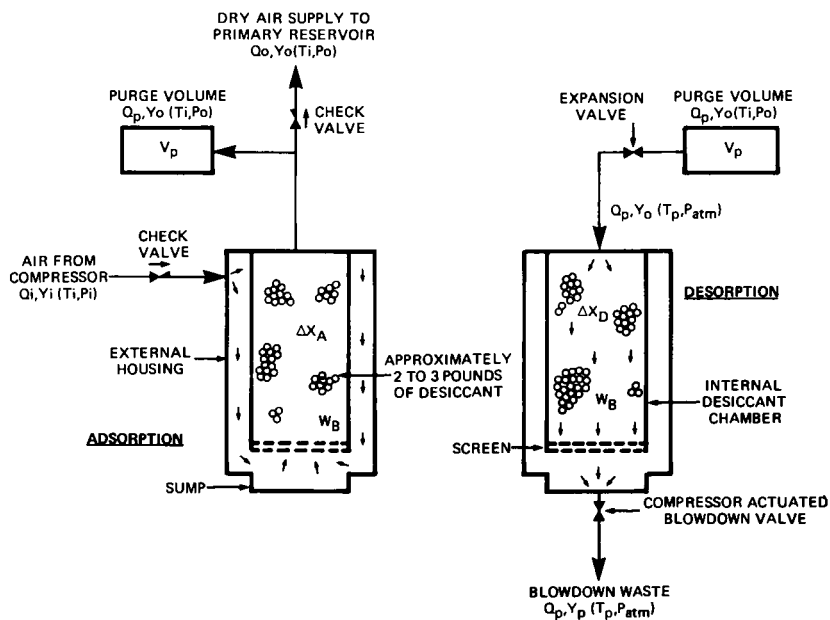


Figure 3. Schematic flow diagram of a pressure swing desiccant dryer

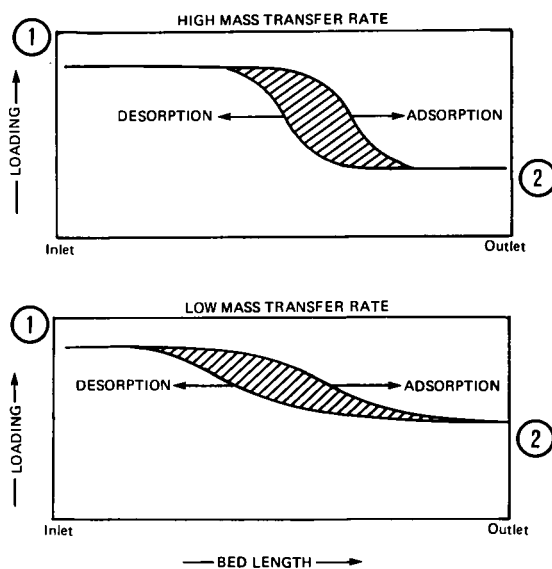


Figure 4. Characteristic shape of adsorption and desorption mass transfer fronts in a pressure swing dehydrator

- ① - LOADING IN EQUILIBRIUM WITH INLET COMPRESSED AIR
- ② - LOADING IN EQUILIBRIUM WITH PRODUCT OR OUTLET AIR

of adsorbent (as assumed in a mass balance), the water is spread out over a large amount of adsorbent due to the fixed rates at which it is removed. The shape of the zones is determined by the mass flowrate of air, temperature, pressure, adsorbent type and adsorbent particle size. The location of the zones is determined by a flow balance between the adsorption stroke and the desorption stroke. Increasing the amount of incoming water during the adsorption stroke tends to push the front towards the outlet end which results in high water concentrations in the product air. Too much purging with a dried product tends to push the desorption front out the influent end and thereby reduces the yield of dried product air per cycle. Thus the volume of purge gas used must be determined by a trade off between dryness and the volume of dried air produced. The amount of adsorbent required for such rapid cycle systems must be determined empirically. For a specific level of dryness, the adsorbent requirements may be considered nearly proportional to the volume of air entering per cycle as long as the yield remains constant.

Empirical Performance Model

Knowing the theoretical limitations of the performance of a pressure swing desiccant dryer, it is possible to develop a simple mathematical model to simulate the operation of such units under various conditions. A rigorous dynamic model of the system is not warranted because of the variable nature of the system. The variables which affect performance, such as compressed air temperature, air flowrate, and ambient temperature, could easily be changing from cycle to cycle. The simple mass balance model which follows will serve the purpose better.

The amount of compressed air entering the primary reservoir per cycle is expressed as:

$$Q_i = Q_o + Q_p$$

where,

$$Q_o = \text{dried outlet air, SCF/cycle}$$

$$Q_i = \text{wet inlet air, SCF/cycle}$$

$$Q_p = \text{purge air, SCF/cycle}$$

By mass balance, the amount of water adsorbed by the desiccant per adsorption cycle is expressed as:

$$\Delta X_A = \frac{Q_i Y_i - (Q_o + Q_p) Y_o}{W_B} \times 100 = \frac{Q_i (Y_i - Y_o)}{W_B} \times 100$$

where,

ΔX_A = differential loading during adsorption, lb
H₂O/100 lbs. adsorbent

Y_i = water concentration of inlet air, lb. H₂O/SCF air

Y_o = water concentration of outlet air, lbs. H₂O/SCF air

W_B = weight of adsorbent bed, lbs. adsorbent

The differential amount of water rejected from the desiccant per cycle is expressed as:

$$\Delta X_D = \frac{Q_p(Y_p - Y_o)}{W_B} \times 100$$

where,

$$\begin{aligned} \Delta X_D &= \text{differential loading during desorption,} \\ &\quad \text{lb. H}_2\text{O}/100 \text{ lbs. adsorbent} \\ Y_p &= \text{water concentration of purge air, lb.} \\ &\quad \text{H}_2\text{O}/\text{SCF air} \end{aligned}$$

Since the differential amount of water rejected per cycle dictates the differential amount of water adsorbed per cycle at steady state,

$$\Delta X_A = \Delta X_D$$

Therefore,

$$Q_i(Y_i - Y_o) = Q_p(Y_p - Y_o)$$

By rearrangement, the outlet water content of the compressed air can be expressed as:

$$\eta = \frac{Y_p}{Y_{p^0}}$$

where,

$$\eta = \text{overall efficiency, dimensionless}$$

However, there is another constraint imposed upon the maximum water content of the purge air exiting the desiccant per cycle. This constraint results from the fact that the amount of water rejected per cycle cannot be greater than the amount of water entering the desiccant per cycle at steady state. Figure 5 graphically demonstrates the definition of efficiency and its interrelationship with the mass balance. A function which has this proper double asymptotic constraint and is suitable for this model was found to be:

$$Q_p Y_p = (\eta Q_p Y_{p^0}) \tanh \left(\frac{Q_i Y_i}{\eta Q_p Y_{p^0}} \right)$$

Therefore, by substitution, the outlet water content of the product air from the desiccant dryer can be calculated as:

$$Y_o = \frac{Q_i Y_i - (\eta Q_p Y_{p^0}) \tanh \left(\frac{Q_i Y_i}{\eta Q_p Y_{p^0}} \right)}{Q_i - Q_p} \quad (1)$$

The last requirement for the model is necessitated by the actual mechanical operation of the desiccant and surrounding hardware.

The model as previously written states that the purge volume is pumped up to P_0 before any air reaches the primary reservoir. This, in actuality, is not the case because both volumes receive air simultaneously. Therefore, Q_p becomes a function of Q_i at low values of Q_i . Depending on the relative volumes of the two reservoirs and the flow restrictions in transit to each, the maximum Q_i to insure Q_p has achieved its maximum constant level may be two to five times Q_p . For the purpose of this model, four purge volumes will be assumed to be the minimum SCF of air fed per cycle to achieve complete pressurization of the purge volume. Thus for

$$Q_i \geq 4 Q_p$$

equation (1) holds and for

$$Q_i < 4 Q_p$$

the equation below is used:

$$Y_o = \frac{Q_i Y_i - (n Q_p Y_{p0}) \tanh \left(\frac{Q_i Y_i}{n Q_p Y_{p0}} \right)}{0.75 Q_i}$$

Experimental Data

The performance of any pressure swing adsorption unit is not only a strong function of the adsorbent used but of the mechanical design. There are a variety of commercial pressure swing desiccant dryers available for which the designs are fixed. Therefore, a pressure swing dehydrator was constructed to provide the following information: 1) to investigate the key variables in the design, 2) to confirm the mathematical model with experimental data, and 3) to determine the performance of different desiccants in order to provide the optimal adsorbents for this application.

Effect of Length To Diameter Ratio. Figure 6 shows the results of the first mechanical design parameter investigated. This parameter was the length to diameter ratio of the chamber containing the desiccant. As the L/D of the adsorbent bed increases, the efficiency as determined by the computer model increases. This efficiency was determined as being the maximum efficiency attainable with other design parameters, excluding L/D, optimized. Also as the average size of the Linde Molecular Sieve Beads are reduced from 4X8 to 8X12 mesh, the efficiency is also slightly improved. Thus any factors which improve flow distribution also improve the operating efficiency. However, the penalty that is incurred by going to a large L/D bed is twofold. The first is that the pressure drop across the

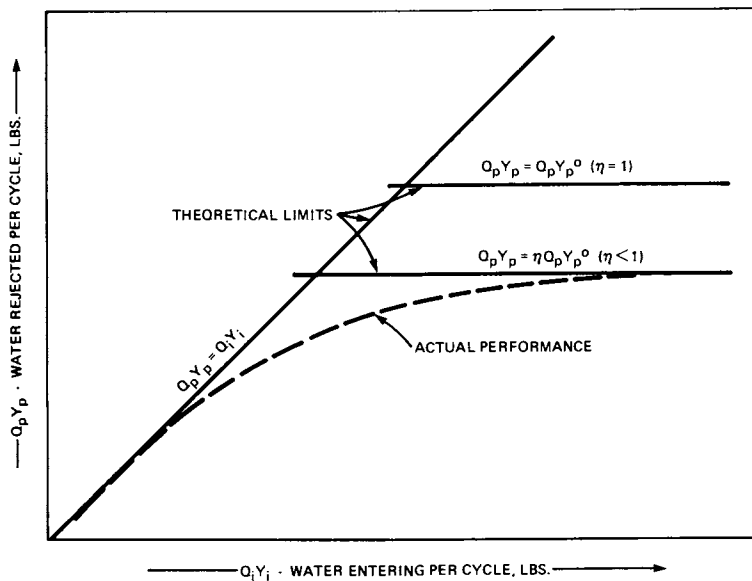


Figure 5. Constraints of mass balance and efficiency of desorption step on simulated performance

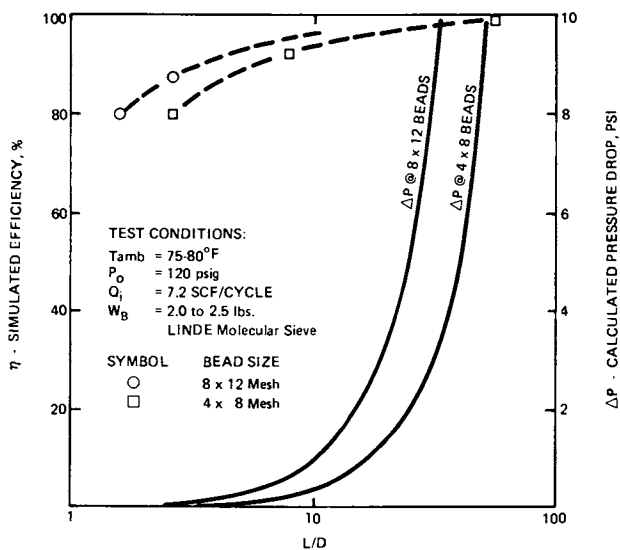


Figure 6. Efficiency and pressure drop at fixed experimental conditions as a function of length to diameter ratio of the desiccant bed

desiccant bed increases with increasing L/D. The second penalty is that the physical dimensions of a large L/D unit severely limit the overall compactness of the desiccant dryer.

Effect of Purge Flowrate. The second critical mechanical design parameter investigated was purge flowrate. Figure 7 shows the result of testwork on two adsorbent beds. Both bed configurations demonstrate the existence of an optimum purge flowrate. At low purge flowrates the relatively small amount of air is insufficient to produce a uniform distribution of air. At high flowrates, the rate at which the purge gas passes through the bed may exceed the rate for which maximum water rejection occurs.

Effect of Purge Volume. Figure 8 shows the effects of both Y_p and Q_j on the dew point depression at 80°F and 120 psig. The experimental data correlates quite well to the purge volume used when expressed as a function of the amount of air dried per cycle. It is expected that most commercial desiccant dryers would be operating somewhere between the two lines. Thus it is apparent, that product dryness is achieved only at the expense of product yield. However, the expense of approximately 15 to 20% of feed air to use as purge to achieve a 40 to 65°F dew point depression is a significant gain in protection for the compressed air system.

Effect of Temperature. The third and most significant operating variable is temperature. Operation at higher ambient temperatures results in only a small change in performance. Because the performance parameter, "Dew Point Depression", is based on the relationship below;

$$\text{Dew Point Depression} = \text{Ambient Temperature} - \text{Dew Point of Effluent Air.}$$

The inlet air temperature does not enter into this expression and will only affect the final dew point of the air. In order to have the most efficient water rejection system, the hot air from the compressor should be allowed to cool as much as possible to allow the desiccant dryer to suppress the outlet air dew point far below ambient temperature.

In Figure 9, the ambient temperature was assumed to be fixed at 80°F and the inlet air is saturated at the elevated temperatures. This is the worst case since the hot air may not contain enough water to become saturated (see Figure 1). The performance based on isothermal operation at the elevated inlet temperature is depicted in the figure as the solid lines. This shows a very dramatic effect on performance. However, this is not to say that little drying is done. For a saturated inlet air temperature of 160°F for which a 10°F Dew Point Depression is

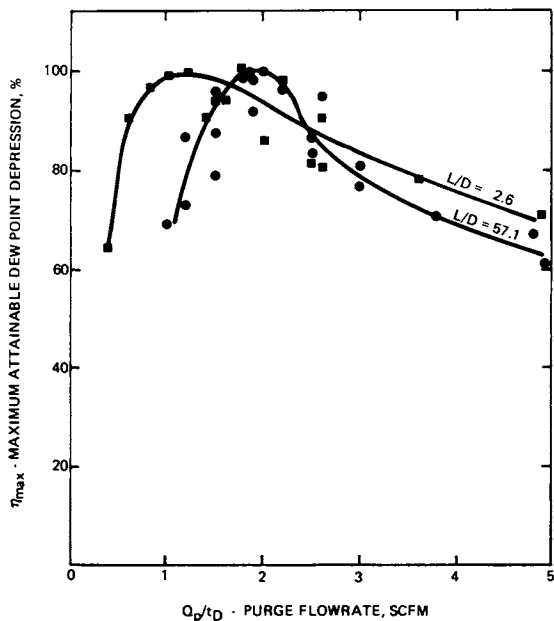


Figure 7. Maximum performance vs. purge flowrate for two-bed geometries

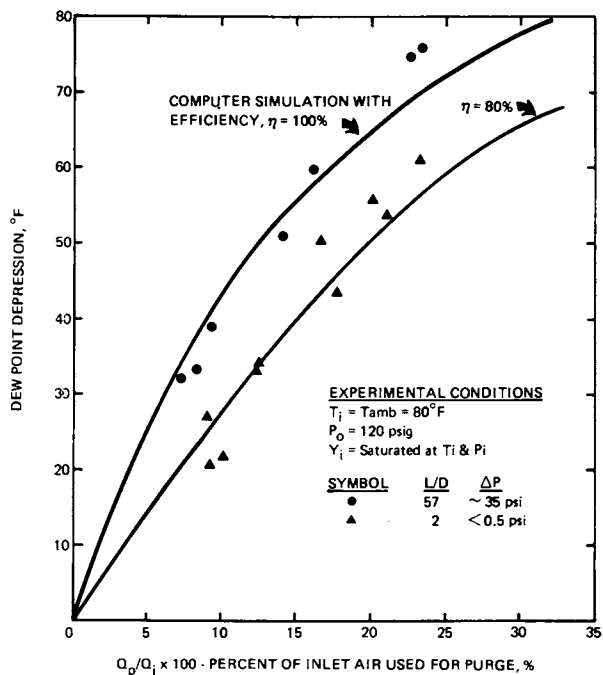


Figure 8. Effect of percentage of inlet air used for purge on dew point depression for two beds with varying L/D ratios

attained, the dew point of the product air has dropped 10°F from the ambient temperature of 80°F, which is 90°F from 160°F. If the pressure swing desiccant dryer was assumed to be a poor to fair heat exchanger, achieving only a 40% approach to ambient temperature, the performance improves markedly as represented by the dashed line on Figure 9. If the dryer were an average heat exchanger, which is a good assumption, then an 80% approach to ambient temperature is not extravagant. For this case the inlet air temperature has only a moderate effect on the performance.

Effect of Desiccant Selection. The final area of interest is in the selection of the desiccant itself. An operating parameter which may be optimized, even in an existing unit is the desiccant itself. In order to demonstrate this concept three desiccants were evaluated at similar operating conditions. The tests were carried out at an ambient temperature of 80°F and two inlet saturated air temperatures were evaluated for each desiccant. In addition, each desiccant was retested after it was thoroughly soaked with compressor oil. In order to approach the worst thermal conditions, the desiccant dryer housing was insulated from the surroundings to prevent temperature losses during the drying cycle. Thus the zero percent approach to ambient temperature case of Figure 9 is being approximated.

The desiccants tested were Silica Gel, Activated Alumina and Molecular Sieve in the form of 4X8 beads. The molecular sieve used was especially selected for this application because of high overall water capacity, high water mass transfer rates, good mechanical strength, and selectivity for water in the presence of oil.

Figure 10 shows the resultant performance of Linde MOLSIV versus Silica Gel and Activated Alumina. Since the unit was only insulated and not heated, condensation results and thereby distorts some of the greater-than-ambient-temperature dew point data. The performance of the desiccants in the "as received" state are compared by determining the efficiency which best fits the data. This indicates that by selecting the optimal desiccant an overall gain in operating efficiency is realized at fixed mechanical operating and design conditions. The performance loss for the "oil soaked" case, is largely attributable to an increase in mass transfer resistance due to the layer of oil which impedes the rate at which water vapor is transferred from the gas phase to the desiccant surface. For the Silica Gel and Alumina there is also expected to be a loss in equilibrium capacity since the oil is not excluded from the micropores due to "molecular-sieving" action.

Summary

The amount of drying achieved by a pressure swing desiccant

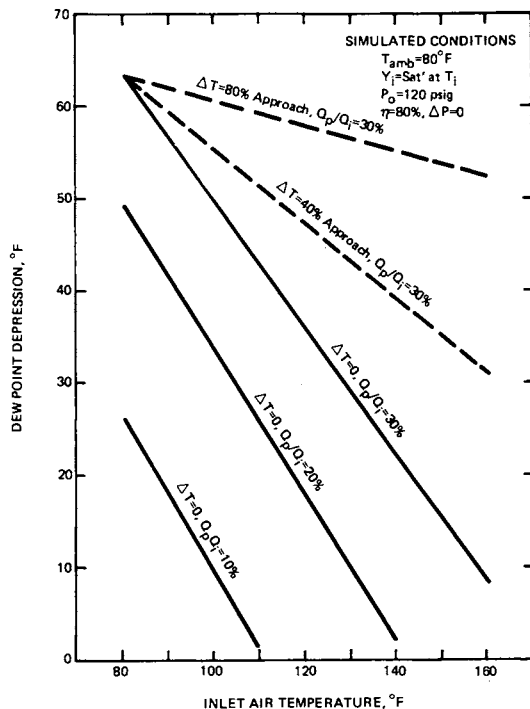


Figure 9. Simulated effect of inlet air temperature on the performance of a pressure swing desiccant dryer at various purge-to-feed ratios and approaches to ambient temperature

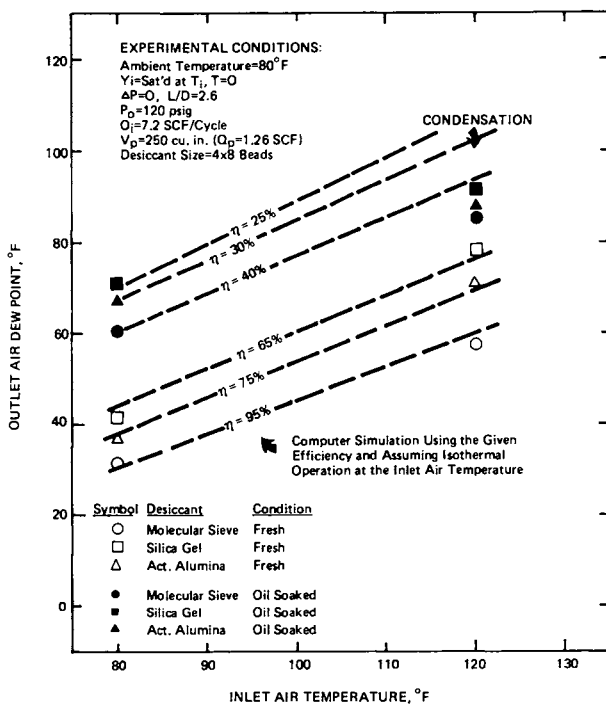


Figure 10. Effects of elevated temperature and oil on the performance of selected desiccants at a fixed experimental operating cycle

dryer compared to other devices, when considering the percentage of inlet water rejected, clearly shows that the desiccant dryer has a significant advantage over aftercoolers, heat exchangers, and separators. In order to predict the performance of pressure swing desiccant dryers over a variety of operating conditions, and duty cycles, a simplified mathematical model was developed. In order to account for the intrinsic mechanical characteristics of most commercial desiccant dryers, an efficiency parameter was defined to account for these variations from ideality in the model. As confirmation of this mathematical model, experiments were performed and mechanical variables were optimized with respect to the predicted performance. Although it may not always be practical to design a pressure swing desiccant dryer to operate at all of these optimum values, it was also demonstrated that the selection of the desiccant is the single most important design consideration. Molecular sieve was determined to have significant advantages over silica gel and activated alumina over a broad range of conditions.

Sodium-Aluminium Silicates in the Washing Process.

III. Ion Exchange and Detergency

M. J. SCHWUGER and H. G. SMOLKA

Henkel & Cie GmbH, Düsseldorf, West Germany

ABSTRACT

Crystalline Na-Al-silicates of the NaA-Type exhibit significant washing performance as a consequence of their good ion exchange capacity. In a laundry detergent their action is complemented by water-soluble complexing agents; this is due to differences in temperature and electrolyte influences on the calcium binding capacity.

Introduction

Previous work has shown that Na-Al-silicates with a high exchange capacity for calcium ions possess significant washing power and are therefore principally suitable as partial phosphate substitutes in laundry detergents (1,2,3). So far, these products appear to be satisfactory concerning practical application, hygiene, toxicology and ecology (4).

The positive effect in the use of Na-Al-silicates is based not only on the ion exchange capacity but also on the binding capacity for dirt present in monomolecular form, as colloidal pigments and sparingly soluble salts. Best results are obtained in the use of systems consisting of Na-Al-silicates and soluble complexing agents - e.g. sodium triphosphate (STP). The modes of action of the two classes of substances are principally different and ideally complement each other (3,5,6). In the present study, recent findings concerning the individual influences on ion exchange and their significance for the washing process are discussed. Results communicated so far are discussed in further detail and depth.

Results and Discussion

So far, investigations have shown that the binding capacity for metal ions, in particular calcium, is to be regarded as essential for the use of Na-Al-silicates (SASIL)* as partial phosphate substitute in laundry detergents.

Besides the binding mechanisms for different materials mentioned in the introduction, the most important mechanism of elimination operates via ion exchange. In this context it must be considered that in commercial laundry detergents the concentration of cations is relatively high, as most of the detergent ingredients are introduced as sodium salts (e.g. anionic surfactants, sodium perborate, sodium triphosphate, sodium sulfate, etc.). Therefore, any knowledge about the influence of cations as counterions on the calcium binding capacity of Na-Al-silicates as compared to STP is of highest importance.

It is concluded from the mass action law that principally both in the case of ion exchangers and in the case of complexing agents an increasing counter-ion concentration will result in a decrease of the calcium binding capacity. Fig. 1 demonstrates this effect in the case of SASIL and STP under washing conditions. It is shown that in the case of STP the decrease in calcium binding capacity is less than in the case of SASIL. On the other hand, due to the different binding mechanisms, there is marked temperature dependence in the case of STP as compared to SASIL - even the sign being different. While in the case of most soluble complexing agents there is a strong decrease in calcium binding capacity with increasing temperature (5), in the case of Na-Al-silicates under washing conditions, even an increase is observed. This increase is to be seen with the hydration reduction of the exchanging ion, the increase of the diffusion coefficient and the conditions thus improved for the diffusion into narrow pores (3,7). This increase is especially marked in the case of magnesium (3), the hydration shell of which is voluminous and stable (7). Thus, as far as calcium

*) The trademark SASIL is derived from the term "sodium-aluminium-silicate". In the present study, SASIL is a synthetic crystalline zeolite of the NaA-type with an outer surface of $1.6 \text{ m}^2/\text{g}$ and an average particle diameter of 5.6μ .

binding is concerned, the two different types of compounds will ideally complement each other in the mixture of SASIL/STP under the conditions of actual washing processes at high counter-ion concentration and variable washing temperatures.

Sodium will normally be the counter-ion in the washing process. Other counter-ions will influence the ion exchange basically in the same fashion; however, there will be gradual differences depending on the ionic species being present. The ion exchange of ions A and B of different valencies i and j may be described according to the general equation [1] (8)

$$Q_{A^i} = \frac{Q_m \frac{b_1 c_{A^i}^j}{c_{A^i}^i}}{b_1 \frac{c_{A^i}^j}{c_{A^i}^i} + b_2 \frac{c_{B^j}^i}{c_{B^j}^j}} \quad [1]$$

Q_{A^i} - amount of ion A^i exchanged in the ion exchanger

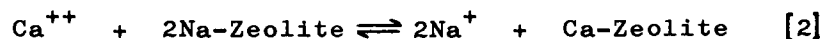
Q_m - maximum exchangeable amount of ion A^i

c_{A^i} - equilibrium solution concentration of ion A^i

c_{B^j} - equilibrium solution concentration of ion B^j to be exchanged

b_1 and b_2 - ion-specific constants accounting for the energy of adsorption of the ions

In the particular case of calcium ion exchange against the sodium of a sodium aluminum silicate according to equation [2]



the concentration changes of the ions involved will be given by equation [3]

$$c_{Na^+} = c'_{Na^+} + 2 Q_{Ca^{++}} \quad [3]$$

c'_{Na^+} - initial sodium ion concentration

Equation [4] is obtained by applying the general equation [1] to the exchange of calcium against sodium ions in SASIL taking equation [3] into account:

$$Q_{Ca^{++}} = \frac{Q_m c_{Ca^{++}}}{c_{Ca^{++}} + 2 \frac{b_2}{b_1} (c'_{Na^+} + 2 Q_{Ca^{++}})} \quad [4]$$

A linear form of equation [4] is particularly suitable for the evaluation of experimental data:

$$\frac{c_{Ca^{++}}}{2Q_{Ca^{++}} (c'_{Na^+} + 2Q_{Ca^{++}})} = \frac{b_2}{b_1 Q_m} + \frac{c_{Ca^{++}}}{2Q_m (c'_{Na^+} + 2Q_{Ca^{++}})} \quad [5]$$

Equation [5] is especially useful for the determination of b_2/b_1 and Q_m by graphical methods.

Equations [4] and [5] are modified versions of the Langmuir equation applied to the case of exchanging univalent and divalent ions, the univalent ions being present at excess concentration.

Fig. 2 shows to what extent there is agreement between the experimental ion exchange data and the theoretical equations. Within the comparatively small limits of experimental error, there is good fit of the experimental data with the calculated curve. A comparison of the Q_m -values with the amounts absorbed at high equilibrium concentration shows that not only the absolute amount of calcium ions adsorbed decreases with increasing sodium ion concentration, but also the equilibrium is shifted toward higher calcium ion concentrations.

While the isothermal lines describe the equilibrium, the dotted lines connect the equilibrium values with the corresponding initial solution concentration. The actual reduction of water hardness during the washing process is given by the difference between the initial and equilibrium concentrations*. The results concerning counter-ion dependancy of ion exchange show that the washing performance of binary systems consisting of ion exchangers and electrolytes must necessarily decrease with increasing electrolyte concentration. Fig. 3 shows the experimental confirmation of this prediction. This basic influence of

*) Two systems of coordinates are given in fig. 2 to facilitate the comparison between physical standard units and the units more commonly used.

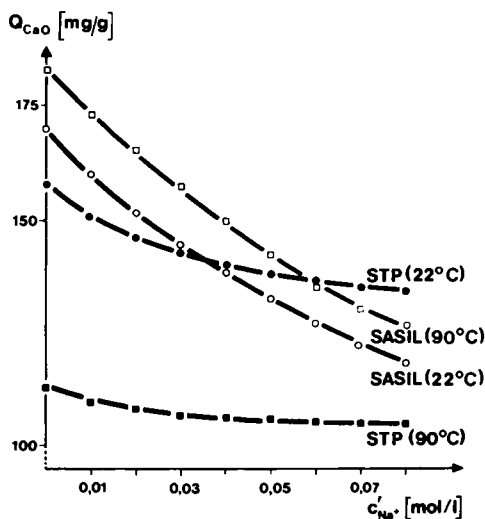


Figure 1. Influence of counter-ions on the calcium binding capacity (Q_{CaO}) at various temperatures. Conditions SASIL: 1(g/l); 30(°d); 15(min); pH 10. Conditions STP: see (5).

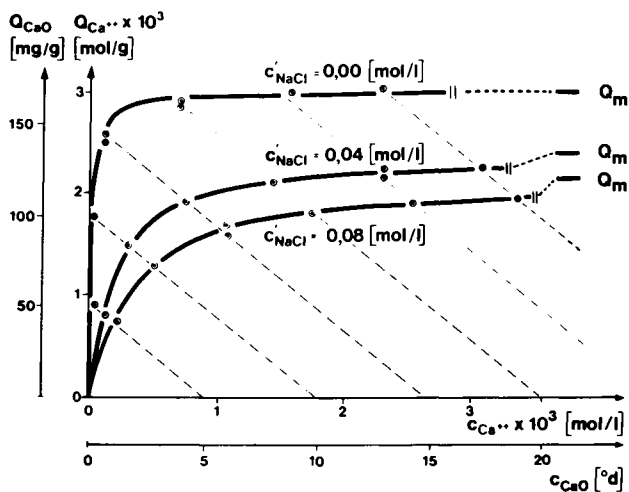


Figure 2. Comparison of calculated and measured isotherms. Conditions: $22 \pm 1(^{\circ}C)$; 1(hr). Solid line and Q_m -values calculated according to equation (4).

counter-ions on the calcium binding capacity and thus on washing performance is found with all ion exchangers and water-soluble complexing agents studied.

The observed influences of electrolytes on ion exchange and thus on washing performance are largely indirect. The washing performance will mainly depend on the capacity of the ion exchanger for calcium (kinetical factors remaining constant). Fig. 4 shows, how the washing performance depends on the calcium load (Q) of SASIL. It is seen that all experimental values are aligned - within the limits of experimental error - along one single curve, independent of water hardness, counter-ion concentration and total amount of SASIL. Fig. 4 shows that - as assumed - the washing performance depends directly on the calcium load of SASIL. Particularly good results are thus obtained in this simple system at calcium loads up to 25-30%. Therefore, a high concentration gradient between calcium in SASIL and calcium in the aqueous phase is required. In the case of a multi-component laundry detergent the curve discussed above will be displaced toward higher remission values (see Table I) - depending on the detergent composition. However, the curve will be flattened. It can be seen that the laundry detergent containing SASIL is comparable to the laundry detergents commonly used today.

Table I

Washing effect of detergents, based on 40% STP, 20% STP + 20% SASIL and 20% STP on artificially soiled textiles (4).

washing temperature	fabric	dosage (g/l)	performance R (%)		
			40% STP	20% STP 20%SASIL	20%STP
95°C	unfinished cotton	6,6	81	79	63
		10,0	83	81	69
60°C	resin finished cotton	6,6	64	62	56
		10,0	66	65	59
60°C	polyester/cotton blend	6,6	63	62	59
		10,0	65	64	61

In view of the application of SASIL in commer-

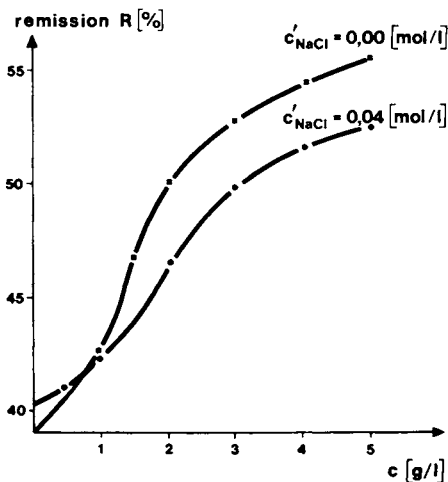


Figure 3. Influence of counter-ion concentration on the washing performance (R) of SASIL. Conditions: 16($^{\circ}$ d); 95($^{\circ}$ C); 30(min); pH 9; unfinished cotton; launder-o-meter.

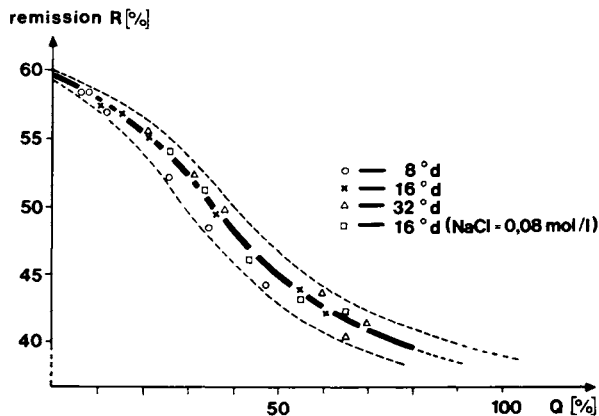


Figure 4. Influence of the Ca-load (Q) on the washing performance (R) of SASIL. Conditions: 95($^{\circ}$ C); 30(min); pH 9.2; SASIL 0-6(g/l); unfinished cotton; launder-o-meter.

cial laundry detergents, information concerning interactions with various ingredients of laundry detergents is of considerable importance. Under washing conditions, no direct interactions - such as adsorption or precipitation - could be observed with the important components of laundry detergents. This means that there will be no mutual interference concerning the individual effects in the washing process.

An exception to this rule is found in the significant degree of precipitation of phosphate on aluminum silicates containing calcium. Such precipitates are formed during the washing process and during transport from the washing machine to the sewage plant via the sewerage system. The degree of precipitation depends on the calcium load of SASIL and on the saturation of STP with calcium. In the application of conventional laundry detergents, sparingly soluble calcium salts are formed during rinsing (dilution), which may lead to textile incrustations and the formation of deposits in the sewerage system. In this respect the function of SASIL as a substrate for the deposition of calcium phosphates is relevant in the washing and rinsing processes, as well as in the sewerage system. Calcium containing sodium aluminum silicates are thus competing with textile fibers and the pipe walls of the sewerage system and principally counteract the formation of deposits on the other substrates.

Fig. 5 shows phosphate elimination Q as a function of residual STP concentration in solution c_r at various levels of calcium in SASIL. The amount of phosphate precipitated increases with increasing calcium content. This is true not only in the case of increasing calcium ion concentration in SASIL, but also in the case of increasing dilution of the wash liquor. In the latter case, the precipitation is caused by the solubility product. In view of the fact that the water used in the rinsing process or present in the sewerage system will always have a certain hardness, critical Ca^{++}/STP -ratios - as regards precipitation - will always be encountered. This is illustrated in fig. 6 for the three most common phosphorus salts in the case of water of 16°d. Fig. 6 shows that the tendency to precipitate in the dilution stage is much less pronounced in the case of STP than in the cases of ortho-phosphate and di-phosphate. At higher levels of water hardness, the precipitation maximum will be shifted toward lower dilutions, resulting in larger absolute amounts of phosphates pre-

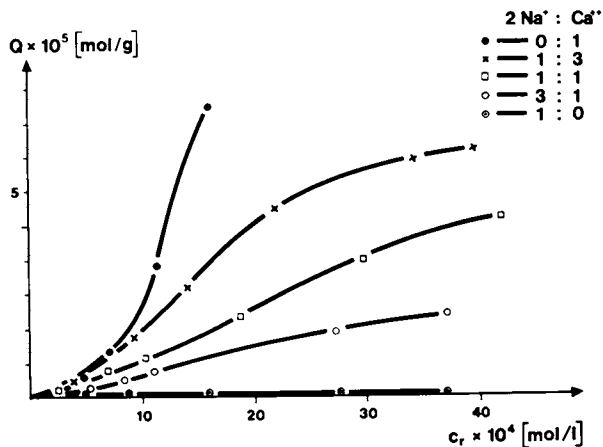


Figure 5. Precipitation of phosphate (Q) on various SASIL containing Ca. Conditions: 25(°C); 1(hr); NaCl 0,17(mol/l); SASIL 0,08(g/cm).

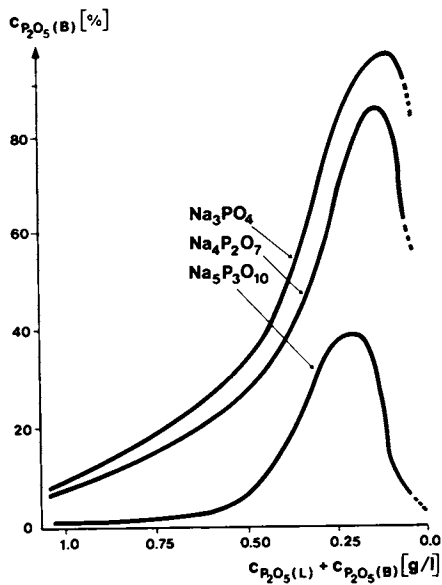


Figure 6. Precipitation of insoluble phosphates as a function of dilution. Conditions: 16(°d); initial $c_{P_2O_5}$ 2,315(g/l); $c_{P_2O_5}$ (L) (concentration in solution); $c_{P_2O_5}$ (B) (concentration in precipitate).

cipitated. At lower levels of water hardness, however, the maximum is shifted toward higher dilutions; as a consequence most of the precipitation will occur outside of the washing machine. A variation of the initial phosphate concentration at constant water hardness will give analogous results.

The same basic considerations are also valid in the case of laundry detergent formulations, as shown in fig. 7, in which a conventional laundry detergent and a laundry detergent containing SASIL are compared. The maximum of precipitation is shifted toward higher dilution in the case of the laundry detergent containing SASIL; the total amount precipitated is smaller and the danger of precipitation of calcium phosphates on the washed textiles decreases, because of this shift to higher dilution.

Besides calcium phosphates, there are other kinds of salts (such as carbonate, sulfate, silicate, hydroxide), which have to be considered, particularly in the case of non-phosphate formulations with regard to precipitation reactions and the formation of textile incrustations and soil deposition. As the novel SASIL-detergents should preferably - in view of physico-chemical considerations - contain a certain amount of water-soluble complexing agents, these other kinds of salts are of minor importance as compared to the water-insoluble calcium phosphates.

In view of the fact that the pH-values encountered during the washing process are predominantly alkaline, the formation of hydroxides of alkaline earths had to be investigated. In the presence of water-insoluble Na-Al-silicates, precipitations occur between pH-values of 10.5 (MgO) and 12.5 (CaO). Therefore, laundry detergents should be formulated to give pH-values below 10.5 in the wash liquor, which also happens to be the pH-range (8.5-10.5) at which ion exchange of SASIL is optimal. Thus, the novel phosphate substitute is particularly effective in the conventionally preferred pH-range. These predictions are confirmed by the experiments shown in fig. 8.

Conclusions

SASIL and STP ideally complement each other in laundry detergents, as the temperature dependancies of the calcium binding capacity and the electrolyte influences are of different sign or magnitude, respectively. Particularly favorable conditions for the application of SASIL are found in the pH-range of 9.0-10.5 in systems, in which the counter-ion content is

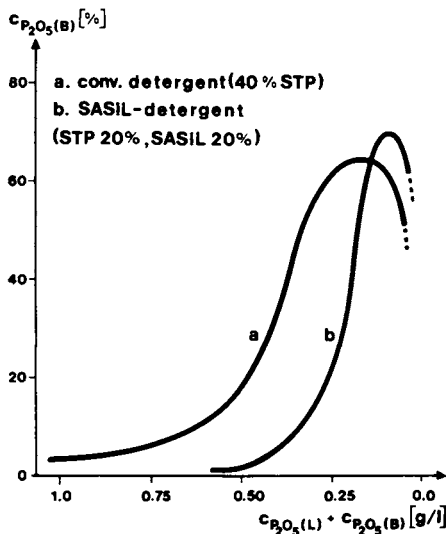


Figure 7. Precipitation of insoluble phosphates from laundry detergents as a function of dilution. Conditions: 16($^{\circ}$ d); initial detergent concentration 10(g/l); other data Figure 6.

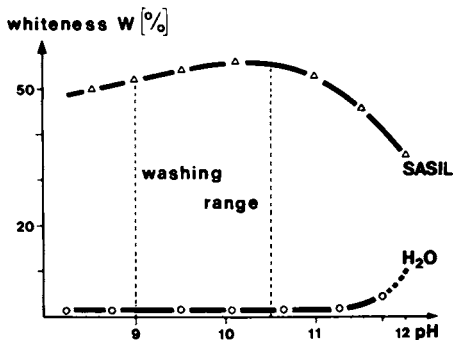


Figure 8. Washing performance (W) of SASIL as a function of pH. Conditions: 95($^{\circ}$ C); 16($^{\circ}$ d); 30(min); SASIL 5,0 and 0,0(g/l); unfinished cotton; launder-o-meter.

as small as possible. The final calcium load resulting during the washing process should preferably not exceed 30 % in the case of pure SASIL. SASIL was found not to interfere with active ingredients of conventional laundry detergents in a manner which might influence its mechanism of action. Quite to the contrary, a decrease in the precipitation tendency of sparingly soluble calcium phosphates is observed particularly during dilution (rinsing processes) as a consequence of the partial replacement of laundry detergent phosphates by SASIL. The ion exchange encountered under actual use conditions may be described by a theoretical equation, which is analogous to the Langmuir-equation.

Literature Cited

1. Schwuger, M.J., Smolka, H.G., Rostek, H.M., DOS 2412837 (1974) Henkel & Cie GmbH
2. Smolka, H.G., Schwuger, M.J., DOS 2412838 (1974) Henkel & Cie GmbH
3. Schwuger, M.J., Smolka, H.G., Colloid Polymer Sci. (part I of this paper - in print)
4. Berth, P., Jakobi, G., Schmadel, E., Schwuger, M.J., Krauch, C.H., *Angewandte Chemie* (1975), 87, 115 (International Edition in English (1975), 14, 94)
5. Jakobi, G., Schwuger, M.J., *Chemiker Zeitung* (1974), 99, 182
6. Smolka, H.G., Schwuger, M.J., Colloid Polymer Sci. (part II of this paper - in print)
7. Wolf, F., Fürtig, H., *Kolloid Z. Z. Polymere* (1965), 206, 48
8. Boyd, G.E., Schubert, J., Adamson, A.W., *J. Amer. Chem. Soc.* (1947), 69, 2818

Kinetics of Crystallization of Zeolite A in a Continuous Stirred-Tank Reactor

ALI ÇULFAZ and PINAR ORBEY*

Middle East Technical University, Department of Chemical Engineering,
Ankara, Turkey

ABSTRACT

Zeolite A was crystallized in a continuous stirred-tank reactor at 1 atm and 98°C. The fractional conversion of SiO₂ to zeolite A was varied from 0 to 0.92 by varying the feed flow rate. The reaction was found to be catalyzed by the external surface area of the formed zeolite A crystals.

Introduction

Studies on zeolite crystallization have been mainly concentrated on the synthesis of new zeolite structures and the modification of the known ones with some work on the kinetics of zeolite crystallization and the growth of large single crystals (1). The kinetic studies on the mechanism of zeolite crystallization were conventionally based on the quantitative analysis of the solid product of crystallization (2-5). The nature of the induction period, the mechanism of nucleation and crystallization, and the effect of the reactant materials have received considerable emphasis (6,7). An attempt to describe quantitatively the overall crystallization process on the basis of the conversion of the limiting reactant to the zeolitic phase was done by Çulfaz and Sand (8). However, in all these studies syntheses were almost invariably carried out in batch systems. No experimental work on the continuous crystallization of zeolites has appeared

*Present address: Mining Research Institute,
Technology Division, Ankara, Turkey.

in the literature except the theoretical treatment of Liu (9) for a continuous process of zeolite A crystallization based on the experimental data of Kerr (4) obtained in a semi-continuous system under transient reaction conditions.

This is the first reported study of a zeolite crystallization in a continuous system. Zeolite A was crystallized in a continuous stirred-tank reactor at steady state with constant flow rate of the reactant materials in and the product stream out of the reactor. The extent of conversion of the amorphous feed stream into zeolite A was studied by varying the retention time in the reactor.

Experimental

Reactants. The reactant materials were a sodium silicate solution prepared from 133 grams of water glass ($\text{Na}_2\text{O}-2.14\text{SiO}_2-9.33\text{H}_2\text{O}$), 30 grams of sodium hydroxide and 1300 grams of water, and a sodium aluminate solution prepared from 25.5 grams of aluminum chips, 81.4 grams of sodium hydroxide and 700 grams of water.

Apparatus. The experimental set-up consisted of a one-liter pyrex reactor heated by a mantle and kept at 98°C by a water-cooled reflux condenser. The silicate and aluminate solutions were fed to the reactor through two separate channels of a peristaltic pump. Sodium silicate solution was pumped through a tygon tubing of $3/32$ " diameter and the sodium aluminate solution was pumped through another tygon tubing of $1/16$ " diameter. The feed solutions were partially heated to the reactor temperature by keeping the stock solutions at about 60°C and by passing the two tubings through the reflux condenser. The ratio of the volumetric flow rate of the silicate solution to the aluminate solution was thus fixed at $4\text{Na}_2\text{O}-\text{Al}_2\text{O}_3-1.7\text{SiO}_2-250\text{H}_2\text{O}$. In various experiments by varying the speed of the peristaltic pump the combined feed rate of the two solutions was changed while keeping the ratio of the volumetric flow rates of the two solutions constant. Therefore the retention time

of the feed in the reactor was varied without changing the overall feed composition.

Sampling. The reactor was fitted with a stirrer and a suction discharge line. By fixing the stirrer speed and the level of the suction line, the amount of the reacting material was kept constant at 0.60 liters. The product was removed continuously from the reactor and samples of it were set aside after every hour of operation for analysis of its zeolite A content. At any given flow rate of the reactants the operation was continued until steady-state was reached.

Analysis. The product stream from the reactor consisted of zeolite A crystals, unreacted gel and solution. Weighed samples of product were filtered, washed free of excess alkali, dried in an oven at 110°C, brought to equilibrium with water vapour in a constant humidity atmosphere, and weighed again. The amount of zeolite A in these samples was quantitatively determined by measuring the ion-exchange capacity for silver ions. In this manner both the percentage of zeolite A in the solid product (grams zeolite A per 100 grams of dried product) and the rate of zeolite A production (grams of zeolite A in the product stream per hour) were determined.

Filtered and dried samples were analyzed by X-ray powder diffraction and the only crystalline phase was shown to be zeolite A. Crystal size distribution of the samples were determined by an optical microscope at 675 magnification and some of these data are shown in Figure 1.

Results and Discussion

Operation at Steady-State. For each flow rate of the reactant materials, the reactor was operated for 5-6 hours before steady-state was reached. All the data reported in this paper refer to the steady-state operation. In a separate experiment, the reactor was initially filled with zeolite A crystals to check whether the same steady-state conversion level would be reached when the reaction was started up with no

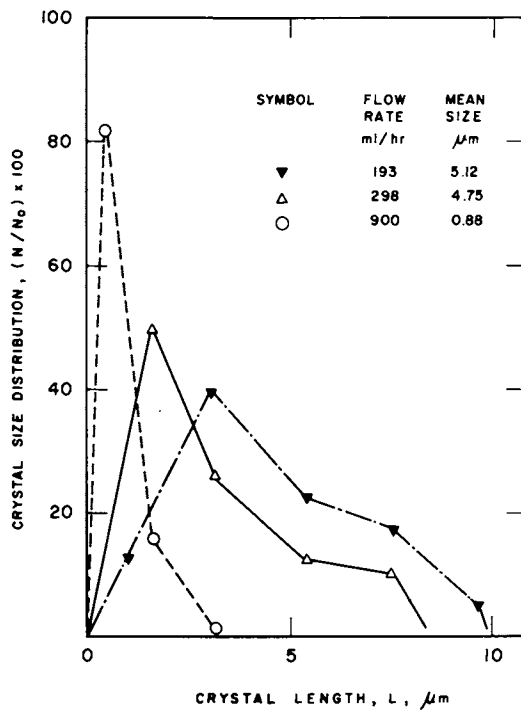


Figure 1. Crystal size distribution of zeolite A crystals. (▼), $X_A = 0.920$, $Z_A = 100\%$; (△), $X_A = 0.900$, $Z_A = 100\%$; (○), $X_A = 0.327$, $Z_A = 36.0\%$.

crystalline material in the reactor. The results are shown in Figure 2.

Analysis of Experimental Data. On the basis of the quantitative determination of the flow rates of feed and product streams and the percentage of zeolite A crystals in the solid phase, the fractional conversion of the limiting reactant SiO_2 to zeolite A was calculated as a function of the flow rate of the reactants under steady-state conditions. The rate of reaction, $-r_A$, was expressed as the moles of SiO_2 reacted to yield zeolite A per unit time per unit reactor volume from the design equation

$$\frac{V}{V_0} = \frac{C_{A0} X_A}{-r_A} \quad (1)$$

where V is the reactor volume (600 ml), V_0 is the flow rate of the combined silicate and aluminate feed solutions (in ml/hr), C_{A0} is the concentration of SiO_2 in the combined feed (0.47 moles/liter), X_A is the fractional conversion of SiO_2 to zeolite A. The fractional conversion versus rate data shown in Figure 3 is typical of an autocatalytic reaction. The dependence of fractional conversion and the mean crystal size of the product on the retention time in the reactor is shown in Figure 4.

The rate of formation of zeolite A was first order with respect to SiO_2 concentration only at low conversions, and attempts to correlate the reaction rate with integer orders of reaction over the whole conversion range were unsuccessful. The autocatalytic nature of the crystallization process was expressed by incorporating the product zeolite A concentration into the reaction rate expression

$$-r_A = k_1 C_A + k_2 C_A C_R \quad (2)$$

or

$$-r_A = C_{A0} (1 - X_A) (k_1 + k_2 C_R) \quad (3)$$

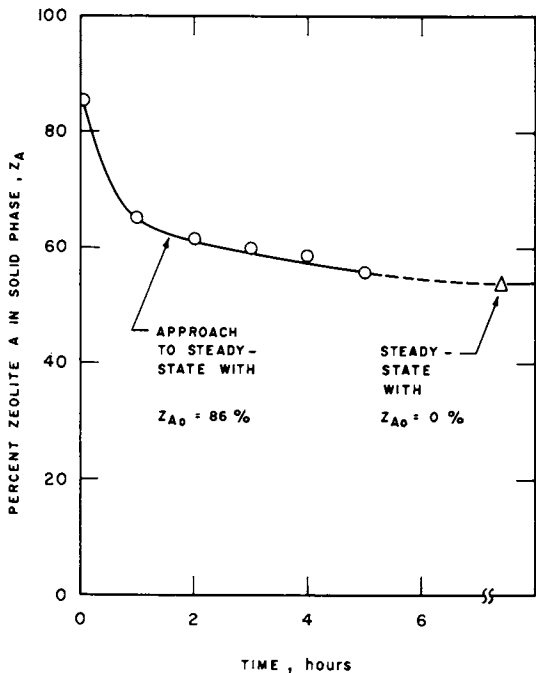


Figure 2. Test for steady state. (O), Initially the reactor was seeded with zeolite A crystals; (Δ), steady-state attained in a separate experiment with no seed. In both cases, the flow rate of the feed stream was 771 ml/hr and the overall feed composition was $4 \text{ Na}_2\text{O}-\text{Al}_2\text{O}_3-1.7 \text{ SiO}_2-250 \text{ H}_2\text{O}$.

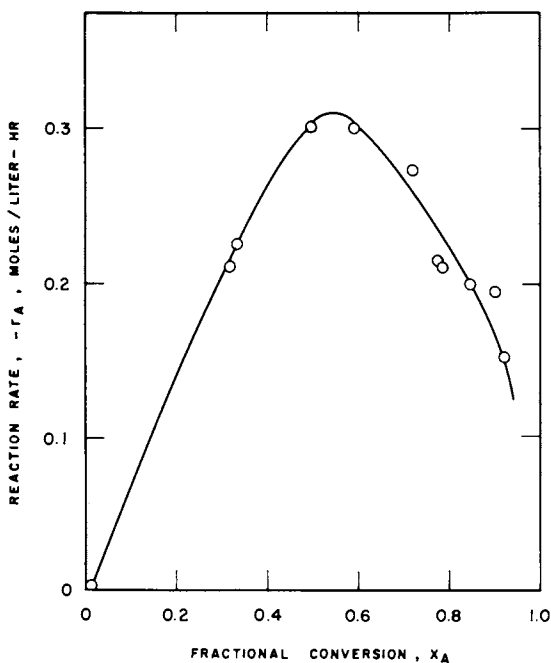


Figure 3. The retention time vs. fractional conversion

where C_R was taken as the rate of formation of the external surface area of the zeolite A crystals (in cm^2/hr). C_R was calculated from the expression

$$C_R = \frac{W Z_A}{\rho_c} \frac{A_c}{V_c} \dots \dots \dots (4)$$

where W is the weight of the solid product removed (g/hr), Z_A is the fraction of zeolite A in the solid product, ρ_c is the crystal density of zeolite A (1.99 g/cm^3), A_c and V_c are the total external surface area and total crystal volume of the same counted number of zeolite A crystals used in the crystal size distribution analysis (10).

Equation 3 was tested by plotting $-r_A/C_{A0}(1-X_A)$ versus C_R as shown in Figure 5. The rate constants k_1 and k_2 were determined from Figure 5 as 5.4 hr^{-1} and $1.7 \times 10^7 \text{ cm}^{-2}$, respectively.

Conclusions

The apparent autocatalytic nature of the rate of formation of zeolite A makes it necessary to include a product zeolite A term in the reaction rate expression. A conventional type of a concentration term for the product in grams zeolite A per unit volume of reactor was found not to correlate well with the experimental data. The catalyzing nature of the product zeolite A is in supplying nucleation sites on its surface and the growth of zeolite A crystals are by the transport of the amorphous material and its diffusion to the nucleation sites on the solid-liquid interface. The correlation of the autocatalytic rate expression with the external surface concentration of the zeolite A crystals is supporting evidence for the hypothesis that the growth rate of crystals are limited by an interface diffusion mechanism proposed earlier by Çulfaz and Sand (8).

The use of a continuous stirred-tank reactor to obtain reaction rate data is very common in chemical

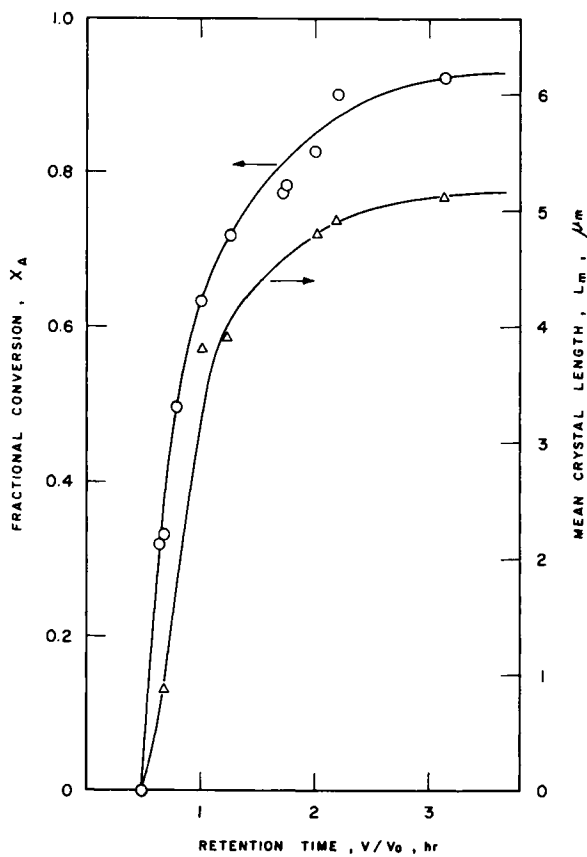


Figure 4. Fractional conversion and mean crystal length of zeolite A as a function of retention time in the reactor

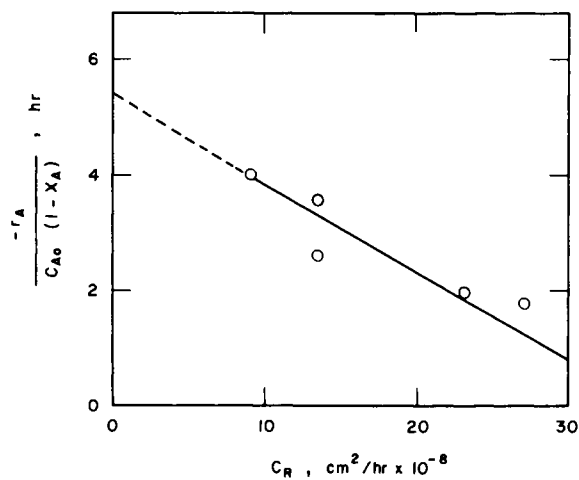


Figure 5. Correlation of reaction rate with the external surface area of the zeolite A crystals produced in the reaction

engineering practice. This well known technique was applied to a zeolite crystallization system for the first time. The crystallization rate data obtained under steady-state conditions proved to be very useful in the interpretation of the mechanism of crystal growth in the zeolite A system. The techniques used in this study is well suited to the investigation of the concentration and temperature dependence of reaction rate in zeolite synthesis and the optimization of reactor performance within industrially applicable operating ranges.

Literature Cited

1. Flanigen, E.M., ADVAN. CHEM. SER. (1973) 121, 109.
2. Breck, D.W., J. Chem. Educ. (1964) 41, 678.
3. Sand, L.B., "Molecular Sieves," pp. 47-61, Society of Chemical Industry, London, 1968.
4. Kerr, G.T., J. Phys. Chem. (1966) 70, 1047.
5. Ciric, J., J. Colloid Interface Sci. (1968) 28, 315.
6. Zhdanov, S.P., ADVAN. CHEM. SER. (1973) 101, 20.
7. Meise, W., Schwochow, F.E., ADVAN. CHEM. SER. (1973) 121, 169.
8. Çulfaz, A., Sand, L.B., ADVAN. CHEM. SER. (1973) 121, 140.
9. Liu, S.L., Chem. Eng. Sci. (1969) 24, 57.
10. Orbey, P., M.S. Thesis, Middle East Technical University, 1976.

INDEX

- A**
- A, zeolite (*See* Zeolite A)
- Absorption bands of N₂O and CO₂
on Cr₁(II)-A 128
- Absorption frequency of supercage
OH groups, IR 613
- Acetylene 639
cobalt(II) complexes with 483
nickel(II) complexes with 488
zeolitic Co(II)A complexes 484
- Acid
-base properties 459
centers 462
gases 639
sites
Brönsted and Lewis 93
generation of 456
number and strength 458
- Acidic properties of dealuminated
NH₄L 601
- Acidic properties of zeolites 453
- Acidity
and catalytic activity 461
with H⁺ content, change in 603
measurement 454, 598
models 453
of mordenite 96
superficial composition and 86
of transition metal zeolites 460
zeolite 453
- Activation
on cis/trans but-2-ene ratio, effect
of mode of 579
energies 361
apparent 225
from chromatographic data 322
for nucleation of zeolite A,
apparent 209
for cracking and isomerization
of *n*-hexane 522
mode, effect of 579
temperature, effect of 229, 579
on yield and melting point, effect of 629
- Active
centers in cerium-exchanged
zeolites 572, 581, 582
sites 462, 630, 656
zeolites A by Co²⁺ exchange 549
- Activity
of bifunctional catalysts 508
for C₃H₆ hydrogenation 545
- Activity (*continued*)
of cis-2-butene isomerization 621
of composite catalysts 655
for the conversion of *n*-hexane 507
effect of feedstock type and feed
hydrotreating on 662
as a function of mean metal
crystallite diameter 511
influence of the structure parameters
on catalyst 504
kinetic considerations of 658
measurements, catalytic 506
metals and coke effects on 658, 660, 662
testing 654
for ring conversion of tetrahydro-
pyran into piperidine 598
- Adsorbed
hydrocarbons, samples with 360
molecule, trigonal site with 116
molecules, influence of 357
phases
density variation of 376
molar integral entropy 374
specific heat of 374
thermodynamic data for 372
pyridine, effect of 554
- Adsorbent
applications, molecular sieve 637
COS formation over 674
performance requirements 670
- Adsorption 89, 92, 303
on activation temperature,
dependence of 229
of bases 586
of benzene 588
on 1-butene isomerization, effect
of pyridine 555
of carbon dioxide 396, 399
carbon monoxide 157, 398, 399
on cation and acid centers,
competitive 462
of *n*-decane and trans-butene-2 315
effect of water on 158
of equilibrium of rare gases and
n-paraffins 313
equilibrium, thermodynamic
functions of 8
of ethylene 588
experiments 394
of gases 1
heats of 9, 367, 368, 380, 385, 397

Adsorption (<i>continued</i>)	
isotherm(s)	375
equilibrium	231
for nitrous oxide	123
of Xe	9
mass transfer fronts	686
measurements	44
of metal carbonyls	144
in microphores, osmotic theory of	2
by microporous adsorbents	10
of Mo(CO) ₆	150
of NH ₃	133, 316
organic molecules	89, 92
osmotic theory of	7
oxygen	158
by pressure	681
of pyridine	601
of Re ₂ (CO) ₁₀	152
at room temperature	89, 92
of Ru ₃ (CO) ₁₂	153
SO ₂	214
thermodynamics of	8, 305, 316
values	9
of water	133
of Xe	9
Air	
drying by pressure swing	
adsorption	681
oxygen from	648
separation, cryogenic	638, 639
used for purge	692
water content of saturated	684
Alkylation of benzene	587, 590
Alumina ratio, silica/ (See Silica/alumina ratio)	
Aluminum content of the faujasite	611
Aluminosilicates	69
Aluminum	
electrons in the zeolites	77
ratio, Si/ (See Silica/alumina ratios)	
-deficient zeolites	465
in the hydrothermal treatment of ammonium-exchanged zeolite Y	271
AlK _β results	68
AlK _β shifts	72
Al _{2s} binding energies	79
Amine scrubbing of regeneration gas	645
Ammonia	277
adsorption of	133, 316, 586
complexes, Cu(II)	137
partial pressure of	600
synthesis	644
Ammoniated Cu(II)-exchanged zeolites X and Y	132
Ammonium	
-exchanged zeolite Y	271
mordenite	102, 103
zeolite	93
Ammonium (<i>continued</i>)	
NH ₄ A system LiA-	443
NH ₄ L, dealuminated	601
NH ₄ X system, LiX-	443
NH ₄ Y, steamed	275, 278
Anharmonicity	117
Arrhenius plot of intracrystalline diffusion coefficient	435
Arrhenius plot of rate constants	502
Asymmetry parameters	56
Atoms in the tetrahedral frame- works, M.O. calculations for	19
Axial distortions	114
	B
B, zeolites	211, 212
Band energies, SiK _β	69
Base(s)	
adsorption of	586
cation interactions	460
load LNG	641
Batch compositions	210, 222, 225
Benzene	
adsorption of	588
alkylation of	587, 590
chromium(I) complex with	488
Beryllium mordenite OH group	587
Bifunctional catalysts	504, 507, 508
Binary isotherm, modified	385
Binary systems involving ethylene	386
Binding energies	79, 81
Biporous molecular sieves	417
Bond length, observed T-O	24, 25
Bond overlap population	24, 25
Bromobenzene in active carbon granule	13
Brönsted acid sites	93
Brown-Sherry-Krambeck model	189
Bulk separations	647
Butane treater	672, 678, 679
<i>n</i> -Butane in zeolite NaX	401
<i>n</i> -Butenes in Ca, Na-Y-zeolite	619
<i>n</i> -Butene isomeriza- tion	555, 576, 578, 606, 610
But-2-ene ratio, cis/trans	579
	C
Calcination of NH ₄ -mordenite	102
Calcium	27
binding capacity	700
-exchanged Y zeolites	396
Ca ²⁺ ions, oligomerization on the dehydrated	554
Ca ²⁺ exchange in NaCaA zeolites	326
Ca-A, zeolites	553
CaA system, LiA-	443, 444
CaNaY zeolites	395, 616, 619, 621
CaX(Na) pellets	432
CaY zeolites	341, 396, 507

- Carbon
- dioxide 641
 - adsorption 399
 - on Cr₁(II)-A 128
 - isotherms of 367
 - in NaY and CaY zeolites 396
 - removal 642
 - rich natural gas desulfurization unit 645
 - as sensitive probe molecules 393
 - sorbed on small-pore Na'-mordenite 349
 - from synthesis gases 643
 - disulfide 352
 - granule, active 13
 - monoxide 352
 - adsorption 157, 398
 - cobalt(II) complexes with 485
 - copper(I) complexes with 479
 - effect of addition of 633
 - gravimetric analysis of Cr₁(II)-A interaction with 125
 - in NaY and CaY zeolites 396
 - NO reduction with 561
 - oxidation 559, 565, 567
 - physisorption 498
 - as sensitive probe molecules 393
 - 13-NMR mordenite sorption sites
 - by 344
 - C₂-C₄ mono-olefins, diffusivities of .. 623
 - C₃H₆ hydrogenation, specific activity for 545
 - C₃H₈-C₂H₄ in 5A zeolite, sorption of 387
 - C₃H₈-C₃H₆, sorption of 384
 - C₆H₆ 277
 - n*-C₇H₁₆ in 5A and 13X zeolites 328
- Catalyst(s)
- activity in isomerization of but-1-ene 576
 - activity and selectivity
 - for the conversion of *n*-hexane 507
 - effect of feedstock type and feed hydrotreating on 662
 - effects of zeolite concentration
 - on 655
 - with H-mordenite as support 508
 - influence of the structure parameters of the 504
 - kinetic considerations of 658
 - metals and coke effects on 658
 - testing of cracking 654
 - bifunctional 507
 - composite 655
 - Cr-Y 633
 - deactivation of Pd-H-mordenite 515
 - isomerization of *n*-hexane and *n*-pentane over 504
 - platinum 538
- Catalyst(s) (*continued*)
- reduced in NaNiY zeolite 528
 - zeolite cracking 650
- Catalytic
- active centers in cerium-exchanged faujasite zeolites 572
 - activity
 - correlations between acidity and measurements 461
 - of transition metal complexes 466
 - behavior of Ca, Na-Y-zeolite 616
 - properties
 - of aluminum-deficient, deep-bed or ultra-stable zeolites 465
 - of Pd-H-mordenite 525
 - of zeolites 453
 - sites 464
 - studies 464
 - on mordenite-like zeolites 584
- Cation(s)
- centers, competitive adsorption on 462
 - contents and percentage elutions
 - of M-L zeolites 171, 172, 174
 - on diffusion, effects of exchangeable 428
 - distributions in M-L zeolites 172, 174, 176
 - effect in recrystallization of
 - clinoptilolites 239
 - exchangeable 134
 - influence of mono- and divalent 357
 - interactions, base- 460
 - migration effects of 393
 - sodalite units of faujasites with different 335
 - recoil studies, Szilard-Chalmers .. 166
 - in zeolite L 168
- Cationic forms of zeolites 562
- Caustic treatment of mordenite and high-silica materials 236
- Cavities, accessibility of 463
- Cell, exchangeable cations per unit 134
- Cerium-exchanged zeolites 572, 578, 581, 582
- Chabazite, ion exchange equilibria in 187
- Chemical regime 620
- Chemical shifts in zeolites by x-ray emission 64
- Chemisorption of SiH₄ on H-mordenite 265
- Chloride promotion, recrystallization of clinoptilolites with 239
- Chloride on recrystallization, effect of 241
- Chromatographic data, activation energies from 322
- Chromatographic measurements 320
- Chromium
- (II) complexes 485, 486
 - exchanged zeolite, anhydrous 123
 - ion-exchanged zeolite A, divalent .. 120

Chromium (<i>continued</i>)		
Cr ₁ (II)-A	125, 128	
Cr-Y zeolite	626, 633	
Cis-2-butene isomerization	621	
Cis/trans but-2-ene ratio	579	
Clinoptilolites, recrystallization		
of	237-240, 241	
Cobalt		
(II) complexes	480, 483, 485	
(II) isocyanide complexes	482	
(II)A zeolite	484, 487	
ion, coordination of NO to	487	
Co ³⁺ exchange	549, 551	
Co ²⁺ oligomerization on the		
dehydrated	554	
Coke	658, 659	
Competitive adsorption on cation		
and acid centers	462	
Complex(es)		
chromium(I)	485, 488	
chromium(II)	485, 486	
cobalt	480	
cobalt(II)	480, 482-485	
copper	474, 479	
copper(II) amine	474, 476	
copper(II) ammonia	137	
ions	188	
iron(II)	489	
nickel	488	
nitrosyl	481	
rhodium	156	
transition metal	466, 473	
Complexation of divalent chromium		
ion-exchanged zeolite A	120	
Composite catalysts	655	
Composition, superficial	86, 88, 90	
Computer simulation of the		
measured spectra	53	
Concentration gradients, high	207	
Constant volume sorption chamber	431	
Continuous stirred-tank reactor	708	
Conversion		
fractional	713	
of <i>n</i> -hexane	509, 511	
of 2-methylpropene	555	
Coordination of NO to cobalt ion	487	
Copper		
complexes	474	
-amine	474, 476, 478	
-ammonia	137	
-carbon monoxide	479	
-nitric oxide	479	
-pyridine	478	
-exchanged zeolites, X and Y	132	
ions in zeolites X and Y,		
aqueous	139, 140	
in NaX and NaY	186	
CuY with ND ₃	484	
Corrected diffusivities	326	
COS formation over adsorbents	674	
Counter diffusion studies	331	
Counter ions	700, 702	
Coupling		
constants	56, 60, 141	
Jahn-Teller	117	
spin-orbit	114, 116	
Cracked gases	639	
Cracking		
activity of zeolites	660	
catalysts, zeolite	650	
activity and selectivity	654, 658, 662	
of <i>n</i> -hexane	522	
products, formation of	519, 521	
rate, total	520	
CRC and severity effects,		
comparison of	660, 661	
Critical molecular diameter	324, 327	
Cryogenic air separation	638, 639	
Cryogenic extraction of helium	638	
Crystal(s)		
external surface area of zeolite A	715	
size distribution in zeolite A	711	
structure determination	146	
Crystallite size	511, 533, 534	
Crystallization		
curves	210, 255	
energies	226	
kinetics	210, 225, 708	
rates	212	
reaction rate order for	227, 229	
Crystallographic parameters	147	
Cubooctahedron	60	
Cyclopropane		
binary, propane-	381	
on 5A zeolite	382	
hydrogenation	538, 542, 544	
nickel(II) complexes with	488	
over Pt-NaY, Pt-SiO ₂ , and Pt-Al ₂ O ₃	543	
D		
Data, treatment of	617	
Davison 5A sieve	424	
Deactivation	612	
of Pd-H-mordenite catalyst	515	
rate of	52	
Dealumination	81, 598	
Dealuminized mordenite	105	
<i>n</i> -Decane, adsorption of	315	
Decomposition		
of metal carbonyls	144, 149	
of Mo(CO) ₆	150	
of Re ₂ (CO) ₁₀	152	
of Ru ₃ (CO) ₁₂	153	
thermal	145, 153	
Deep-bed zeolites	465	
Degenerate electronic state	117	
Dehydrated Ca ²⁺ ions	554	

- Dehydrated Co²⁺-exchanged zeolite A 551, 554
 Dehydration, effect of 552
 Dehydrator, natural gas 642, 670-673
 Dehydroxylation of hydrogen mordenite 105
 Density variation of adsorbed phases 376
 Desiccant dryers, pressure swing 682
 Dessiccant selection, effect of 693
 Desorption
 of *n*-butane in zeolite NaX 401
 mass transfer fronts 686
 of NH₃ 133
 step efficiency of 690
 of water 133
 Desulfurization unit, CO₂-rich natural gas 645
 Detergency 696
 Detergents, washing effect of 701
 Diameter ratio, effect of length- 689
 Differential heat(s) of adsorption 9, 367, 368
 Diffraction patterns, x-ray 442, 444, 445, 447
 Diffuse reflectance spectra 123, 484
 Diffusion
 of *n*-butane in zeolite NaX 401
 in CaX(Na) pellets 432
 coefficient 189, 435
 effects on the catalytic behavior of Ca, Na-Y-zeolite 616
 in faujasite pellets 428
 of ions in zeolites 439
 of isobutane in LaX(Na) pellets 431
 in large port zeolites 325
 in LaX(Na) pellets 434
 limited regime 620
 in molecular sieves 320
 in NaX pellets 432
 in small port zeolites 323
 studies, counter 331
 time constants 422
 Diffusivity(ies)
 of *n*-butenes in Ca, Na-Y-zeolite 619
 of C₂-C₄ mono-olefins 623
 for *n*-C₇H₁₆ 328
 corrected 322, 326
 limiting 324
 NMR self 326
 tracer 322, 326
 Digestion time on recrystallization, effect of 241
 Dispersion of Ag^o in the mordenite pores 501
 Dispersion of the metal phase 506, 508
 Distortions, axial 114
 Distortions, off-axial 115
 Divalent cations, influence of 357
 Dryers, conventional 682
 Dryers, pressure swing desiccant 682
 Drying, non-regenerative 640
 Drying, pneumatic system air 681
 Dual resistance models 422
- E**
- Earth metal ion exchange 182
 Efficiency 690
 EFR line density 533
 EFR parameters 532
 Electrical charges for oxygen 24, 26
 Electron repulsion 111
 Electronic state, degenerate 117
 Elutions of M-L zeolites 171, 172, 174
 Energy
 spectra of ions in trigonal fields 111
 surfaces 117
 term diagram 113
 Entropy of adsorbed phase, molar integral 374
 Equilibria of gases on zeolites 1
 Equipment changes, refinery 663
 ESR studies 156, 158, 628
 Ethane hydrogenolysis 538, 540, 542
 Ethane recovery, deep 639
 Ethylene
 adsorption 588
 binary systems involving nickel(II) complexes with 488
 polymerization of 626
 on 5A zeolite 382
 zeolitic Co(II)A complexes 484
 Exchange extent 575
 Exchange percentage 612
 Exchangeable cations 428
- F**
- Faujasite(s) 60
n-butenes isomerization near 606
 cerium-exchanged 572
 diffusion in 428
 growth of 244
 isomerization over germanic near 606, 608
 on the isomerization reaction, influence of 611
²³Na-resonance in 53, 61
 sodium ions in 56
 synthesis of 233
 type, effect of 657
 water inside the sodalite units of 335, 341
 Feed hydrotreating on zeolite cracking catalyst, effect of feedstock type and 662
 Formation
 of C₆ isomers 520
 of cracking products 519, 521

- Ion exchange (*continued*)
 reactions, thermodynamic formalism for 179
 in zeolites 179, 182, 184
 formation of zeolite N-A with sodium 248
 localization in hydrated zeolites 189
 in trigonal fields 111
 in zeolites
 aqueous Cu(II) 139, 140
 complex 188
 inter- and intraparticle diffusion of 439
 Ionization cross section 83
 Iron
 clusters in zeolites 291
 complexes 489
 Fe(II)Y 490
 Isobutane in LaX (Na) pellets 431
 Isomerization
 n-butene 555, 576, 578, 606, 610
 cis-2-butene 621
 over germanic near faujasite 608
 n-hexane 504, 515, 519, 522
 influence of the aluminum of the faujasite on the 611
 of n-pentane 504
 products, formation of 521
 to total cracking rate, ratio of total 520
 Isotherm(s)
 adsorption 375
 binary 385
 carbon dioxide 367
 comparison of calculated and measured 700
 constants 313
 statistical thermodynamic 385
 Isotopic exchange, Zn 189
- J**
- Jahn-Teller coupling 117
- K**
- K 27
 K₂O-Al₂O₃-SiO₂-H₂O system, zeolites synthesized in the 30
 K⁺ zeolites 41
 Kaliophilite, Linde F/Linde M/ 37, 38
 K-E/K-A/Kalsilite 39
 Ketjen series, dealuminated 83
 Kinetic(s) 599
 of adsorption of gases on zeolites .. 1
 considerations of zeolite catalyst activity and selectivity 658
 crystallization 225, 708
 data on isomerization of but-1-ene .. 578
- Kinetic(s) (*continued*)
 dependencies of pressure change .. 563
 of the oligomerization 554
 of sorption in biporous molecular sieves 417
 of sorption, desorption, and diffusion 401
 studies, batch compositions used in the 225
 studies of zeolite growth 244
 KL, dealuminated 601
- L**
- L zeolite 166, 168, 596
 Large port zeolites 325
 Lattice parameter data, cubic 51
 LaX (Na) pellets 431, 434
 LaY, sodalite cages of 342
 Length to diameter ratio, effect of 689
 Lewis acid sites 93
 LiA-CaA system 443, 444
 LiA-NaA system 441, 442
 LiA-NH₄A system 443
 LiX-NaX system 443, 445-447
 Li⁺-ions in A-zeolite, arrangement and mobility of 357, 363
 Ligand field model for intrazeolitic transition metal ion complexes 110
 Limiting diffusivity 324
 Linde F/Linde M/kaliophilite 37, 38
 Linde F/Zeolite Z (K-F) 33, 34
 Linde Q/Linde H/Zeolite K-G 37, 38
 Linde W/phillipsite/zeolite K-G 39, 40
 Linde 13X, sodalite cages 338
 Line density, EFR 533
 Lineshape analysis 345
 Line width 359
 Liquid phase 640
 Liquified natural gas (LNG) 639, 641
 Loading level 349
- M**
- Magnetic parameters for cobalt(II) isocyanide complexes 482
 Mass
 balance 690
 transfer limitation, intraparticle 512
 transfer fronts 686
 Matrix effects on yield and selectivity 655
 Melting point of polyethylene 629
 Metal
 carbonyls adsorbed on HY zeolite .. 149
 carbonyls loaded in Y-type zeolite .. 144
 contacting time 525
 crystallite diameter 511
 effects on zeolite cracking catalyst activity and selectivity 658
 phase, dispersion of the 508

Methylisocyanide, cobalt(II) complexes with	480	Mordenite (<i>continued</i>)	
2-Methylpropene	555, 556	transition metal ion exchange in	184
Magnesium	27	Mössbauer spectra	295, 297
Micropore diffusivity	425	Mulliken bond overlap populations	24
Micropores, adsorption in	2	Multicomponent sorption equilibria	379
Microporous adsorbents	10		
Migration effects of cations in zeolites	393	N	
M-L zeolites	169, 170, 171, 174, 176	N-A, zeolite (<i>See</i> Zeolite N-A)	
M(95)-L zeolites	169, 171, 172, 174	Natural gas	638
M-L(650)N zeolites	169, 174, 176	dehydrator	642, 670
M-O bond lengths	27	desulfurization unit, CO ₂ -rich	645
M.O.'s coefficients of	141	liquefaction, peakshaving	641
Mobility of Li ⁺ -ions in A-zeolite	357	liquids dehydrator	672, 673
Mo(CO) ₆	150	liquids recovery system	674
Modification	177	liquified	639
Molar integral entropy of adsorbed phase	374	processing	669
Molar ratio data for zeolite Rho samples	45	sweetening, wellhead	643
Molecular		ND ₃ , Epr spectrum of CuY with	484
diameter, critical	324, 327	Neutralization after induction period, partial	242
orbital calculations	19	Nickel	
sieve(s)		complexes	488
adsorbent applications	637	crystallites	534
diffusion in	320	(I) ions, formation of	281
kinetics of sorption in biporous	417	(II)-loaded Y zeolite, reduction of	281
natural gas dehydrator	642	in reduced NaNiY zeolite catalysts, metallic	528
X and Y	606	reduction, temperature dependence of	532
Molecules		(I) species, reactivity of	288
anisotropically and isotropically rotating	349	surface area	534
influence of adsorbed	357	NiCaNaY zeolite	283, 285
non-rotating	349	NiY, NO absorbed on	490
Monovalent cations	357	Nitric oxide	479
Mono-olefins in zeolites, C ₂ -C ₄	623	absorbed on NiY	490
Mordenite		chromium(II) complexes with	486
acidity of	96	-CO mixture	562, 563
analyses of	260	to cobalt ion, coordination of	487
beryllium	587	copper complexes with	479
caustic treatment of	236	effect of addition of	632
dealuminated	267	iron(II) complexes with	489
dealuminized	105	nickel(II) complexes with	488
gas uptake of NaAgz	496	reduction	559, 561, 566
hydrogen		Nitrogen, sorption of	268, 269
(<i>see</i> Hydrogen mordenite)		Nitrosyl complexes in zeolites	481
hydronium	97, 101	Nitrous oxide	123, 125, 128, 488
hydroxyl, stretching band of	587	Nonbonding repulsion, geminal	26
ion exchange equilibria in	187	Non-rotating molecules	349
-like zeolites	584	Nuclear magnetic resonance	54, 326, 329, 335, 344
of NH ₄ ⁺	102, 103	Nucleation	
pores, dispersion of Ag ⁺ in	501	activation energies for	209
reactions of SiH ₄ with	261	energies	226
silanation of	259	reaction rate order for	229
silver	493		
small-port Na ⁺	349	O	
sodium	97, 349	OD-region CO physisorption	498
sorption site	344	Off-axial distortions	115
synthetic	367		

- Offretites 24, 27
 OH groups (*See* Hydroxyl)
 Olefin separation 648
 Olefins, cobalt (II) complexes with 483
 Oligomerization activity,
 2-methylpropene 556
 Oligomerization, kinetics of 554
 Optical spectroscopy of Cu(II)-
 exchanged zeolites 132
 Orders of specific activity for C₃H₆
 hydrogenation 545
 Organic molecules adsorption 89, 92
 Osmotic theory of adsorption 2, 7
 Oxidizabilities 117
 Oxidized samples 282
 Oxygen (O₂)
 adsorption 158, 487
 from air 648
 Ce-exchanged zeolites reactivated
 in 582
 chromium(II) complexes with 485
 Cr₁(II)-A interaction with 125
 effect of addition of 633
 electrical charge for 24, 26
 sorption at 269
 uptake, stoichiometry of 495
- P**
- Palladium
 content of H-mordenite 519
 Pd-H-mordenite catalyst 515, 525
 Paraffin separation, normal/iso 647
n-Paraffins on zeolite, adsorption
 equilibrium of 313
 Particulates, pseudomorphic zeolite 216
 Peakshaving natural gas liquefaction .. 641
 Performance for two-bed geometric,
 maximum 692
n-Pentane, isomerization of 504
 pH, washing performance of SASIL
 as a function of 706
 Phase transformation, metastable 222, 224
 Phosphates, precipitation of
 insoluble 704
 Phillipsite(s)
 Na, K- 219
 nucleation and crystallization 227
 silica-alumina ratios of synthetic 225
 synthesis runs producing pure 223
 thermal stability of 229
 uptake of potassium by 224
 /zeolite K-G, Linde W/ 39, 40
 Piperidine, conversion of
 tetrahydropyran 576, 598, 600
 Platinum catalysts supported on
 zeolite 538
 Pt-Al₂O₃ 543
 Pt-NaY 543
- Pt-NH₄Y 544
 Pt-SiO₂ 543
 Pneumatic system air drying 681
 Polyethylene 628-630, 632
 Population parameters 20
 Potassium by phillipsite, uptake of 224
 Potentials, redox 112
 Precipitation of insoluble phosphates 704
 Pre-exponential factors for cracking
 and isomerization of *n*-hexane 522
 Pressure
 change of NO-CO mixture on
 reaction time 562, 563
 dependence of reaction rate on
 partial 600, 603
 drop 690
 effects on cis-2-butene
 isomerization 621
 swing desiccants dryers 682
 swing theory 685
 Pretreatment 617
 Probe molecules for migration effects
 of cations 393
 Products, rate of deactivation for
 formation of 521
 Product ratios 609
 Propane
 on 5A zeolite 382
 -cyclopropane binary 381
 hydrogenolysis of 542
 treater 671, 676
 Propylene 639
 nickel (II) 488
 zeolitic Co(II)A complexes 484
 Proton
 -catalyzed reactions 463
 free induction decay of water 341
 mobility 462
 Pseudomorphic zeolite particulates 207
 Ptilolites 24, 27
 "PURASIV" systems 646
 Purge
 flowrate 691, 692
 percentage inlet air used 692
 volume 691
 Purification 638
 Pyridine
 adsorption
 of bases 586
 1-butene isomerization, effect of .. 555
 on dealuminated KL 601
 complexes, copper (II) amine 478
 effect of adsorbed 554
- Q**
- Quadrupole
 coupling constants 56
 effects 54
 interaction of the second order 57

R			
Range		Ring conversion of tetrahydropyran into piperidine 596, 598	
initial	369	Rotating molecules, anisotropically and isotropically 349	
maximum	369	Ru ₃ (CO) ₁₂ 153	
terminal	369	S	
Rate constants		SASIL, washing performance of 702, 706	
apparent reaction	535	Scrubbing of the regeneration gas, amine	645
Arrhenius plot of	502	Selectivity	600
log relation between exchange percentage and	612	of bifunctional catalysts	508
for phillipsite nucleation and crystallization	227	of cis-2-butene isomerization	621
relative	609	of composite catalysts of for the conversion of <i>n</i> -hexane over bifunctional catalysts	655
for the self-diffusion of Zn	189	effect of feedstock type and feed hydrotreating on zeolite cracking catalyst	507
Reaction conditions on yield and melting point, effect of	629	influence of the structure para- meters of the catalysts on	662
Reaction rate		kinetic considerations of zeolite catalyst	504
constants	535	matrix effects on	658
order for nucleation and crystallization	227, 229	metals and coke effects on zeolite cracking catalyst	655
on partial pressure, dependence of	600, 603	products at different temperatures ..	658
Reactivity of Ni(I) species	288	ratios, temperature dependency of ..	609
Reactor	617	testing of cracking catalysts	622
Recoil studies	166, 169	Self-diffusion, rate constants for	654
Recovery system, natural gas liquids ..	674	Separation, olefin	189
Recrystallization		Separation, xylene	648
of clinoptilolites	237, 239-241	Severity effects	648
effect of chloride on	241	Sieve, Davison 5A	660, 661
of high-silica zeolite	233	Sieve, molecular (See Molecular sieve)	424
Redox		Silanation of mordenite	259
behavior, kinetic study of the	499	Silanation of zeolites	258, 259
chemistry of divalent chromium ion-exchanged zeolite A	120	Silica	
potentials	112	-alumina ratio(s)	256, 575, 656
reactions, stoichiometry of the	497	formation of zeolite N-A with different	250
Reduced samples	282	products with different	248
Reduction		of synthetic phillipsites	225
of Co ²⁺ -exchanged A-zeolite	551	electrons in the zeolites, energies of ..	77
of Na Ag 2-94	498, 502	materials, caustic treatment of	236
of nickel	532	zeolites, recrystallization of high- ..	233
of nickel(II)-loaded Y zeolite	281	Silicon	
of silver-mordenites	493	zeolites	88
temperature of	533, 535	Si _{2p} and Al _{2s} binding energies	79
Refinery operational and equipment changes	663	SiH ₄	261, 265
Reflective visible measurement	628	SiK _β	67, 69
Regeneration gas, amine scrubbing of the	645	Silver	
Regeneration gas treater	672, 678	-mordenites	493
Rehydration, effect of	552	ions, reduction of	502
Relative rate constants	609	in mordenite pores, dispersion of ...	501
Reoxidation of silver-mordenites ...	493, 498	Single resistance models	422
Repulsion, electron	111	Site(s)	
Repulsion, geminal nonbonding	26	accessibility of	463
Re ₂ (CO) ₁₀	152	occupancies by cations in zeolite L ..	168
Rho, zeolite	43, 45, 51		
Rhodium complexes in zeolites, bivalent	156		

- Site(s) (*continued*)
 occupation in calcium-exchanged
 Y zeolites 396
 Size distribution of platinum particles 541
 Small port zeolites 323, 349
 Sodalite cages 335, 338, 341, 342
 Sodium 27
 aluminate solutions, batches from 250
 -aluminum-silicates in the washing
 process 696
 aluminosilicate gel 253
 ions, formation of zeolite N-A from
 batches with 248
 ions in zeolites of the faujasite type
 mordenite 56
 small-port 349
 zeolites 260
 NaAg 2-75 and NaAg 2-85, reduc-
 tion of Ag ions in 502
 NaAg 2-84, hydrogen uptake of 500
 NaAg 2-94, reduction and
 reoxidation of 498
 NaAgz mordenite, gas uptake of 496
 NaCaA 326, 313
 Na,K-phillipsites 219
 NaLiA 360, 364
 NaLiMe₂A 360, 364
 NaMgA, adsorption on 315, 316
 NaNiY zeolite catalysts, reduced 528
 NaX, zeolite (*See* Zeolite NaX)
 NaY zeolites 186, 396
²³Na-resonance of faujasite 53, 61
 Solids content as a function of time 199
 Sorbate concentrate 425
 Sorption 320
 in biporous molecular sieves 417
 of *n*-butane 401
 of C₃H₈-C₂H₆ in 5A zeolite 387
 chamber, constant volume 431
 curves 425
 data 329
 equilibria of hydrocarbon gases,
 multicomponent 379
 of nitrogen 268, 269
 of oxygen 269
 sites, mordenite 344
 studies 330
 Sorptive properties of ion-exchanged
 forms of zeolite Rho 45
 Sour gas regeneration 677, 679
 Specific activity for C₃H₈ hydro-
 genation 545
 Specific heat of adsorbed phase 374
 Spectra, computer simulation of the
 measured 53
 Spectral measurements 134
 Spectrometer calibration 79
 Spectroscopic studies of mordenite-
 like zeolites, infrared 584
 Spectroscopic parameters for com-
 plexes in zeolites 476, 481
 Spin-orbit coupling 114, 116, 141
 Stability, thermal 229, 601
 Stabilization energies 112, 117
 Statistical
 isotherm, modified 385
 -thermodynamic approach 309
 thermodynamic isotherm 385
 Steady-state, operation at 710
 Steam-methane reforming for
 ammonia synthesis 644
 Stoichiometry of hydrogen and
 oxygen uptake 495
 Stoichiometry of the redox reactions 497
 Stretching bands of various
 mordenites, OH 587
 Structural parameters of the metallic
 phase 510
 Structure 17
 ALK₃ shifts with 72
 parameters of the catalysts 504, 505
 Sulfur compounds 643
 Sulfur dioxide adsorption 214
 Supercage OH groups 613
 Supercage sizes 291
 Superficial acidity 86
 Superficial composition 86, 88, 90
 Surface(s)
 area, specific nickel 534
 area of zeolite A crystals, external 715
 composition by X.P.S., zeolite 76
 contour, rough 78
 energy 117
 of zeolites, analysis of the 80
 Synthesis 177
 of polyethylene 628
 of pseudomorphous zeolite
 particulates 207
 runs producing pure phillipsite 223
 solids content during 199
 Szilard-Chalmers cation recoil studies
 in zeolite L 166
- T**
- T-O bond lengths 24, 25
 Technology 635
 Temperature(s)
 dependence 619
 of adsorption capacity 229
 of apparent reaction rate
 constants 535
 of crystallite size and F-value on 533
 of degree of nickel reduction 532
 of EFR parameters 532
 of Henry's Law constants 383
 of selectivity ratios 622
 effect of 370, 579, 599, 691

- Zeolite A (*continued*)
- particulates, pseudomorphic 210
 - self-diffusion of Zn in 189
 - synthesis mechanism 194
 - transition metal ion exchange 184
 - 4A, anhydrous CoC(II)-exchanged 484
 - 5A
 - diffusivities for $n\text{-C}_7\text{H}_{16}$ in 328
 - multicomponent sorption equilibria of hydrocarbon gases in 379
 - propane, cyclopropane, and ethylene on 382
 - sieve, Davison 424
 - sorption of $\text{C}_3\text{H}_8\text{-C}^2\text{H}_4$ in 387
 - acidic and catalytic properties of 453
 - acidity 453
 - of transition metal 460
 - adsorption of gases on 1
 - aluminum-deficient, deep-bed, or ultra-stable 465
 - B particulates, pseudomorphic 211
 - bivalent rhodium complexes formed in 156
 - Ca-A 553
 - CaNaY 395
 - cis-2-butene isomerization over 621
 - diffusion effects on the catalytic behavior of 616
 - effective diffusivities of n -butenes in 619
 - catalyst activity and selectivity, kinetic considerations of 658
 - cationic forms of 562
 - CaY 396
 - cerium-exchanged 572, 578, 581, 582
 - chemical shifts in 64
 - chromium-exchanged 123, 626
 - Co(II)A 487
 - complex ions in 188
 - concentration on the activity and selectivity of composite catalysts, effects of 655
 - containing transition elements 559
 - copper amine complexes in 476
 - cracking activity of 660
 - cracking catalyst(s) 650
 - activity and selectivity 622, 658
 - with different supercage sizes 291
 - diffusivities of $\text{C}_2\text{-C}_4$ mono-olefins in 623
 - energies of the Al and Si electrons in the 77
 - of the faujasite type 53, 56, 244
 - germanium 88
 - H- 264
 - high-silica 233
 - HS particulates, pseudomorphic 211
 - HY 86, 149
 - hydrated 135, 189
 - hydrogenation of cyclopropane 538
 - hydroxyl groups 459
 - inter- and intraparticle diffusion of ions in 439
 - ion exchange in 179
 - ion localization in 189
 - IR spectra of 580
 - other K⁺ 41
 - K-G 37-40
 - L 166, 168
 - large port 325
 - M-L 169, 171, 172
 - M(95)-L 171, 172, 174
 - M-L(650)N 174, 176
 - migration effects of cations in 393
 - modified 267
 - molded 13
 - mordenite-like 584
 - N-A
 - crystallization curves for 255
 - formation
 - from batches with sodium ions 248, 250
 - with different Si/Al ratios 250
 - from TMA-silicate and sodium aluminosilicate gel 253
 - influence of TMA/Na on the amount of 248
 - kinetic studies of the growth of 244
 - Na-
 - NaCaA 313, 326
 - NaMgA 315, 316
 - NaNiY 528
 - NaX
 - adsorption of n -decane and *trans*-butene-2 on 315
 - adsorption isotherm of Xe on 9
 - differential heat of adsorption of Xe on 9
 - ion exchange isotherm for Cu in 186
 - pellets, diffusion results in 432, 435
 - sorption, desorption, and diffusion of n -butane in 401
 - system, LiA- 446, 447
 - system, LiX- 445
 - NH₄ 93
 - NiCaNaY 283, 285
 - nitrosyl complexes in 481
 - particulates, pseudomorphic 207, 216
 - partially hydrated 135
 - Rho 43, 45
 - samples, analytical data of the 359
 - silanation of 258
 - silicon 88
 - small port 323
 - structure parameters 505
 - surface analysis of 80

Zeolite(s) (<i>continued</i>)			
surface composition by X.P.S.	76		
synthesized in the $K_2O-Al_2O_3-SiO_2-H_2O$ system	30		
tetrahedral frameworks of	19		
thermochemical treatments of	70		
thermodynamics of adsorption on ..	305		
transition			
elements in	567		
metal complexes in	466, 473		
metal ions in	108		
X	611		
alkali and alkaline earth metal			
ion exchange in	182		
aqueous Cu(II) ions in	139, 140		
<i>n</i> -butenes isomerization over			
protonated germanic near	606		
Cu(II)-exchanged	132		
transition metal ion exchange in ..	184		
13X, diffusivities for <i>n</i> - C_7H_{16} in	328		
		Y	611
		alkali and alkaline earth metal	
		ion exchange in	182
		ammonium-exchanged	271
		aqueous Cu(II) ions in	139, 140
		<i>n</i> -butenes isomerization over	
		protonated germanic near	606
		calcium-exchanged	396
		Cu(II)-exchanged	132
		metal carbonyls loaded in	144
		nickel (II)-loaded	281
		reactions with	262, 263
		silated	259, 269
		transition metal ion exchange	184
		Z	33, 34
		Zeolitic Co(II)A complexes	484
		Zinc isotopic exchange, kinetic data	
		for	189
		Zinc in zeolite A, self-diffusion of	189